PROCEEDINGS OF

14th Biennial International Symposium

on

ANTENNAS AND PROPAGATION

17-19 December, 2014

APSYM 2014
Dec. 17 - 19

DEPARTMENT OF ELECTRONICS
Cochin University of Science and Technology
Kochi – 682 022

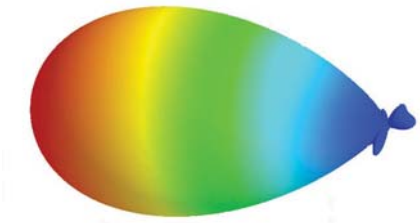

Co-sponsored by:

IEEE APS Kerala Chapter
IEEE Student Branch, Cochin
University Grants Commission
Indian National Science Academy
All India Council for Technical Education
Department of Atomic Energy (Govt. of India)
Department of Science & Technology (Govt. of India)
Council of Scientific and Industrial Research (Govt. of India)
Kerala State Council for Science Technology and Environment (Govt. of Kerala)
GE- General Electric Company, Bangalore
CST- Computer Simulation Technology
Entuple Technologies Pvt Ltd
Keysight Techologies Inc.

ISBN: 978-93-80098-60-8

Published by the Directorate of Public Relations and Publications, Cochin University of Science & Technology, for Department of Electronics,
Cochin 682 022, INDIA

December 2014

Proceedings of APSYM 2014

Organised by

Department of Electronics
Cochin University of Science and Technology
Kochi, India
Phone: 91 484 2576418
Fax : 91 484 2575800
URL : www.doe.cusat.edu

Editors

Prof. K.G. Nair
Prof. K. Vasudevan
Prof. C.K. Aanandan
Prof. P. Mohanan

Co-sponsored by

IEEE APS Kerala Chapter
IEEE Student Branch, Cochin
University Grants Commission
Indian National Science Academy
All India Council for Technical Education
Department of Atomic Energy (Govt. of India)
Department of Science & Technology (Govt. of India)
Council of Scientific and Industrial Research (Govt. of India)
Kerala State Council for Science Technology and Environment (Govt. of Kerala)
GE - General Electric Company, Bangalore
CST- Computer Simulation Technology
Entuple Technologies Pvt Ltd
Keysight Techologies Inc.

Copyright © 2014, CREMA, Department of Electronics, Cochin University of Science and Technology, Kochi, India.

All rights reserved. No part of this publication may be reproduced, stored in a retrieval system or transmitted in any form or by any means, electronic, mechanical, photocopying and recording or otherwise without the prior permission of the publisher.

This book has been published from Camera ready copy/softcopy provided by the contributors.

INCLUDE INDEX

ISBN: 978-93-80098-60-8

Published by the Directorate of Public Relations and Publications for CREMA, Department of Electronics, Cochin University of Science & Technology, Cochin 682 022, INDIA and printed at Print Express, Cochin, INDIA.

CHAIRMAN WELCOMES YOU

Dear friend,

We are happy to note that you are visiting Cochin, the vibrant city in the beautiful state of Kerala, India to attend APSYM 2014, the Antennas and propagation Symposium, 2014. We, the members of the organizing committee of APSYM- 2014, are looking forward to meet you soon.

"APSYM-2014" is the 14th Symposium in the series, which we started in 1988. In spite of demands from many corners to organize the Symposium in some City Hotels in Cochin, we decided to have it in our University Campus because of two reasons. Mainly, the distinguished visitors from various parts of the world will see our University along with our antenna laboratory which we built with utmost care and hopes. Secondly our research students and faculty members get ample opportunities to interact with the visiting intellectuals and experts. These expectations came true in many occasions in the past. We are thankful to all great personalities, who contributed in this regard.

Over 106 papers are scheduled to be presented during APSYM in 2014. The organizing committee have planned an excellent technical programme with a number of invited talks by great Scientists, Engineers in this field.

Proceedings of the earlier Symposia are available with organizers of APSYM-2014. Those who want to purchase copies may please contact them.

Wish you all a warm welcome once again and hoping very interesting discussions.

Cochin
November 28, 2014

Prof.K.G.Nair

OUR TRIBUTE TO GREAT PIONEERS

JAMES CLERK MAXWELL

Developed electromagnetic theory of radiation by his mathematical magic. His theoretical prediction of the existence of electric and magnetic fields associated with wave propagation carrying energy of electromagnetic nature was a breakthrough in the history of science. A new era of electromagnetism was thus opened by this great scientist.

HEINRICH HERTZ

Experimentally demonstrated the generation, propagation and detection of electromagnetic waves. Thus he gave a firm experimental support for the theoretical conclusions drawn by James Clerk Maxwell.

JAGADISH CHANDRA BOSE

The first Indian scientist who marked his footprints in the world of electromagnetics. In fact, Bose generated millimeter waves using a circuit developed in his laboratory and used these waves for communication, much earlier than the western scientists. He also developed microwave horn antennas which are still employed in many communication applications.

ORGANISING COMMITTEE

Chairman	**Prof. K.G. Nair** Emeritus Professor
Vice-Chairman	**Prof. K. Vasudevan** Emeritus Professor
Director	**Prof. C.K. Aanandan** Professor & Head
Technical Programme	**Prof. P. Mohanan**
Registration	**Prof. P.R.S.Pillai** **Assoc. Prof. James Kurien**
Accommodation	**Prof. Tessamma Thomas** **Assoc. Prof. Supriya. M. H**

Members

Mr. Aji George	Mrs. Roshna T K
Mrs. Anila P V	Mrs. Sajitha V R
Mrs Anitha R	Mrs. Sarah Jacob
Mr. Deepak U	Mr. Satheesh Chandran
Ms. Dibin Mary George	Mrs. Sabna N
Mr. Dinesh R	Mr. Shameer Mohammed
Mr. Jayakrishnan M P	Mr. Suraj Kamal
Mrs. Libi Mol V A	Ms. Sreekala P S
Mr. Lindo A O	Mr. Sujith Kumar S Pai
Mr. Mohan Kumar	Mrs. Sumitha Mathew
Mrs. Nayana	Mrs. Revathi
Mr. Neeraj Puskaran	Ms. Theresa Bernard
Mr. Nijas C M	Mr. Ullas G Kalappura
Mr. Prakash K C	Mr. Vinesh P V
Mr. Prasanth P P	Mr. Vivek R Kurup

Board of Referees

Prof. K G Nair	Dr.Thomaskutty Mathew	Dr. P Abdulla
Prof. Ramesh Garg	Dr. Mythili Palayyan	Dr. Shameena V.A
Prof. K T Mathew	Dr. Suma M N	Dr. Deepthi Das Krishna
Prof. K.J. Vinoy	Dr. Sarin V.P	Dr. Sujith R
Dr. P. Muralikrishna	Dr. Gopikrishna	Dr. Gijo Augustine
Dr. Raveendranath U Nair	Dr. Sreejith M Nair	Dr. Manoj Joseph
Dr. S Mridula	Dr. Rohit K Raj	Dr. Nisha Nassar
Dr. Binu Paul	Dr. Anupam ramachandran	Dr. Deepu V

MILESTONES IN THE HISTORY OF ELECTROMAGNETICS

1747	Benjamin Franklin	Types of Electricity
1773	Henri Cavendish	Inverse square law
1785	Coulomb	Law of electric force
1813	Gauss	Divergence theorem
1820	Ampere	Ampere's experiment
1826	Ohm	Ohm's law
1831	Faraday	Electromagnetic Induction
1837	Morse	Telegraphy
1855	Sir William Thomson	Transmission lines theory
1864	Lord Rayleigh	Theory of Sound Propagation
1865	James Clerk Maxwell	Electromagnetic field equations
1873	James Clerk Maxwell	Unified theory of Electricity and Magnetism
1876	Graham Bell & Gray	Telephone
1883	Thomas Alva Edison	Electron Emission from Heated Filament
1885	Heinrich Hertz	Electromagnetic Wave Propagation
1887	Heinrich Hertz	Spark plug experiment
1888	Heinrich Hertz	Half-wave dipole antenna
1890	Ernst Lecher	Lecher wire
1893	Heinrich Hertz	Spark Gap Generator
1893	Thomson	Waveguide theory
1894	Marconi	Wireless Telegraphy
1895	Jagadish Chandra Bose	5-6 mm wavelength Signal Transmission
1897	Lord Rayleigh	Boundary values and modes in Metallic cylinders
	Jagadish Chandra Bose	Horn antenna and Millimeter wave Source
1898	Lodge	Tuned Transmitters and Receivers
1900	Marconi	TransAtlantic Communication
1902	Weber	Propagation in Hollow Tube1902
	Fleming	Vacuum Tube
1903	Hulsmeyer	Radar
1906	Fessenden	Rotating Alternator and audio modulation
	Thomas et.al	Crystal Detector
	Fessenden	Radio broadcasting
	Dunwoody	Crystal detectors
1907	DeFroest	Triode
1912	Eccles	Ionospheric propagation
1914	AT & T	170 kHz Radio
1915	Carson	Single side-band transmission
1918	Watson	Ground wave propagation
1919	Southworth	Lecher line circuit
	Heinrich Barkhausen & Kurz	Triode electron tube at 1.5 GHz
1920	Hull	Magnetron
	Yagi and Uda	Yagi-Uda antenna
1921	HuII	Smooth bore Magnetron
1922	Affel	Directional Coupler
	Brillouin	Acoustooptic Effect
1923	HH Beverage	Beverage antenna
1925	Van Boetzelean	Short wave Radio
	Appleton	Ionospheric layer
1927	Okabe	Split-anode Magnetron
1929	Clavier	Microwave Communication
1930	Hansen	Resonant cavity
	Karl G Jansky	Bruce Curtain antenna
	Barrow L	Waveguides
1931	Marconi	600 MHz radio link in Italy
	Andre G Clavier	Microwave Radio transmission across English Channel
1932	Southworth	Circular Waveguide
	Marconi	57 cm Radio telephone and teleprinter service
	Claud Cleton	Microwave spectroscopy
1933	Barrow	Circular Wavegiude Propagation
	Armstrong	Frequency modulation
1934	Schelkunoff	TE01 mode in Circular Waveguide
	Watson-Watt	Experimental Radar Station
1935	Oscar Heil	Velocity modulation
	Watson watt	RADAR
1936	Southworth and Barrow	Microwave propagation in Circular Waveguide
	G. H. Brown	Turnstile antenna
1937	Varian Brothers	Klystron
	Janskey	Radio Astronomy
	Manson	Waveguide Filter
	Russel & Varian Bros	Klystron
	A, H. Boot , J T. Randall	
	M. L. Oliphant	Magnetron
	Pollard Radar aiming	anti-aircraft guns
1938	J. D. Kraus	Corner reflector
1939	Barrow	Magic Tee
	Peterson et.al	Diode Mixer
1939	P. H. Smith	Smith impedance

1940	Hansen	Leakywave Antenna
	Quakenbush	UHF coaxial Connector
	Bowen, Dummer et al	P P I Scope
1942	Wheeler	Stripline Technology
	Neill	N-type connector
1943	AT&T	4.5 GHz Multichannel PPM digitally modulated microwave Radio
1944	Meyers et.al	Reflectometers
1945	Kompfner	TWT
1946	Clarke	Forecasts geosynchrous Satellite
	J. D. Kraus	Helical antenna
	Percy Spencer	Microwave oven
1947	AT &T	3.7-4.2 LOS link
1948	Van der Ziel	Non-linear capacitors
1950	C. L. Dolph	Dolph-Tchebyscheff array
1953	Townes	Ammonia Maser
	Deschamps	Microstrip antenna
1954	Towns	Maser
1955	Page	Monopulse Radar
1956	Esaki	Tunnel Diode
	Bloembergen	Three level Maser
1957	Kroemer	Hetrojunction Transistor
	Bakanowski et.al	Varactor
	Hines et.al	Parametric Amplifier
	V. H. Rumsey	Frequency independent antenna
	Weiss	Parametric amplifier
1958	Bloembergen	Solid state Maser
	John D Dyson	Spiral antenna
	Read	Read diode
		Space Communication
	Maiman	Ruby Laser
1959	D. Wigst Isbell	Log periodic antenna
1968	Victor Veselago	Predicted DNG Materials
1969	Wen	Coplanar Line
1970	Silvester	FEM
	Byron	Microstrip array
1971	Itoh and Mittra	Wave Analysis of Microstrip
1975	Bekati	Relativistic cavity Magnetron
1980	Mimura	HEMT
1986	Didenko et. al.	Advance relativistic Magnetron
1988	S. K. Khamas	High Tc Super conducting dipole
1992	Victor Trip, Johnson wang	Paste-on Antenna
1993	Te-Kao Wu et.al	Multiple Diachronic Surface Cassegrain Reflector
1996	Clorfeine & Delohh	TRAPATT diode
1996	John W Mc Carkle	Microstrip DC to GHz Field Stacking Balun
2002	George V Eleftheriades	Planar Negative LC loaded Refractive media
2004	Thomas Purr et.al	Miniaturized Directional Antenna
2006	John C Mather & George F Smoot	Microwave Back ground 2006 (CMB) Cosmic Microwave Background Radiation
2008	Queens University, Belfast	Skin-tenna
2010	Michael Strano, Jae-Hee Han, and Geraldine Paulus	Solar Funnel Antenna
	SPAWAR System Center Pacific	Sea water antenna
2011	Gaeta et.al	Slit time lenses
2012	Duke University	Better invisibility cloak
2014	Universiti Teknologi Malaysia	smart fluorescent antenna

CONTENTS

Session	Title	Page
I	Microstrip antennas 1	13
II	Microwave Devices 1	39
III	Biomedical Applications	55
IV	Antenna Arrays	77
V	Microwave Devices 2	129
VI	Computer Aided Design and Communications	155
VII	Microstrip Antennas -2	181
VIII	UWB Antennas	221
IX	Antennas	253
X	RFID and FSS	299
XI	Microwave Devices 3	335
XII	Microstrip Antennas 3	383
XIII	Invited Talks	431
XIV	Author Index	441

RESEARCH SESSION 1

MICROSTRIP ANTENNAS I

03.00PM TO 04.00PM
RESEARCH SESSION 1
MIRCOSTRIP ANTENNAS 1
J C BOSE - HALL

Chair: Prof. Satish Sharma, San Diego State University, USA.

No	Paper	Page
1.1	**Distributed Reactive Nearfield Parasitic Element Based Compact CPW Fed Antenna for Nearfield Sensor Applications** Sujith Raman, Robin Augustine, Anders Rydberg Microwave Group, Dept of Engineering Sciences, Angstrom Laboratory, Uppsala University, Uppsala, Sweden. *E-mail:- Sujith.Raman.1983@ieee.org*	15
1.2	**Beam Switching Antenna at 2.45 GHz for Wireless Body Area Network Application** Anupam R Chandran, Senan Morrison, Ruifeng Zhang, Nick Timmons & Jim Morrison. WiSAR Lab, Letterkenny Institute of Technology, Letterkenny, Ireland. *E-mail: Anupam.Ramachandran@lyit.ie*	20
1.3	**Compact single shorted hexagonal microstrip patch antenna** K. P. Ray[1], Suchitra Majumdar[2], S. S Kakatkar[1], R.G Karandikar[2]. [1]SAMEER, IIT Campus, Powai, Mumbai - 400076, India. [2]K.J Somaiya COE, Vidyavihar, Mumbai - 400077, India. *E-mail: kpray@rediffmail.com*	24
1.4	**Broadband offset CPW-Fed Square Slot Antenna** Amit A. Deshmukh[1], Ameya A. Kadam[1], Sudesh Agrawal[1] and K. P. Ray[2] [1]D. J. Sanghavi College of Engineering, Vile Parle, Mumbai – 400056. *Email: amitdeshmukh76@rediffmail.com* *[2]RFMS Division, SAMEER, IIT Campus, Mumbai-400076*	28
1.5	**Design, Fabrication and Performance Analysis of Microstrip Antenna with MIMO Implementation.** Mohammad Ameen[1], Mohammed Ismail. H[2] Communication Engineering, KMEA Engg College, Kerala, India. *E-mail:[1]*mohammadmn61@gmail.com, *[2]ismail@kmeacollege.ac.in*	32

DISTRIBUTED REACTIVE NEARFIELD PARASITIC ELEMENT BASED COMPACT CPW FED ANTENNA FOR NEARFIELD SENSOR APPLICATIONS

Sujith Raman, Robin Augustine, Anders Rydberg

Microwave Group, Solid State Electronics, Dept of Engineering Sciences, Angstrom Laboratory, Uppsala University, Uppsala, Sweden. Email:- Sujith.Raman.1983@ieee.org

Abstract— *An Electrically Small metamaterial inspired antenna with narrow bandwidth suitable for nearfield sensor application is presented. The operation principle is based on a Distributed Reactive Nearfield Parasitic Element (DRNPE). The DRNPE unit cell with high distributed inductive reactance is introduced near a highly capacitive open ended CPW transmission line, resulting in good impedance matching. The resonant behavior is independent of the transmission line parameters and hence can be tuned with respect to the DRNPE parameters. The prototype used as a sensor for the measurement of dielectric constant variation is also discussed. The simulation (Ansoft HFSS) and measurement (HP8510C Vector Network Analyzer) results are in good agreement.*

I. INTRODUCTION

Nowadays the developments of electrically small antennas have attracted researchers and scientists due to their vast application in wireless industry. A large impedance transformation will be required to match electrically small antennas to a typical 50Ω system, because of their very small radiation resistance and very large capacitive reactance. A compensating element with large inductive reactance and radiation resistance can mitigate this to provide good impedance matching.

There have been wide varieties of recent approaches to achieve electrically small antennas. Ziolkowski have been overcome this problem on small electric dipoles [1] by placing Epsilon Negative(ENG) materials and by designing antennas for VHF and UHF applications [2] These also include the usage of space filling (Meandering signal strip) antennas [3], fractal based antennas [4] and Geometrically modified antennas [5].

Introduction of capacitive or inductive elements both lumped and integral in and around the radiating structure is also used to generate electrically small antennas [6]. That is the usage of inductors and capacitors as a matching circuit to achieve resistive matching is the common design options available. Metamaterials based or Metamaterial inspired antennas are other important techniques widely used to develop electrically small antennas [7-8].

But the exploration of electrically small antennas on planar structures especially on coplanar waveguide structures is found to be very useful for wireless and Integrated Circuit(IC) industry. Coplanar waveguide based structures (Transmission lines, antennas, filters etc.) have received great attention in recent years due to their ease of integration with Monolithic Microwave Integrated Circuits(MMIC), wide bandwidth, flexibility towards multiband operation, low radiation leakage, less dispersion etc. Studies on Coplanar Waveguide Transmission line by introducing metamaterial structures to convert them to filters [9], suitable for MMIC [10] and for antennas [11] have been carried out by researchers, but these are achieved either by modifying the signal strip or ground plane of CPW. A temperature sensor showing a corresponding frequency shift with respect to temperature is presented [12] based on a resonant antenna and a dielectric resonator. But antenna itself acting as a sensor is the area to be explored. In this paper an electrically small metamaterial inspired element is used to find the change in resonant frequency with respect to the dielectric constant of medium. It is found that the impedance matching at the resonant frequency of this resonant antenna is stable, and hence is suitable for nearfield applications.

The investigation of the developed novel antenna, depicted here, clearly explains the conversion of high impedance open ended CPW-Fed transmission line into a resonant antenna. A Distributed Reactive Nearfield Parasitic Element (DRNPE) is used to reduce the effective electrical length of the resonator. The total size reduction of 94% is obtained as compared to a normal Coplanar Waveguide fed monopole antenna. This sensor is found to be successful in recognizing the variation in dielectric constant from air (1) to water (80) without much change in impedance matching. Moreover only two DRNPE parameters are governing the resonant frequency and hence providing a significant degree of freedom to the designers.

II. GEOMETRY OF ANTENNA

The geometry consists of an open ended CPW transmission line (figure 1(a)) etched on one side of the substrate with signal strip width S_W and lateral ground plane dimension Lg x Wg = $0.05\lambda_0$ x $0.05\lambda_0$ mm^2, where λ_0 is the free space wavelength corresponding to the resonant frequency. The signal strip width (W) and gap (g) are chosen for 50Ω impedance. DRNPE; a vertically meandered metallic structure is on other side of the same substrate as shown in (figure1 (b)). The width of the element (W_s) is constant throughout the structure. The prototype fabricated for 1GHz on a substrate of dielectric constant 4.4 and thickness 1.6mm has an overall dimension of $0.05\lambda_0$ x $0.12\lambda_0$ x $0.005\lambda_0$ = 34x15x1.6 mm3. The side view of antenna is shown in figure 1(c).

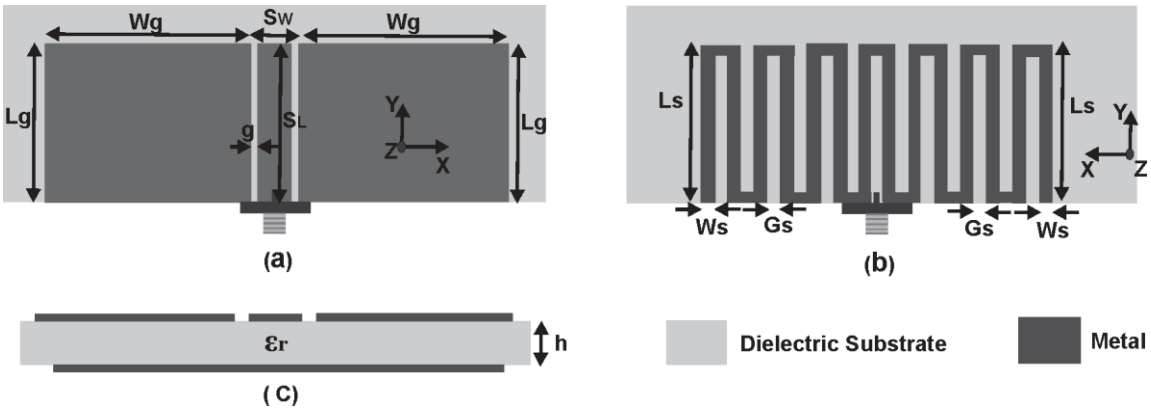

Figure.1 Geometry of Antenna a) Front view b) Back view (DRNPE) c) Side view
(Wg= 15mm, Lg=15mm, S_W=3mm, S_L=Ls=15mm, g=0.35mm, W_S=1mm, G_S=1mm , h=1.6mm and ϵ_r=4.4)

III. RESULTS AND DISCUSSIONS

At the resonant frequency of any antennas the real part of impedance is equal to 50Ω and imaginary part is nearly zero. The reflection coefficient of a normal open ended CPW-Fed transmission line is 0dB as shown in figure 2. This is because of the high reflection at the open circuited end of the transmission line. Thus an open ended CPW transmission line is an inefficient radiator at frequency ranges 1-10GHz. The high capacitive reactance and small radiation resistance creates a large impedance mismatch. Thus it is a challenging task for the antenna designers to convert this in to an efficient radiator. By adding the DRNPE forces the structures total reactance to nearly zero by introducing a large distributed inductive reactance to compensate the very large capacitive reactance of the open ended CPW. Moreover it forces the input resistance of the resonant system to nearly 50Ω. The reflection characteristics of the open ended CPW, with and without DRNPE shown in figure 2 indicates that the prototype has a reflection coefficient at lower frequency regions with DRNPE. The real and imaginary part of impedance with DRNPE is also shown in figure.2. Thus DRNPE is therefore exploited in order to compensate the capacitive imaginary part of the input impedance and match it to 50Ω. DRNPE is a different approach; it is parasitic element contributing to the resonance and makes the antenna electrically small and is easily matched to the source without using any external matching elements

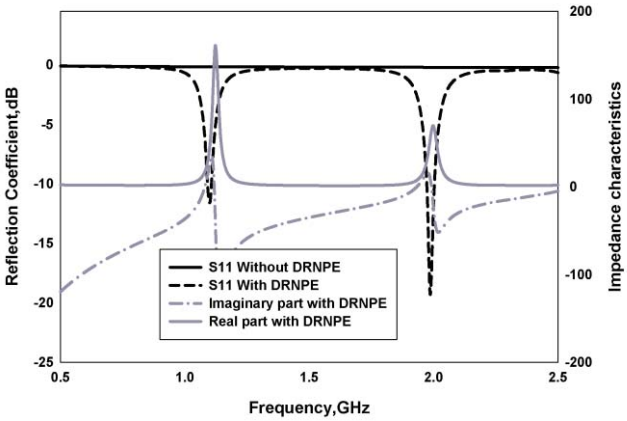

Figure.2 Reflection and Impedance characteristics of the antenna (Wg= 15mm, S_W=3mm, Ls = 15mm, g=0.35mm, W_S=1mm, G_S=1mm, h=1.6mm and ϵr=4.4)

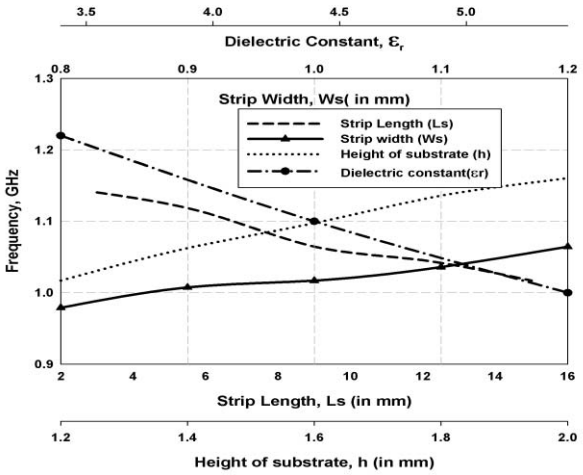

Figure.3 Antenna parametric variation (Wg= 15mm, Lg=15mm, S_W=3mm, S_L=15mm, Ls=15mm, g=0.35mm, W_S=1mm, G_S=1mm, h=1.6mm and ϵr=4.4)

The variation studies have been performed to know the effect of one parameter by keeping all the other parameters constant and are shown in figure 3. The strip length (Ls) is decreased on both sides (figure 1) and the frequency is found to increase due to the reduction in resonant length and vice versa. Similarly as the strip width (Ws) increases the resonant frequency increases. As substrate height (h) increases, the coupling between DRNPE and CPW decreases with a corresponding decrease in capacitance(C) and inductance(L), so frequency increases($f=1/(2*pi\ \sqrt{LC})$) . Thus these parameters show direct (Ws & h) as well as indirect (Er and Ls) monotonic variations with frequency.

The length of the transmission line is varied by changing lateral ground plane length (Lg) and Signal strip length (SL) of CPW. All other parameters remain constant. As the transmission line length is 15mm, the DRNPE aligns exactly since Ls=Lg as in figure 1. It is interesting to note that as the transmission line length is less than DRNPE element, the resonant frequency is on the higher region and is shifted to the fundamental resonance as it approaches DRNPE length as shown in figure 4. Further increase in the transmission line length is not at all affecting the real and imaginary part of impedance and hence there is no shift thereafter in resonant frequency as in the impedance diagrams.

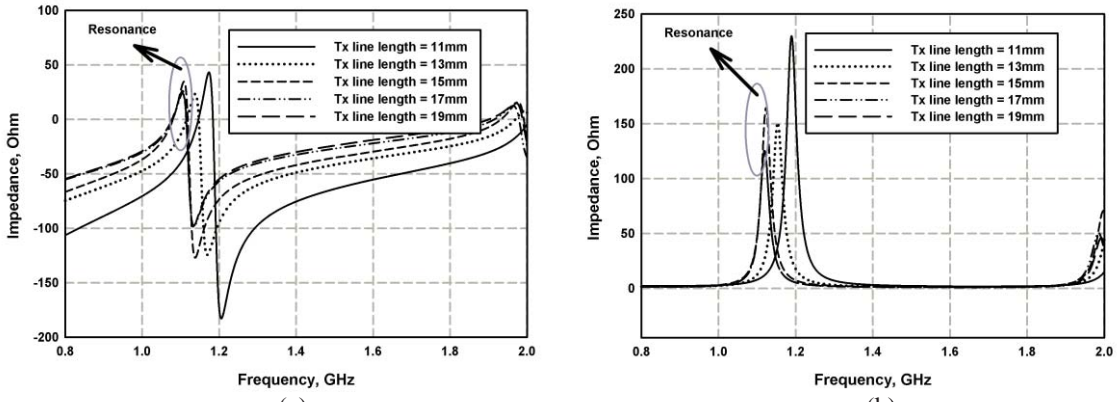

(a). (b).

Figure.4 a) Imaginary and b) Real part of impedance with transmission line length variation (Wg= 15mm, Ls=15mm, S_W=3mm, g=0.35mm, W_S=1mm, G_S=1mm , h=1.6mm and ϵr=4.4)

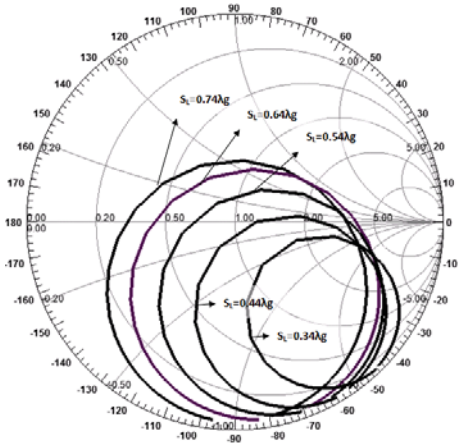

Figure.5 Smith chart showing Impedance variation with signal strip length (Wg= 15mm, Lg=15mm, S_W=3mm, g=0.35mm, Ls=15mm, W_S=1mm, G_S=1mm, h=1.6mm and ϵ_r=4.4)

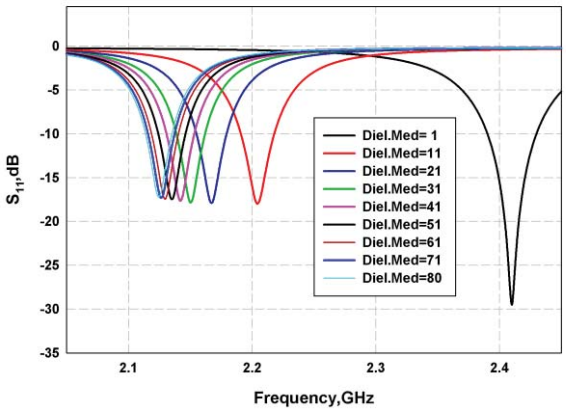

Figure.6 Frequency sensitivity with respect to the dielectric constant of surrounding medium (Wg= 8mm, Lg=8mm, S_W=3mm, g=0.35mm, Ls=8mm, W_S=0.53mm, G_S=0.53mm and h=1.6mm)

The impedance mismatch of the antenna due to any fabrication misalignments can be easily overcome by tuning the reactance by varying the signal strip length. The variation of impedance with respect to signal strip is shown in figure 5. As the signal strip length is reduced the inductive reactance predominates with a corresponding change in the real part. Moreover it is found that the signal strip length is only affecting the impedance matching without change in the resonant frequency.

Different antennas are developed on substrate of dielectric constant 4.4 and thickness 1.6mm for different application bands and their corresponding parameters are given in table 1.

Table.1. Antenna parameters for different application bands

Frequency bands	Ls =Lg =Wg	Gs =Ws
900MHz	17.6mm	1.18mm
1.8GHz	10.3mm	0.68mm
2.4GHz	8mm	0.53mm
5.2GHz	4.16mm	0.27mm

An antenna resonating at 2.4GHz for sensor measurements was surrounded with a medium of varying dielectric constant starting from air(1) to water(80), and its sensitivity is analyzed. The resonance frequency shifts with the change in dielectric constant, but the percentage shift decreases as dielectric constant increases as shown in figure 6. The impedance matching of the antenna is not degrading, which is essential for sensor applications. Thus by measuring the shift in frequency, the dielectric constant can be calculated. This is highly useful for the dielectric constant measurement of bulk liquid materials, by simply inserting in the liquid. The relationship between the resonant frequency (Fr) and dielectric constant (ε_r) is calculated and anlysed;

$$\varepsilon_r = \varepsilon_{rc} + \delta_c \quad \text{----------(1)}$$

Where, $\varepsilon_{rc} = 9.41E{+}12*(F_r)^{-34.34}$ ---------- (2)

$\delta_c = (4.97E{-}06)*(\varepsilon_{rc})^4 + 1.34E{-}05*(\varepsilon_{rc})^3 - 2.03E{-}03*(\varepsilon_{rc})^2 - 3.18E{-}0.1*(\varepsilon_{rc}) + 8.18E{-}01$ ---------- (3)

The Coefficient of Determination for eqn (2) and (3) are 0.9674 and 0.991 respectively.

To understand the resonant behavior the current distribution of antenna is analyzed. It is found that the current distribution of CPW transmission line shown in figure 7(a) is modified as in figure 7(b) with the parasitic DRNPE element. The odd mode distribution of CPW transmission lines remains as such but there is a continuous vertical variation on the direction of current along the lateral ground planes as clearly indicated in the figure. But the direction of current along the edges remains as such with a variation in intensity. The current distribution of DRNPE element alone is shown in figure 7(c). There is a half wave variation on both of the lateral ground planes with an overall full wave variation of 1.1λg.

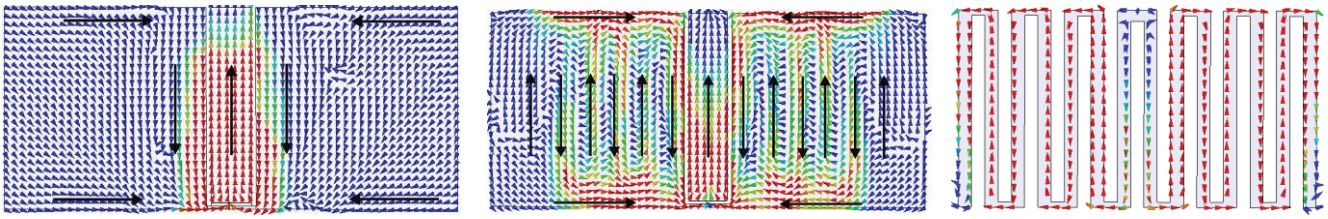

(a). (b). (c).

Figure.7 Current distribution of a) CPW transmission line without DRNPE b) CPW transmission line With DRNPE c) DRNPE structure (Wg= 15mm, Lg=15mm, S_W=3mm, S_L=15mm, g=0.35mm, W_S=1mm, G_S=1mm, h=1.6mm and ϵr=4.4)

Since Ls=Lg=Wg=SL and Ws=Gs for a 50Ω CPW transmission line there are only two parameters determining the resonance of the antenna and is convenient for the designers. For the proposed antenna resonating at 1GHz the parameters are, Lg=0.08λg and Ws=0.005λg. The measured polarization along the bore sight of the antenna is in Y-direction and the gain is -1.5dBi.

IV. CONCLUSION

Compact Coplanar Waveguide fed antenna with Distributed Reactive Nearfield Parasitic Element (DRNPE) as a nearfield sensor is presented. The DRNPE together with CPW transmission line acts as the radiating element. The width, gap and length of DRNPE are primarily affecting the impedance and resonance of the structure. The proposed antenna is compact having a size reduction of 94%, when compared to a CPW-fed antenna fabricated on the same substrate. This antenna is highly suitable for nearfied phantom dielectric measurements.

V. REFERENCES

[1] Richard W. Ziolkowski, and Aycan Erentok "Metamaterial-Based Efficient Electrically Small Antennas", IEEE Trans. Antennas Propag., Vol. 54,No.7,pp 2213-2130, July 2006

[2] Richard W. Ziolkowski, "An efficient, Electrically Small Antenna Designed for VHF and UHF applications", IEEE Antennas and Wireless Propag. Letters., Vol.7,pp 217-220, 2008

[3] S. Back and Y. Jee, " Compact integrated monopole antenna with CPW-fed meander resonators" , Electron. Lett., Vol. 47, No.2, pp 79-80, Jan 2011. 2004.

[4] Deepti Das Krishna, M. Gopikrishna, C.K. Anandan, P.Mohanan and K.Vasudevan, "CPW-Fed Koch Freactal Slot Antenna for WLAN/WiMAX Applications", IEEE Antennas and Wireless Propag. Letters., Vol.7,pp 389-392, 2008

[5] S.R. Best, "The radiation properties of electrically small folded spherical helix antennas", IEEE Trans. Antennas Propag., vol. 52, no.4, pp. 953-960, Apr.2004.

[6] Gokhan Mumcu, Saurabh Gupta, Kubilay Sertel, John L. Volakis " Small Wideband Double-Loop Antennas using Lumped Inductors and Coupling Capacitors", IEEE Antennas and Wireless Propag. Letters., Vol 10,pp 107-110, 2011

[7] Aycan Erentok and Richard W. Ziolkowski "Metamaterial Inspired Efficient Electrically Small Antennas", IEEE Trans. Antennas Propag., vol. 56, no.3, pp. 691-707, Mar.2008.

[8] Marco A Antoniades and George V. Eleftheriades, " A Folded-Monopole Model for Electrically Small NRI-TL Metamaterial Antennas", IEEE Antennas and Wireless Propag. Letters., Vol 7, pp 425-428, 2008

[9] A.L.Borja, A. Belenguer, J. Cascon, H. Esteban and V.E. Boria, "Wideband Passband Transmission Line Based on Metamaterial-Inspired CPW Balanced Cells", IEEE Antennas and Wireless Propag. Letters., Vol 10,pp 1421-1424, 2011

[10] Wei Tong, Zhirun Hu, S. Chua, Philip D. Curtis, Andrew. A.P. Gipson and Mohamed Missous, "Left-Handed Metamaterila Coplanar Waveguide Components and Circuits in GaAs MMIC Technology", IEEE Trans. Microwave Theory Tech., Vol.55, No.8,pp 1794-1800, August 2007

[11] J.Zhu and G.V. Eleftheriades, 'Dual-band metamaterial-inspired small monopole antenna for WiFi applications',Electron. Lett., Vol. 45, No.22, pp 1104-1106, oct. 2009.

[12] Haitao Cheng, Siamak Ebadi and Xun Gong 'A Low-Profile Wireless Passive Temperature Sensor Using Resonator/Antenna Integration Up to 1000^0 C', IEEE Antennas and Wireless Propag. Letters., Vol 11, pp 369-372, 2012.

Beam Switching Antenna at 2.45 GHz for Wireless Body Area Network Application

Anupam R Chandran, Senan Morrison, Ruifeng Zhang, Nick Timmons & Jim Morrison
WiSAR Lab, Letterkenny Institute of Technology, Letterkenny, Ireland
Email: Anupam.Ramachandran@lyit.ie

Abstract: *In this paper, a microstrip patch antenna with parasitic arms for controlling the direction of the radiated beam for wireless body area network is presented. The realized gain of the antenna in the off-body mode is 1.93 dB and that in the on-body mode is 1.4 dB. The operating frequency band centered at 2.45 GHz frequency remains unaltered with a bandwidth of 80 MHz irrespective of the switching states.*

Introduction: Wireless Body Area Network (WBAN) is an inter connection of wireless links between sensor nodes located at different locations on the human body. In WBAN, there exists two modes of communications; on-body mode and off-body mode. On-body mode refers to the communications between different sensor nodes located at different areas on the body. Whereas in the case of off-body mode, the communication exist between body worn devices and a remote base station or a mobile device through which the data recorded can be transmitted to a medical practitioner for analysis or can be used to track down the soldiers health conditions in a battle field. Fig. 1 shows the two different modes of communications in WBAN.

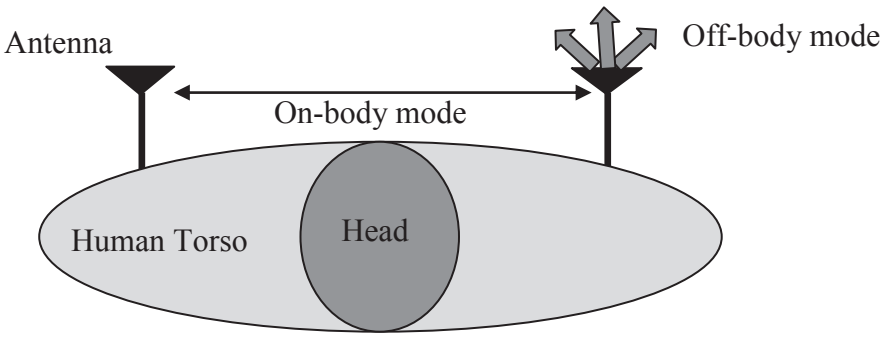

Fig.1 Mode of propagation for WBAN

In order to switch the signal from on-body mode to off body mode, there is a need for an antennas system that is capable of switching the signal from on-body mode to off-body mode of communication. The frequency of operation of the antenna should be in the designated ISM band irrespective of the direction the beam is switched In recent years, there has been a significant amount of work published in the literature relating to WBAN. But there has been only very few papers that are available in the literature regarding a sensor node that is capable of switching the beam from on-body mode to off-body mode. Some of the recent research works published in this area includes stacked patch antennas with switchable propagating mode for UHF body centric communications [1]. The paper describes the use of the lower patch antenna to generate monopole like radiation pattern for the use in on-body mode of communication while the upper patch radiates in the bore sight direction that serves for the off-body communication mode. A microstrip patch antenna based on textile material is used

to realize a switchable on/off-body communication system with pin diodes in [2]. A dual feed, dual radiation pattern dielectric resonator antenna for BAN applications has been proposed in [3], where one of the two feeds is excited at a time to switch the beam pattern. In this paper, we introduce a novel pattern reconfigurable microstrip patch antenna suitable for wireless body area network application.

Antenna Design:

Geometry of the proposed antenna is shown in fig. 2. For studying the effect of the antenna when in close proximity to a human muscle tissue at 2.45 GHz, the antenna is placed 2mm above a cubical cylindrical phantom [4]. The permittivity and conductivity used for the numerical muscle tissue phantom model at 2.45 GHz were $\varepsilon_r = 53.57$, $\sigma = 1.81$Sm-1.

The inset fed microstrip patch antennas with on-phantom optimized dimensions is used as the radiating element. Two parasitic elements with switches SW_L (SW_{L1} + SW_{L2}) and SW_R (SW_{R1} + SW_{R2}) are placed at a specific distance from the radiating element. For proof of concept copper strips were used instead on switches. In the ON-state, the switches were replaced by a shorting strip, and the OFF states were realized by open. Switches are connected in such a way that the beam can be tilted by controlling their ON/OFF states. Here the concept is to change the parasitic arms as reflector and director alternatively to achieve on-body and off-body mode of communications. The microstrip patch and parasitic arms are printed on the same side of a FR4 substrate of dielectric constant $\varepsilon_r = 4.4$ and thickness 1.6 mm. The dimension of the ground plane underneath the patch is optimized as 28 mm X 60 mm for the specific application. All the simulations were carried out using CST microwave studio.

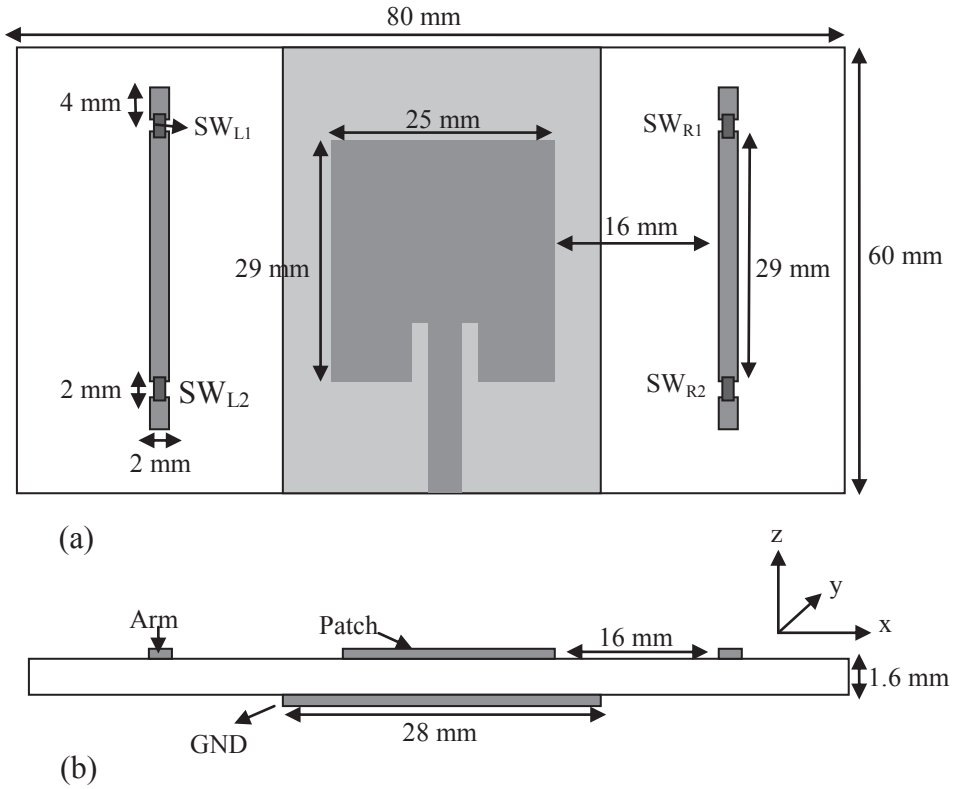

Fig. 2 Geometry of the antenna (a) Top view (b) Side View

Results and Discussions:

Fig. 3 and Fig. 4 shows the simulated and the measured reflection coefficient results of the antenna for three different configurations of the switching states. When switches SW_L (SW_{L1} + SW_{L2}) and SW_R (SW_{R1} + SW_{R2}) are in the OFF state, the antenna radiates in the boresight direction suitable for off-body mode of communications. The corresponding radiation pattern for the off-body mode in free space and on-phantom is depicted in Fig. 5(a) and 6 (a) respectively. When SW_{L1} and SW_{L2} are in the ON state and SW_{R1} and SW_{R2} are in the OFF state, the corresponding parasitic arm acts as a reflector tilting the beam to ±60 degrees from the normal when in free space and ±20 degrees from the normal when in close proximity to the phantom muscle tissue. The corresponding radiation pattern plot in free space and on-phantom is shown in Fig 5 (b) and 6 (b) respectively, which makes this antenna suitable for on-body mode of communications. Similarly, when SW_{L1} and SW_{L2} are in the OFF state and switches SW_{R1} and SW_{R2} are in the ON state, the parasitic arm on the right acts as a reflector and direct the beam as shown in Fig. 5 (c) when in free space and as in Fig. 6 (c) when in close proximity to the phantom. In all these switching states, the frequency of operation remained the same. The prototype of the proposed beam switching antenna is shown in along with the graph in Fig. 4 (a).

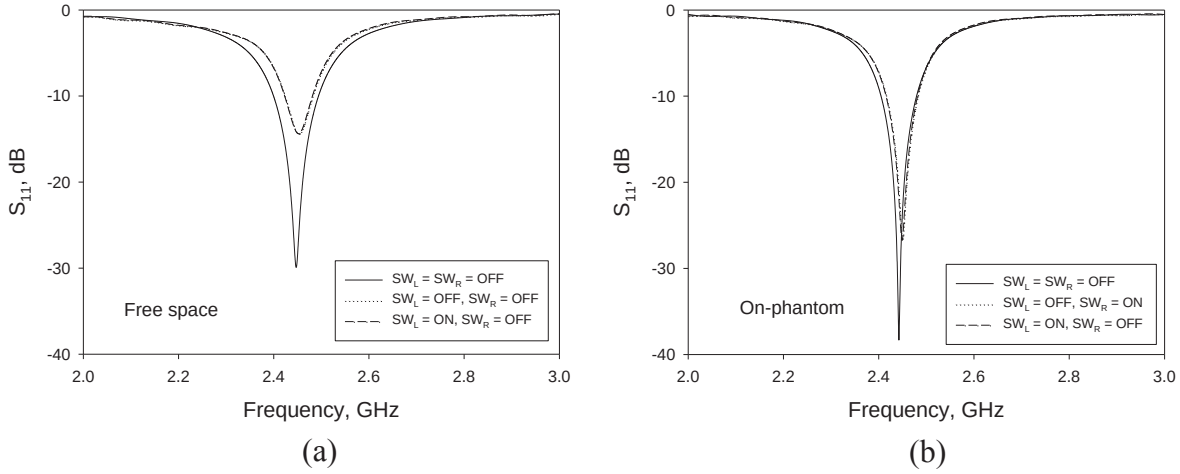

Fig. 3. Simulated reflection coefficient of the antenna for different switching conditions
(a) Free space (b) On-phantom

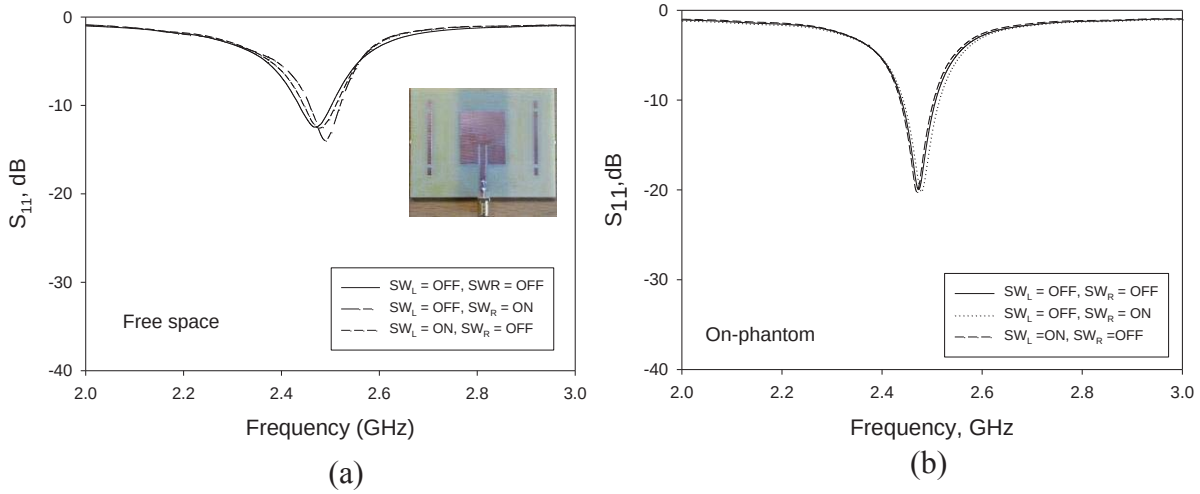

Fig. 4. Measured reflection coefficient of the antenna for different switching conditions
(a) Free space (b) On-phantom

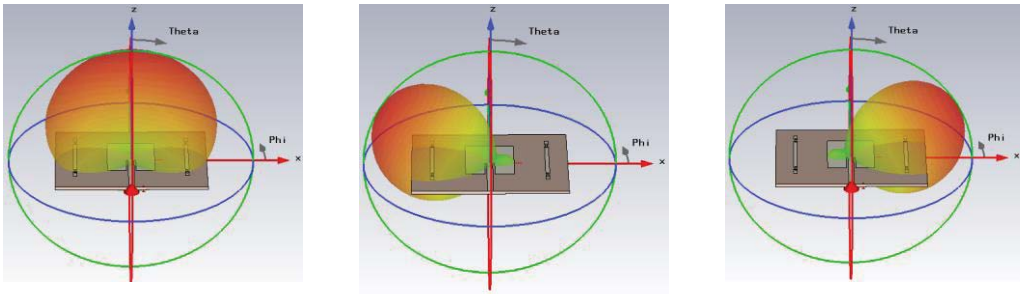

(a) (b) (c)

Fig.5. Free space radiation pattern of the antenna

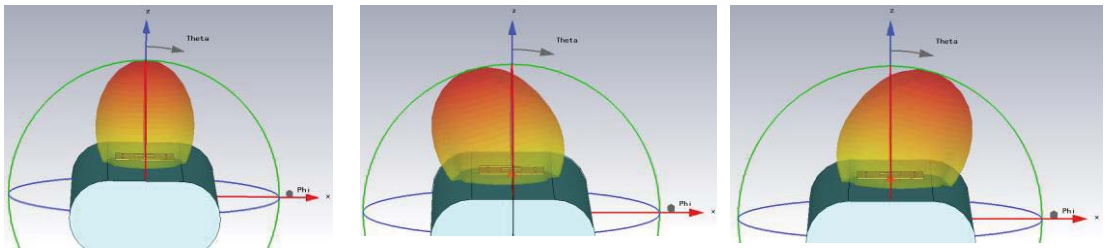

(a) (b) (c)

Fig.6. On-phantom radiation pattern of the antenna

Conclusion:

A pattern reconfigurable antenna at 2.45 GHz has been developed for wireless body area network applications. The resonance frequency of the antenna remains the same for the different configurations of the pattern despite being in close proximity to human muscle tissue. A ±20 degree of beam tilt was achieved for the antenna while on-phantom.

Acknowledgement:

The authors would like to acknowledge Enterprise Ireland for their financial support.

Reference:

[1] W. G. Scanlon and A. R. Chandran, "Stacked patch antenna with switchable propagating for UHF body centric communications", IEEE International Workshop on Antenna Technology, iWAT 2009, pp. 1-4, 2009.

[2] H. J. Lee, K. L. Ford and R. J. Langley, "Switchable on/off-body communication at 2.45 GHz using textile microstrip patch antenna on stripline", IET Electronics Letters, Vol.48, No. 5, pp. 254-256, 2012.

[3] A. M. Faiz, T. Alves, B. Poussot and J. M. Laheurte , "Diversity antenna combining slot-loop DRA for BAN applications", Electronics Letters, Vol. 48, No.1, 2012.

[4] G. A. Conway and W. G. Scanlon, "Antennas for Over-Body-Surface Communication at 2.45 GHz", IEEE Transactions on Antennas and Propagation, Vol. 57, No. 4, 2009.

Compact single shorted hexagonal microstrip patch antenna

K. P. Ray [1], Suchitra Majumdar[2], S. S Kakatkar[1], R.G Karandikar[2]
[1]SAMEER, IIT Campus, Powai, Mumbai - 400076, India
[2]K.J Somaiya COE, Vidyavihar, Mumbai - 400077, India
E-mail: kpray@rediffmail.com

Abstract: *In this paper, it has been shown that the resonant frequency of a hexagonal patch antenna can be lowered significantly by loading a single shorting pin at the edge of microstrip patch antenna, leading to a remarkable reduction in the size of the antenna and saving in real estate for a given operating frequency. Simulated and experimental results of such a Hexagonal microstrip antenna are presented. Comparisons of the Shorted and conventional Hexagonal microstrip antennas are also presented and discussed.*

Introduction: Emerging technology has paved the way for miniaturization of devices which in turn has led to the need for miniaturization of antennas suitable for such modern devices used in personal communication equipments. Compact antennas are also required for applications like missiles and other airborne applications where space is at a premium. Shorting pin loaded microstrip antennas have recently gained much attention due to the increasing demand of compact antennas for personal communication equipment. It has been demonstrated that loading a rectangular, circular or triangular microstrip patch antenna with a shorting pin can effectively reduce the required patch size for a given operating frequency [l-3]. In the shorted patch technique, a radiating microstrip patch antenna is shorted by a shorting pin through ground via substrate material. This short circuit may be complete, by wrapping a copper strip around the edge of the antenna, or by placing a shorting post at an optimum location [2]. It is easier to use a shorting post as compared to wrapping a copper strip around the edge. It has been demonstrated that a smaller shorted microstrip antenna has the same resonance frequency as that of an unshorted but bigger microstrip antenna [3].The shorting posts or plate along the zero potential line, perpendicular to the feed axis, leave the field distribution unperturbed [4].

Compact shorted variations of circular and triangular microstrip antennas have already been reported in the literature [5, 6]. A shorted Hexagonal microstrip antenna (HMSA) has however, not been investigated as thoroughly as shorted patch antennas of other shapes. A Hexagonal Microstrip Antenna (HMSA) has the advantage that its shape/area can be closely approximated to that of a circle and it can be packed closely together in an array. Also, straight edge of HMSA configuration helps in parasitic coupling with other similar patches for bandwidth improvement which would have become difficult with curved edges of circular microstrip patch antenna. Recently, HMSA and its variations have been reported in the literature and a resonance frequency formulation has been proposed to match with the experimental results [7 – 12].

A single shorted HMSA has been designed and fabricated and the simulated and measured results are presented in the next section. The conventional HMSA has also been designed and fabricated and the results for these variations of HMSA have been compared. In

[14], a compact configuration of Hexagonal microstrip antenna using multi shorting has been proposed. The area has been shown to reduce by a factor of four for the quarter patch using multi shorting techniques, while maintaining approximately the same resonance frequency as that of conventional HMSA. In this paper, a single shorting pin has been used to reduce the resonance frequency of a given size of hexagonal microstrip patch antenna. The reduction in area for an antenna designed at a given operating frequency using this technique is seen to be almost 10 times as compared to a conventional HMSA.

Antenna Configuration:

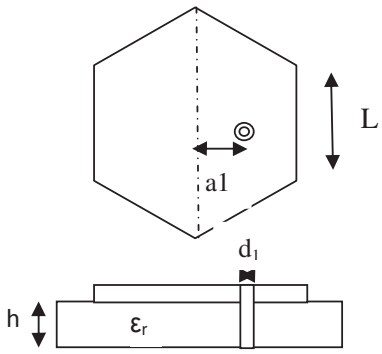

Fig1a Conventional HMSA

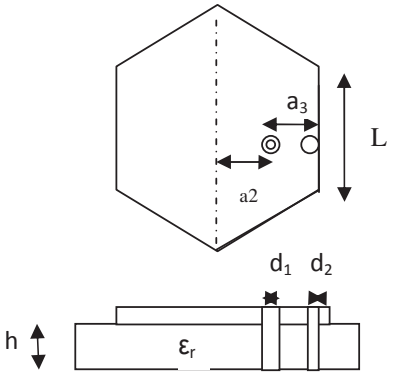

Fig1b Single Shorted HMSA

Fig.1 Geometrical Configuration. a) Conventional HMSA b) single shorted HMSA
Antenna Parameters: Substrate Dimension 75 mm x 75 mm x 1.59 mm, L =40 mm, h=1.59mm, a_1=17.5mm, a_2=31mm, a_3=5mm, d_1=1.4mm, d_2=1mm where d2 is shorting pin location with respect to feed point., ε_r=4.3, loss tangent tanδ=0.02

Fig 2a. Photograph of HMSA

Fig 2b. Photograph of S-HMSA

Fig.2 Photographs of fabricated antennas a) HMSA b) single shorted HMSA

The geometry of the proposed conventional Hexagonal Microstrip patch antenna and Single shorted Hexagonal Microstrip patch antenna is shown in Fig.1a and Fig 1b respectively. The antennas are etched on a substrate of height h having dielectric constant ε_r and loss tangent tan δ. The side length of the regular hexagon is shown as L in Fig.1a. The antenna is fed at a distance a_1 from the centre of the hexagon for the unshorted case while the feed distance is a_2 for the S-HMSA. The shorted HMSA is shorted to ground at a distance a_3 from the feed location. The diameter of feeding pin is taken as d_1 while that of the shorting post is taken as d_2.

The antenna was extensively studied through simulations and optimised for maximum reduction in resonant frequency. It was observed that maximum reduction is achieved when a

single shorting pin is located along the edge of the microstrip patch antenna. The antenna parameters for the final fabricated HMSA and S-HMSA are given in Fig.1a and Fig 1b respectively. The antenna is mounted on FR4 substrate which has a dielectric constant of 4.3 and fed using a coaxial probe. Both Hexagonal Microstrip Patch Antenna and Shorted Hexagonal Microstrip Patch Antenna have the same physical dimension. A conventional HMSA and shorted antenna was fabricated based on the optimised simulated configuration. A photograph of the fabricated antenna is shown in Fig 2a. In the fabricated antenna, the shorting pin is located at the centre of one of the edges as shown in 2b.

Results and Discussion: The simulated and experimental results for the return loss of conventional and single shorted hexagonal microstrip patch antenna are shown in fig 3a and 3b, respectively. As seen from Fig.3a, a hexagonal microstrip patch antenna of 40mm side length resonates at 1.095GHz. The corresponding return loss plot for a shorted HMSA is shown in Fig.3b. It may be seen from the figures that after loading with a single shorting pin, the Hexagonal microstrip patch antenna resonance frequency reduces to 331MHz. The Shorted Hexagonal Microstrip patch antenna is thus seen to achieve significant reduction in resonance frequency as seen from fig 3a and 3b. Measured and simulated results are seen to agree well from Fig.3a and 3b. Thus, 69% reduction of resonant frequency is achieved by locating a single shorting pin at one of the edges of hexagonal microstrip patch antenna. This reduction in resonant frequency can be attributed to the increase in current path length due to loading of single shorting post in microstrip patch antenna. Current path distributions of both hexagonal microstrip patch antenna and Single shorted Hexagonal Microstrip Patch antenna are shown in fig 4a and 4b, respectively. Further it has been observed through simulation that same resonance frequency of 331 MHz is achieved for a conventional hexagonal microstrip patch antenna of side length 14cm as shown in Fig.5. This shows that using single shorting technique the area required for antenna has been reduced from 509 cm^2 to 41 cm^2 for the same resonant frequency of 331 MHz. This amounts to a remarkable reduction of 91.84% in area leading to a highly compact, lightweight antenna and making more space available for other subsystems and electronics on board.

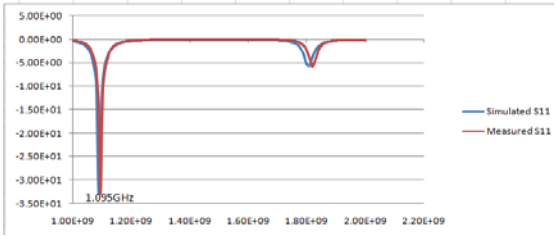

Fig.3a Return loss of conventional HMSA

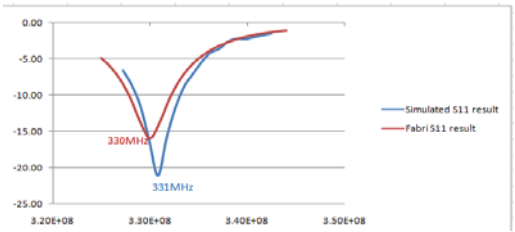

Fig.3b Return loss of single shorted HMSA

Fig.3 Simulated and measured Return loss for a) conventional and b) single shorted HMSA

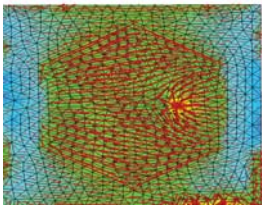

Fig 4a Current distribution of HMSA.

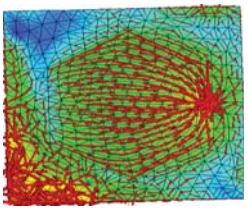

Fig 4b Current distribution of S-HMSA

Fig.4 Current distribution of conventional and single shorted HMSA (L= 4cm)

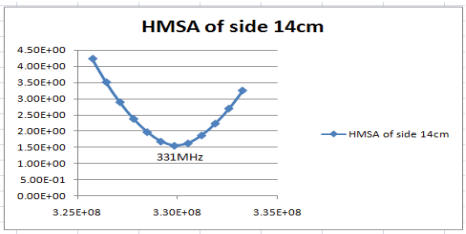

Fig 5. VSWR of HMSA of side length 14cm.

Conclusion

A hexagonal microstrip patch antenna with a single shorting pin at the edge was designed to realize significant reduction in the resonance frequency leading to more than 90% reduction in the size of the antenna and an extremely compact, lightweight design at the desired frequency. More than 69% reduction in resonant frequency was achieved. Simulated and measured results were shown to be in good agreement with each other. This antenna is useful in applications like mobile handsets, missiles, aircrafts, and other compact systems having severe space constraints and where size and weight are of major concern.

References

[1] WATERHOUSE, R.: 'Small microstrip patch antenna', *Electron. Lett.,*1995, **31,** (8), **pp.** 604-605

[2] G. Kumar and K. P. Ray, Broadband microstrip antenna, Artech House, USA, 2003

[3] K. Hirasawa and M. Haneishi, Analysis, design, and measurement of small and low-profile antennas, Artech House, Boston, 1992.

[4] M. Sanad, Effect of shorting posts on short circuit microstrip antennas, IEEE Antenna Propagat. Symp., 1994, pp. 794-797.

[5] S. K. Satpathy, K. P. Ray, and G. Kumar, Compact shorted variations of circular microstrip antenna, Electron Lett 34(1998), 137-138.

[6] S. K. Satpathy, K. P. Ray, and G. Kumar, Compact shorted variations of triangular microstrip antenna, Electron Lett 34(1998), 709-711.

[7] I. J. Bahl, and P. Bhartia, Microstrip Antennas, Artech House, Dedham, 1980.

[8] K. S. Arvind and J.R. Wolfgang, Spectral domain analysis of a Hexagonal microstrip resonator, IEEE Trans. Microwave Theory and Tech 30 (1982), 825-828.

[9] K. P. Ray, M. D. Pandey, S. Krishnan, Determination of resonance frequency of hexagonal and half-hexagonal microstrip antenna, Microwave Opt Technol Lett 49(2007), 2876-2879.

[10] K. P. Ray and M. D. Pandey, Resonance frequency of hexagonal and half hexagonal microstrip antennas, Microwave Opt Technol Lett 51(2009), 448-452.

[11] K. P. Ray, M. D. Pandey and A. Deshmukh, Broadband gap-coupled half hexagonal microstrip antennas, Microwave Opt Technol Lett 50 (2008), 271-275.

[12] K. P. Ray , M. D. Pandey,R. Rashmi and S.P. Duttagupta, “Compact configurations of hexagonal microstrip antennas”, Microwave and Optical Technology Letters, Issue Volume 55, Issue 3, pages 604–608, March 2013

Broadband offset CPW-Fed Square Slot Antenna

Amit A. Deshmukh [(1)], Ameya A. Kadam[(1)], Sudesh Agrawal[(1)] and K. P. Ray[(2)]
(1) D. J. Sanghavi College of Engineering, Vile Parle, Mumbai - 400056
Email: amitdeshmukh76@rediffmail.com
(2) RFMS Division, SAMEER, IIT Campus, Mumbai-400076
Email: kpray@rediffmail.com

Abstract: *A new Coplanar Waveguide fed square slot rectangular microstrip antenna for broader bandwidth is proposed. An impedance bandwidth of more than 82% in 3000 MHz frequency band which covers Wi-MAX and WLAN bands is obtained. The proposed antenna shows broadside radiation pattern over the bandwidth with gain of 5.6dBi.*

Introduction: The interest of using Coplanar Waveguide (CPW)-fed for microstrip antennas (MSA) has been increasing over in recent years [1]. The CPW fed MSAs have many attractive features like low radiation loss, less dispersion, ease of integration with monolithic microwave integrated circuits (MMIC's). The single layer substrate is used which enables integration with active and passive devices. One of the main issues with CPW fed slot antennas is to provide an easy impedance matching to the CPW line. In order to obtain broadband CPW-fed slot antennas, several impedance tuning techniques have been reported in the literature like, change of slot dimensions in bow-tie slots [1 – 3], a wide rectangular slot [4 - 5], coupling mechanism including inductively-coupled slot [6], dielectric resonator coupling [7], and other techniques such as harmonic control used by photonic band-gap (PBG) [8]. However, bandwidth realizing CPW-fed slot antennas is generally less than 60%. In this paper, a new technique has been employed to increase the impedance bandwidth of the CPW-fed slot antenna, which uses the coupling between the CPW feed line and the square slot to facilitate the impedance matching of the antenna and reduce the cross-polarization level. The simulation and experimental results of the proposed antenna show the impedance bandwidth (BW) of more than 82% at the center frequency of around 3000 MHz thereby covering Wi-MAX and WLAN frequency bands. The antenna was first simulated and optimized using IE3D software followed by experimental verifications [9]. The patch was fabricated on FR4 substrate and the measurement was carried out using R & S Vector network analyzer (ZVH-8). The radiation and gain properties were measured using R & S RF source and spectrum analyzer in the minimum reflection surroundings with required minimum far field distance between reference antenna and antenna under test.

2. Antenna Design

The geometry of the reported CPW-fed slot antenna is shown in Fig. 1(a). The printed square radiating slot has a side length of L and a width of G. A 50Ω CPW has a width W_f and a gap of spacing ***g*** between the connecting strip and the coplanar ground plane. The tuning stub is connected to the end of CPW feed line. In this design, the dimensions are chosen to be G =72 mm, L = 44 mm, W_f = 6.37 mm, and g = 0.5 mm. The return loss and resonance curve of the reported structure is shown is Fig 1(b) and (c), respectively. The VSWR $\leq$ 2, BW for the reported configuration was found to be 1.5 GHz at center frequency of 2.6 GHz which gives total bandwidth of 67% [10]. Also, current distribution at the resonant modes is shown in Fig. 2(a – d). The surface currents show half wave and wavelength variations along the patch and outer square slot dimensions which are due to fundamental and second order modes. To understand the functioning of this antenna and the effect of stub, an analysis of this antenna was carried out by removing tuning stubs placed towards the corner of the square slot as shown in Fig. 3(a). The return loss and resonance curve plot of this modified structure is

shown in Fig 3(b) and (c), respectively. As seen from Fig 3(b), the change in BW is not significant. Further a CPW-fed simple RMSA with offset feed is investigated. The geometry of the antenna is shown in Fig. 4(a). The proposed antenna was fabricated on an FR4 substrate with thickness (h) of 1.6 mm and relatively permittivity (ε_r) of 4.4 as shown in fig. 4(b) and tested. The parametric study for variation in CPW fed line position on the realized BW was carried out and optimum result was obtained for strip position of 9 mm from the center. The effect of offset feed on impedance is shown in fig.4(c). With an offset feed location at 9mm the impedance is below 100Ω for a wide range of frequencies indicating a good impedance match. The simulated BW was found to be 2.1 GHz at center frequency of 2.6 GHz (82%) and measured BW is 2.96 GHz. The measurement was carried out to validate the simulation. The measured BW is as shown in fig. 5 (a) and (b). The resonance curve shown in fig 6(a) shows excitation of additional modes as compared to the center feed configuration what results in increased BW. The resonance plot of CPW fed stub loaded square slot MSA indicates a high and varying impedance in desired frequency range while that of offset fed CPW fed MSA is almost equal to 80Ω over wide frequency range indicating a good match. The antenna efficiency plot is shown in fig. 6 (b) .The antenna efficiency is about 96% in the lower frequency range which decreases to less than 60% towards higher frequencies, since FR4 substrate is lossy substrate. The current distribution at the resonant modes is shown in Fig. 7(a – d). The measure of co-polar radiation pattern plots in y-z and x-z planes at 2.4 GHz, 3.6GHz and 4GHz are shown in Fig. 8. The pattern remains in broadside direction over most of the BW.

Conclusions: A new wideband CPW-fed square slot cut RMSA is proposed. Using the offset feed location, an increased input impedance BW of 82 % center at around 3.0 GHz is obtained. The increased antenna BW is due to the additional modes introduced in offset feed configuration. The antenna gives broadside radiation pattern over most of the BW.

References:

[1] P.L.Chin, A.Z. Elsherbeni, and C.E. Smith, "Characteristics of Coplanar Bow-Tie Patch Antennas," Antennas and Propagation Society International Symposium, vol. 1, pp.398-401, 2002.

[2] P.L.Chin, A.Z. Elsherbeni, and C.E. Smith, "A Coplanar Waveguide Bow-Tie Aperture Antennas," Antennas and Propagation Society International Symposium, vol.1, pp.564-567, 2002.

[3] E.A. Soliman, S. Brehels, P. Delmotte, G.A.E. Vondenbosch, and E. Begne, "Bow-tie Slot Antenna Fed by CPW," Electron. Len, vol.35, pp.514-515, 1999.

[4] M. Miao, B.L. Ooi, and P.S. Kooi, "Broadband CPW-fed Wide Slot Antenna," Microwave Opt. Technol. Lett., vol. 25, pp. 206-211, 2000.

[5] E.A. Soliman, S. Brehels, P. Delmotte, G.A.E. Vondenbosch, and E. Begne, "CPW-fed Cusp Antenna," Microwave Opt. Technol. Lett., vol. 22, pp. 288-290, 2000.

[6] S.-S. Garcia and J.-J. Laurin, "Study of a CPW Inductively Coupled Slot Antenna," IEE. Proc. Microwave Antennas Propagation, vol. 87, pp. 58-64, 1999.

[7] M.S. Al Salameh, Y.M.M. Antar, and Guy Segulin, "Coplanar Waveguide-Fed Slot-Coupled Rectangular Di-electric Resonator Antenna," IEEE Trans. Antennas Propagation. , vol. 50, pp. 1415-1419, 2002.

[8] X.-C. Chang and L.-T. Wang, "A Broadband CPW-Fed Loop Slot Antenna with Harmonic Control," IEEE Antennas and Wireless Lett, vol. 2, pp. 323-325, 2003.

[9] IE3D 14, Zeland software Inc., Fremont, CA.

[10] J.Y. Chiou, J.Y. Sze, and K.L. Wong, "A Broadband CPW-fed Strips-Loaded Square Slot Antenna," IEEE Trans. Antennas Propagation, vol.51, 2003.

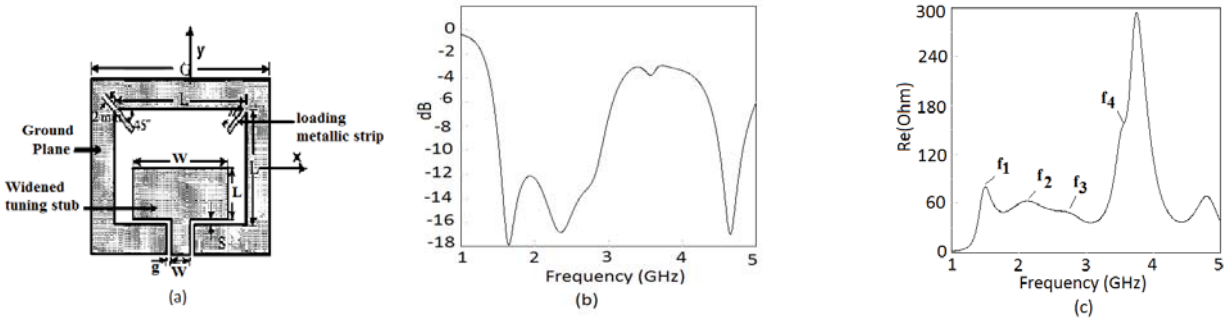

Fig 1 (a) CPW fed stub loaded square slot RMSA, its (b) return loss, and (c) resonance curve plots

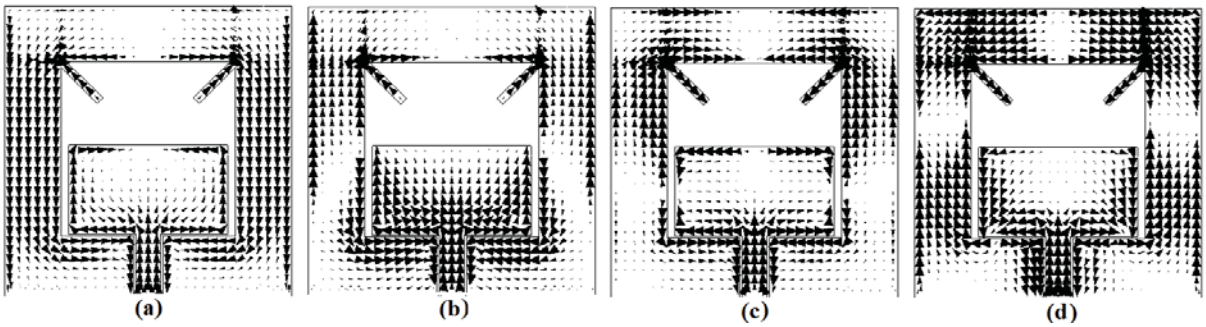

Fig 2 Current distribution at various resonant modes, (a) f_1=1.504GHz, (b) f_2 =2.104GHz, (c) f_3= 2.744GHz, (d) f_4 =3.248 GHz, for stub loaded CPW fed RMSA

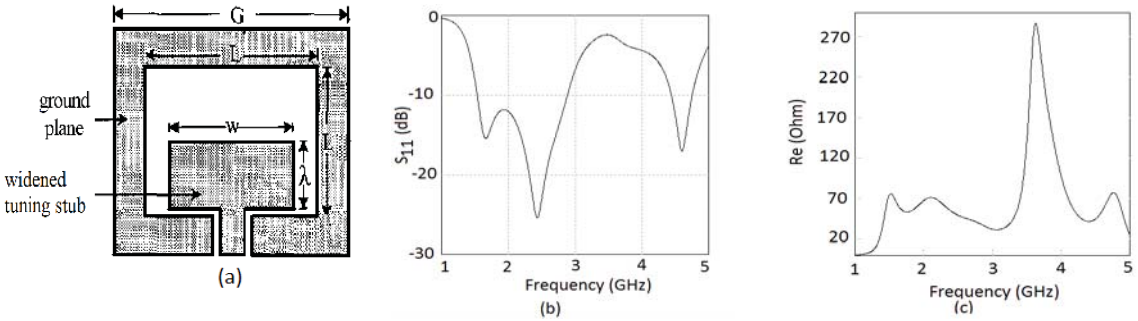

Fig 3 (a) Geometry of CPW fed RMSA without stubs, its (b) return loss, and (c) resonance curve plots

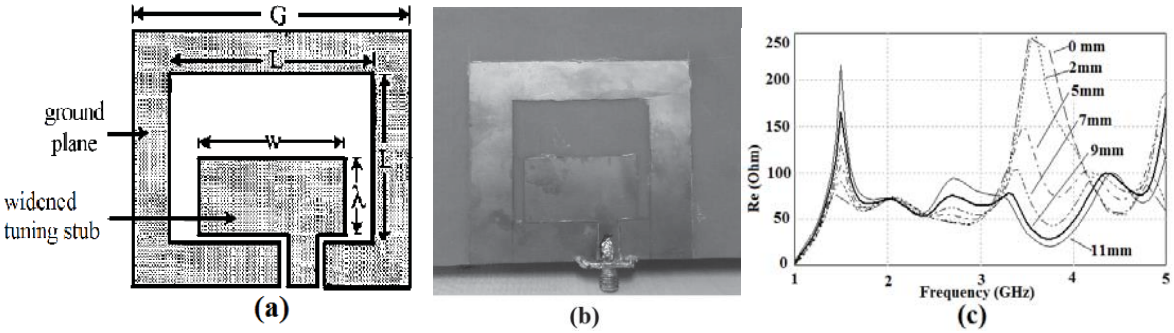

Fig 4: (a) Geometry of offset fed CPW fed RMSA, (b) fabricated prototype and (c) effect of offset feed on resonance plot.

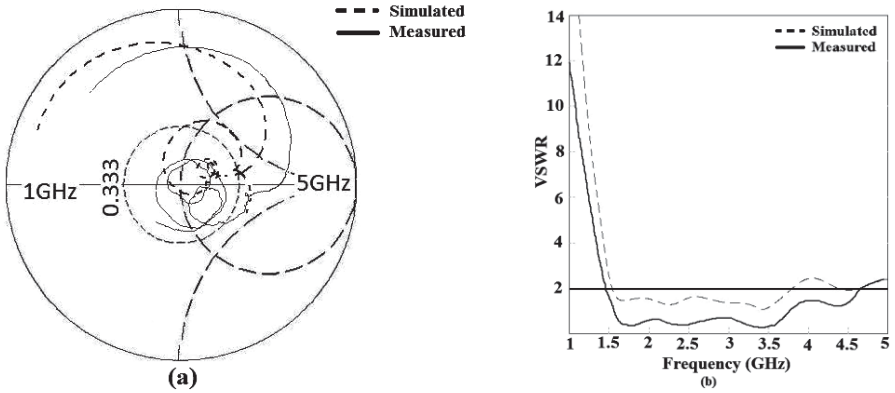

Fig 5: (a) Impedance loci and (b) VSWR plot for offset fed CPW fed RMSA

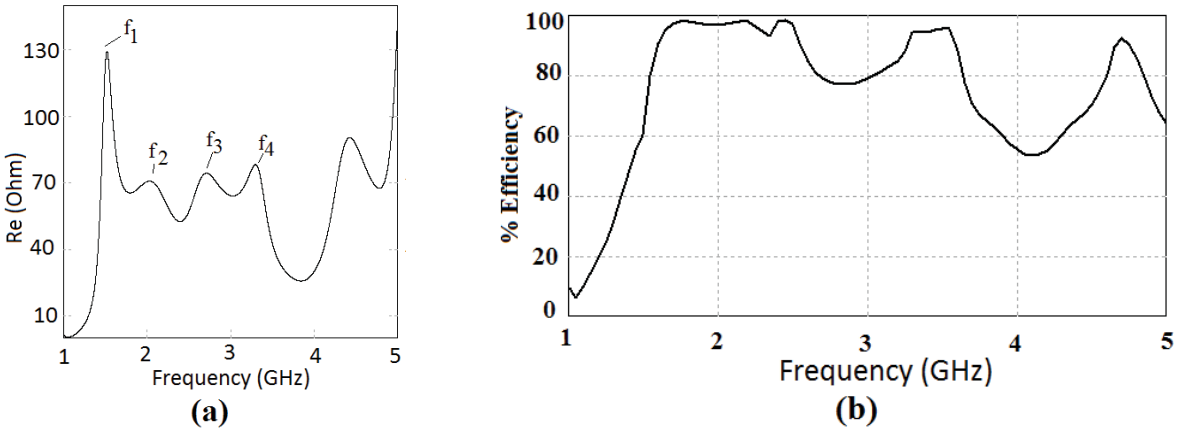

Fig 6: (a) Resonance curve, (b) Antenna efficiency plot for offset fed CPW fed RMSA

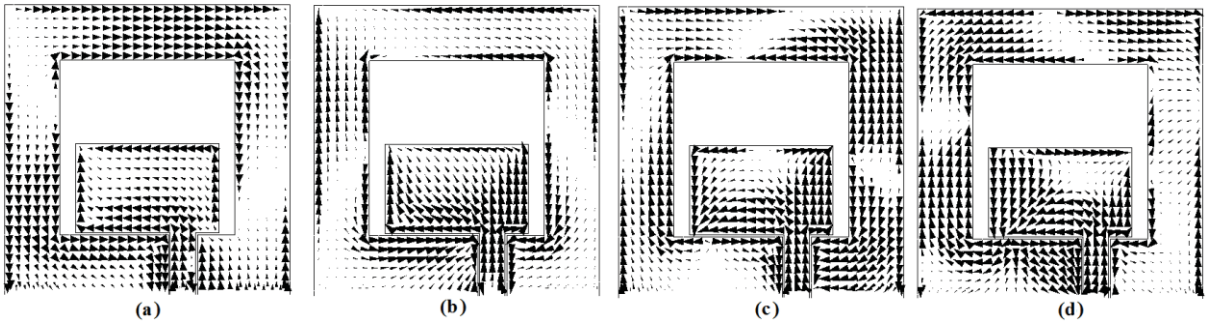

Fig 7: Current distribution at the resonant frequencies (a) f_1= 1.504 GHz, (b) f_2= 2.034 GHz, (c) f_3=2.632 GHz, (d) f_4=3.127 GHz for offset fed CPW fed RMSA

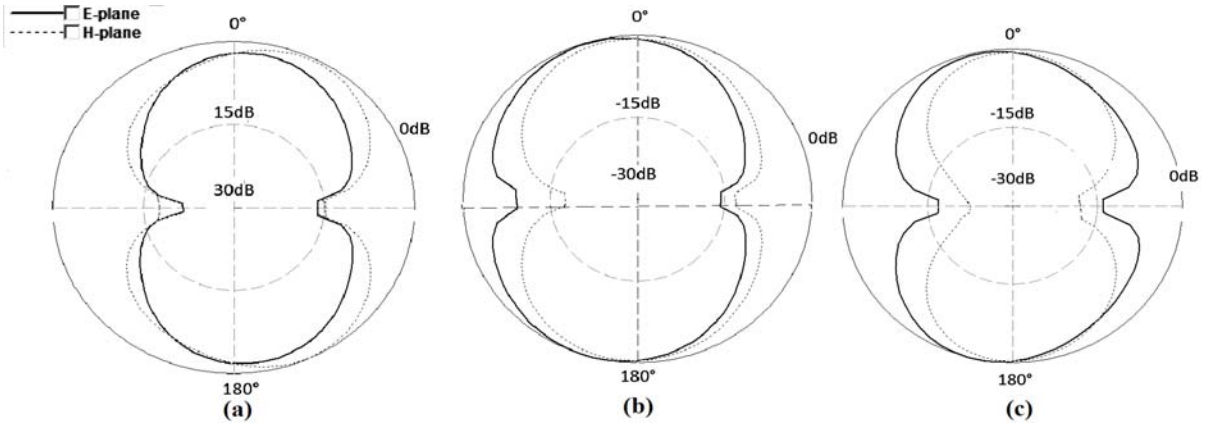

Fig 8: Radiation Patterns at (a) lower frequency of 2.4 GHz, (b) center frequency of 3.6 GHz and (c) upper frequency of 4 GHz for offset fed CPW fed RMSA

Design, Fabrication and Performance Analysis of Microstrip Antenna With MIMO Implementation For Wireless Applications

Mohammad Ameen[(1)], *Mohammed Ismail. H*[(2)]
(1) Communication Engineering, KMEA Engg College, Kerala, India
Email: mohammadmn61@gmail.com

(2) Department of Electronics and Communication Engineering, KMEA Engg College, India, Email: Ismail@kmeacollege.ac.in

Abstract—This paper presents the design of a small and compact triple band Microstrip slot antenna and their 2 x 1 MIMO implementation for Bluetooth, 4G LTE, WLAN, and WiMAX applications. The proposed slot antenna consist of a microstrip feed line , a ground plane on the other side on which slot etched and some L strips are added. Two S shaped parasitic elements are added back to back on another side The simulation results of the single antenna shows that the designed antenna is capable of operating over 2.39 to 2.86 GHz, 3.13 to 3.68 GHz, and 5.08 to 5.97 GHz frequency bands while rejecting frequency ranges between these three bands. Next, a study was performed to implement this antenna in 2x1 MIMO arrangement on the same circuit space. The simulation result shows that it is suitable for working for Bluetooth, 4G LTE, WLAN and WiMAX applications. Nearly Omn-directional radiation pattern, acceptable antenna gain, better mutual coupling and better envelope correlation coefficient are achieved over the three operating bands.

Index Terms—Multiple Input Multiple Output (MIMO), Wireless Local Area Networks, Long Term Evolution, Worldwide Interoperability for Microwave Access.

Introduction: Presently the wireless communication is one of the fastest growing segment of the communication field. There are many commercial and government applications such as Satellite communication, mobile radio, and Wireless communication where size, weight, cost, ease of installation, performance, aerodynamics profile are major constraints. The vision of the wireless communication supporting information exchange between people and devices is the communication frontier of the next few decades. This vision will allow multimedia communication from anywhere in the world. In the last few years, the development of WLAN (wireless local area networks) and WiMAX (Worldwide Interoperability for Microwave Access), Bluetooth, 4G LTE (Long Term Evolution) represented one of the principal interests in the information and communication field [1-5]. Also, in today's environment, technology demands antennas which can operate on different wireless bands and should have different features like low cost, minimal weight, low profile and are capable of maintaining high performance over a large spectrum of frequencies. The paper presents the design, fabrication and performance analysis of microstrip slot antenna with MIMO implementation. The designed and fabricated antenna is very small and table I gives a comparison of the existing MIMO antennas and newly designed antenna.

Table: I Comparison between existing and newly designed MIMO antenna

Reference Number	Dimensions (mm^3)	WLAN (2.4/5.2/5.8)	WIMAX (2.5/3.5/5.5)	4G LTE (2.6)
[]	80 x 18 x 1.6 mm^3	(2.4/5.8)	(2.5/3.5/5.5)	-
[8]	85 x 40 x 0.64 mm^3	(2.4/5.2)	(3.5)	-
[9]	110 x 52 x 1.6 mm^3	(2.4)	(3.5/5.5)	-
[10]	48.5 x 40 x 1.6 mm^3	(5.2)	(3.5)	-
[11]	110 x 52 x 1.6 mm^3	(2.4)	(3.5/5.5)	
[12]	110 x 160 x 0.8 mm^3	(2.4)	(2.5)	(2.6)
[13]	99 x 55 x 1.6 mm^3	(2.4)	(3.5)	-
[14]	125 x 85 x 0.8 mm^3	(2.4)	(5.5)	-
[15]	79 x 1.6 x 1.524 mm^3	(2.4/5.2/5.8)	(3.5)	-
[16]	40 x 90 x 0.79 mm^3	(2.4)	(3.5)	-
Proposed MIMO Antenna	**77 x 30 x 3.2 mm^3**	**(2.4/5.2/5.8)**	**(2.5/3.5/5.5)**	**(2.6)**

Antenna Design: The proposed antenna may be considered as a transformer of the slot antenna. As shown in Figure 1, the configuration of the triple-band slot antenna is designed and substrate with FR4, relative permittivity of 4.4, and a loss tangent of 0.02. The entire size of the antenna is only 30x30x3.2 mm^3. Without loss of generality, a 50Ω microstrip feed line with a width of 3 mm is given for centrally feeding the antenna at one side of the substrate and two S shaped parasitic elements are added on one side of the substrate and Some simple slots are etched on the ground plane to give all the work bands.

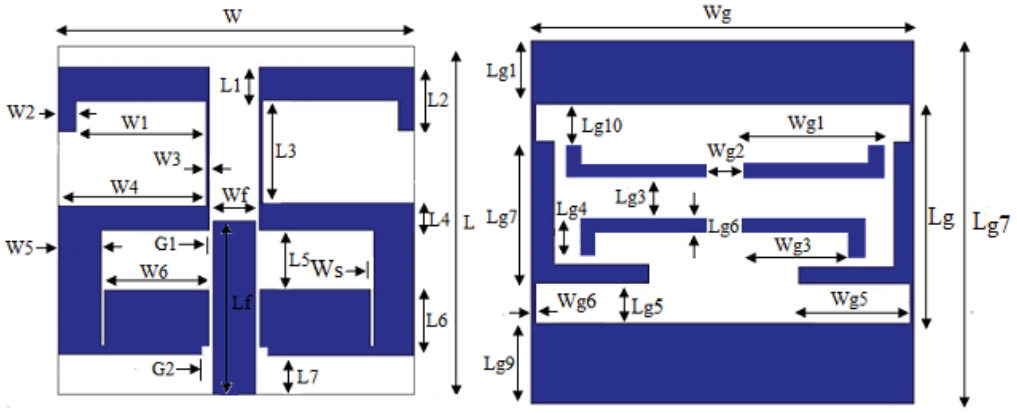

Figure:1 Dimensions of front and backside (unit: mm).

The rectangular slot in the ground plane can get the lowest resonant frequency of 2.52 GHz. There are some L shaped strips are added on the ground plane to get the middle resonant frequency of 3.5 GHz. The addition of two slots the S shaped symmetric parasitic elements provides the highest resonance and makes impedence matching in the wide band range. The L strips embedded on the rectangular slot are used for feeding and providing the middle band work.The initial length of slot embedded on the S shape and L strip is approximated according to,

$$l = \frac{\lambda_p}{4} = \frac{c}{4f\sqrt{\varepsilon}}, \varepsilon = \frac{\varepsilon_r + 1}{2} \quad (1)$$

Where, c is the speed of light in vacuum, f is the resonant frequency, and ε_r is the relative permittivity of the substrate. The whole antenna is optimized with the commercial software CST Microwave studio and values of some optimized parameters are shown in table 1I. The figure 3 shows the front and back view of fabricated single microstrip antenna.

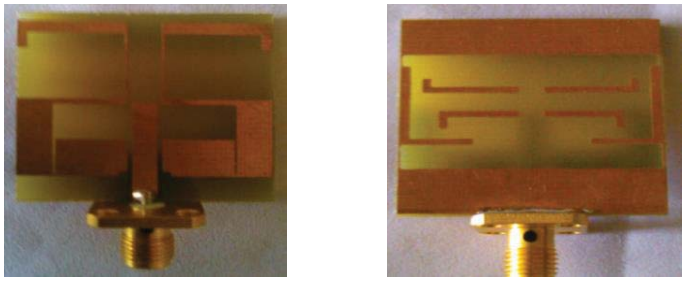

Figure: 22 Front view and Back view of fabricated single Microstrip Antenna

Table.II The values of parameters for the design of the proposed antenna (mm).

Parameters	L	W	L_g	W_g	W_f	L_f	W_1	W_3	W_6
Dimension	30	30	30	30	3	16	11.4	0.3	8.5
Parameters	W_7	W_8	L_6	L_5	L_3	L_2	L_8	L_{G2}	L_{g3}
Dimension	13	0.27	6	5.5	16.5	4.57	4	2.25	2.75
Parameters	L_{g4}	L_{g5}	L_{g1}	L_{g9}	L_{g7}	W_{g1}	W_{g2}	W_{g3}	W_{g5}
Dimension	2.75	1.5	5.75	6.75	11.25	11	4	8.1	8.1

The simulated return loss versus frequency curve is shown in Figure 4. The designed antenna resonates at 2.52 GHz, 3.47 GHz and 5.68 GHz respectively. The return loss for 2.52 GHz is -30.24 dB, for 3.47 GHz is -32.09 dB and the return loss for 5.68 GHz is -27.10 dB which covers the minimum required value of return loss of -10 dB. The bandwidth of the proposed patch antenna is 470 MHz (2.39 GHz – 2.86 GHz), 550 MHz (3.13 GHz – 3.68 GHz) for 3.47 GHz and 900 MHz (5.08 GHz – 5.97 GHz) for 5.68 GHz.

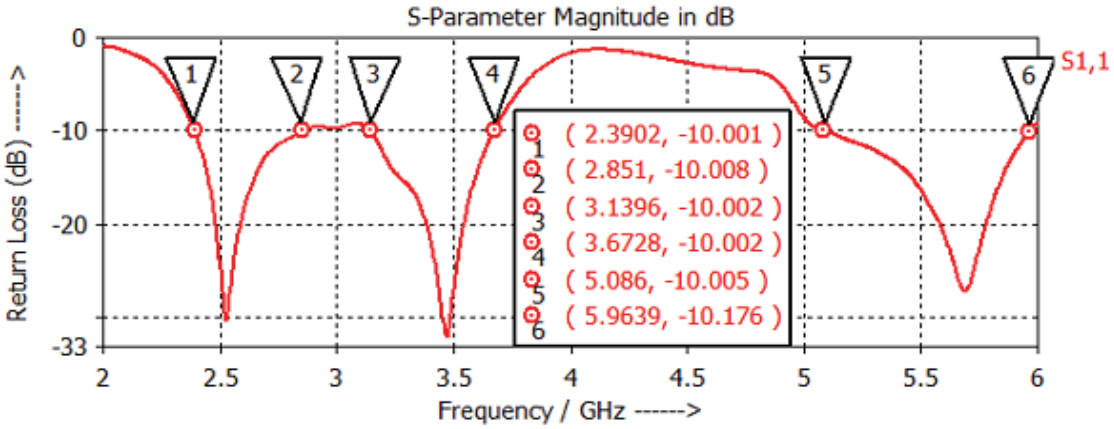

Figure:4 Simulated Return loss curve of the proposed antenna.

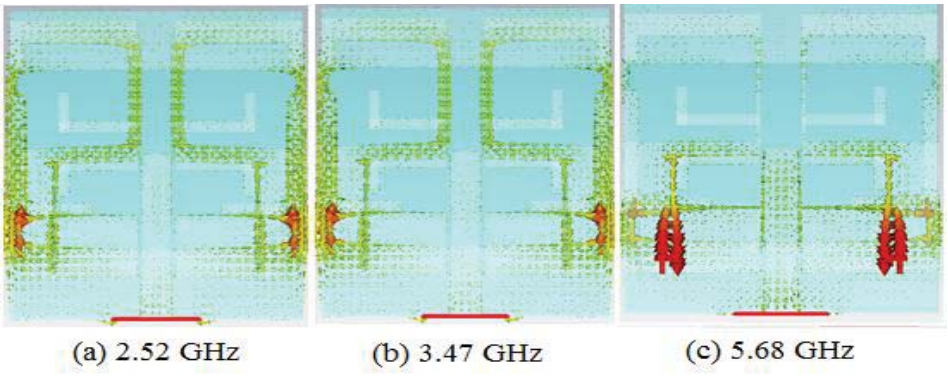

Figure:5. Current distribution of the proposed antenna (a) 2.52 GHz, (b) 3.47 GHz and (c) 5.68 GHz

The current distribution at different frequencies are illustrated in figure5(a), 5(b) and 5(c), The figure 5(a) shows that the current distributes mainly along the edges of the rectangular slot of the ground plane at 2.52 GHz. In figure 5(b) the current flowing along the two L strips embedded in the ground plane at 3.47 GHz and in figure 5(c) the current mainly concentrates in the slots provided in the parasitic elements at 5.68 GHz.

INTEGRATION OF 2x1 MIMO ANTENNA: Figure 6 shows four common configurations of the combination of two such antennas. The simulated S-parameters of the MIMO/diversity configurations are shown in Figure 7.

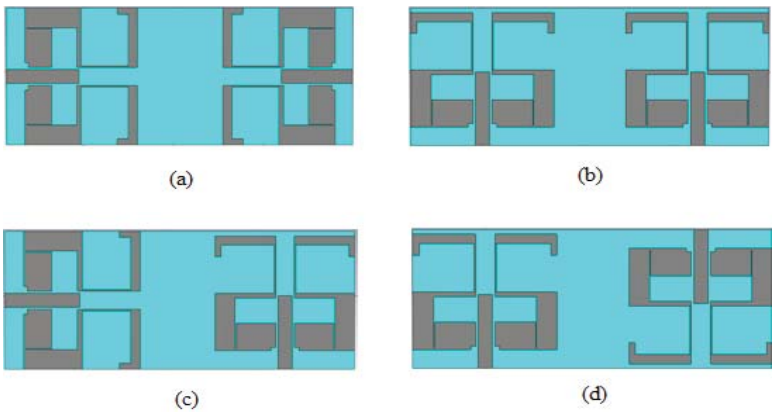

Fig: 6 MIMO/diversity triple-band configurations, (a) front-to-front, (b) side by side, (c) orthogonal and (d) parallel.

The proposed antenna provides good impedance matching with slight variation and high isolation between the two antenna ports without the use of any external slot/slit. It is seen that in the front-to-front configuration, the value of S_{12} is completely below the -10dB while in the other configurations the S_{12} goes above the -10 dB. The envelope correlation coefficient of the array configuration can be determined through the use of the S-parameters and is given in the following.

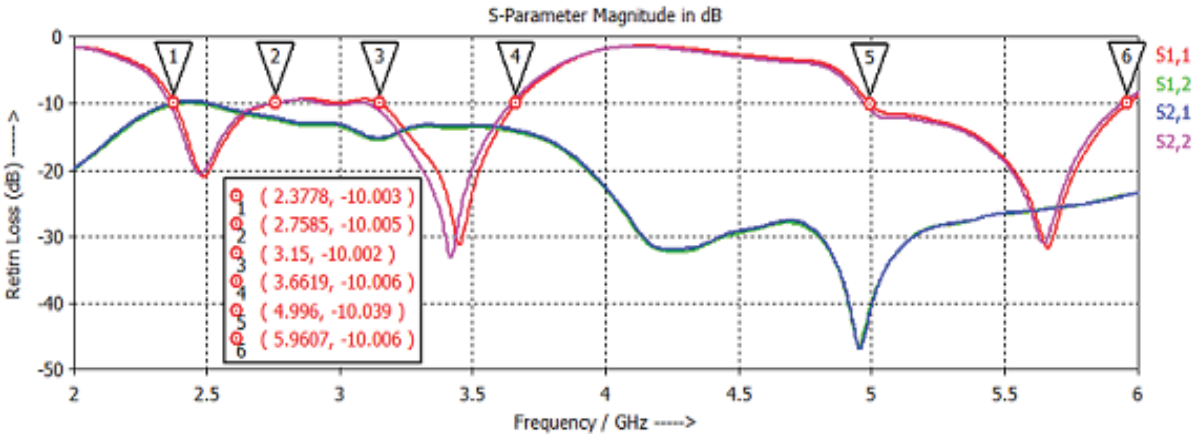

Fig: 7. Simulated plots for the proposed MIMO antenna.

Examining the simulation results shown in Figure 7, the return loss plots S_{11} and S_{22} are approximately same, the mutual coupling S_{12} and S_{21} are same. These bands are marked as band 1 (2.37 GHz – 2.76 GHz), band 2 (3.15 GHz – 3.67 GHz), and band 3 (4.99 GHz – 5.97 GHz). The bandwidths for these bands are determined by the reflection coefficient (S_{11} and S_{22}) of -10 dB or lower. The bandwidths are 400 MHz, 520 MHz, and 980MHz of the three bands respectively. In band 1 the S_{11} and S_{22} is -20 dB, band 2 at -31 dB and band 3 at -31 dB. In band 1 the mutual coupling S_{12} and S_{21} is below -10 dB, band 2 at -13 dB and band 3 at -25 dB. The figure 8 shows the comparison of simulated and measured S_{11} plot for MIMO antenna.

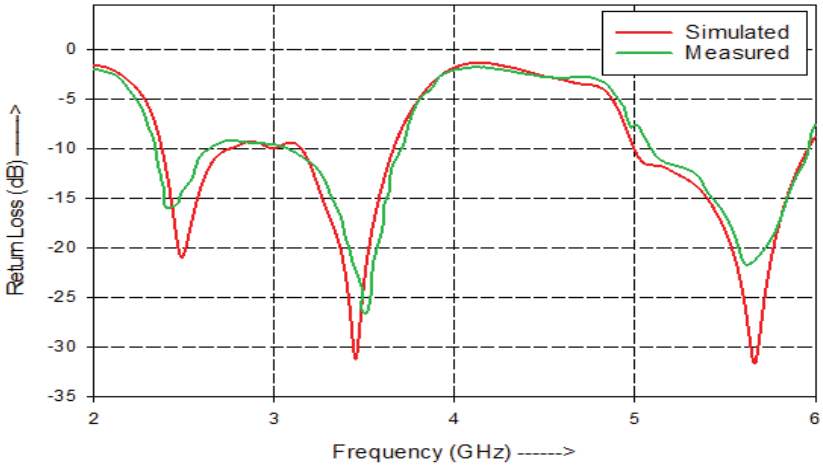

Figure: 8 Simulated and Measured Return loss of the MIMO antenna

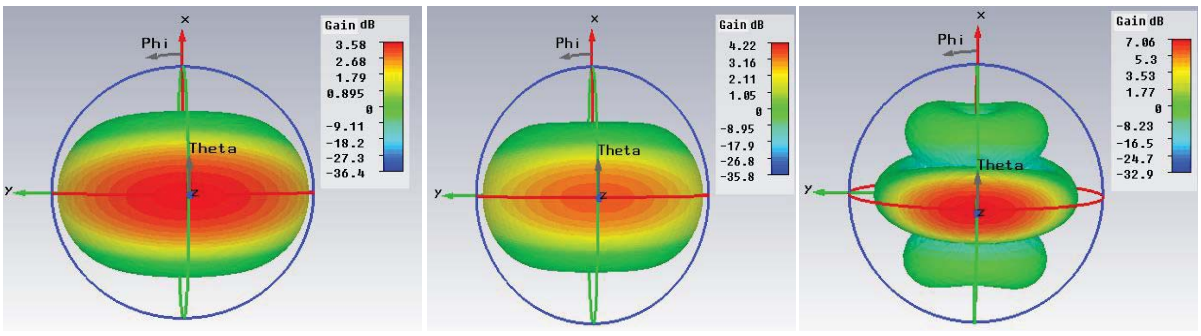

(a) (b) (c)

Figure: 9 1D and 3D Radiation Pattern (a) 2.49 GHz, (b) 3.45 GHz, (c) 5.66 GHz.

The ideal value of Envelope correlation coefficient (ρ) should be less than 0.07 for a mobile base station. Then for mobile terminals, the value for ρ should be 0.5 or less. From the figure 10 the Envelope correlation coefficient will be less than 0.05 for all the operating frequencies. Figure 11 shows the photographs of fabricated multiple input multiple output antenna.Table III gives the comparison of simulated results for single antenna and multiple input multiple output antenna.

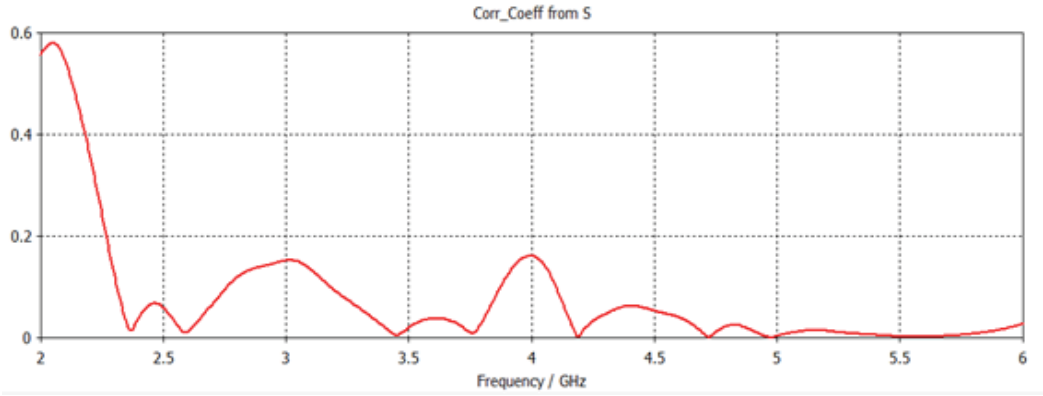

Figure:10. Envelope correlation vs frequency for MIMO.

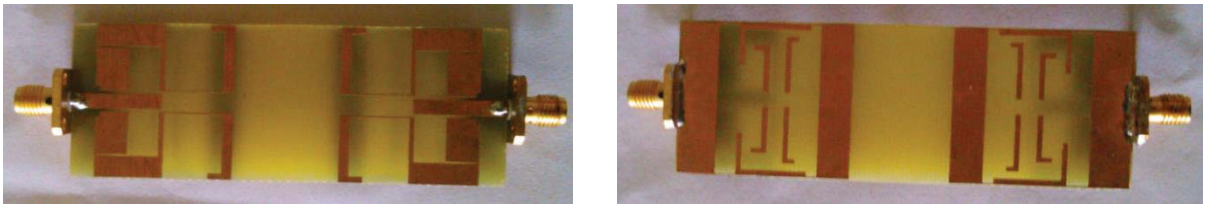

Fig. 11 Back view of fabricated MIMO Microstrip Antenna

Table:III Comparison of designed antennas.

Antenna Type	Frequency Range	Return Loss	Bandwidth	Gain
SISO	2.39 GHz - 2.86 GHz	-30 dB	470 MHz	2.66 dB
	3.10 GHz - 3.68 GHz	-32 dB	550 MHz	3.02 dB
	5.08 GHz - 5.96 GHz	-27 dB	900 MHz	4.09 dB
MIMO	2.37 GHz - 2.76 GHz	-21 dB	400 MHz	3.58 dB
	3.15 GHz - 3.67 GHz	-31 dB	520 MHz	4.22 dB
	4.99 GHz - 5.96 GHz	-31 dB	980 MHz	7.06 dB

Conclusion: A compact microstrip slot antenna is designed for a triple band operation is presented. The proposed antenna is composed of a ground plane on which a rectangular slot is etched and a Pair of L strips embedded in the slot and S shaped parasitic elements are added on other side of the substrate that enables proper adjusting of the resonant bands. The simulation results of the triple band microstrip slot single antenna with bandwidths of 470 MHz (2.39 GHz - 2.86 GHz), 550 MHz (3.13 GHz - 3.68 GHz) and 900 MHz (5.08 GHz - 5.97 GHz) are obtained. Next, a study was performed to implement the single antenna into 2x1 MIMO arrangements on the same circuit space. The simulation results of the MIMO antenna with bandwidths of 400 MHz (2.37 GHz - 2.76 GHz), 520 MHz (3.15 GHz - 3.67 GHz) and 980 MHz (4.99 GHz - 5.96 GHz) are obtained and it shows that the MIMO antenna is suitable for working in Bluetooth (2.4GHz – 2.5 GHz), 4G LTE (2.5 GHz – 2.69 GHz), WLAN (2.4/5.2/5.8 GHz), and WiMAX (2.5/3.5/5.5 GHz) applications. Because of the good electromagnetic property and compact size, the antenna is competitive candidate for

multimode wireless communication applications. The proposed antenna can be an excellent choice for Bluetooth, 4G LTE, WLAN and WiMAX applications due to its small size, simple structure, good multi-band characteristics, nearly omnidirectional radiation pattern, better mutual coupling and envelope correlation coefficient over the three bands.

References

[1] Lin Dang, Zhen Ya Lei, Yong Jun Xie, Gao Li NIng, and Jun Fan, " A Compact Microstrip Slot Triple-Band Antenna for WLAN/WiMAX Applications," *IEEE Antennas and Wireless Propagation Letters, Vol.9.2010.*

[2] J. Zhang, X.-M. Zhang, J.-S. Liu, Q.-F. Wu, T. Ying and H. Jin, "Dual-band bidirectional high gain antenna for WLAN 2.4/5.8 GHz applications", *Electronics Letters, 1st January 2009 Vol.45 No.1.*

[3] T. Wang, Y.-Z. Yin, J. Yang, Y.L. Zhang, and J.J. Xie, "Compact Triple-Band Antenna Using Defected Ground Structure for WLAN/WIMAX Applications", *Progress In Electromagnetics Research Letters, Vol. 35,164, 2012.*

[4] C.R. Byra Reddy, N.C. Easwar Reddy and C.S. Sridhar, "A Compact Triple Band Rectangular Microstrip Slot antenna for WLAN/WIMAX applications". *Journal of Theoretical and Applied Information Technology*, October 2011.

[5] Pradutt K. Bharti, H. S. Singh, G. K. Pandey, and M. K. Meshram, "Slot Loaded Microstrip Antenna for GPS, Wi-Fi, and WiMAX Applications Survey", *International Journal of Microwaves Applications,* April 2013.

[6] Ramesh Garg, Prakash Bartia, Inder Bahl, Apisak Ittipiboon, ''*Microstrip Antenna Design Handbook'', 2001,* pp 1-68, 253-316 Artech House Inc. Norwood, MA.

[11] Pozar, D. M., and D. H. Schaubert (Eds), ''*The Analysis and Design of Microstrip Antennas and Arrays,* IEEE Press, New York, 1996.

[13] Nurulrodziah BT Abdul Ghafar, ''*Design of a Compact Microstrip Antenna at 2.4 GHz'',* MSc thesis, Department of Electrical – Electronics & Telecommunications, Faculty of Electrical Engineering, Universiti Teknologi, Malaysia, Nov, 2005.

[14] Pozar, D. M., ''*Microstrip Antennas'', Proc. IEEE,* Vol. 80, 1992, pp. 79-91.

[15] MSc Thesis, ''Design of a patch Antenna'', chapter 3, Internet source,Florida State University, [http://etd.lib.fsu. edu/theses/ available/etd -0412004-143656 /unrestricted/ Chapter3.pdf] as on 2009/01/10

[16] Z. I. Dafalla, W. T. Y. Kuan, A. M. Abdel Rahman, and S. C. Sudhakar, ''*Design of rectangular Microstrip patch antenna at 1GHz''*, Multimedia University, Faculty of engineering and technology, Melaka, Malaysia. 2004, ''*RF and Microwave Conference, October 5-6''*. Malaysia.

DECEMBER 17, WENESDAY
03.00PM TO 04.00PM
RESEARCH SESSION 2
MICROWAVE DEVICES 1
S N MITRA - HALL

Chair: Dr. D. Guha, Univeristy of Calutta, Calcutta, India.

No	Papers	Page
2.1	**Design of a Four-Way 5 kW, 325 MHz Wilkinson Power Combiner for RF Accelerator** B. V. Ramarao[1], S. Sonal[1], J. K. Mishra[1], M. Pande[1], P. Singh[1], G. Kumar[2], and J. Mukherjee[2] [1]Ion Accelerator Development Division, BARC, Mumbai-85 E-mail: bvram@barc.gov.in [2] Indian Institute of Technology, Bombay, Powai, Mumbai – 400076	41
2.2	**Design and Development of A Novel Mitre Bend for Interferometer Used in Plasma Density Measurement** [1] P. K. Atrey, [2] D. A. Pujara and [1] S. Mukherji [1]Institute for Plasma Research (IPR), Gandhinagar *E-mail: atrey@ipr.res.in* [2]Institute of Technology, Nirma University, Ahmedabad-382481, *dhaval.pujara@nirmauni.ac.in*	45
2.3	**Single Conversion Frequency –Hopped L-Band Transceiver for Software Defined Radio** Sanjib Kumar Mandal [1], Sachin Oberai [2], V.N.Singh [3], and R.S.Pundir [4] Defence Electronics Application Laboratory Dehradun - 248001, Uttarakhand [1]*E-mail: sanjibkumar.mandal@deal.drdo.in*	47
2.4	**SOLID STATE RF POWER AMPLIFIER AT 27.12 MHz** Sujo C.I and Gopal Joshi, BARC, Mumbai, India, 400085. *E-mail: sujo@barc.gov.in*	51

Design of a Four-Way 5 kW, 325 MHz Wilkinson Power Combiner for RF Accelerator

B. V. Ramarao (1), S. Sonal (1), J. K. Mishra (1), M. Pande (1), P. Singh (1), G. Kumar (2), and J. Mukherjee (2)*

(1) Ion Accelerator Development Division, BARC, Mumbai-85 mail: bvram@barc.gov.in

(2) Indian Institute of Technology, Bombay, Powai, Mumbai - 400076

Abstract: A four way high power combiner has been designed at 325 MHz. Equivalent circuit parameters have been calculated, which simplified the design by providing initial physical parameters of the combiner for EM simulation. Electromagnetic simulations have been carried out to estimate the effects of physical dimensions over the RF performance parameters of the power combiner. The fabricated power combiner has insertion loss of 0.23 dB and output return loss better than 30 dB. The power combiner has been tested up to 3.2kW, CW at 325 MHz using four solid-state high power amplifier modules. The efficiency of the power combiner is better than 94%.

Introduction: Due to the advancement of Laterally Diffused Metal Oxide Semiconductor (LDMOS) technology, the development of high power Solid-State Power Amplifier (SSPA) for RF accelerators has become practicable even up to power levels of tens of kilo watts. The SSPA has several advantages over the vacuum tubes and klystrons like low voltage power supplies, low power circulators, long life time, etc. In addition to these advantages, the cost of the SSPA is also comparable to vacuum tubes and klystrons [1].

Since the power output of the solid-state devices is limited to less than one-kilo watts at UHF band, a high power combiner is essential to develop high power solid-state amplifier. The power combiners have been designed in both planer and waveguide technology. Since the planer devices have limited power output, a waveguide type power combiner is preferred at output power >2 kW. Design of a coaxial waveguide type 8-way radial power combiner with both circuit analysis and EM analysis has been presented in [2]. This power combiner has power handing capacity of 2.5kW, CW. The design equations and 3D electromagnetic modeling of the radial power combiner is presented in [3]. More simpler and compact 18-way radial power combiner for 5 kW output power has been designed and used for RF accelerator at 500 MHz [4]. All these designs are based on radial power combiners only. The radial power combiners have less isolation at smaller number of input ports (<5). They have better isolation of >10 dB for 16-way and 18-way devices. A 4-way and 8-way Wilkinson power combiners rated for 1 kW and 2.5 kW at 350 MHz have been designed and used for RFPA development [5].

In this paper, hybrid method of designing the four-way Wilkinson type power combiner is presented. Initial design is based on the formulas and circuit simulations. EM simulations have been carried on the initial design to optimize the power combiner. The field strength simulation of the power combiner indicates the device can be usable up to 50 kW pulse and 5 kW, CW at 325 MHz.

Design of Power Combiner: The geometry of the power combiner is shown in Fig. 1 (a). It is a basic Wilkinson type 4-way power combiner with radial input signal launches [6]. It consists of an inner cylinder which has been split into four equal splines, a thin metal disc joining the splines, an outer cylinder, a taper section, and a teflon disc to support the splines and also to maintain the spacing between the splines. Longitudinal and radial parameters of

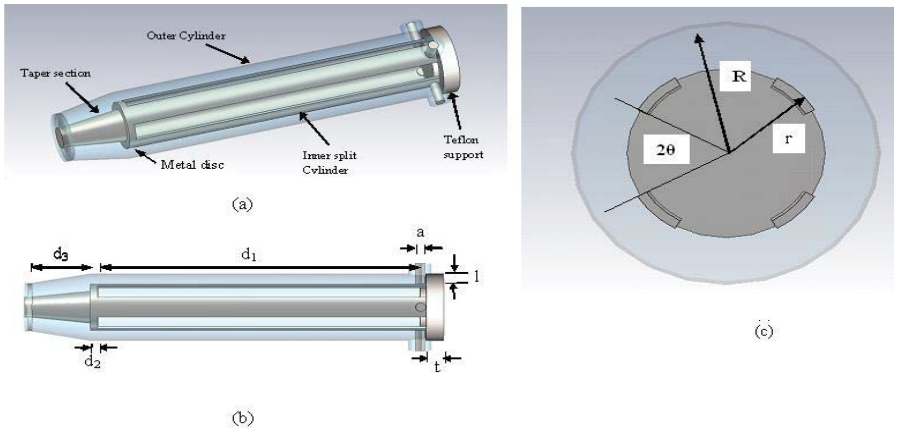

Fig. 1. (a) Geometry of the 4-way power combiner, (b) radial and (c) longitudinal parameters

the power combiner are shown in Figs. 1(b) and 1(c), respectively. The descriptions of the physical parameters of the power combiner are given in Table 1.

TABLE 1: DESCRIPTION OF THE PHYSICAL PARAMETERS OF 4-WAY POWER COMBINER

Parameter	Description	Value (mm or deg.)
d_1	Length of the splines from launch point to metal disc	220
d_2	Thickness of the metal disc joining the splines	7
d_3	Length of the taper section	40
l	Length of the input launch pin	7
a	Diameter of the input launch pin	4
t	Spacing between splines end and back plate (thickness of Teflon disc)	12
r	Outer radius of the inner split cylinder	20
R	Inner radius of the outer cylinder	27
θ	Half of the cut angle of the inner cylinder	20
s	Radial spacing between two adjacent splines(=r*2 θ)	13.96

The electrical equivalent circuit of the RF power combiner is shown in Fig. 2. Ports 1 to 4 are input ports and port 5 is the output or combining port. The terminating impedance of these ports is Z_o. The series inductance L_1 of the equivalent circuit is due to finite length of the input feed pins. The shunt capacitance C_1 accounts for the capacitance between splines and the back plate with PTFE (Teflon) as dielectric material. The coupling capacitor C_2 between the splines is the result of capacitive coupling between the adjacent splines. Z and d_1 are the characteristic impedance and length of the splines, respectively. The capacitance C_3 arises from the metal disc, which joins all the splines at the combiner end. Its value depends upon the thickness, d_2 of the disc and spacing between metal disc and outer cylinder. The characteristic impedance of the taper is Z_o and its length is d_3. The initial circuit parameters are calculated based on the design of Wilkinson power combiner [7].

The main coaxial line is air dielectric and the length of the splines is quarter wave length, $\lambda_o/4$ at the operating frequency of 325 MHz, which is calculated to be 220 mm. The characteristic impedance of the splines Z depends on the circumferential spacing between the two splines and the outer conductor. The initial value of the Z is given by $Z = Z_o * sqrt(N)$ where, Z_o is impedance of the external source or load and N is the number of input ports, which is 4 in this 4-way power combiner. The Z is calculated to be 100 Ω. The characteristic impedance of the un-split coaxial line is $Z_c = Z_o/sqrt(N)$, which is 25 Ω. Since it is a high power combiner, the spacing between the two conductors is chosen to avoid the break down between the conductors. The spacing between the conductors, s is chosen as 7 mm with safety factor of >10 for 5 kW CW operation. The inner radius (r) and outer radius (R) are

calculated using $Z_c = 60 \ln(R/r)$, where outer radius, $R = r+s$. The capacitor C_3 is a coaxial capacitor with plate thickness of d_2, $C_3 = 2\pi\epsilon d_2 / \ln(R/r)$. The length of the constant impedance taper line, d_3 is chosen as 40 mm to have smooth transition of electric fields and also to match output 1-5/8" EIA dimensions. The inductance L_1 is calculated using the input ;th, l=7 mm). The calculated circuit

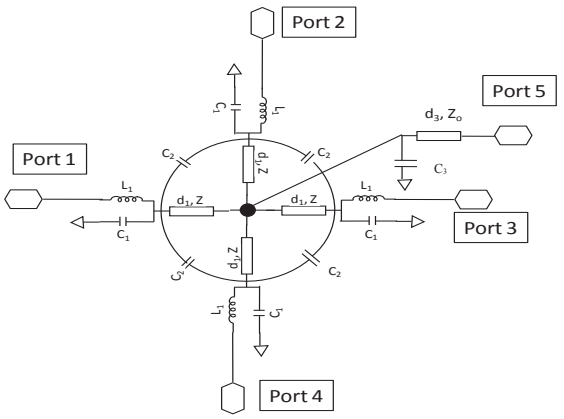

LE 2: CIRCUIT PARAMETERS

t eter	Calculated value
	2 pH
	2 pF
	0.2 pF
	100 Ω, 220 mm
	50 Ω, 40 mm
	1.2 pF

EM Simulation: Based on the calculations and circuit simulations, the initial geometrical parameters are shown in Table 1. Electromagnetic (EM) simulation is carried out on this geometry with these initial geometrical parameters in microwave studio. The cutting angle between the adjacent strips 2Θ, the distance to back cover plate (thickness of Teflon disc) t, and metal disc thickness d_2 are chosen as variable parameters. RF performance parameters of the power combiner have been studied against the variation of these parameters.

The change in the output match, input match, insertion loss, and isolation with respect to 2Θ is shown in Fig. 3. At the cutting angle of 60^o, output match $|S_{55}|$ is better than 40 dB at 325 MHz but the isolation is poor and it is >25 dB. Also input match is only at -13 dB. At the cutting angle of 40^o both isolation and input match are better, and output match is also better than 35 dB. The output match is better at the disc thickness d_2 of 4 mm. There is no pronounced effect on isolation and input matching parameters. The input return loss is better than 20 dB for a Teflon disc thickness of 6 mm. Other parameters are least affected. Optimized input and output return losses of the combiner are 18 dB and 43 dB, respectively at 325 MHz. The isolation among the input ports is better than 30 dB at 325 MHz. The insertion loss is <0.25 dB over a frequency bandwidth of 100 MHz.

Power handing capacity: The power combiner has been simulated with the actual power inputs. E and H field monitors have been observed for maximum field strengths. Under simultaneous excitations with each input of 850 W at 325 MHz, the maximum E-field is 1.21 MV/m at the metal disc joining ring, which is well below the break down limit of dry air (3 MV/m). The H-field is maximum near the input launches. The maximum surface currents (power losses) are well below the melting of copper (Cu) surfaces.

Results and discussion: The device has been fabricated in Copper material to have minimum insertion losses. To avoid the oxidation of its surfaces, inner parts are Gold plated with 1 micron thickness and outer parts are powder coated. Input power level is at ~1.3 kW, a suitable RF connector for this is 7/16" DIN connector, which is used for input signals. Whereas output or combined power is close to 5 kW at 325 MHz, so a suitable RF connector EIA:1-5/8" has been used at the output. The designed power combiner has been

characterized using a 4-port VNA. The measurement set-up of the fabricated power combiner is shown in Fig. 4. The measured input match is shown in Fig. 5(a). The $|S_{55}|$ is -33 dB at 325 MHz. The combiner has 30 MHz bandwidth over $|S_{55}|$<-20 dB. The measured transmission coefficients are shown in Fig. 5 (b). The maximum insertion loss is 0.23 dB. The amplitude imbalance between the ports is <0.25 dB at 325 MHz. The measured maximum phase imbalance is <2 degrees at 325 MHz. The measured results are in close agreement with the simulated results.

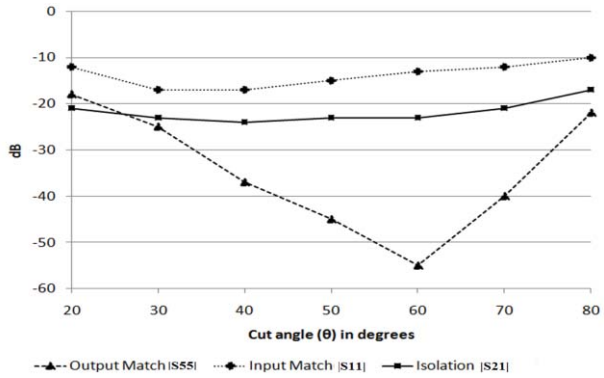

Fig. 3. Effect of cut angle (2Θ) on $|S_{55}|$, $|S_{11}|$ and $|S_{21}|$

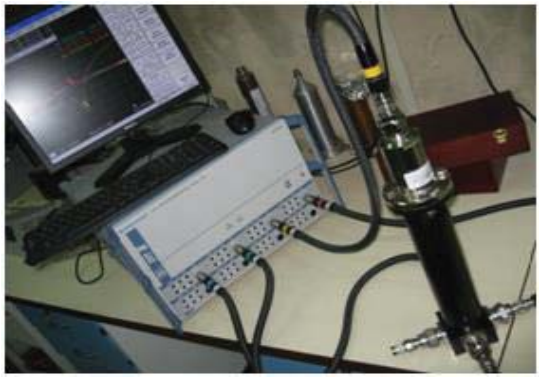

Fig. 4. Measurement set-up for combiner

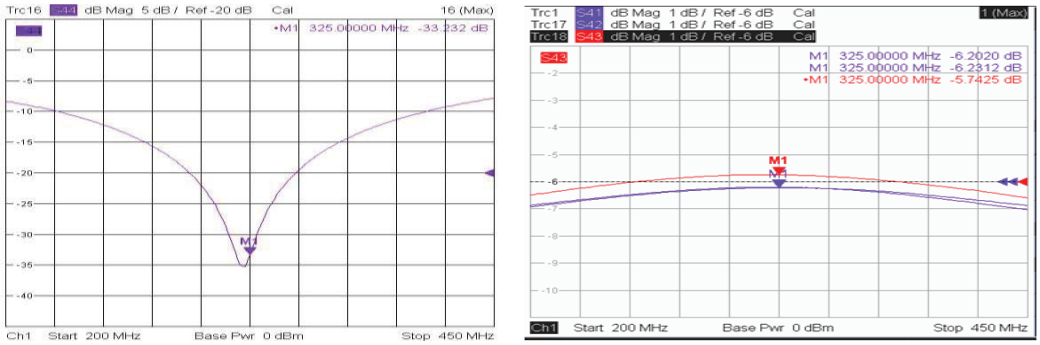

Fig. 5. (a) Measured $|S_{55}|$, and (b) $|S_{51}|$, $|S_{52}|$, $|S_{53}|$ of 4-way high power combiner

The 4-way high power combiner has been tested by combining four phase coherent power amplifier modules of 850 W each. The measured combined power output is 3.2 kW, so the total power loss is <6% of the input power implying efficiency of >94%. Also, at the power output of 3.2 kW, 325 MHz, no damage was noticed to the power combiner proving its high power capability.

References:

[1] M. Gasper, Solid-state RF PA: practicality, cost, potentials, feasibility, trend and outlook in: *5th CW and high average power RF work shop*, CERN, Geneva, Mar. 2008.

[2] M. Amjadi and E Jafari, "Design of a broad band eight way coaxial waveguide power combiner", *IEEE Trans. Microw. Theory and Tech.*, vol.60, no.1, pp. 39-44, Jan. 2012.

[3] A. E. Fathy, S. Lee, and D. Kalokithis, "A simplified design approach for radial power combiner" *IEEE Trans. Microw. Theory and Tech.*, vol. 54, no.1, pp. 247-255, Jan. 2006.

[4] M. Gasper, "A compact 500 MHz 4 kW solid-state power amplifier for accelerator applications", *NIMA, Section A*, 637(2011), pp. 18-24, 2011.

[5] J. K. Mishra, B. V. Ramarao, and Manjiri Pande, "Design and analysis of RF power combiner/splitters at 350 MHz", in Proc. InPac-2011, New Delhi, p. 251, Jan. 2011.

[6] E. Wilkinson, "An N Way Hybrid Power Divider", *IRE Trans. Microw. Theory and Tech.*, pp. 116-118, Jan. 1960.

Design and Development of a Novel Mitre Bend for Interferometer used in Plasma Density Measurement

P. K. Atrey[1,2], Dhaval Pujara[1] and S. Mukherjee[2]

[1]Institute of Technology, Nirma University, Ahmedabad
[2]Institute for Plasma Research, Gandhinagar
Email: atrey@ipr.res.in

Abstract — The guiding devices like transmission lines and wave-guides are generally used to transport the electromagnetic power from a source to a load. For such power transfer in millimeter wave interferometer and reflectometer employed for diagnostics in *TOKAMAKS,* oversized wave-guides and bends are often used. A mitre bend, described in the present paper is a special type of bend, with very low mode-conversion losses. The design and development of a double corner mitre bend is discussed in the paper. Testing of mitre bend is carried out on a test-bench with 136 GHz interferometer system. The measured transmission loss is found to be ~ 0.4 – 1.2 dB, which is very less as compared to a conventional round bend loss having loss of the order of 4 dB.

Index Terms — Interferometer, mitre bend, mode conversion losses, plasma density.

I. Introduction

Amongst the modern diagnostics of fusion plasmas, millimeter wave methods, both passive and active, play an important role. Millimeter wave interferometer and reflectometer are used to measure the properties of plasma such as the plasma density and its fluctuations in *TOKAMAKS* [1-2]. Ordinary waveguides become smaller and smaller as the frequency increases and the associated waveguide losses become intolerable even for relatively short distances. A 136 GHz interferometer is designed and developed to measure the plasma density in SST-1 *TOKAMAK* [3]. An interferometer is in fact used to measure the difference in path length between a reference beam, which is kept constant in path length, and a beam transmitted through the plasma. Since the losses in fundamental waveguides are very high, oversized waveguides are often used, especially at higher frequencies in the interferometer. The loss in fundamental waveguide (WR-8) is 6.5 dB/m, hence oversized waveguide (WR–90) is used which has low loss (i.e. 0.3 dB/m) at 136 GHz. To avoid mode conversion losses, a gradual transition from the fundamental to the oversized waveguides is used. In practical purposes, we need to have bends since the transmission paths need not be collinear. A bend in the oversized waveguide WR–90 can cause, mode conversion losses (~ 4 dB) at 136 GHz. A mitre bend is a type of bend in oversized waveguide, which has low mode conversion losses [4]. Since, we have ten bends in 136 GHz interferometer in SST–1 tokamak, it is better to use mitre bend to reduce the losses in the waveguide path.

II. Design and Fabrication

The design of a double corner mitre bend is shown in Fig. 1. The standing wave ratio introduced by such a corner is even less than 1.05. Such a mitre bend is designed and fabricated from a X-band (WR–90) copper waveguide. For $\theta = 90^{\circ}$, the angle θ /4 as shown in Fig. 1 is 22.5°. The length of an X – band waveguide is cut in three pieces at the angle of 67.5°as shown in Fig. 2 (a) and joined as shown in Fig. 2 (b) with silver brazing. The calculated length between the points A and C is 33.29 mm. Two square flanges are also brazed at the both ends of bend. Electroplating is done inside the waveguide.

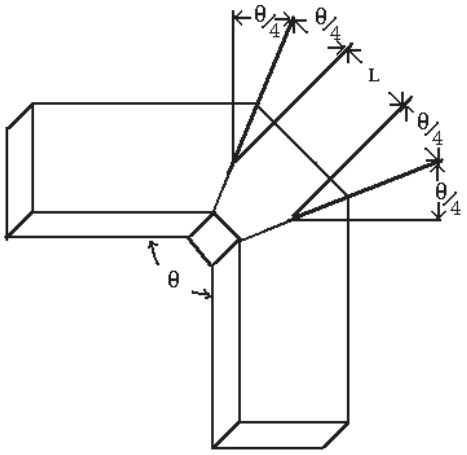

Fig. 1 Proposed double corner mitre bend

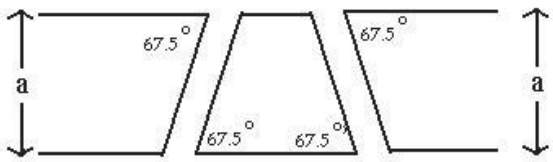

(a)

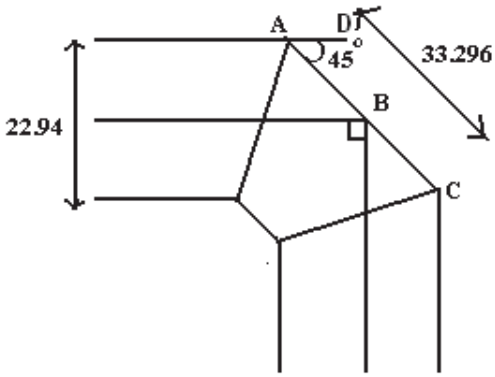

(b)

Fig. 2 Mitre bend fabrication steps (a) and (b)

III. Experimental Set-up, Results and Discussion

Once the mitre bends were designed and fabricated, they were tested on a specially developed experimental set-up. The photograph of the complete set-up is shown in Fig. 3.

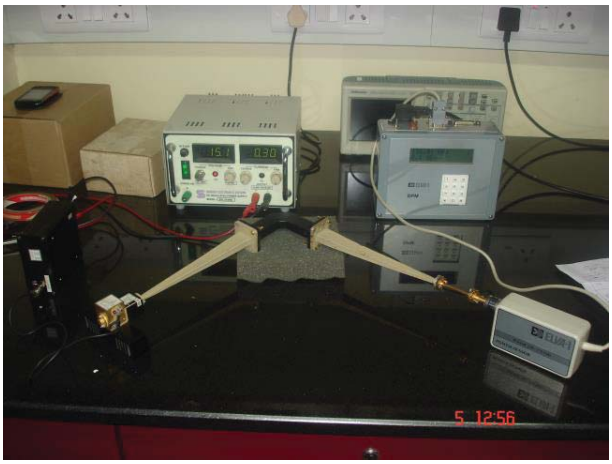

Fig. 3 Photograph of an experimental set-up

The set up includes a Gunn Oscillator as a source operating at 136 GHz with power output of approximately 8 dBm. The output of the source is fed to an isolator. Two transitions (F - band to X - band) are used after the isolator. The power meter is used after the second transition to detect the output power. First, output power (P_1) is measured without the bend between the transitions. Then bend (conventional round or mitre bend) is connected between two transitions and output power (P_2) is measured. The power loss is calculated using the formula:

Power Loss (dB) with conventional bend = $P_1 - P_2$ (1)

Both conventional bend and mitre bends are tested and the results are summarized in Table I. All the ten mitre bends are tested and found the loss between (0.4 dB to 1.2 dB). As shown, the measured power loss in case of a mitre bend is very less (~0.4 – 1.2 dB) as compared to the measured power loss of a conventional round bend (~4 dB). The variation in loss of mitre bends may be attributed to fabrications and measurements error.

IV. Conclusion

A double corner mitre bend is designed and fabricated in X – band waveguide. Testing of the mitre bend is carried out on a special test bench with 136 GHz system. The measured power loss is found to be in the range of 0.4 to 1.2 dB, which is quite less as compared to a conventional round bend loss i.e 4 dB.

TABLE I
Summary of Measured Results

S. No.	Power Output without Bend P_1 (dBm)	Power Output with Conventional Bend P_2 (dBm)	Power Loss due to Conventional round Bend (dB)	Power Output with Mitre Bend P_2 (dBm)	Power Loss due to Mitre Bend (dB)
1.	7.3	3.3	4.0	6.9	0.4
2.	7.3	3.3	4.0	6.1	1.2
3.	7.3	3.3	4.0	6.5	0.8
4.	7.3	3.3	4.0	6.7	0.6
5.	7.3	3.3	4.0	6.9	0.4
6.	7.3	3.3	4.0	6.8	0.5
7.	7.3	3.3	4.0	6.3	1.0
8.	7.3	3.3	4.0	6.5	0.8
9.	7.3	3.3	4.0	6.8	0.5
10.	7.3	3.3	4.0	6.8	0.5

References

[1] M. A. Heald and C. B. Wharton, "Plasma Diagnostics with Microwaves" J. Wiley, New York, 1978, pp-121.
[2] P. K. Atrey, S. B. Bhatt etal., "Measurement of chord averaged density in Aditya using 100 GHz and 136 GHz interferometer" Indian J. Phys., 66B, pp. 489-492, 1992.
[3] Y. C. Saxena and SST-1Team, "Present status of SST-1 project" Nuclear Fusion, 40, pp. 1069 , 2000,.
[4] J. L. Doane and T. N. Anderson, Microwave Journal, pp. 153-160, 1989.
[5] P. K. Atrey and K. K. Jain, *"Design and Fabrication of Mitre Bend",* Presented in 18th National Symposium on Plasma Science and Technology (Plasma-2003), BIT Mesra, Ranchi, Dec. 8-11, 2003.

Single Conversion Frequency –Hopped L-Band Transceiver for Software Defined Radio

*Sanjib Kumar Mandal [(1)], Sachin Oberai * [(2)], V.N.Singh [(3)], and R.S.Pundir [(4)]*
(Defence Electronics Application Laboratory)
Dehradun-248001, Uttarakhand
Phone: (0135)2223085, Fax No: (0135) 2787265
[1]e-mail: sanjibkumar.mandal@deal.drdo.in

***Abstract:** in this paper a compact integrated transceiver module at L-Band is described that was designed for Software Defined Radio application. A single down conversion with fixed IF at 70 MHz is used for compact size and direct up-conversion architecture is adopted for transmitter path. This transceiver is capable of frequency hopping in its entire band (940 to 1260 MHz) of operation. Electrical imperfections of the circuit like non linearity, gain compression,inter modulation,spurious,harmonic level, gain variation over frequency band has been simulated in Agilent's ADS(Advance Design System) software for the prediction of performance as well as optimization of gain for both receiver as well transmitter path for required specification. A PSOC is also introduced for required control signal generation and baseband interface. To fabricate the transceiver commercially available ICs are used on multi-layer (ten) FR4 PCB. The experimental result shows that RF Transceiver has perfect performance for SDR Application.*

Introduction: The well known types of the conventional communication systems are designed to transmit and receive on a single fixed frequency channel. These systems are vulnerable to jamming, interference, and multipath problems. It was found that, the repeated switching of frequencies during RF transmission according to specific techniques which is known as frequency hopping will minimize the sensitivity of the system to jamming and interference as well as solves some of the multipath problems. Software Defined Radio (SDR) is that in which the radio parameter i.e. transmitter modulation, B.W, Channel etc can be totally configured by the software so that a common platform can be used across a number of users and applications.SDR may provide flexible ,upgradable ,multi standard terminals for the military communication infrastructure[1].

Transceiver development for SDR is a challenge to design which include size weight, power issues, frequency hopping capability, portability of different waveform for different bandwidth application.Fig.1 below shows the typical Software Defined Radio implementation using current technology. This L-Band (960-1240MHz) frequency hopped RF-Transceiver includes receiver, transmitter, frequency synthesizer, Integrated PLO, and programmable system Chip (PSOC) controller which means the transceiver is mix of RF, Analog and Digital components. A need to deal concurrently with all these technology requires versatile software with capability of co-simulation of multidisciplinary models. Agilent ADS has been utilized for simulation of this transceiver

unit. This compact transceiver has been fabricated on multilayer FR4 Substrate and RF-IC package like QFM, LFCSP and TSSOP has been selected to suite the application.

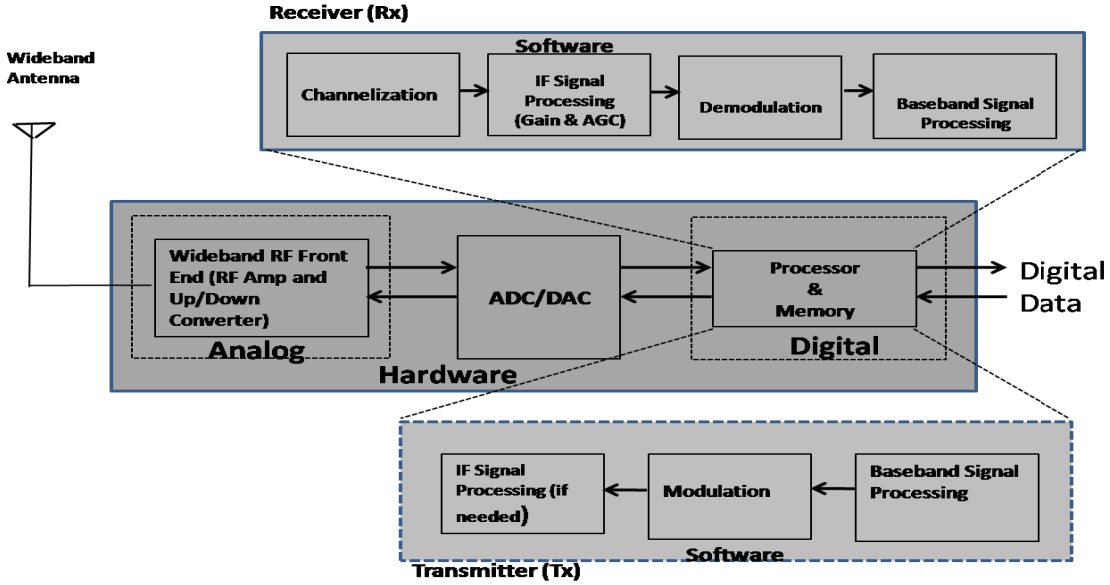

Fig.1. Typical SDR implementation using Current technology.

Description of Transceiver: The transceiver architecture include RF front end for frequency up and down conversion, LO circuitry to generate the required signals, PSOC (Programmable System On Chip) for generating control signals for DDFS(Direct Digital frequency Synthesizer),PLO(Phase lock Oscillator), Hopping Filter Frequency Selection , Tx/Rx selection and baseband interface .The RF subsystem is shown in figure-2& 3.

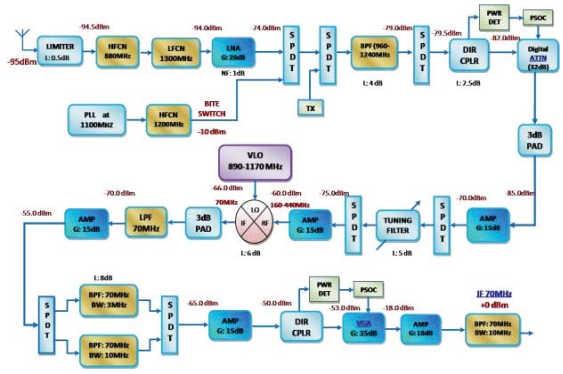

Fig.2. The block Schematic of Receiver

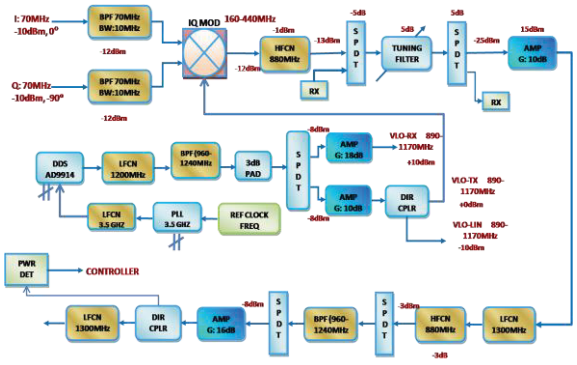

Fig.3. The Block Schematic of Transmitter & LO

The I/Q signal from baseband is filtered before getting in the I/Q modulator in the transmit path. The I/Q modulator is formed by image rejection mixers and a combination circuit for output. It converts the baseband I @70 MHz 0^0 and Q @ 70 MHz 90^0 phase signal to RF signal (960 MHz to 1240 MHz).A tunable band pass is inserted in between modulator and gain block to meet our requirements such as Adjacent channel power rejection(ACPR) and EVM. The receiver is based on single conversion superhetrodyne architecture. The receive path include Low noise amplifier (LNA), mixer and limiter and a directional coupler for RSSI input for VGA gain selection. The Dynamic Range (80 dB) is achieved using one VGA and one Digital attenuator. The mixer convert the incoming RF (960 MHz to 1240 MHz) to a fixed IF @ 70 MHz with the help of variable LO (890 to 1170 MHz) generated by DDFS. The SAW Filter at o/p gives the required S/N for the signal. At IF two selectable different

bandwidth saw filter is incorporated for different waveform application. The LO circuitry, Band pass filter and tunable hopping filter is shared by both Tx/Rx using T/R switch, to reduce the size of half-duplex mode of operation of the transceiver for SDR. The clock for DDFS is provided by on board PLO at 3.5 GHz.

Design Flow & Simulation of the Transceiver: A typical design approach for any system can be broken down into steps like specification of the design goal, formulation of the design constraints, trade-off Analysis, preliminary design. Design analysis, optimization, interface parameter sensitivity analysis and experimental design verification. A most popular approach for modeling and simulation of the mix signal systems is behavior modeling which is efficient and invaluable for verification purpose has been utilized for the said purpose. Behavior model of the RF blocks like amplifier, filters, frequency converters, carrier synthesizers and power distribution have been considered for the design of RF transceiver. These models play a key role in deciding the design flow[2].

The design of the Transceiver has been carried out with a mix of two design approaches i.e. Top-Down and Bottom up approach. Design was initiated from highest level of abstraction i.e. specifying required performance of the system and transforming to the lowest level of abstraction i.e. Design details up to schematic and layout level. Top down design approach of realizing systems confirms best performance but at the expense of time and cost. Bottom up design is carried out by configuring the system around available components. We have designed RF transceiver using mix of these two approaches. Details of the components have been worked out for required performance after simulation of the signal flow through the system. Wide range of tolerances has been considered at the interface levels and RFIC/MMIC modules have been selected from various vendors. The simulation schematic for receiver and its results is shown in figure 4 & 5 respectively [3,4].

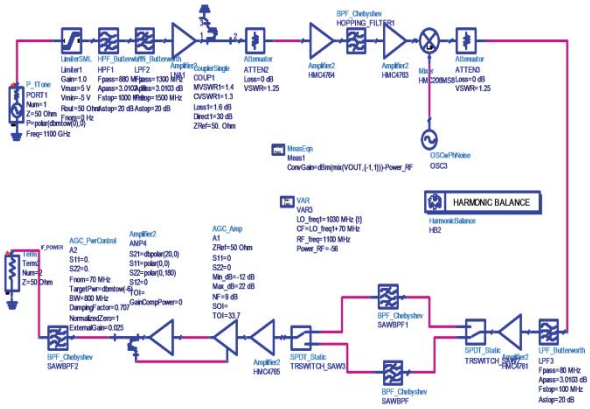

Fig.4 Simulation schematic of Receiver

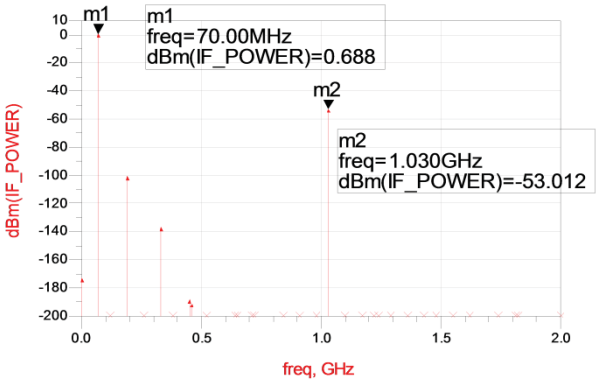

Fig.5 Simulated IF spectrum at output.

The transmitter simulation schematic and its simulation result is shown in Figure 6 & 7 respectively.

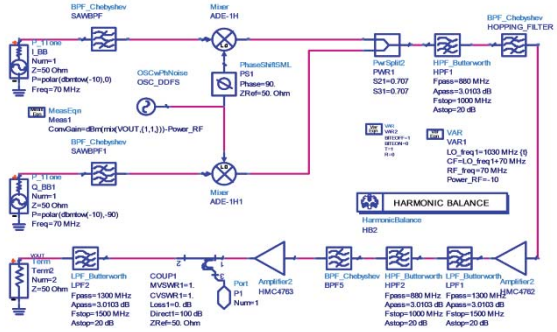

Fig.6 Simulation schematic of transmitter

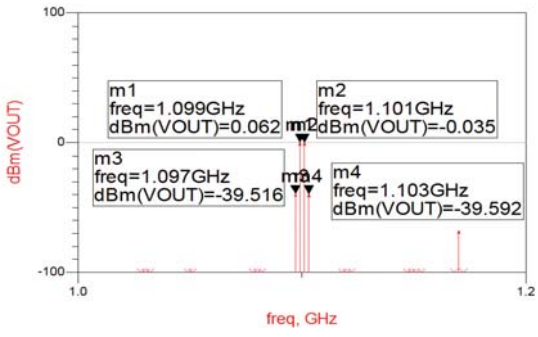

Fig.7. Simulated Result for IMD at 1100 MHz

Hardware fabrication and Test results: At microwave and RF frequencies the use of micro strip circuitry has many advantages over other methods, particularly because chip components can be mounted directly on to the micro strip tracks on the outer surface of the board. The high density of the components mounted on the transceiver unit board meant that a multilayer board was used in order to make various powers and circuit connections. A 10 layer PCB is used in an epoxy /glass FR4 material. The tested noise figure of the receiver is 3.4dB, which is better than the required specification and very close to the simulated result. The measured LO phase noise is perfect: - 92dBc @ 10 kHz offset and -113dBc @ 100 kHz offset. An OCXO is used as the reference source for the synthesizers, the frequency stability is better than 0.5ppm. The measured Tx output power is + 0 dBm±3 dB and spur level is greater than -50dBm.

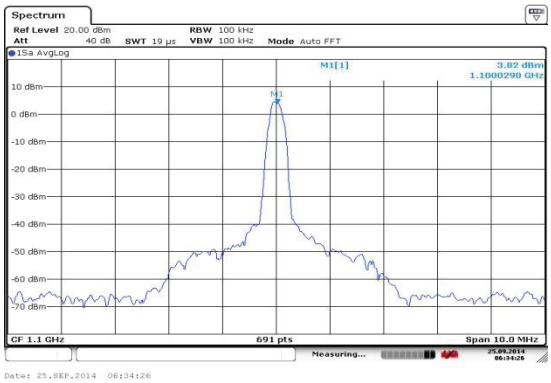

Fig.8 Transmitted output spectrum at 1.1 GHz

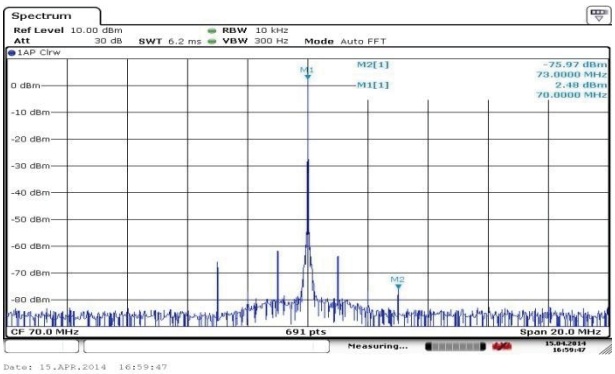

Fig.9. Receiver IF spectrum for i/p -60 dBm

Conclusion: In this paper the methodology for the frequency domain system-level analysis of transceiver front end architectures for SRD was presented. The simulation tool takes into account of models for all relevant non-ideal effects in front-ends such as noise, aliasing, distortion, phase noise etc. The simulations are performed with dedicated frequency –domain simulation tools that processes input power spectra. The DDFS (Direct Digital Frequency Synthesis) used as variable LO with on-board PLO at 3.5 GHz as clock enable the RF transceiver for frequency hopping application in SDR.The design also validated by fabricating its PCB and different waveform also have been tested with baseband module of SDR which meet the system requirement.

Acknowledgement: The authors express their sincere gratitude and thanks to Shri RC Agarwal, Director DEAL for his kind permission to publish the paper. Authors are thankful to Shri S.O.Gupta, Group Head RFSG for continuous guidance and technical discussion.

Reference:

[1] B. Razavi, "Challenges in portable RF transceiver design," Circuits Devices,pp. 12–25, Sept. 1996.
[2] System-level analysis of RF transceiver-integrated circuits, Donnay, S. ; IMEC, Leuven, Belgium Geilen, G. Mixed-Signal Design, 1999. SSMSD '99. 1999 Southwest Symposium .
[3] B. Razavi, RF Microelectronics, Prentice-Hall,1998.
[4] K. Mayaram, et.al., "Overview of computer-aided analysis tools for RFIC simulation: algorithms, features and limitations", Proc. CICC 97, pp.505-5 12.
[5] J. Crols, S. Donnay, M. Steyaert, G. Gielen, "A high-level design and optimization tools for analog RF receiver front-ends", Proc. ICCAD 95, pp.550-553.
[6] Min et al. "An all-CMOS architecture for a low-power frequency hopped 900 MHz spectrum transceiver,- Proc of the IEEE Custom Integrated circuit Conference, pp. 379-382, 1994.

SOLID STATE RF POWER AMPLIFIER AT 27.12 MHz

Sujo.C.I and Gopal Joshi

BARC, Mumbai, India, 400085,Email: sujo@barc.gov.in

Abstract: *A solid state RF power amplifier has been developed and tested at 27.12 MHz, up to 900W.Class AB configuration has been used in this design. The RF amplifier is built in two stages and N channel Enhancement type MOSFET has been used in the power stage. Control electronics to monitor various parameters of the RF amplifier and also to protect the RF amplifier against over temperature, over drive and high reflected power has been developed. The unit is water cooled and 19" rack mountable. It is observed that the temperature is less than 60^{o}C when measured very close to the power MOSFET.*

Introduction: A solid state RF power Amplifier has been designed, developed and tested at 27.12 MHz, up to 900W, with 50 ohm load in Electronics Division, BARC. The RF amplifier was also tested with plasma load for mass spectrometric applications with impedance matching unit. N channel enhancement mode MOSFET which can withstand high load mismatch (vswr 65:1) has been selected for the design. The RF amplifier has been tested successfully under different mismatched load conditions also. This paper describes the design, development and salient features of the RF power amplifier developed.

Description of 900W,27.12MHz RF Power Amplifier: The RF power amplifier which is developed in class AB has been tested up to 900W at 27.12 MHz. It has been developed in two stages .The total gain of the RF amplifier is found to be 71db at an output of 900W. Sinusoidal or pulsed RF input to the amplifier can be given from an external RF source. In the first stage, 4W RF power is generated. It is housed in a separate instrumentation bin. The 900W RF power is generated in the main power amplifier bin.

50V, N channel enhancement type MOSFET has been used in the power stage. It is a single device which can deliver up to 1KW and can withstand full reflected power. Gain of the device is found to be 27dB.The device consists of two N channel MOSFETS and Push pull configuration has been implemented in the design. Thermal resistance of the device is 0.15^{o}C/W. Centre tapped transformer has been used at the input to generate 180 degree phase shifted outputs.

The output power is available through a directional coupler on the front panel on an N type connector. Control electronics have been developed to monitor various parameters of the RF amplifier and also to protect the amplifier against over temperature over-drive and excess reflected power.

The forward and reflected power from the directional coupler are routed to the front panel through the control electronics board. Electronics has also been developed to display the forward and reflected power and temperature on the front panel. Though RF power amplifier can safely withstand the full reflected power as per specifications of the device, control electronics was developed to limit the forward power, in case the reflected power exceeds 500W.

Fig.1 Preamplifier with control electronics

The transistors are mounted directly on a copper heat spreader with thickness of 1cm (fig.2). The surface smoothness is important and special care has been given to it. The heat spreader is then attached to the main heat sink made of aluminum. Heat sink compound is used at all thermal interfaces and the recommended transistor mounting procedure has been followed.

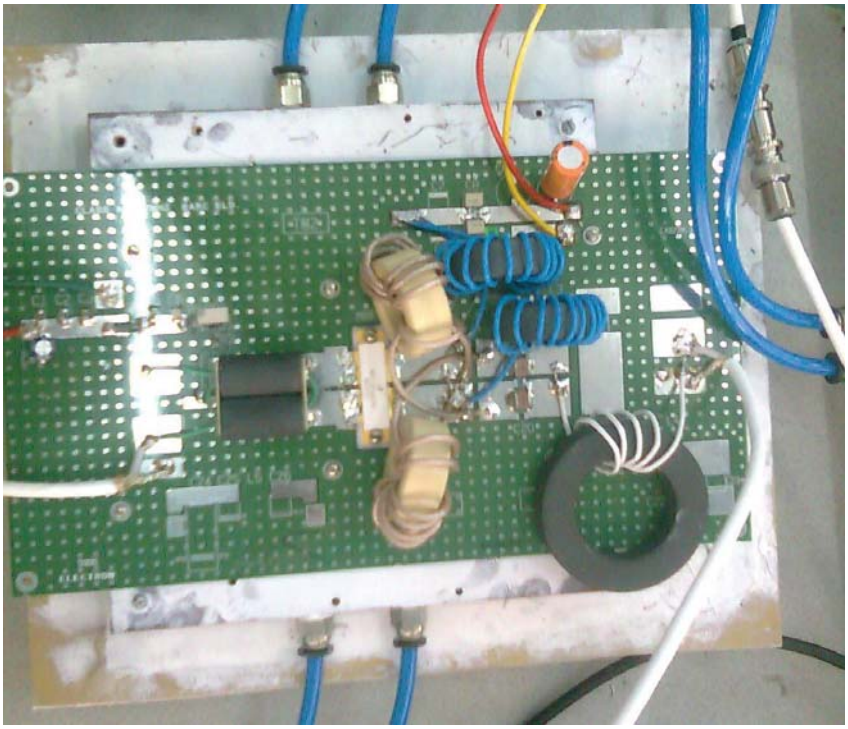

Fig.2 Power stage of 900W, Solid State RF Power Amplifier

Impedance Matching: Transformers have been used at the input and output of the device to match with 50 ohm . 2:1 coaxial type RF transformer has been used at the input side which acts as a splitter and also converts the input impedance of the device to 50 ohm.1:3 transmission line type transformer has been implemented at the output side which acts as a combiner and also matches the device to 50 ohm. LC networks has been used at the input and output side so as to optimize the performance of the device at 27.12 MHz.

RF simulation package was used to characterize the device and also to simulate the impedance matching .The simulation results are shown in fig (3)

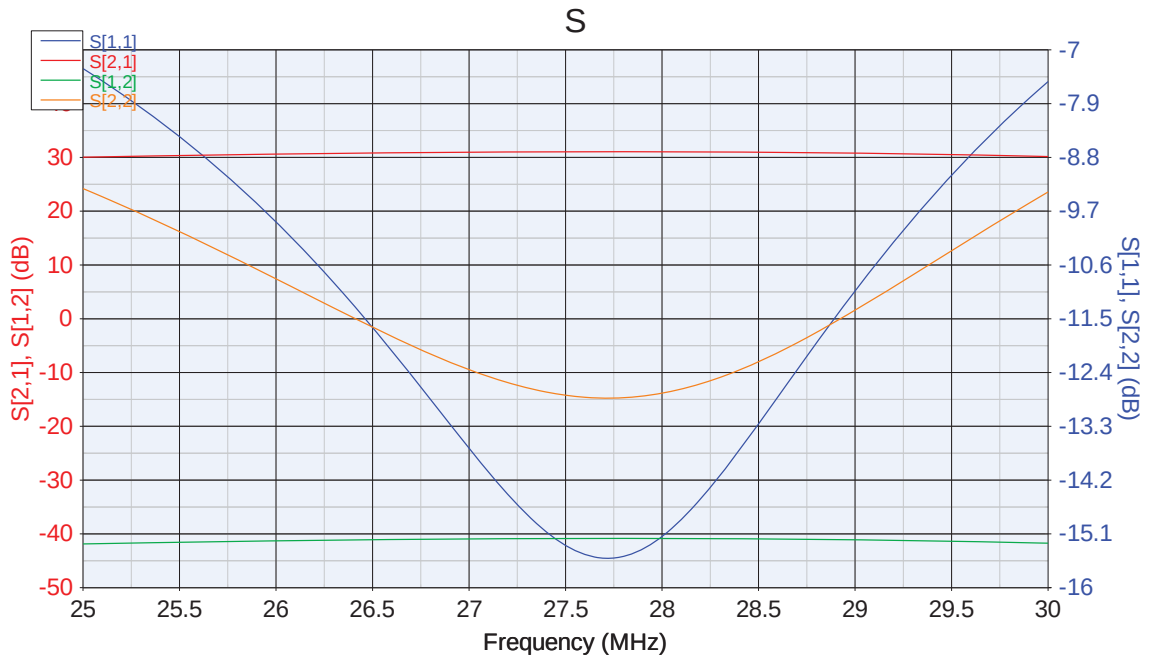

Fig.3 Optimized S parameters of RF Device obtained after simulation.

Test results of RF power Amplifier: The RF Power amplifier was tested at different drain voltages. An input of 48V, 26A has given output power of 900W with 72% efficiency. The RF amplifier was tested up to 925W with 50 ohm load. Table 1 gives the results of the testing.

Table1: Testing of gain and efficiency

INPUT (dBm)	CURRENT (A)	RF POWER (W)	EFFICIENCY %
-30	1.92	25	27.0
-27	4.22	60	29.5
-24	.01	140	36.3
-21	12.48	300	50.0
-18	18.45	540	60.8
-17	20.62	640	64.5

-16	22.68	740	67.8
-15	24.2	820	70.4
-14	25.37	860	70.5
-13.4	25.86	890	71.5
-12	26.8	925	71.7

Testing of the RF amplifier was also done under extreme load conditions. Different lengths of transmission lines were used in order to simulate different load conditions including open and short. It is found that the device is capable of withstanding full reflected power.

Development of Control Electronics: The RF input signal from a signal generator at 27.12 MHz is given to the Pre amplifier stage through the control electronics board. An RF switch is placed in the drive path of the low power stages of Power Amplifier. The RF switch will be made off in case of over-drive or over temperature situations. This removes the RF input signal to the Pre amplifier.

If the reflected power exceeds more than 500W, the forward power of the main RF amplifier will be limited to 500W using a limiter. A filter of required bandwidth has been used after the limiter so as to remove the higher harmonics. The reflected power has to be brought down below 100W so as to increase the forward power again.

Temperature sensor is located very near to the power device and if the temperature of the heat sink exceeds 70 degrees RF input to the power amplifier is switched off.

Conclusion: 900W ,27.12 MHz, solid state RF power amplifier has been designed ,developed and tested with 50 ohm load in class AB push pull configuration. Required control electronics to protect the power devices under extreme load conditions, over temperature and over-drive has been developed. This general purpose RF power amplifier can be used for different applications including plasma loads and NMR/ NQR. Recently the RF power amplifier was tested with plasma load at 900W RF power.

Acknowledgement: The encouragement and support given by Shri C.K. Pithawa, Director, E &I group and Dr. T.S.A. Krishnan, Head, Electronics Division are highly acknowledged. The authors are also thankful to Electronics division work shop and Ms. Charulatha Shinde for their help in realizing the power amplifier.

References:

1. Motorola Device Data (Vol-II)
2. Norm Dye and Helge Granberg, “Radio frequency Transistors”,2001
3. Mali Mahalingam and Edward Mares, “Thermal measurement methodology of RF Power Amplifier”,AN1955,Rev.1,4/2014

DECEMBER 17, WENESDAY
03.00PM TO 04.00PM
RESEARCH SESSION 3
BIOMEDICAL APPLICATIONS
G S SANYAL - HALL

Chair: Dr. K.P. Ray, Sameer, Mumbai. India.

No	Papers	Page
3.1	**Interaction of Mobile Phone radiation with Brain** [1]C. K. Smitha , [2]N. K. Narayanan [1]Department of Electronics & Instrumentation Engg. College of Engineering, Vadakara, Kerala- 673105, *E-mail: smi_c_k@yahoo.com,* [2]Department of Information Technology Kannur University, 670567, *E-mail: nknarayanan@gmail.com*	57
3.2	**Experimental validation of the numerical model of a commercial mobile phone for specific absorption rate assessment** Ashish Rojatkar and Vikass Monebhurrun Department of Electromagnetics, DRE-L2S, SUPELEC, 3 rue Joliot-Curie, 91192 Gif-sur-Yvette Cedex, France. *E-mail: ashish.rojatkar@supelec.fr*	61
3.3	**Investigation of Microwave Resonators for Monitoring Biological Parameters** M.P. Jayakrishnan, Divya Sathyanath, Sruthy Skaria, Thushara H.P., Karthika S. Nair , Anju Pradeep , S. Mridula and P. Mohanan Centre for Research in Electromagnetics and Antennas, Cochin University of Science and Technology, Cochin -682022, Kerala. *E-mail:jkmpjk@gmail.com,drmohan@gmail.com*	65
3.4	**Analysis of SAR of a Multi-Band Planar Inverted-F Antenna** Hrudya.B.Kurup[5], Vijesh.K.R[1], P.Mohanan[2], V.P.N.Nampoori[1] and Bindu.G [4] [1.]International School of Photonics CUSAT, Cochin- 22, [2.]Center for Research in Electromagnetics and Antennas Department of Electronics, CUSAT, Cochin- 22, Kerala, India, [3.]Swadesi Science Movement, [4.]Nansen Environmental Research Center, Cochin [5.]KMEA Engineering College. *E-mail: vijeshkr33@yahoo.com*	71

Interaction of Mobile Phone radiation with Brain

[1]C. K. Smitha , [2] N. K. Narayanan
[1]Department of Electronics & Instrumentation Engg.
College of Engineering, Vadakara, Kerala- 673105, smi_c_k@yahoo.com,
[2] Department of Information Technology Kannur University,
Kerala- 670567, nknarayanan@gmail.com

Abstract : *The concern about the adverse effects of mobile phone radiation on the nervous system has increased due to the drastic increase in mobile phone usage. In this paper, the mean value of sample entropy of EEG data set of 35 volunters with and without phone for 6 pairs of channels around ear is analysed using Kruskal Wallis test. The test result is significant for 6 channels. The maximum variation in percentage change of sample entropy is -1.21 to 8.22, while keeping GSM phone at Cz position.*

Keywords: *Mobile phone radiation, Sample Entropy, Kruskal Wallis test .*

I. INTRODUCTION

Some of the studies [1-5] conducted shows that long-term usage of mobile phones can damage health. Mobile phone generates a modulated radio frequency electromagnetic field (RF-EMF), which is a form of non-ionizing radiation, since the field cannot break chemical bonds. However, it is unknown whether mobile phone radiation could affect cellular and physiological activities by other mechanisms. Thermal effects are based on energy absorption from the field to the tissue, which causes the oscillation of molecules.

The high frequency microwave field cannot cause any regular changes in the ion movement due to their small absorption cross-section, inertial properties and viscosity of the liquid medium. But high frequency field can cause fluctuations and vibration of the charged particles and membranes. This phenomenon is similar to the effect of Brownian motion initiated by temperature rise. As a result of this the mobility of the ions and fluctuations in membrane motions are increasing without rise in temperature. The high frequency EM field and temperature have analogous effects on biological structures. The similarity of the effects is supported that low-level microwave exposure as well as low frequency EMF exposure induce changes in heat shock proteins as the temperature does.

The fluctuations, initiated by the high frequency EMF affect the gating variables and nerve cell properties. The impact of a low-intensity microwave radiation of order 0.1 - 10 W/m^2 is enough for redistribution of protein ion channels. This makes an impact on the value of the threshold for the action potentials initiation in the neural network. The change in the density of ion channels within ten percent of the equilibrium state can significantly alter the action potential threshold. This increases the probability of the spontaneous formation of the action potential. The change in the electrical potential of brain can be measured by EEG, hence we choose EEG signal for the analysis to find the effects of radiation on the brain.

Non linear dynamical systems such as neuronal networks generating EEG signals can display chaotic behavior and EEG generation can be described using sets of non linear differential equations. The level of chaos can be measured using entropy of the system [6]. Entropy is a measure of uncertainty. Higher entropy represents higher uncertainty and a more chaotic system. Sample entropy (SampEn) a nonlinear measure is selected to quantify the degree of complexity in EEG due to mobile phone radiation.

In the previous work by the same authors, signal complexity of single channel radiation is measured using various fractal methods includes Higuichi's method [7, 8]. The variation in the energy of single channel of the EEG signal at various frequency bands were analyzed using normalized wavelet energy and wavelet power [9, 10]. The result shows that there are some changes in the fractal dimension, wavelet Energy and wavelet power while using mobile phone. So in this paper we attempted to study the effect of mobile phone radiation on brain by analyzing sample entropy of EEG signals from 6 pairs of electrodes placed around ears.

This paper is organized as follows: Methods of feature extraction and analysis included in section 2. Results obtained and discussion in section 3 and conclusion and scope of further work in section 4.

II. METHODS

EEGs were recorded with 21 scalp electrodes placed as per conventional 10–20 system of electrodes, from EEG Lab under Neurology Department of Malabar Institute of Medical Sciences Hospital, Calicut using Galelio N.T machine.

A. ***Data Acquisition:*** This data set containing EEG record of 35 subjects of different age groups (27 to 67) for 5 minutes each for following 5 conditions : at rest, GSM phone at ears, GSM phone at vertex or Cz, CDMA phone at ears and CDMA phone at vertex or Cz. The volunteers were informed about the procedure of the study and all were participated voluntarily. During the procedure the volunteers were instructed to lie down and relax, EEGs were taken initially at rest and then the phone is switched on (in talking mode) and kept at the above described positions in succession. The volunteers were unaware of the instant of switching of mobile phone.

B. Preprocessing: Unwanted signals or artifacts (noises) can be removed by visual inspection and by filtering. A notch filter is used to remove 50 Hz line frequency. Wavelet algorithm using threshold filtering [11] is applied to de-noise the signal.

C. Feature Extraction: Behavior of EEG signals is unpredictable for relatively longer periods due to chaotic characteristics. The lengths of samples were taken as 128 points, equivalent to sampling rate, to get almost constant characteristics. Sample Entropy [12, 13] of each segment is calculated and average of this is used as feature parameter. Sample Entropy, $\mathrm{SampEn}(m, r) = \lim_{N\to\infty}\left(-\ln\left[\frac{B^{m+1}(r)}{B^{m}(r)}\right]\right)$ Where '*r'* is a coefficient of tolerance, '*m'* is the dimension of the template vector X_m. B_i is the count of distance between $X_m(i)$ and $X_m(j)$ is less than or equal to 'r'. For an embedding dimension m, the m-vector $X_m(i)$ is defined as $X_m(i) = [x(i), x(i+1), x(i+m-1)]$, i= 1, 2 … N-m+1. During each computation, 'm' is fixed to 2 and the width of the boundary is set as 'r' multiplied by the standard deviation (SD) of the original data set for the calculation of sample entropy.

D. ***Statistical Analysis- Kruskal Wallis Test:*** A hypothesis test [14, 15] is a method of making decisions using data from a scientific study. The two samples from a population have same statistical parameters, if measurements are made at similar conditions. Here non parametric test named Kruskal Wallis test is used for hypothesis testing since the feature parameter does not follow normal distribution characteristics. Kruskal Wallis test compares samples from two or more groups based on the median.

III. RESULTS & DISCUSSIONS

The sample entropy of six pairs of channels namely A1 - A2, Fp1 - Fp2, F3 - F4, F7 - F8, C3 - C4 and T3 - T4 is taken as feature parameter. Average values of entropies are calculated and plotted in Figure-1, shows an increase in entropy while using phone. The percentage

change in sample entropy of the data set for above mentioned 4 conditions (with phone) with respect to entropy of the data set at rest (without phone) is tabulated as in Table-1.

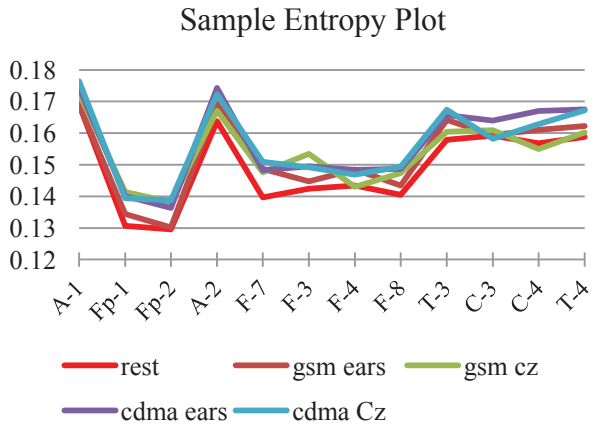

Fig-1 Plot of Sample Entropy for different conditions of datasets

TABLE -1
Percentage increase in Sample Entropy (in %)

Channels	gsm ears	gsm cz	cdma ears	cdma Cz
A-1	-0.02	2.11	3.16	4.34
Fp-1	2.84	8.22	7.2	6.65
Fp-2	0.46	6.69	5.23	7.15
A-2	3.32	1.99	6.39	5.17
F-7	6.51	5.72	6.17	8.05
F-3	1.6	7.77	4.97	4.77
F-4	3.57	-0.29	3.46	2.41
F-8	2.09	4.92	5.85	6.4
T-3	4	1.64	4.98	6.03
C-3	0.09	1.05	2.95	-0.65
C-4	2.68	-1.21	6.49	3.83
T-4	2.16	0.87	5.48	5.27

On analysing the percentage change in entropy, it is observed that percentage change in entropy is greater for CDMA phone in most of the cases. The data set (with and without phone) of feature parameters is analysed using Kruskal Wallis test and the result is shown in Table-2.

TABLE -2
Kruskal Wallis test statistics of Sample Entropy

Channels	A1	Fp1	F7	F3	T3	C3	A2	Fp2	F8	F4	T4	C4
p value	0.537	0.023	0.012	0.02	0.044	0.518	0.093	0.026	0.16	0.349	0.057	0.043

In hypothesis testing, null hypothesis and alternate hypothesis are fixed on the basis of prior knowledge. Here null hypothesis is taken as the median of all the feature set are same or median of feature data set with and without phone are same. The test statistic (p value) is calculated and the decision is taken based on that. The purpose of Kruskal Wallis teat is to find out whether data from several groups have a common median. If p-value is less than significance level (here 0.05) then the null hypothesis is rejected, or can be interpreted as the data set of feature parameter at rest (without phone) is different from that of feature parameter with phone. As per the test result, the values of data set is different in channels Fp1, F7, F3, T3 in left lobe and Fp2 and C4 in right lobe.

IV. CONCLUSION

On analyzing percentage change in entropy, variation between low to high varies between 0.02 to 6.91 for GSM at ears, -1.21 to 8.22 for GSM at Cz , 2.95 to 7.2 for CDMA at ears and 0.65 to 8.05 for CDMA at Cz for different channels. The Kruskal Wallis test is significant in 6 out of 12 number of channels. This shows the variations in EEG signal while using the mobile phone, which demonstrate transformation in the activities of the brain due to radiation.

The change in complexity has to be taken into account in view of right of brain will control left side and vice versa. As per the above discussions, it is seen that the difference in complexity is produced on the Left side of the brain in channels Fp1, F7, F3, and T3 and in channels Fp2 and C4 in right side of the brain. In the experiment the phone is kept next to right ear, nearer to channel A2. There is no change in complexity in this channels and its pair A1. But changes in other electrodes have to be taken seriously to be further investigated.

The effect of radiation may vary due to gender difference, age difference, and mode of usage of phone (frequent or occasional usage) has to be further investigated. In this study 2 mobile phones with SAR values of 1.3W/Kg(GSM) and 0.987 W/Kg(CDMA) is used, further investigations must be carried out to find the changes in brain while using phone with higher values of SAR.

REFERENCES

[1]. Min Kyung Chu et al, " Clinical features of headache associated with mobile phone use: a cross-sectional study in university students", BMC Neurology 2011

[2]. Ashok Agarwal et al, "Effect of cell phone usage on semen analysis in men attending infertility clinic: an observational study", 2008 American Society for Reproductive Medicine, Published by Elsevier Inc. 124-128

[3]. James C Lin, "Cellular Telephone Radiation and EEG of Human Brain',IEEE Antennas and Propagation Magazine. Vol 45, No -5 October 2003.

[4]. Andrew A.Marino, Erik Nilsen,Clifton Frilot,"Nonlinear changes in Brain Electrical Activity due to Cell Phone Radiation", Bioelectromagnetics 24:339-346(2003).

[5]. H. D'Costa, et al" Human brain wave activity during exposure to radiofrequency field emissions from mobile phones", Australasian Physical & Engineering Sciences in Medicine Volume 26 Number 4, 2003

[6]. Saeid Sanei and J.A. Chambers, "EEG Signal Processing|", 2007 John Wiley & Sons, UK

[7]. C. K. Smitha and N. K. Narayanan" Effect of mobile phone radiation on brain using EEG nalysis by Higuichi's fractal dimension method ", Proc. of ICCESD-2013, SPIE 8760, doi 10.1117/12.2012177

[8]. C.K. Smitha, N. K. Narayanan "Brain Dynamics under Mobile Phone Radiation Using Various Fractal Dimension Methods", IJIRs, Volume 13, Issue Number 2, 2014 (ISSN: 2231-525X) p 166-180

[9]. C. K. Smitha & N.K.Narayanan " Effect of Mobile Phone Radiation on Brain using Wavelet Energy", IFMBE Proceedings of ICBME 2013, Volume 43, 2014, pp 192-195 DOI :10.1007/978-3-319-02913-9_49, Print ISBN :978-3-319-02912-2 Series ISSN 1680-0737

[10]. C. K. Smitha & N.K.Narayanan " Effect of Mobile Phone Radiation on Brain – Wavelet Power Approach" Proceedings of WMSCI 2014, Volume 1, pp 213-218

[11]. Abdullah Al Jumah "Denoising of an Image Using Discrete Stationary Wavelet Transform and Various Thresholding Techniques" Journal of Signal and Information Processing, 2013, 4, 33-41 doi:10.4236/jsip.2013.41004

[12]. Eugene N. Bruce et.al, "Sample Entropy Tracks Changes in EEG Power Spectrum With Sleep State and Aging",. J Clin Neurophysiol. 2009 August; 26(4): 257–266.doi: 10.1097/WNP.0b013e3181b2f1e3

[13]. Jeng-Rung Huang, Abbod et al ,"Application of Multivariate Empirical Mode Decomposition and Sample Entropy in EEG Signals via Artificial Neural Networks for Interpreting Depth of Anesthesia" Entropy 2013, 15, 3325-3339, ISSN 1099-4300. doi:10.3390/e15093325

[14]. A Stuart and M G Kendall, "Statistical Inference and Statistical Relationship The advanced theory of Statistics vol-2', Hafers Press ,1986

[15]. Irwin Miller and John E Freund, "Probability and Statistics for Engineers" 4th Edition, Prentice Hall, 1985

Experimental validation of the numerical model of a commercial mobile phone for specific absorption rate assessment

Ashish Rojatkar* and Vikass Monebhurrun
Department of Electromagnetics, DRE-L2S, SUPELEC, 3 rue Joliot-Curie, 91192 Gif-sur-Yvette Cedex, France
*Corresponding author e-mail: ashish.rojatkar@supelec.fr

Abstract: *The computer aided design (CAD) models of commercially available mobile phones are usually not openly available for electromagnetic simulations. A simplified reconstructed CAD model proves useful to gain insight about the radio frequency performance of the mobile phone that can complement the measurement. Herein a commercially available mobile phone is characterized both numerically and experimentally. The numerical model of the mobile phone is reconstructed by examining the locations and dimensions of the main components that influence the electromagnetic fields. The near field is characterized by comparing the specific absorption rate (SAR) distributions obtained numerically and experimentally.*

Introduction:

The radio frequency (RF) exposure due to mobile phones is currently characterized by measuring the specific absorption rate (SAR) using a standard dosimetric test facility [1,2]. Numerical dosimetry is not yet applied for the SAR compliance because the electromagnetic simulation of computer aided design (CAD) models of commercially available mobile phones is not straightforward [3,4]. Furthermore the CAD models of commercially available mobile phones are usually not openly available. Obviously the availability of numerical simulation results proves particularly useful to gain insight of the experimental data.

A set of software and/or hardware modified commercially available mobile phones have been previously employed for the evaluation of the real-life exposure both indoor and outdoor [5]. However, since the CAD models of these mobile phones are not available, it becomes difficult to confront measurement and numerical simulation results. Nonetheless, by carefully examining the essential components of the mobile phone and performing a comprehensive numerical analysis of the mobile phone in terms of return loss, radiation pattern, total radiated power (TRP) and specific absorption rate (SAR), a simplified numerical model may still be reconstructed [6]. Herein the numerical model of one of the mobile phones previously used for the real-life exposure assessment is reconstructed and validated experimentally.

Since the return loss of the actual triple-band –Global System for Mobile (GSM) communication 900 MHz and 1800 MHz, and Universal Mobile Telecommunication System (UMTS) 2100 MHz– mobile phone can only be measured using a network analyzer after soldering a coaxial cable at the input of the antenna, and not possible in this study. The numerical simulation results are considered valid when the resonance frequencies match the operating frequencies for which the device was designed by the manufacturer. The distributions of the surface currents are then assessed by comparing the SAR distributions obtained numerically and experimentally.

Numerical Model:

A commercial package of the finite integral technique (FIT) is employed for the numerical simulations [7]. A simplified model of the triple-band commercial mobile phone with a bottom-mounted antenna is generated by examining the physical dimensions of the different elements –antenna, antenna support, battery, casing, etc. – constituting the actual device. The

freely available information contained in the mobile phone manual proves useful in designing the internal structure and the different components. Since FIT is based on hexahedral meshes i.e. voxels, all objects having curved shapes are preferably substituted by equivalent linear shapes in the reconstructed CAD model whenever possible.
The reconstructed mobile phone antenna model and the mobile phone component structure are presented in Figure 1. Some components are expected to have negligible impact on the simulation results and they are herein omitted to simplify the numerical model e.g. the camera which is located far from the antenna structure is not expected to highly influence the surface currents.
Since the actual dielectric properties of the different components are unknown, a trial and error parametric investigation is undertaken using typical values to achieve the best match of the three expected operating frequencies of the mobile phone.
The return loss of the numerically reconstructed mobile phone is shown in Figure 2. The return loss profile exhibits a sufficiently good match at the three operating frequencies: 900 MHz, 1800 MHz and 2100 MHz. This is further confirmed by examining the radiation pattern characteristics at the two GSM frequency bands with a maximum free space gain of 2.25 dBi at 900 MHz and 5.26 dBi at 1800 MHz.

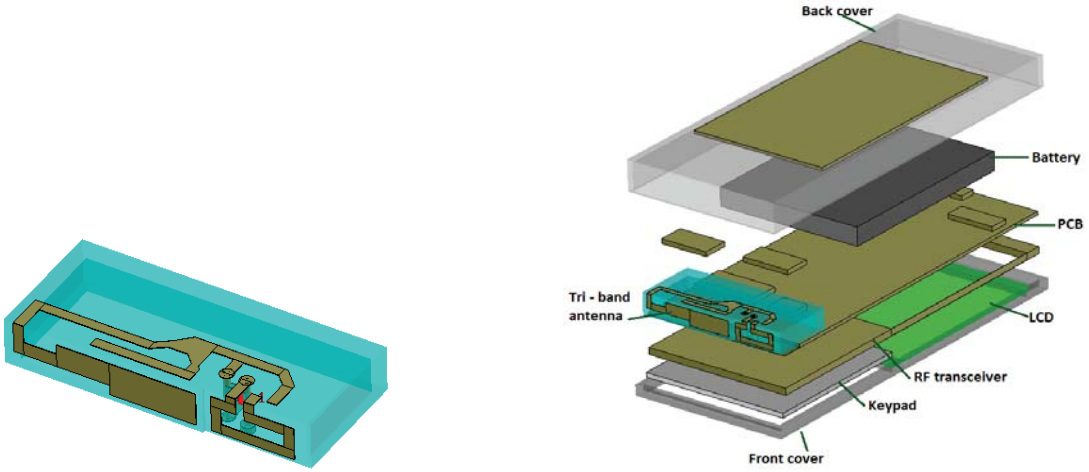

Figure 1: The antenna shape integrated with the mobile phone model (left) and the expanded view of the bottom mounted antenna mobile phone model (right)

Since the SAM head model recommended by the SAR measurement standards involves uncertainty due to the head/phone positioning that may add up in the uncertainties of the mobile phone CAD model, a flat phantom is herein preferred for the comparison of the SAR results. The experimental SAR assessment is performed using a fully automated standard dosimetry test facility. The mobile phone is placed with its front side in contact with the low loss dielectric flat phantom filled with the tissue equivalent liquid. The relative permittivity and conductivity values of the tissue equivalent liquid are 41.5 and 0.97 S/m, and 40 and 1.4 S/m at 900 MHz and 1800 MHz, respectively. All metal objects are modeled as perfect electric conductors (PEC) and the material properties assigned to various surrounding components are inclusive of the typical loss values. The numerical model of the mobile phone is discretized as 2.7 million hexahedral mesh cells (15 lines per wavelength, smallest mesh step of 0.05 mm). In the presence of the flat phantom, the total number of voxels reaches 7 million.

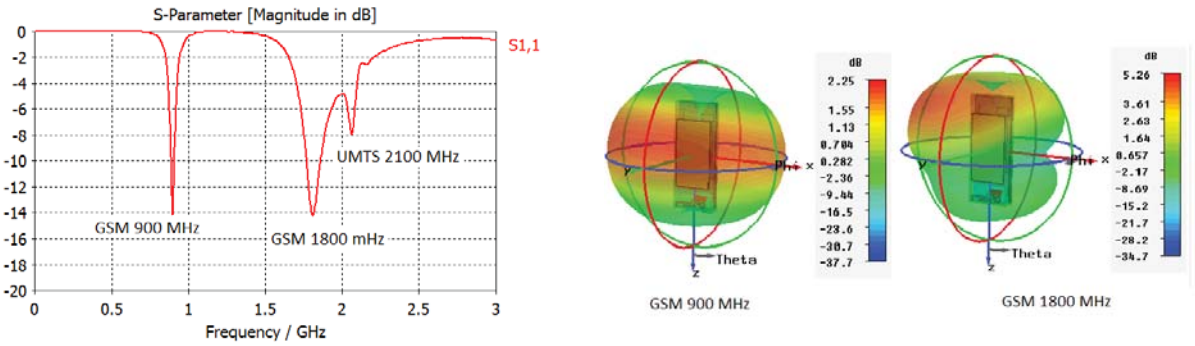

Figure 2: The return loss profile of the mobile phone (left) and the radiation patterns at the two GSM frequencies of interest (right).

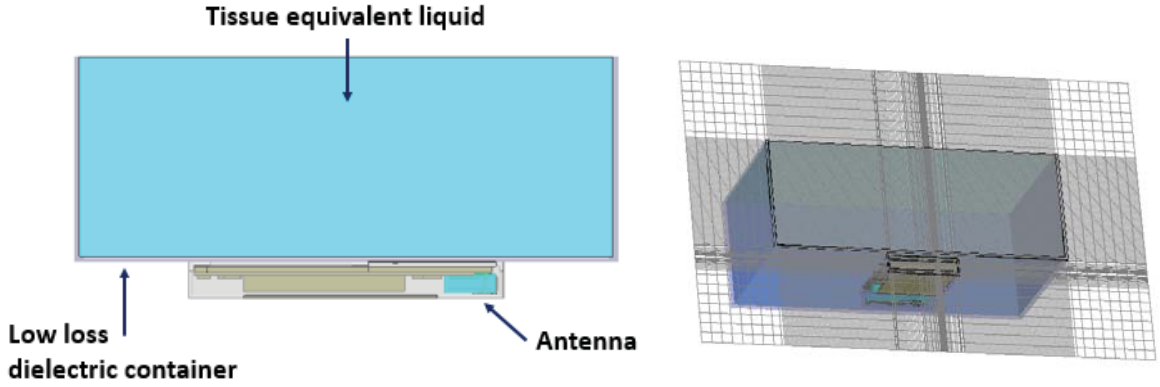

Figure 3: Mobile phone positioned beneath the flat phantom (left) and the corresponding mesh density (right).

Experimental SAR validation:

The comparison of the SAR distributions obtained by numerical simulation and measurement at 900 MHz and 1800 MHz are shown in Figures 4 and 5, respectively. Herein the average powers emitted by the mobile phone at 900 MHz and 1800 MHz are 250 mW and 125 mW, respectively. Table I provides the comparison of the peak point-SAR values for these two frequency bands with a quantitative match observed at 900 MHz while the simulated SAR value at 1800 MHz is relatively lower than the measured value. A possible explanation could be the difference in the return losses and the material losses between the actual device and the numerical model.

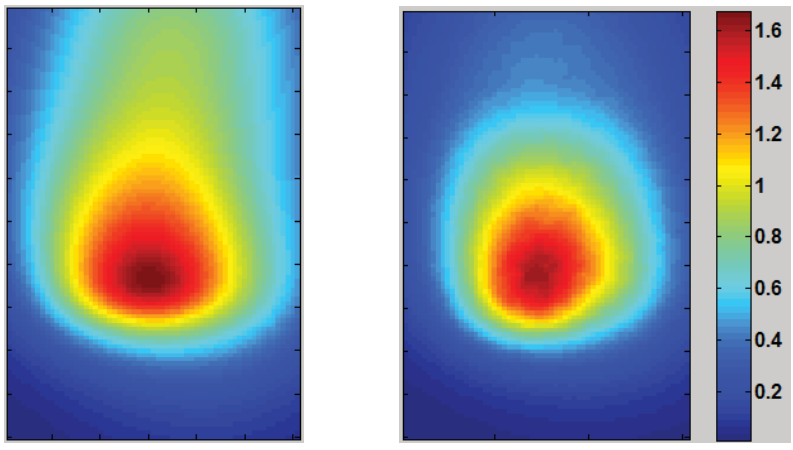

Figure. 4: Local SAR distribution at 900 MHz, simulation (left) and measurement (right).

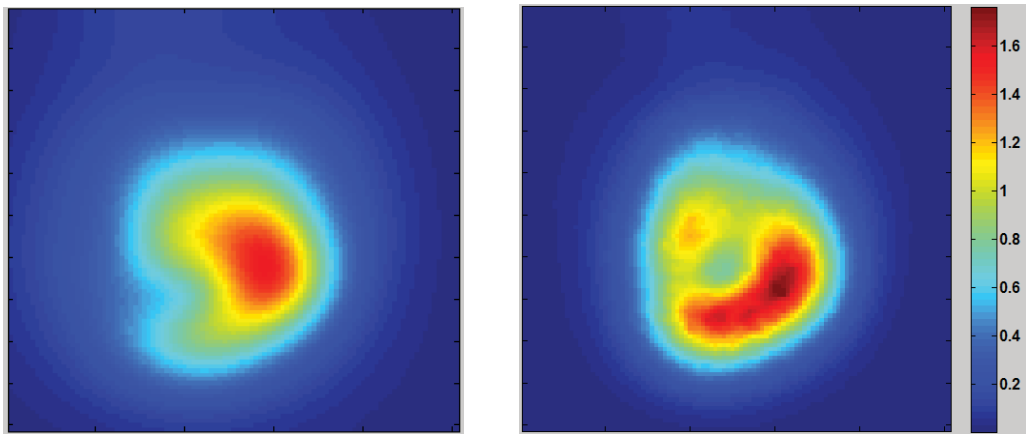

Figure. 5: Local SAR distribution at 1800 MHz, simulation (left) and measurement (right).

Table I: Peak point-SAR (W/kg) measured at a distance of 7.2mm from the base of the flat phantom

900 MHz		1800 MHz	
Simulation	**Measurement**	**Simulation**	**Measurement**
1.67	1.65	1.56	1.76

Conclusion:

The simplified CAD model of a commercially available mobile phone is herein generated to complement the experimental evaluation for real-life exposure assessment. The reconstructed numerical model exhibits good return loss and radiation pattern characteristics at the frequencies of interest. The variations observed in the point-SAR distributions, specially at the higher frequency are likely due to the difference in the current distribution across the components which are omitted and/or presently represented by simplified shapes. Overall satisfactory qualitative and quantitative agreements are observed for the point-SAR distributions for both frequency bands.

Reference:

[1] Recommended practice for determining the peak spatial-average specific absorption rate (SAR) in the human head from wireless communications devices: measurement techniques, IEEE Standard 1528, 2003.

[2] Human exposure to radio frequency fields from hand-held and body-mounted wireless communication devices—human models, instrumentation, and procedures—Part1: Procedure to determine the specific absorption rate (SAR) for hand-held devices used in close proximity to the ear (frequency range of 300 MHz to 3 GHz), IEC Standard 62209-1, 2005.

[3] M. Siegbahn et al, "An international interlaboratory comparison of mobile phone SAR calculation with CAD-based models," *IEEE Transactions on Electromagnetic Compatibility*, 52, 4, 2010, pp. 804-811.

[4] V. Monebhurrun et al, "A benchmark CAD mobile phone model for specific absorption rate calculations", *IEEE Transactions on Magnetics*, 50, 2, 2014, pp. 1-4.

[5] Ashish Rojatkar and Vikass Monebhurrun, "Evaluation of the real life exposure due to GSM mobile phones, in Proc. URSI-GASS, Beijing, Aug. 2014.

[6] V. Monebhurrun et al, "Numerical and experimental investigations of a commercial mobile handset for SAR calculations", in *Proc. 2nd Int. Conf. Bioinformat. Biomed. Eng.*, May 2008, pp. 784–787.

[7] CST: http://www.cst.com

Investigation of Microwave Resonators for Monitoring Biological Parameters

M.P. Jayakrishnan, Divya Sathyanath, Sruthy Skaria, Thushara H.P., Karthika S. Nair , Anju Pradeep , S. Mridula and P. Mohanan
Centre for Research in Electromagnetics and Antennas, Cochin University of Science and Technology, Cochin -682022, Kerala.
jkmpjk@gmail.com, drmohan@gmail.com

Abstract: This study focuses on feasibility analysis of different planar microwave resonators to monitor different biological parameters in human and animals. The methodology is based on the principle of change in resonance of the resonator due to the change in dielectric properties of surrounding tissues correlated with metabolism. Two Resonators namely; Split Ring Resonator and Stepped Impedance Resonator are subjected to study. The resonance frequency of the resonator is found to be a function of their geometry and dielectric constant of the medium surrounding it. The responses of the resonators for various resonator geometries are subjected to analysis and the optimum geometries are employed for experimental validation. The responses of resonators to different fluids are observed and the feasibility as an implantable sensor is investigated by embedding the resonators in animal tissue.

Introduction: Monitoring of biological parameters is a challenging and inevitable stream in medical diagnostic field. Among the various diagnostics methods used extensively, microwave based methods are getting more attention recently. Microwave based methods have the advantage of being non invasive or minimally invasive, improved accuracy, desired precision etc. The present study focuses on the investigation of two simple microwave resonators for monitoring the biological parameters based on change in the dielectric properties of the surrounding tissues correlated with metabolism. The current study is a leading step towards an efficient bio-sensor.

Methodology: The measurements are conducted using an Agilent PNA-E8362B. The resonator is excited using a broadband horn antenna in the monostatic mode and the reflected (Backscattered) energy from the resonator is monitored. The measurement setup is illustrated in figure 1.

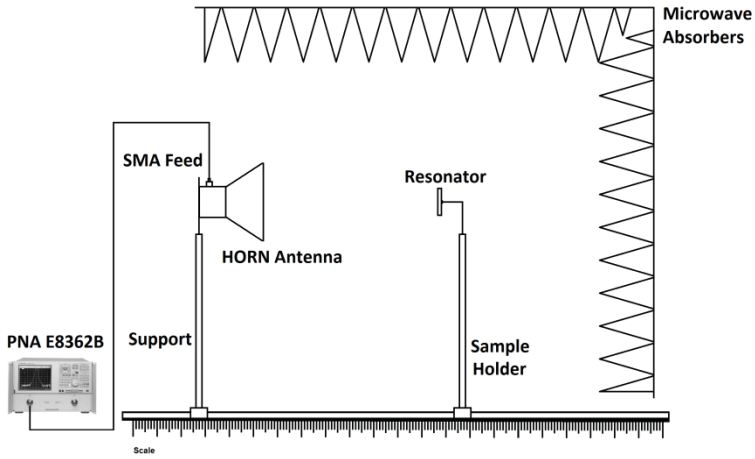

Figure 1 *The Measurement setup.*

The return loss measurement of the empty room is stored in the memory of the PNA. Now the sample is inserted in the sample holder and measurement is repeated. Using the built in 'Data – Memory' operation the clutter due to static objects in the room can be easily removed.

The Split Ring Resonator (SRR): A circular double ring split ring resonator is used for the present study, as depicted in figure 2(a). An approximate equivalent circuit of a split ring resonator is an LC tank circuit as depicted in figure 2(b). The Split ring resonator resonates at a frequency which is a function of its geometry and the dielectric medium surrounding it.

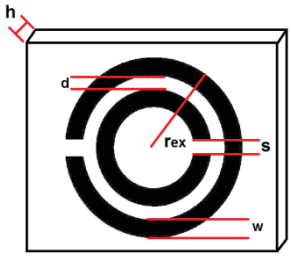

2(a)

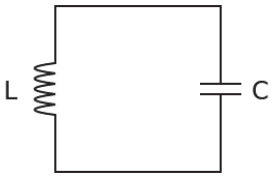

2(b)

Figure 2 **a.***The Split ring resonator,* **b.** *The Electrical equivalent.*
(h = height of the substrate, rex = external radius, w = width of the rings (same for both rings), d = gap between the rings, s = width of the slot (same for both rings).)

The L and C values for the equivalent circuit of the SRR can be calculated using the equations given in [1]. A Matlab based GUI calculator [1] is used to calculate the dimensions of the SRR. The parameters of the Split Ring Resonator are as follows: Substrate used is Rogers RT/Duroid 5880 (Relative permittivity 2.2, height (h) 0.8mm), External radius (rex) 5mm, Width of rings (w) 0.4mm, Gap between the rings (d) 0.4mm, Operating Frequency 2.700 GHz.

Spatial Resolution of the SRR: An important parameter of a sensor is its spatial resolution. In this study it refers to the vicinity of the sensor where the field is highly influenced. The following method is used to investigate the spatial resolution of the SRR structure. The SRR is excited using a small loop antenna placed near it as shown in the figure 3 and the sensitive region in front of the SRR is investigated by placing a dielectric slab of thickness 0.4mm in front of it at a distance D and moving the slab along the Z-axis. It is found that the structure shows a considerable shift in the resonance frequency and the sensitive region is limited to 1mm in front of it (figure 3). This offers adequate spatial resolution so that it could be used for localized measurements.

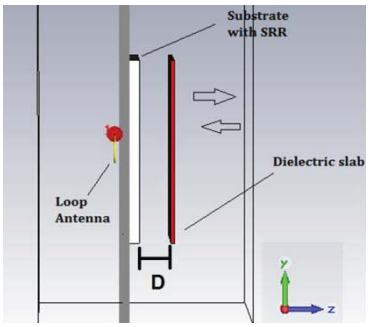

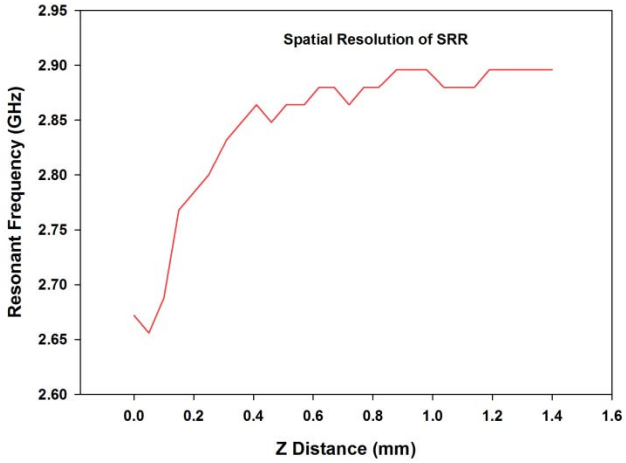

Figure 3 *The setup used for spatial resolution analysis (The Arrows shows the direction of movement of the dielectric slab), and the result.*

Measurements and Results: The resonator is given a thin coating of the fluid on top and then illuminated using the setup given in figure 1. It is seen that the SRR shows a shift in its resonance for different dielectrics in proximity with it , but the drawback is that the readability of the backscattered signal is reduced for lossy fluids like water , hydrogen peroxide etc. Since the aim of the study is an implantable sensor, all these lossy fluids are of great interest and hence a method for backscatter enhancement has to be adopted. After numerous experimental iterations, it is found that the resonator shows distinguishable backscattered energy when the fluid is placed at the region of maximum field. Since the electric field of the SRR structure is confined within the rings and the magnetic field is spread across the structure, it is very difficult for the fluids to interact with the field. However in

case of the Complementary-SRR structure the Electric and Magnetic fields also follow a complimentary pattern to the SRR [7], and hence the fluids interact more with the electric field and thus the CSRR is expected to show a better response. Experimental observations reveal that the complimentary structure to the SRR (CSRR) resonates at two frequencies 4.1120GHz and 5.8100GHz, with the higher mode showing considerable shift (in GHz) when a dielectric is placed in proximity with it, as shown in figure 5, 6. The structure is found to exhibit enhanced backscatter level when a dielectric backing with a ground plane is given to it as shown in figure 4.

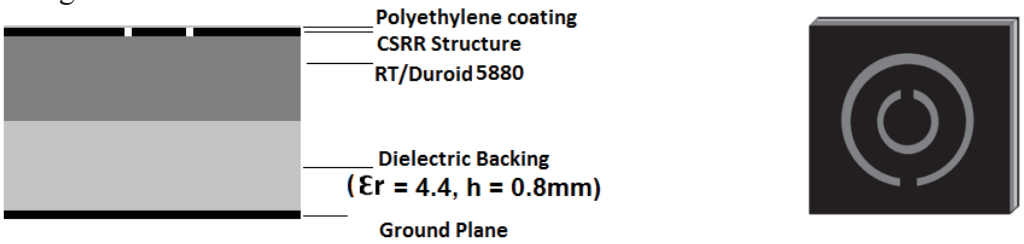

Figure 4 *Cross Section (left), Front (Right).*

The figure 5 shows the response of the CSRR to different fluids (with constant volume). A very thin coating of polyethylene film is given on top of the CSRR structure to prevent it from any possibility of short circuit.

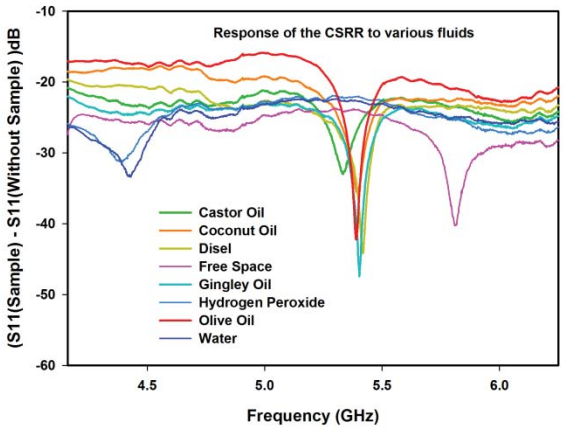

Figure 5 *Responses of the CSRR to various Fluids.*

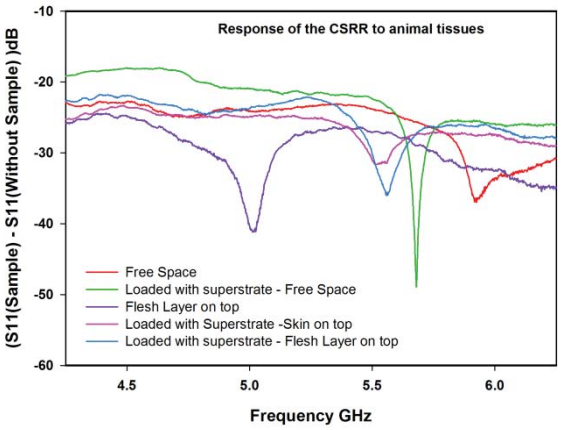

Figure 6 *Response of the CSRR to Animal Tissues.*

It is apparent from the plots that the CSRR structure exhibits very good performance. To validate the suitability of CSRR as an implantable antenna in human/animal tissues, experiment is done, by embedding the sensor in animal tissues. The animal tissues used are the blood drained flesh and skin (Hypodermis) of a buffalo. The results of the experiment are depicted in Figure 6. The experiments are also conducted by covering the CSRR structure with a superstrate (FR4 0.8mm).

The Stepped Impedance Resonator: A microstrip line based quarter wavelength Stepped Impedance Resonator (SIR) is also used for the study. The geometry of the stepped impedance resonator is depicted in figure 7. The design is based on the following design equations [6].

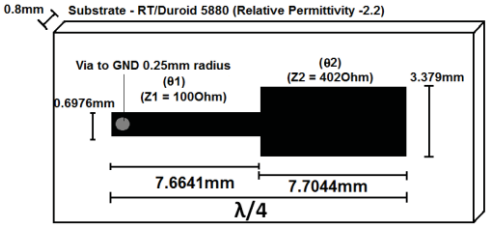

Figure 7 *The Geometry used for the experiment.*

$$\tan\theta_1 * \tan\theta_2 = k \quad (1)$$

Where k is the impedance ratio defined as

$$k = \frac{z_2}{z_1} \quad (2)$$

Similar to the SRR, the resonance frequency of the SIR is a function of its geometry and the dielectric medium surrounding it, and is expected to behave in a manner similar to the SRR when a dielectric is kept in proximity. The SIR is excited using the same setup explained in figure 1. The observations reveal that the SIR has an undistinguishable response to lossy fluids like water and hydrogen peroxide etc, similar to SRR and shows distinguishable response when fluid is kept at maximum field regions on the geometry. This is an encouraging result, but it is very difficult to maintain constant volume of the fluid. As a solution, after a number of iterations, the complimentary geometry of the SIR with a few modifications as explained in figure 8 is found to resonate at two frequencies 3.03GHz and 8.725GHz. When a dielectric is placed in proximity with it, the lower resonant frequency shows a lesser shift (in MHz range) compared to the higher frequency (in GHz range), and hence higher frequency invites more attention.

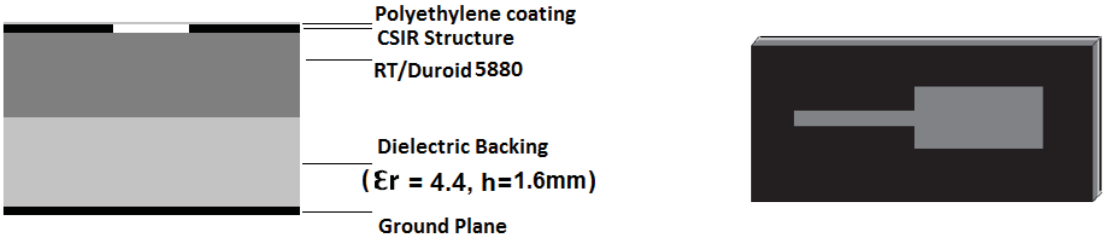

Figure 8 *The CSIR structure - Cross section (left), Front view (Right).*

The responses of the CSIR to various fluids are illustrated in figure 9; the measurements are taken after giving a protective polyethylene coating on the CSIR surface to prevent short circuit due to the fluids.

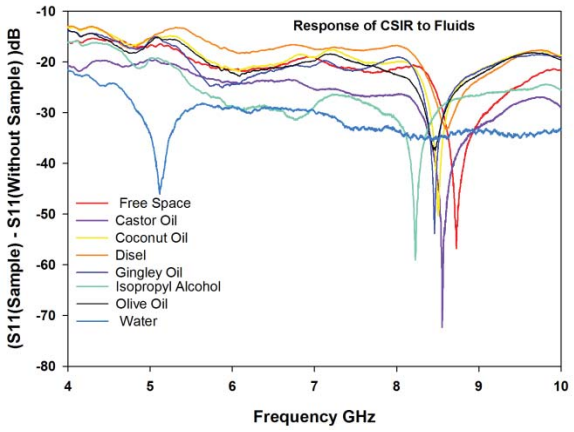

Figure 9 *Response of CSIR to various Fluids*

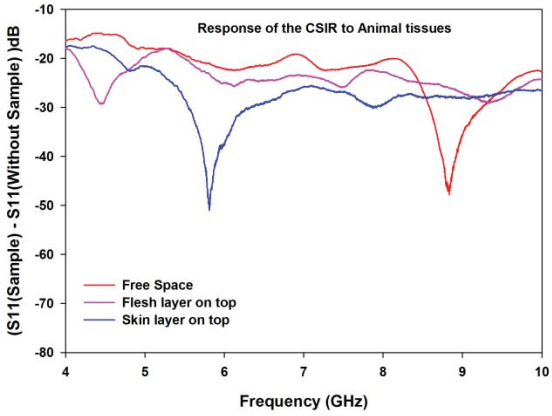

Figure 10 *Response of CSIR to Animal tissues.*

The result parts confidence that the resonator can be used for dielectric measurements. The feasibility of this as an implantable sensor is analyzed as in the previous case by embedding the CSIR in animal tissue. The results are shown in figure 10.

Discussion and Future Plans: This study highlights the concept of the feasibility of the proposed resonators for continuous biological parameters monitoring, as implanted sensors. They are capable of producing readable backscatter levels when embedded in animal tissues and are capable of distinguishing dielectrics in proximity by showing proportional shift in their resonance frequencies. Now the challenges pending are the biocompatibility of the resonators, the characteristic resolution of the sensors, and mathematical analysis of the observations. These challenges can be solved one by one, as explained in the following paragraphs. The biocompatibility issue of the resonators can be solved by fabricating the resonators using a biocompatible material. This problem can be approached with another perspective too, that is by covering the structure using a biocompatible superstrate. If one

requires monitoring the blood glucose level, the CSRR structure can be used with a slight modification as explained. The response plot of the CSRR clearly shows that if the structure is covered by a superstrate it shows almost same result for both the skin and flesh layer in which it is embedded. This means that the spatial resolution is limited to the height of the superstrate and the observed shift in resonance is mostly due to the effect of the superstrate and the effect of the animal tissues are almost nil. Now if the superstrate is glucose selective, i.e. the dielectric properties of the superstrate varies with the amount of glucose in the blood, one could plainly say that the shift in resonance of the resonator is purely due to the variation of the blood glucose level, and hence we can achieve the required characteristic resolution. The CSRR based sensor could be now implanted in the body in proximity with blood /interstitial fluid as shown in figure 11. Similarly the CSIR structure can also be used as a sensor by covering the structure with a parameter selective superstrate.

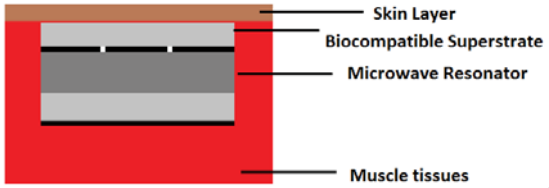

Figure 11 *An illustration of the implant*

The mathematical analysis of the resonators can be done by extracting the equivalent circuit of the resonators and correlating the same to the response to various materials with known dielectric constants.

The future work of this study concentrates on the development of a parameter selective superstrate and the mathematical analysis of the behavior of the resonators. In-vivo implementation as an implantable sensor for monitoring biological parameters based on metabolism, which can provide with a rejuvenated life for people suffering from diseases like diabetes mellitus, leukemia etc. is also envisaged.

Acknowledgement

The authors wish to acknowledge the Board of Research in Nuclear Science (DAE-BRNS) Govt. of India, for their valuable support and funding for the project entitled "Implantable Sensor Antenna System for Medical Application" under which this work is carried out. The Authors also would like to acknowledge Dr. R. Ratheesh, Scientist, C-MET Trichur, for his immense support and valuable suggestions throughout the work.

References

[1] Anju Pradeep, S. Mridula and P.Mohanan, "Design of an Edge-Coupled Dual- Ring Split-Ring Resonator", Antennas and Propagation Magazine, IEEE Volume: 53, Page(s): 45 – 54, 2011.

[2] Frank Hesmer, et al. "Coupling mechanisms for split ring resonators: Theory and experiment" phys. stat. sol. (b) 244, No. 4, 1170 – 1175 (2007) / DOI10.1002/pssb.200674501, © 2007 WILEY-VCH Weinheim.

[3] Christophe Caloz and Tatsuo Itoh, "Electromagnetic Metamaterials: Transmission Line Theory and Microwave Applications", John Wiley & Sons, INC., Hoboken, New Jersey, 2006.

[4] FilippoCapolino, "Metamaterials Handbook: Theory and Phenomena of Metamaterials", CRC Press - Taylor & Francis Group, 2009.

[5] Edward C. Jordan and Keith G. Balmain, "Electromagnetic Waves and Radiating Systems", Prentice Hall, New-Delhi, 1994.

[6] M.Makimoto and Y.Yamashita, "Microwave Resonators and Filters for Wireless communication, Theory Design and Application", Springer series in Advanced Microelectronics, vol.4, 1994.
[7] Muhammed said Boybay and Omar M. Ramahi, "Material characterization Using Complimentary Split- Ring Reasonators", IEEE Transactions on Instrumentation and Measurement, 2012.
[8] Nijas C.M, Deepak U, Vinesh P.V., Sujith R., Mridula S.,K. Vasudevan , and P. Mohanan, "Low Cost Multiple Bit Encoded Chipless RFID Tag Using Stepped Impedance Resonator", IEEE Transactions on Antennas and Propagation, 2013.

ANALYSIS OF SAR OF A MULTI-BAND PLANAR INVERTED-F ANTENNA

Hrudya.B.Kurup[1,3,5],Vijesh.K.R[1,3] , P.Mohanan[2], V.P.N.Nampoori[1,3], Bindu.G[3,4]
1.International School of Photonics, 2.Center for Research in Electromagnetics and Antennas (CREMA) Department of Electronics CUSAT 3.Swadesi Science Movement,
4. Nansen Environmental Research Center, Cochin 5.KMEA Engineering College, Department of Electronics
Cochin- 22, Kerala, India.

Abstract: This paper proposes a novel multi-band PIFA structure with reduce exposure of the human head to mobile-set antenna radiation. It also analyses the SAR of the triple band at various distances from the head model. The PIFA structure proposed in this paper is designed to operate at GSM 900, GSM 1900 and Wi-Fi bands. SAR is decreased by reducing the radiation towards human head, while maintain significant radiation in all other directions. This SAR reduction is accomplished by inserting suitable slots in the top radiating patch and ground plane of PIFA at appropriate positions so as to modify the current distribution and radiation pattern.

INTRODUCTION: Recent years has witnessed a very rapid expansion of wireless communications. This has driven the development of multiple wireless standards and portable communication devices (especially mobile phones) capable of numerous operating modes. Antennas are the key elements in these devices which equip them with its various capabilities. For antennas to satisfy the requirements of the current market, they must be compact along with multi band capability. To handle multiple frequency bands and standards, a versatile antenna such as a PIFA is required. Due to the rapid growth in the use of mobile phones and other wireless communication systems there's a huge public health crisis looming from this one particular threat: electromagnetic radiation from cellular phones. Therefore, it is necessary to decrease the interaction of electromagnetic energy towards human head when mobile handset is in operation. For electromagnetic wave exposures, these guidelines are based on peak specific absorption rate (SAR).

This paper discusses the design of a simple , compact, multi-band planar inverted F-antenna (PIFA) working in GSM 900 , GSM 1900 WI-Fi and Bluetooth bands . By adopting sutable techniques , the SAR of the proposed antenna is reduced. Analysis of the SAR value of the antenna at various distances from the head model is also done.

PIFA Structure

PIFA structure consists of a large metallic ground plane, a resonating metallic plate at the top i.e. a patch, a feed wire & one or more shorting pins or plates to connect the top patch and the ground plane. The antenna is fed through feeding pin which connects to the ground plane. This type of feeding technique allows designer to place it at any desired location in the patch. The shorting pin and shorting plate allows good impedance matching achieved with the patch above ground plane of size less than $\lambda/4$. Resulting PIFA structure is of compact size than conventional $\lambda/2$ patch antennas.This structure resembles a short-circuit micro strip antenna .Therefore PIFA can be thought of as a shorted micro strip patch antenna with air as dielectric.[1]. Fig. 1 shows a basic PIFA structure which is fed at the base by a feed wire.

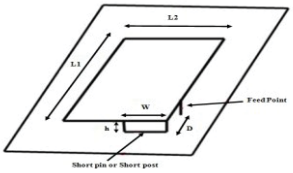

Fig.1: Basic PIFA Structure

Basic Design Equation:

The frequency at which PIFA resonates can be calculated by using a basic formula as given below

$$L_1+L_2-W = \lambda_g/4 \quad (1)$$

Where L_1 is Top patch length ,L_2 is Top patch Width,λ is the wavelength corresponding to resonant- frequency.

Above equation represents that the sum of the width and length of the top plate should be $\lambda/4$. The performance of the antenna can be enhanced by varying ground plane length. Optimum length of the ground plane is 0.4λ at the operating frequency [2]. This approximation is very rough and does not cover all the parameters that significantly affect the resonant frequency of the antenna [3].

Specific Absorption Rate

Specific Absorption Rate (SAR) is the rate at which Radio Frequency energy is absorbed in the human body over a given time and expressed as the power absorbed per unit mass.SAR is usually averaged either over the whole body, or over a small sample volume (typically 1 g or 10 g of tissue).This measurement is used to determine whether a device complies with safety norms/guidelines.SAR for electromagnetic energy can be calculated from the electric field within the tissue as:

$$SAR = C\frac{dT}{dt} = (\frac{\sigma E^2}{\rho}) \quad (6)$$

σ = conductivity of the tissue (S/m), ρ = mass density of the tissue (kg/m_3),E = rms electric field strength (V/m) [4]

SAR reduction techniques over these years

Various methods have been proposed over the last years to reduce the SAR to levels below the current maximum exposure levels of the international standards. Increasing the distance between the antenna and head is the easiest way to reduce SAR.However this can cause an increase in the volume of the device which is not much appreciated. Auxiliary antenna elements and ferrite loading are other methods commonly used for reducing SAR. But using these techniques increases the size and cost .

Artificial magnetic conductors (AMC), electromagnetic band gap (EBG) surfaces and metamaterials are also effectively experimented for reducing SAR. These are special high impedance surfaces which are based on a single conductor cell that can resonate to a design frequency in order to trap the electromagnetic energy that otherwise would be directed to the user. They are typically realized as a metallization pattern of many single cells over a dielectric substrate and a ground plane.[5]-[9]. The design and implementation of these surfaces are difficult when it comes to complex cell structures.

Another effective way of reducing SAR is by introducing slits in the antenna structure. By introducing suitable slits in the antenna, the radiation pattern of the antenna can be modified so as to reduce radiation tremendously towards human head, without sacrificing the radiation characteristics. The radiation pattern and functionality of an antenna are related to current distribution on its surface. Any slight change in the geometrical configuration of the surface will create new current paths and new radiation edges, which will give the antenna new resonance, different radiation pattern and operation.[10] These structures are much simpler, cost effective and efficacious when compared to the other methods.

Proposed Antenna

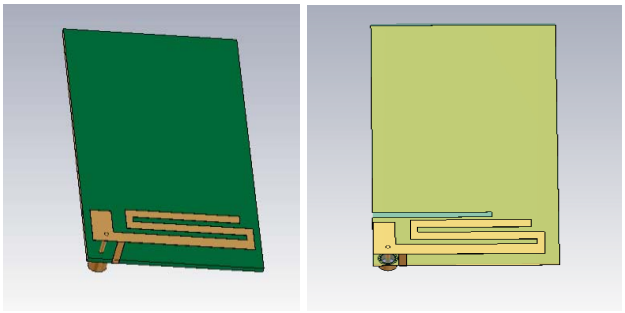

Fig.2: a) Proposed antenna b) 3-D view in CST

The proposed antenna is shown in Fig.2 (a) and 3D structure of the proposed PIFA antenna is shown in Fig.2 (b). The proposed PIFA antenna is designed using a dielectric material as FR-4 which has loss tangent, δ=0.02, dielectric constant, ε_r = 4.4 and substrate height, h = 1.6 mm. Slots of optimum dimensions are inserted at appropriate positions in the ground plane and top radiating patch so as to obtain multi-band operation. Feeding point source is used to excite the structure. Total dimensions of the radiating parts of the antenna are 46 x 14 mm^2. And that of ground plane are 100 x 50 mm^2 .Fig 3 and 4 shows the detailed dimensions of the top radiating patch and the ground plane

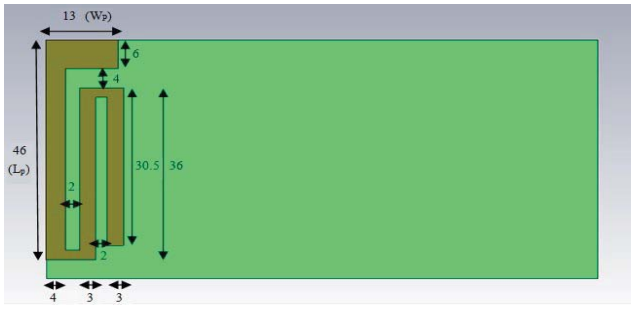

Fig.3: Dimensions of Top Radiating Patch

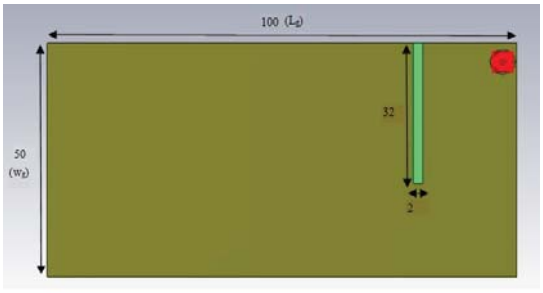

Fig.4: Dimensions of Ground Plane

The simulation and analysis of the proposed antenna is done using CST microwave studio. The simulated reflection coefficient (S_{11}) also known as return loss is presented in Fig. 5. It can be observed from S_{11} plot that the antenna covers the GSM900, GSM 1900, Bluetooth and Wi-Fi bands. To get good return loss and gain, the height of top plate selected is 10 mm. The ground plane, shorting plate and top plate are made perfect electrical conductor (pec) .

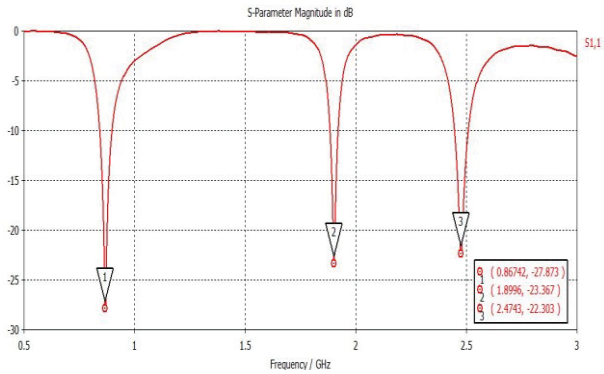

Fig. 5: The Simulated S11 (dB) of proposed PIFA

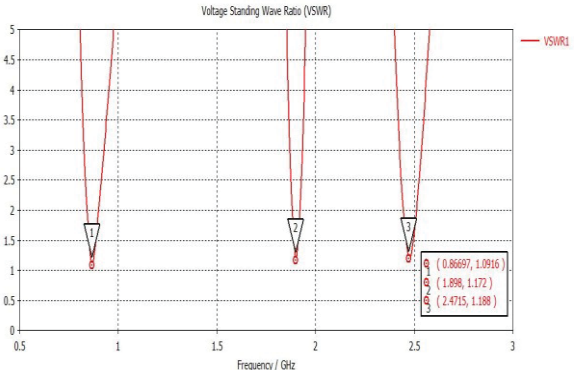

Fig. 6: The Simulated VSWR of proposed PIFA

Return loss of -27.87 dB obtained at resonant frequency of 867 MHz, -23.36 dB at 1899MHz and -22.30 dB at 2.47 MHz Also, it is observed from results that at resonant frequency the Voltage Standing Wave Ratio (VSWR) is well below 2dB [16] i.e. at 867 MHz value of VSWR is 1.09, at 1899 MHz VSWR is 1.17 and at 2.47 GHz VSWR is 1.18. The bandwidth here can be specified as impedance bandwidth for which return loss S11 is -6 dB as this value is good enough for mobile handset applications.The impedance bandwidth of the proposed PIFA design is the difference between upper and lower frequency which is 0.07 GHz, 0.05GHz and 0.06GHz.

The simulated 3-D radiation pattern of the proposed PIFA is shown below. The simulated 3D radiation pattern at 867 MHz, 1899MHz, and 2.47GHz in xyz and xy-z planes is obtained from the simulation results using CST microwave studio is shown in Fig 7(a),(b),(c).

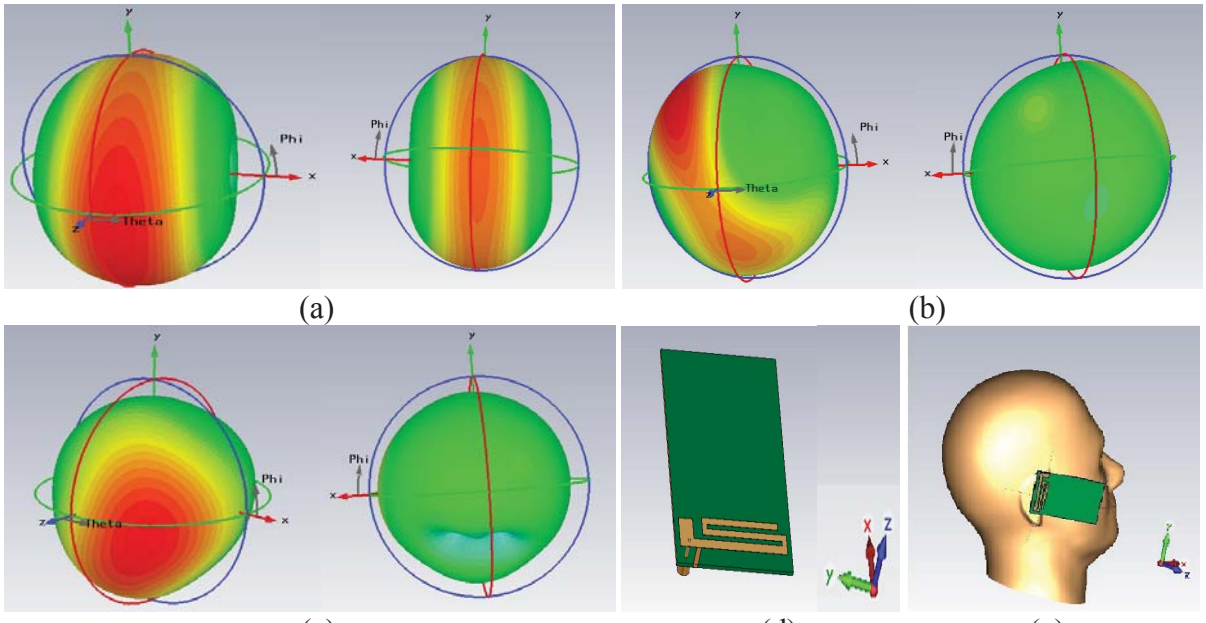

Fig.7: Simulated radiation pattern in XYZ plane and XY-Z plane at a) 867MHz b) 1899 MHz c) 2.42GHz d) proposed antenna geometry with co-ordinates e) +z and –z directions when antenna is placed near the phantom model

It can be seen from the plot that the antenna is having good electromagnetic radiation intensity in the +Z plane where as radiation is considerably reduced in the –Z direction. [11] The red, orange,yellow,green and blue regions represents radiation intensity in the decreasing order. Therefore the antenna radiation pattern itself clearly shows a decrease in

intensity of electromagnetic radiation in the –Z direction (ie towards user head, when the phone is in use).The cellular bands covered by the simulated antenna are GSM900,GSM1900 ,Bluetooth and Wi-Fi bands. The antenna has good radiation characteristics in all directions except to the user head side thus reducing electromagnetic radiation interaction with user head, which is suitable for mobile handsets.

SAR calculation with phantom head model

Various public organizations in the world have established safety guidelines for electromagnetic wave absorption. For electromagnetic wave exposures, these guidelines are based on peak specific absorption rate (SAR). SAR value is an important tool in judging the maximum possible exposure to RF energy from a source. FCC and DOT has regulated SAR value as 1.6 W/Kg averaged over 1 gm of tissue.

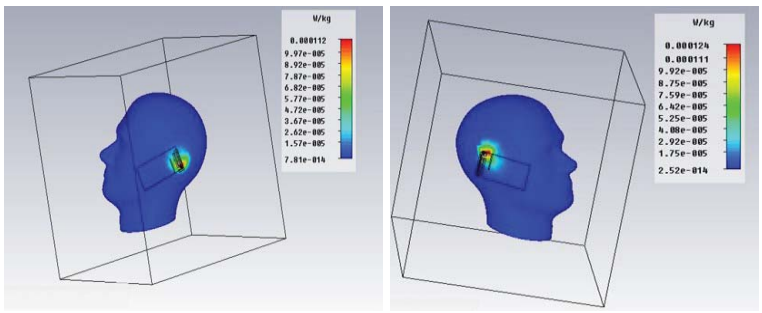

(a) (b_1) (b_2)

Fig.8 Proposed PIFA structure at a distance of 1mm from the head model when antenna is placed a)Right side of head model b) Left side of head model

The simulation model of SAM phantom head model provided by CST Microwave Studio®(CST MWS) along with the designed antenna is used for calculation of SAR .The SAR values are simulated by placing the antenna at various distances from the head model.

TABLE I
SIMULATED SAR VALUE OF THE ANTENNA WITH DIFFERENT RESONANT FREQUENCY

Distance from head model	Frequency under consideration	SAR w/kg(1gm) Antenna on Left side of head model	SARw/kg(1gm)Antenna on Right side of head model
1mm	867MHz	0.000127	0.000127
1mm	1899MHz	0.000957	0.00104
1mm	2.42GHz	0.00237	0.00240
10mm	867MHz	7.3514e-005	2.90767e-006
10mm	1899MHz	0.000286246	5.16984e-005
10mm	2.42GHz	0.000912081	0.000184495
20mm	867MHz	1.64438e-005	1.03705e-006
20mm	1899MHz	0.000105218	2.48611e-005
20mm	2.42GHz	0.000375272	0.000112568

It is seen that as the distance between the head model and antenna increases, the specific absorption rate decreases. The 1-g SAR results for the respective resonant frequencies at various distances are listed in table I, it is clearly seen that 1-g SAR results at all frequencies are well below the SAR limits of 1.6 W/kg standards. Here, the minimum SAR value obtains at lowest resonant frequency 0.9 GHz and this could be attributed due to the largest

wavelength having minimum ability of penetration in the human head. The SAR value can be reduced even more, if casing of the antenna is considered and if it is placed far away from the body.

Acknowledgement

Authors are thankful to KSCSTE for financial assistance through emeritus scientist scheme. They are also thankful to Director ISP and Head of the Department ISP CUSAT for providing facilities to carry out the project. Authors also acknowledge interest in the project by Swadesi science movement Kerala.

Reference:

[1] Kin-Lu Wong, "Compact and broad-band micro strip antennas", Published by John Wiley & Sons, Inc., Chapter: 2, Page(s): 46-78, 2003.

[2] C. Picher, J. Angueral, A. Andújar, C. Puente1, and S. Kahng, "Analysis of the Human Head Interaction in Handset Antennas with Slotted Ground Planes", IEEE Antennas and Propagation Magazine, Vol. 54, No. 2, Page(s): 36 – 56, April 2012.

[3] W. Geyi, Q. Rao, S. Ali, and D. Wang, "Handset Antenna Design: Practice And Theory", Progress In Electromagnetic Research Journal (PIER) , Vol. 80, Page(s) : 123–160, 2008.

[4] Lin J C "Cellular Mobile Telephones and Children," IEEE Antennas and Propagation Magazine, vol. 44 (5), pp.142-145, 2002.

[5] K. Takagi, Y. Furukawa, et. al., Portable telephone with reduced specific absorption rate and improved efficiency, U.S. Patent 7 274 953 B2,Sept. 25, 2007.

[6] M.A. Mangoud, R.A. Abd-Alhameed, N.J. McEwan, P.S. Excell and E.A. Abdulmula, SAR reduction for handset with two-element phased array antenna computed using hybrid MoM/FDTD tech- nique,Electronics Letters, vol. 35, no. 20, pp. 272-275, 30th Sep. 1999.

[7] M. Kitra, C. Panagamuwa, P. McEvoy, J. Vardaxoglou and J. James Low SAR Ferrite Handset Antenna Design,IEEE Transactions on Antennas and Propagation, vol. 55, no. 4, pp. 1155-1164, Apr. 2007

[8] S. Kwak, D. Sim, J. Kwon, and H. Choi, Comparison of the SAR in the Humand Head using EBG structures applied to a Mobile Handset,Proc.37th European Microwave Conference, pp. 937-940, Munich Germany, Oct. 2007.

[9] M. Tariqul, N. Misran, T. Sue, and M. Rashed, Reduction of Specific Absorption Rate (SAR) in the Human Head with Materials and Metamaterials,Proc. Int. Conf. on Electrical Engineering and Informatics, pp. 707-710, Selangor, Malaysia, Aug. 2009.

[10] D. Laila, R. Sujith, C. M. Nijas, C. K. Aanandan, K. Vasudevan, P.Mohanan Modi ed CPW Fed Monopole Antenna with Suitable Radiation Pattern for Mobile Handset, Microwave Review, Sept, 2011.

[11] Tefiku, F. , "A Mobile Phone PCS PIFA with Low SAR", IEEE Antennas and Propagation Society International Symposium, Page(s): 4685 – 4688, 2007.

DECEMBER 17, WENESDAY
04.15PM TO 05.30PM
RESEARCH SESSION 4
ANTENNA ARRAYS
J C BOSE - HALL

Chair: Dr. S.N. Joshi, CEERI, Pilani, India.

No	Papers	Page
4.1	**Gain Enhancement of Antenna Array using Metamaterial Inspired Superstrate** Bybi P Chacko, Gijo Augustin and Tayeb A Denidni Center for Energy, Materials and Telecommunications (EMT), National Institute of Scientific Research (INRS), University of Quebec, Montreal QC H5A 1K6, Canada. *E-mail:bybichacko@emt.inrs.ca*	79
4.2	**Role of Edge Elements and Mutual Coupling Effect in Active Cancellation of Probing in Phased Arrays** N. Bala Ankaiah, Hema Singh, and R. M. Jha Centre for Electromagnetics (CEM), CSIR – National Aerospace Laboratories, Bangalore., India, 560017. *Email: hemasingh@nal.res.in, jha@nal.res.in*	83
4.3	**Design Technique to Enhance Axial Ratio Bandwidth of Circularly Polarized Microstrip Array Antenna** Rajpal Singh, Anurag Sharma, Pramod Kumar Verma, Vinod Kumar Singh, and Mahakar Singh Defence Electronics Applications Laboratory (DRDO), Raipur Road, Dehradun, India-248001. *E-mail: dealrajpal@gmail.com*	87
4.4	**C-Band Monopulse Antenna Array based on Proximity Coupled U-slot Element** Pramod Kumar Verma, Rajpal Singh, Anurag Sharma, and Vinod Kumar Singh. Defense Electronics Applications Laboratory (DRDO), Raipur Road, Dehradun, India-248001 *E-mail: pramodkumarverma@deal.drdo.in*	91
4.5	**Linearly Polarized Stub Loaded Microstrip Reflectarray with Microstrip Antenna Feed** Amit A. Deshmukh[1], Ameya A. Kadam[1], Kshitij Lele[1] and K.P.Ray[2] [1]Department of EXTC, D. J. Sanghvi College of Engineering, Vile-Parle (W), Mumbai, India. [2]RFMS Division, SAMEER, IIT Campus, Powai, Mumbai-400076. *E-mail:amitdeshmukh76@rediffmail.com, kshitij.lele@gmail.com*	95
4.6	**Broaband Directional Triangular Monopole Antenna Array with Reflector** Mahima Arrawatia[1], Maryam Shojaei Baghini [1],Girish Kumar [1] [1]Electrical Engineering Department, Indian Institute of Technology Bombay Powai, Mumbai-400076, India	99

E-mail: mahima87@ee.iitb.ac.in, mshojaei@ee.iitb.ac.in, gkumar@ee.iitb.ac.in

4.7 **Conventional beamformers based on One Dimensional Reduced Mapped Real Transform** 103
P. R. Mini [1] , S. Mridula [2] , Binu Paul [2] and P. Mohanan [3]
[1]Department of Electronics and Communication Engineering, Federal Institute of Science and Technology, Kerala, India.
E- Mail: mini@fisat.ac.in
[2]Division of Electronics Engineering, School of Engineering, Cochin University of Science and Technology, Kerala, India.
E-Mail:mridula@cusat.ac.in, binupaul@cusat.ac.in
[3]Department of Electronics, Cochin University of Science and Technology, Kerala, India.
E-Mail: drmohan@cusat.ac.in

4.8 **Design of an Analogue Beam-former Network for Low Frequency Radio Telescopes** 107
Mugundhan V., Kathiravan C., Rajalingam M. and Ramesh R.
Indian Institute of Astrophysics, Bangalore-570034, India.
Email: mugundhan@iiap.res.in

4.9 **MSRR Loaded Microstrip Patch Antenna Array for 5.8 GHZ Wi-Max Applications** 113
Chirag Arora [1] , Shyam S. Pattnaik [2] , R. N. Baral [3]
[1]Krishna Institute of Engineering & Technology , Ghaziabad, (UP),
Email: c_arora2002@yahoo.co.in
[2]ETV Department, NITTTR, Chandigarh**.**
Email: profshyampattnaik@gmail.com
[3] IMS Engineering College , Ghaziabad (UP).
E-mail: r.n.baral@gmail.com

4.10 **Design, Development and Installation of Meteor Antenna System at NARL, Gadanki** 119
M. Durga Rao[1], P.Kamaraj and P. Srinivasulu
National Atmospheric Research Laboratory, Gadanki, India, 517112.
[1]*Email: mdrao@narl.gov.in*

4.11 **Design And Development Of Yagi Antenna Array For Stratosphere-Troposphere Radar** 123
Binoy Babu B, Titu K. Samson, Rejoy Rebello, K. R. Santosh, K. Vasudevan, K. Mohankumar and P. Mohanan
Advanced Centre for Atmospheric Radar Research, ST Radar Facility, CUSAT.
E-mail: binoy212@gmail.com

Gain Enhancement of Antenna Array using Metamaterial Inspired Superstrate

Bybi P Chacko, Gijo Augustin and Tayeb A Denidni
Center for Energy, Materials and Telecommunications (EMT), National Institute of Scientific Research (INRS), University of Quebec, Montreal QC H5A 1K6, Canada.
(email:bybichacko@emt.inrs.ca)

Abstract: *The effective utilization of a zero-index metamaterial unit-cell for broadside gain enhancement of conventional microstrip antenna array is presented. The 2 x 2 microstrip patch antenna array with metamaterial superstrate layers display, S11 ≤ -10 dB and gain of 14.5 – 15.6dBi over 5.63-5.89 GHz. The zero index unit-cell based metamaterial superstrate exhibits a gain enhancement up to 2.3dB. The experiment results show a good agreement with the simulated values.*

Introduction: Being the most sensitive element in any wireless communication system, antennas play a major role in the overall system performance. Traditionally, microstrip antennas are widely employed since they provide many prominent features such as small size, light weight, and easy mounting in various scenarios. In spite of all the merits, one of the challenging obstacles for a microstrip patch antenna is the lack of high gain, good enough for long range communication in urban crowded environments. A widely used traditional solution is the deployment of arrays with appropriate beam forming network (BFN) [1].

Metamaterials offers a broad range of possibilities for modern researchers working in the fascinating field of applied electromagnetics. This new paradigm offers numerous types of metamaterials with broad range of effective dielectric characteristics and operates from microwave band to visible spectrum. Among various metamaterials low index metamaterials (LIM) possess refractive index in the range of zero to one ($0 \leq n \geq 1$) resulting either effective permeability or permittivity reaches a value close to zero [2, 3]. This results in very small phase variations for electromagnetic waves passing through these types of structures. This 'freezing' of the phase inside a LIM material helps to focus the refracted waves along the direction perpendicular to the flat interface [4]. This property can be effectively utilized in many applications such as wave front transformer [3] and antenna radiation beam focusing [5].

In this work, we investigate the design strategies for effective gain enhancement of a 2 x 2 antenna array by employing zero-index metamaterial based superstrate. The antenna geometry was optimized for maximum gain without degrading the impedance matching. Analysis shows that, the proposed unit-cell when loaded with an optimum periodicity and inter-layer spacing facilitates significant gain enhancement for the planar microstrip array.

Antenna geometry: The proposed metamaterial high-gain antenna array is shown in Fig. 1(a). It comprises of a 2 x 2 microstrip patch antenna array operating at 5.8GHz and three layers of ZIM unit-cell based superstrate. The patch antenna array (Fig. 1(b)) is designed on a Rogers 6035HTC substrate of dielectric constant 3.45 and thickness t2 = 1.52 mm. The structure of the ZIM unit-cell with geometrical parameters is shown in Fig. 1(c). It consists of a single-open electric-field-coupled resonator realized on Rogers® R04350B laminate with dielectric permittivity (εr) 3.48, loss tangent 0.0031 and thickness (t1) 0.762mm. The unit-cell is studied using the full wave electromagnetic simulation software CST microwave

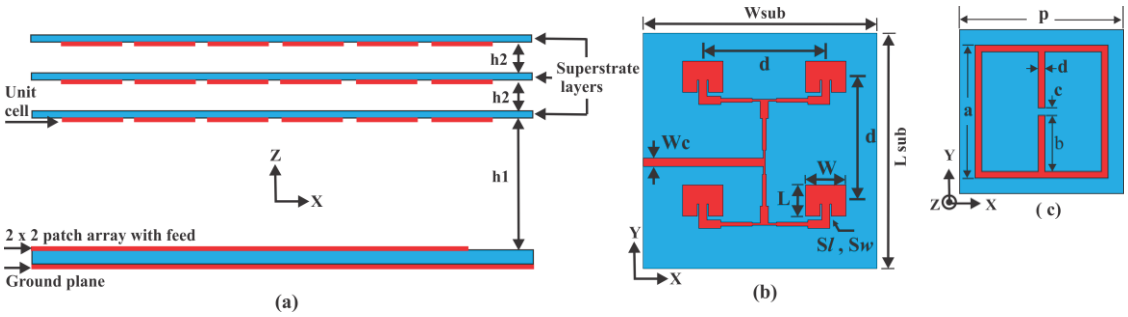

Fig. 1 Proposed high-gain metamaterial superstrate antenna array (a) Side view of the whole structure, (b) Array antenna at 5.8 GHz (c) unit-cell geometry (Wsub = Lsub = 100, W = 16.7,L = 13.2, Sl = 5, Sw = 0.5, Wc = 3.4, s = 2, h1 = 27, h2 = 1, d = 50.8[units in mm]), (unit cell dimensions: a = 11.75, b = 5.13, c = d = 0.5, p = 13.75 [units in mm]),)

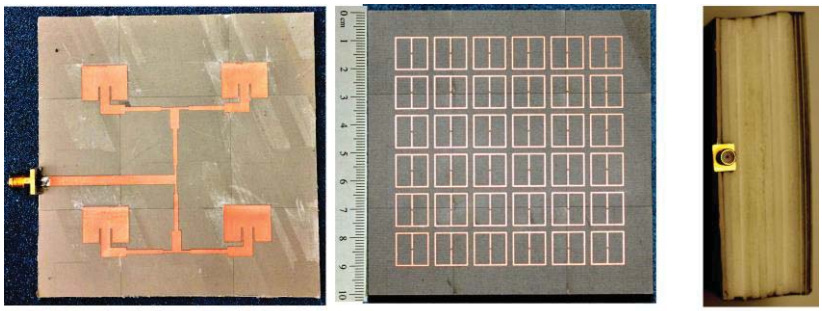

Fig. 2 Proposed high-gain metamaterial superstrate antenna array (a) Array antenna (b) superstrate geometry (b) Fabricated prototype of the proposed antenna

studio® whose characteristics were presented in [6]. At the optimized design, the unit-cells were arranged with a periodicity 6 x 6 and inter-unit-cell spacing of 2mm. Three-layer superstrate was placed at a height of h1 = 27 mm (approximately equal to half wave length) from the patch antenna array with an inter-layer spacing of h2 = 1mm.

To offer a solid mechanical support for the thin metamaterial superstrate layer, Rohacell® high frequency foam material of permittivity 1.05 are added in the gaps h1 and h2. The superstrate layers and the source antenna are aligned at the center and have dimensions of Lsub x Wsub = 100 x 100 mm^2.The fabricated high-gain metamaterial antenna array prototype is shown in Fig. 2. The measurement were carried out using Anritsu® MS4647A vector network analyzer in an anechoic chamber.

Results and discussions:

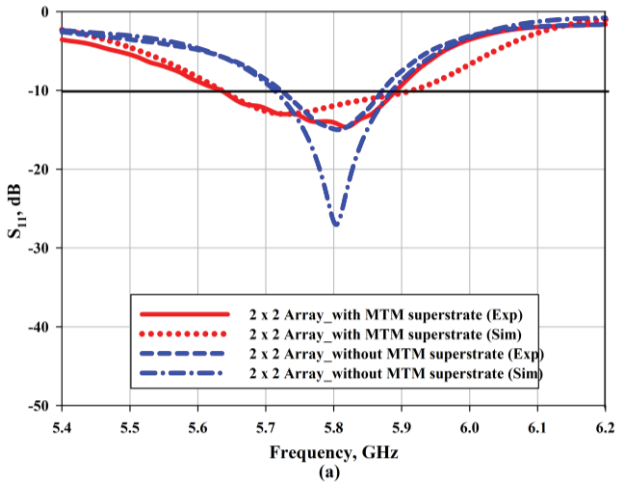

Fig. 3. Simulated and measured S_{11} characteristics of the MPA with and without metamaterial superstrate layers

The simulated and measured S_{11} characteristics of the MPA array with and without the metamaterial superstrate layers are presented in Fig.3. At the optimized design, the antenna array with metamaterial superstrate displays a slight enhancement in bandwidth compared to the source antenna array. This is due to the change in the near field properties of the MPA array when the superstrate is added. The source antenna (MPA array) offers S11 ≤ -10dB bandwidth from 5.72 to 5.87GHz, while the proposed metamaterial antenna design provides a bandwidth from 5.63GHz to 5.89GHz. The simulated and measured results are in good agreement.

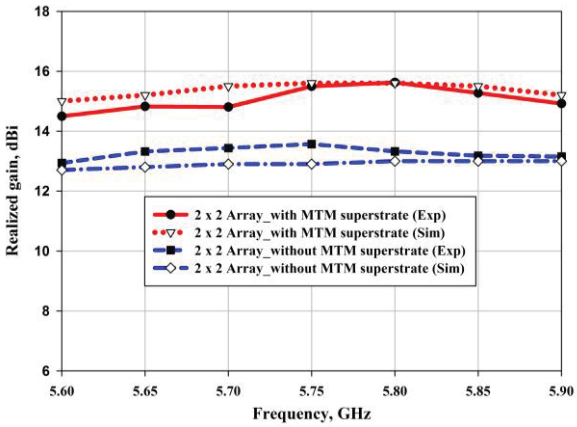

Fig. 4. Simulated and measured realized gain of the MPA with and without metamaterial superstrate layers

The gain of the MPA array with and without the MTM layers was also measured separately using gain comparison method and is displayed in Fig.4. The MTM superstrate layers enhance the source antenna gain over the operating frequency band. It is observed that ,by loading three layers of superstrate material, the measured maximum gain of the source antenna array went up from 13.3dBi to 15.6dBi at 5.8GHz. Thus the MTM superstrate delivered a gain enhancement up to 2.3dB. The measured results agree with the simulated ones. The antenna also has a maximum gain of 15.6 dBi at 5.8 GHz.

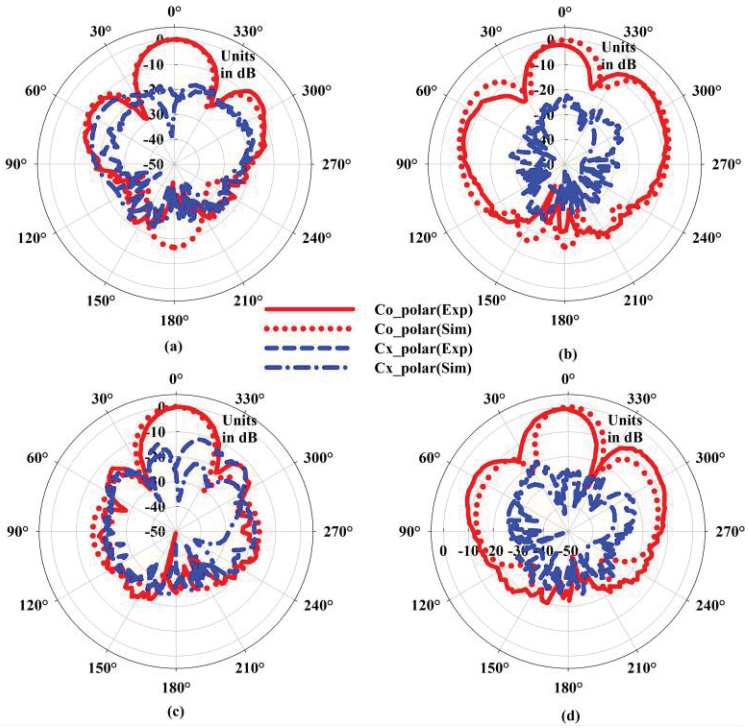

Fig. 5. Simulated and measured Radiation patterns at 5.8 GHz (a) XZ plane pattern of the MPA array (b) YZ plane pattern of the MPA array (c) XZ plane pattern of the MPA array with superstrate (d) YZ plane pattern of the MPA array with superstrate

The far-field radiation pattern of the proposed array antenna in XZ and YZ planes at 5.8 GHz is measured and compared with the simulated one as depicted in Fig.5. The radiation patterns are similar to those observed for base-station antenna applications. A good agreement between the simulation and experiment is also observed.

Conclusions: In this work, we have proposed a novel high-gain antenna array with ZIM based metamaterial superstrate layers. The measurement results have shown that the 2x 2 metamaterial based antenna array exhibits S11 $\leq$ -10dB and Gain $\geq$ 14.5dBi in the entire IEEE 802.11a band. A gain enhancement up to 2.3dB has been obtained.

Reference:

[1] H.-D. Chen, C. Y. D. Sim and Y.J. Wu, "Broadband high-gain microstrip array antennas for WiMAX base station," IEEE Trans. Antennas Propag., vol. 60, no.8, pp. 3977-3980 Aug. 2012.

[2] R. W. Ziolkowski, "Propagation in and scattering from a matched metamaterial having a zero index of refraction," Phys. Rev. E - Statistical, Nonlinear, Soft Matter Phys., vol. 70, no. 42, pp. 046608-1-046608-12, 2004.

[3] M. Silveirinha, and N. Engheta, "Design of matched zero-index metamaterials using nonmagnetic inclusions in epsilon-near-zero media," Phys. Rev. B - Condensed Matter Mater. Phys., vol. 75, no.7, 2007

[4] D. Li, Z. Szabo, X. Qing, E. -P. Li and Z. N. Chen, "A high gain antenna with an optimized metamaterial inspired superstrate," IEEE Trans. Antennas Propag., vol. 60, no.12, pp. 6018-6023,2012.

[5] H. Zhou, Z. Pei, A. Qu, Song Zhang, J. Wang, Z. Duan, H. Ma and Z. Xu, "A novel high-directivity microstrip patch antenna based on zero-index metamaterial," IEEE Antennas Wireless Propag. Lett., vol.8, pp. 538-541,2009.

[6] B. P. Chacko, G. Augustin and T. A. Denidni, " A High-Gain Antenna based on Zero-Index Metamaterial Superstrate," Proceedings of IEEE Antennas and Propagation society International Symposium (APSURSI), pp. 122-123, 2013.

Role of Edge Elements and Mutual Coupling Effect in - Active Cancellation of Probing in Phased Arrays

N. Bala Ankaiah, Hema Singh, and R. M. Jha
Centre for Electromagnetics (CEM),
CSIR – National Aerospace Laboratories, Bangalore., India, 560017
Email: hemasingh@nal.res.in, jha@nal.res.in

Abstract: *A modified improved LMS algorithm is used for active cancellation of probing sources in linear phased array. The edge effect and mutual coupling is included in the formulation for the steering vector and weight adaptation towards the generation of adapted pattern for a given signal environment. The array performance in adaptive nulling is analyzed in terms of output signal-to-interference-noise ratio, output noise power and the adapted pattern.*

Introduction: The performance of phased array is analyzed in terms of nullifying the probing sources and maintaining the gain towards each of desired sources. The modified improved LMS algorithm is an efficient adaptive algorithm used for active cancellation of probing sources in phased arrays. When the antenna elements are closed to each other mutual coupling effect [1] arises. The coupling between the antenna elements affects the antenna radiation pattern and array manifold. The mutual and self impedance of antenna elements depend on the geometric configuration of the array. Further, the edge effect in finite antenna arrays has been the subject of interest towards performance optimization [2]. For a finite array, the behavior of edge elements is in general different from the rest of the array. The real part of the input impedance of antenna array does not depend on the element position in the array while this is not true for the imaginary part of the impedance matrix. This effect alters the array response towards the impinging signals [3]. The performance of the phased array degrades after including the edge and mutual coupling effect.

In this paper, the modified improved LMS algorithm is used for adaptive nulling in linear phased array including edge and mutual coupling effects. The signal environment considered consists of multiple desired and probing sources. The active cancellation of probing sources in dipole phased array is demonstrated by comparing the adapted and the quiescent patterns. The performance of phased array is further analyzed in terms of output signal-to-interference-noise ratio (SINR).

Formulation for Array Response including Edge and Mutual Coupling Effect: The array response towards the signal incident at an angle θ including edge effects is given by

$$S_t = f(\theta,\phi)\cdot\left(C_{ii}\cdot e^{-j(kd\cos\theta+\alpha)} + \sum_{k=1;k\neq i}^{N} S_{ik}\cdot e^{-j(kd\cos\theta+\alpha)} \right) \quad (1)$$

where, S_{ik} is the coupling scattering coefficient [4], given by

$$S_{ik} = \begin{cases} 0 & i = k \\ \dfrac{2 \cdot Z_{ik}}{(Z_{ii}+1)\cdot(Z_{kk}+1) - Z_{ik}\cdot Z_{ki}} & otherwise \end{cases} \quad (2)$$

Where, k is the wave number, d is the inter-element spacing, Z is the impedance matrix consisting of both self and mutual impedances, C_{ii} denotes the coupling of the array aperture to the output port, α is the phase excitation, and $f(\theta,\phi)$ is the radiation pattern of the antenna element.

Results and Discussion: In this paper, a 16-element uniform linear dipole array is considered. The dipole length is taken as half-wavelength with h=0.25λ. The inter-element spacing is 0.484λ. The edge and mutual coupling effects are included in computations for the output SINR, and adapted pattern for different signal environments. The results are shown for side-by-side and parallel-in-echelon dipole arrays for different signal environments. In adapted pattern, the desired sources are shown as green arrows while probing sources are represented by red arrows. Figure 1 compares the output SINR of the dipole array with and without edge effect. The signal scenario consists of one desired signal (90°; 1) and two probing sources (45°; 135°, 150, 200). As expected the output SINR degrades slightly when edge and mutual coupling effects are included. However the variation is not much significant.

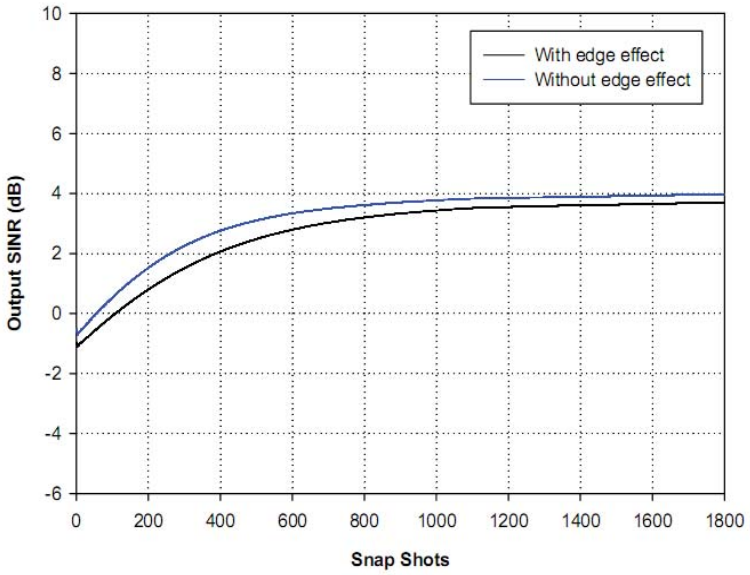

Figure 1 Output SINR of 16-element linear side-by-side dipole array. One desired signal (90°; 1) and two probing sources (45°, 135°; 150, 200).

Figure 2 shows the quiescent and adapted patterns of 16-element linear side-by-side dipole array including edge and mutual coupling effects. The signal environment consists of two desired signals (40°, 140°; 1 each) and two probing sources (80°, 95°; 800, 1000). The adapted pattern shows mainlobe towards each of the desired signals with accurate and deep nulls towards each of probing sources. These probing sources will not be able to receive any signal from the array. In other words the array is invisible to them. Thus one can infer that the modified improved LMS algorithm is an efficient weight adaptation algorithm, which can efficiently cater to arbitrary signal environment including edge and mutual coupling effect.

Figure 3 shows the output SINR of 16-element linear parallel-in-echelon dipole array. The array signal environment consisting of one desired signal (90^o; 1) and one probing source (145^o; 100). As expected the output SINR of array reduces a little when edge effects are taken into account. It can be observed that the performance of parallel-in-echelon array without edge effect is better as comapred to the case parallel-in-echelon array with edge effect

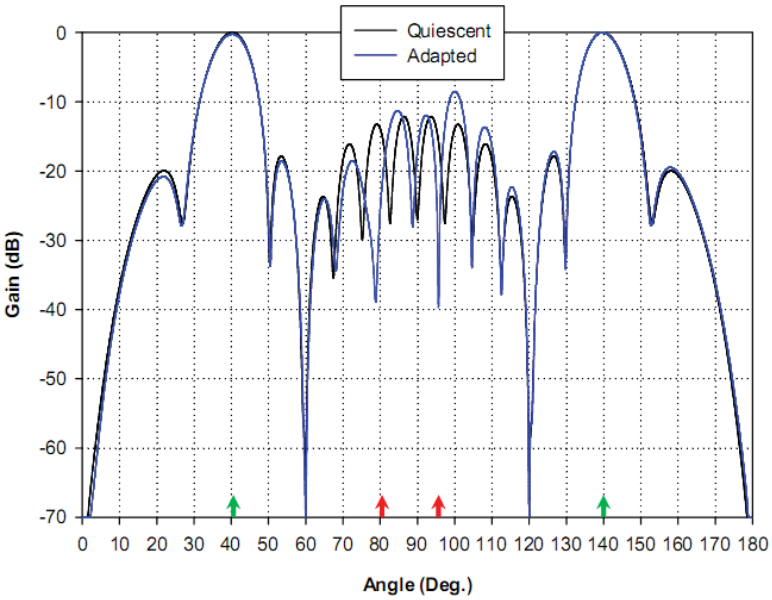

Figure 2 Adapted pattern of 16-element linear side-by-side dipole array.
Two desired signals (40^o, 140^o; 1 each) and two probing sources (80^o, 95^o; 800, 1000).

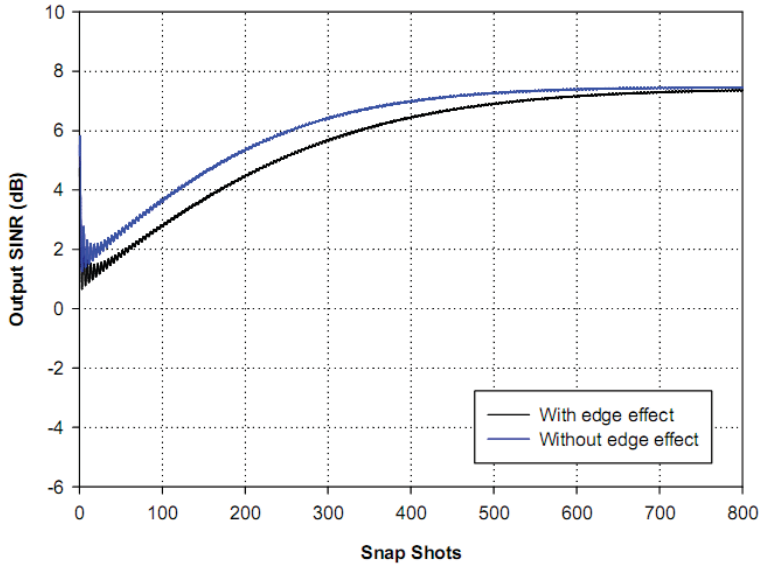

Figure 3 Output SINR of 16-element linear parallel-in-echelon dipole array.
One desired signal (90^o; 1) and one probing source (145^o; 100).

Figure 4 presents the adapted pattern of 16-element linear parallel-in-echelon dipole array. The array configuration consists of two desired signals (40^o, 140^o; 1 each) and one probing source (100^o; 200). It may be observed that array maintains mainlobe towards each of the

desired sources with a deep null towards the probing source. It is apparent that the array is able to cater to the signal scenario even when the edge and mutual coupling effects are taken into account. This demonstrates the efficiency of adaptive algorithm used for weight adaptation in array. This helps the phased array in catering complicated signal environments consisting of multiple sources.

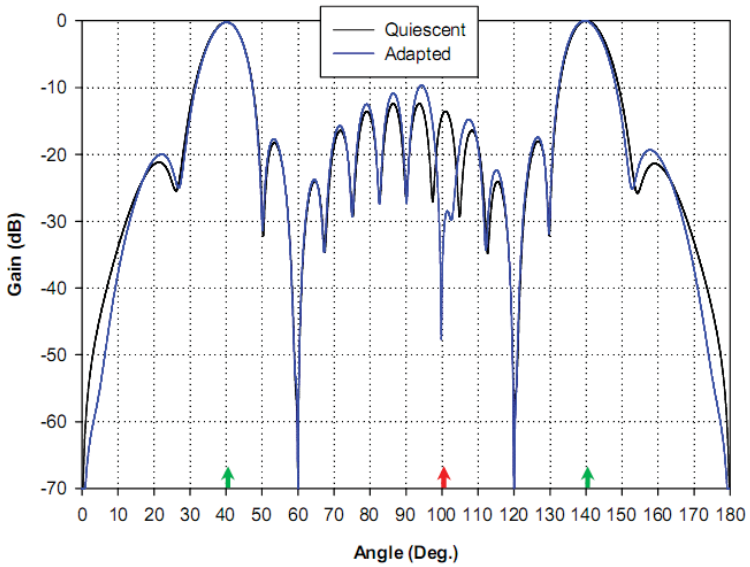

Figure 4 Adapted pattern of 16-element linear parallel-in-echelon dipole array. Two desired signals (40^o, 140^o; 1 each) and one probing source (100^o; 200).

Conclusion: The modified improved LMS algorithm is an efficient adaptive algorithm towards suppression of probing in phased arrays. It is capable of catering arbitrary signal environment consisting of multiple desired and probing sources, even when edge effect and mutual coupling is taken into account. The edge effect and mutual coupling alters the steering vector and hence the weight adaptation. This affects the adaptive nulling performance of the phased array. The optimal weights used to estimate the output noise power and SINR of linear dipole array. The generated adapted pattern maintains mainlobes towards each of the desired sources efficiently with accurate and deep nulls in the probing directions. This capability of adaptive algorithm can be exploited towards active radar cross section reduction of the aerospace platforms over which phased arrays are mounted.

References:

[1] I. J. Gupta, and A. A. Ksienski, "Dependence of adaptive array performance on conventional array design," *IEEE Transactions on Antennas and Propagation*, vol. AP-30, pp. 549-553, July 1982.

[2] R. C. Hansen, "Anomalous edge effects in finite arrays," *IEEE Transactions on Antennas and Propagation,* vol. 47, no. 3, pp. 549-554, March 1999.

[3] R. C. Hansen, "Linear connected arrays," *IEEE Antennas and Wireless Propagation Letters*, vol. 3, pp. 154-156, May 2004.

[4] V. Rabinovich and N. Alexandrov, *Antenna Arrays and Automotive Applications*, ISBN: 978-1-4614-1073-7, 191 p., 2013.

Design Technique to Enhance Axial Ratio Bandwidth of Circularly Polarized Microstrip Array Antenna

Rajpal Singh, Anurag Sharma, Pramod Kumar Verma, V. K. Singh, Mahakar Singh
Defence Electronics Applications Laboratory (DRDO), Raipur Road, Dehradun, India-248001
Email: dealrajpal@gmail.com

Abstract: *The paper presents a new technique to achieve wide axial ratio bandwidth using a feeding technique based on corporate feeding network. The Simulated results of designed 4x4 stacked patch array antenna exhibit the wide 3 dB axial ratio bandwidth of more than 20 percent and gain better than 17.5 dBi over the band.*

Introduction: The microstrip antennas have light weight, small volume, low profile and can be made conformal to the host surface. Therefore it is suitable for the present scenario of telecommunication. Power is fed to the Microstrip array antenna through a corporate feed network having a single input and multiple feed lines constituting the output ports. Each of these feed lines terminating at an individual radiating element has equal length and therefore transfers its power to the elements in same phase.

When an electromagnetic wave impinges on an array antenna it strikes on an element where it causes a current flow, part of the incident wave will be re-scattered into space and other will be directed towards other elements, where it will add vectorially with the incident wave. The amount of signal received by an element of array antenna is the vector sum of the direct wave and that are coupled to it through (a) parasitically from other elements and (b) by surface waves in the antenna [1].

Conventional corporate feed network: The conventional corporate feed network is generally used to feed the power to Microstrip array antenna. This feed network splits power in the ratio of 2^n (where n=1,2,3,4,.....etc.) [2]. The matching of different feeding lines are accomplished by quarter wavelength transformers.

When two microstrip patch antennas are in proximity and one is transmitting, the second will receive some of the transmitted signal, with the amount depending on their separation and relative orientation. If both antennas are transmitting they will simultaneously receive a part of each other transmitted power. Antennas re-scatter a portion of incident wave and act like a transmitter even when they are only in receiving mode. The result is that energy interchange between a radiating element of an array and a remote point element occurs not only by the direct path but also indirectly via scattering from other radiating elements of the array. The total effect of this phenomenon is called mutual coupling, which depends on the radiation characteristics of the element, relative separation between the elements and the relative orientation of each element [1-3]. Mutual coupling may be reduced by increasing the inter-element spacing (d), restricted by $\lambda_0/2 \leq d < \lambda_0$ to avoid the occurrence of grating lobes in the scan angle.

Proposed Feed Network: The mutual coupling depends on the inter-element spacing and orientation of radiating elements. The inter-element spacing lies in the fixed range of $\lambda_0/2$ to λ_0. Now only the orientation of the radiating elements may be used to control the mutual coupling. Therefore an unconventional corporate feed network is designed, in which the power is fed by microstrip line connected to alternate face of the radiating elements and the

feed-line length is increased by $\lambda_g/4$ with respect to the previous one in the fashion of 0, 90, 180 and 270 degrees arrangement [4-5] as shown in fig-5. In this configuration only the co-poles are reinforced. The cross-poles of the diagonal elements cancel each other because of 180 degree phase reversal while the coupling between the adjacent elements is reduced due to orthogonal orientation with 90 degree phase difference of the radiating elements. Therefore the mutual coupling of the array is significantly less as compared to conventional feeding network. The comparison of cross-pols for both the configurations is shown in the simulated results in figs-1, 2 and 3 respectively.

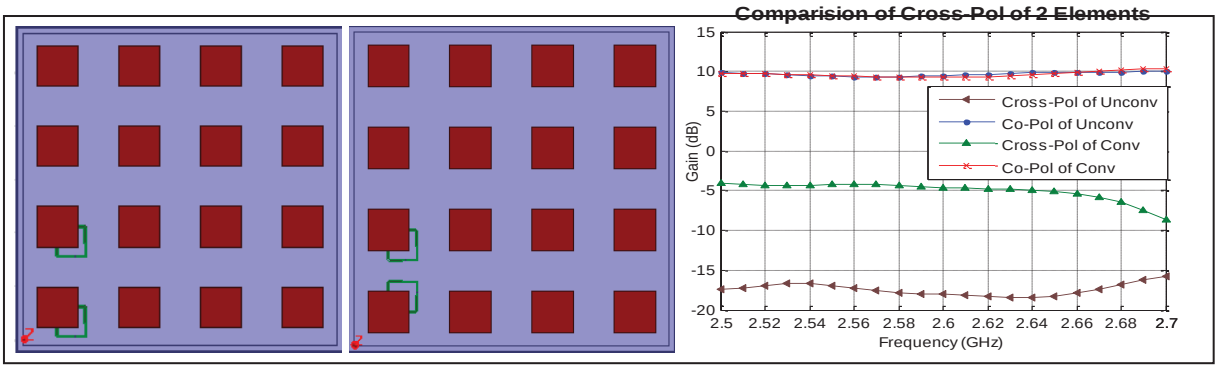

Fig 1 Comparison of Cross-pol of antenna with conventional and unconventional feed of two elements

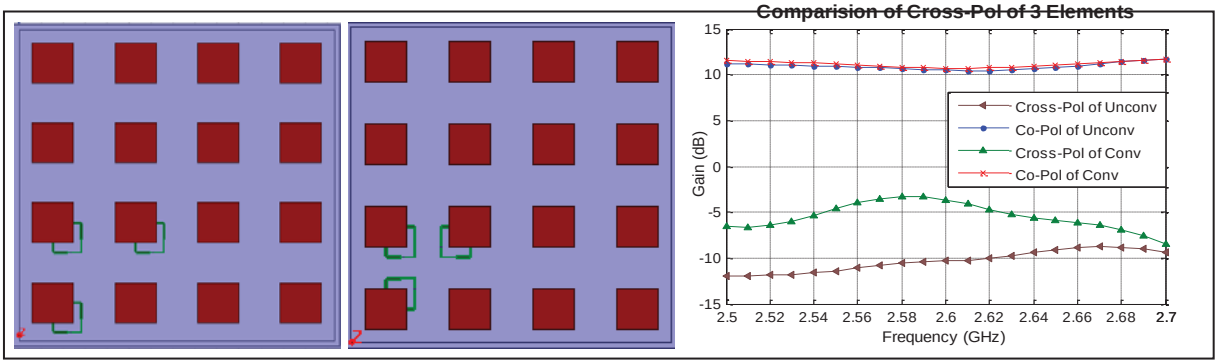

Fig 2 Comparison of Cross-pol of antenna with conventional and unconventional feed of three elements

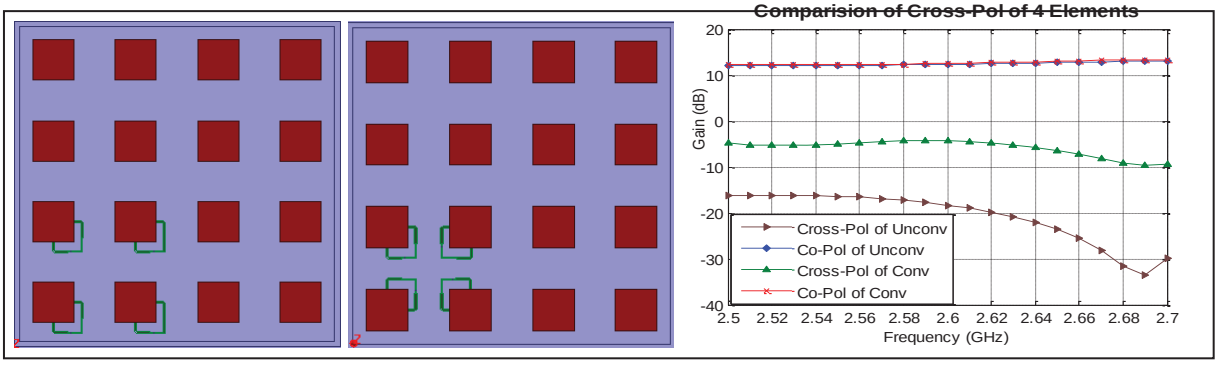

Fig 3 Comparison of Cross-pol of antenna with conventional and unconventional feed of four elements

Description of Array Antenna: The microstrip array antenna is designed at S-band with conventional and unconventional feed network [2-3]&[6]. The configurations of the sixteen patches conventional and un-conventional array antenna are given in fig-4 and fig-5 with simulated co-pol and cross-pol levels respectively. The dimension of the both lower and upper square patches is 37.5 mm and the inter-element spacing is 37.5 mm. The overall size

of the antenna is 300 x 300 x 12 mm^3. The lower patches and the feeding network are printed on 1.575 mm thick substrate of RT Duroid-5880 (ε_r=2.2). The upper patches are printed on the bottom side of 1 mm thick FR-4 substrate (ε_r= 4.4). The upper and lower patches are separated by a 8 mm thick spacer (ROHACEL, ε_r=1.05). FR-4 substrate is also working as the radome. In designed microstrip array antenna with unconventional feed, the orthogonal face of each patch with respect to patch one as shown in fig-5 is fed with microstrip quadrature feed with a phase difference of 90, 180 and 270 degrees configuration. The 100 Ω feed line is used to feed the power to each element with a $\lambda_g/4$ impedance matching transformer of 70.7 Ω.

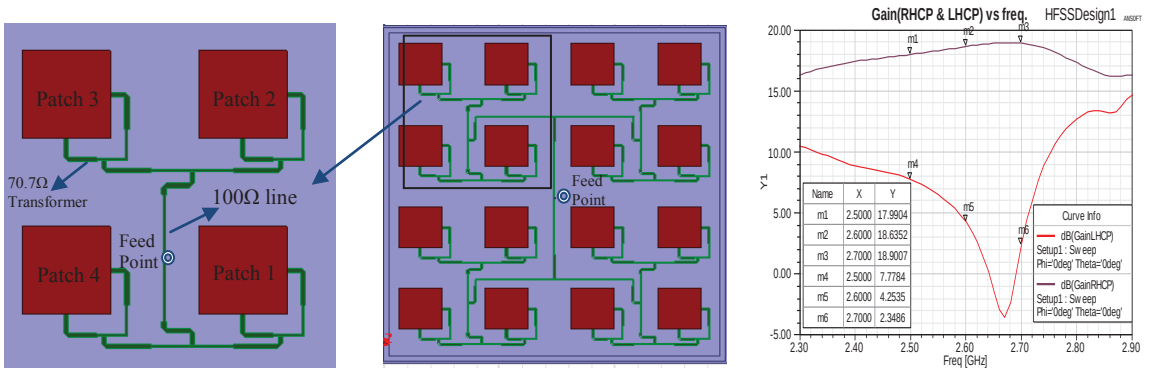

Fig. 4: Microstrip array antenna with conventional feed network and simulated Co-pol & Cross-pol level

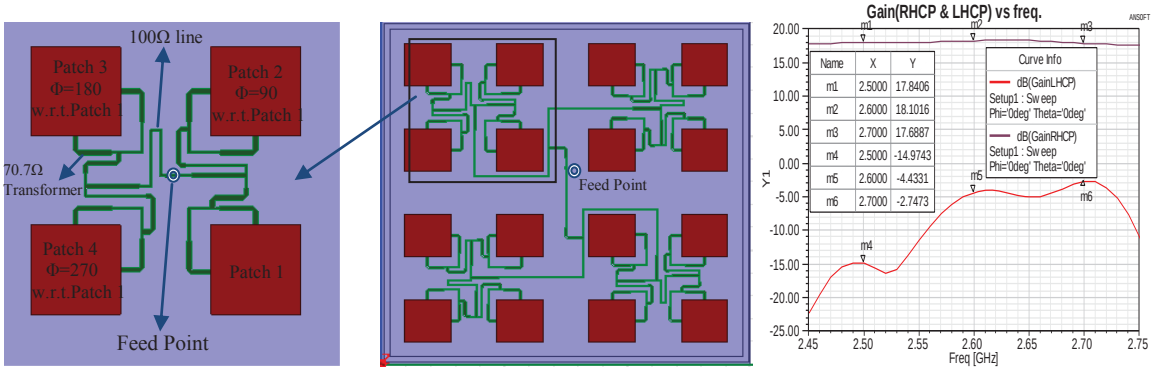

Fig. 5: Microstrip array antenna with unconventional feed network and simulated Co-pol & Cross-pol level

Results and Technical discussion: The microstrip array antennas with conventional and unconventional feed network are modeled, simulated and optimized on HFSS software.

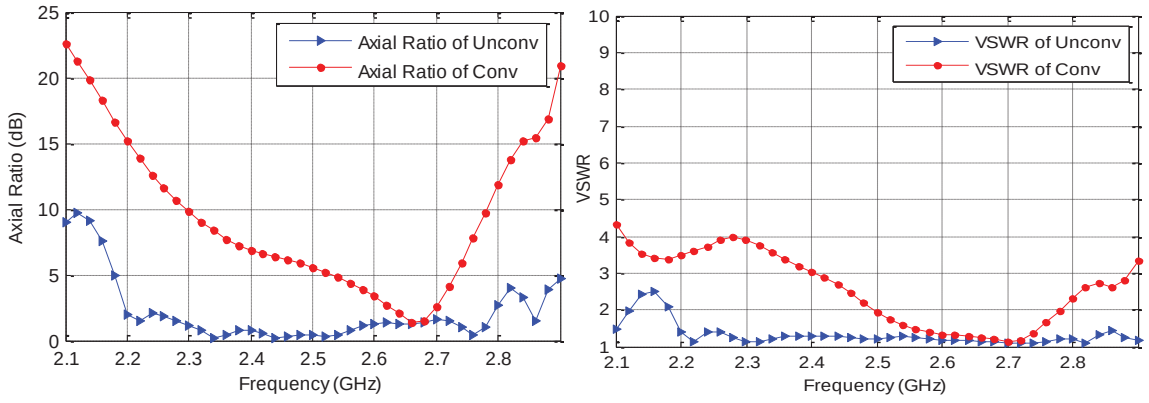

Fig. 6: Simulated Axial Ratio and VSWR of Microstrip array antenna with conventional & unconventional feed network

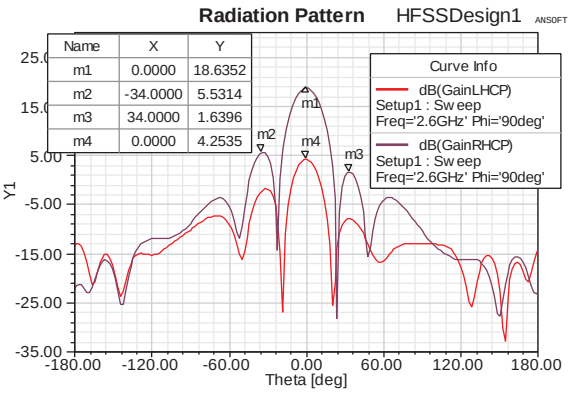

Fig. 7(a): Radiation pattern @ 2.6GHz with conventional feed network

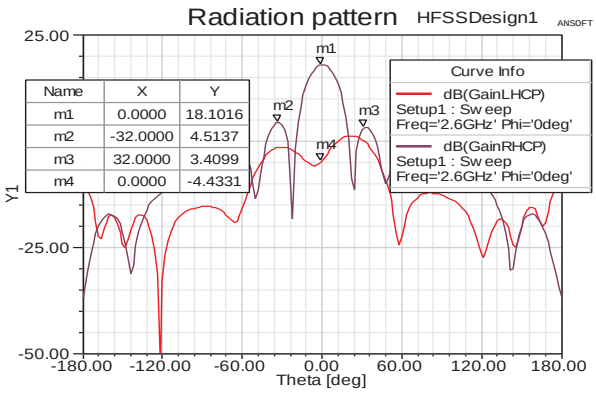

Fig. 7(b): Radiation pattern @ 2.6GHz with unconventional feed network

The simulated axial ratio plots and VSWR plots with the conventional and unconventional feed are shown in fig-6 and the radiation patterns at 2.6 GHz are shown in figs-7(a) and 7(b) respectively that shows tremendous improvement in the axial ratio bandwidth as well as in VSWR with unconventional feed network. It can be seen that the cross-pol level for the unconventional feed is reduced as compared to the conventional one. This reduction in the cross-pol is due to orthogonal orientation and phase difference on the input of the radiating elements.

Conclusion: The paper presents a new feeding technique for a 4x4 circularly polarized microstrip patch array antenna. Simulated axial ratio (<2dB) bandwidth of 24 percent has been achieved over the frequency range of 2.2-2.79 GHz. Simulated impedance bandwidth (VSWR<1.5) is more than 24 percent over the frequency range of 2.2-2.95 GHz and the gain of the antenna is more than 17.5 dB.

Acknowledgement: The authors thanks Director, DEAL, for permission to publish the paper.

Reference:

[1] Emmanuel H. Van Lil and Antoine R. Van DE Capelle, "Transmission line model for mutual coupling between microstrip antennas", IEEE Trans. on Antennas & Propagation, Vol. AP-32, No. 8, pp. 816-821, 1984.
[2] Ramesh Garg, Prakash Bhartia, Inder Bahl "Microstrip Antenna Design Handbook ", Artech house, Boston, London, 2000.
[3] Girish Kumar, K. P. Ray, "Broad Band Microstrip Antennas", Artech house, Boston, London, 2003.
[4] Huang J., "A Technique for an array to generate circular polarization with linear polarized elements" IEEE Trans on Ant. and prop., vol. AP-34, No. 9, PP 1113-1123, Sept.1986.
[5] Kapil R. Dandekar, Hao Ling and Guanghan Xu, "Experimental study of mutual coupling compensation in smart antenna applications", IEEE Trans. on wireless comm., Vol. 1, No. 3, pp. 480-487, 2002.
[6] V. K. Singh and Virpal Singh, "Design of C-band RHCP microstrip Antenna array", Proc. ICAT-2005.

C-Band Monopulse Antenna Array based on Proximity Coupled U-slot Element

Pramod Kumar Verma, Rajpal Singh, Anurag Sharma and V K Singh
Defense Electronics Applications Laboratory (DRDO), Raipur Road, Dehradun, India-248001
Email: pramodkumarverma@deal.drdo.in

Abstract: *The paper describes design of a wideband monopulse antenna array of U-slot rectangular patch. The U slot rectangular patches are fed by means of proximity coupling by microstrip feed line with pi shaped stub. Measured Impedance bandwidth (SWR≤2) of antenna is 22% ranging from 4.3 GHz to 5.4 GHz. Antenna has simulated gain of 18 dBi and null depth of better than 30 dB.*

Introduction: It is well known that microstrip antennas have very narrow impedance bandwidth typically a few percent. Impedance bandwidth of microstrip patch antennas can be enhance by noncontact feeding techniques i.e. aperture coupling and proximity coupling [1-3]. These feeding methods have helped to overcome the bandwidth limitation associated with direct contact excitation procedures (edge and probe feeding). The direct contact feed suffers from spurious radiation from feed line and also associated with the current discontinuity where the patch joins feed. Other methods for widening bandwidth are to cut the patch with U-slot and to use stacked patch structure [4-5].

The paper discusses the simulated and measured results of a planar 8x2 microstrip antenna array based on U-slot rectangular patch elements. This may be used for monopulse tracking as it is fed by microstrip based Rat-Race to get Sum and Difference pattern.

Rat Race: In general Rat-Race is designed in circular shape but here we have designed a compact rectangular shape Rat-Race to accommodate in between antenna elements. HFSS CAD model of rat race is shown in fig-1. If we feed port 2 and port 4 equally then port 3 will receive combined power and no power would be received at port 1.This is the reason port 3 is referred to as the sum port and port 1 is referred as delta / difference port. Comparison of theoretical and simulated results of designed Rat-Race is shown in table-1. As per simulated results shown in fig-2(a) and fig-2(b), the power imbalance of designed Rat Race is less than 0.3dB and the phase imbalance of Rat-Race is less than 3 degree at center frequency.

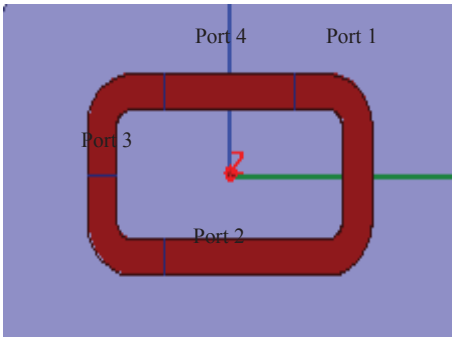

Fig.1 HFSS CAD Model of Rat Race

Table 1: Simulated phase difference between output ports

Excited port	Output port	Isolated port	Phase difference between two output ports	
			Theoretical	Simulated
1	2,4	3	180°	181.2
2	1,3	4	180°	177.3
3	2,4	1	0°	1.7
4	1,3	2	0°	2.2

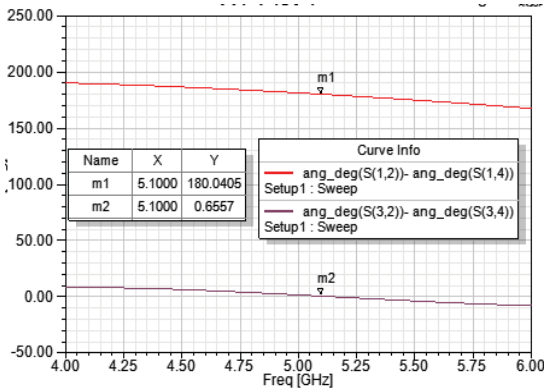

Fig.2 (a) Phase difference between output arms

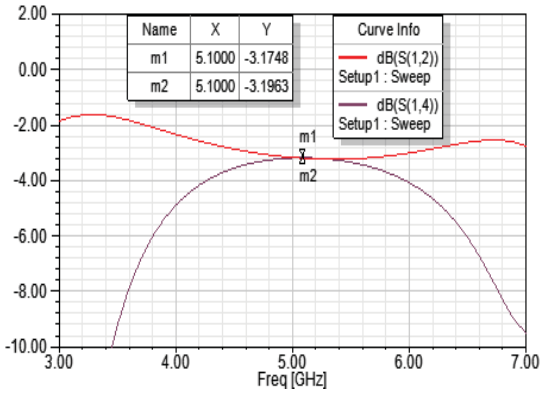

Fig.2(b) Power split of rat race

Concept of Monopulse: Monopulse gives much better target measurements than the estimating of the angular position. Monopulse systems usually contain enhanced signal processing to give better quality target information. Designed single axis monopulse antenna uses two sections i.e. upper eight elements and lower eight elements of planar array. In transmission mode both sections of antenna arrays will be fed in phase and the corresponding radiation pattern is called the sum pattern. In reception mode, from the received signal of both section of antenna array it is possible to get sum pattern and difference pattern in elevation. For sum pattern all two sections are fed in same phase and equal amplitude while for difference pattern two sections are fed in opposite phase (180^0) and equal amplitude. Both signals are then compared and their difference is used to estimate the elevation tracking of target accurately.

Description of Antenna Array: The geometry of designed antenna element with detailed dimension is shown below in fig-3(a).

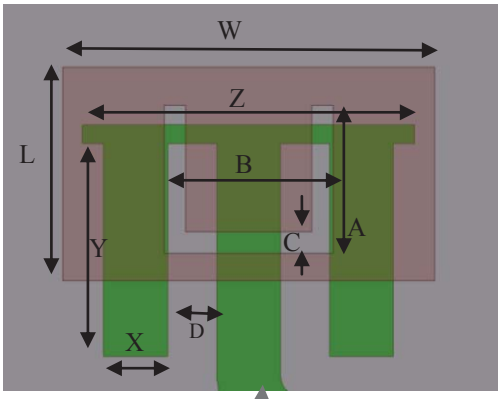

Fig.3(a) HFSS CAD Model of Antenna Element

Antenna Parameter		Dimension
Patch Dimensions	W	18.0 mm
	L	16.0 mm
Π - Stub Dimensions	X	4.80 mm
	Y	16.0 mm
	Z	25.0 mm
	D	3.70 mm
Slot Dimension	A	11.1 mm
	B	12.7 mm
	C	1.60 mm

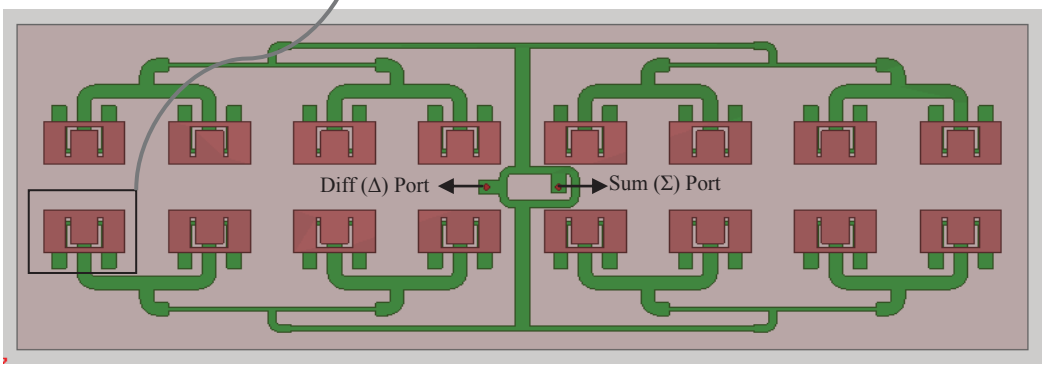

Fig.3(b) Top View of HFSS CAD Model of Mono-Pulse Antenna Array

The bottom dielectric layer is made of 1.575mm thick RT Duroid 5880 substrate (ε_r=2.2). Top layer is made of FR-4 epoxy (ε_r= 4.4) with thickness of 1 mm. Top and bottom dielectric layers are separated by 3mm thick rohacel HF 51 foam (ε_r=1.05). Foam is used as a supporting material to maintain the gap between the upper and lower layer. It also reduces the excitation of surface wave between layers. The rectangular U-slot patch is located on lower side of top dielectric layer which act as a radome for antenna. The pi shaped feed line and Rat- Race has been printed on the upper side of lower dielectric layer. Ground is printed on bottom side of lower dielectric layer. Top view of HFSS CAD Model of antenna is shown in fig-3(b). Fabricated antenna prototype has dimension 360 mm x 140 mm x 8 mm.

Simulated and Measured Results

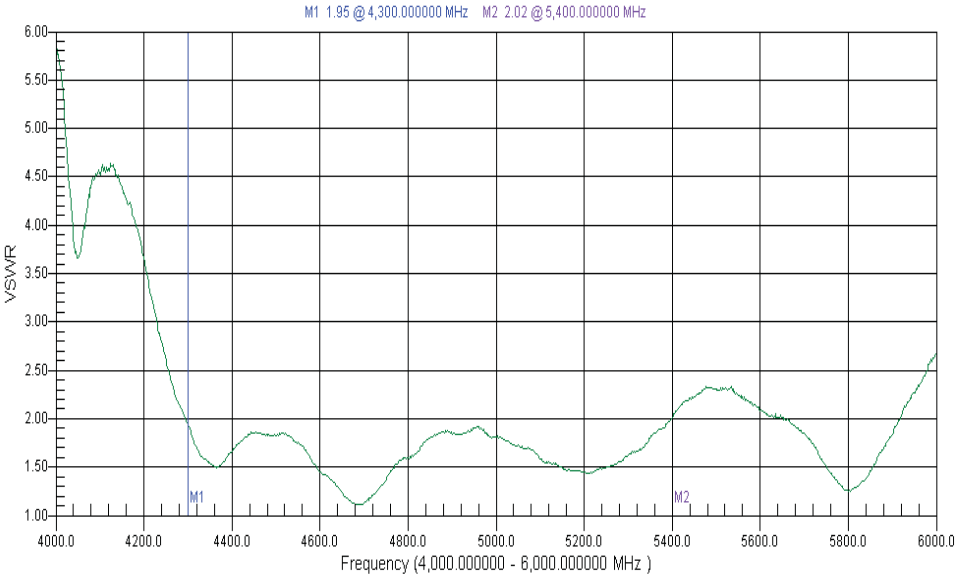

Fig.4(a) Measured VSWR of Sum Port of Mono-Pulse Array Antenna

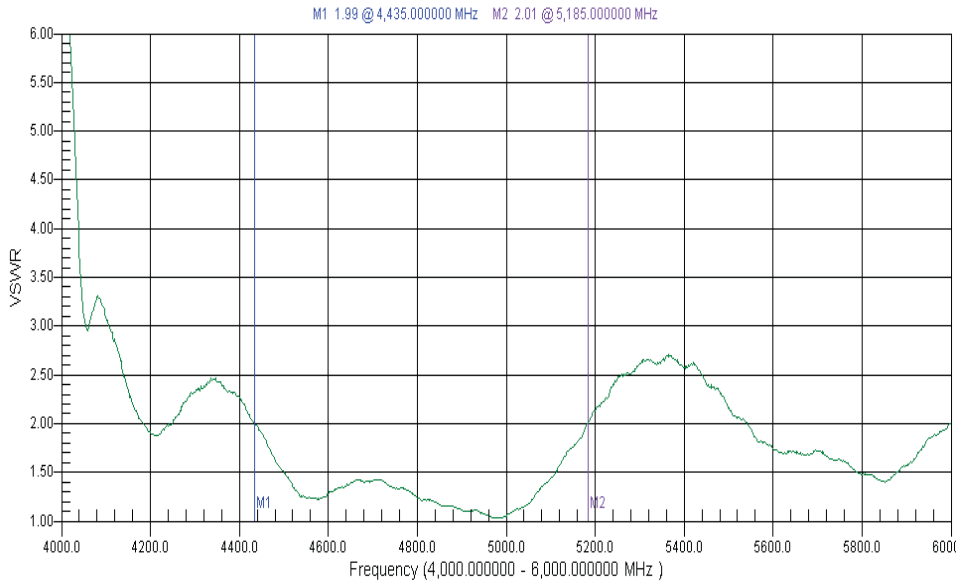

Fig.4(b) Measured VSWR of diff. Port of Mono-Pulse Array Antenna

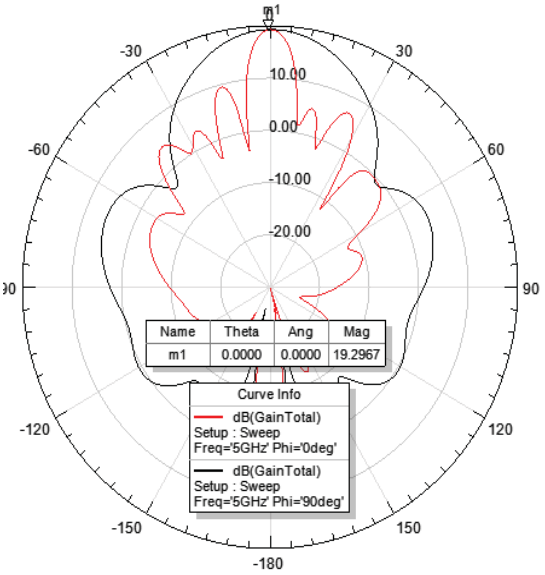

Fig.5(a) Simulated E and H Plane Radiation Pattern with Sum Port Excited

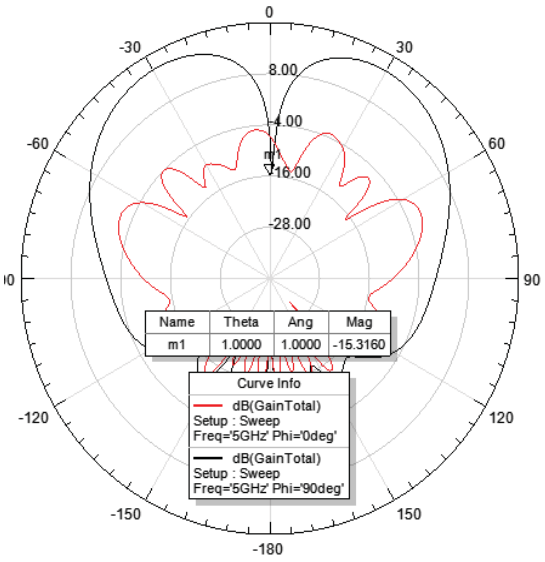

Fig.5(b) Simulated E and H Plane Radiation Pattern with diff. Port Excited

Measured VSWR of sum and difference port are shown in fig-4(a) and fig-4(b). Measured impedance bandwidth (VSWR<2) for sum port and difference port is 22.6% in range of 4.3 GHz to 5.4 GHz and 14% in range of 4.435 GHz to 5.105 GHz respectively. Simulated E and H plane radiation pattern of antenna with sum and difference port excitation at 5 GHz is shown in fig-5(a) and fig-5(b) respectively. Simulated peak gain of antenna is better than 18 dBi and null depth is better than 30 dB.

Conclusions: A multilayer proximity-coupled U-slot rectangular microstrip antenna array composed of sixteen elements has been described. A Compact rectangular shaped Rat-Race has been designed for monopulse feeding of antenna. Antenna has simulated gain of 18 dBi and the null depth is better than 30 dB. VSWR bandwidth at Sum and Difference port has been achieved 22% and 14% respectively.

Acknowledgement: The authors thank Director, DEAL, for permission to publish the paper.

Reference:

[1] K. L. Lau, K. M. Luk and K. F. Lee, “Wideband U-slot microstrip patch antenna array”, IEEE Proc. Microwave Antennas Propagation., Volume148, No. 1, pp. 41-44, 2001.

[2] C. L. Mak, K. M. Luk and K. F. Lee, “Proximity coupled U-slot patch antenna ”, Electronics Letters, Volume 34, No. 8, pp. 715, 1998.

[3] W. S. T. Rowe and R. B. Waterhouse, “Investigation of proximity coupled antenna structures,” in IEEE Int. Antennas and Propagation Symposium, Columbus, OH, Jun 2003, vol. 2, pp. 904–907.

[4] Girish Kumar, K. P. Ray, "Broadband Microstrip Antennas", Artech House Inc., Norwood, NJ, 2003.

[5] D. M. Pozar and B. Kaufman, “Increasing the bandwidth of a microstrip antenna by proximity coupling”, Electronics Letters, Volume 23, pp.368–369, Apr1987.

Linearly Polarized Stub Loaded Microstrip Reflectarray with Microstrip Antenna Feed

Amit A. Deshmukh[1], Ameya A. Kadam[1], Kshitij Lele[1] and K.P.Ray[2]

[1] Department of EXTC, D. J. Sanghvi College of Engineering, Vile‐Parle (W), Mumbai, India

[2] RFMS Division, SAMEER, IIT Campus, Powai, Mumbai-400076

E-mail ID: amitdeshmukh76@rediffmail.com, kshitij.lele@gmail.com

Abstract: *A microstrip reflectarray with patches of variable stub lengths to realize progressive phase shift is proposed. Three different configurations namely, 1 × 3, 3 × 1 and five element arrays are studied. The beamwidth in all three configurations in the E and H- plane is around 21˚ with a gain of 11 dBi in five element array.*

Keywords: Microstrip Reflectarray, Microstrip Antenna Feed, Linear Polarization.

INTRODUCTION: Commonly, a high gain antenna is realized using parabolic reflector configuration [1]. However, due to their curved reflecting surface they are bulky in size. As an alternative, a flat or slightly curved reflector, namely the printed reflectarray, can be conformably mounted on to the existing supporting structure with relatively small increments in size [1]. The microstrip line‐fed MSA arrays are planar but have low efficiency due to losses in the microstrip line. Also they suffer from higher cross‐polar radiation resulting from the feeding network. Recently, horn- fed reflectarray antennas have been reported which are large in size [2, 3]. A printed reflectarray antenna consists of two basic elements, the feed and a thin reflecting surface consisting of an array of printed elements. The feed element illuminates these patches, which are designed to re‐radiate the incident fields with phases which form a planar phase front. However, the low‐profile printed reflectarray is a fairly new concept that combines some of the best features of the printed array technology and the traditional parabolic reflector antenna concept [4, 5]. In order to compensate for the varying path lengths between the parasitic and center patches, MRAs with variable size patches are used as reported in [6]. Changing the patch length detunes the parasitic elements from the resonance frequency which is done to obtain the required progressive phase. Another method of compensating the phase difference, is the use of variable stub length patches. To prove the concept, results for 1×3 MRAs, 3×1 MRAs and MRAs with five elements arranged in two orthogonal axes are presented. These configurations are shown in Figure 1(d), 2(a) and 3(a), respectively. For all three configurations the beamwidth in E and H- plane is around 21˚. As the no. of patches increases, the gain increases and so does the directivity. The array theory has been applied to obtain the necessary phasing between adjacent array elements. These antennas have been analyzed using the IE3D software [7].

MRA CONFIGURATIONS: An MRA placed on top of the co‐axially fed MSA, is shown in Figure 1(a). The patch length governs the frequency of the RMSA. A 1 × 3 MRA with variable size patches is shown in Fig. 1(c). Alternatively, by adding a stub as shown in Fig. 1(d), the effective length of the patch is increased, thereby realizing detuning of its frequency. By detuning, i.e., by changing its effective length, a space‐fed patch element with the desired phase of the far field can be obtained and this is one of the techniques used in reflectarrays, to get

the same phase as that of a parabolic reflector [1]. In order to have the same phase of the re‐ radiated waves, the effective length of the central element is increased by adding a stub to detune it with respect to the length of the non-centered array elements, thereby resulting in the uniform phase of the reflected wave front. The length of the stub is calculated using the formulas given in [8]. The formulation is carried out to design MRA in the C‐ band frequency (3800 MHz to 4200 MHz). The feed RMSA is designed at 4000 MHz and its dimensions are: L =1.955 cm, W = 2.5 cm on the Taconic substrate having substrate parameters: h = 0.16 cm, $\varepsilon_r = 3.2$, and tan $\delta = 0.001$. To minimize the aperture blockage, a smaller finite ground plane of dimension: Length $L_g = 2.915$ cm and width $W_g = 3.4$ cm, is used. To avoid the mutual coupling, the placing between the two centers of adjacent RMSAs is taken as $0.54\lambda_0$ in both the directions. The effect of variation of distance D on gain, directivity, efficiency, and beam widths for different configurations has been studied in [8]. The maximum gain and directivity is obtained at $D = 5\lambda_0/2$. Hence, the optimum D for this configuration is taken as $5\lambda_0/2 = 18.75$ cm. The simulated and measured parameters for different configurations at 4 GHz are given in Table 1.

1 × 3 MRA: The simulated input impedance loci plot for 1 × 3 reflectarray antenna is shown in Fig 1(e). The simulated radiation pattern plots of 1 × 3 configuration in E‐ plane and H‐ plane are shown in Fig 1(f). The beam width in the E and H – planes is 21.44˚ and 22.05˚ respectively. Since there are more elements along the E- plane the beamwidth in the E- plane is narrower than the H- plane. It is noted from the simulated and measured values of gain and directivity in Table 1, that the radiation efficiency of the antenna is high. The length of the stub for the center patch, which is used for phase compensation, is taken to be 1.4 mm.

3 × 1 MRA: Similar to the 1 × 3 MRA, the analysis of the 3×1 MRA is carried out and the results are summarized in Table 1. The simulated plot of the input impedance loci for this reflectarray antenna is shown in Fig 2(b) and the simulated radiation pattern plots of crossed MRA in E‐ plane and H‐ plane at 4 GHz are shown in Fig 2(c). The beam width in the E and H-planes is 21.57˚ and 20.44˚ respectively. Since there are more elements along the E- plane the beamwidth in the H- plane is narrower than the E- plane. Similar to the 1 × 3 reflectarray, a stub of length 1.4 mm is used for the center patch.

PLUS-SHAPED MRA: Similar to the above MRA configurations, the analysis for crossed MRA has been carried out and the simulated and measured parameters are given in Table 1. The simulated input impedance loci plot for crossed MRA is shown in Fig 3(b). The simulated radiation pattern plots for crossed MRA in E‐ plane and H‐ planes are shown in Fig 3(c). The beam width in the E and H- planes is 20.95˚. Since the patches in this configuration are at the same distance from the center patch as in the previous two configurations, the stub length for the center patch is the same, that is, 1.431 mm. For all these cases, the first side lobe level (FSLL) is poor. When a larger MRA for much higher gain is designed with elements in excess of 64, the FSLL lower than −13 dB is achieved.

Table 1: Simulated and measured parameters for different configurations at 4 GHz.

Configuration	VSWR		Gain (dBi)		Beam width in E and H- planes (degrees)			
	Simu.	Meas.	Simu.	Meas.	E- plane		H- plane	
					Simu.	Meas.	Simu.	Meas.
1x3	1.469	1.449	9.58	9.41	21.44˚	21.39˚	22.05˚	21.98˚
3x1	1.509	1.492	8.34	8.14	21.57˚	21.51˚	20.44˚	20.36˚
Plus	1.618	1.603	11.11	10.98	20.95˚	20.83˚	20.95˚	20.86˚

CONCLUSIONS: A high‐efficiency, three‐dimensional MRA with microstrip antenna feed has been developed for concept proving. Of all the MRA configurations, an optimum gain of nearly 11.11 dBi is realized for the crossed MRA with a spacing of $5\lambda_0/2$ between the MSA and MRA. The antenna efficiency and gain can be further improved by using a low loss dielectric substrate. This reflectarray has to be scaled up to replace a parabolic reflector to realize higher gains. As the number of array elements increases, the FSLL becomes much lower and directivity increases.

REFERENCES:

1. J Huang, and R J Pogorzelski, "A K_a band microstrip reflectarray with elements having variable rotation angles", IEEE Trans. Antennas Propagation, Vol. AP‐46, no. 5, pp. 650‐6, May 1998.
2. D M Pozar, S D Targonski, and H Syrigos, "Design of millimetre wave microstrip reflectarrays", IEEE Trans. Antennas Propagation, Vol. AP‐45, no. 2, pp. 287‐95, Feb. 1997.
3. R D Javor, X D Wu, and K Chang, "Design and performance of a microstrip reflectarray antenna", IEEE Trans. Antennas propagation, Vol. AP‐ 43, no. 9, pp. 932‐9, Sep. 1995.
4. G Berry, R G Malech, and W A Kennedy, "The reflectarray antenna", IEEE Trans. Antennas Propagation, Vol. AP‐11, no. 6 pp. 645‐51, Nov. 1963.
5. D M Pozar, and T A Metzler, "Analysis of a Reflectarray Antenna Using Microstrip Patches of Variable Size", Electronics Letters, Vol. 29, no. 8, pp. 657‐8, 1993.
6. K. P. Ray, Amit A. Deshmukh and Ameya A. Kadam, "Linearly Polarized Microstrip Reflectarray with Microstrip Antenna Feed", IETE Journal of Research, Vol. 59, Issue 4, pp. 294-301, July-August 2013.
7. IE3D 12.1, Zeland Software, Fremont, USA, 2004.
8. Lenin Naragani and Dr. P. Hanumantha Rao, "Stub Loaded Microstrip Reflect Array", in ElectroMagnetic Interference and Compatibility (INCEMIC), pp. 486-9, Feb. 2006.

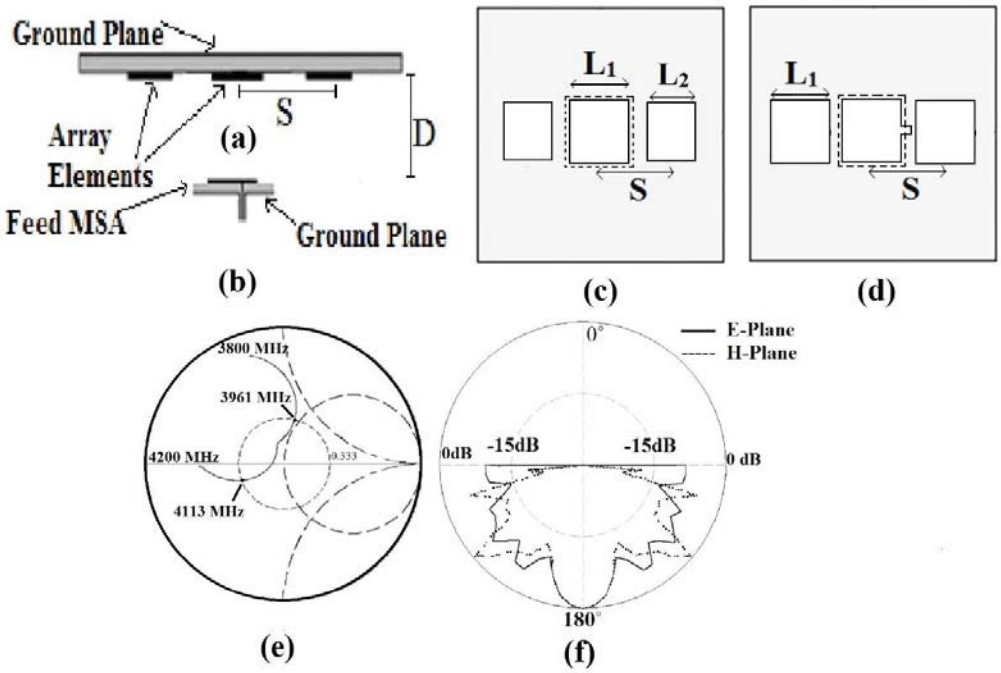

Fig 1: 1 × 3 MRA: Side view of (a) reflectarray and (b) feed patch and topview of reflectarray with (c) variable patch size and (d) same patch size with stub. (e) Impedance loci and (f) radiation pattern plot.

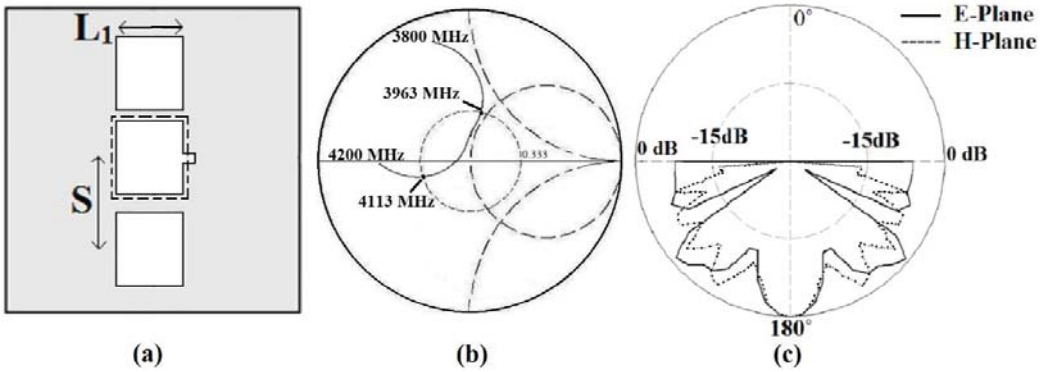

Fig 2: 3 × 1 MRA: (a) Configuration (b) Impedance loci and (c) radiation pattern plot.

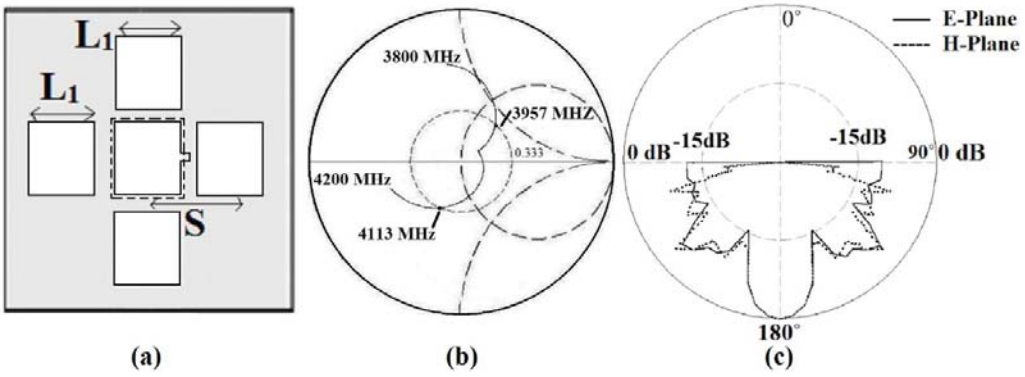

Fig 3: Crossed MRA: (a) Configuration (b) Impedance loci and (c) radiation pattern plot.

Broadband Directional Triangular Monopole Antenna Array with Reflector

Mahima Arrawatia[(1)], Maryam Shojaei Baghini [(1)],Girish Kumar [(1)]
(1) Electrical Engineering Department, Indian Institute of Technology Bombay
Powai, Mumbai-400076, India
mahima87@ee.iitb.ac.in, mshojaei@ee.iitb.ac.in, gkumar@ee.iitb.ac.in

Abstract: *In this paper, a broadband triangular monopole antenna array with improved gain is presented. A two element triangular monopole antenna array having VSWR<2 bandwidth from 590MHz to 2GHz is designed on FR4 substrate. The 2-element array has a gain of 3dBi at 900MHz and 7dBi at 1.8GHz. The radiation pattern is bi-directional and uniform over the entire bandwidth. The triangular monopole antenna array is re-designed with a reflector to achieve a unidirectional radiation pattern. The antenna has a VSWR<2 bandwidth from 740MHz to 1.9GHz and the gain is 8dBi at 900MHz and 10.6dBi at 1.75GHz. A uniform unidirectional radiation pattern with less than 2dB variation in the broadside over the entire bandwidth is also achieved.*

Introduction: Growth of mobile communication in recent years has led to the need of broadband directional antennas with uniform radiation pattern in the frequency range of 800MHz to 2GHz. Many broadband omnidirectional antennas have been reported [1]. These broadband antennas have gain of only 2dBi and the radiation pattern degrades at higher frequencies. In [2], a broadband antenna having a bandwidth from 560MHz to 1060MHz is reported but the gain is only 4.2dBi over the bandwidth. Some directional antennas for UWB applications are reported in [3-7]. In [3], a broadband antenna having a bandwidth from 2.26 - 12.26GHz is developed but the gain of the antenna varies from -3.4 to 4.3dBi. In [4], a cavity backed UWB antenna with gain of 8.4dBi and a bandwidth of 7.5GHz is designed but the radiation pattern is not uniform over the entire bandwidth. In [5], a compact horn antenna is designed. A bandwidth of 14GHz is achieved with 10.5dBi gain but horn antennas are not planar. In [6], a Vivaldi antenna is designed with a bandwidth from 1.4GHz to 12GHz, but it has an endfire radiation pattern. In addition, it also has high cross-polar level at higher frequency. In [7], a gain of 6.5dBi is achieved over a wide bandwidth of 8.82GHz but the radiation pattern is not uniform over the entire bandwidth. In [8], a broadband high gain antenna for WLAN application is developed, but the bandwidth is only 200MHz. In this paper, a low cost directional broadband triangular monopole antenna array with uniform radiation pattern over the entire bandwidth is designed to cover various cell phone bands.

Broadband Triangular Monopole Antenna Array: A single feed 2-element broadband triangular monopole antenna array is designed to achieve wide bandwidth along with improved gain. The antenna is designed on FR4 substrate with $\varepsilon_r = 4.4$, h = 1.6mm and $\tan\delta$ = 0.02 and simulated using IE3D [9]. The patch is fabricated on one side of the substrate and ground plane on the other side. Each element of the array is designed for an antenna input impedance of 100Ω. Two triangular monopole antennas [1] with 100Ω input impedance are combined to achieve a 50Ω broadband antenna with improved gain. The designed triangular monopole antenna array is shown in Fig.1. The width W_1 = 78mm and flare angle φ is 46^0 for 100Ω antenna impedance. The width of the feed line (s) is 1.3mm and length (L_1) is 97.5mm. The antenna is co-axially fed. The dimensions of the ground plane are length (L_g) =178mm and width (W_g) = 60mm.

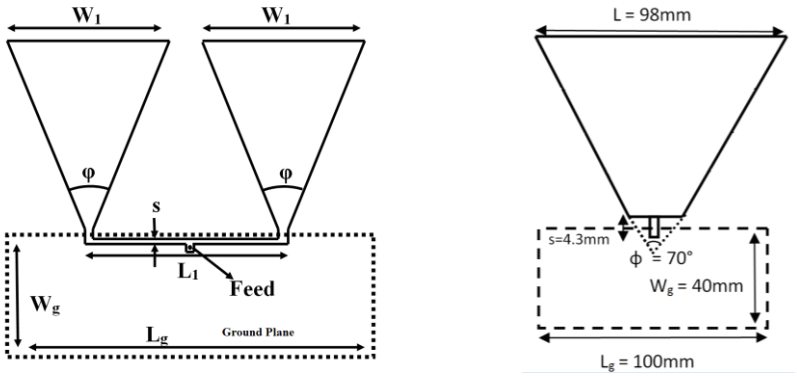

(a) (b)

Fig.1 (a) Two-element broadband triangular monopole antenna array and (b) Truncated triangular monopole antenna

The VSWR plot of the array is shown in Fig.2 (a). The VSWR < 2 bandwidth is from 590MHz to 2GHz, which covers CDMA, GSM900 and GSM1800 bands. A truncated triangular monopole antenna, shown in Fig.1 (b) is designed for comparison. It has a VSWR<2 bandwidth from 790MHz to 1.1GHz and 1.76GHz to 5.8GHz. The simulated gain plots of both the antennas are shown in Fig.2 (b). The gain of the two-element broadband triangular monopole antenna array is 3dBi at 900MHz and 7dBi at 1.8GHz. However, the gain of the truncated triangular monopole antenna is only 1.5dBi at 900MHz and 3dBi at 1.8GHz. The radiation pattern of the array at 920MHz and 1.82GHz is shown in Fig. 4. The radiation pattern is bi-directional. At 920MHz the HPBW in E-plane is 78° and in H-plane, it is 126°. At 1.82GHz HPBW in H-plane is 42° and in E-plane, there is slight tilt from the broadside direction but the magnitude is only 0.7dB less along the broadside direction than maximum value. A discontinuity is observed at ±90° in the radiation pattern because an infinite dielectric is considered in simulation using IE3D.

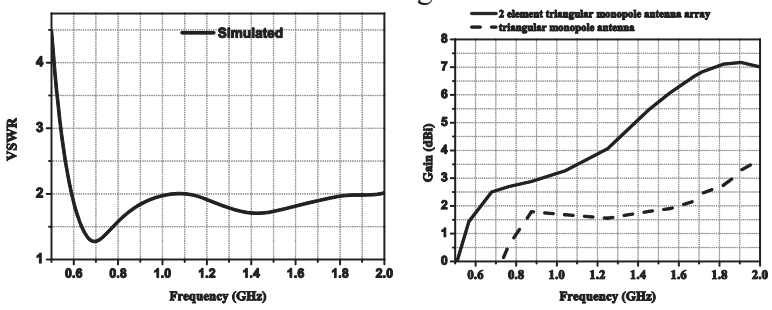

(a) (b)

Fig.2 (a) VSWR and (b) Gain plots of broadband triangular monopole antenna array

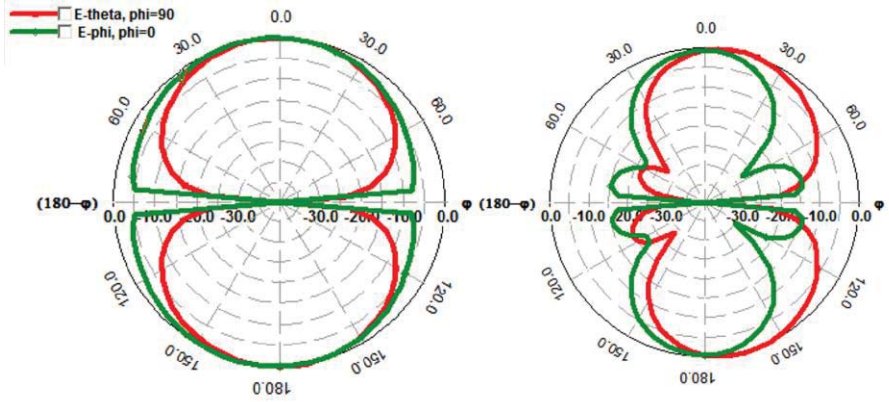

(a) (b)

Fig.3 Radiation pattern of the broadband triangular monopole antenna array at (a) 900MHz and (b) 1.82GHz

Broadband Triangular Monopole Antenna Array with Reflector: The gain of the broadband triangular antenna array can be increased further by placing a reflector behind the antenna at an optimum distance. The reflector should be placed around a distance of $\lambda_h/4$ at the highest frequency (2GHz for this design) so that the radiation pattern of the antenna at high frequency does not distort. Placing the reflector close to antenna degrades the matching of the antenna at lower frequencies. The antenna array is re-designed to achieve both impedance bandwidth and radiation pattern uniformity. The designed antenna with reflector at 50mm is shown in Fig. 4. The width (W_1) is 78mm and the flare angle φ is increased to 74°. The width of the feed line (s) is 1.3mm and length (L_1) is 97.5mm. The antenna is co-axially fed. The size of the ground plane is L_g = 178mm and Wg = 60 mm and the size of the reflector is (W_r) = 239mm and (L_r) = 252mm. The measured VSWR < 2 bandwidth is from 740MHz to 1.9GHz as shown in Fig. 5(a). The antenna covers CDMA, GSM900 and GSM1800 bands. The gain of the antenna with reflector is shown in Fig.5 (b). The gain of the antenna with reflector is 8dBi at 900MHz and 10.6dBi at 1.75GHz. The radiation pattern of the antenna at 925MHz and 1.86GHz is shown in Fig. 6. At 925MHz the HPBW in E-plane is 66° and in H-plane, it is 72°. The cross-polar level is less than -25dB in both the planes. At 1.86GHz, HPBW in H-plane is 46°. In E-plane, there is a slight tilt from the broadside direction but the magnitude is only 2dB less along the broadside direction than maximum value. The cross-polar level in E-plane is less than -20dB and in H-plane, it is less than -30dB.

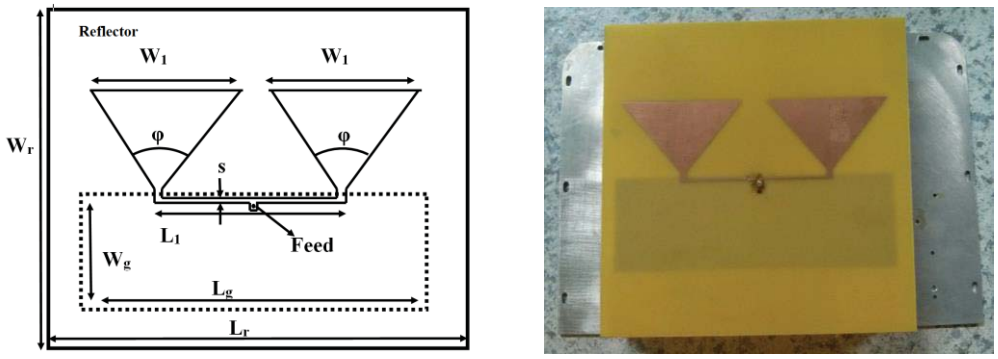

(a) (b)

Fig.4 Two element broadband triangular monopole antenna array with reflector (a) Simulated (b) Fabricated

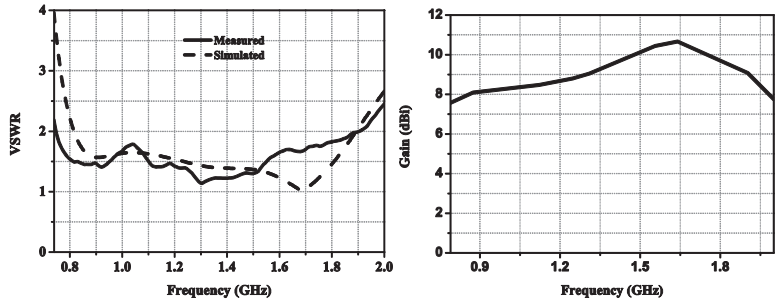

(a) (b)

Fig. 5 (a) VSWR and (b) Gain plots of broadband triangular monopole antenna array with reflector

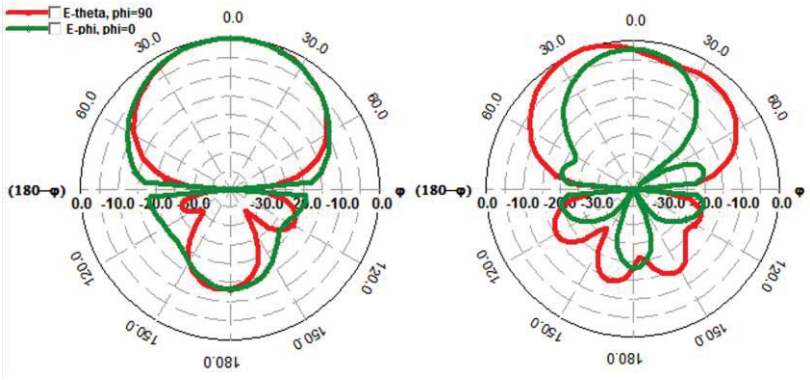

(a) (b)

Fig.6 Radiation pattern of the broadband triangular monopole antenna array with reflector at (a) 925MHz and (b) 1.86GHz

Conclusion: In this paper, a broadband triangular monopole antenna array with improved gain is presented. The antenna has a bidirectional radiation pattern. A 2-element triangular antenna array with reflector is also designed. The designed antenna has a VSWR<2 bandwidth from 740MHz to 1.9GHz. The gain of the antenna is 8dBi at 900MHz and 10.6dBi at 1.75GHz. The radiation pattern is also uniform over the entire bandwidth. The antenna covers CDMA, GSM900 and GSM1800 bands.

Reference:

[1] G. Kumar and K. P. Ray Broadband Microstrip Antenna, Artech House, USA 2003

[2] Rezaeieh, S.A; Abbosh, AM., "Wideband and Unidirectional Folded Antenna for Heart Failure Detection System," *IEEE Antennas and Wireless Propagation Letters*, vol.13,pp.844,847, 2014

[3] Xianming Qing; Zhi Ning Chen, "A miniaturized directional UWB antenna," *IEEE International Symposium on Antennas and Propagation (APSURSI),* pp.1470,1473, 3-8 July 2011

[4] Awan, D.; Bashir, S.; Whittow, W., "High gain cavity backed UWB antenna with and without band notch feature," *Antennas and Propagation Conference (LAPC), 2013 Loughborough* , pp.299,302, 11-12 Nov. 2013

[5] Ranga, Y.; Esselle, K.P.; Weily, AR.; Verma, AK., "Compact high-gain short-horn antenna for UWB applications," *Proceedings of the 5th European Conference on Antennas and Propagation (EUCAP)*, pp.1511,1513, 11-15 April 2011

[6] Xu Han; Lei Juan; Cui Changjuan; Yang Lin, "UWB dual-polarized Vivaldi antenna with high gain," *International Conference on Microwave and Millimeter Wave Technology (ICMMT)*, vol.3, pp.1,4, 5-8 May 2012

[7] Ranga, Y.; Esselle, K.P.; Weily, AR.; Verma, AK., "A compact antenna with high gain for ultra wide band systems," *European Microwave Conference*, pp.85,88, Sept. 29 2009-Oct. 1 2009

[8] Qiu-Yi Zhang; Qing-Xin Chu; Han-Qing Ma, "High-gain broad-band cavity-backed slot antenna for WLAN applications," *International Conference on Microwave and Millimeter Wave Technology*, pp.1866,1868, 21-24 April 2008

[9] IE3D software from Mentor Graphics, USA

Conventional Beamformers based on One Dimensional Reduced Mapped Real Transform

P. R. Mini[(1)], S. Mridula[(2)], Binu Paul[(2)] *and* P. Mohanan [(3)]
(1) Department of Electronics and Communication Engineering, Federal Institute of Science and Technology, Kerala, India (mini@fisat.ac.in)
(2) Division of Electronics Engineering, School of Engineering, Cochin University of Science and Technology, Kerala, India(mridula@cusat.ac.in), (binupaul@cusat.ac.in)
(3) Department of Electronics, Cochin University of Science and Technology, Kerala, India (drmohan@cusat.ac.in)

Abstract: *Conventional beamformers offer the advantages of simplicity and robustness. A reduced form of One Dimensional Mapped Real Transform for obtaining reduction in computational complexity and computation time in beamformers without significant reduction in gain is proposed.*

1. Introduction:

Beamforming controls the beam maxima and nulls of a radiation pattern using signal processing techniques on an array of sensors and is commonly employed in Radar, Sonar and Adaptive Mobile Communications. One of the most commonly used types of non-adaptive beamformers is conventional beamformers. Using a fixed set of weightings and time delays (or phasings) the signal from the sensors in the array are combined, primarily using only information about the location of the sensors in space and the signal direction of interest. It is easy to implement conventional beamformers. They also offer robust performance in single target scenarios [1].In this paper a novel method derived from One Dimensional Mapped Real Transform (1D-MRT) is applied to conventional beamformers. The proposed One Dimensional Reduced Mapped Real Transform (1D-R-MRT) exhibits reduced computational complexity and computation time.The signal model for conventional beamforming is described in Section 2. MRT and its coefficients are introduced in Section 3. The proposed algorithm is presented in Section 4. Simulation results are presented in Section 5. Conclusions are presented in Section 6.

2. Signal model:

Consider a uniform linear array of Ns omni directional antennas with a spacing d between individual elements. Each array element of a uniform linear array will receive the signal at different time instants. The difference in phase shift of the wave between the first element (reference element) and the nth element of the array is given by

$$\psi = \frac{2\pi(n-1)d\sin\theta}{\lambda}; 1 \le n \le Ns \quad \ldots. \quad (1)$$

where, d is the inter element spacing and λ is the wavelength of the signal [1].
The data vector at the sensor inputs is represented by

$$X(t) = [x_1(t) \quad x_2(t) \cdots x_{Ns}(t)]^T \quad \ldots. \quad (2),$$

$$X(t) = A(\theta)s(t) + n(t) \quad \ldots.. \quad (3)$$

where s(t) is the signal vector, n(t) is the noise term and A(θ) is the array factor.

$$A(\theta) = [1 \quad e^{j\psi} \quad e^{j2\psi} \cdots e^{j(Ns-1)\psi}] \quad \ldots\ldots (4)$$

The beamformer output is the sum of the weighted inputs of the array elements.

$$Y(t) = W^H X(t), \quad \ldots.. \quad (5)$$ where, W is the weight vector ,

$$\overline{W} = [w_1 \quad w_2 \cdots w_{Ns}], \qquad \ldots. \quad (6)$$

and W^H is the Hermitian of the weight vector. In a conventional beamformer the weights are chosen as the conjugate of the array factor.

3. One dimensional Mapped Real Transform:

The Mapped Real Transform (MRT) performs the frequency domain analysis of one and two dimensional signals in terms of additions only [2]. It is obtained by exploiting the periodicity and symmetry of exponential terms in the Discrete Fourier Transform relation and grouping related data. Here the MRT for one dimensional signal is utilised. The One Dimensional Mapped Real Transform (1D-MRT) as explained by Roy and Gopikakumari [2][3] is as follows.

Let x_n, $0 \le n \le N-1$ be a 1-D sequence and let Y_k, $0 \le k \le N-1$ be its DFT. The DFT is given by

$$Y_k = \sum_{n=0}^{N-1} x_n W_N^{nk}, \quad 0 \le k \le N-1 \quad \ldots.(7)$$

where $W_N^q = e^{\frac{-j2\pi q}{N}}$ and k is the frequency index. Using the periodicity of the twiddle factor W_N, (7) can be expressed as

$$Y_k = \sum_{n=0}^{N-1} x_n W_N^{((nk))_N} \qquad \ldots(8)$$

The exponent $((nk))_N$ can have a value p, where p is the phase index with $0 \le p \le N-1$. For a given value of k, by grouping the data that share the same value p for the exponent $((nk))_N$, and also using the relation $W_N^{p+(N/2)} = -W_N^p$, Y_k can be expressed as

$$Y_k = \sum_{p=0}^{M-1} Y_k^{(p)} W_N^p \qquad \ldots..(9)$$

where $Y_k^{(p)}$ is the 1D–MRT of x_n, $0 \le n \le N-1$, defined as

$$Y_k^{(p)} = \sum_{\forall n \Rightarrow ((nk))_N = p} x_n - \sum_{\forall n \Rightarrow ((nk))_N = p+M} x_n \qquad \ldots.(10)$$

with M=N/2. Unlike DFT, the computation of the MN coefficients of MRT is performed in terms of additions only. The 1-D MRT maps a one dimensional array of length N into M one dimensional arrays, each of length N, resulting in a matrix of M x N elements [2][3].Since the relation $W_N^{p+(N/2)} = -W_N^p$ is exploited, the 1-D MRT is valid for all even values of N.

4. One Dimensional Reduced MRT.

The elements of the 1D-MRT are represented as $Y_k^{(p)}$ where $0 \le k \le N-1$ and $0 \le p \le M-1$. Out of the MN elements of the 1D-MRT matrix, different applications can be performed by selecting only a few elements appropriate for the application. In the proposed 1D-R-MRT algorithm for beamforming, only the elements of the second column of the 1D-MRT matrix, corresponding to k = 1, are chosen for processing. The suitability of the second column (corresponding to k=1) for beamforming is confirmed after repeated trials.The coefficients corresponding to frequency index k=1 are obtained by simply subtracting the elements in the second half of the input vector from the corresponding elements in the first half. The data size for processing is reduced by half and the coefficients are obtained without involving any complex

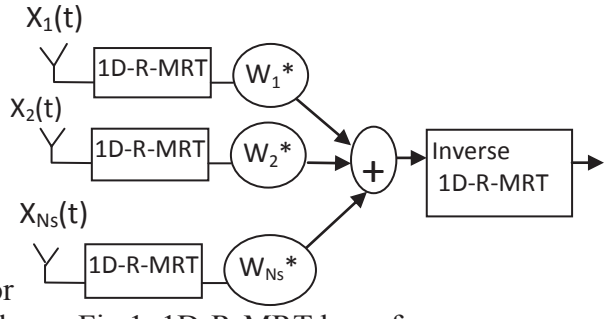

Fig 1: 1D-R-MRT beamformer

multiplication. A schematic diagram of the 1D-R-MRT based conventional beamformer is shown in Fig 1.

5. Simulation results.

For the proposed study, an array of eight sensors with the source at 40 degrees is considered. The input signal frequency is 1 MHz and is corrupted by Additive White Gaussian Noise. The one dimensional data vector size is 64 and SNR is 30 dB. After computing the 1D-R-MRT, the data vector size will be 32. By trial and error method, it is found that faithful reproduction of the input signal is obtained only if sampling frequency is 4.93 times the input signal frequency for vector size of 64 as observed in Fig 2(a). It can be seen that the input signal and beamformer output closely match. But from fig 2(b) and 2(c), it can be observed that when the input signal is sampled at a higher than optimum sampling frequency (fs=5.5f) or at a lower than optimum sampling frequency (fs=4.5f), the beamformer output differs considerably from the input signal.

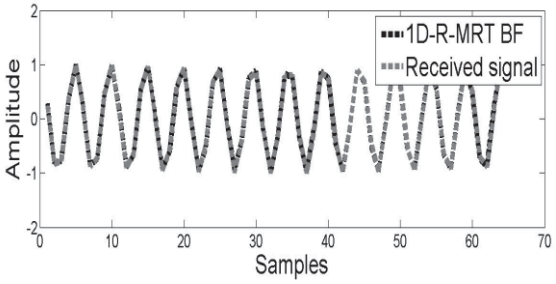

a) fs =4.93f

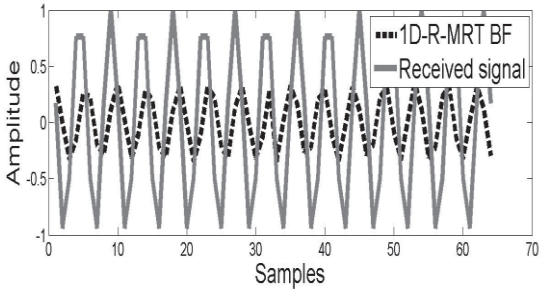

b) fs = 4.5 f

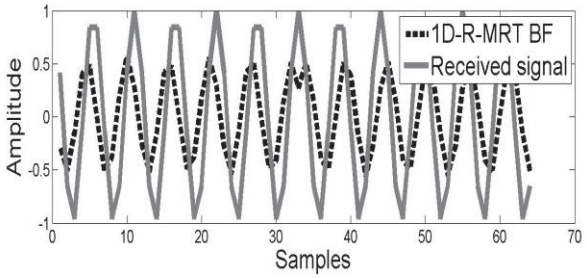

c)fs=5.5 f

Fig 2(a-c) Comparison of beamformer outputs[8 sensors, DOA=40°,64 samples, SNR=30 dB].

The sampling frequency corresponding to various sample vector sizes is optimized by trial and error as illustrated in Table 1. The computation time required by the 1D-R-MRT conventional beamformer is compared with that of time domain and frequency domain conventional beamformers as illustrated in Tables 2(a-b).

Table 1: Sampling frequency for sample sizes

Sample size	Sampling frequency
16	5.33 f
32	4.57 f
64	4.93 f
128	4.129 f
256	4.655 f
512	4.096 f

Table 2(a): Comparison of computation time

Sample size	Computation Time (Secs)- 8 sensors		
	Time domain	Frequency domain	1D-R-MRT
16	0.0243	0.0243	0.0241
32	0.0247	0.0245	0.0243
64	0.0255	0.0255	0.0245
128	0.0269	0.0271	0.0252
256	0.0289	0.0289	0.0264
512	0.0336	0.0337	0.0287
1024	0.0467	0.0499	0.0327
2048	0.0640	0.0638	0.0449
4096	0.0941	0.0964	0.0604
8192	0.1521	0.1607	0.0950

Table 2(b): Comparison of computation time

Sample size	Computation Time (Secs) -100 sensors		
	Time domain	Frequency domain	1D-R-MRT
1024	0.0772	0.0804	0.0544
2048	0.2363	0.2423	0.0877
4096	0.4859	0.4801	0.2696
8192	0.8725	0.8798	0.5552

As observed in Table 2(a) and 2(b), the simulations show that 1D–R-MRT beamformer requires lesser computation time.

The beampatterns of the conventional beamformers based on 1D-R-MRT, time and frequency domain are compared for varying values of sensors, DOA and SNR as shown in Fig 3(a-b).

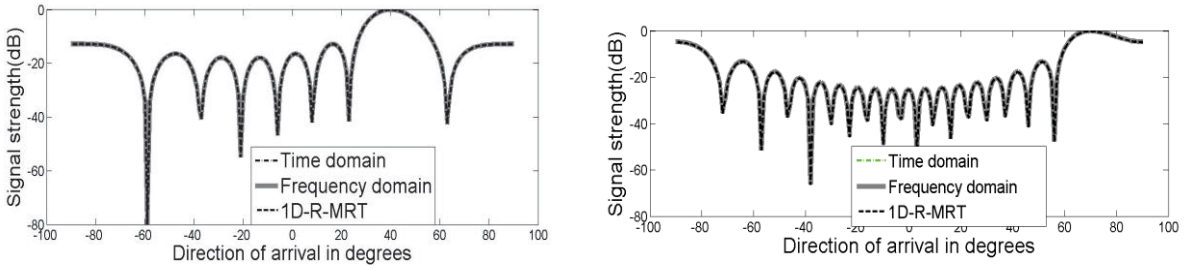

a) 8 sensors, DOA= 40 deg, SNR =30 dB b) 18 sensors, DOA= 70 deg, SNR =10 dB

Fig. 3(a-b): Comparison of normalized beampatterns of conventional beamformers. [No: of samples =64, Sampling frequency = 4.93 f].

It is seen from figures 3(a) and 3(b), that for high and low SNR as well as for varying DOA and varying number of sensors , the beampattern obtained using 1D-R-MRT is comparable with that of time domain and frequency domain conventional beamformers.

The simulation is performed using MATLAB version 7.2 on an Intel core i3 processor running at 2.4 GHz with 4 GB RAM.

6. Conclusion.

In this work a new algorithm for beamforming, referred to as One Dimensional Reduced Mapped Real Transform algorithm is proposed. In the 1D-R-MRT algorithm, only a few selected coefficients of the 1D MRT of a signal are used for beamforming. The advantages of the proposed algorithm are: 1) The data for processing is only half the size of the original signal. 2) The transform and its inverse can be computed easily using addition and does not involve any complex multiplication. 3) The computation time is lower than that of time domain and frequency domain beamformers. 4) The gain is comparable to time domain and frequency domain conventional beamformers.

Reference:

[1] Van Veen, B.D., and Buckley, K.M. "*Beamforming: a versatile approach to spatial filtering",* IEEE ASSP Magazine, vol 5, pp 4-24, 1988.

[2] Rajesh Cherian Roy, "Development of a new transform-MRT", PhD thesis,CUSAT,2009.

[3] K. Meenakshy and R Gopikakumari, "Texture descriptors based on 1-D MRT", International Journal of recent trends in Engineering, Vol 2,No 6, pp 1-3, Nov 2009.

[4] Preetha Basu, Bhadran. V, R. Gopikakumari,"A new algorithm to compute forward and inverse 2-D UMRT for N - a power of 2", IEEE International Conference on Power, Signals, Controls and Computation (EPSCICON), pp 1-5 , 2012.

[5] Juan A. Torres-Rosario, "Implementation of a phased array antenna using digital beamforming", Master Of Sciences, In Electrical Engineering, University Of Puerto Rico, Mayagüez Campus, 2005.

[6] H. Krim, M. Vibert, "Two decades of array signal processing research", *IEEE Signal Processing Magazine*, Vol 13, pp 67-94, July 1996.

Design of an Analogue Beam-former Network for Low Frequency Radio Telescopes

Mugundhan V.[(1)],*Kathiravan C.* [(1)],*Rajalingam M*[(1)]., *Ramesh R.*[(1)]
(1) Indian Institute of Astrophysics, Bangalore, India, 570034, Email: mugundhan@iiap.res.in

Abstract: *This paper describes the prototype design, development and characterization of a new Analog Beam-former Network (ABFN), a RF switch setup that facilitates the electronic steering operation of physically non-steerable radio antenna systems in order to follow the movement of celestial radio sources either in Right Ascension (RA) or Declinatinon (Dec). Trial observations made with the prototype ABFN using a new radio interferometer facility operating at the Gauribidanur Radio Observatory are presented to show the tracking performance of the ABFN.*

1. Introduction: Antenna arrays are used in low frequency radio astronomy to increase the resolution and sensitivity of the radio telescope. Arrays contain more than one antenna that are spatially distributed. In order to make these individual elements act as one single synthesized element, beam-formers are a necessity. Beam-formers are used to steer the response (field of view) of the array to a desired direction and track a source for the duration of observation.

When the source is at the zenith, all the antennas in the array receive the source signal at the same time without any phase or time difference. But when the source has moved to some position away from the zenith, different antennas in the array receive the source signal with a phase/time difference. This phase or time difference, which is purely because of the position of the source in the sky is called *geometric phase/delay* and is given by the following equations:

$$\Delta\phi = \frac{2\pi}{\lambda} d \sin\theta \qquad 1$$

$$\tau = \frac{d \sin\theta}{c} \qquad 2$$

Where $\Delta\phi$ is the geometric phase, τ is the geometric delay, θ is the zenith angle of the source. Due to this phase shift/delay, the signals from the antennas do not combine coherently. Coherent addition can be achieved by compensating for the phase shifts/time delays. This compensation is done by beam-formers. Beam-formers can be phase or delay shifting type, based on the frequency band of interest. In case of narrow band operation, phase compensation is used, but for wide band operation delay compensation is preferred. Beam-formers were first employed in RADAR arrays during the 1960s [7]. Phase shift beam-forming is still predominantly used in RADAR systems. First usage of beam-forming in radio astronomy is found in the Ohio Radio Telescope, which had scanning capabilities in the declination direction [8]. The above telescope and those which followed this telescope were narrow-band survey instruments, which used phase-shift beam-forming for declination pointing. The instruments at Gauribidanur Radio Observatory, which operate from 40-120 MHz use time delay beam-forming for declination pointing.

The conventional architecture of a time delay BFN used in radio telescopes is presented in the next section, the design and the characterization of the new BFN is described in section 3.

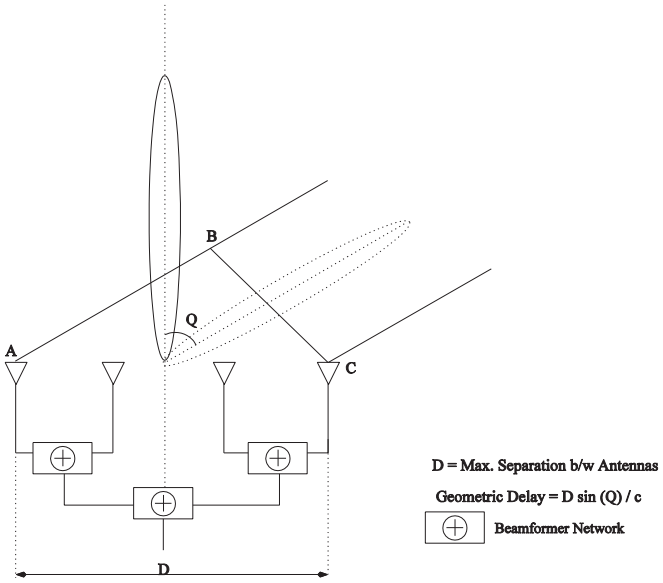

Figure 1 Concept of a Beam-former

Section 4 describes the observational setup and we conclude in section 5 with a discussion of results and future works.

2. Conventional Beam-former Network Design: Conventionally, diode based delay switching networks have been used in synthesis radio telescopes for beam-forming [1]. Each stage of these networks was centered on four PIN diodes, which would have a lot of discrete components for biasing networks and impedance matching (Ref. fig 2). When Port 2 is held Low, the diodes D5 and D6 are switched ON and allow the RF signal to travel through the No Delay Path (NDP), which is just a small length of PCB track. When Port 1 is held low, the RF signal is routed through the Delay Path (DP), which is a low loss co-axial cable whose length is:

$$L = 0.66d\sin(\theta) \qquad 3$$

Where L is the length of the cable, .66 is the velocity factor of co-axial cable. It is important to note that the amount by which the signal is delayed in the DP is with reference to the NDP. Based on the tilt-angle resolution needed, many stages like the one described above would be needed. Same number of stages must be repeated once more to allow the beam to be tilted either side of the zenith. This would require at least 8*n* RF diodes and 4*n* control signals for each ABFN network. In order to overcome this, a single compensatory cable stage would be introduced in the ABFN. The compensatory stage also has a delay cable that is capable of providing a delay that is $(n+1)\tau$. For source position on one side of the zenith, the normal, n stage delay network would be used and for the other side, the normal and the compensatory stages would be operated in combination to provide the tilt angles. This would result in the beam having unequal gain on either side of the zenith. The above BFN design is used for the instruments at the Gauribidanur Radio observatory, namely Gauribidanur Radio Heliograph (GRH) [2] - a 2D interferometric imaging system, Gauribidanur Low Frequency Solar Spectrograph (GLOSS) [3] – A high resolution spectrograph array of 8 antennas and Gauribidanur Radio Interference Polarimeter (GRIP) [4] – A 1D interferometric polarimeter. The BFN is arranged in a Christmas tree configuration and is currently used only for declination pointing. The existing beamformer works satisfactorily only up-to ≈120 MHz (Ref. Figure 3). It was recently decided to increase the frequency coverage of the imaging instrument and include tracking capabilities to get more on-source time. So, a new BFN design was required for the above reasons.

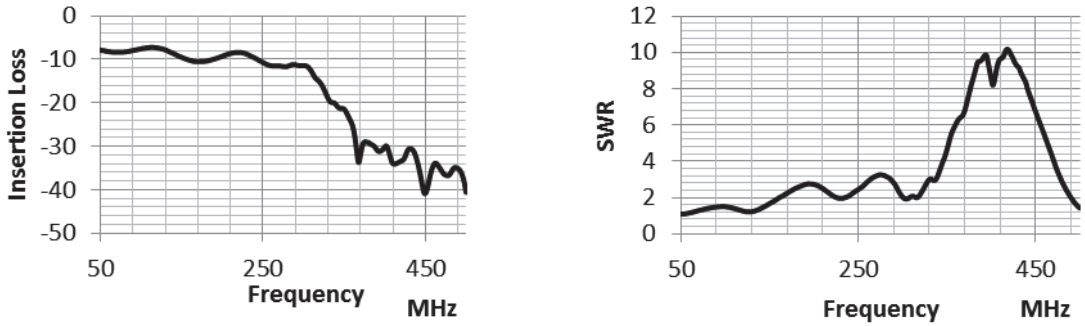

Figure 2 Characteristics of the conventional BFN

3. New Beam-former Network Design: The advent of MMIC technology has made way for highly modular RF switches in place of the PIN diode and the accompanying lumped element circuitry. For the present application, Double Pole Double Throw (DPDT) switches were used so that a single switch may be used in place of 4 PIN diodes and the accompanying circuitry (as shown in figure 3).

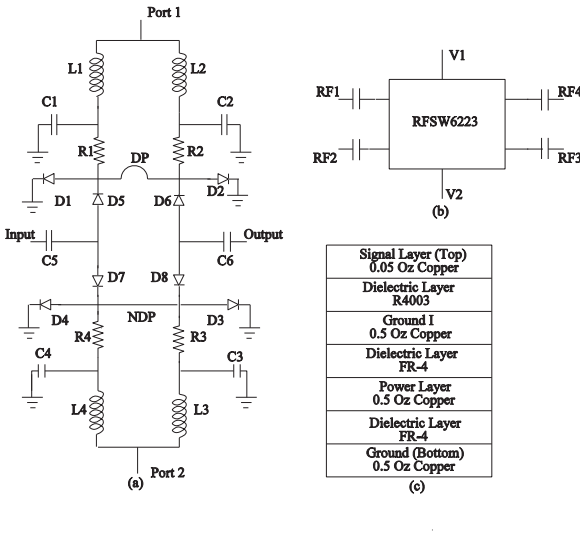

Figure 3 Single stage of (a.) Conventional BFN and (b.) New BFN. (c.) Layer Stack-up.

The switches needed to have a constant impedance of 50Ω over a large operating bandwidth. After a thorough market survey, we found that RFSW6223[4] suited our requirements. The switch had a low insertion loss (~ 0.5 dB from ~ 40 - 500 MHz) and the maximum operating frequency was ~6 GHz. The isolation between the RF paths is ~ 37 dB. A single BFN can take two antenna analog inputs and has one analog output. The BFN has 4 switches for 4 possible tilt angles, with minimum tilt angle resolution of 7°. The delays were introduced using co-axial cables. The length of the co-axial cable is given by the following formula in equation 3. LMR100 cables were used as delay cables. The circuit was fabricated on a four layer PCB (ref. Figure 2.c). The parameters were calculated to provide impedance control so that the PCB has a stabilized performance over the desired frequency range of operation (refer Figure 3). Impedance control is achieved by changing the width of the track and height of the dielectric layer as follows:

$$Z = \frac{120\pi}{\sqrt{\epsilon}\left(\frac{w}{h}+1.393+.667\ \ln\left(\frac{w}{h}+1.444\right)\right)} \qquad 4$$

Other than the four switches to choose between the DP and NDP, the BFN also had two other switches: one at the input, before the first delay switch and one at the end, after the final delay switch. The first switch will let us choose the antenna whose signal has to be routed through the DP or the NDP based on the source position. This switch gets rid of the compensatory cable network used in the conventional setup. The arrangement is also inherently symmetric and thus the gain on both sides of the zenith is the same, making this

ABFN suitable for transient observations and also suitable for RA tracking also. The switch at the output of the final delay switch is used to choose between the final switch's delay and no-delay paths.

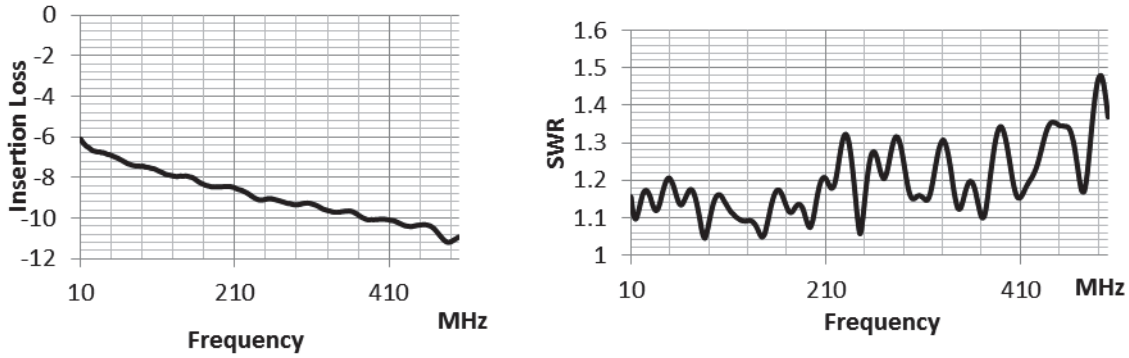

Figure 4 Characteristics of the New BFN.

4. Observations: For trial observations, a four element antenna array (ref. Table 1) was formed using LPDAs. The LPDAs were designed to operate from 150 to 350 MHz. This was to demonstrate the wide-band beam-forming ability of the designed BFN. Since a half-wavelength spacing introduced mutual coupling between the antennas, the antennas were spaced 1λ apart. According to the equation 5, the location of grating lobes are given by:

$$\theta_g = \sin^{-1}\frac{n\lambda}{d} \qquad 5$$

Where n is the grating lobe number. A spacing of 1λ will ensure that the first grating lobe is present at 90° which falls out of the 3dB beam-width of the main lobe, giving us freedom to steer the array response inside the primary beam freely. The λ chosen corresponded to 191.4 MHz.

The antennas were arranged with their E-plane in the E-W direction. The RF signal from each of the antennas were amplified by ≈ 30 dB and brought to the receiver room via co-axial cables. In the receiver room, the antenna signals were combined in a Christmas-Tree configuration. Three BFNs, were required for the test array. A LabView based programmable interface was used to send the control word to an Arduino microcontroller board which was used for transmitting the control signals to the RF switches in the BFN for switching the beam after every 28cosδ minutes, where δ is the declination of the source. The output of the third beam-former at 191.4 MHz was down-converted to 10.7 MHz in a single mixing receiver system and then filtered with a band-pass filter with f_c = 10.7 MHz, Δf ≈ 1 MHz. 191.4 MHz was chosen because this was a relatively interference free frequency band and also we had off the shelf backend equipment for this frequency. The band-limited signal was sampled at Nyquist rate and transmitted through an FPGA data Acquisition module to the PC through USB interface. The observation is carried out for ≈6 hours duration.

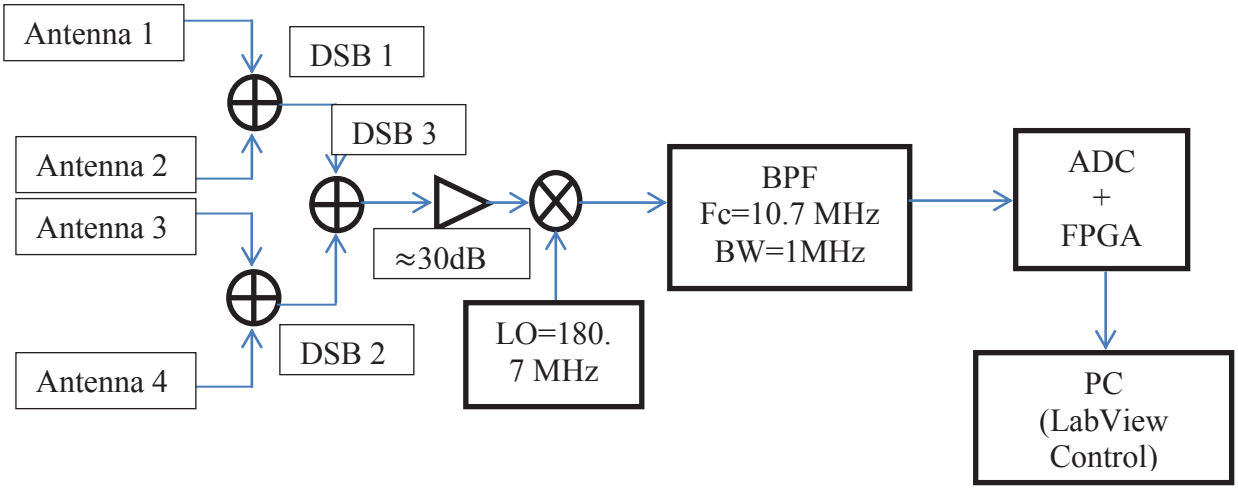

Figure 5 Observational Setup.

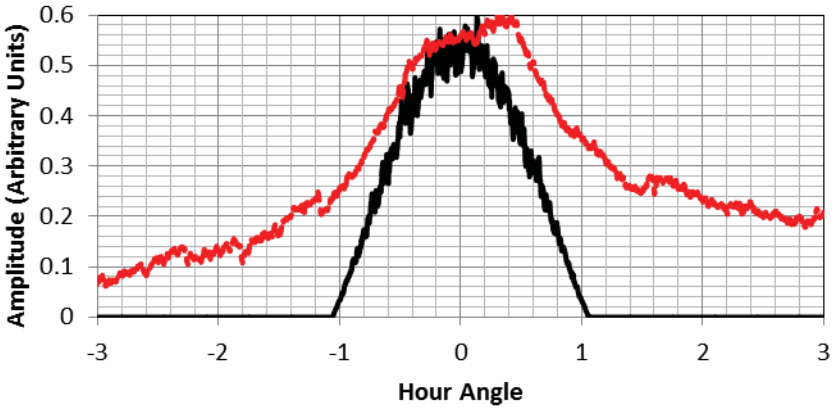

Figure 6: Tracking (red) and Transit (black) observations of Sun on May 17, 2014.

Table 1: TEST ARRAY PARAMETERS

Number of Elements	4
Frequency of Operation	191.4 MHz
Collecting Area	4 m^2
Sky Coverage (Transit mode)	~19°
Sky Coverage (Tracking mode)	~60°

5. Conclusions and Future work: From the S-Parameter plots, it is seen that the new beam-former achieves better performance than the diode-based beam-formers. Also wide frequency response is achieved, making it suitable for both imaging and spectral applications. The beam-formers are designed to be used for any low frequency, wide-band radio telescope system. Currently, we're working on two fronts: one, implementation of the new beam-formers presented in this work for the spectrograph array, GLOSS; two, design of a prototype 8 input beam-former such that there is only a single beam-former board for a single group (a group contains 8 antennas) where the delay cables will be replaced with microstrip tracks.

References:

[1] T.L.Landecker, "Co-axial Cable Delay system for Synthesis Radio Telescopes", IEEE Transactions on Instrumentation and Measurements, Vol. IM-33, No. 02, pp. 78 – 83, 1984.

[2] R.Ramesh, K.R. Subramanian, M.S. Sundararajan, Ch. V. Sastry, "The Gauribidanur Radio Heliograph", Solar Physics, Vol. 181, pp. 439 – 453, 1998.

[3] P. Kishore, C. Kathiravan, R. Ramesh, M. Rajalingam, Indrajit Barve, "Gauribidanur Low Frequency Solar Spectrograph", Solar Physics, Vol. 289, pp. 3995-4005, 2014.

[4] R. Ramesh, C. Kathiravan, M.S. Sundararajan, Indrajit Barve, Ch. V. Sastry, "A Low-Frequency Antenna System for Observations of Polarized Radio Emissions from the Solar Corona", Solar Physics, Vol. 253, pp. 319-327, 2008.

[5] Data-sheet of RFSW6223, www.rfmd.com.

[6] G.W. Swenson Jr., Y.T. Lo, "The University of Illinois Radio Telescope", IRE Transactions on Antennas and Wave Propagation, January 1961.

[7] K.F.Molz, "Phased Array Radar Systems", Proc. Of Signal Processing in RADAR and SONAR Directional Systems, July 1964.

MSRR LOADED MICROSTRIP PATCH ANTENNA ARRAY FOR 5.8 GHz Wi-MAX APPLICATIONS

Chirag Arora[1], Shyam S. Pattnaik[2], R. N. Baral[3]

[1]Krishna Institute of Engineering & Technology, Ghaziabad, (UP), c_arora2002@yahoo.co.in
[2] ETV Department, NITTTR, Chandigarh, profshyampattnaik@gmail.com
[3]IMS Engineering College, Ghaziabad (UP), r.n.baral@gmail.com

Abstract: *The paper communicates a unique technique for gain and bandwidth improvement of a microstrip patch antenna array for IEEE 802.16a 5.8 GHz Wi-MAX applications. A conventional microstrip patch antenna array is loaded with a pair of metamaterial multiple split ring resonators (MSRR). The unloaded antenna array provides a bandwidth of 425 MHz at 5.8 GHz, whereas under loaded conditions the bandwidth increases to 610 MHz corresponding to bandwidth enhancement of 3%. Under loaded conditions gain improvement of 1.1 dBi is observed in the elevation plane while a similar gain of 5.3dBi is observed in the azimuth plane. Reduction in mutual coupling between the elements of antenna array, due to MSRR loading, has been analyzed. The electrical dimension of the patch is 0.23λ x 0.3λ. The proposed array has been fabricated on FR-4 substrate with thickness (h) = 1.48 mm, dielectric constant (εr) = 4.3 and loss tangent = 0.01. Equivalent circuit of the proposed array has also been presented.*

INTRODUCTION: Recently, the wireless communication technology is developing rapidly, resulting in wide use of wireless local area network (WLAN) in office or home. Due to various advantages such as light weight, low profile, planar configuration, less fabrication cost and capability to integrate with microwave integrated circuits technology, the microstrip patch antenna is quite well suited for applications such as wireless communications system, cellular phones, radar systems and satellite communications systems[1-2]. Wing Chi Mok *et al.* presented a single patch dual and triple band patch antenna for WCDMA and Wi-MAX applications [1]. However, sometimes it becomes hard to achieve high gain and wide bandwidth from a single element. One of the ways to achieve them is to make array of patch antennas [3-4]. However, due to existence of surface waves some mutual coupling exists between the patches of the array, resulting in severe degradation in antenna's radiation characteristics, reduction in gain and bandwidth, errors in beam forming, scanning etc [5].

Several methods to reduce the mutual coupling between the elements of antenna array are reported in the literature [6]. However, these methods generally require complex fabrication techniques. Recently, metamaterials are being used widely due to their unique features [7]. These materials have the capability to suppress electromagnetic wave propagation in certain frequency band and therefore, they can reduce the mutual coupling between the elements of array antenna by suppressing surface wave propagation [8].

In this work, a pair of multiple split ring resonator is used to decrease the mutual coupling between the patches of microstrip antenna arrays. The proposed MSRR is used to load

the antenna array. Simulation results are obtained with the method of moment based full wave IE3D electromagnetic simulator.

ANTENNA ARRAY DESIGN: Fig. 1(a) shows the geometrical structure of two element antenna array and Fig.1 (b) presents the antenna array loaded with MSRR, which act as artificial magnetic resonator [9]. A 50Ω SMA coaxial connector is used to the feed the array. The dimensions of each patch, as calculated using the transmission line model equations [10], are 15.88 mm and 11.95 mm respectively.

The corporate feed network, which provides power split using quarter wave impedance transformer [10], is used to edge feed the elements of the array. The dimensions of the feed network, as calculated from [10] are: b = 0.5327, c =2.8758, d = 0.5237, e = 1.38, and f = 7.55, j = 7.55 and h = 1.48. The spacing between the two patches of the antenna array is 0.96 (λg/2), where λg is the guided wavelength.

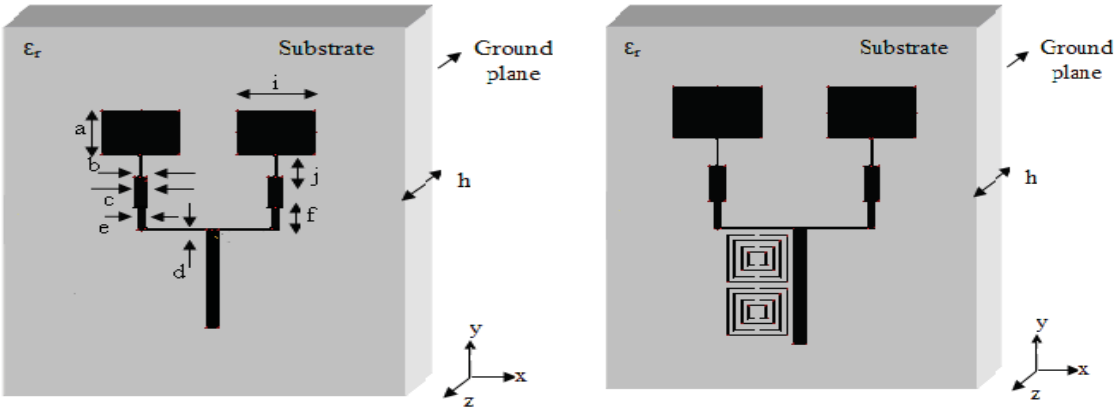

Fig. 1 Geometrical Sketch of (a) 2-element Antenna array (b) Proposed Antenna Array Loaded with MSRRs.

MSRRs, each containing four split rings, are integrated into the array in such a way that they do not increase the overall size of the proposed antenna array, that is, the dimensions of loaded as well as unloaded antenna are same. The geometrical dimensions of the MSRR are: length of outer split ring is 12.50 mm, width of rings is 0.2mm, gap at split of rings is 0.2 mm and separation between each ring is set to as 1mm. The distance between antenna array and MSRRs is 0.5 mm in both vertical as well as horizontal direction. The spacing between two MSRRs is fixed at 0.1 mm.

RESULTS AND DISCUSSION: This section presents the simulated results of the proposed antenna array in loaded and unloaded conditions. Fig. 2 depicts the return loss characteristics of the proposed array under both, loaded and unloaded conditions. It is observed that the unloaded antenna array resonates at 5.8 GHz with bandwidth of 425 MHz, whereas, under loaded conditions the bandwidth increases upto 625 MHz at the same resonant frequency, thus corresponding to the bandwidth improvement of 3%. The dimensions of the array under both the conditions are same.

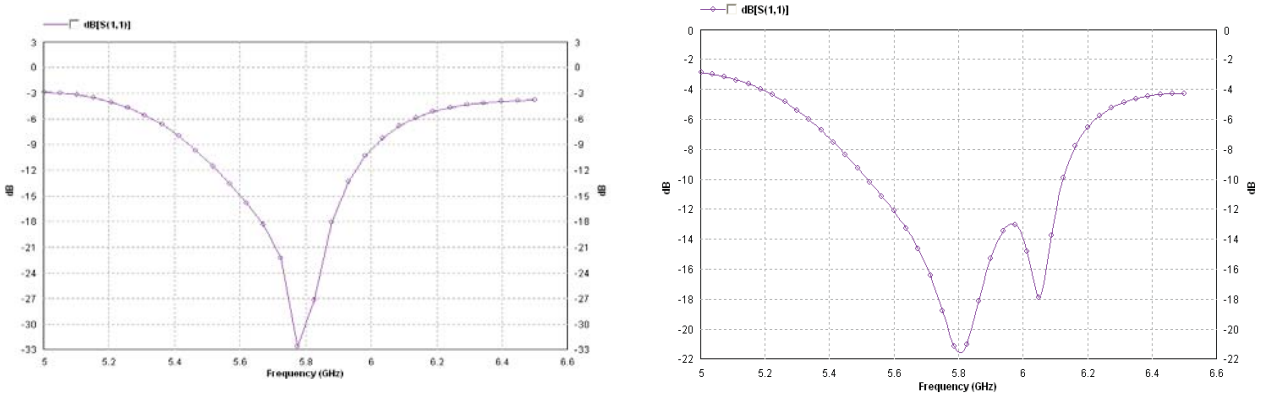

(a) (b)

Fig. 2 S_{11} Characteristics of (a) Unloaded Antenna Array (b) MSRR Loaded Proposed Antenna Array

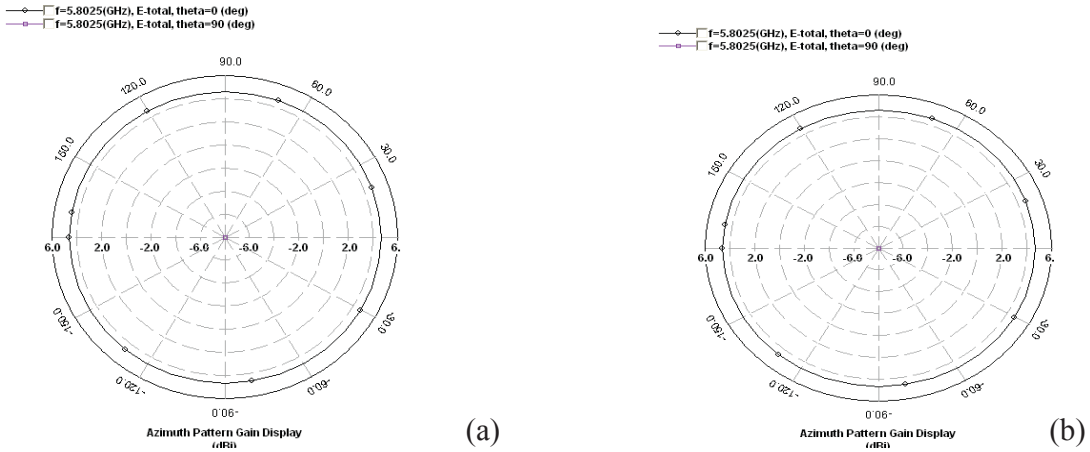

(a) (b)

Fig. 3 Azimuth Plane Radiation Pattern Characteristics of (a) Unloaded Antenna Array (b) Proposed Loaded Antenna Array.

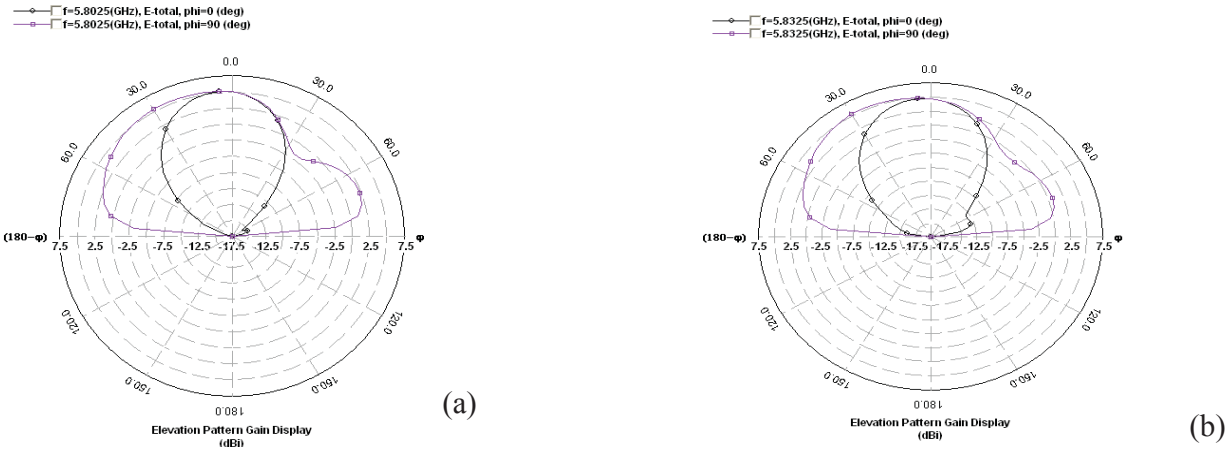

(a) (b)

Fig. 4 Elevation Plane Radiation Pattern Characteristics of (a) Unloaded Antenna Array (b) Proposed MSRR Loaded Antenna Array.

Fig. 3 represents the radiation pattern characteristics of loaded and unloaded antenna array, from which it is observed that the array resonates with gain of 5.3 dBi in azimuth plane, under both the conditions. However, in elevation plane (Fig. 4) *gain improvement of 1.1 dBi is observed in elevation plane* of the loaded array as compared to the unloaded array, as a result of which the elevation plane radiation pattern of MSRR loaded antenna array starts resembling like that of a conventional patch antenna radiation pattern. However, a dip in the elevation plane radiation pattern is observed due to the excitation of the some spurious modes on patch conductor. Fig 5 represents the plot for gain Vs frequency of the loaded array.

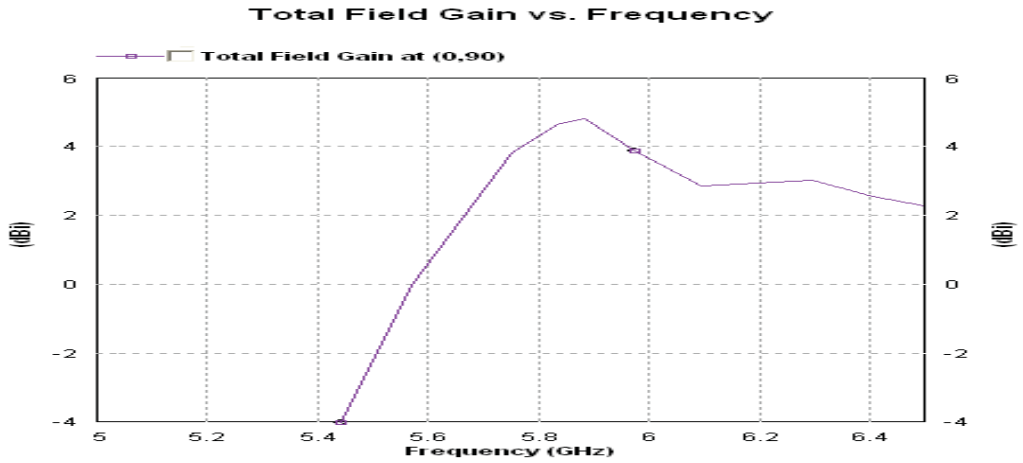

Fig. 5 Gain Vs frequency curve for the loaded array

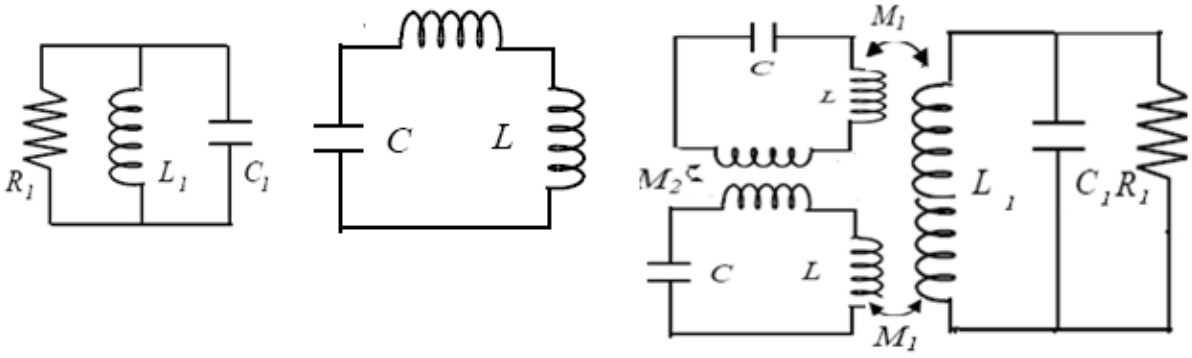

(a) (b) (c)

Fig. 6 Equivalent circuit of (a) Microstrip Patch Antenna (b) MSRR (c) Proposed Antenna Array

Equivalent Circuit Analysis and Theoretical Discussion: Fig. 6 depicts the equivalent circuit of (a) microstrip patch antenna (b) MSRR (c) proposed antenna array. According to the principles of equivalent theory, the MSRR can be modeled as a LC resonant circuit. The values of L and C (which are equivalent inductance and capacitance of MSRR, respectively) are calculated using equations (1) and (2) [9].

$$L = \frac{\mu_0}{2}\frac{L_{savg}}{4}4.86\left[\ln\frac{0.98}{\rho}+1.84\rho\right] \quad (1)$$

Where, μ_0 is the permeability of free space, ρ is the filling ratio, Lm_{avg} is the average length of the square SRR, which is given as $Lm_{avg} = 4[Lm - (N - 1)(w + s)]$ and N is the number of split rings. The equivalent capacitance (C) MSRR is given as [9]

$$C = \varepsilon_0\frac{N-1}{2}\left[2L_s-(2N-1)(w+s)\frac{K\sqrt{1-k_1^2}}{K(k_1)}\right] \quad (2)$$

Where, ε_0 is the permittivity of free space, K is complete elliptic integral of first kind; k_1 is argument of integral. The values of L_1, C_1 and R_1 (which are equivalent inductance, capacitance and resistance of the patch antenna respectively) can also be calculated using various mathematical relations [11].The inductance of the patch antenna array with the capacitance of MSRRs and the mutual inductances forms the LC resonant circuit of the loaded antenna. This capacitance compensates the inductance of antenna array and hence good matching is obtained at the resonant frequency. In loaded conditions, magnetic coupling between antenna array and MSRR (M_1) develop the electric field across the gap capacitance at the splits and capacitance between inner and outer split rings of MSRR. Due to this magnetic coupling between antenna array and MSRR, the mutual inductance between the elements of the array gets reduced. Also, under loaded conditions, the time varying magnetic flux generated by the antenna induces current on MSRR. It results in large electric field across the capacitance associated with the MSRR. This capacitance of MSRR is sufficiently large to match with the inductance of the array which leads to the reduction in mutual coupling between the elements of the array. Feed lines provide the coupling paths between array elements and the MSRRs. These feed lines also act as the additional conducting strips to reduce the existing mutual coupling. This reduction in mutual coupling between the array elements results in gain and bandwidth enhancement of the proposed loaded array.

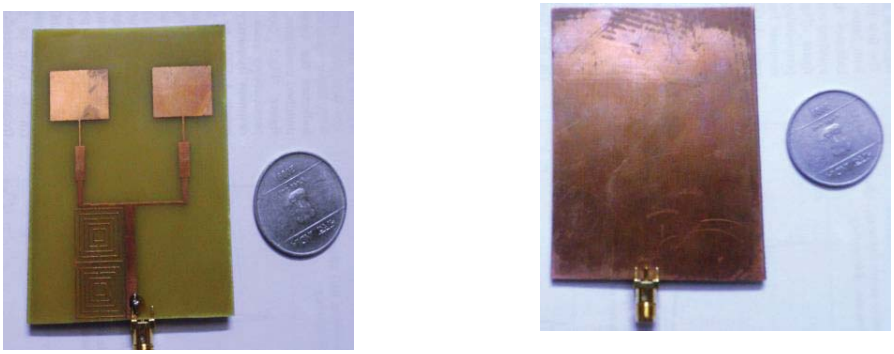

Fig. 5 Photograph of Fabricated Proposed Antenna Array (a) Radiating Patch View (b) Ground Plane View.

CONCLUSION: Loading of MSRR reduces the surface waves and mutual coupling between the elements of array and hence there is improvement in gain and bandwidth of proposed array. The advantage of this proposed antenna is that its performance gets improved at no extra size. The performance comparison of the proposed loaded antenna array and conventional unloaded antenna array show that metamaterial has a good potential to reduce the mutual coupling between the elements of the array. Measured results shall be presented in the subsequent publications.

REFERENCES

[1] Wing Chi Mok, Sai Hoi Wong, Kwai Man Luk, Kai Fong Lee, "Single-Layer Single-Patch Dual-Band and Triple-Band Patch Antennas", IEEE Transactions on Antennas and Propagation, Vol. 61, No. 8, pp. 4341- 4344, Aug 2013.

[2] Sharma M D, Kataria A, Meena R S, "E Shaped Patch Microstrip Antenna for WLAN Application Using Probe Feed and Aperture Feed", IEEE International Conference on Communication System and Network Technologies, pp. 66 – 70, May 2012, Rajkot.

[3] Nasser Ghassemi, Ke Wu, Stephane Claude, Xiupu Zhang, Jens Bornemann, "Low-Cost and High-Efficient W-Band Substrate Integrated Waveguide Antenna Array Made of Printed Circuit Board Process," IEEE Transactions on Antennas and Propagation, Vol. 60, No. 3, pp. 1648- 1653, March 2012.

[4] Chandan Kumar Ghosh, Bappaditya Mandal, Susanta Kumar Parui, "Omni-Directional Printed Antenna Array for MIMO Application," 5th International Conference on Computers and Devices for Communication (CODEC), pp. 1-4, Kolkata, Dec 2012.

[5] Heema Singh, H L Sneha, R M Jha, "Mutual Coupling in Phased Arrays: A Review", Hindawi International Journal of Antennas and Propagation, Feb. 2013.

[6] Revera Ablino, Balanis C. A. ,"Gain Enhancement in Microstrip Patch Antennas using Ferrite Rings" AP-S Symposium- Radio Science Meeting USNC-URSI, pp. 228, Lake Buena Vista, FL, July 2013.

[7] Ferdous S, Hossian, Chowdhury S. M. H., Mahdi M. R. C., "Reduced and Conventional Size Multi-Band Circular Patch Antennas Loaded with Metamaterials", IET- Microwave Antenna and Propagation, Vol. 7, No 9, pp 768-776, June 2013.

[8] Zhenzhe Liu, "Suppression of The Mutual Coupling Between Microstrip Antenna Arrays Using Negative Permeability Metamaterial on LTCC Substrate," IEEE Antenna and Propagation Symposium Society, pp. 1258-1259, 2013.

[9] F. Bilottil, A. Toscano, L. Vegni, K. Aydin, K.M. Alici, E. Ozbay, "Equivalent Circuit Models for the Design of Metamaterials Based on Artificial Magnetic Inclusions," IEEE Transactions on Microwave Theory and Techniques, Vol. 55, No. 12, pp. 2865-2873, December 2007.

[10] R. Garg, P. Bhartia, I. Bhal, A. Ittipiboon, "Microstrip Antenna Design Handbook," Artech House, Boston, UK, 2001.

[12]J.G. Joshi, Shyam S. Pattnaik, S. Devi, "Geo-textile Based Metamaterial Loaded Wearable Microstrip Patch Antenna," International Journal of Microwave and Optical Technology, Vol. 8, No. 1, pp. 25-33, Jan 2013.

Design, Development and Installation of Meteor Antenna System at NARL, Gadanki

M. Durga Rao[(1)], P.Kamaraj [(1)] and P. Srinivasulu[(1)]
(1) National Atmospheric Research Laboratory, Gadanki, India, 517112, Email: mdrao@narl.gov.in

Abstract: *Meteor observations take place in the Meteor Region of the atmosphere between 80 and 120 km. In this region the molecules in the atmosphere produce frictional heating, which causes an incoming particle to ablate, or convert from a solid into plasma. This produces an ionized trail of electrons, which reflect incoming radiowaves. It is very interesting to have the measurement of the echo directions of radio meteors, which is important in several fields of study. To have the provision for the meteor study, recently developed 30-MHz ionospheric radar at NARL, Gadanki is being augmented with a separate antenna system. This antenna system consists of two-element crossed yagi antennas at 30-MHz frequency. This paper will describe the design, development and installation aspects of meteor antenna system.*

Introduction: Ionospheric research has been a continued topic of interest both for academic interest and applications. A 30-MHz radar has been developed recently at National Atmospheric Research Laboratory to study the low latitude ionospheric plasma irregularities. While technological advances have provided expanded scope of observing the ionosphere both from ground and space with different techniques with improved accuracy, theoretical advances have taken place using the new information coming through new experiments, resulting in continued progress in our understanding. Meteor observation capability is made available with the existing radar by augmenting with separate antenna system with circular polarisation.

Configuration of antenna array: The configuration of the antenna system is very crucial to obtain accurate estimate of the angle of arrival of meteors as well as the configuration should not suffer from the mutual coupling effects. Hence, it is proposed to use antennas arranged to be spaced by distances differing by λ/2. The overall configuration receive antenna system is having five independent Yagi antennas arranged in 2λ and 2.5λ spacing as shown in figure1 and four Yagi antennas separated by 0.6λ spacing for transmission. These antennas are realized with crossed two-element vertical looking Yagi to have circular polarization. These antennas are oriented 45^{o} w.r.t North to minimize the mutual coupling effect with the existing main antenna array.

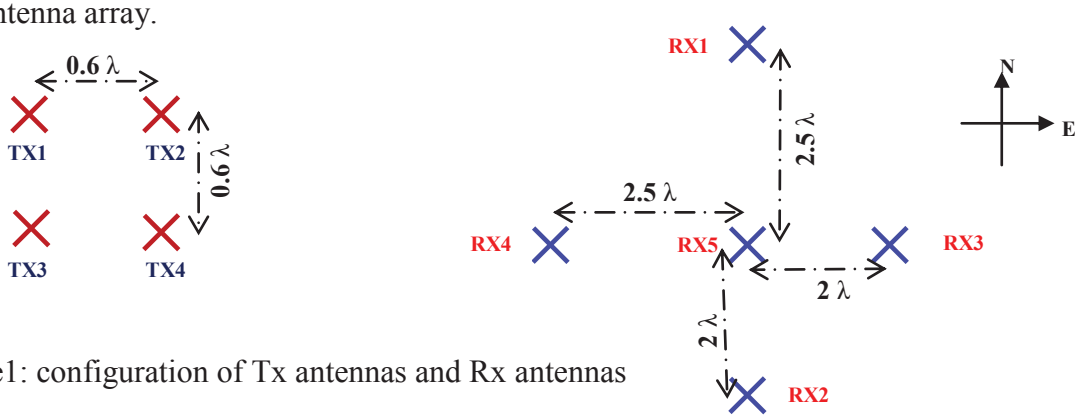

Figure1: configuration of Tx antennas and Rx antennas

Antenna specifications: Yagi antenna (30 MHz) is a 3-m vertical boom, with a firm base made of Seamless/ERW Steel material attached with the two elements (reflector & dipole) along with balun box. The electrical and mechanical specifications to design and realize the antenna are given in the Table-1&2.

Parameter	value
Centre frequency	30- MHz
band width	2- MHz
Return Loss	20 dB
Power Handling	10 kW (peak) with10% DR
Beam width	> 70^o
Gain	4.7 dB or better
Front/Back ratio	10 dB or better
Impedance	50 Ohms
Balun	1:4 Transformer ($\lambda/2$ cable)

Table-1: Electrical Specifications

Parameter	value
Dipole diameter	25mm
Dipole thickness	4 mm
Folded dipole gap	125 mm
Feed gap	15 mm
Boom diameter	90 mm
Boom thickness	5.5 mm
Base plate	320 mm square, Thickness: 12mm
Grouting bolt	EN24, 18 mm diameter and 230mm length

Table2: Mechanical Specifications

Design of Yagi antenna: Yagi antenna is a directional antenna consisting of a driven element (typically folded dipole) and additional parasitic elements (usually a so-called reflector and one or more directors). These antennas are directional along the axis perpendicular to the dipole in the plane of the elements, from the reflector toward the driven element and the director(s). Typical spacing's between elements vary from about 1/10 to 1/4 of a wavelength, depending on the specific design. The lengths of the directors are smaller than that of the driven element, which is smaller than that of the reflector(s) according to an elaborate design procedure. The present configuration employs only folded dipole and reflector elements to achieve wide beam width.

Simulation with 4NEC2: The simulation is carried out with the help of 4NEC2 software. NEC (= Numerical Electric Code) is a simulation method for wire antennas, developed by the Lawrence Livermore Laboratory in 1981 or the Navy. To realize this antenna is divided into "short segments" with linear variation of current and voltage. The Numerical Electromagnetics code (NEC-2) is a computer code for analyzing the electromagnetic response of an arbitrary structure consisting of wires and surfaces in free space or over a ground plane.

The analysis is accomplished by the numerical solution of integral equations for induced currents. The excitation may be an incident plane wave or a voltage source on a wire, while the output may include current and charge density, electric or magnetic field in the vicinity of the structure, and radiated fields. To start with the basic design, the following values are followed; later on these values are optimized with 4NEC2 to achieve the required specifications. The values are given in Table-3. The steps followed in design of total antenna system are given below and the simulated radiation patterns single crossed dipole antenna is shown in figure-2. The overall simulations for the Rx and Tx antenna array and the corresponding radiation patterns are shown in figures-3 and 4.

Parameter	Initial value	Optimized value
Dipole Length	0.47 λ	0.4475 λ
Reflector Length	0.51 λ	0.52 λ
Spacing between Reflector and Dipole	0.2λ	0.155 λ
Reflector distance from gusset	0.1λ	0.11 λ

Table-3: Estimation of antenna parameters

Step1: Design of two-element yagi antenna with the initial values and optimising the values.
Step2: Design of two-element crossed dipole yagi antenna with the optimised values.
Step3: Design of Meteor Rx antenna system with 2λ and 2.5λ spacing.
Step4: Design of Meteor Tx antenna system with 0.6λ spacing.

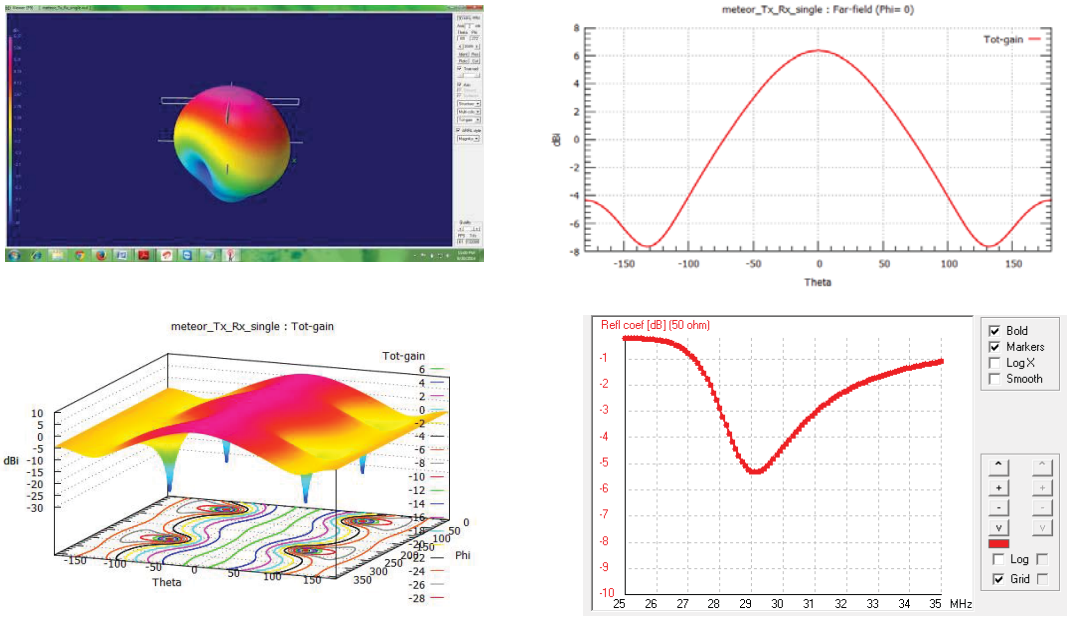

Figure-2: (a) Single crossed dipole antenna structure (b) 2-D radiation pattern (c) 3-D pattern with contour and (d) Return loss without impedance matching

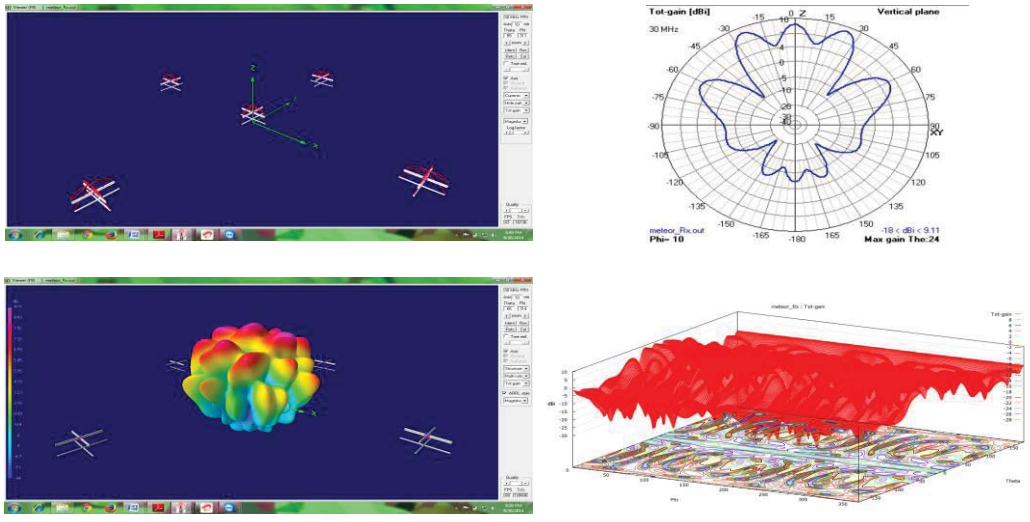

Figure-3: (a) Rx antenna system with currents (b) 2-D radiation pattern (c) 3-D radiation pattern with structure and (d) 3-D pattern with contour plot

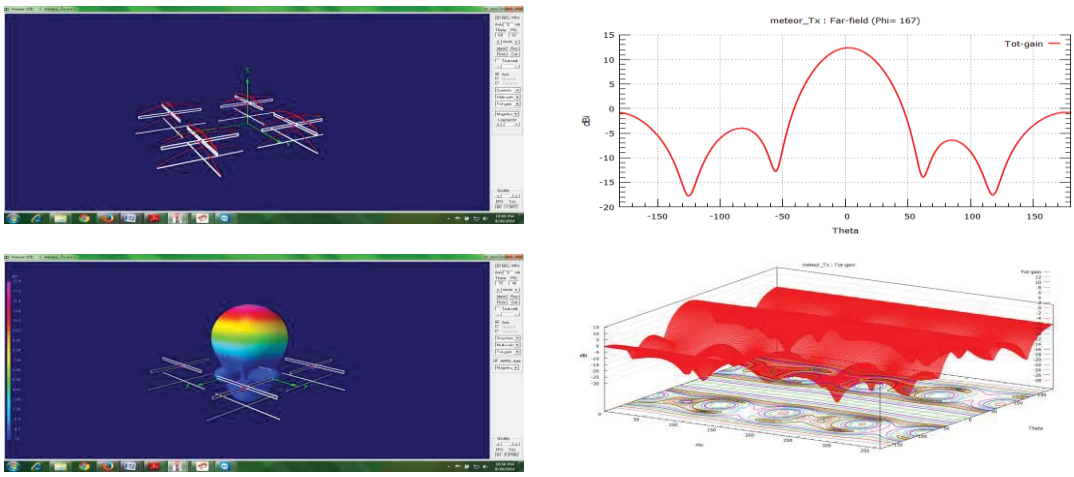

Figure-4: (a) Tx antenna system with currents (b) 2-D radiation pattern (c) 3-D radiation pattern with structure and (d) 3-D pattern with contour plot

Fabrication of the antenna: The electrical parameters as per table-1&2 are used for fabrication. The radar antennas are meant for tropical climate with high incidence of moisture and high ambient temperature; all the metallic components are to be suitably protected.The mild steel components used for Boom and other angular clamps are sand blasted and dip galvanized for 200 micron thickness. The following materials are used for the antenna parts, viz., "MSERWSTEEL" for Boom, "Al alloy 63400 (WP)" for folded diplole, reflector and "SS AISI 304" for angle clamps.

Installation and RF characterization: Installation of the antenna plays a crucial role in achieving the desired results of the overall system. The weight of each antenna is about 75 kg and these antenna elements have to sustain the wind speed of 100 kmph. In view of this the pedestals are constructed to withstand the same. The antenna array photograph is shown in figure 4. The base line of Tx antenna array and three out of five Rx antennas are aligned in geo magnetic north-south direction, where as the baseline of remaining two Rx antennas are aligned perpendicular to the baseline of other Rx antennas. The alignment w.r.t magnetic N-S is achieved with the help of dual frequency DGPS instrument. The return loss measured with antenna site master S311D are shown in figure 4.

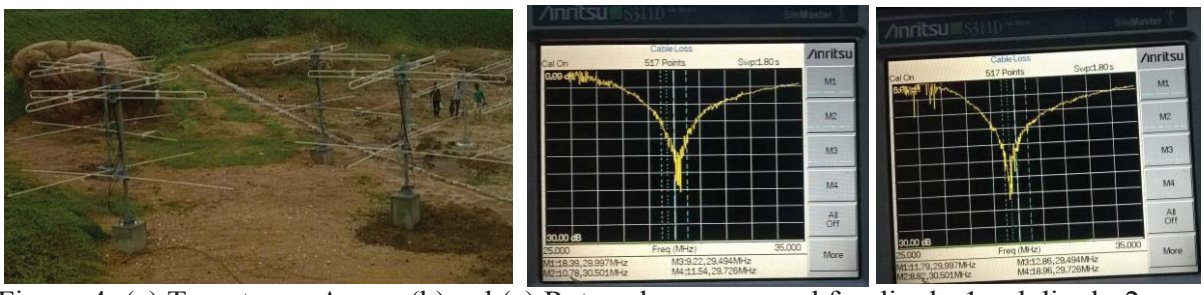

Figure-4: (a) Tx antenna Array (b)and (c) Return loss measured for dipole-1and dipole-2

Reference:

[1] Balanis C A, "Antenna Theory, analysis and design", 3rd edition, 2005.
[2] J.Jones, "An improved interferometer design for use with meteor radars", Radio Science, Vol. 33, No. 1, pp. 55 – 65, Jan-Feb 1998.
[3] K.P. Ray, Nandini M.Ammanagi, "Investigation of mutual coupling effect on the performance of 3-element Yagi-Uda antenna in linear array configuration", Int. J. Electron. Commun. (AEÜ),No.65, pp.510-515, 2011.

DESIGN AND DEVELOPMENT OF YAGI ANTENNA ARRAY FOR STRATOSPHERE-TROPOSPHERE RADAR

Binoy Babu B, Titu K. Samson, Rejoy Rebello, K. R. Santosh, K. Vasudevan, K. Mohankumar and P. Mohanan
Advanced Centre for Atmospheric Radar Research, ST Radar Facility, CUSAT.
acarr.cusat@yahoo.com

Abstract: *This paper describes the design of a 3-element yagi-uda antenna for a frequency of 205MHz, with a band-width of 5MHz, and optimization of the antenna parameters to work it for Stratosphere Troposphere (ST) Radar. It also included the design of a 619-element yagi antenna array for the above radar, and to obtain the phase distribution, to electronically steer the beam in desired directions. Theoretical calculations and simulations are done to fix the requirements and specification for ST Radar. Effect of lightning arrester on the total system is also studied.*

Introduction: The knowledge of earth's atmosphere is very important for human existence. Meteorological instrument have been devised and used over the time and routine surface measurements of temperature, pressure, humidity, precipitation, wind etc. Radar wind profiler (RWP) has evolved as the potential tool for measuring the height profile of wind vector with high time and height resolutions in all-weather condition. RWPs are suitable as research tools in assisting scientists in a wide spectrum of research interests, or as operational systems, helping to provide benefits to users in a variety of applications. Here yagi antenna design for ST Radar is described, which probes into the atmosphere upto 20km and finds the wind vector from the reflections.

YAGI ANTENNA FOR 205MHz ST RADAR

The specifications for yagi antenna for ST Radar were frequency of operation: 205MHz, Gain >7 dBi, F/B ratio >15dB, Bandwidth (10dB): 5MHz. Simulation studies are conducted on CST to find the effect of *reflector spacing and length, director spacing and length, element diameter, size of supporting boom* on realizable gain of the antenna. For different configurations of yagi radiation pattern is taken. From these parametric studies a yagi antenna of three elements is designed, with optimum gain and performance to meet the requirements of ST Radar. It offers a gain of 8.5dBi and front to back ratio greater than 15 dB, along with an operating bandwidth of 5 MHz. Further increase in antenna gain will degrade the front to back ratio and half power beam width and coming to an array of 619 yagi antennas, single element gain has little effect on overall gain of the array. However, if we improve the front to back ratio, it will reduce the radiation towards rear and increase the antenna efficiency. The final design parameters are Dipole Length 0.44λ, Director Length 0.42λ, Reflector

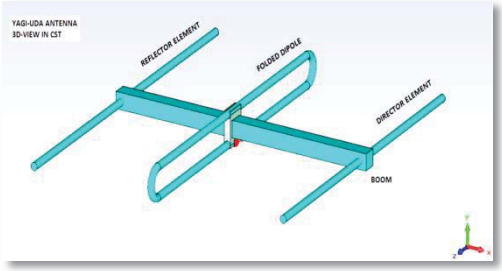

Figure 1: A single Yagi antenna

Length 0.482λ, Director Spacing 0.18λ, Reflector Spacing 0.16λ, Element Radius 0.0048λ, where Lambda (λ) 1465mm for 205MHz.

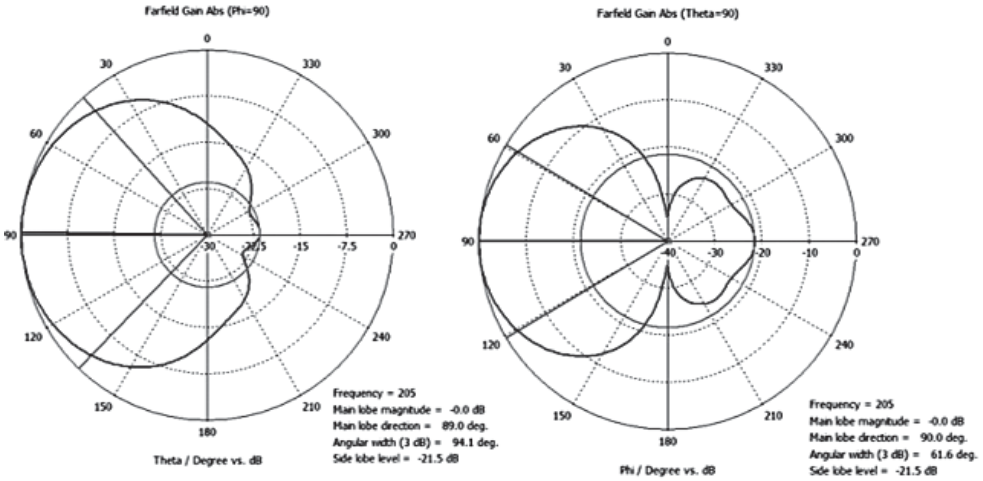

Figure 2: Polar Plot of radiation pattern, for Yagi antenna with gain 8.5 dBi, beam width 61.6^0 in Azimuth and 94.1^0 in Elevation, F/B ratio -17 dB, SLL -21.5dB and bandwidth 5.56 MHz

Feeding the antenna from coaxial cable a folded balun[7] is designed. The balun provides better matching and balancing for the antenna and the radiation patterns remain undistorted.

619-ELEMENT ARRAY FOR ST RADAR

A 619-element array is required to provide total gain of 35dB and beam width of 3^0, for the ST Radar to cover a height of 20km. For a radiation pattern without grating lobes, triangular grid arrangement is proposed. And the 619 elements or 619 yagi antennas are arranged in a manner, so that overall array structure forms a circle. The element spacing is chosen to be 0.7*λ. The figure shows the arrangement of 619 Yagi antennas in the array. Each dot in the figure 3 represents a yagi antenna.

The complete array is modeled and simulated in CST simulation software. The array elements are simultaneously excited with uniform amplitude and phase, for a frequency of 205MHz. Simulated radiation pattern in azimuth and elevation planes are shown in Figure 4. Obtained results are, angular width (3dB) = 3.2^0, first side lobe level = -18 dB, total gain = 35dB, F/B ratio = > 20dB.

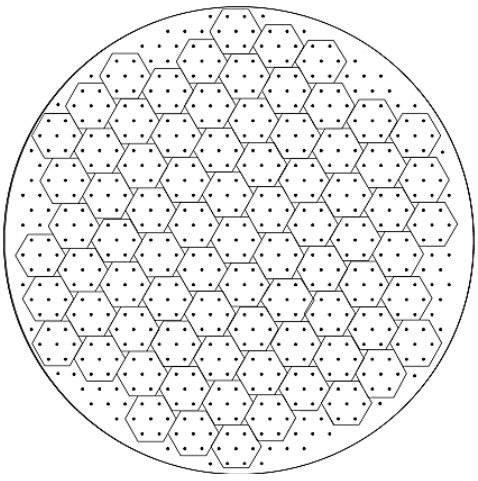

Figure 3: Yagi antenna arrangements in the array (each dot represents a yagi) as 7- element cluster

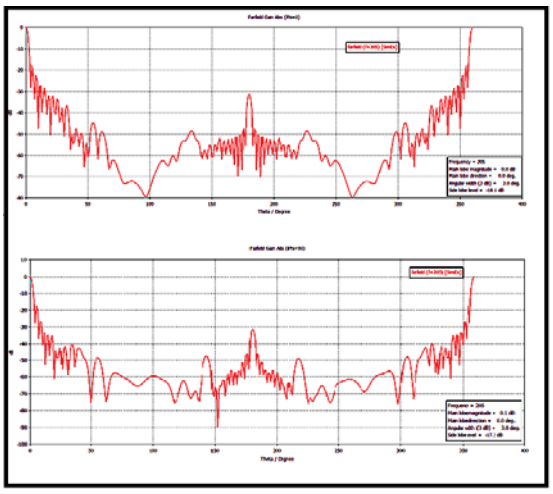

Figure 4: Array pattern – azimuth and elevation

BEAM STEERING

Beam steering in ST radar is used for obtaining wind vector components. A planar array is capable of steering the beam in two dimensions by changing the phase applied to each element. The element lattice with a planar array is shown in the figure 5. The same can use as triangular array by properly selecting excitation values, see figure 6.

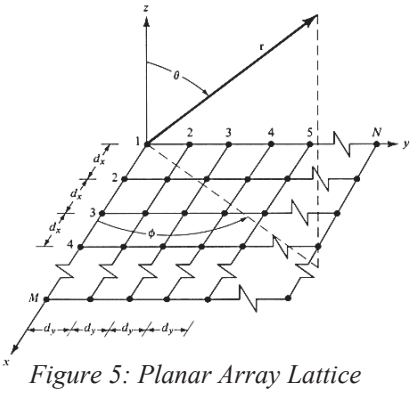

Figure 5: Planar Array Lattice

$$AF = I_0 \sum_{m=1}^{M} e^{j(m-1)(kd_x \sin\theta \cos\emptyset + \beta_x)} \sum_{n=1}^{N} e^{j(n-1)(kd_y \sin\theta \cos\emptyset + \beta_y)}$$

Where AF is the array factor, I_0 the current or excitation given to each element, m and n are the number of elements in row and column (x and y axis), k the propagation constant, dx and dy are the spacing between the elements in x and y directions and $\beta_x = -k_x sin\,\theta_0\, cos\,\emptyset_0$ and $\beta_y = -k_y sin\,\theta_0\, sin\,\emptyset_0$.

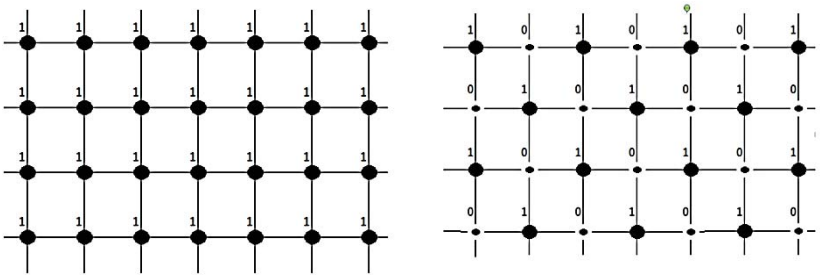

Figure 6: Rectangular grid to triangular grid conversion by selecting excitation

The phase's βx and βy are independent of each other, and they can be adjusted so that the main beam can pointed to different azimuth and elevation angle. The phase values for 619 elements are calculated using the above equations.

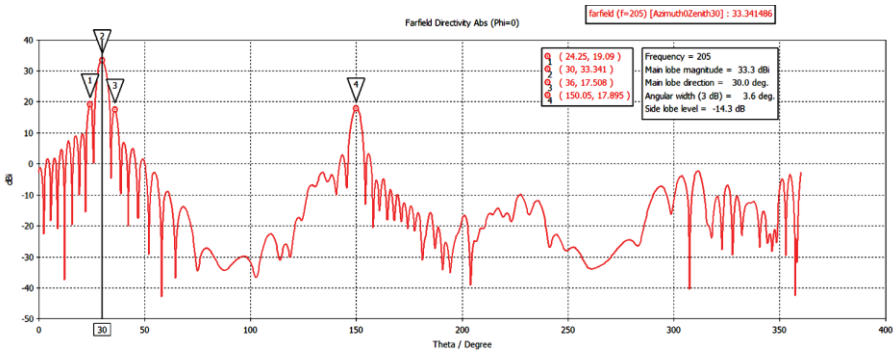

Figure 7: Beam tilted to an angle for 30 degree

With the phase calculation, the beam can be tilted in any direction with an accuracy of 0.2°.

49-ELEMENT ARRAY CONFIGURATION

The SAM[8] (Spaced Antenna Mode) which is an alternative approach for measuring winds, by making use of scattering and reflection from variations in the refractive index and it requires dedicated transmitting and receiving antennas. For this a cluster of 49 elements in

the centre act as transmitters, and another act as receiver. Simulation studies are conducted to find the effect of sleeping elements on radiating antenna pattern.

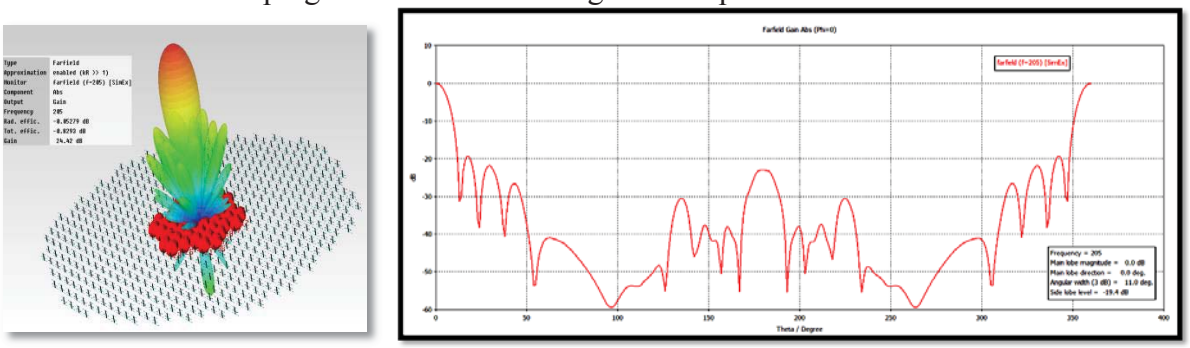

Figure 8: Array pattern in SAM mode (3D plot and Cartesian plot)

A cluster of 49 elements in the 619 elements is excited, keeping other element in unexcited. Results showed that those antennas will not affect the operation of exciting antennas. This configuration gives a gain of 24dB and HPBW of 11^0 and SLL -19.4dB. It is found that even the other elements are kept unexcited, the 49-elements in the whole array can radiate independently.

LIGHTNING ARRESTER DESIGN FOR RADAR

Simulation studies are done to see the effect or lightning arrester position in the antenna array pattern. Radiation pattern with and without lightning arrester are compared.

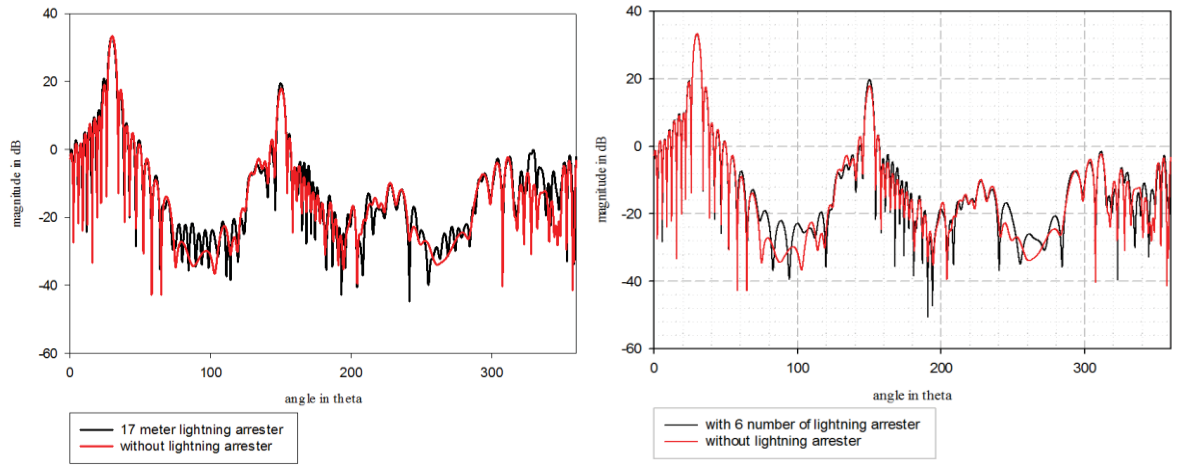

Figure 9: Array Pattern with and without lightning arrester of 17 meter and 6 meter height

First, effect of a lightning arrester of height 17 meter that is equivalent to the radius of the array is studied. Next with a lower height of 6 meter, and located at five different positions- four points on the edges, and one at the center of the array is studied. Both the arrangement will cover the entire array, and protect from lighting. From the results, it is clear that the metallic poles will not affect the radiation pattern of the array adversely.

RESULTS AND CONCULSIONS

A three elements yagi antenna, with a gain of 8.5dBi and front to back ratio greater than 15 dB is designed. 619 element triangular grid array is modeled in CST excited simultaneously with uniform phase and the gain of 35dB and beam width of 3.2^0 observed. Phase calculation

is done for beam steering the array. The tilted beam is evaluated for various azimuth and elevation angle and an accuracy of 0.02^0 is observed. Effect of lightning arrester system on radiation pattern of the array is studied. Observations showed that a lightining arrester placed parallel to boom of the yagi antenna will have no electrical effect as radiator, irrespective of its height or number of elements. Increasing the fence height will improve the radiation shielding.

An array to work for ST radar is designed and evaluated with possible theoretical means. It is found that the designed three-element yagi antenna array, with 619-antenna array met the requirements and specifications for ST radar.

REFERENCES

1. Constantine A. Balanis, "ANTENNA THEORY analysis and design," John Wiley & sons publication.
2. Theodore C. Cheston, Joe Frank, "Phased array Radar antennas", RADAR HANDBOOK.
3. R. Latteck, W. Singer, M. Rapp, and T. Renkwitz Leibniz, "MAARSY – the new MST radar on Andøya/Norway," Institute of Atmospheric Physics at the Rostock University, Schloss-Str. 6, 18225 K¨uhlungsborn, Germany.
4. James K Hsiao, " Properties of non-isosceles triangular grid planar phased array," IEEE transactions on antennas and propogation, Vol AP-20, No.4, July 1972.
5. Scott A. McLaughlin, Bob L. Weber, David A. Merritt, Gary A. Zimmerman, Maikel L. Wise, Frank Pratte, "New stratosphere-troposphere radar wind profiler for national networks and research".
6. Venkata Kishore K., Nalini K., B. T. P. Madhav, B. V. Raj Gopala Rao, Surendra Kumar B., Naga Harsha Vardhan K., "Design and Analysis of 3-Element yagi-uda Antenna for Wind Profiling Radar," International Journal of Computer Science & Communication Networks, Vol 1(3), 242-246.
7. Roy W Lewallen, "Baluns: What they do and how they do it," ARRL antenna compendium, vol1.
8. M. F. Larsen and J. Röttger, "The Spaced Antenna Technique for Radar Wind Profiling," Journal of Atmospheric and Oceanic Technology, Volume 6 Issue 6, 1989.
9. E. Hermawan, T. Tsuda and T. Adachi, "MU radar observations of tropopause variations by using clear air echo characteristics," Radio atmospheric science center, Kyoto University, Uji, Kyoto, Japan.
10. S. C. Chakravarti and JayatiDatta, ISRO "Mesospheric back scatter echoes as observed by Indian MST radar facility at Gadanki," Indian Journal of Radio and Space physics, Vol.6, December 2007.
11. F. S. Marzano and G. Ferrauto, "Relation between weather radar equation and first-order backscattering theory," Atmospheric Chemistry and Physics 3,813-821, 20 June 2003.

DECEMBER 17, WENESDAY
04.15PM TO 05.30PM
RESEARCH SESSION 5
MICROWAVE DEVICES 2
S N MITRA - HALL

Chair:Dr. U Raveendra Nath, NAL, Bangalore.

No	Papers	Page
5.1	**RF Circuit Design on Molded Interconnect Device** Divya Unnikrishnan, Darine Kaddour, Smail Tedjini ORSYS Group, LCIS laboratory, Grenoble INP, Valence, France. *Email:- divya.unnikrishnan@lcis.grenoble-inp.fr*	131-
5.2	**Passive Millimeter-wave Imaging for Detection of Objects Under Low Visibility** Anindya Harchowdhury[1], Binay Kumar Sarkar[2] Indian Institute of Technology Kharagpur, India, *721 302.* *Email:harchowdhuryanindya2@gmail.com[1], binaysarkar@yahoo.com[2]*	136
5.3	**Analysis and Characterization of Dual-loop Phase-locked Synthesizer to Realize Improved Performance in Millimeter-wave Frequency** Sukhendu Bhanja, Mousumi Sarkar, Arijit Majumdar SAMEER , Kolkata, India,700 091. *Email:sukhendu.bhanja@mmw.sameer.gov.in, mousumi.kundu@mmw.sameer.gov.in, arijit@mmw.sameer.gov.in*	140
5.4	**Monopack Transmit/Receive Module in X-Band.** Beenamole K.S., Vibishna B., Ashish Meena, Devaraj V., Hemprasad Ghanta. Electronics and Radar Development Establishment, Bangalore. *E-mail: beena.mole.ks@lrde.drdo.in*	144
5.5	**8-Way Unequal Amplitude Equal Phase Power divider Design Using Arbitrary Impedance for 430MHz Tropospheric Wind Profiling Radar** Venkata Kishore.K [1] ,Galaba Sai Rajesh [1] , Vijay Kumar [2] , P.Srinivasulu [3] [1,2]SENSE Department, VIT University, Vellore, Tamilnadu, India-632014.*E-mail:kothapudi@gmail.com* [3]NARL, Thirupathi, Government of India, Gadanki, AP, India, 517112.	148

RF CIRCUIT DESIGN ON MOLDED INTERCONNECT DEVICE

Divya Unnikrishnan, Darine Kaddour, Smail Tedjini

ORSYS Group, LCIS laboratory, Grenoble INP, Valence, France.
Email:- divya.unnikrishnan@lcis.grenoble-inp.fr

Abstract—*This paper presents the potential application of MID (Molded Interconnect Device) technology in the radio frequency domain. The dielectric characterization of two different thermoplastic substrates LCP (Liquid Crystal Polymer) Vectra E820i and ABS PC (Acrylonitrile Butadiene Styrene Poly Carbonate) is carried out using a resonant cavity. Microstrip transmission lines are also realized on these two substrates by patterning the metal using LDS (Laser Direct Structuring) and inkjet printing techniques. Transmission line measurements allowed the permittivity extraction in continuous frequency domain. Extracted permittivities are nearly 4.3 and 2.8 respectively for LCP Vectra E820i and ABS PC, which are comparable to those obtained from the resonant cavity. Based on these characterized dielectric values, two microstrip patch antennas optimized at 2.63 GHz were designed and fabricated. The LDS based antenna on LCP has a maximum gain of 5.1 dBi and inkjet printed antenna on ABS PC has a maximum gain of 3 dBi. The measurement and simulation results for the material and antenna characterization is also presented.*

I. INTRODUCTION

MID (Molded Interconnect Devices) technology is one of the trend setting innovative technology in the field of electronic circuit design. This technology allows the direct integration of electrical conductor patterns onto injection molded thermoplastic substrates on either two dimensional or three dimensional surfaces allowing thus reduced number of components and process steps [1-2]. Compared to conventional PCBs (Printed Circuit Board), MID offers higher degree of design flexibility especially in the RF (Radio Frequency) domain and enormous environmental, ecological and technological advantages [3]. For example, thermoplastic materials used in MID as substrates are easily recyclable. Also, it allows reduced number of components in the circuits as switches, wires, connectors etc. can be integrated on the circuit itself. Smaller size, reduced weight and assembling time, lower complexity can be achieved with MID technology providing thus a low cost of fabrication. MID has been made footprints in various applications such as medical, automobile and telecommunication domains [4-6].

The advantages of MID technology can be exploited in the field of RF circuit design. The selection of thermoplastics as substrate is often a complex choice, given a proper balance between electrical, thermal and mechanical properties and ease of fabrication and cost. Some of the important parameters that must be taken into account while choosing a substrate material in the RF circuit design is its complex dielectric permittivity and losses. Indeed, dielectric properties of the substrate can influence the electrical performance and reliability of the RF circuits. In addition, dielectric properties of the media interacting the EM (electromagnetic) waves can influence its field distribution and propagation [7]. To this end, characterization of EM properties of thermoplastic substrates have been carried out before moving to the RF circuit design.

Several methods of MID fabrication exist such as LDS (Laser Direct Structuring), LSS (Laser Subtractive Structuring), inkjet printing etc., where molded thermoplastics are produced by single injection molding. Single injection molding is the process of producing the required thermoplastic substrate by injecting their granulate into a mould for a single shot time [6]. LDS grabs more attention among other MID fabrication methods due to its great flexibility for design changes, possibility of making circuits on 3D surface, higher level of product integration with improved quality and reduced cost etc. A great interest has been recently developed on inkjet printing since it allows circuit fabrication [8] at reduced cost and completion time of conductive patterns. Both LDS and inkjet printing thus offer

great advantage of change in conductor pattern design in each circuit realization which in turns allow customization and specialization pattern printed.

In this paper, two low cost thermoplastics substrates, LCP (Liquid Crystal Polymer) Vectra E820i and ABS PC (Acrylonitrile Butadiene Styrene Poly Carbonate) are considered for the dielectric characterization and further antenna design. RF circuit fabrication on LCP Vectra E820i were carried out using LDS process due to the high temperature performance, chemical resistance, precise and stable dimensions of the substrate. RF circuits on ABS PC were fabricated using ink jet printing due to the substrate's low surface roughness which makes it suitable for achieving high quality printed electronic traces. Both substrates are injection molded in plates of dimensions 10x10x0.2 cm^3. Dielectric properties' characterization of these MID substrates have been done using a resonance cavity and two transmission lines method which respectively provide discrete frequency and continuous frequency characterization. Based on these extracted dielectric properties of two substrates, two MID microstrip patch antennas are designed and analyzed based on their reflection coefficient and radiation pattern.

II. DIELECTRIC PROPERTIES OF MID MATERIALS

Various methods of material characterizations can be found in literature [9-11]. Resonance cavity method is an accurate method of measurements for low loss dielectric substrates. In this method, a small piece of the material under test is placed in a high quality factor metallic resonant cavity. The resonant cavity method is based on the perturbation theory which allows an accurate determination of the permittivity based on a comparative analysis of certain EM characteristics such as resonance frequency and quality factor between empty and a partially loaded resonance cavity. The dielectric sample under test is placed at the position of maximum electric field. The required size of the dielectric sample should be small enough so that the electric distribution of the empty cavity changes slightly when the cavity is loaded. A shift in resonance frequency and quality factor of the cavity occurs when the sample is inserted. From measurements of empty and partially loaded cavity, the complex permittivity of the material can be calculated at various resonance frequency points [10]. The cavity shape as well as the dimensions of the sample determine resonance frequencies and hence this method of characterization can be used only for discrete frequency measurements.

A typical measurement system consists of a network analyzer, a resonant cavity and a software to make the calculations. Figure 1 (a) presents the measurement set up of dielectric characterization using Damaskos thin sheet tester cavity [12] and Figure 1(b) shows the extracted dielectric properties of the two substrates. Extractions have been done for first seven resonance frequencies; 0.809 GHz, 1.266 GHz, 1.872 GHz, 2.521 GHz, 3.186 GHz, 3.863 GHz and 4.541 GHz. LCP Vectra grabs higher permittivity of nearly 4.3 and lower loss of 0.004 whereas permittivity of ABS PC is nearly 2.8 and tangent loss is nearly 0.006. The measurement provides a good accuracy of extraction with a precision less than 2.6%. The accuracy is calculated based on the precision provided by the Damoskos cavity measurement which is less than 0.1% and substrate thickness precision of less than 2.5 %.

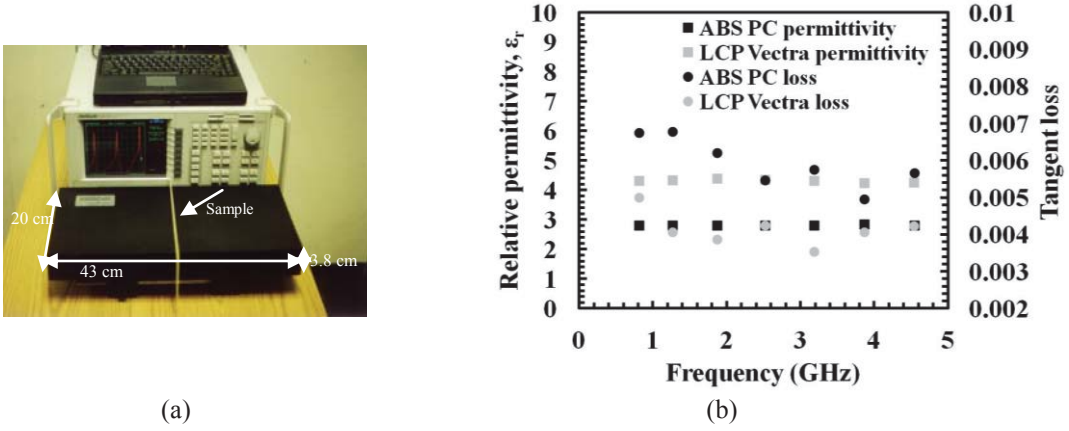

(a) (b)

Figure.1 MID dielectric characterization (a) Damaskos thin sheet tester cavity, (b) Characterized dielectric properties of LCP Vectra E820i and ABS PC.

Based on these extracted results, MID transmission lines and antennas were designed and realized and following section discusses them in details.

III. MID MICROSTRIP TRANSMISSION LINES AND PATCH ANTENNAS

A. MID Transmission lines

One of the fundamental components of RF system is transmission lines. In order to study the compatibility of MID technology in RF applications, microstrip transmission lines were fabricated on LCP Vectra E820i by LDS and on ABS PC by inkjet printing.

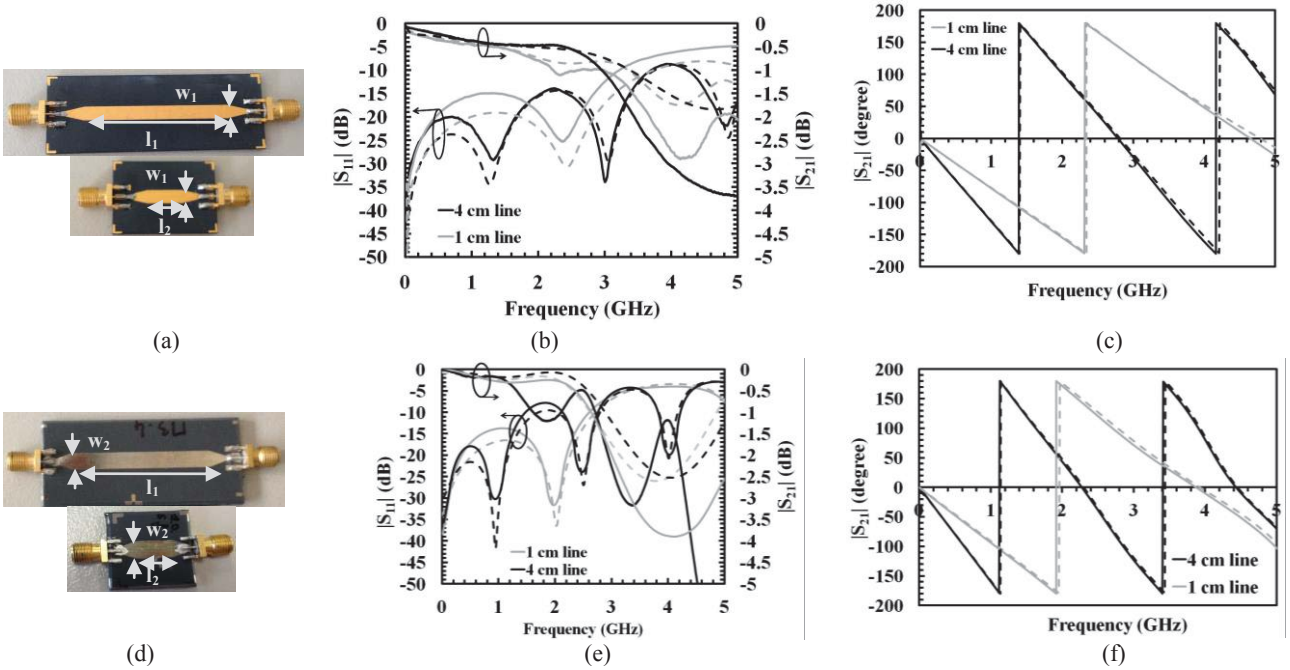

Figure.2 MID transmission lines and their characteristics, (a) lines on LCP Vectra E820i by LDS, (b) and (c) S parameter in dB and degree of LDS lines, (d) lines on ABS PC by inkjet printing, (e) and (f) S parameters in dB and degree of inkjet printed lines (w_1= 3.8mm, w_2= 5.1mm, l_1=4cm and l_2=1cm, dotted lines: simulations and solid lines: measurements)

The transmission lines on LCP Vectra E820i and ABS PC are respectively shown in Figure 2 (a) and (d). All lines are designed to have an impedance of 50 Ω. As mentioned before, LDS is used for device fabrication on LCP Vectra E820i. Three main steps involved in LDS process: injection molding, laser structuring and electroless plating. Thermoplastic molded parts are manufactured in single-shot injection molding. The molded part is subjected for laser activation, a process to activate the surface of the molded thermoplastic and to further undergo selective metallization. The process defines a circuit trace with a combination of Nickel, gold and copper having conductivity 5.48 x10^{06} S/m and thickness of 10µm. For inkjet printed transmission lines, metal ink with silver nanoparticles is inkjet-printed and subsequent curing and sintering step is performed to create metal thin-films of thickness 4.5µm with electrical conductivity in the order of 10^6 S/m. Tapered access and soldering pads are mounted on either side of the transmission lines to have better access to connecting lines.

Figure 2 also compares the *S* parameters of these transmission lines obtained from measurement and simulations. All measurements have been carried out using N5222A Agilent PNA using electronic calibration and simulations have been carried out using Ansys HFSS considering SMA connectors on either side of lines. Measurement results of all transmission lines show good agreement with simulations. If a frequency at 2 GHz is considered, LDS transmission lines provides an insertion loss of 1 dB whereas inkjet printed lines provide loss of 1.25 dB. This is due to the higher tangent losses in ABS PC compared to LCP Vectra E820i. LDS line of 4 cm and 1 cm lines respectively show a 15 dB matching till 2 GHz and 2.8 GHz. In similar, inkjet printed lines show a matching of better than 15 dB till 1.5 GHz for 4 cm line and till 2.3 GHz for 1 cm line. Lower mismatching level occurs at higher frequencies is due to the tapered access for connecting lines.

These *S* parameters were taken into account in order to extract the relative permittivity of the substrates in continuous frequency domain. Two transmission line method [9] which provides accurate dielectric

properties extraction is utilized for the extraction. The basic concept of this method is to deembed the parasitic effects of connectors, cable access, etc. from *S* parameters measurements and then extract the substrate's permittivity. Detailed mathematical calculations involved in this method can be found in [9]. The *S* parameters are used in order to extract the characteristic impedance (Z_c) and propagation constant (γ) of the line. Based on the extracted γ, the effective dielectric permittivity can be extracted based on the equation (1).

$$\varepsilon_{reff} = \left(\frac{\beta c}{\omega}\right)^2 \tag{1}$$

where β is the imaginary part of γ which defines the phase of a line, c is the speed of light in vacuum in meter per second and ω is the angular frequency in rd/s. Further extraction of relative dielectric permittivity (ε_r) can be done by taking into account the analytical model of transmission lines in microstrip technology [12].

Based on the above calculations, the effective and relative permittivity of LCP Vectra E820i and ABS PC were extracted and are given in Figure 3. LCP Vectra holds an effective permittivity of nearly 3.2 which in turns provide the relative permittivity near to 4.3. Similarly, the effective permittivity extracted for ABS PC is around 2.2 and relative permittivity is near to 2.8. The extracted permittivity show good agreement with that obtained from resonant cavity method with a small variation of 3%.

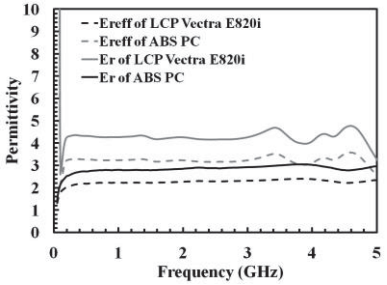

Figure.3 Effective permittivity (dotted lines) and relative permittivity (solid lines) of ABS PC and LCP Vectra E820i extracted from two transmission lines method.

Finally, two microstrip patch antennas optimized for a resonance frequency of 2.63 GHz were designed on ABS PC and LCP Vectra in order to investigate the potential of MID for RF applications.

B. MID Microstrip patch antennas

Microstrip patch antennas have gained much attention as popular radiators due to their compact shape, less design complexity, low fabrication cost and ease of integration with microwave circuitry [14]. For this reason, we started the analysis of MID technology in antenna design by designing a rectangular microstrip patch antennas.

Figure 4 (a) and (b) respectively show rectangular microstrip patch antennas fabricated on 2mm thick LCP Vectra E820i by LDS and on ABS PC by inkjet printing. The conductivity and thickness of metallization are the same as that used for transmission lines presented above.

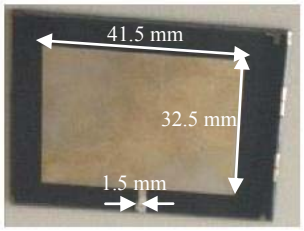

(a)

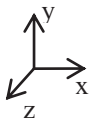

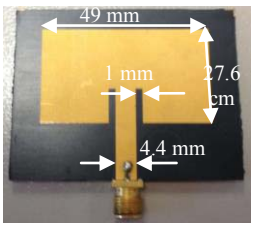

(b)

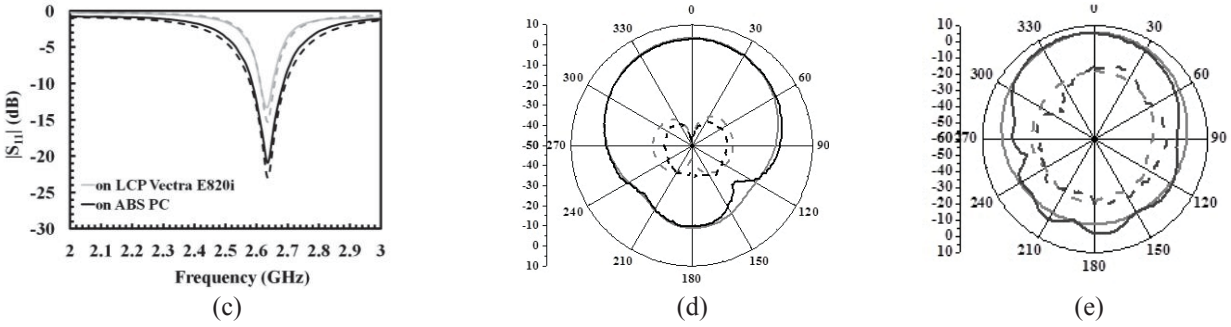

Figure.4 (a) MID microstrip patch antennas on ABS PC by inkjet printing and (b) on LCP Vectra E820i by LDS, (c) reflection coefficient of two antennas, (d) gain of inkjet printed antenna in dBi and (e) gain of LDS antenna in dBi.

The reflection coefficient in dB of two antennas are presented in Figure 4 (c). Measurement results of both antennas show resonances at 2.63 GHz with return loss better than 14 dB. Inkjet printed and LDS antennas respectively provide maximum gain of 3 dBi and 5.1 dBi (in Figure 4 (d) and (e). For inkjet printing technology, the low antenna gain is due to the higher conductive losses compared to LDS technology. Good agreement between measurements and simulation results validate thus the potential of MID technology for RF applications.

IV. CONCLUSION

This work discusses the application of MID technology on RF domain. The study is based on the measurements of MID microstrip transmission lines and antennas realized by LDS and inkjet printing techniques respectively on LCP Vectra E820i and ABS PC thermoplastics. First of all, the dielectric properties of these thermoplastic substrates were extracted using resonance cavity method. Permittivity of nearly 4.3 and 2.8 and low tangent losses of 0.004 and 0.006 were observed respectively for LCP Vectra E820i and ABS PC, validating thus the potential of MID for RF applications. Further design of 50Ω transmission lines on these two substrates were designed and fabricated. Measurements are in good agreement with simulations. Extracted permittivities of these two substrates from transmission lines' *S* parameter measurements show similar results as that obtained from resonance cavity method. In addition, two microstrip patch antennas optimized for 2.63 GHz were designed and measured. LDS antenna provides a gain of 5.1 dBi whereas inkjet printed antenna provides a gain of 3 dBi. The inkjet printed antenna performance can be improved by increase in metallization thickness. Measurements results are in agreement with simulation results validating thus the potential of MID for RF applications.

V. REFERENCES

[1] W. Xu, "Research on Key Technology of MID, " 2010 Second Pacific-Asia Conference on Circuits, Communications and System (PACCS), pp. 133–135.
[2] C. Orlob, D. Kornek, S. Preihs, and I. Rolfes, "Characterization of Electromagnetic Properties of Molded Interconnect Device Materials," German Microwave Conference, 2009.
[3] A. Housden and J.Gould, "Molded Interconnect Devices", Prime Faraday Technology Watch, pp.1-2, February 2002.
[4] D. Moser, J. Krause, "Multi functional package sensors in Automotive Applications", in the book of Advanced Microsystems for Automotive applications, 2006.
[5] D. Reynaerts and H. Van Brussel, "Design of an Advanced Computer Writing Tool", Sixth International Symposium on Micro Machines and Human Science, IEEE, pp. 229-234, 1995.
[6] LPKF Laser and Electronics, www.lpkf.com.
[7] A. R. Von Hippel, Dielectric Materials and Applications, New York: J. Wiley & Sons,1984.
[8] H. J. V. Osch, J. Perelaer, A. W. M. Laat and U. S. Schubert, " Inkjet Printing of Narrow Conductive Tracks on Untreated Polymer Substrates ," Advanced Materials, vol. 20, pp. 343-345, 2008.
[9] A. M. Mangan, S. P. Voinigescu, M. T. Yang and M. Tazlauanu, "De- Embedding Transmission Line Measurements for Accurate Modeling of IC Designs," IEEE Transactions on Electron Devices, vol. 53, pp. 235- 241, February 2006.
[10] R. A. Waldron, "Perturbation theory of resonant cavities," Proc. ht. Elect. Eng.," vol. 107C, pp. 272-214, Sept. 1960.
[11] Y. H. Chou, M. J. Jeng, Y. H. Lee and Y. G. Jan, Measurement of RF PCB Dielectric Properties and Losses, Progress in Electromagnetics Research Letters, Vol. 4, pp. 139-148, 2008.
[12] Damaskos, Material Measurement Solutions.
[13] D. Pozar, Microwave Engineering, New-York: J. Wiley & Sons, 2005.
[14] J. R. James, and P. S. Hall, Handbook of Microstrip Antennas. Peter Peregrinus, London, UK, 1989.

Passive Millimeter-wave Imaging for Detection of Objects Under Low Visibility

Anindya Harchowdhury
Kalpana Chawla Space Technology Cell
Indian Institute of Technology, Kharagpur
Kharagpur, India
harchowdhuryanindya2@gmail.com

Binay Kumar Sarkar
Kalpana Chawla Space Technology Cell
Indian Institute of Technology, Kharagpur
Kharagpur, India
bks@ece.iitkgp.ernet.in

***Abstract*— Passive Millimeter Wave (PMMW) imaging is used to form image through passive detection of natural radiation from a scene. The interest in this area is driven by the ability to form images in clear weather or in low visibility such as fog, cloud and rain. In this paper, we discuss the possible use of PMMW imaging system using a frequency scanning antenna to detect distant objects on railway track to avoid a scope of accident. Results are shown for both clear weather as well as poor visibility conditions.**

Keywords— PMMW; imaging; frequency scanning antenna; poor visibility.

I. INTRODUCTION

Passive Millimeter-Wave (PMMW) imaging is a technique that uses radiometers to detect thermal radiation emitted and reflected by metallic and non-metallic objects. While visual and infra-red (IR) emissions are attenuated by atmospheric constituents, PMMW emissions are transmitted resulting in consistent contrast between different objects from day to night in clear weather as well as in low-visibility conditions to form images for a range of security and inclement weather applications [1, 2].

The use of PMMW imaging technique in Unmanned Aerial Vehicle (UAV) for search and surveillance [3], opens up the possibilities of using it in civil applications like obstacle detection on road in poor visibility.

The medium separating the radiometer from the target area plays a significant role in affecting the level of emissions that reach the radiometer. MMW imaging systems operate within 30 GHz to 300 GHz frequency [4]. Imaging within the MMW region in inclement weather is possible because the MMW region contains atmospheric transmission windows around 35 GHz, 94 GHz, 140 GHz and 220 GHz, where the attenuation caused by atmospheric constituents is relatively low as shown in Fig.1. In these sub-millimeter wave ranges, the imaging of a scene in close proximity (in the order of few hundreds of meters) demands near field (NF) imaging techniques [5, 6].

In this work, the problem is framed to reconstruct images of a scene in front of a locomotive either stopped or in motion. The train is considered to be at least 200 m. far from the scene so as to take precautions so that any possible collision can be avoided. NF-far field (FF) transform technique discussed in [6] is considered here with the prior assumption of availability of received FF radiated pattern for image reconstruction.

The organization of this paper is as follows. The passive imaging technique is discussed in section II. Frequency scanning antenna used in this purpose is detailed in section III with the design details. Passive imaging simulation set-up used in this problem is discussed in section IV. Graphical results of reconstructed images are shown in section V comparing with original images. Finally the conclusion is drawn in section VI.

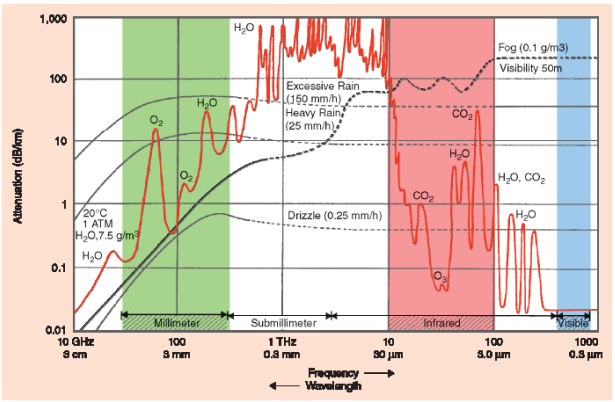

Fig.1 The attenuation at millimeter wave frequencies by atmospheric gas, rain, fog [4]

II. PASSIVE IMAGING TECHNIQUE

PMMW imaging technique consists of creating an image of one scene or Field of View (FOV) by detecting the radiometric temperature radiated by the objects and the background inside the scene [3].

Each object in the scene radiates power in the millimeter wave range with an emissivity ε compared to the radiation of a black body. The radiation acquired by the sensing element is a sum of contributions from the natural emission of the objects inside the scene, and the energy they reflect from illumination sources inside and outside of the scene. More specifically, the effective temperature of an object (Te), as given by (1), is the contribution of the physical temperature of the object (T) itself, modified by its emissivity ε, the temperature of the background behind the object (Tb) modified by its transmissivity τ, and the temperature of the other background

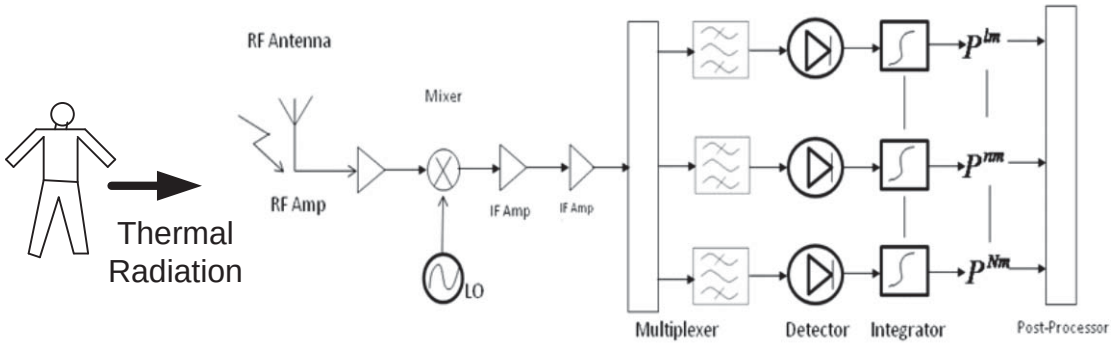

Fig.2 Simple Block diagram of PMMW imaging system

objects as given in (2). The relation among the emissivity, reflectivity and transmissivity are given in (2).

$$T_e = \varepsilon T_s + \tau T_i + \rho T_t \quad (1)$$

$$\varepsilon + \tau + \rho = 1 \quad (2)$$

A simplified block diagram of a PMMW imaging system is shown in Fig.2, where a human body is taken as an object and millimeter wave radiation is captured by the frequency scanning antenna and after RF to IF conversion, the power is detected by the detector. The detector is followed by an integrator, and the post processing is carried out by a computing system.

III. FREQUENCY SCANNING ANTENNA

Frequency scanning is the special application of phased array antenna, where the main beam steering occurs by the frequency scanning of the exciter. This type of antenna is called as frequency scanning antenna. The normal arrangement is to feed the different radiating elements from one folded waveguide as shown in Fig.3. Increasing the inter-element path length may result in small frequency change that will scan the beam in the direction normal to the face of the antenna. Assume that the radiating elements spaced *d* apart are connected by a serpentine (snake) feed of length *s*. The phase equation can be written as,

$$\sin\theta_m = \frac{s\lambda}{d\lambda_g} - \frac{m\lambda}{d} \quad (3)$$

where, θ_m is the beam pointing angle and *m* is an integer number. Larger s/λ and correspondingly larger *m* gives a faster change in the beam angle with the frequency [9-11].

A. Design Parameters

According to the system design, the receiving antenna should receive at 94 GHz from broadside i.e. at 90° with the railway track. We considered $d = 0.5\lambda_0$. From the prior conditions and using (3), we find that $s = 5.14\lambda_0$ where λ_0 is the free space wavelength at the operating frequency and *m* = 4. Antenna length (L) = 2 m, λ_0 = 3.2 mm at 94 GHz. (Half Power Beam Width) HPBW= $\frac{\lambda_0}{L} = 0.0016 rad$. The spatial

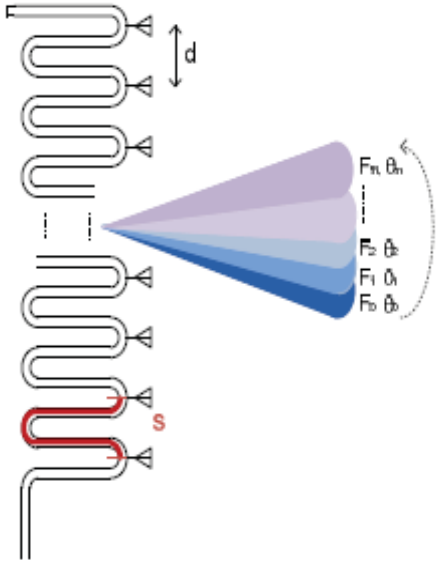

Fig.3 Frequency Scanning Array

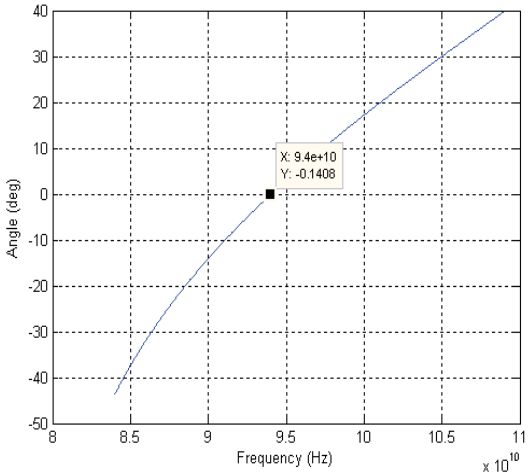

Fig.4 Beam pointing direction vs. frequency variation

resolution is computed as, $\Delta R = HPBW * R$ at the broadside. For other directions $\Delta R = R(\tan\theta_1 - \tan\theta_2)$, where θ_1 and θ_2 are the angles between the broadside distance and the

directions from which different frequencies with fixed offset are received. As, the antenna is going to receive from both the directions of broadside, a total of 84° scanning can be obtained with the specified parameters. It is divided into -44° and 40° in the left and right half and frequency vs beam pointing direction result is plotted in Fig.4.

IV. PASSIVE IMAGING SIMULATION SET-UP

Instead of a human body, few metallic and non-metallic objects are considered on a railway track as contents of the scene in this imaging simulation set up. The received power can be expressed as,

$$P = KT_e\Delta f * \exp(-2\alpha z) \quad (4)$$

where, T_e, Δf, K, α are the effective temperature of the object, bandwidth of individual resolution cell, Boltzman's constant and attenuation coefficient in linear scale respectively. α is obtained from [4]. Scene width is the same as Locomotive width≈ 3m. Major objective is to detect objects on railway track in low visibility. Safe distance of detection is considered to be 200 m. from the receiving antenna mounted in train. The attenuation at 94 GHz is about 0.6384 at 200 m distance in the presence of O_2 [4]. From the antenna design parameters and the range (200 m), we find that spatial resolution is about 32 cm. So, number of resolution cells (pixels) in the scene is equal to 3m/32cm ≈ 10. Two different scenes are considered for the simulation.

Scene-I: Here we place a metal and a concrete object between the railway tracks. The dimension of each of the objects is kept same as the dimension of a resolution cell. In case of metal, $\varepsilon = 0$ and $\rho = 1$. τ is 0 at millimeter wave frequency. The background illuminating temperature is around 100 K. Therefore, *Te* = 100 K. The effective temperature of the concrete and granite are 292.85 K and 187.3 K respectively. As granite stones and concrete sleepers are distributed between the two metal tracks, the effective temperature of this section is the average of both of them =240.075 K. The rail tracks and adjoining metals together is considered to have dimension equal to one resolution cell.

Scene-II: Here, the scene objects are considered same as in scene-I, but the width of the metallic object is (1+2/3=5/3) of a resolution cell. The width of other objects are same as in scene-I.

V. RESULTS AND DISCUSSION

Three different cases are demonstrated in Fig.5; a metal, a concrete slab, railway tracks, concrete sleepers, and granite stones comprise the scene in (a) normal weather, (b) fog (50 m. visibility), and (c) heavy rain (25 mm/h). Reconstructed images are compared with the original image in Fig.5. Received power by the detector from different objects considered in the scene are provided in Table-I. Received power from individual resolution cell is scaled up to form the reconstructed image. The received power fro. Reconstructed image in clear weather does not make any difference with the reconstructed image in fog and therefore appears to be visible to MMW detectors. Received power in heavy rain needs more amplification than in clear weather due to large attenuation and objects can then be detected from the reconstructed image. It is also recognized that, though both granite and concrete sleepers are present in the original image, average received radiometric temperature does not provide the scope to detect either of them. Fig.6 shows imperfect reconstruction of the scene at 200 m distance from the receiver. The original scene contains metallic object with 52 cm width, which is 5/3 of a resolution cell in dimension. So, a part of the object with one

TABLE I. Received power from different objects

Cases	Object	Received power
Clear weather	metal	2.7531e-14 W
	Concrete	8.0625e-14 W
	granite	5.1566e-14 W
Heavy rain	metal	7.7625e-17 W
	Concrete	2.2732e-16 W
	granite	1.4539e-16 W

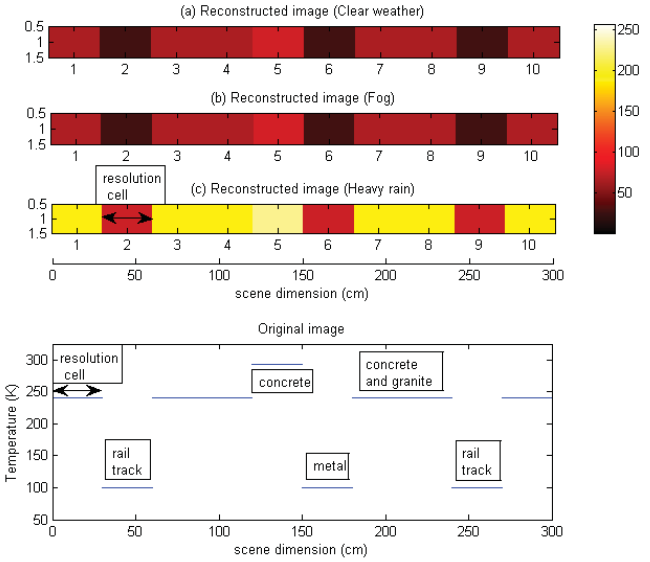

Fig.5 Reconstruction of concrete and metal in fog (200 m distance)

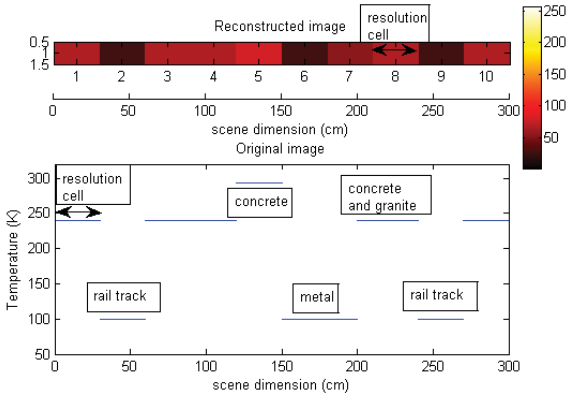

Fig.6 Imperfect scene reconstruction (200 m distance)

resolution cell width is identified in the sixth cell of the reconstructed image. The radiometric temperature of the rest of the part i.e. last (52-32) =20 cm of the metallic object is averaged out with that of the granite and concrete sleepers and received at the receiver. The radiometric temperature of this seventh cell is (292.85+187.3+100)/3 =193.3833 K. Though the metallic section of the seventh cell cannot be distinguished from the reconstructed image, the distinct intensity of this cell may help to predict about the existence of any other object apart from granite and sleepers. In Fig.7, the scene contains the same elements considered in Fig.5 with same dimension. The scene images are acquired over five discrete successive acquisition time interval. As the distance between scene and receiving antenna is set to 200 m, the image of the area is formed due to the movement of the train. It can be noticed that for the first three acquisitions the

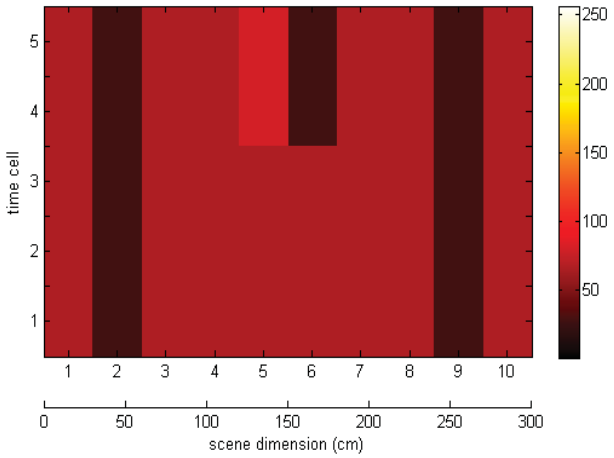

Fig.7 Reconstruction of concrete and metal in fog over five time cells

concrete and the metal object do not come in the scene. From the 4th acquisition, they are within 200 m distance from the train and therefore available in the image. The same happens for the 5th time cell due to the length of the two objects in along the railway track.

VI. CONCLUSION

PMMW imaging technique is used in this paper to identify distant objects as a means of collision avoidance of trains on railway track. It is shown that poor optical visibility due to fog and heavy rain can be negated by developing identifiable reconstructed image of static objects situated far from the observer. Imperfect reconstruction of objects having width of non-integer multiple of unit resolution cell is demonstrated here. The image of the area of the scene created due to train movement is also discussed, which may help to understand the dimension of unwanted objects on the path along with direction of train movement.

REFERENCES

[1] Roger Appleby, Rupert N. Anderton, "Millimeter-Wave and Submillimeter-Wave Imaging for Security and Surveillance", 95, No. 8, August 2007 | Proceedings of the IEEE.

[2] Juan B. Nogueira-Nine, R. A. Stirling-Gallacher Sony Deutschland GmbH, Reducing the acquisition time in a single sensor passive millimeter wave (PMMW) imaging system utilizing compressive sensing Proc. of SPIE Vol. 8188818803-2.

[3] David Michael Patrick Smith, Aspects of Small Airborne Passive Millimeter-Wave Imaging Systems, PhD Thesis, March 2010.

[4] Larry Yujiri, Merit Shoucri, and Philip Moffa, Passive Millimeter wave Imaging, 1527-3342, September 2003, *IEEE Microwave magazine*.

[5] Y. Álvarez, Fernando Las-Heras, and M. R. Pino, "Reconstruction of equivalent currents distribution over arbitrary three-dimensional surfaces based on integral equation algorithms" *IEEE Trans. Antennas Propag.*, vol. 55, no. 12, Dec. 2007.

[6] C. Vázquez, C. García, Y. Álvarez, S. Ver-Hoeye, and Fernando Las-Heras "Near Field Characterization of an Imaging System Based on a Frequency Scanning Antenna Array", *IEEE Trans. Antennas Propag.*, vol. 61, no. 5, May. 2013.

[7] Y. Álvarez et.al, "Submillimeter-Wave Frequency Scanning System for Imaging Applications" *IEEE Trans. Antennas Propag.*, vol. 61, no. 11, Dec. 2013.

[8] P.F.Goldsmith, "Focal plane imaging systems for millimeter wavelengths", *IEEE Trans. Microwave Theory Tech.*, vol. 41, no.10, Oct. 1993.

[9] Thomas A. Milligan, "Modern Antenna Design", 2005, Second Edition, IEEE Press.

[10] Merill.I.Skolnik, "Introduction to Radar Systems", 2001, Third Edition, The McGrawhill Publications.

[11] R.C. Hansen, Phased Array Antennas, 2009, Second Edition, John Wiley Press.

Analysis and Characterization of Dual-loop Phase-locked Synthesizer to Realize Improved Performance in Millimeter-wave Frequency

Sukhendu Bhanja[(1)], Mousumi Sarkar[(2)], Arijit Majumdar[(3)]
(1) SAMEER , Kolkata, India, Pin 700091, Email: sukhendu.bhanja@mmw.sameer.gov.in
(2) SAMEER , Kolkata, India, Pin 700091, Email: mousumi.kundu@mmw.sameer.gov.in
(3) SAMEER , Kolkata, India, Pin 700091, Email: arijit@mmw.sameer.gov.in

Abstract: A generalized transfer function based analysis for characterization of multi-loop phase-locked synthesizer has been carried out. Using this formulation time domain and frequency domain characterization of a dual loop synthesizer has been done in terms of the noise characteristics of each component of the synthesizer. The stability performance has been studied in time domain and phase noise performance in frequency domain. Loop filter parameters has been obtained for optimum phase noise. The performance of the synthesizer has been evaluated through experiment and it has been observed that the system is highly stable with 47.5 deg phase margin and 15.7 dB gain margin respectively. Phase noise of - 87 dBc/Hz at an off-set of 100 kHz from the carrier frequency of 34.65 GHz has been realized.

Introduction: Microwave and millimeter wave RADAR & communication system in recent times uses synthesized source realized by Phase Lock Loop (PLL) in receiver system for improved stability and phase noise of the system. In such synthesized sources one can use either single loop or multi-loop (normally dual-loop) phase-locked oscillator.

A typical Dual-loop phase-locked source can be realized using the scheme proposed in [1]. In [1] the dual loop PLL is characterized by extending the transfer function of single loop PLL. Studies on single loop PLL [2-4] and dual loop PLL [5-8] has been reported in literature for synthesizer design. A generalized approach to analyze and characterize the time domain and frequency domain performance of synthesizer using dual loop PLL is presented in this communication.

In this paper we have made detailed analysis and derived generalized phase transfer function for a multi-loop PLL useful for synthesizer application. While doing this we have initially made measurement on VCO and the synthesizer and used these measured data to optimize the dual loop performance in terms of stability and phase noise. The system is highly stable with phase margin of 47.5 deg and gain margin of 15.7 dB. The phase noise at 34.65 GHz system is measured to be - 87 dBc/Hz @ 100 kHz off-set from the carrier.

Description of the Dual Loop PLL: A scheme for a dual loop PLL [1] is shown in *Fig.1*. The main loop stabilizes the voltage controlled oscillator (VCO) in the frequency range of 34.4 GHz to 34.7 GHz while the auxiliary loop (C-band synthesizer) with same configuration stabilizes the VCO at a frequency from 4.21 GHz to 4.375 GHz. Using a harmonic mixer and the output signal of C band loop , the frequency of the main loop (Ka-Band) is down-converted to 700 MHz where frequency divider is readily available. The reference frequency is generated from a crystal oscillator (OCXO) at 10 MHz which is used as reference for both the synthesizers .The reference frequency is compared with the down-converted signal at 700 MHz using phase frequency detector IC (ADF4106) .The charge pump output is filtered and is used to stabilize the VCO at Ka-Band.

Stability Analysis : The fundamental equations for stability analysis are open loop equation, closed loop equation and phase error response .All these functions has been determined

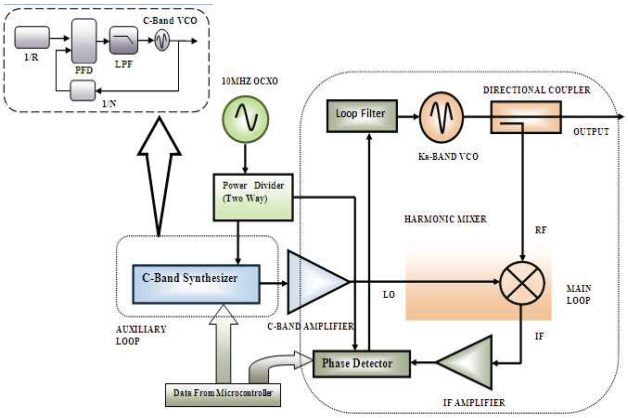

Fig.1 Block Diagram of dual loop PLL at Ka band

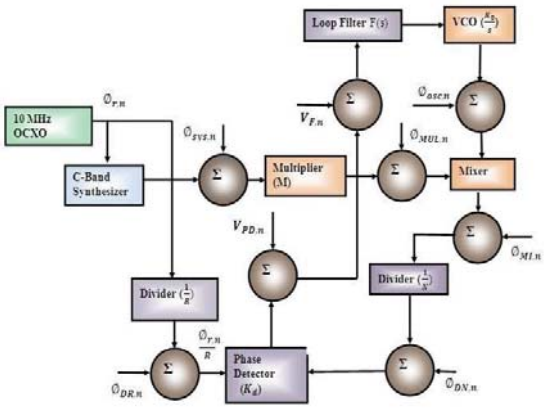

Fig.2 Block Diagram of Total PLL with Additive Noise Sources

from the transfer function of the loop filter [3-4].

The phase transfer function for the total loop is given in (1)

$$H(s)=\frac{\theta_o}{\theta_i}=\frac{\dfrac{K_d K_o F(s)}{sR}+\dfrac{MC(s) K_d K_o F(s)}{sN}}{1+\dfrac{K_d K_o F(s)}{Ns}} \quad (1)$$

Where , $C(s)=\dfrac{\theta_c}{\theta_i}=\left[\dfrac{\dfrac{K_{dc}K_{oc}F_c(s)}{s}}{1+\dfrac{K_{dc}K_{oc}F_c(s)}{N_c s}}\right]\dfrac{1}{R_c}$, the phase transfer function for the auxiliary loop.

θ_o / θ_c is output phase of total loop & auxiliary loop respectively.

θ_i is input phase of total loop

K_d / K_{dc} is Phase detector gain for main loop & auxiliary loop respectively.

K_o/ K_{oc} is VCO-gain constant for main loop & auxiliary loop respectively.

N/ N_c is Feedback path divider value for main loop & auxiliary loop respectively.

R/ R_c is Reference divider for main loop & auxiliary loop respectively.

M is the multiplying factor of the harmonic mixer

$F(s)$ / $F_c(s)$ is transfer function of the loop filter for main loop & auxiliary loop respectively.

The generalized equation (1) may be used to obtain the single loop equation as described in [2].

The phase transfer function is optimized for different parameters by changing the values of the loop filter components. The transfer function has been chosen to place all the poles in the right half plane implying the system to be stable. The transient response due to frequency switching can be determined by the step response of the closed loop transfer function. Assuming linear operation of the phase detector it will be sufficient to calculate only the unit step response .The phase margin and gain margin can also be optimized by using Bode diagram of the total transfer function. Table I shows the optimized values of loop filters for both the loops.

Phase Noise Calculation: Superposition principle has been applied for noise calculation of the total loop as shown in *Fig.2*. Noise generated or added in individual block has been added either at their respective inputs or outputs [7]. Noise being random in nature and

uncorrelated , respective spectral densities corresponding to SSB response can be added to derive the overall noise.

TABLE I

LOOP	LOOP FILTER COMPONENTS							
	Component values					*Phase Margin (Deg)*	*Gain Margin (dB)*	*Settling time (ms)*
	R1 (Ω)	*R2 (Ω)*	*C1*	*C2*	*C3*			
Main Loop	820	10	6.8pF	4.7pF	150pF	47.5	15.7	0.2
C-Band Loop	150	320	33nF	156nF	5pF			

$$S_{o,n}(f) = [S_{r,n}(f)\left(M + \frac{N}{R}\right)^2 + S_{DR,n}(f)N^2]|H(s)|^2 + \left[\begin{array}{l} S_{MUL,n}(f) + S_{SYS,n}(f)\frac{M^2}{N^2} \\ - S_{MI,n}(f) - N^2 S_{DN,n}(f) \end{array}\right]\left|H^{'}(s)\right|^2 + \left[\frac{N^2}{K_d{}^2}\left(S_{V_{PD},n}(f) + S_{V_F,n}(f)\right)\right]\left|H^{'}(s)\right|^2 + S_{OSC,n}\left|1 - H^{'}(s)\right|^2 \quad (2)$$

Where $H^{'}(s) = \dfrac{F(s)K_0K_d / Ns}{1 + \dfrac{F(s)K_0K_d}{Ns}}$

Experimentally obtained phase noise data of VCO in the main loop and that of auxiliary loop is fitted in the general phase noise equation (3) as detailed in [9]:

$$S\phi(f) = k_0 + \frac{k_1}{f} + \frac{k_2}{f^2} + \frac{k_3}{f^3} + \frac{k_4}{f^4} \quad (3)$$

The constants in the above equation are evaluated by equating the measured experimental data with the above general equation.

The noise from loop Filter ($S_{V,F}$), phase detector($S_{\Phi,F}$), N-divider ($S_{\Phi,D,n}$) and multiplier ($S_{\Phi,MU,n}$) in *Fig.2* has been modeled using equations given in [7].

The total phase noise is obtained from (2) and plotted using MATLAB which closely matches with the experimental data as shown in *Fig3.*

Experimental study : To realize the hardware of the dual loop phase lock source shown in Fig.1 we have designed the C band synthesizer, Ka band directional coupler ,C band amplifier , IF amplifier ,Phase Frequency Detector (PFD) card with loop filter. To obtain a good phase noise of the dual loop a ultra low noise fractional-N type C-band synthesizer has been designed and developed using Mini-circuit VCO and Analog Device Phase Frequency Detector card ADF4156.The loop filter used in the loop is optimized and a phase noise of -97 dBc/Hz @ 10 kHz is obtained within the frequency range of 4.21 to4.37 GHz. Minimum step size obtained for the loop is 1.5 kHz. Output of the C-Band synthesizer is amplified using two stage amplifier to drive the local oscillator port of the harmonic mixer. The IF output of the harmonic mixer is amplified and fed to the PFD card. The amplifier at C-band and IF is designed using Minicircuit IC GVA-84+ and MAR-6+ respectively. The output of the PFD card is filtered using optimized loop filter and it drives the VCO control. The output of the VCO is passed through a cross slot narrowband directional coupler having coupling of 12 dB .

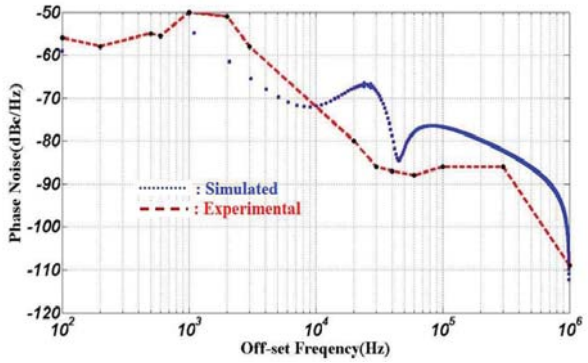

Fig.3 Comparison of Phase Noise of the Total Loop

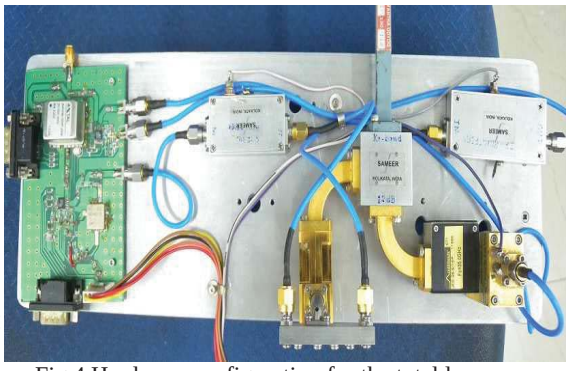

Fig.4 Hardware configuration for the total loop

Using these designed components and the harmonic mixer from Agilent Technology , VCO from Millitech , OCXO from Axtal , the total hardware of the dual loop phase lock source had been assembled which is shown in Fig.4. Phase noise of -87 dBc/Hz @ 100 kHz is achieved within a band width of 300 MHz (From 34.4 to 34.7 GHz).

CONCLUSION : In this paper a generalized approach for multiloop PLL design dual loop synthesizer at Ka band has been analyzed and designed. The components in the loop filter are optimized for maximum stability and improved phase noise. The optimized values are experimentally verified in C-band and Ka band loops. The experimentally measured phase noise data of C band synthesizer and Ka band VCO is used to model the phase noise of the total loop. Phase noise of -87 dBc/Hz @ 100 kHz has been achieved at Ka Band. Experimentally measured phase noise closely matches with the simulated one.

Acknowledgment: We are thankful to Director, SAMEER, DeiTy for his help and encouragement and for allowing us to carry out this work. We are also thankful to Professor Subal Kar, IRPE, Calcutta University for guiding us in presenting the work in current form.

Reference:

[1] Waldow,P.; Follmann,R.; Stehr,U. Beyer,A.; "'Advanced phase-locked - loop oscillators", 'Microwave Magazine, IEEE , Vol.02, No. 02, pp. 70 – 76, 2002.
[2] Malik,Z.Y.; Yasin , M.; Kayani, J.K.; "Design and Implementation of an X Band Frequency synthesizer for RADAR Application ", Applied Science & Technology ,pp. 10-14, 2007.
[3] Nakagawa,T.; Okazaki,H.; Yamaguchi,Y.; "A Low-Power X-Band Frequency Synthesizer Module ", Microwave Symposium Digest ,pp. 1209-1212, Vol.03, 1997.
[4] Ahmed,F.; Furqan,M; "A Digital S-Band Phase Locked Loop Based Frequency Synthesizer For On-Board Satellite Transmitter", JESTECH ,pp. 1-7, 2005.
[5] Kamata,M.; Shono,T.; Saba,T.; Sasase,I.; Mori,S.; "Third-Order Phase-Locked Loops using Dual Loops with Improved Stability", IEEE PACRIM, pp. 338-341, Vol.01, 1997.
[6] Kim, T.H.; Kim,B.; "Dual-loop Digital PLL Design for Adaptive Clock Recovery", Design Automation Conference, pp. 347-352, 1997.
[7] Kroupa ,V.; "Noise properties of PLL systems", IEEE Transaction on Communication, pp. 2244-2252, Vol.COM-30,No 10,1997.
[8] Shi,C.; Wang,W.; Ye,L.; Liao,H.;" ,"- 99dBc/Hz@10kHz 1MHz-Step Dual-Loop Integer-N PLL with Anti-mislocking Frequency Calibration for Global Navigation Satellite System Receiver", ISCAS, pp. 1876-4879, 2011.
[9] Drucker,E.; "Model PLL Dynamics And Phase-Noise Performance", Microwave & RF, pp. 73-117, 2000.

Monopack Transmit/Receive Module in X-Band.

Beenamole K.S, Vibishna. B, Ashish Meena, Devaraj V, Hemprasad Ghanta.
Electronics and Radar Development Establishment, Bangalore.
email: beena.mole.ks@lrde.drdo.in

Abstract: *This paper discusses about active and passive phased arrays and the importance of transmit/receive modules for active phased array applications. This paper details about the configuration, architecture and functions of transmit/ receive modules highlighting the importance of phase shifter and attenuator inside the T/R module. This paper also discusses about the features of a realised monopack Transmit/ Receive module in X-band and its suitability to be used in active phased arrays based on the phase and amplitude characteristics.*

Introduction: Active Phased Arrays(APAs)[1,2] have become the practical propositions for modern day radar systems due to their high efficiency and reliability compared to Passive Phased Arrays(PPAs). Active phased arrays(Fig.1), employs distributed Transmit/Receive(T/R) modules to replace the single central transmitter(Fig.2), used by passive phased arrays and thus introducing *Graceful Degradation* to the radar system making it more reliable to the user. Each single module generates a low output power, which when multiplied by the number of elements in an active phased array results in a very large output power. The power aperture product of active phased arrays are higher than that of their counterparts, passive phased arrays. Active phased arrays offers many advantages viz., rapid electronic scanning in one or several planes, low sidelobes or flexible sidelobe control, multiple clustered scanning beams, adaptive pattern control against jammers or clutter, frequency agility etc. The antenna elements are an integral part of these T/R modules with each antenna element connected to one T/R module. The antenna elements used with active phased arrays are capable of operating over the full field of view of the radar and throughout the bandwidth of the radar without any degradation in any of its characteristic features viz. gain, polarization, Voltage Standing Wave Ratio(VSWR) and cross polarization.

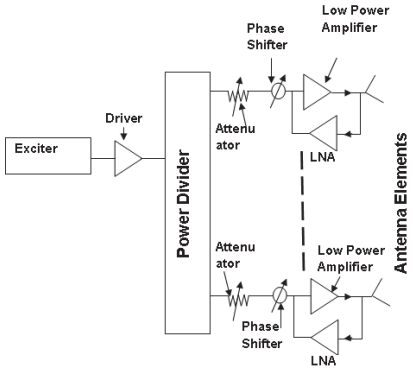

Fig. 1 Active phased array schematic

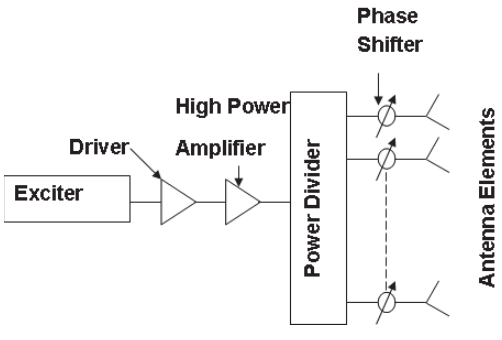

Fig. 2 Passive phased array schematic

Transmit/Receive(T/R) Module Configuration: The T/R Modules(TRMs) are the key elements in active phased arrays. The cost and performance of the active array critically dependent on the availability of compact, light weight, low consumption and high reliability T/R modules. The major functions of the T/R module include the generation of transmit power, low noise amplification of the received signals from the respective radiating element, required phase shift in the transmit and receive mode for beam steering and variable gain setting for aperture weighting through attenuators and proper interface to the array beam steering controller as well as array beam former and radiating element.

The schematic diagram of the T/R module used in the active phased array described in this paper is shown in Fig. 3. Here, the transmit chain of the T/R Module consists of Solid state power amplifiers to boost the signal from the Array RF manifold and pass it on to the antenna. The output may be of a few watts to several 100 watts depends on the application requirement. The receive chain consists of a Limiter followed by a Low Noise Amplifier(LNA).

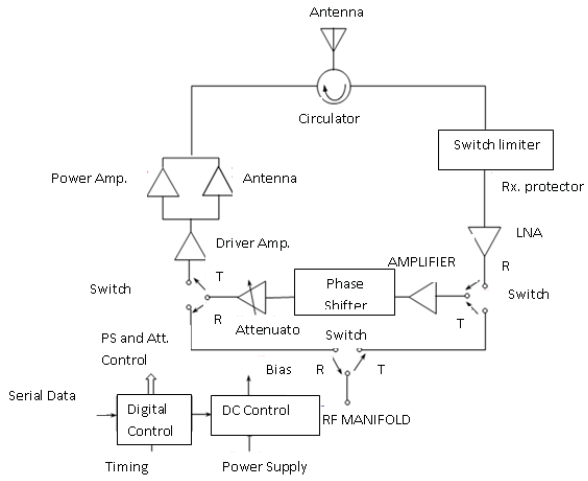

Fig. 3 Block diagram of Transmit/Receive Module

Architecture : An innovative architecture has been conceived for the Transmit/Receive Module (TRM) in X-Band. In this design, a monopack housing has been chosen and hence the size of TRM is very much constrained and challenge lies in identification of suitable components which can be housed in a single enclosure. The digital attenuator and phase shifter are placed in the common path of transmit and receive module. The RF chain of the TRM is made out of a 3 chip configuration which consists of MMIC(Microwave Monolithic Integrated Circuit) based core chip, Power Amplifier and LNA. the core chip contains the phase shifter and attenuator and also the buffer amplifiers. A temperature monitoring system also has been built into the module for monitoring the online temperature of the module. A T/R Module controller based on FPGAs housed inside the T/R Module. The key functionality of a TRMC is to latch the phase and attenuation values to phase shifter and attenuator in the common leg of the RF chain in a synchronized way, so that beam can be shaped and steered in the space for both transmit and receive modes. Besides, it should monitor the health status of the module in terms of temperature, power and DC supply check. This X-Band TRM has been realized for the first time in India.

Functions of T/R Module: The Transmit/ Receive Modules[3] are used in active phased arrays to scan the beam over the frequency band of interest with a specified sidelobe level. This is accomplished by the use of a digital attenuator and digital phase shifter MMICs. The antenna elements in an array will receive an incident plane wave with different phases if it is not parallel to the array face. If a phase shifter is connected to each antenna element the incident energy can be coherently combined by applying suitable phases to the antenna elements. In active arrays, the spacing between the antenna elements will be determined by the scan coverage and grating lobe limitations. If the spacing between the antenna elements(dx~ $\lambda_0/2$, λ_0=free space wavelength[4]) is constant then the difference in phase shift between adjacent elements is constant. The incremental amount of phase shift, P_x between elements to receive the energy coherently from θ_0 is given by the equation [4].

$$progressive\ phase\ shift, P_x = 2\pi\left(\frac{dx}{\lambda}\right)\sin(\theta_0)$$

where, dx is the inter element spacing. The progressive phase shift depends on the frequency, spacing between elements and the incident angle of the wave with respect to array face. The phase shifters will have different phases depends on the frequency for each beam position. The phase shifters must be reset each time the frequency of operation is changed. The digital phase shifter values for an M-bit phase shifter can be given as $2\pi/2^M$, $2\pi/2^{M-1}$, … ,π. The maximum amount of phase shift within a T/R Module is 360 deg. limited by the sinusoid function.

In a phased array if all the elements are excited with the same amplitude the resultant radiation pattern will have a peak sidelobe level of ~ -13dB with respect to the main beam. The digital attenuators are used for tapering the amplitude of array elements in order to get low sidelobe levels. In case of digital attenuators used in T/R modules the performance of the individual bit is determined by the maturity of the device technology, and the realizable limit on the required resistance values and the resistors' parasitics[1]. The design is usually a compromise between the insertion loss at zero state and the maximum attenuation value which can be achieved over the frequency bandwidth. Generally the highest attenuation bit is limited to 16dB and the lowest bit is 1dB incase of 5 bit attenuator and 0.5dB in case of a 6 bit attenuator. The maximum attenuation which can be provided by an attenuator is -31.5dB.

In order to maintain good performance the attenuator should maintain a constant phase over the attenuation states(2^n, where n is number of attenuator bits) and the phase shifter should maintain a constant attenuation over the entire phase states(2^n, n is the number of phase shifter bits) over the frequency bandwidth of operation. Practically there will be some error in the attenuation and phase values which can be set by the phase shifter and attenuator. These errors have to be corrected in active arrays by suitable methods in order to obtain optimum array performance. There employs a digital control circuitry to activate/deactivate the phase shifter and attenuator bits depends on the sidelobe level and scan requirements.

Features of the Realized T/R Module: The T/R Module(TRM) has been housed in its own package in order to minimize coupling effects between adjacent TRM paths when used in active phased arrays. The TRM consists of MMIC based Transmit//Receive chains with a core-chip consists of phase shifter, and attenuator placed in the common leg of the T/R Module. The Architecture of the TRM has been selected to fit within a size of 100mm x 14mm x 4.5mm with

a weight of 20gm. The TRMC is able to transmit/receive serial data with speed around 20Mbps in full duplex mode. Fo

r ensuring good signal integrity, the TRMC has LVDS lines for sending and receiving data and command respectively. The TRMC monitor the temperature of power amplifier in the RF chain continuously and send the values serially to the other controller up the hierarchy on a query basis. The TRM digital controller has to switch the attenuation and phase values for both transmit and receive modes, meeting the required timing specifications.

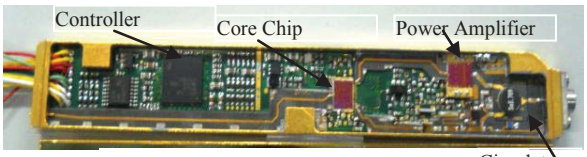

Fig.4 TRM : EXPLODED VIEW

Fig.5. TRM WITH TOP COVER

Results and Conclusion: The realised T/R Module has been tested for its phase and attenuation behaviours over the phase shifter and attenuator states. Fig. 6 shows the measured and optimised phase errors for each of the phase shifter states. Fig. 6 shows the measured and optimised attenuation errors for each of the attenuator states. The corrections have been performed by suitable algorithms and the results shows an rms phase error of ~1.8° and an rms attenuation error of 0.28dB which are very promising values to be used with active phased arrays to achieve very good antenna array performance.

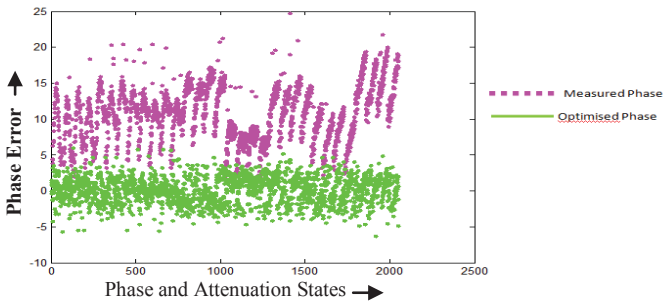

Fig.6 Measured and optimised Phase errors

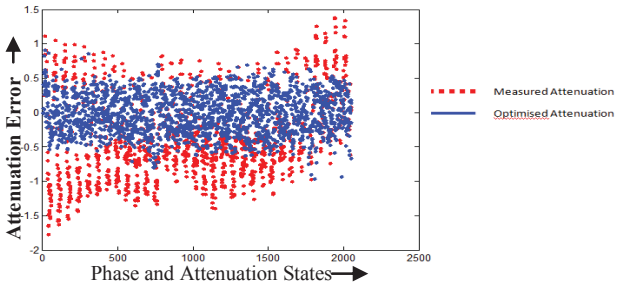

Fig.7 Measured and Optimised Attenuation errors

Acknowledgment: The authors are thankful towards the Director, LRDE for his kind permission to publish this paper.

References

[1]. Fourikis (Nicholas), Phased Array-Based Systems And Applicatons. John Wiley & Sons Inc;
[2]. Eli Brookner, "Phased arrays for the new millennium", Proc.of the IEEE 2000, pp.3-13.
[3]. Bruce A.Kopp, George Jerinic, "Transmit/Receive Modules", IEEE Transactions on Microwave Theory and Techniques, vol.50, No.3, March 2002.
[4]. Robert J.Mailloux, " Phased Array Antenna Handbook", Artech House, pp 15-20.

8-Way Unequal Amplitude Equal Phase Power divider Design Using Arbitrary Impedance for 430MHz Tropospheric Wind Profiling Radar

Venkata Kishore.K[(1)],Galaba Sai Rajesh [(1)], Vijay Kumar[(2)], P.Srinivasulu[(3)]
1. SENSE Department, VIT University,Vellore, Tamilnadu, INDIA-632014.
2. SENSE Department, VIT University,Vellore,Tamilnadu,INDIA-632014
3. RADG, NARL, Department of space, Government of India,
Gadanki, Chittoor District, AP, INDIA, Pincode-517112
1.Email:kothapudi@gmail.com

Abstract: *In this paper, an 8-port unequal amplitude equal phase power divider with arbitrary power divisions terminated by arbitrary impedance is considered and is useful for both component miniaturization and easy design facilities due to as many sets of design equations as possible. Arbitary design impedance technology in the UHF band is proposed. The Power divider with input transformer & arbitrary design impedance (A) is introduced to control high impedance values. Here the impedance of one of the transmission line selected is 15 ohm[a], which is best suited for the impedance limitation of 20Ω-80Ω with a large power dividing ratio in tropospheric wind profiling radar operating at 430MHz applications where the low side lobe levels are required. The simulated results are presented to verify our proposed design.*

Index Terms — Characteristic impedance, UHF, Arbitary impedance

1. Introduction

Wind profiling Radar system provides wind speed and direction values as a function of altitude. The primary role for wind profiler Radar is in weather observation and forecasting however, other applications have been identified, including severe wind condition warnings, flight planning, space shuttle support, and pollution studies. Wind profiler radars (WPR) play an important part in our understanding of the atmosphere. T-Radar operates at 430 MHz frequency band. The major subsystems of the Radar wind profiler are as follows, Antenna Subsystem (Phased array antenna), Feeder network, Transmit Receive (TR) modules, Radar Controller. Corporate-fed networks are used to provide power splits of , such as n = 2, 4, 6… and so on, and are commonly used in arrays. For an antenna array, this type of feed is more general and versatile because it provides the designer more control over the amplitude and phase of each element[1].

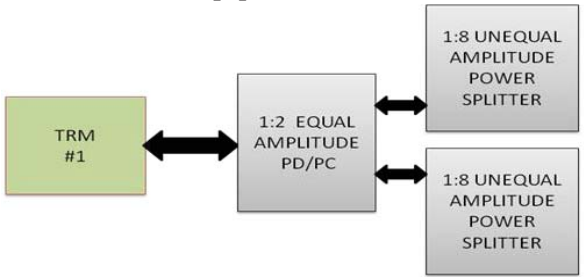

Figure 1 :Corporate binary feeder network

Unequal amplitude equal phase power dividers are very important components especially in a low side lobe antenna arrays. It is well known that one of the common ways to get a radiation plot with low side lobes using antenna array is feeding the elements of the array with unequal amplitudes equal phase signal and it decreases in other elements. Especially, in the case of high power dividing ratio, the line width of the high characteristic impedance branch implemented in Microstrip might be too narrow to be fabricated. To avoid such fabrication difficulties, some structures have been reported to realize high characteristic impedance line, such as arbitrary design impedance (a) with input transformer [5] [6]. The amplitude weights are designed for a side lobe level of -17dB down from the main beam by using antenna synthesis technique a so called taylors 1-parameter method.

Table 1: Power divisions for all 8-way power divider

Parameter	Ps-1	Ps-2	Ps-3	Ps-4	Ps-5	Ps-6	Ps-7
Ptotal	5.62012	3.65319	1.96696	0.73408	1.23285	1.68974	1.96345
P1	1.96693	1.68974	0.73408	0.30777	0.55318	0.79622	0.96345
P2	3.65319	1.96345	1.23285	0.42631	0.67967	0.89352	1
K	1.3628	1.077	1.2959	1.176	1.108	1.059	1.0187
Ksquare	1.8573	1.161	1.679	1.3851	1.228	1.1222	1.0379
K qube	2.531	1.2525	2.176	1.63	1.316	1.188	1.0574
K ^4	3.4492	1.348	2.8202	1.9126	1.5071	1.2577	1.0769

2. Design analysis

Design equation for an N-way power divider with arbitrary power split ratio is suggested. It consists of N transmission lines and N resistors and may be terminated in arbitrary impedances. Since a transmission line with too high characteristic impedance is difficult to realize in microstrip technology, an arbitrary design impedance A is introduce to control it. The A is arbitrary and positive value, and as many sets of design equations as possible may be produced depending design situation. Therefore, the design formulas containing A may be called “Arbitary design equations.

A. characteristic impedance design

The power and impedance relationship among each port will satisfy the following conditions. The design equations for arbitrary design impedance with input transformer The characteristic impedance and the isolation resistor can be derived in terms of z0 and k as following equations 1-3.

$$R_{TN} = \frac{P_{total}}{P_N}.A \qquad (1)$$

$$Z_N = \sqrt{R_a R_{TN} \frac{P_{total}}{P_N}} \qquad (2)$$

$$Z_{TN} = \sqrt{R_{TN} R_N} \qquad (3)$$

Where R_{TN} =isolation resistor, A =arbitary design impedance, P_{total} =total input power, P_N =power at port-N, Z_N =characteristic impedance of the main transmission line, R_a =input transformer, R_N =termination impedance 50Ω, Z_{TN} = characteristic impedance of the additional impedance transformer to match 50Ω termination.

B. Amplitude Weights, Lengths and Widths of Characteristic impedances and Substrate selection and specifications of feeder network

The calculated parameters i.e Power at different ports, impedances, microstrip transmission line lengths and widths of the corresponding characteristic impedances, feeder network using FR4 substrate and Specifications of feeder network (8-way unequal amplitude equal phase power divider) is shown in tables 2,3 ,4 & 5.

Table 2: Amplitude weights

Port No.	Amplitude weighting coefficients[power in watts]	Amplitude weighting coefficients[power in dbm]
1	0.30777	-5.1177
2	0.42631	-3.7021
3	0.55318	-2.5713
4	0.67967	-1.67701
5	0.79622	-0.9896
6	0.89352	-0.4889
7	0.96345	-0.1617
8	1	0

Table 3: Substrate information

Parameter	Symbol	Unit	Case-1
Frequency		GHz	0.43
Substrate			FR-4
Relativepermittivity	εr		4.4
Loss tangent	tanδ		0.02
Substrate height	H	mm	1.6
Line impedance	Z0	Ω	50
Wavelength	λ	m	0.6976
Width	W	mm	3.06
Electrical length		degrees	90^0

Table 4: Specifications

Parameter	Specifications
Frequency	430MHz
Type of network	Corporate binary fed network
Feeder network component	Unequal amplitude equal phase power splitter using arbitrary design impedance and input transformer
No. of inputs	1
No. of outputs	8
Illumination taper	Taylors1-parameter method
Inter-element spacing	0.71λ
Bandwidth	> 40MHz
Coupling	-12.6,-11.2,-10.06,-9.17, -8.48,-7.98,-7.65,7.49dB
Insertion loss	less than 0.5dB
Isolation	greater than 20dB
Phase variation	up to 6 degrees
VSWR	1.5(max)
Impedance	50Ω

Table 5: Impedances, lengths and widths

Parameter	Impedance (Ω)	Length(mm)	Width(mm)	Radius
Unequal amplitude equal phase Power splitter-1 a=15Ω,Rn=50Ω				
Ra	35.35	93.4	5.223	-
Z1	55.33	96.23	2.572	31.1
Z2	29.79	92.41	6.633	29.89
ZT1’	46.29	95.06	3.47	-
ZT2’	33.96	93.16	5.531	-
Unequal amplitude equal phase Power splitter-2				
Ra	35.35	93.4	5.223	-
Z1	51.88	95.8	2.876	30.97
Z2	30.98	92.61	6.312	29.95
ZT1’	44.82	94.86	3.656	-
ZT2’	34.59	93.27	5.388	-
Unequal amplitude equal phase Power splitter-3				
Ra	35.35	93.4	5.223	-
Z1	41.86	94.43	4.06	30.53
Z2	36.03	93.51	5.08	30.24
ZT1’	40.26	94.19	4.314	-
ZT2’	37.35	93.73	4.82	-
Unequal amplitude equal phase Power splitter-4				
Ra	35.35	93.4	5.223	-
Z1	46.18	95.05	3.486	30.73
Z2	33.34	93.06	5.676	30.09
ZT1	42.29	94.49	4	-
ZT2	35.93	93.5	5.102	-
Unequal amplitude equal phase Power splitter-5				
Ra	35.35	93.4	5.223	-
Z1	43.15	94.62	3.88	30.59
Z2	35.12	93.36	5.272	30.19
ZT1	40.88	94.28	4.21	-
ZT2	36.88	93.65	4.913	-
Unequal amplitude equal phase Power splitter-6				
Ra	35.35	93.4	5.223	-
Z1	41.09	94.31	4.18	30.49
Z2	36.62	93.61	4.963	30.27
ZT1	39.89	94.13	4.374	-
ZT2	37.66	93.78	4.76	-
Unequal amplitude equal phase Power splitter-7				
Ra	35.35	93.4	5.223	-
Z1	39.46	94.06	4.44	30.41
Z2	38.02	93.84	4.698	30.34
ZT1	39.09	94.01	4.509	-
ZT2	38.37	93.89	4.635	-

3. Results and discussions

The unequal power divider for 8-way layout design in IE3D electromagnetic simulation software is done with the help of calculated parameters in table-5.

Case-1:- Design of 1:8 unequal amplitude equal phase Power divider

Figure 2(a)(b)&(c) shows the layout and computed S-parameters for the 8-way unequal amplitude equal phase power divider has a transmission lines with proper lengths and widths with 50 Ω terminations designed at the operating frequency of 430MHz.

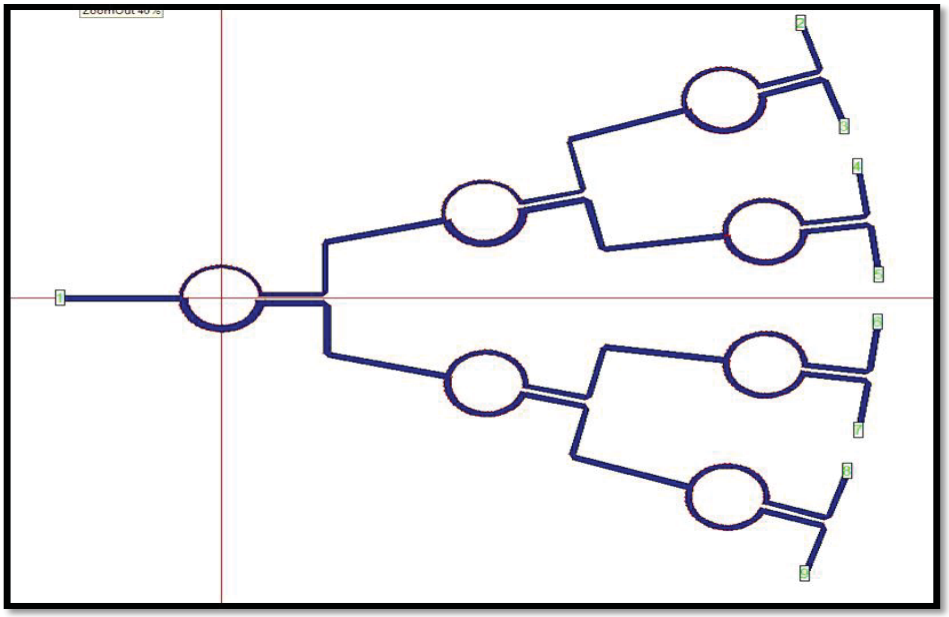

Figure 2(a):1:8 unequal amplitude power divider layout design in IE3D

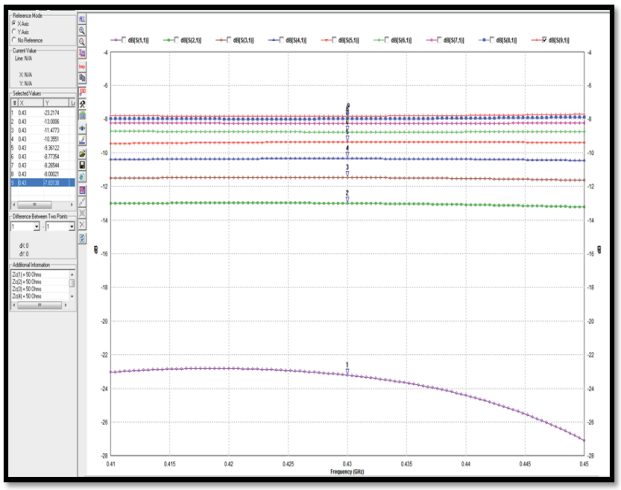

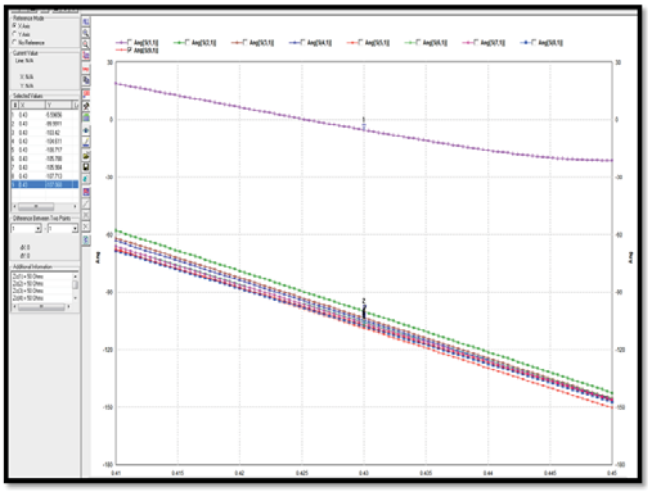

Figure 2(b):Return loss and power divisions for 1:8 unequal amplitude power divider
Figure 2(c): phase angle for 1:8 unequal amplitude power divider

Case-2:- Results Analysis

Table 6: Comparision of ideal and simulated results

S.no	Coupling ideal in dB	Coupling simulated in dB	Insertion loss in dB	Phase angle in degrees
1	-12.614	-13.006	-0.4	99.9
2	-11.20	-11.4773	-0.2	103.4
3	-10.06	-10.3551	-0.3	104.6
4	-9.174	-9.36122	-0.2	108.7
5	-8.487	-8.77351	-0.25	105.7
6	-7.986	-8.26544	-0.3	105.9
7	-7.659	-8.00021	-0.35	102.7
8	-7.497	-7.8338	-0.3	102.6

Therefore, judging from the preceding results, there is a good agreement between our design goal and the actual performance of the unequal amplitude equal phase power divider.

CONCLUSION

The Power coupling, Return loss, phase angle and impedances are showing the applicability of the 8-way unequal amplitude equal phase power divider in the desired field and expected to have high performance. The results giving the motivation towards new designs like 1:16 and 1:32 port unequal amplitude power dividers as a feeder network in the linear and planar arrays by using appropriate amplitude weights based on side lobe reduction and beam width control. The proposed structure is easy to design and therefore very attractive for high power dividing ratio applications and essential component of a feeder network and Beam forming network.

ACKNOWLEDGEMENT

Authors would like to express their gratitude to Dr. P. Srinivasulu, Scientist/Engineer-SG, Head RADG, NARL, Tirupathi for giving constant guidance and support. The authors would like to thanks the reviewers of this manuscript for their helpful comments.

REFERENCES

[1] Venkata Kishore.K, Nalini.K, P.Srinivasulu, "Design and simulation of Microstrip Unequal amplitude quadrature hybrid coupler as a feeder network component for 430MHz Tropospheric wind profiling Radar."Accepted for publication in International Journal of Advanced Scientific Research and Technology, Issue (2), Volume2 (April2012), 251-264.
[2] E. J. Wilkinson, "An N-way hybrid power divider," *IEEE Trans. Microw. Theory Tech.*, vol. MTT-8, no. 1, pp. 116–118, Jan. 1960.
[3] J.-S. Lim, S.-W. Lee, C.-S. Kim, J.-S. Park, D. Ahn, and S. Nam, "A 4:1 unequal Wilkinson power divider," *IEEE Microw. Wireless Compon. Lett.*, vol. 11, no. 3, pp. 124–126, Mar. 2001.
[4] J.-X. Chen and Q. Xue, "Novel 5:1 unequal Wilkinson power divider using offset double-side parallel-strip lines," *IEEE Microw. Wireless Compon. Lett.*, vol. 17, no. 3, pp. 175–177, Mar. 2007.
[5] D. M. Pozar*, Microwave Engineering*, 2 ed. New York:Wiley, 1998.
[6] Hee-Ran Ahn, and Ingo Wolff. "General Design Equations of Three-Port Unequal Power-Dividers Terminated by Arbitrary Impedances."Dept. of Elec. Engineering Gerhard-Mercator-University Duisburg Germany.
[7] Hee-Ran Ahn, kwyro Lee and Noh-Hoon Myung "General Design Equations of N-Way Arbitrary Power Dividers" Dept. of Electrical Engineering, KAIST, Korea.

DECEMBER 17, WENESDAY
04.15PM TO 05.30PM
RESEARCH SESSION 6
COMPUTER AIDED DESIGN AND COMMUNICATIONS
G S SANYAL- HALL

Chair:Prof. Rabindra K. Mishra, Berhampur University.

No	Papers	Page
6.1	**Proof of Concept Implementation of a Polyphase Channelizer with USRP** P. Murali Krishna, T. P. Sameer Babu Naval Physical and Oceanographic Laboratory, Cochin - 682021, India. *Email: mk.npol@gmail.com, sameerbabu@gmail.com*	157
6.2	**Underwater Acoustic OFDM: Synchronization under High Doppler** Sameer Babu T.P.[1], Murali Krishna P.[1], and R. David Koilpillai [2] [1]Naval Physical and Oceanographic Laboratory, Defense Research and Development Organization, Cochin, 682 021, India. *Email: sameerbabu@gmail.com, mk.npol@gmail.com* [2] Dept. of Electrical Engg. Indian Institute of Technology Madras, Chennai, 600 036, India. *Email: koilpillai@iitm.ac.in*	161
6.3	**Equivalence of Digital Travelling Wave (DTW) and FDTD** Rabindra K. Mishra. Electronic Science Department, Berhampur University, India. *E-mail: r.k.mishra@ieee.org*	165
6.4	**Application of Levin's t-Transform in Image Series Analysis of Rectangular Waveguide Slot** S.S.Kakatkar and K.P.Ray SAMEER, IIT Campus, Powai, Mumbai- 76, *Email: sskakat@rediffmail.com*	169
6.5	**FLANN-SM based CAD model for Deformed –Ω atom synthesis** Sambhudutta Nanda[1], P.K. Sahu[2], R.K. Mishra[3] [1,2]Dept of Electrical Engineering, NIT Rourkela, *E-mail: 514EE1012@nitrkl.ac.in, pksahu@nitrkl.ac.in* [3]Dept of Electronic science, Berhampur University, *E-mail: r.k.mishra.ieee@gmail.com*	173
6.6	**Demonstration of A Wireless Communication System Using SDR Platform** Ansha K K[1], Mary Rani Abraham[2], and Sameer Babu T P [2] [1]School of Engineering, CUSAT, Cochin – 682022. *Email:anshakk91@gmail.com.* [2] Naval Physical & Oceanographic Laboratory, Kochi. 6982021, *Email:sameerbabu@gmail.com*	177

Proof of Concept Implementation of a Polyphase Channelizer with USRP

P. Murali Krishna, T. P. Sameer Babu
Naval Physical and Oceanographic Laboratory, Cochin - 682021, India
Email: mk.npol@gmail.com, sameerbabu@gmail.com

Abstract: *A proof of concept implementation of a polyphase channelizer is discussed in this paper. Polyphase channelizers are a computationally efficient receiver structure in case where the channelization is uniform. The algorithm effectively combines a polyphase decimator and a FFT to effectively realize multi channel receivers. We have implemented a four channel channelizer for commercial FM reception to demonstrate the application of the same.*

Introduction: This paper describes a proof of concept implementation of a four channel commercial FM channelizer. The authors aim to convey the message that with improvements in reusable hardware and processing power available, it is possible to implement highly complex signal processing algorithms and evaluate them in the real world. Such a possibility was not imaginable even a decade earlier and it throws up opportunities to test proposed techniques at a very minimum hardware cost. The popular USRP platform is used to demonstrate the design in real time with the FM demodulation done in an Intel i3 based laptop. The paper is organized as follows: We introduce the problem of multi channel reception which the paper addresses and the requirement need for an efficient method. The channelizer algorithm is described briefly and DSP techniques used to implement the same are listed. The details of the design and implementation of the proposed channelizer is provided and the implementation results are illustrated. We conclude the paper by citing the relevant literature in the subject.

Need for Channelization Algorithm: The architecture of a typical receiver front end is depicted in Fig 1. The RF signal is band pass filtered, amplified and then down converted to base band where it is digitized and further demodulated using DSP techniques [1]. In order to receive and process multiple channels simultaneously, the signal flow illustrated in Fig 1 is normally repeated with different local oscillator parameters corresponding to the channels of interest.

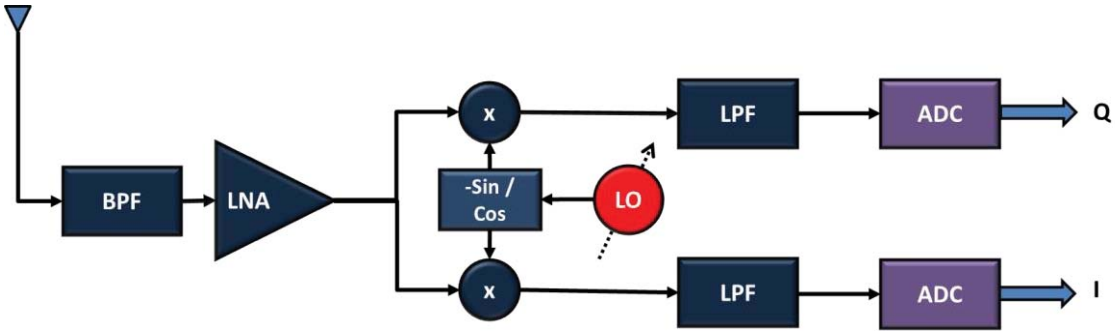

Figure 1: Front End Architecture of a Typical Single Channel Receiver

The multiple channel receiver using separate modules is not a good engineering solution if the channel parameters like inter channel spacing and data bandwidth are constant and pre

defined as in an FDM system. An elegant implementation for the multichannel receiver is possible by using the channelization algorithm [2].

Channelizer Algorithm Development: Consider the case a FDM transmission system where the channels to be received are distributed evenly as given Fig 2. The frequency axis is normalized with respect to half the sampling rate and only the positive side of the spectrum is illustrated.

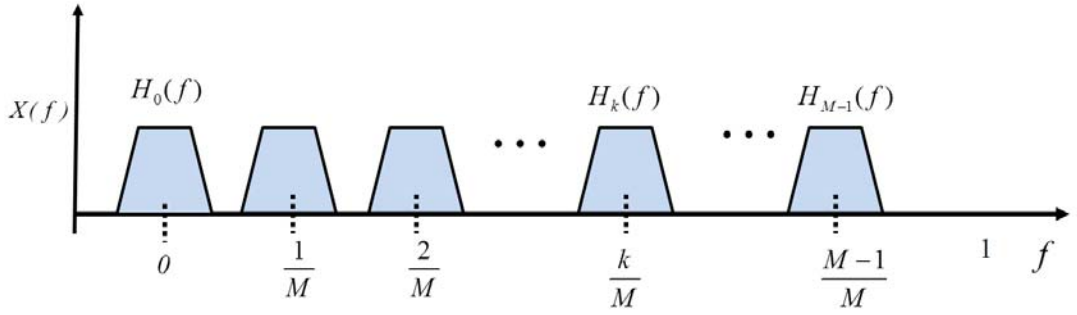

Figure 2: Channel Distribution in a Broadcast System

It is evident from Fig 2 that a suitably modulated / frequency shifted prototype filter *H(f)* can be used to demodulate the different channels. The relation that needs to be satisfied for the k^{th} channel response $H_k(f)$, is

$$H_k(f) = H\left(f - k\tfrac{1}{M}\right) \quad k = 0,...,M-1 \tag{1}$$

The frequency response of the shifted prototype filter can be expressed to be

$$H_k(f) = \sum_{n=-\infty}^{+\infty} h[n]\, e^{-j2\pi\left(f-\frac{k}{M}\right)n} \tag{2}$$

where *h[n]* is the impulse response of the prototype filter. Since time reversal of the impulse response *h[-n]* does not vary the magnitude response, using the DFT notation, it is possible to rewrite (2) using the time flipped impulse response *h[-n]* in the following form

$$H_k^*(z) = H\left(e^{j2\pi\frac{k}{M}}z^{-1}\right) = H\left(e^{-j2\pi\frac{k}{M}}z\right), \quad k = 0,...,M-1 \tag{3}$$

Each filter is now a band shifted version of the prototype response centered at the location of the carrier frequencies of interest. The expression in (3) can be decomposed based on the M – fold polyphase decomposition of the modulated / frequency shifted impulse response sequence [3]. The analysis will become simpler if the choice of *M* in the polyphase decomposition coincides with the number of channels under consideration. In our analysis we consider them equal and correspondingly obtain the decomposition given in (4)

$$H_k^*(z) = H\left(e^{j2\pi\frac{k}{M}}z^{-1}\right) = \sum_{\ell=0}^{M-1} e^{-j2\pi\frac{k}{M}\ell} z^{\ell} E_{\ell}\left(z^{-M}\right) \tag{4}$$

where $E_l(z^{-M})$ are the polyphase components. The z^l term in (4) introduces a non-causality which can be modified by introducing a delay term in the beginning thus giving the final polyphase decomposed form [3]

$$z^{-M} H_k^*(z) = \sum_{\ell=0}^{M-1} e^{-j2\pi\frac{k}{M}\ell} z^{-(M-\ell)} E_{\ell}\left(z^{-M}\right) \tag{5}$$

The expression in (5) can be thought of a linear combination operation of the outputs from a set of sub band filters. The linear combination operation is done by the DFT matrix. The interesting fact to note is that the channel specific operation is done by the DFT matrix which can be separated from the polyphase filtering stage. An implementation structure arising from (5) will be as depicted in Fig 3. The input x[n] is having a spectral distribution as given in Fig

2 and each of the DFT bin outputs will correspond to one of the channels shifted to the base band.

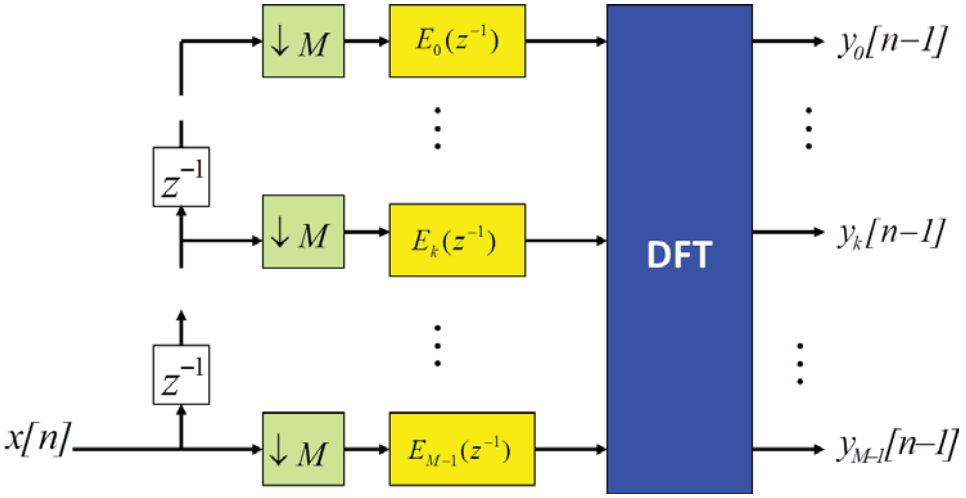

Figure 3: Polyphase Channelizer Structure

DSP Techniques Present in Channelizer: The DSP techniques used to achieve this feat are (i) the original spectrum is down sampled by *M* which creates all the channels to alias to the base band, (ii) the individual polyphase arms introduce a proportional phase shift to the aliased channel spectra, (iii) using appropriate phase shifters (complex multipliers), the outputs of the polyphase arms can be linearly combined to separate the individual channels in a manner similar to that of solving a set of consistent linear equations [4]. Mathematically the entire set of operations can be compactly expressed using the *Z* domain relationship in (6)

$$\begin{bmatrix} Y_0(z) \\ \vdots \\ Y_{M-1}(z) \end{bmatrix} = \begin{bmatrix} \ddots & & \\ & e^{-j\frac{2\pi}{M}kl} & \\ & & \ddots \end{bmatrix} \begin{bmatrix} z^{-0}\ H_0^*(z^M) \\ \vdots \\ z^{-(M-1)}\ H_{M-1}^*(z^M) \end{bmatrix} X(z) \qquad (6)$$

Proof of Concept Experiment: To validate the theory, we implemented a 4 channel channelizer operating in the commercial FM band. The popular USRP SDR platform was used to implement the front end hardware [5]. In the vicinity of Cochin, there are three FM channels at 91.9MHz, 93.5MHz and 94.3MHz. Using one USRP module, a FM transmission was done at 92.7MHz so as to have 4 channels available with a channel spacing of 800 kHz.

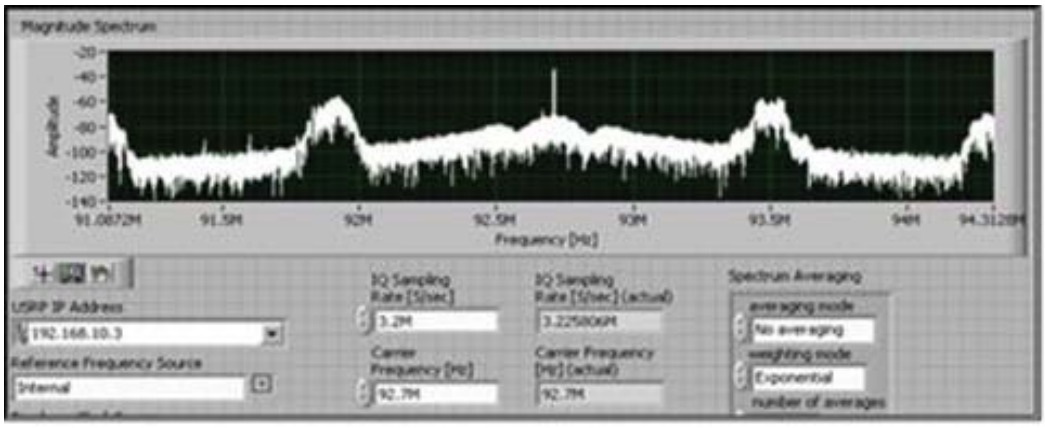

Figure 4: Combined Channel Spectrum at Channelizer Input

Fig 4 illustrates the spectrum at the input to the channelizer. The front end sampling rate was fixed at 3.2 MHz and the base band data obtained was decimated using a polyphase down sampling structure by a factor of 4. A prototype digital filter of order 128 was designed using the Parks McClellan method [3] which resulted in each polyphase component having a length of 32 samples. The entire channelization code was implemented in LabView running in a Intel second generation i3 processor based laptop.

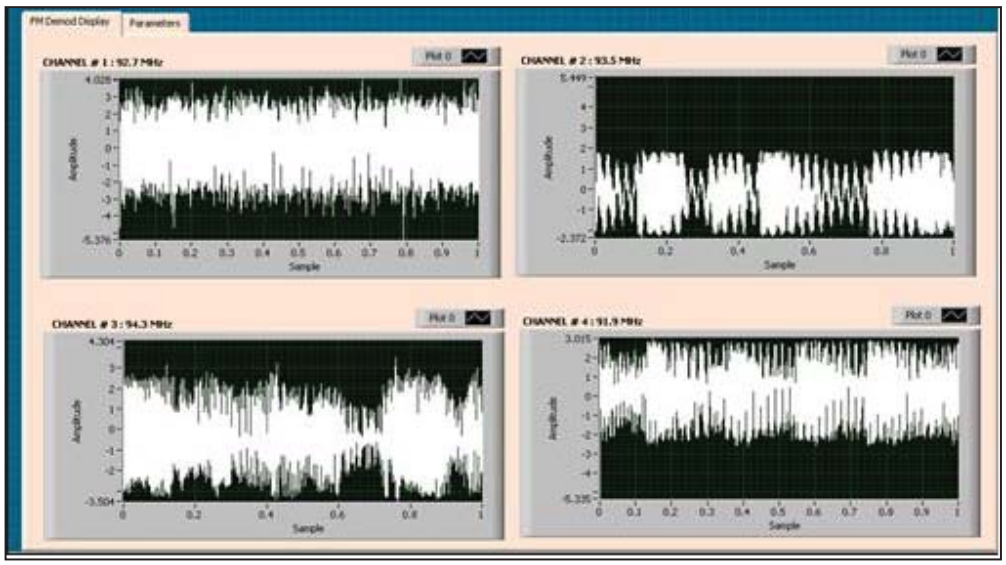

Figure 5: Demodulated FM Signal at Channelizer Output

The base band converted channels were FM demodulated in real time and were down sampled to 44.1 kHz sampling rate. These were played back through the speaker in the laptop. Fig 5 illustrates the demodulated FM signals. All the demodulated outputs exhibited very good fidelity when played back. It was also possible to store the demodulated outputs as four separate .WAV files in real time.

Conclusion: In this paper, we have described the implementation of a proof of concept demonstration of a channelizer using popular USRP hardware modules. To provide completeness, we have included a brief of the underlying theory. An overview of the design with key parameters used for the implementation has also been provided. This paper illustrates that it is possible to implement seemingly very complex signal processing techniques in real time using standard computing units. The applications that are possible with such techniques are only limited by the imagination. We refer to the MATLAB code given in [4] for visualizing the operation of the channelizer to interested readers.

Reference:

[1] M. Henker T. Hentschel and G. Fettweis, “The digital front-end of software radio terminals”, Proc. of IEEE Personal Communications, Vol. 6, No. 4, pp 612, 1999
[2] T. Hentschel, “Channelization for software defined base stations”, Annales des Telecommunication, Vol 57, No. 5-6, pp 386-420, 2002
[3] Norbert Fliege, “Multirate Digital Signal Processing : Multirate Systems, Filter Banks and Wavelets.”, John Wiley, New York, 1994
[4] F. J. Harris, C. Dick and M. Rice, “Digital Receivers and Transmitters using Polyphase Filter Banks for Wireless Communications”, IEEE Transactions on Microwave Theory and Techniques, Vol. 51, No. 4, pp 1395–1412, 2003.
[5] Ettus Research. http://www.ettus.com.

Underwater Acoustic OFDM: Synchronization under High Doppler

Sameer Babu T.P [(1)], Murali Krishna.P [(1)], and R.David Koilpillai [(2)]
(1) Naval Physical and Oceanographic Laboratory, Defense Research and Development Organization, Cochin, 682 021, India
Email: sameerbabu@gmail.com, mk.npol@gmail.com
(2) Dept. of Electrical Engg.
Indian Institute of Technology Madras
Chennai, 600 036, India
Email: koilpillai@iitm.ac.in

Abstract: *The problem of Doppler compensation for multicarrier acoustic communications is investigated in this paper. The underwater acoustic channel poses problems due to the constraints of the medium and related propagation laws. The solutions to the same are hence unique in both theoretical aspects and practical implementation. We are comparing the performance of pulse compression waveforms which are used to compensate the Doppler Effect. The choice of the waveform is decided by the robustness in the estimation of the Doppler scaling parameter.*

Introduction: In recent years, OFDM systems have become a popular choice in underwater acoustic communication. The OFDM signal is broadband in nature. The impact of Doppler in broadband waveforms is compression/dilation in time domain or non-uniform Doppler shift in the frequency domain. The method of Doppler compensation for OFDM adopted in underwater acoustics is to re-sample the Doppler distorted waveform [1], [2]. The key step in this technique involves the estimation of the Doppler time scale parameter. In this paper, we compare the performance of the Doppler scaling parameter estimation using different pulse compression waveforms. In particular, we are comparing the traditionally used LFM waveform with the HFM waveform.

Packet length based Doppler time scale estimation: Let $s(t)$ and $r(t)$ denote the transmitted and received signals respectively and let T_s be the sampling interval at transmitter and receiver. The attenuation and propagation delay can be safely ignored without loss of generality for the analysis. It is possible to express the relation between $s(t)$ and $r(t)$ in the presence of Doppler as

$$r(nT_s) = s\left((1+a)nT_s\right) \tag{1}$$

with the time scale parameter a= v/c where 'v' is the relative velocity between the platforms and 'c' is the velocity of acoustic propagation. If the relative Doppler time scale is known, the Doppler Effect can be negated by inverse time scaling the received signal. In a multi rate parlance this is equivalent to re-sampling the received signal by the factor (1+a) given as

$$s\left(nT_s\right) = r\left(\left(\frac{n}{1+a}\right)T_s\right) \tag{2}$$

To facilitate the estimation process, the packet structure is modified by amending a preamble and post-amble waveforms [1], [2]. The assumptions involved in this method are 1) all multi

paths have the same Doppler rate and 2) the path gain and Doppler rate are constant over the packet duration. The waveform should have very low delay tolerance since the estimation method essentially measures scaling in time delay of the received packet. The waveform should have high Doppler tolerance since the matched filter designed for the transmitted waveform must be able to effectively detect the Doppler scaled version of the same to identify the time index accurately. The Linear Frequency Modulated (LFM) signal is proposed as a candidate for the pre-amble and post-amble waveform. When there is a large relative velocity, the pulse compression performance of a linear frequency modulation suffers from significant degradation due to the mismatch between the received signal and the matched filter used.

Performance Comparison of LFM and HFM in Presence of Uniform Doppler: The transmitted LFM waveforms in the pass band can be expressed as

$$s(t) = A(t)\cos\left[2\pi\left(f_0 t + \frac{1}{2}kt^2\right)\right] \tag{3}$$

where $A(t)$ is the envelope function, f_0 is the starting carrier frequency, and k is the frequency sweep rate. The instantaneous frequency is the derivative of the phase term inside the cosine function,

$$f_s(t) = f_0 + kt \tag{4}$$

The hyperbolic frequency modulated waveform can be written as

$$s(t) = A(t)\cos\left[\frac{2\pi}{k}\log(1 + kf_0 t)\right] \tag{5}$$

where k is a constant factor and f_0 is the starting carrier frequency. The instantaneous frequency for HFM is given by the expression

$$f_s(t) = \frac{1}{1/f_0 + kt} \tag{6}$$

The received LFM waveform in the presence of Doppler time scaling can be written as

$$r(t) = A((1+a)t)\cos\left[2\pi\left(f_0(1+a)t + \frac{1}{2}k(1+a)^2t^2\right)\right] \tag{7}$$

The instantaneous frequency of the received signal $f_r(t)$ for LFM is obtained as earlier and is given by the expression

$$f_r(t) = f_0(1+a) + kt(1+a)^2 \tag{8}$$

For a Doppler-invariant waveform, the following condition should be satisfied:

$$f_s(t) = f_r(t - t_0) \tag{9}$$

where t_0 is a constant time shift independent of t [3]. Substituting (4) and (8) into (9), we can solve for t_0 to obtain the relation

$$t_0 = \frac{a\,f_0 + ((1+a)^2 - 1)k\,t}{k(1+a)^2} \tag{10}$$

which is a function of t and therefore, (9) is not satisfied. For LFM the Doppler time scaling results in shifting the starting frequency as well as the rate of frequency modulation. The

Doppler scaled received signal $r(t)$ is not matched to $s(t)$ and will lead to loss of pulse compression at matched filter output. For HFM, the received signal in the presence of Doppler time scaling can be expressed as

$$r(t) = A((1+a)t)\cos\left[\frac{2\pi}{k}\log(1+kf_0(1+a)t)\right] \tag{11}$$

The instantaneous frequency of the received HFM signal with Doppler time scaling is obtained in a similar manner as

$$f_r(t) = \frac{1}{(1/f_0(1+a)) + k(t)} \tag{12}$$

Again, substituting (6) and (12) into (9), we obtain

$$t_0 = -\frac{a}{k\, f_0(1+a)} \tag{13}$$

In the case of HFM, t_0 is a constant and independent of t if we are assuming that the relative velocity between the transmitter and the receiver remains the same. Fig. 1 compares the LFM and HFM matched filter response to different relative velocities. An LFM/HFM signal having a time bandwidth product of 750 is used for the simulations.

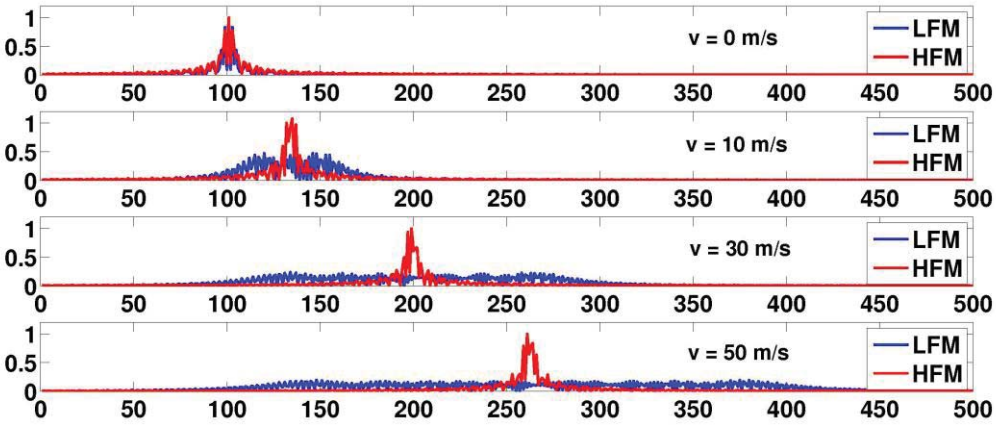

Fig. 1 Compressed pulse for the LFM and HFM with different relative velocities

Comparison of Scaling Factor Estimation Performance: The performance comparison of LFM and HFM waveforms for the estimation of Doppler scale factor is shown in Fig. 2. It is clear that when the relative Doppler is greater than 10m/s, the HFM waveform clearly out performs LFM waveform in the estimation of the Doppler scaling factor. Within this range of relative Doppler, both LFM and HFM waveforms have identical performance.

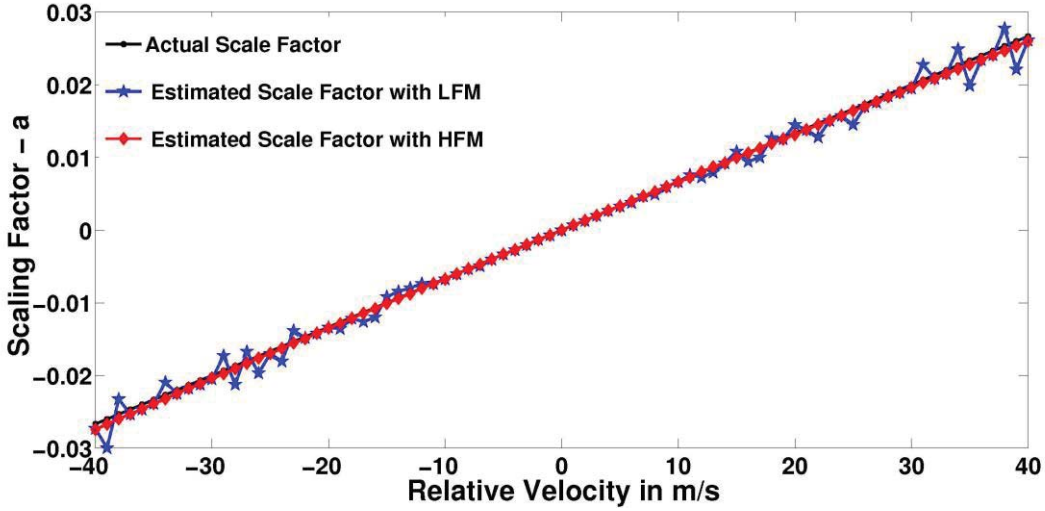

Fig. 2. Comparison of LFM and HFM in the estimation of scaling factor

Conclusion: In this paper, we have compared the performance of LFM and HFM waveforms in the estimation of Doppler time scaling parameter. It is seen that the Doppler invariant nature of HFM results in improved estimation performance in the presence of high relative Doppler. This result will be of practical significance in the design of OFDM based acoustic modems for mobile platforms.

Acknowledgment: The authors would like to express their gratitude to Prof. Arogyaswami Paulraj who evinced keen interest and suggested crucial steps in the study.

Reference:

[1] B. Sharif and J. Neasham and O. R. Hinton and A. E. Adams,"A Computationally Efficient Doppler Compensation System for Underwater Acoustic Communications",IEEE Journal of Oceanic Engineering,vol. 25, no. 1, pp. 52–60, 2000

[2] Baosheng Li and Shengli Zhou and Milica Stojanovic and Lee Freitag and Peter Willett, "Multicarrier Communication Over Underwater AcousticChannels With Nonuniform Doppler Shifts", IEEE Journal of Oceanic Engineering, vol. 33, no. 2, 2008

[3] J. Yang and T. K. Sarkar, "Doppler-Invariant Property of Hyperbolic Frequency Modulated Waveforms", Microwave and Optical Technology Letters, vol. 48, no. 6, pp. 1174–1179, 2006

Equivalence of Digital Travelling Wave (DTW) and FDTD

Rabindra K. Mishra
Electronic Science Department, Berhampur University, India; r.k.mishra@ieee.org

Abstract: *After revisiting the 1-D Digital Travelling Wave concept for a lossless transmission line, it is shown analytically that this technique is equivalent to the FDTD technique formulated for the transmission line. A section of a transmission line terminated with different types of loads is then simulated with both these techniques & their results are compared to establish their equivalence.*

Introduction: The Digital Travelling Wave (DTW) concept, based on acoustic DSP models [1], is being developed as a possible new computational electromagnetic technique [2]. Though there are many similarities between the proposed method and the established acoustic models, it is impossible to directly implement the acoustic models as electromagnetic models. This work briefly explains the DTW technique and then analytically proves that this technique is equivalent to the FDTD method which is well established computational EM technique. Finally the Transmission Line (TL) model of a rectangular microstrip antenna is analyzed using FDTD for a terminated TL and the results are compared with those obtained from DTW method.

Digital Travelling Wave:

For a lossless, source-free, homogenous, unbounded transmission line the wave equation is given in the form $\psi_{tt} = c^2 \psi_{zz}$, where the variable ψ can represent either the voltage 'V' or the current 'I' on the line. The subscripts zz and tt respectively mean second partial derivatives in space and time and c is the speed of the EM wave on the TL. For numerical simulation the common method of discretizing this wave equation is the FDTD Technique. However, there is another method of discretizing this using the D'Alembert's travelling wave solution $\psi(t, z) = \psi^{+}(t - z/c) + \psi^{-}(t + z/c)$. Here, the supercripts + & '–' indicate the forward & backward travelling waves respectively. Since the travelling wave is discretized in this later method, we call it the Digital Travelling Wave (DTW) method. For discretization, we assume that the EM wave is band limited to half of sampling rate and sample by selecting T as time sample interval and Z as position interval between two consecutive time samples making $Z = Tc$. By applying sampling on a discrete time-space grid, in

which n & k represent respectively time & space, the discretized traveling wave is represented as

$$\psi(n, k) = \psi^{+}(n-k) + \psi^{-}(n+k) \quad (1)$$

Thus to compute the wave propagation, state variables in two delay lines should be updated by

$$\psi^{+}(n+1, k) = \psi^{+}(n, k-1) \text{ and } \psi^{-}(n+1, k) = \psi^{-}(n, k+1) \quad (2)$$

It means the samples are shifted to left and right respectively. Thus for the modeling a pair of delay lines can implement the shift.

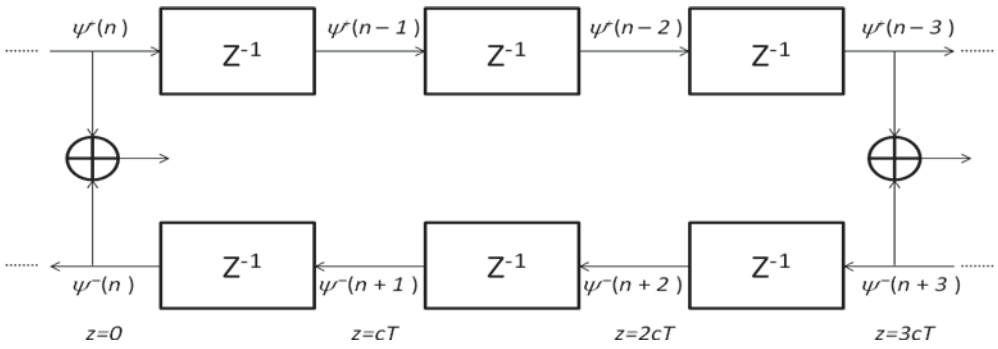

Figure 1: DWT simulation of the ideal, lossless Transmission Line with observation points at z = 0 and z = 3Z = 3cT . (z^{-1} represents unit-sample delay.)

FDTD Modeling:

Using a short-hand notation $\psi_{z,t}$ for $\psi(t, z)$, the central difference approximation for second-order partial derivatives are obtained as

$$\psi_{zz} = \frac{(\psi_{t,z+\Delta z} - 2\psi_{t,z} + \psi_{t,z-\Delta z})}{2\Delta z^2} \quad (3.a)$$

$$\psi_{tt} = \frac{(\psi_{t++\Delta t,z} - 2\psi_{t,z} + \psi_{t-\Delta t,z})}{2\Delta t^2} \quad (3.b)$$

Adopting index notation of $n = t/\Delta t$ and $k = z/\Delta z$ and choosing $\Delta t = \Delta z/c$, the wave equation in discretized form becomes

$$\psi_{n+1,k} = \psi_{n,k-1} + \psi_{n,k+1} - \psi_{n-1,k} \quad (4)$$

Proof of Equivalence:

Fixed linear combinations of past state are formed for computing the time updates, in both these schemes. To establish their equivalence, we need to define a one-to-one transformation showing that given any common initial state for both schemes, the next state can be computed in both the scheme.

From fig (1) it is obvious that the DTW scheme, given in eq. (1) preserves mapping. For the FDTD scheme, let us expand the RHS of eq. (4) using eq. (1) and verify that the LHS also satisfies the map, i.e. $\psi(n+1,k) = \psi^{+}(n+1-k) + \psi^{-}(k+n+1)$.

Proof:

$$\begin{aligned}\psi_{n+1,k} &= \psi_{n,k-1} + \psi_{n,k+1} - \psi_{n-1,k} \\ &= \psi^{+}(n-k+1) + \psi^{-}(n-1+k) \\ &\quad + \psi^{+}(n-1-k) + \psi^{-}(n+k+1) \\ &\quad - \psi^{+}(n-1-k) - \psi^{-}(n-1+k) \\ &= \psi^{+}(n-k+1) + \psi^{-}(k+n+1) \\ &= \psi^{+}[(n+1)-k] + \psi^{-}[(n+1)+k] \\ &= \psi(n+1,k) = \psi_{n+1,k}\end{aligned}$$

Application to Microstrip Antenna:

As a proof of the concept, we applied both these schemes to the transmission line model of a rectangular microstrip antenna to find the input impedance of the antenna and compare it with the results obtained from CST Microwave Studio. For modeling the antenna using DTW, three loss-less Transmission lines are considered. The 1st and 3rd lines are connected to the 2nd line at its two ends and are terminated in open circuit. The junctions of the 1st-2nd and 2nd-3rd lines are loaded with 'G', the slot admittance in Transmission Line Model for Microstrip Antenna [3]. The characteristic impedance of 1st & 3rd line was taken to be 'G' and their length was determined so that the susceptance is 'Y' at the junction.

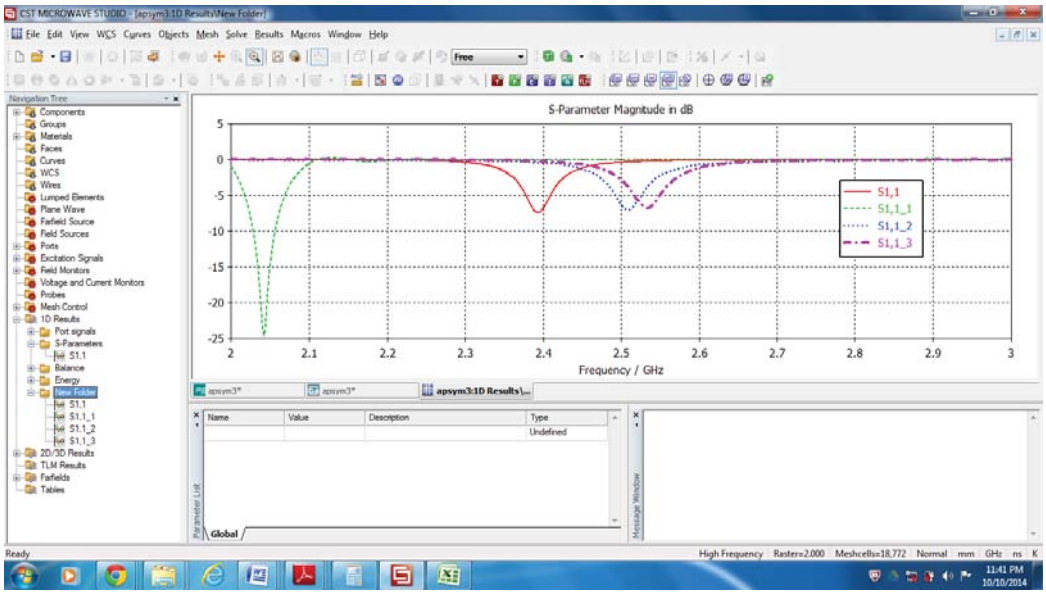

Figure 2: Comparison of S-Parameters (S11: CST, S11_1: Transmission Line Model, S11_2: FDTD and S11_3: DTW)

Results and Discussion:

Figure 2 compares the S_{11} parameter for Microstrip Antenna obtained from CST, FDTD Model, Transmission Line Model and the DTW model. For

the antenna resonating at 2.4 GHz simulated using a substrate of thickness 2mm, permittivity 2.8 @ 2.4 GHz, length 45.34 mm & width 37.56 mm, it is observed that the FDTD model follows the CST result very closely while the transmission line model shows a deviation of around 15% from the CST model. However, the DTW model shows a deviation of around 3%. Though is it primarily based on the normal transmission line model, to improve the accuracy, effects of 5 higher order modes TM_{10}, TM_{11}, TM_{12}, TM_{21} & TM_{22} were also included by modeling each as a transmission line, loading the dominant mode. Thus it is seen that by judicious modeling, the DTW model can be used for microstrip and other antennas.

.

Reference:

[1] J. O. Smith, "Efficient yet accurate models for strings and air columns using sparse lumping of distributed losses and dispersion", in Proceedings of the Colloquium on Physical Modeling, Grenoble, France, 1990, ACROE.

[2] R. K. Mishra, "Digital Travelling Wave: A Computational Electromagnetic Technique", Proceedings of AEMC 2009, Kolkata, 2009.

[3] C. A. Balanis, Antenna Theory: Analysis and Design, 3rd Edition, Wiley, 2005.

Application of Levin's t-Transform in Image Series Analysis of Rectangular Waveguide Slot

S.S.Kakatkar and K.P.Ray
SAMEER, IIT Campus, Powai, Mumbai- 76, Email: sskakat@rediffmail.com

Abstract: *A longitudinal slot in a waveguide has been analysed using image series representation along with the recently developed closed form point dipole and double dipole approximations. The image series convergence has been accelerated by applying Levin's t-transform for better accuracy. The results from this analysis agree well with those from other techniques as well as with measurements.*

Introduction: Waveguide fed slots have been used as radiating elements in antenna arrays for a long time. Recently, these slots have been analysed using the infinite set of images formed by the slot in waveguide walls [1]. Entire slot and its images are considered in this approach as opposed to the periodic Green's function where basically the images of point sources are considered for deriving the Green's function [2]. The internal admittance required for matching the tangential magnetic field is derived as the sum of self admittance of slot radiating in free space (for air filled waveguide) and the sum of mutual admittance of all the image slots.

This sum of mutual admittances is oscillatory in nature and requires the summation over a number of images for reasonable accuracy. Recently, techniques such as Shanks' transformation and Chebyshev-Toeplitz (CT) algorithm have been used to accelerate the convergence of this series [1]. In this paper, we have used Levin's t-transform [3] for series convergence and compared the results with other techniques such as modal analysis with waveguide Green's function and image series with other convergence accelerators. Levin's t-transform has the advantage that it may be applied iteratively without loss of accuracy or round-off errors as the successive higher order sums are calculated directly from the initial partial sums as opposed to Shanks' transformation or CT algorithm, where lower order intermediate sums are used for computing the higher order sums. Although the method is sufficiently general, the proposed technique is demonstrated by applying it to shunt slots in the broadwall of a waveguide.

Theory: The geometry of the problem is illustrated in Fig.1. The waveguide broad dimension is *a* and the narrow dimension is *b*. The wall thickness is denoted by *t* and the waveguide is assumed lossless. The slot as shown in Fig.1a and 1b is assumed to be parallel to the z- axis. The centre of slot, C is at $(x_0, 0, 0)$ i.e. the slot offset from the wall is x_0 and that from the centre is $x_c = a/2 - x_0$. The slot is of length *2l* and width *w*. The width *w* is assumed to be much less than its length i.e. narrow slot approximation is employed. As is usual in the method of moments (MoM) formulation of such problems [4], the problem is broken up into three regions viz. internal to the waveguide, external region and the cavity region formed by the finite waveguide thickness. The internal (external) slot electric field $E_{i(e)}$ is expanded in terms of *p* cosinusoidal basis functions or expansion modes with coefficients *e* and in the

Galerkin formulation, the magnetic fields are expanded using the same basis functions with coefficients *h* and the internal (external) aperture admittance is denoted by $Y^{i(e)}$.

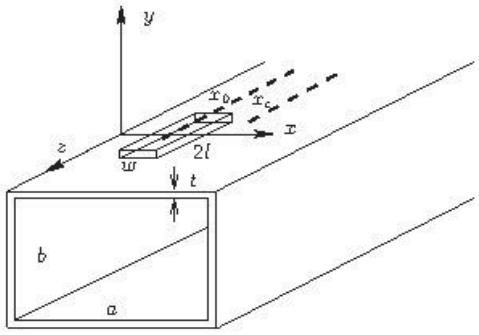

Figure 1a: Geometry of the problem

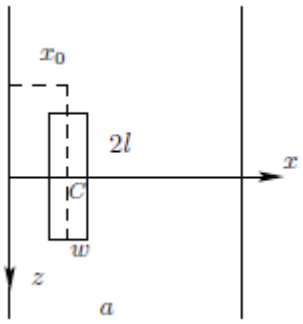

Figure 1b: Slot details

$$E_{i(e)} = \sum_{p=1}^{P} e_{i(e)p} \sin\left[\frac{p\pi}{2l}(l+z)\right]\hat{x} \qquad (1)$$

$$h_{i(e)} = Y_{ps}^{i(e)}\, e_{i(e)s}\; n\times\hat{x} \qquad (2)$$

The coefficients $e_{i(e)p}$ are found by enforcing the continuity of magnetic field along the centreline of internal and external slot surfaces through the wall thickness cavity region and solving the resulting coupled equations [1]. The slot admittance seen by the waveguide is then found from backscattering amplitude and the slot is said to be resonant when the slot presents a pure real admittance.

The external aperture admittance Y^{e}_{ps} in Eq.2 can be found using spectral domain analysis [4]. The internal admittance Y^{i}_{ps} is found using the waveguide Green's function. The internal admittance matrix elements involve an infinite double summation over all the waveguide modes and their computation is often tedious and time consuming. More than 2500 modes are needed for reasonable convergence. Expressions for Y^{i} can be found in [4].

As in [1], we compute the internal admittance by replacing the slot in waveguide with its infinite set of images in the waveguide walls as shown in Fig.2a. The images are numbered as *mn* where *m* is the column number and *n* is the row number. The reference slot is denoted by 00. The magnetic field at the reference slot is the sum of fields due to the slot electric field itself as well as all its images. The internal admittance is then computed as the sum of self admittance of the original slot at C and its mutual admittance with all its images.

$$Y_{ps}^{i} = \sum_{-\infty}^{\infty}\sum_{-\infty}^{\infty} y_{ps}^{mn} \qquad (3)$$

where y_{ps}^{mn} is the mutual admittance between the reference slot 00 and its image *mn* at C_{mn}. y_{ps}^{00} is the same as self-admittance for a slot radiating in homogeneous half-space i.e. same as Y^{e}_{ps} for empty waveguides. The geometry used for evaluating mutual admittance between two parallel slots (or slot and its mn^{th} image) is shown in Fig.2b. Mutual admittance due to image slots is evaluated using the recently derived simple and accurate closed form approximations for mutual coupling between slots with cosinusoidal aperture distribution viz. Point dipole and double dipole approximations [5] as these are shown to give more accurate

results than other closed form approximations. These approximations are discussed in detail in [5].

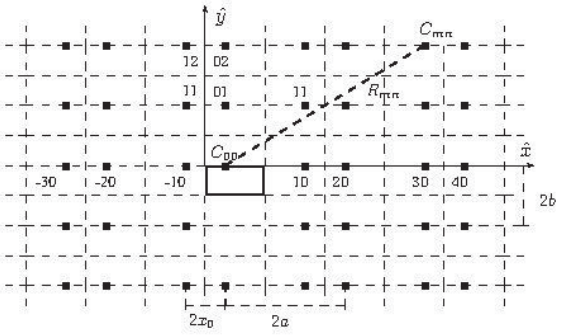

Figure 2a: Images of the slot

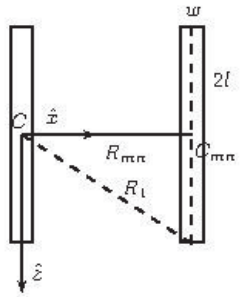

Figure 2b: Geometry for mutual coupling evaluation

By summing alternate columns, the contribution from images is grouped into even and odd series [1]. It can be seen that the contribution from even series is independent of slot offset and once computed can be reutilised for any slot with the same slot length making the analysis more efficient. Only the contribution from odd series needs to be recalculated with change in offset. In practice, each even and odd image series has to be truncated at a finite row and column $\pm N$. Then, $(N + 1)^2 - 1$ mutual coupling terms are required for even series and $2N(N + 1)$ terms are required in the odd series.

The even and odd image series are oscillatory in nature and the convergence of each oscillating image series is further accelerated by employing Levin's t-transform [3] for an efficient and accurate analysis. The Levin's t-transform may be summarised as given below:
Let S_n be the partial sum of n terms of a series such that $S_n \to S \quad as \quad n \to \infty$, where S is the sum of the series. The Levin's t-transform may be computed as follows:

$$t_k^n = \frac{\sum_{i=0}^{k} (-1)^i \binom{k}{i} \left(\frac{n+i}{n+k}\right)^{(k-1)} \left(\frac{S_{n+i}}{S_{n+i+1} - S_{n+i}}\right)}{\sum_{i=0}^{k} (-1)^i \binom{k}{i} \left(\frac{n+i}{n+k}\right)^{(k-1)} \left(\frac{1}{S_{n+i+1} - S_{n+i}}\right)} \qquad \text{for k=0,1,2...} \qquad (4)$$

The k^{th} order transform, t_k^n gives an estimate of the sum S of the series. As has been shown later, application of Levin's t-transform aids in accelerating the convergence of the series.

Numerical results:

The results from this formulation have been studied for a number of slot lengths and offsets. The variation of resonant length against offset is shown in Fig.3 for a slot in X-band waveguide and is compared with Stegen's measured data at 9.375 GHz as reproduced in [4]. The resonant length is also evaluated using the MoM with waveguide Green's function [4] with maximum mode number M=N=1000 or 10^6 modes in waveguide (longer dashes). The results are compared with the resonant length computed from the present analysis taking N=±5 (short dashes) where N is the number of images in each even and odd series of images shown in Fig.2 and expanding the slot field using 9 modes in the slot aperture (P=S=9). The end correction for rounded slots [4] has been added in the results so that $2l_{round} = 2l_{rect} + 0.215\,w$. As shown in Fig.3, the error in resonant length for the present analysis employing Levin's t-transform with respect to Stegen's measured data [4] is seen to

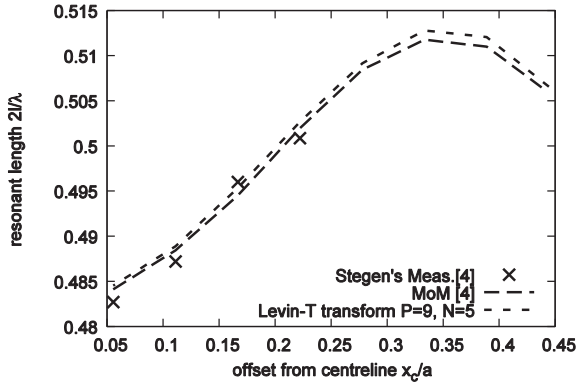

Figure 3: Resonant length for X-band waveguide compared with measured results and MoM modal formulation

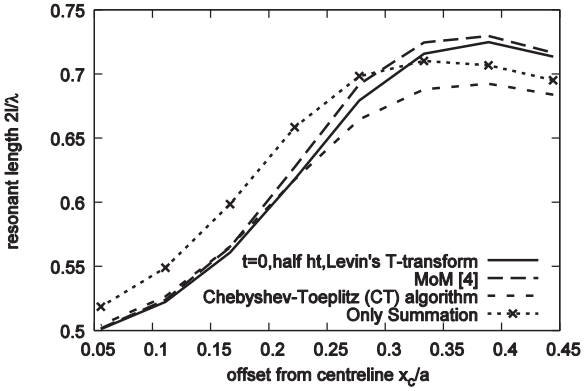

Figure 4: Resonant length for half height waveguide from this theory, MoM modal formulation and CT algorithm

be better than 0.5% even for N=5 case, while the error for this formulation with respect to MoM modal formulation is better than 0.5% at the largest offset and even better at smaller offsets used in practice.

The accuracy in resonant length is much poorer if convergence acceleration techniques like Levin's t-transform are not employed. This becomes clearer from Fig.4 where the resonant length for a slot in a thin (t=0) half height waveguide at 8 GHz is computed using MoM formulation with waveguide Green's function and compared with direct summation of image series admittances. The error for direct summation is seen to be around 5% while the error in resonant length with Levin's t-transform is better than 1% upto $x_c/a < 0.2$ and the error is less than 2% at larger offsets, in spite of the increase in error associated with closed form approximations above a slot length of around 0.65λ [5]. It is also noteworthy that the error in resonant length with CT algorithm [1] is around 5% at larger offsets as seen from Fig.4.

Conclusion: A general method has been developed for the analysis of slots in rectangular waveguide by taking the images of the slot in waveguide walls and using the recently reported point dipole and double dipole approximations for mutual admittance evaluation and Levin's t-transform for convergence acceleration. It has been shown that the Levin's t-transform gives better accuracy than techniques such as CT algorithm. For air filled waveguides, the external admittance data can be reused in the internal admittance series leading to more efficient formulation. The results computed from this method agree very well with the MoM results using waveguide Green's function and with experimental results.

References:

[1] Kakatkar, S.S. and Ray, K.P., "Analysis of longitudinal slot in a rectangular waveguide using image series and Chebyshev-Toeplitz algorithm," International Conference on Microwave and Photonics (ICMAP), 2013, pp.1-5, 13-15 Dec. 2013, Dhanbad, India.

[2] Myun-Joo Park and Sangwook Nam, "Efficient calculation of the Green's function in rectangular waveguides," IEEE Antenn. Propagat. Symp., vol.4 , pp.2354- 2357, 1997

[3] S. Singh and R.Singh, "On the use of levin's t-transform in accelerating the summation of series representing the free-space periodic green's functions," IEEE MTT, vol.41, May93

[4] L. G. Josefsson, "Analysis of longitudinal slots in rectangular waveguides," IEEE Trans. Antennas Propagat., pp. 1351-1357, Dec. 1987

[5] S.S.Kakatkar and K.P.Ray, "Evaluation of mutual coupling between slots from dipole expressions," Progress In Electromagnetics Research M, Vol. 9, pp.123-138, 2009

FLANN-SM based CAD model for Deformed –Ω atom synthesis

Sambhudutta Nanda[1], P.K. Sahu[2], R.K. Mishra[3]

[1]*Dept of Electrical Engineering, NIT Rourkela, 514EE1012@nitrkl.ac.in*

[2]*Dept of Electrical Engineering, NIT Rourkela, pksahu@nitrkl.ac.in*

[3]*Dept of Electronic science, Berhampur University, r.k.mishra.ieee@gmail.com*

Abstract— *this work represents a design of a new CAD model based on neuro-space mapping for synthesis of metamaterial atom such as Deformed Ω atom. In the proposed CAD model, a deformed Ω atom is transformed to a simple SRR atom using Space-Mapping with FLANN. The input to the proposed CAD model is the dimensions of the deformed Ω atom and the output is the equivalent SRR atom. From the obtained SRR atom dimension, the permeability is calculated using the available closed form formula derived from Lorentz method*

Introduction: Metamaterials are widely used as antenna superstrate for cloaking, lens application etc. Realization of metamaterial is achieved by making array of different types of unit cells or atoms. One such unit cell is SRR [1], which is well documented in literature. Another convenient structure is Deformed-Ω [2]. Deformed-Ω atom has an advantage of wide band width of operation hence preferred over other atoms. Before realizing the metamaterial, it is necessary to obtain the permeability and permittivity of these atoms which is a difficult task. Calculation of permeability of LHM consisting of deformed-Ω is difficult and a lengthy process as there is no closed form formulae available for this shape. For calculating the permeability of the deformed-Ω atom, first we have to get the S-parameter by simulating the structure with some costly simulation tool or by testing it practically. Using NRW [3, 4] method, the permeability is extracted from the S-parameter. Whereas closed form formulae for SRR with given dimension is available in literature. In the proposed work we develop a method, through which we can use the formulae of SRR to find the permeability of the deformed-Ω atom, which in turn will reduce the complexity of synthesis of deformed-Ω atom.

Neuro-Space Mapping: An optimisation technique is proposed by Bandler [5] named as space-mapping technique for design of Microwave components using EM tools or Experiments. This technique is based on two models named as fine model and coarse model. Fine model gives the accurate output or result based on costly simulation tools or experimental values or complex mathematical computations. Whereas the coarse model gives less accurate result compared to fine model and needs less computational effort as well in comparison to fine model. Using the mapping technique proposed by Bandler, the input of the coarse model is mapped to another set of inputs using some mapping techniques so as to get accurate results as fine model. In this work, we propose the use of FLANN for mapping of the parameters of the coarse model. Using FLANN, it becomes easier to train the network and the result is obtained in less iterations compared to MLP-NN.

The variation of permeability of metamaterial of any type of unit cell array follows the same pattern, i.e. the frequency dependency of permeability curve for all LHM materials follow the Lorentz model of permeability. From this it can be concluded that deformed-Ω atom and the SRR atom show a common analytical model. So it is assumed that there is mapping relationship between these two types of unit cells. In other words we can say that for each deformed-Ω atom, there exists an equivalent SRR atom and vice-versa such that both the atoms show same permeability characteristics over a certain range of frequency. So in the proposed method, the deformed-Ω atom dimensions are mapped to a simple SRR dimension

using Neuro-Space mapping technique. Then the permeability of the deformed-Ω atom can easily be found from the close form formulae of Lorentz formulation using the mapped SRR dimension. Figure 1 shows the dimension of the deformed-Ω atom is to be mapped with a SRR atom

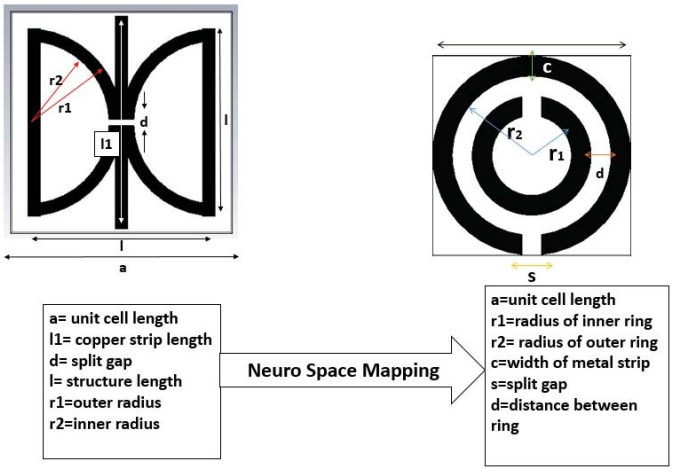

Figure 1(mapping structures)

Implementation of Neuro–Space mapping: The schematic diagram and the implementation of Neuro-Space mapping is shown in Figure 2(a) and 2(b). In this work, CST MWS 2013 along with NRW method has been explored for extraction of the permeability of deformed-Ω atom as the fine model.

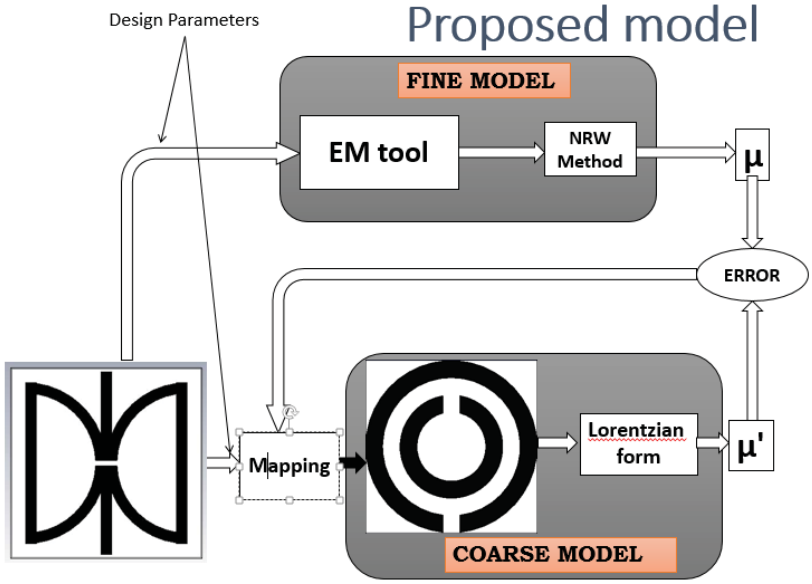

Figure 2(a) Schematic diagram of mapping

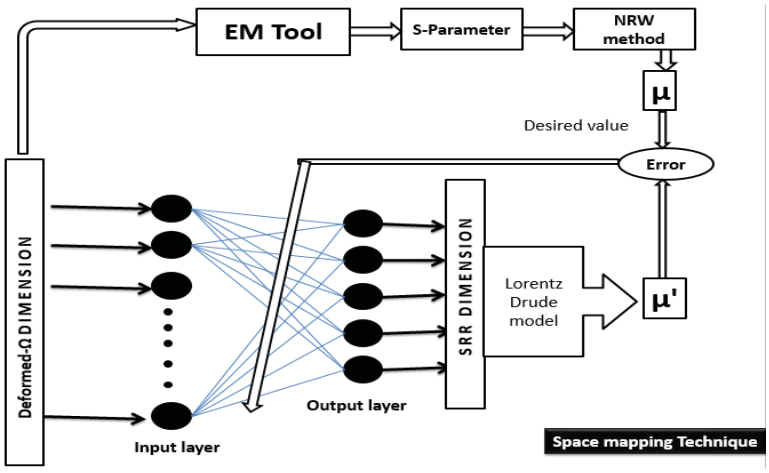

Figure 2(b) Implementation of Neuro-Space mapping

As shown in figure 2(b) the design parameters of the deformed-Ω atom is given as input to the FLANN. Output of the FLANN is the dimensions of the SRR, i.e. our mapped dimensions. From this mapped dimension, the permeability is calculated from Lorentz formulation and compared with the fine model output i.e the permeability obtained from NRW method. The error obtained is used to update the weights of the FLANN.

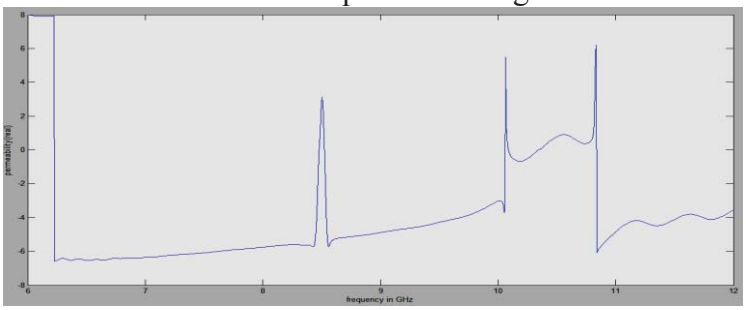

Figure 3 Extracted permeability curve

Figure 3 shows the extracted permeability values simulated for 6 to 12 GHz using MATLAB 2013. Input of the FLANN is expanded using both linear expansion and triginimetric expansion. By expanding the inputs we get 17 input nodes for FLANN.The input database is obtained from the CST results along with the design parameters. The learning factor is initialy taken as 0.001 and varied.

Results and discussions: The FLANN is trained over a small frequency band(required frequency band) between 10 to 12 GHz, where the permeability value is negative with different learning factors(Eta). Results are shown at learning factor 0.005 and 0.007. Better result is obtained at learning factor 0.007. In the figure shown below black curve is the permeability from fine model and the red curve is the permeability curve from mapped dimension.

Eta=0.005

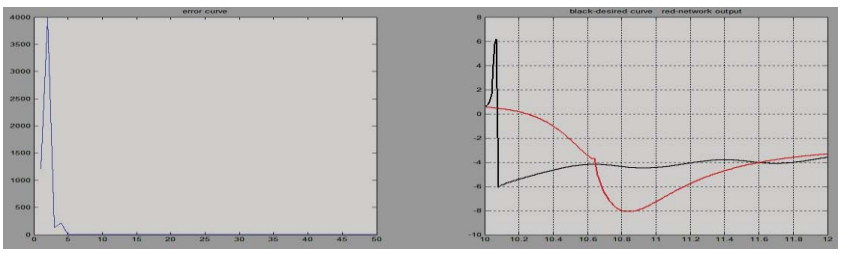

Figure 4(a) Result for Eta = 0.005

Eta=0.006

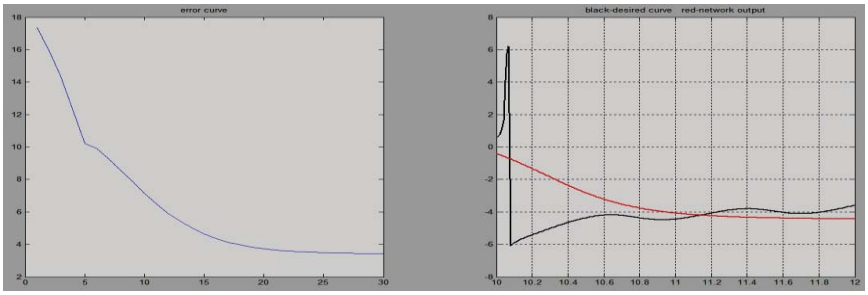

Figure 4(b) Result for Eta = 0.006

Eta=0.007

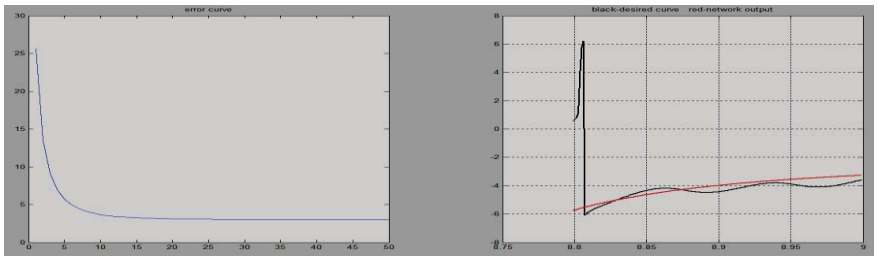

Figure 4(c) Result for Eta = 0.007

A neuro-space mapping based CAD model is developed for calculation of permeability of deformed-Ω atom. The work can be extended for calculation of both permeability and permittivity of LHM.

Reference:

[1] J.B. Pendry, A.J. Holden, D.J. Robbins & W.J. Stewart, "Magnetismfrom conductors and enhanced nonlinear phenomena", *IEEE Trans.Microwave theory and Technique*, vol. 47, no. 11, pp. 2075-2081, Nov.1999.

[2] Debasis Mishra D. R. Poddar and R. K. Mishra, "Deformed Omega Array as LHM" proceedings of international conference on Microwave-8

[3] T. D. Karamanos, A. I. Dimitriadis, and N. V. Kantartzis, "Effectiveparameter extraction of SRR structures by means of first-principleshomogenization techniques", *Metamaterials' 2012: The Sixth International Congress on Advanced Electromagnetic Materials inMicrowaves and Optics*.

[4] Hao Zhou, Guizhen Lu, Yanfei Li, Song Wang, and Yue Wang, "AnImproved Method of Determining Permittivity and Permeability by *S*Parameters", *PIERS Proceedings*, Beijing, China, March 23-27, 2009.

[5] M . Bakr, J. Bandler, R. Biernacki, S. Chen, K. Madsen, "A Trust Region Aggressive Space Mapping Algorithm for EM Optimization" IEEE Transactions on Microwave Theory and Techniques, vol. 46, no. 12, December 1998.

[6] Faissal MILI and Manel HAMDI, "A hybrid Evolutionary FunctionalLink Artificial Neural Network for Data mining andClassification",*(IJACSA) International Journal of Advanced Computer Science and Applications,* Vol. 3, No.8, 2012.

[7] Ganapati Panda and Debi Prasad Das, "Functional Link Artificial NeuralNetwork for Active Control of Nonlinear Noise Processes",*International Workshop on Acoustic Echo and Noise Control (IWAENC2003)*, Kyoto, Japan, Sept. 2003.

DEMONSTRATION OF A WIRELESS COMMUNICATION SYSTEM USING SDR PLATFORM

Ansha K K[(1)], Mary Rani Abraham[(2)], and Sameer Babu T P[(2)]
(1)School Of Engineering, CUSAT, Kochi, Email:anshakk91@gmail.com.
(2) Naval Physical & Oceanographic Laboratory, Kochi. 6982021
Email:sameerbabu@gmail.com

Abstract: *In this paper, we present the design and implementation of an end-to end wireless communication system over the air. Evaluation of the proposed design was conducted using the Universal Software Radio Peripheral (USRP) software defined radio platform and NI- LABVIEW software. The received signal is analyzed using scatter plot, eye diagram and spectrogram.*

Introduction: The traditional hardware radio system consists of a variety of analog elements such as filters, converters, modulators and demodulators. The design of the radio is totally dependent on hardware. The reason why Software Defined Radio (SDR) becomes popular is that people could use SDR technology to realize many applications without a lot of efforts in the integration of different components. The software module can be incorporated to adapt different modulators and demodulators in the SDR platform [1]. This paper presents the implementation of an end to end wireless digital communication system using NI LABVIEW software and USRP Platform.

System overview: SDR is defined as a radio whose functionality is at least partially controlled or implemented in software [2]. To achieve this, RF components such as mixers and filters are moved to the software domain, where a computer or digital signal processor performs baseband signal processing. In the Baseband section of SDR, it performs signal processing in baseband- transmission and reception of data. The software platform used to develop baseband section is Lab VIEW from National Instruments. The baseband signal processed in LABVIEW is then transmitted using a computer hosted RF hardware called USRP. The USRP forms the RF front-end of the transceiver. The Gigabit Ethernet cable connects the PC and USRP.

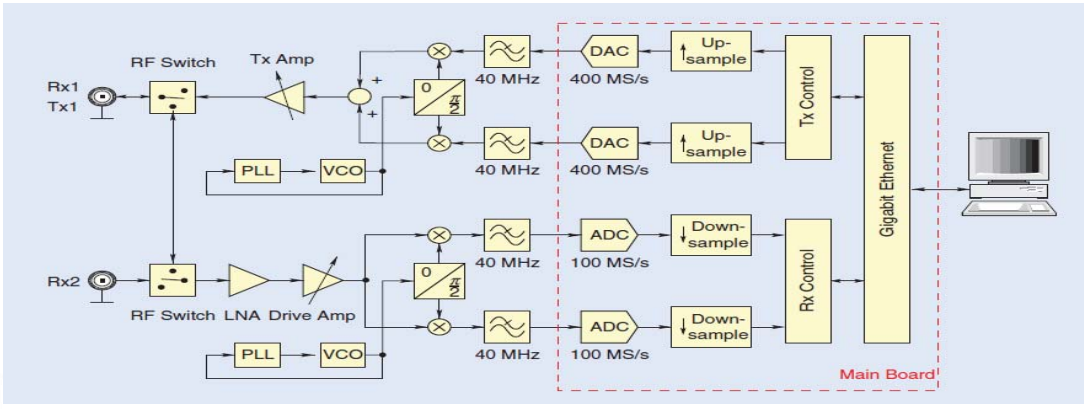

Fig 1. NI USRP 2920 Block Diagram

The USRP device, whose block diagram is shown in Fig. 1 includes two essential components, (i) the main board- carrying the FPGA, the digital-to-analog (DAC) and analog-to-digital (ADC) converters, and a standard interface between the host-computer and the USRP unit- and (ii) the RF transceiver daughter-board that generates the complex envelope from the received RF driving the ADCs in receiver mode and reconstructs the RF signal to be transmitted from the complex envelope provided by DAC in transmitter mode.

Methodology: A basic wireless digital communication system on SDR platform that uses PSK modulation is designed in LABVIEW. The block diagram of transmitter and receiver is shown in the fig. 2

Transmitter

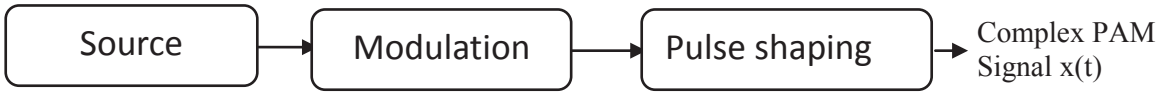

Receiver

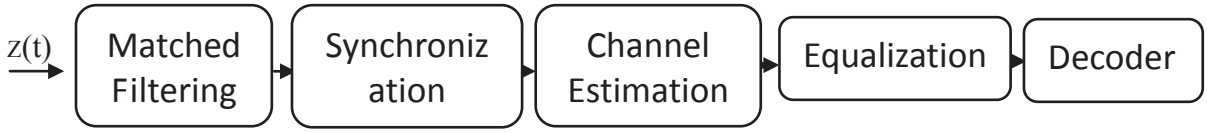

Fig 2. Block Diagram of Transmitter and Receiver

Source: The function of source is to generate data bits that are to be transmitted.

Modulation: Modulator maps the data bits to the elements of a symbol constellation. The modulation scheme used is PSK. The digital signal needs to be mapped to an analog waveform before transmission to a channel.

Pulse shaping: The transmitter uses digital pulse shaping to create the transmit waveform. The up sampled symbol sequence is filtered in discrete-time by a transmit pulse shape. The square root raised cosine Nyquist pulse shaping filter is used for pulse shaping. Its impulse response is

$$g_{\text{sqrc}}(t) = \frac{4\alpha}{\pi\sqrt{T}} \frac{\cos\left[(1+\alpha)\pi t/T\right] + \frac{\sin[(1-\alpha)\pi t/T]}{4\alpha t/T}}{1-(4\alpha t/T)^2}. \quad (1)$$

where T is the symbol period and α is the roll off factor.

The transmitted signal x (t) can be written as

$$x(t) = \sqrt{E_x} \sum_{n=-\infty}^{\infty} s[n] g_{\text{tx}}(t-nT). \quad (2)$$

x(t) is the complex PAM signal, the complex symbols s[n] modulate a succession of pulses given by function $g_{tx}(t)$.

Matched filter: The received signal z(t) is sampled at the receiver.

$$z(t) = x(t) + v(t) \quad (3)$$

where x(t) is the complex baseband signal, v(t) is the noise, and z(t) is the received signal.

The sampled signal is filtered using receiver matched filter. The square root raised cosine filter is used as it is its own matched filter.

Synchronization: Symbol timing recovery is known as synchronization. It is used for correcting the delay caused by the channel. Both the maximum energy solution method and early late gate method were used for synchronization.

Channel Estimation and Equalization: Due to reflection, scattering, diffraction etc. the transmitted signal encounter a multipath propagation.
In general, the received signal can be written as

$$z(t) = \int_{\tau} h_e(\tau)x(t-\tau)d\tau + v(t) \tag{4}$$

where $h_e(\tau)$ is the baseband frequency selective channel. For complex pulse amplitude modulations, the channel distorts the pulse-shaping function. Channel estimation and equalization is used to mitigate the effect of multipath propagation in transmitted symbols. An FIR equalizer is used to employ FIR filter that removes the effect of channel.
Let $\{f_{n_d}[l]\}_{l=0}^{L_f}$ be a FIR equalizer. The equalizer will be applied to the received signal so that

$$r[n] = \sum_{\ell=0}^{L_f} f_{n_d}[\ell]y[n-\ell] \approx \hat{s}[n-n_d] \tag{5}$$

where n_d is the equalizer delay, L_f is the order of filter.

Decoder: The estimated symbols are down sampled and then passed to a detection block which determines the most likely transmitted symbol for that observation. The detected symbols are passed to an inverse symbol mapping block to produce a good guess of the transmitted bits.

Experimental setup, Results and Analysis of Results: The experiment was performed over real wireless link by setting the following baseband parameters on the front panels of transmitter.vi and receiver.vi. Overall setup is shown in Fig 3.

Fig 3. Experimental Setup.

Center Frequency= 100MHz
Packet Length = 500 bits
Symbol Rate =100 k symbols/sec
Modulation Type = QPSK
Pulse Shaping Filter = Root Raised Cosine
Filter Length = 8
Capture Time = 2 msec.
Roll off factor = 1
Baseband Sampling Rate=2MSamples/sec

It was found that when the roll off factor was increased from 0 to 1 in increments of 0.1, the eye of the diagram becomes clearer. This means that increase in the roll of factor causes the reduction of ISI. It was found that when the noise level of signal increases, the constellation spread out. The scatter plot and eye diagram of the received signal with roll off factor =1 is shown in Fig 4. The spectrogram of the received signal is shown in the fig 5. The Null to Null Bandwidth observed on spectrogram is 200 kHz.

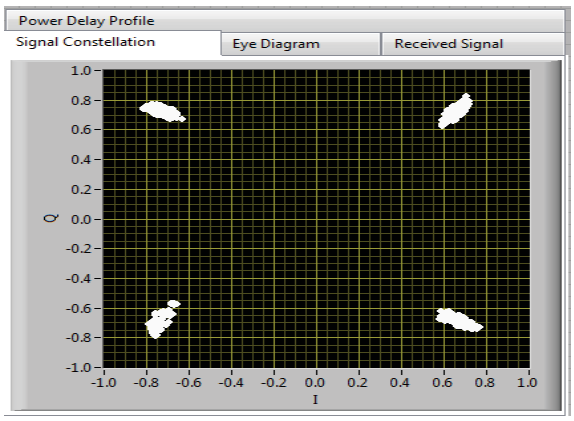

Fig 4.a

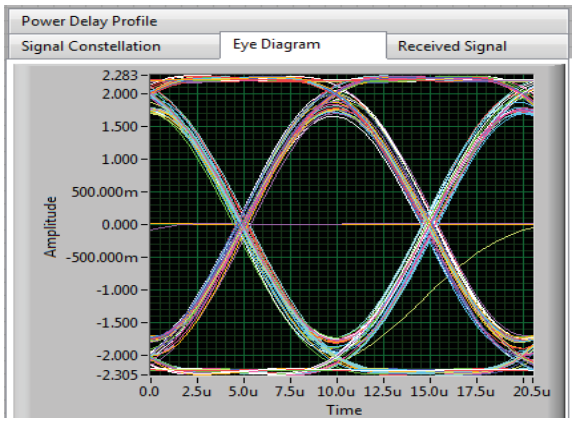

Fig 4.b

Fig 4. Scatter Plot and Eye diagram of received signal for roll of factor =1.

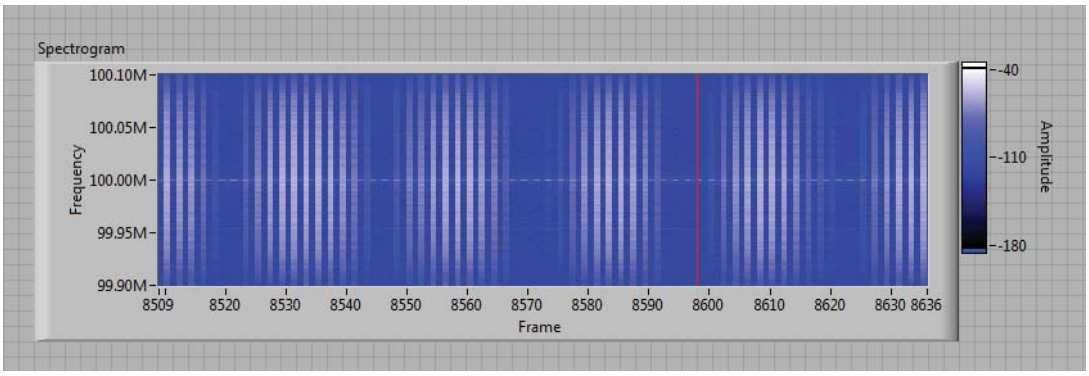

Fig 5. Spectrogram of Received Signal.

Conclusion: An end-to-end wireless communication system is designed and demonstrated over the air using the USRP software defined radio platform. The received signal is analyzed using scatter plot, eye diagram and spectrogram.

Reference:

[1] Chi-Yuan Chen, Fan-Hsun Tseng, Kai-Di Chang, Han-Chieh Chao and Jiann-Liang Chen "Reconfigurable Software Defined Radio and Its Applications" Tamkang Journal of Science and Engineering, Vol. 13, No. 1, pp. 29-38, 2010.

[2] J. Reed, "Software Radio: A Modern Approach to Radio Engineering." Upper Saddle River, NJ, USA: Prentice Hall Press, 2002.

[3] J. Mitola III, "Software radios: Survey, critical evaluation and future directions," Aerospace and Electronic Systems Magazine, IEEE, vol. 8, no. 4, pp. 25-36, Apr. 1993.

[4] Robert W Heath Jr, "Digital Wireless Communication: Physical Layer Exploration Lab Using the NI USRP™", National Technology and Science Press, 2012.

DECEMBER 18, THURSDAY
08.30AM TO 10.30AM
RESEARCH SESSION 7
MICROSTRIP ANTENNA 2
J C BOSE- HALL

Chair: Prof. K.G. Nair C-SiS, CUSAT, India.

No	Papers	Page
7.1	**Broadband Two Half U-slot cut Rectangular Microstrip Antenna** Amit A. Deshmukh[1], Saleha Shaikh [1], Ami Desai[1] and K. P. Ray[2] [1]EXTC, DJSCOE, Vile – Parle (W), Mumbai, India. *E-mail: amitdeshmukh76@rediffmail.com* [2]RFMS, SAMEER, I.I.T. Campus, Powai, Mumbai, India. *Email: kpray@rediffmail.com*	183
7.2	**Analysis of Broadband Shorted Plate Slot cut Rectangular Microstrip Antenna** Amit A. Deshmukh[1], Saleha Shaikh [1], Ami Desai[1] and K. P. Ray[2]. [1]EXTC, DJSCOE, Vile – Parle (W), Mumbai, India. *Email: amitdeshmukh76@rediffmail.com* [2]RFMS, SAMEER, I.I.T. Campus, Powai, Mumbai, India. *Email: kpray@rediffmail.com*	187
7.3	**Broadband Sectoral Microstrip Antennas** Amit A. Deshmukh[1], Neelam V. Phatak [1], S. Nagarbowdi [1], Kshitij Lele[1] and K. P. Ray [2] [1]EXTC, DJSCOE, Vile – Parle (W), Mumbai, *Email: amitdeshmukh76@rediffmail.com* [2]RFMS, SAMEER,IIT Campus, Powai, Mumbai, India. *E-mail: kpray@rediffmail.com*	191
7.4	**Wideband Circularly Polarized Patch Antenna for WIMAX Applications** Sumitha Mathew, R.Anitha and K.Vasudevan Centre for Research in Electromagnetics and Antennas, Department of Electronics, Cochin University of Science &Technology, Kochi-22, Kerala, India. *Email: vasudevankdr@gmail.com*	195
7.5	**A Compact Low Frequency Zeroth Order Resonant Antenna** Basil J. Paul[1], S. Mridula[1], and P. Mohanan[2] [1]School of Engineering, CUSAT, Cochin, India, 682022*, E-mail: basiljpaul@gmail.com, mridula@cusat.ac.in* [2]Dept. of Electronics, CUSAT, Cochin-682022, India. *E-mail: drmohan@cusat.ac.in*	199
7.6	**Metamaterial Loaded High Gain Smiley Antenna** Gurveer Kaur[1], Shyam S. Pattnaik[2], and Balwinder S. Dhaliwal[1] [1]Guru Nanak Dev Engineering College, Ludhiana, India, 141006. *E-mail: c_kgurveer@yahoo.in* [2]National Institute of Technical Teachers Training and Research,	203

Chandigarh.*E-mail:profshyampattnaik@gmail.com*

7.7 **Isolation Enhancement using Thin Wire Metamaterial for closely spaced Microstrip Antenna** 207
A.Nilam.T.Kadam, B.Kiran.S.Janwalkar, C.Anuja.A.Odhekar
[1]D.J.Sanghvi College of Engineering, Mumbai. India-400056.
Email:anuja.odhekar@djsce.ac.in

7.8 **A Compact ACS fed Electrically Small Antenna** 212
U. Deepak[1], Susan Thomas[2], T. K. Roshna[3] and P. Mohanan[4]**.**
Department of Electronics, Cochin University of Science & Technology, Cochin, 682022.
Email:[1]deepak.palath@gmail.com, [2]shonasusan@gmail.com, [3]roshnatk03@gmail.com, [4]drmohan@gmail.com

7.9 **Bandwidth Enchacement of Dual Band David Fractal Microstrip Antenna** 216
Jacob Abraham , and Thomaskutty Mathew
Department of Electronics, School of Technology and Applied Science M G University, Regional Center, Edapally, Kochi India,
E-mail:tjacobabra@gmail.com

Broadband Two Half U-slot cut Rectangular Microstrip Antenna

Amit A. Deshmukh[(1)], Saleha Shaikh [(1)], Ami Desai[(1)] and K. P. Ray[(2)]
(1) EXTC, DJSCOE, Vile – Parle (W), Mumbai, India, Email: amitdeshmukh76@rediffmail.com
(2) RFMS, SAMEER, I.I.T. Campus, Powai, Mumbai, India, Email id: kpray@rediffmail.com

Abstract: *Broadband compact two half U-slot cut rectangular microstrip antenna derived from double U-slot cut rectangular microstrip antenna is proposed. The slot cut antenna gives bandwidth of around 1000 MHz (~50%) with broadside radiation pattern and gain of around 7 dBi over the complete bandwidth*

Introduction: After being reported for the first time, the U-slot shape has been extensively used to increase the bandwidth of microstrip antenna (MSA) [1]. The first reported U-slot cut rectangular MSA (RMSA) yields bandwidth (BW) of around 400 MHz centered at 1000 MHz on foam substrate. Since the MSA is optimized on thicker substrate, the U-slot compensates for the probe inductance thereby acting as a probe inductance compensator [1]. Broadband designs of U-slot using circular and equilateral triangular patch are also reported [2]. Depending upon the frequency range in which they are designed, the coaxially fed U-slot cut MSA yields BW in the range of 30 to 40% with gain of around 6 to 8 dBi. Further increase in RMSA BW is obtained by cutting symmetrical or un-symmetrical U-slot inside the patch [3]. In an unsymmetrically cut U-slot, presence of three resonant modes was noticed which is reported to increase its BW beyond 40%. Using symmetrical U-slot, further increase in antenna BW is obtained either by using different feeding techniques like L-probe feed and proximity feed or by cutting another U-slot inside the first one [2, 4]. These two methods yield an increase in BW by nearly 5 to 10% as compared to coaxially fed MSAs. While designing U-slot cut RMSA in the given frequency range, inner U-slot length is taken equal to half the wavelength and based on this approximation, formulation in slot resonant length is reported [5]. The compact and broadband MSA is obtained by using the symmetry of U-slot cut MSA across the feed point axis and by using only half of the configuration which leads to half U-slot cut MSAs [6]. For the given slot frequency, an inner half U-slot length is taken equal to quarter wave in length.

The double U-slot cut RMSA optimized on foam substrate thickness of 1.65 cm, gives BW of 700 MHz centered at 1591 MHz [4]. In this paper, using the symmetry of double U-slot cut RMSA (as reported in [4]) across the feed point axis, a compact proximity fed two half U-slot cut RMSA is proposed. The resonant modes which are introduced by two half U-slots near the fundamental TM_{01} mode of RMSA, yields broader BW. The simulated and measured BW of around 1000 MHz (>55%) is obtained. The antenna gives broadside radiation pattern with a gain of around 7 dBi over the complete BW. The proposed antenna was first optimized using IE3D software using finite square ground plane of side length 30 cm [7]. To validate the simulated results, measurement was carried out. The patch was fabricated using copper plate of finite thickness and was suspended above the ground plane using foam spacer support placed towards the antenna corners. The slot cut MSA is fed using N-type connector of 0.32 cm inner wire diameter. The measurement was carried out using R & S Vector network analyzer (ZVH – 8). The antenna pattern and gain was measured in minimum

reflection surroundings with required minimum far field distance between reference antenna and antenna under test.

Double U-slot cut RMSA: The coaxially fed double U-slot cut RMSA is shown in Fig. 1(a). The patch fabricated on foam substrate of thickness 1.65 cm, yields BW from 1241 to 1941 MHz (700 MHz centered at 1591 MHz) as shown in Fig. 1(b). The impedance plot shows the presence of two distinct loops indicating the presence of three resonant modes. They are due to the two U-slots and TM_{01} mode of RMSA. The reported antenna gives broadside radiation pattern with gain of more than 7 dBi over the VSWR BW. To realize compact configuration, the symmetry of double U-slot cut RMSA across the feed point axis is used, as discussed in the following section.

Two Half U-slot cut RMSA: The compact dual half U-slot cut RMSA is shown in Fig. 1(c – e). The dimensions shown in all the figures and their captions are in cm. The proximity feed is used as it helps in realizing impedance matching while using thicker substrate. The substrate thickness for the patch (h) is selected to be 1.7 cm and the coupling strip is placed at thickness (h_1) of 1.5 cm below the patch. This substrate thickness is nearly the same as that used in reported dual U-slot cut RMSA. To optimize the configuration, first half U-slot cut RMSA is optimized as shown in Fig. 1(f). The parametric study for variation in half U-slot length is carried out and the input impedance plots for the same are shown in Fig. 1(g). With an increase in slot length the loop formed due to the mode introduced by half U-slot is optimized inside VSWR = 2 circle. The optimum result is obtained for l_{v1} = 4.8 cm and input impedance plot for the same is shown in Fig. 1(h). The simulated BW is 338 MHz (18.2%) whereas the measured BW is 368 MHz (19.85%). The antenna shows broadside radiation pattern over the complete BW with peak gain of around 7 dBi. The input impedance locus for half U-slot cut RMSA shows formation of second loop in the higher frequency region. To optimize the same so as to realize larger BW, second half U-slot inside the first one is cut as shown in Fig. 2(a). The input impedance plots for variation in second half U-slot length are shown in Fig. 2(b). With an increase in half U-slot length, the resonance frequency for the next loop decreases and it comes closer towards the first loop. For l_{v2} = 2.2 cm, it was observed that two loops cannot be optimized inside VSWR = 2 circle. To optimize the same, substrate thickness for patch and strip was increased to, h = 2.0 cm and h_1 = 1.8 cm. The optimum input impedance and VSWR plots are shown in Fig. 2(c). The simulated BW is 998 MHz (50%) whereas the measured BW is 1067 MHz (51.4%). The measured radiation pattern at center frequency and gain variation over BW is shown in Fig. 2(d, e). The pattern shows higher cross polar levels due to the orthogonal surface currents due to modified modes introduced by two half U-slots.

Conclusions: Broadband two half U-slot cut RMSA derived from double U-slot cut RMSA is proposed. The parametric study for optimizing first half U-slot and further double half U-slot cut RMSA is presented. The two half U-slots introduces modes near the fundamental TM_{01} mode of RMSA to realize broader BW of around 1000 MHz (>50%). The proposed slot cut RMSA yields gain of around 7 dBi over most of the BW.

References:

[1] T. Huynh and K. F. Lee, “Single-Layer Single-Patch Wideband Microstrip Antenna”, Electronics Letters, Vol. 31, No. 16, August 1995, pp.1310-1312.

[2] K. L. Wong, Compact and Broadband Microstrip Antennas, John Wiley & sons, Inc., New York, USA, 2002.

[3] J. Ghalibafan and A. R. Attari, “A New Dual-band Microstrip Antenna with U-shaped slot”, Progress In Electromagnetic Research C, Vol. 12, 2010, pp.215 – 223.

[4] Y. X. Guo, K. M. Luk, K. F. Lee and Y. L. Chow, "Double U-slot rectangular patch antenna", Electronics Letters, Vol. 34, No. 19, 17th September 1998, pp.1805 – 1806.
[5] S. G. Weigand, H. Huff, K. H. Pan, and J. T. Bernhard, "Analysis and design of Broadband Single Layer Rectangular U-slot Microstrip Patch Antenna", IEEE Transactions on Antennas & Propagation, AP – 51, 3, March 2003, pp. 457 – 468.
[6] R. Chair, C. L. Mak, K. F. Lee, K. M. Luk and A. A. Kishk, "Miniaturized wide-band half U-slot and half E-shaped Patch Antennas", IEEE Transactions on Antennas & Propagation, AP-53, 8, August 2005, pp. 2645 – 2652.
[7] IE3D 12.1, Zeland Software, Freemont, USA

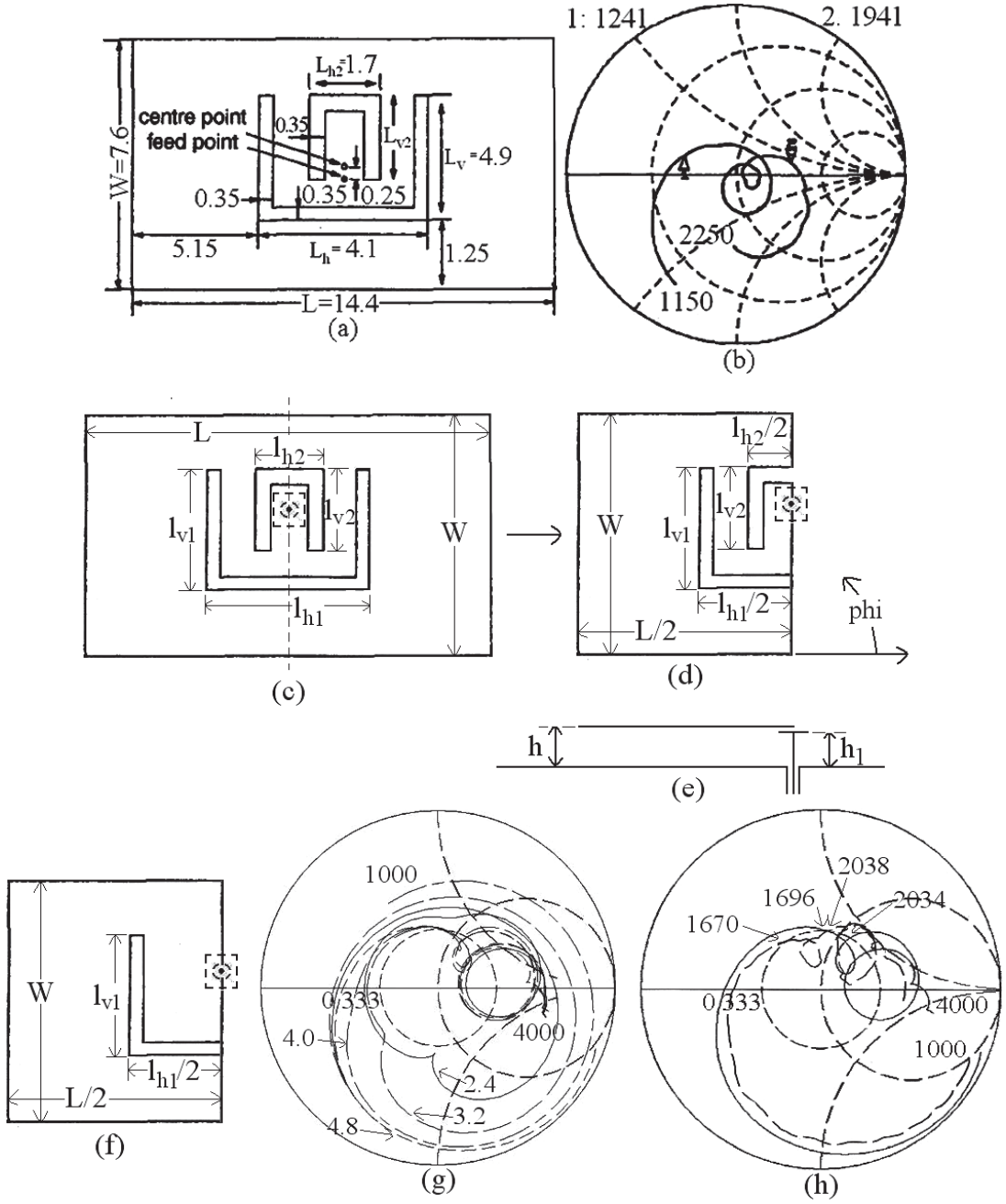

Fig. 1 (a) Reported double U-slot cut RMSA and its (b) input impedance plot [4], proximity fed (c) two U-slot and (d, e) two half U-slot cut RMSA, (f) proximity fed half U-slot cut RMSA, its (g) input impedance plots for varying l_{v1} and its (h) optimized input impedance plot for l_{v1} = 4.8, l_{h1} = 2.2

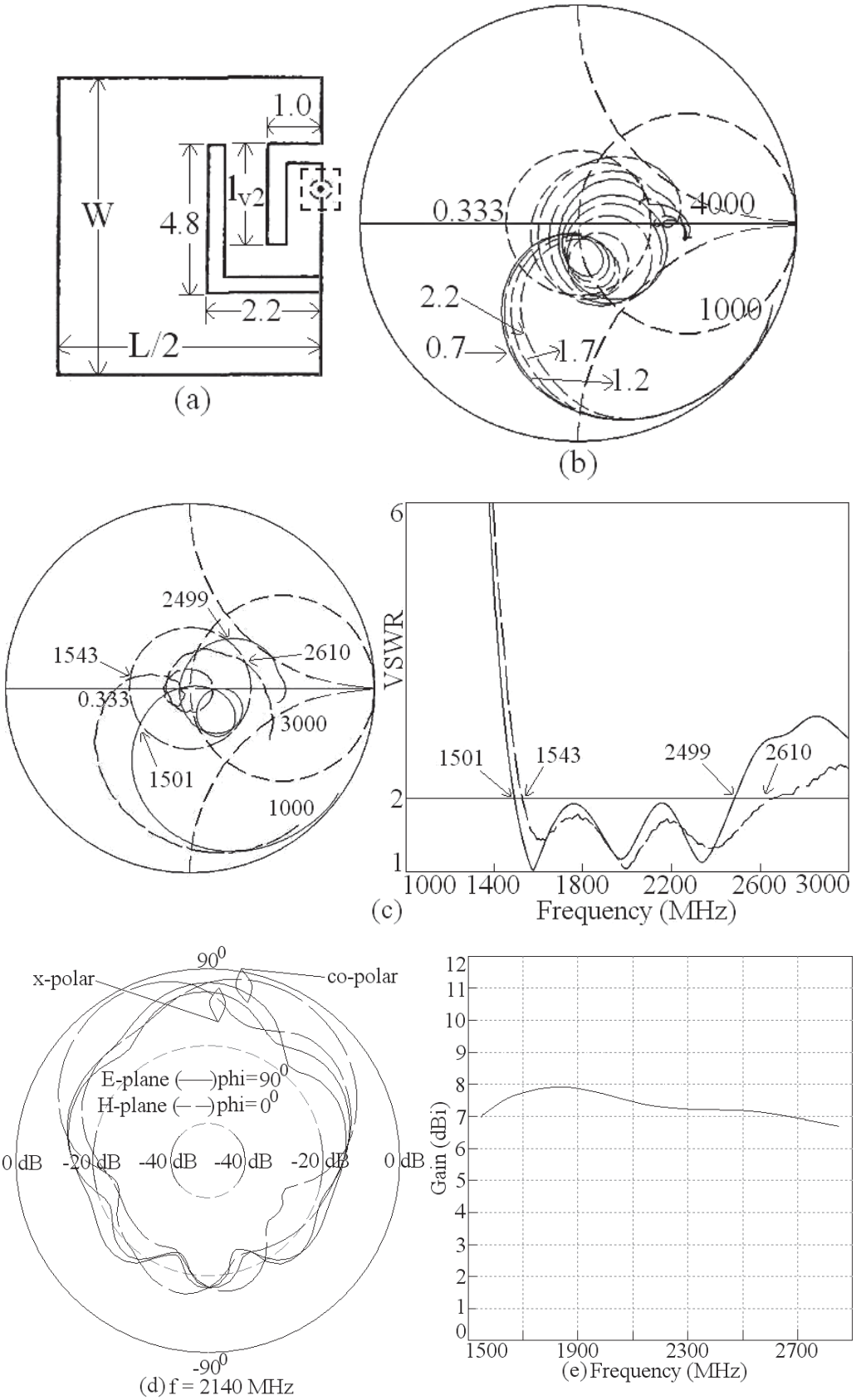

Fig. 2 (a) Proximity fed double U-slot cut RMSA, its (b) input impedance plots for varying l_{v2}, its (c) optimized input impedance and VSWR plots, (—) simulated, (– –) measured, its (d) radiation pattern at centre frequency and (e) gain variation over the BW

Analysis of Broadband Shorted Plate Slot cut Rectangular Microstrip Antenna

Amit A. Deshmukh[(1)], Saleha Shaikh [(1)], Ami Desai[(1)] and K. P. Ray[(2)]
(1) EXTC, DJSCOE, Vile – Parle (W), Mumbai, India, Email: amitdeshmukh76@rediffmail.com
(2) RFMS, SAMEER, I.I.T. Campus, Powai, Mumbai, India, Email id: kpray@rediffmail.com

Abstract: *The analysis to study the broadband response in shorted plate slot cut rectangular microstrip antenna is presented. The slot reduces the resonance frequency of higher order $TM_{1/4,1}$ mode of the shorted patch and along with fundamental $TM_{1/4,0}$ mode yields broader bandwidth of more than 550 MHz (~60%). The proposed analysis will help in understanding the functioning of slot cut shorted antennas*

Introduction: The compact microstrip antenna (MSA) is realized by placing shorting plate/post along the zero field line at the fundamental patch mode, thereby converting half wavelength resonator into a quarter wavelength resonator [1]. The bandwidth (BW) of these quarter wavelength resonators is increased by cutting rectangular slot or U-slot inside the patch which is either fully shorted or partially shorted along one of its edge [2 – 7]. The broadband response in shorted MSAs is realized with respect to the fundamental shorted patch mode. The slot is said to introduce an additional resonant mode near the fundamental patch mode when its length is selected nearly equal to quarter wave in length. However the effects of variation in slot width and its position inside the shorted patch on the slot resonance frequency has not been explained. The broadband and dual band variations of shorted plate slot cut MSAs using bend feeding structure are reported [8 – 10]. However which mode that yields broadband and dual band response is not explained. The BW of conventional half wavelength resonators has been increased by cutting the slot inside the patch [2]. The analysis to study the effects of slot that realizes broadband response is reported [11]. It was observed that slot modifies the resonance frequency of higher order orthogonal patch mode and along with fundamental mode yields broader BW. The slot position was found to be an important parameter for realizing the tuning of orthogonal mode frequency with respect to fundamental patch mode. Similar analysis to study the effects of slot in quarter wavelength resonators is not available.

In this paper, an analysis to study the broadband response in proximity fed shorted slot cut rectangular MSA (MSA) is proposed. The slot reduces the resonance frequency of second higher order $TM_{1/4,1}$ mode of the shorted patch and along with fundamental $TM_{1/4,0}$ mode yields broadband response. The simulated and measured BW of more than 550 MHz (~60%) is obtained. The slot also alters the surface current distribution at higher order mode to yield radiation pattern with no variations in the directions of principle planes. The analysis of shorted RMSA is carried out first using IE3D software followed by experimental verifications [12]. The patch was fabricated using copper plate and was supported in air using foam spacer support. The impedance measurement was carried out using R & S Vector network analyzer (ZVH 8) whereas pattern and gain measurements were carried out using RF source and Spectrum analyzer in the minimum reflection surroundings. In the proposed analysis, MSA with fundamental mode frequency in 900 MHz band is selected as in this frequency range, % antenna BW is smaller. Thus the proposed analysis will give an insight

into the functioning of slot cut compact antennas and will help to design them in desired frequency range.

Shorted Plate slot cut RMSA: The proximity fed RMSA with its voltage distribution at TM_{10} mode is shown in Fig. 1(a). All the dimensions shown in figures and their captions are in cm. The patch length (L) is selected such that its TM_{10} mode frequency is around 900 MHz. By placing the shorting plate along zero field line, its compact variation is realized as shown in Fig. 1(b). The shorted RMSA is simulated for $x_f = 3.5$, $y_f = 0$ and its resonance curve plot is shown in Fig. 1(c). It shows two peaks and surface current distributions at them are shown in Fig. 2(a, b). At first peak, current shows one quarter wavelength variation along shorted patch length and this is due to shorted TM_{10} mode. It is also referred to as $TM_{1/4,0}$ mode since along shorted patch length it shows quarter wavelength variation with field remaining constant along the orthogonal shorted patch dimension. The second peak is due to $TM_{1/4,2}$ mode as current shows one quarter wavelength variation along shorted patch length and two half wavelength variation along patch width. Further shorted RMSA is simulated for $y_f = 2.5$ cm and its resonance curve plot is shown in Fig. 1(c). It shows additional peak at 1129 MHz and surface current distribution at the same is shown in Fig. 2(c). It shows quarter wavelength variation along shorted length and half wavelength variation along the orthogonal dimension. Hence this mode is referred to as $TM_{1/4,1}$ mode. Since surface currents at $TM_{1/4,0}$ mode are horizontally directed, the E-plane is directed along $\Phi = 0^0$. At $TM_{1/4,1}$ mode as maximum contribution of currents are along vertical direction, E-plane is directed along $\Phi = 90^0$. At $TM_{1/4,0}$ mode, by optimizing strip dimension, broadband response was realized. The measured and simulated BW is more than 440 MHz (~50%). To increase the BW, rectangular slot is cut on the vertical edge of the patch as shown in Fig. 2(d). The slot position is selected such that it will not reduce $TM_{1/4,0}$ mode resonance frequency. The resonance curve plots for varying slot length (l) and its position (Y) are shown in Fig. 2(e, f). With an increasing slot length, $TM_{1/4,1}$ and $TM_{1/4,2}$ mode frequencies reduces and they come closer to $TM_{1/4,0}$ mode frequency. With an increase in 'Y' from 2 to 4 cm, reduction in $TM_{1/4,1}$ mode frequency is smaller as compared to that in $TM_{1/4,2}$ mode frequency. This is due to placement of slot more towards the maximum current location along patch width at $TM_{1/4,2}$ mode. The surface current distribution at modified $TM_{1/4,0}$ and $TM_{1/4,1}$ modes for slot length of 3.5 cm is shown in Fig. 2(g, h). With an increasing slot length, surface currents at modified $TM_{1/4,1}$ mode are aligned along horizontal direction inside the shorted patch. The broader BW is realized when the loops formed due to $TM_{1/4,0}$ and modified $TM_{1/4,1}$ modes lies inside VSWR = 2 circle. This is obtained for l = 3.5 cm, w = 0.4 cm and Y = 3.0 cm and its input impedance plot is shown in Fig. 2(i). The simulated BW is 557 MHz (60%) whereas the measured BW is 575 MHz (62%). Due to the shorted patch, the pattern over the BW shows higher cross polar radiation with E and H-plane aligned along $\Phi = 0^0$ and 90^0, respectively. The antenna gain is more than 4 dBi over most of the BW as shown in Fig. 2(j). The proximity fed RMSA of equivalent dimension yields BW of around 350 MHz (>35%). Thus the proposed slot cut configuration yields higher BW as compared to that of RMSA with half the patch size.

Conclusions: The proximity fed broadband slot cut shorted RMSA is proposed. An analysis to study the effects of rectangular slot which yields broadband response is presented. The slot reduces the resonance frequency of next higher order $TM_{1/4,1}$ mode frequency of the shorted patch and along with fundamental $TM_{1/4,0}$ mode yields BW of more than 550 MHz (~60%). The slot also modifies the surface current distribution at $TM_{1/4,1}$ mode to yield radiation pattern with no variation in the direction of principle planes. Due to the shorted patch, antenna gain is more than 4 dBi over the complete BW.

References:

[1] G. Kumar and K. P. Ray, Broadband Microstrip Antennas, 1st edition, Artech House, USA, 2002.

[2] K. L. Wong, Compact and Broadband Microstrip Antennas, John Wiley & sons, Inc., New York, USA, 2002.

[3] A. A. Deshmukh and G. Kumar, "Compact Broadband U-slot loaded Rectangular Microstrip Antennas", Microwave and Optical Technology Letters, Vol. 46, No. 6, 20th Sept. 2005, pp. 556 – 559.

[4] R. Chair, C. L. Mak, K. F. Lee, K. M. Luk and A. A. Kishk, "Miniaturized wide-band half U-slot and half E-shaped Patch Antennas", IEEE Transactions on Antennas & Propagation, AP-53, 8, August 2005, pp. 2645 – 2652.

[5] A. K. Shackelford, K. F. Lee, K. M. Luk and R. C. Chair, "U-slot Patch Antenna with shorting pin", Electronics Letters, Vol. 37, No. 12, 7th June 2001, pp.729 – 730.

[6] C. L. Mak, R. Chair, K. F. Lee, K. M. Luk and A. A. Kishk, "Half U-slot patch antenna with shorting wall", Electronics Letters, Vol. 39, No. 25, 11th December 2003.

[7] Y. X. Guo, K. M. Luk, K. F. Lee, and R. Chair, "A Quarter Wave U-Shaped Patch antenna With two unequal arms for Wide-band and Dual-Frequency operation", IEEE Transactions on Antennas & Propagation, AP – 50, 0, August 2002, pp. 1082 – 1087.

[8] C. Y. Chiu, K. M. Shum, C. H. Chan and K. M. Luk, "Bandwidth Enhancement technique for Quarter-Wave Patch Antennas", IEEE Antennas & Wireless Propagation Letters, Vol. 2, 2003, pp. 130 – 132.

[9] C. Y. Chiu, C. H. Chan and K. M. Luk, "Small Dual band Antenna with folded Patch Technique", IEEE Antennas & Wireless Propagation Letters, Vol. 3, 2004, pp. 108 – 110.

[10] C. Y. Chiu, C. H. Chan, and K. M. Luk, "Study of small Wide-band Patch Antenna With double shorting walls", IEEE Antennas & Wireless Propagation Letters, Vol. 2, 2003, pp. 230 – 231.

[11] Amit A. Deshmukh, K. P. Ray and Ameya Kadam, "Analysis of slot cut Broadband and Dual band Rectangular Microstrip Antennas", IETE Journal of Research, Vol. 59, No. 3, May – June 2013, pp. 193 – 200

[12] IE3D 12.1, Zeland Software, Freemont, USA

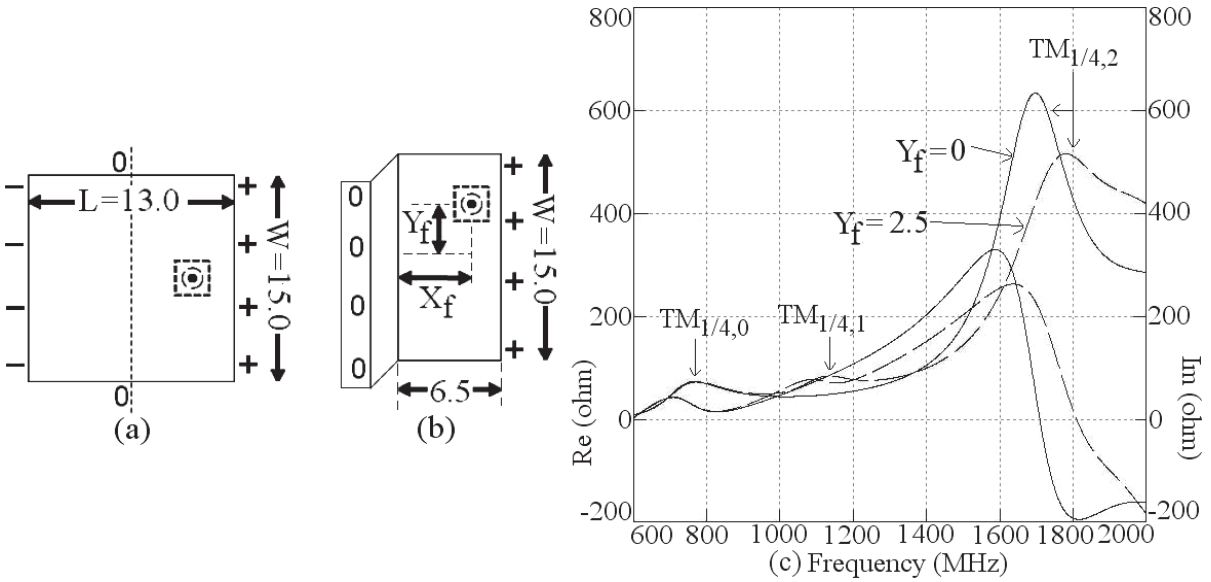

Fig. 1 Proximity fed (a) RMSA and (b) shorted plate RMSA and (c) resonance curve plots for shorted plate RMSA for different feed point locations

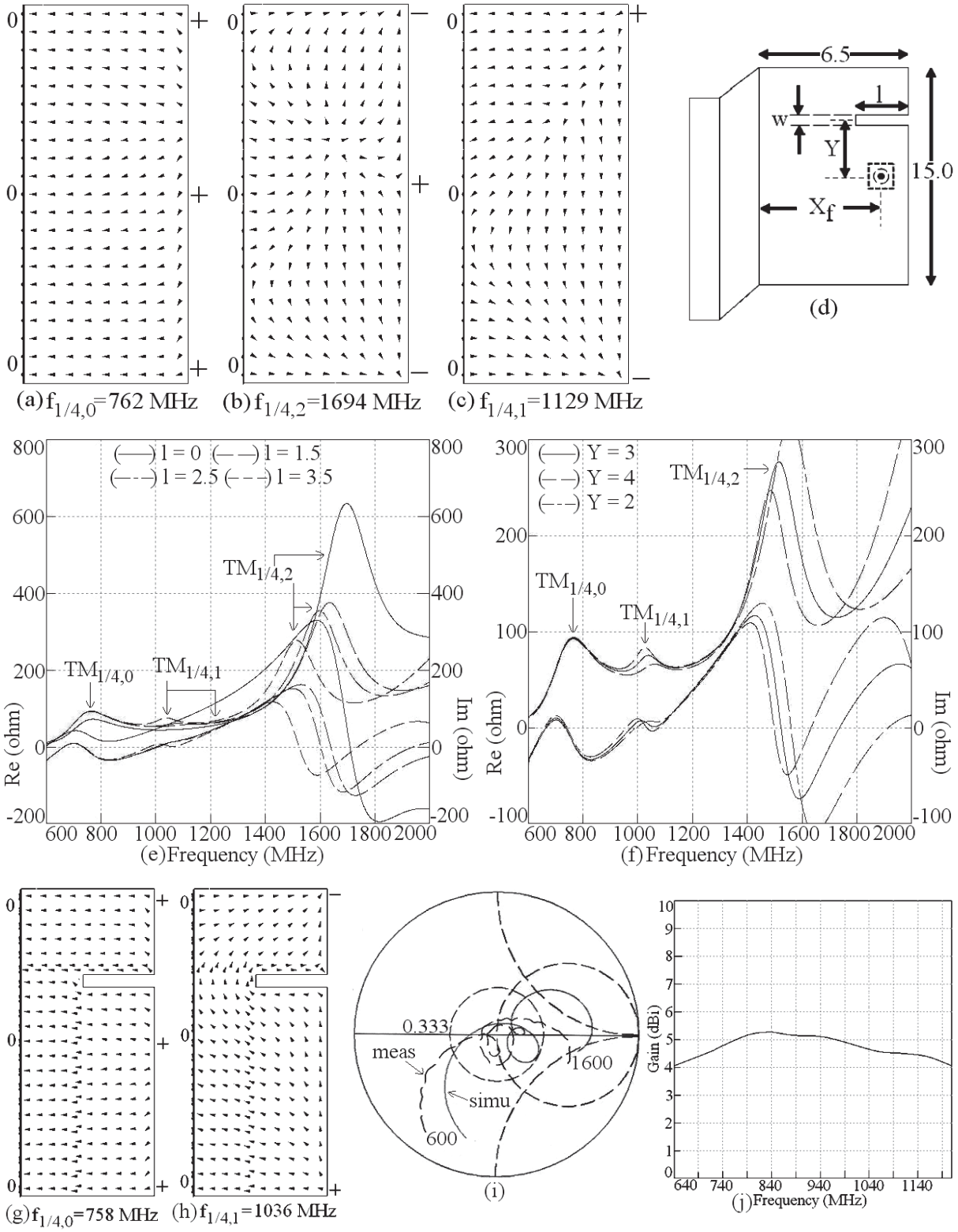

Fig. 2 (a – c) Surface current distribution at various resonant modes for shorted RMSA, (d) slot cut RMSA, its resonance curve plots for variation in (e) l and (f) Y, its surface current distribution at (g) $TM_{1/4,0}$ and (h) modified $TM_{1/4,1}$ modes for l = 3.5 cm, its (i) optimized input impedance plots (—) simulated, (– —) measured, and its (j) gain variation over BW

Broadband Sectoral Microstrip Antennas

Amit A. Deshmukh[(1)], Neelam V. Phatak [(1)], S. Nagarbowdi [(1], Kshitij Lele[(1)] and K. P. Ray [(2)]
(1) EXTC, DJSCOE, Vile – Parle (W), Mumbai, Email: amitdeshmukh76@rediffmail.com
(2) RFMS, SAMEER,IIT Campus, Powai, Mumbai, India, Email: kpray@rediffmail.com

Abstract: *Proximity fed broadband 90^0 and 60^0 Sectoral microstrip antennas are proposed. With decrease in Sectoral angle the bandwidth in Sectoral patch reduces. At fundamental mode, 90^0 and 60^0 Sectoral microstrip antenna yields bandwidth of nearly 1200 MHz (>55%) and 1000 MHz (>50%), respectively. The Sectoral antennas shows broadside radiation pattern with a gain of more than 7 dBi over the complete bandwidth.*

Introduction: The broadband microstrip antenna (MSA) is realized by fabricating the patch on lower dielectric constant thicker substrate and in most of the reported designs the patch is suspended in air thereby realizing dielectric constant of unity [1, 2]. For substrate thickness more than $0.06\lambda_0$, an impedance matching to optimize for broader bandwidth (BW) is realized by using proximity feeding technique [3]. The MSA BW is also increased by using multi-resonator configuration in which additional resonant mode is either introduced by another parasitic patch or by the slot which is cut inside the patch [4 – 9]. The realized BW depends upon the spacing between the individual resonance frequencies. The Sectoral MSA is a variation of circular MSA and without using any additional resonator the BW in Sectoral MSA is increased by varying its angle [10]. In 300^0 Sectoral MSA, angle tunes patch second order mode resonance frequency with respect to first order mode, to yield BW of more than 400 MHz (>30%), [10]. The BW of 270^0 Sectoral MSA is increased by cutting rectangular slot inside the patch. The slot tunes the spacing between first and second order mode to yield BW of more than 500 MHz (>40%) [11].

In this paper, a complementary variation of 270^0 Sectoral MSA, a broadband proximity fed 90^0 Sectoral MSA is proposed. For the proposed Sectoral MSA, the patch radius and air substrate thickness as that used in [10] and [11] are selected. First the fundamental and higher order modes of new 90^0 Sectoral MSA are studied. Due to the reduction in patch area, the fundamental mode resonance frequency in 90^0 Sectoral MSA is higher than that of the 270^0 Sectoral MSA. At the fundamental mode, 90^0 Sectoral MSA yields BW of nearly 1200 MHz (>55%) with broadside radiation pattern and gain of more than 7 dBi over most of the BW. The effect of reduction in Sectoral angle is studied. With decrease in angle from 90^0 to 60^0, the fundamental mode resonance frequency of Sectoral patch slightly reduces. This gives reduced BW nearly 1000 MHz (>50%) in proximity fed 60^0 Sectoral MSA. Further to compare the performance of 90^0 Sectoral MSA with 270^0 Sectoral MSA, 90^0 Sectoral MSA design in 1000 MHz frequency band is proposed. This proximity fed configuration yields BW of more than 600 MHz (~50%), which is more than the BW realized in 300^0 Sectoral MSA as well as the slot cut variation in 270^0 Sectoral MSA. The proposed MSAs were first optimized using IE3D software [12] on finite square ground plane of side length 30 cm. To realize higher BW and maximum radiation efficiency, MSAs were optimized on thicker air substrate ($> 0.1\lambda_0$). In measurements, MSAs were fabricated using copper plate of finite thickness and were fed using N-type connector of 0.32 cm inner wire diameter. The impedance response

was measured using R & S vector network analyzer (ZVH–8). The radiation pattern was measured using R & S RF source and spectrum analyzer with required minimum far field distance between reference antenna and antenna under test.

270^0 AND 90^0 SECTORAL MSA: The proximity fed 270^0 Sectoral MSA and its equivalent 90^0 Sectoral MSA are shown in Fig. 1(a – c). For h = 3.0 cm and h_1 = 2.8 cm, equivalent CMSA radius in 270^0 Sectoral MSA is calculated such that its TM_{11} mode frequency is around 900 MHz [1]. The radius (r) was found to be 7.0 cm. The 270^0 Sectoral MSA for r = 7 cm, is simulated over 800 to 2500 MHz frequency range and its resonance curve plot is shown in Fig. 1(d). In 270^0 Sectoral MSA, new resonant mode (f_1) is present below the equivalent TM_{11} mode of circular patch. The next modes in 270^0 Sectoral MSA are similar to TM_{11}, TM_{21} and TM_{02} modes (f_2, f_3 and f_4) of equivalent CMSA [9]. The equivalent proximity fed 90^0 Sectoral MSA is simulated over the same frequency range and its resonance curve plot is shown in Fig. 1(d). It shows peak at 1562 MHz and surface current distribution at the same is shown in Fig. 2(a). The currents show one half wavelength variations along the diagonal length inside the Sectoral patch. The next mode is present at 2581 MHz at which two half wavelength variations in currents is present along patch diagonal axis as shown in Fig. 2(b). At next higher order modes, the surface currents shows multiples of half wavelength variation along vertical and horizontal directions inside the 90^0 Sectoral MSA.

By optimizing the coupling strip position and its thickness below the 90^0 Sectoral MSA, a broader BW as shown in Fig. 2(c) is obtained. For h = 3.0 cm and h_1 = 2.5 cm, the simulated and measured BW's are, 1180 MHz (57.3%) and 1234 MHz (60%), respectively. The radiation pattern at center frequency and gain variation over the BW using square ground plane of side length 30 cm are shown in Fig. 2(d, e). Since the surface currents are varying along the diagonal axis, the E-plane is directed along $\Phi = 45^0$. The radiation pattern at center frequency and over the complete BW is in the broadside direction with gain of more than 7 dBi over most of the BW. The cross polar levels in broadside direction are less than 12 to 14 dB as compared co-polar levels. Further the effect of variation in sector angle in Sectoral MSA is investigated. With decrease in angle from 90^0 to 60^0, fundamental mode resonance frequency of Sectoral patch reduces from 1739 to 1715 MHz. The proximity fed 60^0 Sectoral MSA yields simulated and measured BW of 1020 MHz (51.8%) and 1045 MHz (52.3%), respectively. The reduction in resonance frequency and BW is due to the reduced patch area in the Sectoral configuration. Further to compare the performance of 90^0 Sectoral MSA with 270^0 Sectoral MSA, patch radius in 90^0 Sectoral MSA was increased such that its fundamental mode frequency is around 1000 MHz. For 1000 MHz and h = 3.0 cm, the patch radius was found to be 12 cm. Its simulated BW is 605 MHz (49.2%), whereas the measured BW is 612 MHz (50.4%). The realized BW in 90^0 Sectoral MSA is more than the BW obtained in 270^0 Sectoral MSA and its slot cut variation. Also 90^0 Sectoral MSA shows better radiation pattern characteristics in terms of cross polar radiation against 270^0 Sectoral MSA.

Conclusions: A new proximity fed 90^0 Sectoral MSA is proposed. For the same patch radius fundamental mode resonance frequency of 90^0 Sectoral MSA is higher than that of its complementary structure, i.e. 270^0 Sectoral MSA. The proximity fed 90^0 Sectoral MSA yields BW of around 1200 MHz (>57%) with broadside radiation pattern and gain of 7 dBi. To compare the performance with 270^0 Sectoral MSA, 90^0 Sectoral MSA is designed in 1000 MHz frequency band. It yields higher BW, better radiation pattern characteristics with nearly 50% reduction in patch area.

References:

[1] G. Kumar and K. P. Ray, Broadband Microstrip Antennas, 1st edition, Artech House, USA, 2002.

[2] R. Garg, P. Bhartia, I. Bahl and A. Ittipiboon, Microstrip Antenna Design Handbook, Artech House, USA, 2001.

[3] R. T. Cock and C. G. Christodoulou, "Design of a two layer capacitively coupled, microstrip patch antenna element for broadband applications", IEEE Antennas Propag. Soc. Int. Symp. Dig., vol. 2, 1987, 936-939.

[4] K. L. Wong, Compact and Broadband Microstrip Antennas, John Wiley & sons, Inc., New York, USA, 2002.

[5] T. Huynh and K. F. Lee, "Single-Layer Single-Patch Wideband Microstrip Antenna," Electronics Letters, vol. 31, no. 16, August 1995, pp. 1310-1312.

[6] K. L. Wong and W. H. Hsu, "A broadband rectangular patch antenna with a pair of wide slits", IEEE Trans. Antennas Propagat., vol. 49, Sept. 2001, pp. 1345 – 1347

[7] K. F. Lee, S. L. S. Yang, A. A. Kishk, and K. M. Luk, "The Versatile U-slot Patch", IEEE Antennas & Propagation Magazine, vol. 52, no. 1, February 2010, 71 – 88.

[8] Y. X. Guo, K. M. Luk, K. F. Lee and Y. L. Chow, "Double U-slot Rectangular Patch Antenna", Electronics Letters, vol. 34, 1998, 1805 – 1806

[9] S. K. Sharma and L. Shafai, "Performance of a Novel Ψ-Shaped Microstrip Patch Antenna with Wide Bandwidth", IEEE Antennas & Wireless Propagation Letters, vol. 8, 2009, pp. 468 –471.

[10] Amit A. Deshmukh, Ankita R. Jain, Apurva A. Joshi, Tejal A. Tirodkar and K. P. Ray, "Broadband Proximity fed modified Circular Microstrip Antenna", Proceedings of ICACC – 2013, 29th – 31st August 2013, Kochi, India.

[11] Amit A. Deshmukh, Ankita R. Jain and K. P. Ray, "Broadband 270^0 Sectoral Microstrip Antenna", Microwave and Optical Technology Letters, Vol. 56, No. 6, June 2014, pp. 1447 – 1449.

[12] IE3D 12.1, Zeland Software, Freemont, USA

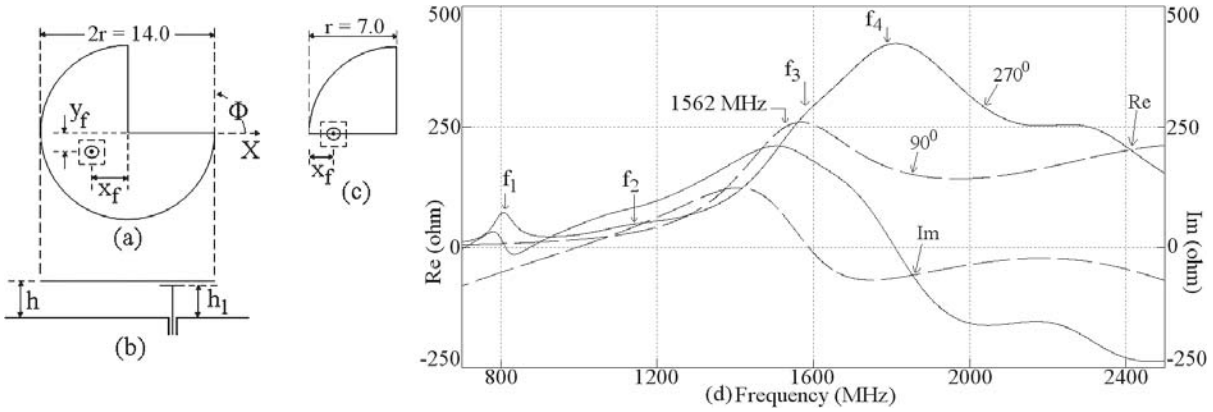

Fig. 1 (a) Top and (b) side views of proximity fed 270^0 Sectoral MSA, (c) 90^0 Sectoral MSA (d) resonance curve plots for (—) 270^0 Sectoral MSA, (— —) 90^0 Sectoral MSA

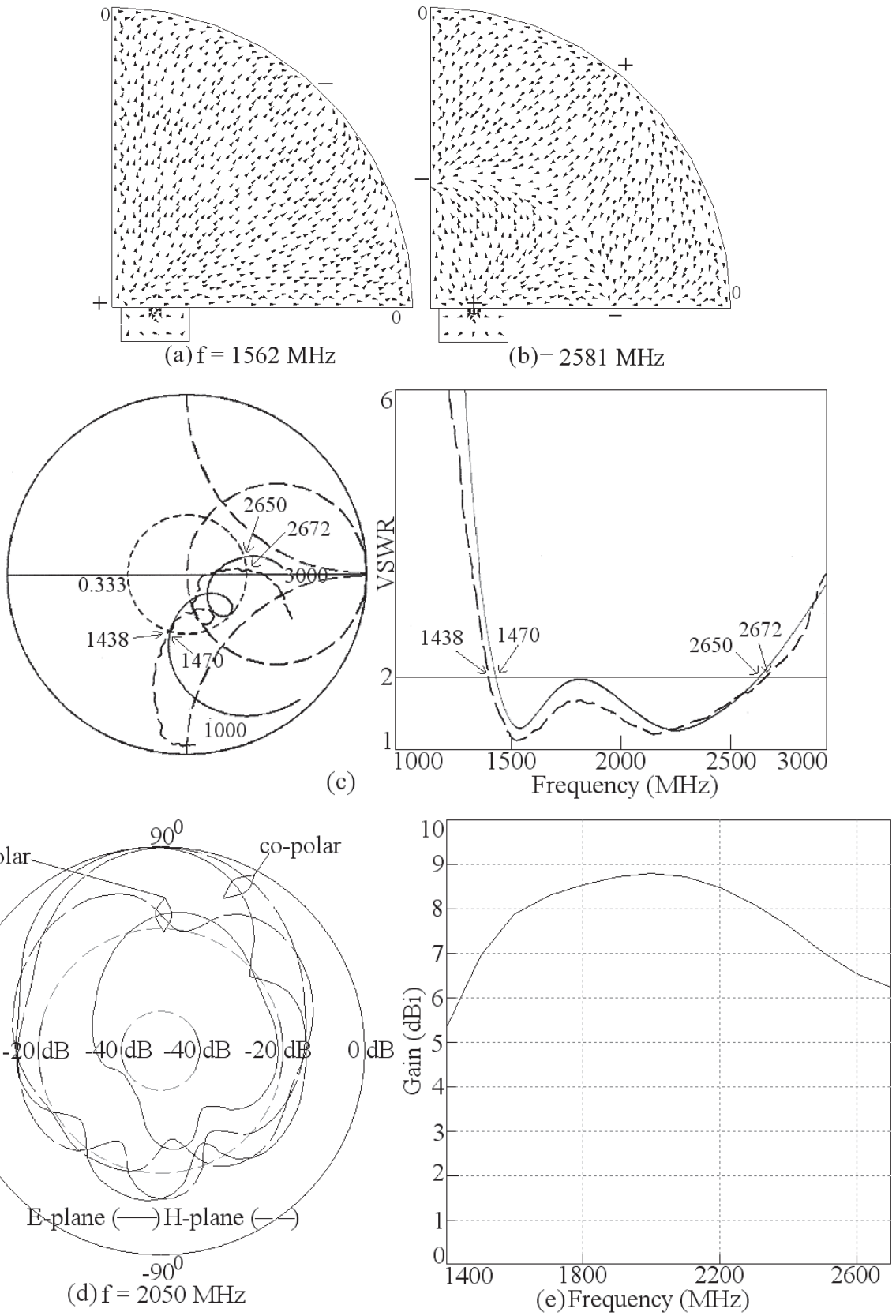

Fig. 2 (a, b) Surface current distribution at first two resonant modes for 90^0 Sectoral MSA, (c) optimized input impedance and VSWR plots for 90^0 Sectoral MSA, (——) simulated, (— —) measured, and its (d) radiation pattern at center frequency and (e) gain variation over BW

WIDEBAND CIRCULARLY POLARIZED PATCH ANTENNA FOR WIMAX APPLICATIONS

Sumitha Mathew, R.Anitha and K.Vasudevan
Centre for Research in Electromagnetics and Antennas,Dept of Electronics,
Cochin University of Science &Technology, Kochi-22, Kerala, India.
Email: vasudevankdr@gmail.com

Abstract: *A simple microstrip circular disc antenna to excite circularly polarized radiation is presented. In a single-probe fed circular disc sector patch, two corners are truncated to obtain circular polarization characteristics. The truncation helps to reduce the ground plane dimensions making the antenna more compact. The antenna is fabricated on an FR4 substrate with volume 25 mm x 30 mm x 1.6 mm.The simulated and experimental results are compared and are found to be in good agreement. The antenna resonates in the WiMAX 3.3 - 3.6 GHz band with 3dB axial ratio bandwidth of 2.3% and -10dB impedance bandwidth of 7.8 %.*

Introduction: Circularly Polarized antennas are more resistant to bad weather conditions and less sensitive to the orientation of the corresponding mobile device. These single feed antennas have simple structures requiring less board space than dual-feed circularly polarized antennas and do not require an external polarizer. Conventional designs of single-feed compact square microstrip antennas for circular polarization (CP) are usually achieved by truncating patch corners, using a nearly square patch, cutting a diagonal or cross slot in the patch and inserting slits of different lengths at the edges of the patch [l]-[4]. These CP designs usually exhibit narrow axial-ratio bandwidth (ARBW) and have stringent manufacturing tolerances. CP antennas for the WiMAX frequency band with lower ARBW values [5] - [8] have been reported. It is also found that most of these designs utilize square and circular patches. However, very few designs for achieving CP operation employing the sector shaped patch [9]-[10] are available in the open literature, although the sectoral shaped microstrip antenna has the advantage of being physically smaller at a fixed frequency, as compared to square or circular microstrip antennas.

A coaxial probe-fed circular disc sector patch antenna with truncation at the two corners is presented for WiMAX applications. The antenna exhibits wideband performance with measured values of 7.8% impedance bandwidth (BW) and 2.3 % ARBW. The simulated and measured results in terms of the return loss, axial ratio (AR) and radiation pattern are compared, and are found to agree perfectly with each other.

Antenna Geometry and Design: The geometry and photograph of the proposed antenna is shown in Fig. 1. The patch is printed on the top side of an FR4 substrate with $\varepsilon_r = 4.4$ and thickness h=1.6mm. A ground plane of size W mm x L mm covers the bottom side. The circular disc sector of radius R mm is modified by truncating two sectoral portions of radii r_1 and r_2 from corner 1 and corner 2 respectively. This forms the basic patch shape and provides the perturbation required to produce CP. Without the truncation, the impedance matching is very poor, even though CP radiation is obtained in the band. This is shown in the simulated return loss characteristics in Fig.2 (a).

The dimensions are chosen as R = 26mm, $\theta = 65^0$, r_1 = 5 mm r_2 = 1.4 mm and W = 30 mm and L = 25mm. The excitation is applied at the feed point A or B as in Fig. 1. Wide band CP operation with fundamental resonance frequency in the WiMAX band is exhibited. The coaxial-probe feed point A (x_p, y_p) is chosen along the locus of 50 Ω characteristic impedance and is adjusted for perfect matching. The coordinates of point A are obtained as x_p = 21 and y_p = 5. Point B, the mirror image of A with respect to the centre of the disc, is the feed point to obtain the opposite sense of circular polarization.The two truncations achieve a size reduction of about 3.7% of the original sectoral patch.

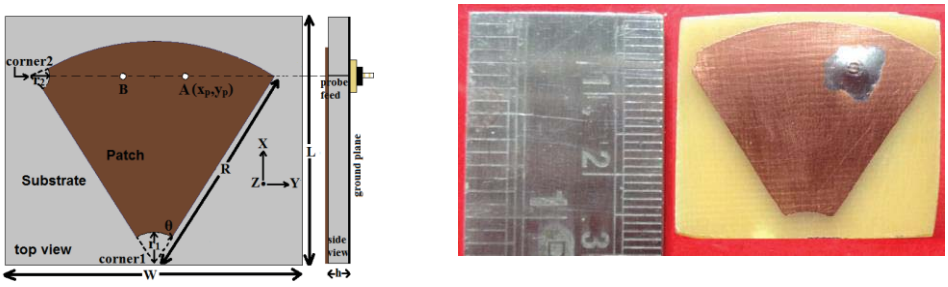

Fig. 1. Geometry and photograph of the proposed Structure

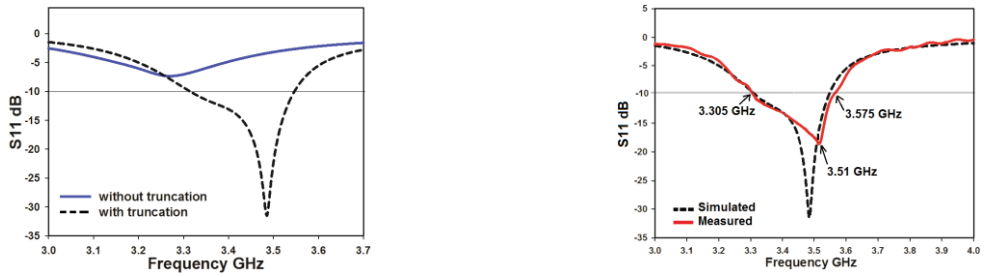

(a) (b)

Fig. 2. Return loss Characteristics of the Proposed Antenna a) Simulated S11without and with the truncation b) Simulated and measured S11 of the proposed antenna

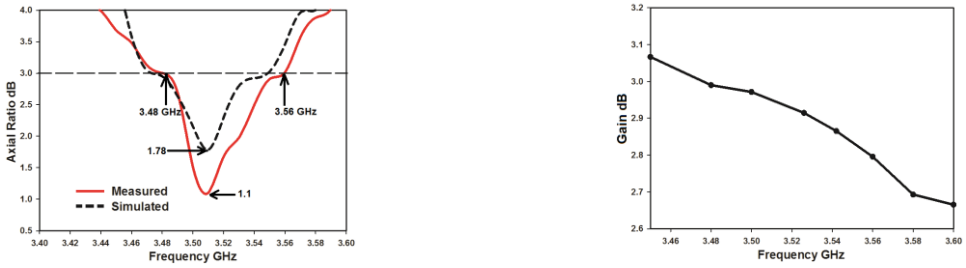

(a) (b)

Fig. 3. Characteristics of the Proposed Antenna a) Simulated and measured Axial Ratio b) Measured Gain

Simulated Results: With the excitation applied at A, the simulated -10 dB return loss characteristics are shown Fig. 2(b).The -10 dB impedance bandwidth is 3.3-3.55 GHz (250 MHz).The simulated axial ratio results in Fig.3(a) show that the -3dB ARBW is from 3.471-3.550 GHz (80MHz) at a centre frequency of 3.5 GHz. Two near-degenerate orthogonal modes TM_{01} and TM_{10} are excited here, which makes CP operation possible. The sense of polarization can be confirmed as left-handed circular polarization (LHCP) by observing the simulated current distributions on the patch at the centre frequency. The current distributions

at four different phase angles are shown in Fig 4.Simulations are performed using the Ansoft HFSS software.

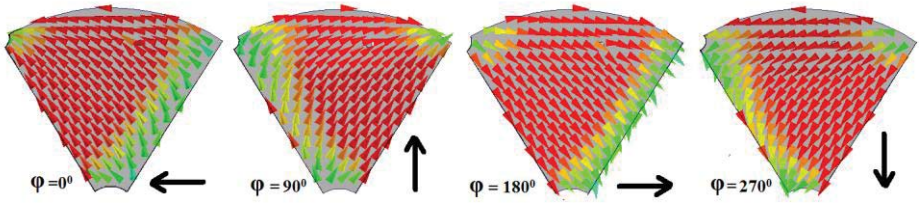

Fig. 4.Simulated current distribution on the patch for Left Hand Circular Polarization at 3.51 GHz.

Experimental Results: The prototype of the structure was fabricated by the conventional photolithographic procedure and tested using the PNAE8362B Vector Network Analyzer and Anechoic Chamber. With the feed applied at A, the return loss was measured and the results are shown in Fig. 2(b).The measured total bandwidth is 270 MHz. It is observed that the simulated and measured results are in good agreement with each other.

Radiation Patterns in two orthogonal planes were also measured in the Anechoic Chamber. The measured Co-Polarization and Cross-Polarization patterns in two orthogonal planes (E plane and H Plane) are shown. Good LHCP radiation is obtained at a CP centre frequency (defined as the frequency with the minimum AR value) of 3.51 GHz and is represented in Fig. 5.The axial ratio was also experimentally measured and the comparison with the corresponding simulated results are shown in Fig. 3(a).The measured and simulated results closely agree with each other. The measured peak gain of the antenna is 3.08 dB in the CP bandwidth as shown in Fig. 3(b).

(a) (b)

Fig. 5.Measured Radiation Patterns for LHCP at 3.51 GHz in two orthogonal Planes a) E-Plane b) H-Plane

TABLE I.COMPARISON WITH EXISTING STRUCTURES

Parameter	Proposed antenna	Triband Koch Fractal boundary microstrip[5]	Dual-band U-slot [6]	Dual-band stacked patch asymmetric U slot[7]	Wideband with vortex slots and shorting vias [8]
Impedance BW (%)	7.8	2.4	7.5	3	51.7
ARBW (%)	2.3	1.6	0.7	1	57.8
Peak Gain (dB)	3.08	4.5	8.5	6.2	1
Feed Method	Coaxial Probe	Coaxial Probe	Coaxial Probe	Coaxial Probe	Coaxial Probe disk loaded
Distinguishing technique	Corner truncation	Fractal slot boundary	U slot	Stacked patch	Shorting vias & vortex slots

Comparison with existing structures: Table I expresses the comparison of the proposed antenna with some of the important works related to CP performance in the WiMAX frequency range. The parameters compared are -10 dB return loss bandwidth, ARBW, Peak gain achieved, feed method and the distinguishing technique or feature applied in each work. The proposed structure has improved performance in terms of total bandwidth and ARBW when compared to [5], [6] and [7].The peak gain realized is also reasonably good, even though lesser than those of the three structures, but greater than that for [8].

Conclusion: A single feed wide band antenna with a simple sector shaped patch has been proposed and experimentally analyzed. The antenna resonates in the WiMAX band with circular polarization of 2.3% axial ratio bandwidth. The patch size reduction is 3.7% on comparison with the untruncated sectoral patch. No external perturbation elements or shorting pins need to be employed. The structure can be made further compact by the use of slots.

Reference:

[1] Sharma, P.C., and Gupta, K.C., "Analysis and optimized design of single feed circularly polarized microstrip antennas", IEEE Transactions On Antennas And Propagation., Vol.29, pp. 949-955, 1983..

[2] Kin-Lu Wong and Yi-Fang Lin, "Circularly polarized microstrip antenna with a tuning stub", Electronics Letters ,Vol. 34 No. 9, pp. 831-832, 1998.

[3] H. Iwasaki, "A circularly polarized small-size microstrip antenna with a cross slot," IEEE Transactions on Antennas and Propagation, Vol. 44, pp. 1399–1401, 1996.

[4] Wen-Shyang Chen,Chun-Kun Wu, and Kin-Lu Wong, "Novel Compact Circularly Polarized Square Microstrip Antenna", IEEE Transactions On Antennas And Propagation, Vol. 49, No. 3, 2001.

[5] V. V. Reddy and N. V. S. N. Sarma, "Triband Circularly Polarized Koch Fractal Boundary Microstrip Antenna", IEEE Antennas and Wireless Propagation Letters, Vol. 13, pp. 1057–1060, 2014

[6] Shuo Liu, Shi-Shan Qi, Wen Wu, and Da-Gang Fang, "Single-Fed Dual-Band Dual-Polarized U-Slot Patch Antenna", Proceedings of IEEE MTT-S International Microwave Workshop Series on RF and Wireless Technologies for Biomedical and Healthcare Applications (IMWS-BIO) 2013.

[7] Payam Nayeri, Kai-Fong Lee, Atef Z. Elsherbeni and Fan Yang, "Dual-Band Circularly Polarized Antennas Using Stacked Patches With Asymmetric U-Slots", IEEE Antennas And Wireless Propagation Letters, Vol. 10, pp. 492-495,2011

[8] Dan Yu, Shu-Xi Gong, Yang-Tao Wan, Ya-Li Yao, Yun-Xue Xu, and Fu-Wei Wang Wideband Omnidirectional Circularly Polarized PatchAntenna Based on Vortex Slots and Shorting Vias IEEE Transactions On Antennas And Propagation, Vol. 62, No. 8, August 2014.

[9] Wen-Hsiu Hsu and Kin-Lu Wong,"Circularly-polarised disk-sector microstrip antenna", Electronics Letters, Vol. 34, No. 23, pp. 2188–2190, 1998

[10] Sumitha Mathew, R. Anitha, T. K. Roshna, C. M. Nijas, C. K. Aanandan, P. Mohanan and K. Vasudevan, "A Fan-shaped circularly polarized patch antenna for UMTS band", Progress In Electromagnetics Research C, Vol. 52, pp.101-107, 2014.

A Compact Low Frequency Zeroth Order Resonant Antenna

Basil J. Paul[(1)], S. Mridula[(2)], and P. Mohanan[(3)]
(1) School of Engineering, CUSAT, Cochin, India, 682022, Email: basiljpaul@gmail.com
(2) School of Engineering, CUSAT, Cochin, India, 682022, Email: mridula@cusat.ac.in
(2) Dept. of Electronics, CUSAT, Cochin, India, 682022, Email: drmohan@cusat.ac.in

Abstract: *A highly miniaturized Zeroth Order Resonant (ZOR) antenna loaded with chip inductor is presented. The ZOR property of the antenna is confirmed by adding additional unit cells on to the basic structure and observing its resonant frequency. The resonance of the antenna is contributed by the shunt inductor and capacitor. The measured resonant frequency of the antenna is 429MHz.The measured gain of the unit cell antenna is -7.5dBi. The return loss characteristics and radiation pattern of the antenna are also presented in this paper.*

Introduction: Antenna miniaturization is an interesting topic among RF Engineers. Successful implementation of this paves way to extremely small hand held devices. Commonly used methods for achieving compactness is by using monopole geometry [1], meander line structures [2], spiral geometry [3], and by using slots [4]. Most of these antennas reported have their resonant frequency in GHz range. Only few works have been reported on antennas that work in low frequencies of the order of few MHz [5] – [6]. But the major drawback of such antennas is the increased size. This paper presents a metamaterial inspired compact antenna loaded with chip inductor that resonates at 429MHz.

Theory: This paper describes an antenna that uses the concept of zeroth order resonance (ZOR) of metamaterials. The concept of ZOR can be easily understood from the dispersion diagram or ω-β diagram of a composite right/left handed transmission line (CRLH-TL) shown in Fig.1 [7]. The ω-β plot is non-linear for CRLH-TL and a non-zero resonant frequency exists at β = 0. This resonant frequency is known as zeroth order resonance frequency. From the curve, it is clear that the electrical length can be zero and negative for a CRLH TL. The advantage of ZOR is that it is possible to design size independent resonators using this concept.

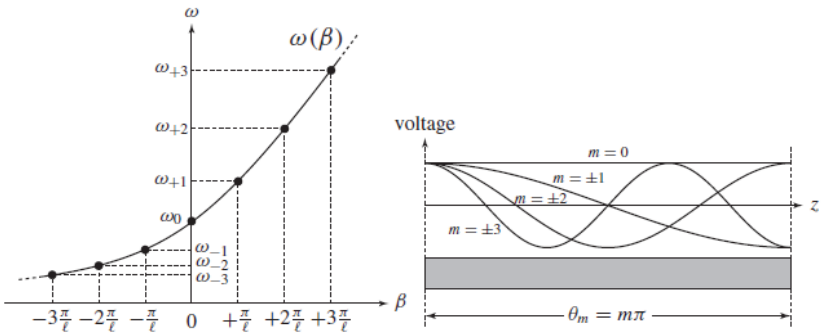

Fig. 1 Dispersion diagram of CRLH transmission line

Geometry: The proposed antenna is derived from an open ended transmission line whose resonant frequency is determined by shunt inductance and capacitance. The shunt inductance is formed by using a chip inductor. The inductor used is 0603HP series 72nH coil wound chip

inductor by Coilcraft Inc. The inductor is selected in such a way that the self resonant frequency of the chip inductor is less than the operating frequency. The shunt capacitance is formed by the distributed capacitance of a patch of size 14mm x 5.5mm. The structure of unit cell antenna is shown in Fig.2. The overall size of the unit cell antenna is only 39mm x 23mm. The antenna is fed with a coplanar waveguide (CPW) feed. The length of the feed is extended by 5mm in order to add additional units on to the unit cell antenna. The CPW fed antenna has a truncated conductor backing on the bottom plane. The width of the conductor backing is 14mm, which is optimized for better impedance matching. The antenna is fabricated on a substrate with $\varepsilon_r = 4.4$, $\tan\delta = 0.02$ and thickness 1.6mm.

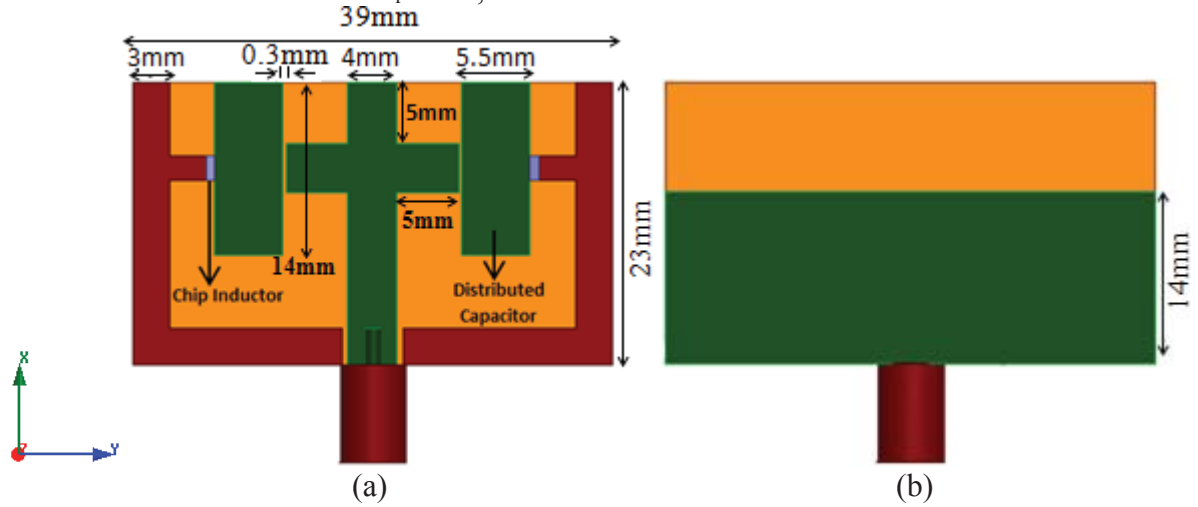

Fig. 2 Structure of unit cell antenna (a) Top plane (b) Bottom plane

The ZOR property of the antenna is confirmed by adding additional cells on to the unit cell. The property that the resonant frequency should be independent of antenna dimensions is being validated here. The higher order structures of the antenna are shown in Fig.3. These higher order structures are designated as 2x2, 3x2 and 4x2. The bottom ground plane is kept as such while adding additional units. The width of the unit cell antenna is optimized to 23mm so as to achieve ZOR.

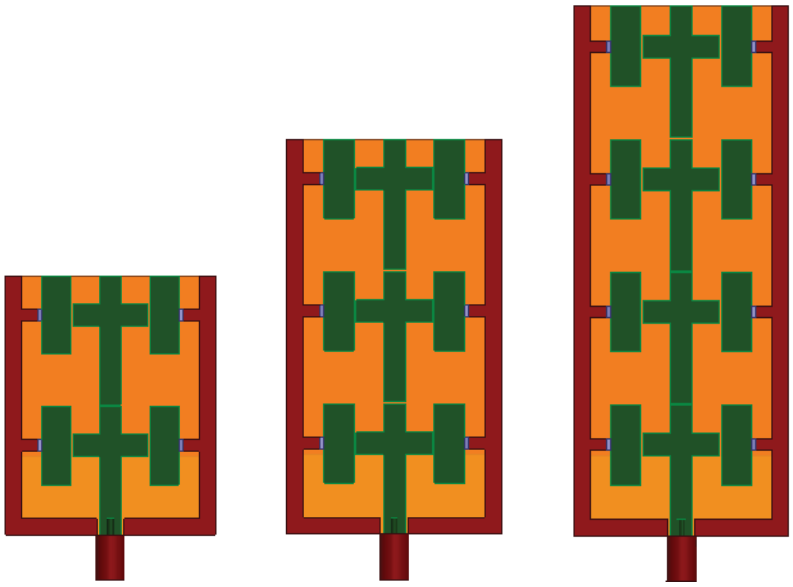

Fig. 3 Higher order structures of the antenna

Results and Discussions: The simulated and measured resonant frequency of the antenna is 393MHz and 429MHz respectively. The difference in simulated and measured characteristics

is due to the non-ideal nature of the chip inductor used. The return loss characteristics of the antenna is shown in Fig.4. It can be observed from return loss characteristics that the change in resonant frequency with the addition of unit cells is negligible. Hence the antenna resonates very close to the zeroth order resonance. In all the cases the antenna is well matched with a return loss less than -10dB. A total size reduction of 97% is achieved with respect to a conventional patch antenna at 429MHz.

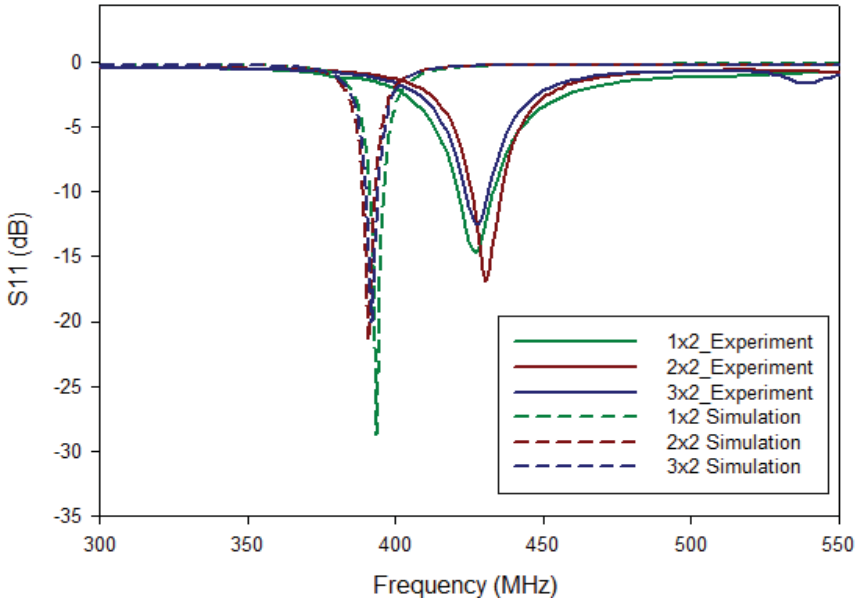

Fig. 4 Simulated and measured return loss characteristics

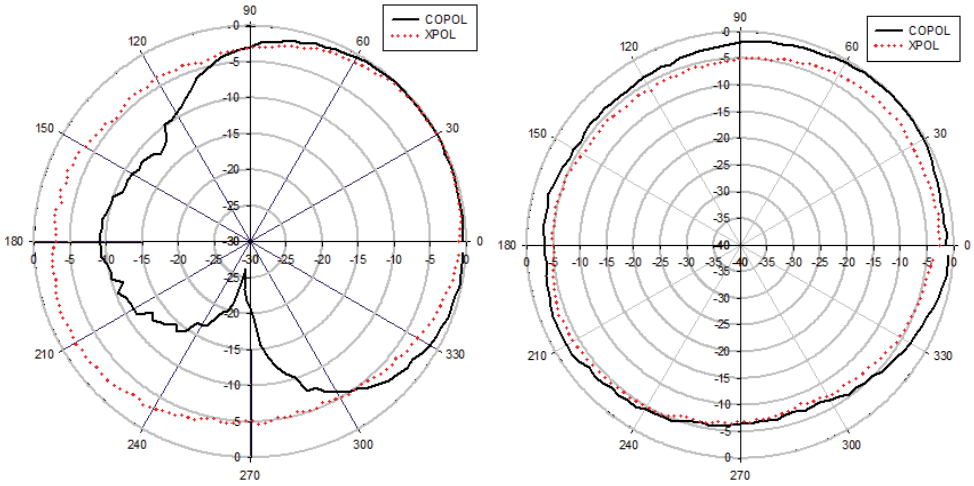

(a) (b)

Fig. 5 Measured radiation pattern of the antenna (a) y-z plane (b) x-z plane

A transmission peak of -32dB is observed at 429MHz which indicates a maximum transfer of energy at resonant frequency from the transmitter to receiver. The measured -10dB bandwidth of the antenna is 11MHz. Hence the bandwidth of the antenna is less. The small bandwidth is attributed to the inherent high Q nature of metamaterial based structures.

The measured radiation pattern of the antenna at 429MHz is shown in Fig.5. From the radiation pattern plots it is evident that the antenna exhibits omnidirectional pattern. The gain of the antenna is measured using three antenna method. The measured gain of the 1x2, 2x2, 3x2 structures are -7.5dBi, -10.2dBi, -10.7dBi respectively. The low gain of the antenna is due to the small size of the antenna, lossy nature of chip inductor used and also due to the substrate losses.

Table 1 gives a comparison of the proposed antenna with other compact antennas already reported in literature. Although the gain of the proposed antenna is low, the size is made much compact by using chip inductor and by applying ZOR concept without using vias to bottom ground plane.

Table. 1 Comparison of proposed antenna with other compact antennas

Parameter	Proposed Antenna	[3]	[8]	[9]
Frequency	429 MHz	4.35 GHz	2.66 GHz	0.96 GHz
ε_r	4.4	4.4	3.5	4.4
Size (mm^3)	39 x 23 x 1.6	10 x 10 x 1.6	40 x 40 x 1.52	11.25 x 13.8 x 1.55
Bandwidth	2.5%	1.2%	12.4%	Not specified
Gain	-7.5dBi	Not specified	1.3dBi	-12.75dBi
Via process	Not required	Not required	Not required	Required

Conclusion: A compact low frequency antenna is presented in this paper. The usage of chip inductor provides another degree of freedom for miniaturization in addition to using ZOR concept for designing the antenna. The price paid for size reduction is the reduced gain and bandwidth of the antenna. Hence the antenna can be further modified for improving the gain and fractional bandwidth. The antenna size can be further reduced by performing rigorous parametric analysis. By introducing slight modifications, antenna can be made suitable for devices working in low frequency bands such as medical implant communication band (402 – 405MHz) and DVB-H band (470 – 862MHz).

Acknowledgements: The authors would like to thank Kerala State Council for Science Technology and Environment (KSCSTE) for providing financial assistance for this research work as per Council File No. 03/FSHP/2013/CSTE, dated 10/01/2014.

Reference:

[1] C. F Tseng, C. L Huang, C. H Hsu, "Microstrip-fed monopole antenna with a shorted parasitic element for wideband application", Progress In Electromagnetics Research Letters, Vol. 7, pp. 115 – 125, 2009.

[2] Xiao-Chuan Wang, Wen-Zhong Lu, Fei Liang, Shuai Wan, "Nonuniform meander-line monopole antenna with back-coupled patch for WLAN applications", International Conference on Microwave and Millimeter Wave Technology, pp. 348 – 351, 2010.

[3] Anju Pradeep, S Mridula, P Mohanan, "Metamaterial based all purpose sensor antenna", International Journal on Communications Antenna and Propagation, Vol. 03, No. 03, pp. 181 – 184, 2013.

[4] J. J Jiao, G Zhao, F. S Zhang, H. W Yuan, Y.C Jiao, "A broadband cpw-fed T-shape slot antenna", Progress In Electromagnetics Research Letters, Vol. 76, pp. 237 – 242, 2007.

[5] C. Y Huang, B. M Jeng, C. F Yang, "Wideband monopole antenna for DVB-T applications", Electronics Letters, Vol. 44, No. 25, pp. 1448 – 1450, 2008.

[6] Matthias John, Max Ammann, "A compact shorted printed monopole antenna for TV white space trials", European Conference on Antennas and Propagation, 2013.

[7] Christophe Caloz, Tatsuo Itoh, "Electromagnetic Metamaterials: Transmission line theory and Microwave applications", John Wiley & Sons, 2006.

[8] M. S Majedi, A. R Attari, "A compact and broadband metamaterial inspired antenna", IEEE Antennas and Wireless Propagation Letters, Vol. 12, pp. 345 – 348, 2013.

[9] Renato Silveira Feitoza, Fernando Rangel de Sousa, "A highly miniaturized patch antenna based on zeroth order resonance", Microwave & Optoelectronic Conference (IMOC), pp. 1 – 5, 2013.

Metamaterial Loaded High Gain Smiley Antenna

Gurveer Kaur [(1)], Balwinder S. Dhaliwal [(1)], and Shyam S. Pattnaik [(2)]

(1) Guru Nanak Dev Engineering College, Ludhiana, India, 141006, Email: c_kgurveer@yahoo.in

(2) National Institute of Technical Teachers Training and Research, Chandigarh.
profshyampattnaik@gmail.com

Abstract- *This paper presents linearly polarized rectangular smiley antenna loaded with metamaterial split ring resonator (SRR) for wearable applications. Slots are etched in simple rectangular patch in the form of eyes and smile to form rectangular smiley antenna. Initially rectangular microstrip patch antenna resonates at 10 GHz. The slotting results in dual band resonance at 5.24 GHz and 9.56 GHz. The SRR loading of rectangular smiley antenna enables the antenna to resonate at 4.46 GHz and 5.31 GHz with enhanced gain and directivity due to metamaterial resonance. The gain is enhanced from 1.38 dBi to 4.82 dBi and directivity too is improved from 1.71 dBi to 5.08 dBi at lower resonant frequency of 4.46 GHz. The size of the metamaterial loaded antenna is reduced by 49.3% for 4.46 GHz frequency.*

I. Introduction

A wearable antenna is considered to be a part of clothing used for communication purposes, which includes medical field, tracking, military, navigation and public safety [1]. Currently much interest is taken in body-worn communication systems for detecting motion on the body during exercise, monitoring functions such as pulse rate and blood pressure, use by the emergency services, and for general network connection [2]. Regardless of the application area, an important aspect of wearable communications is the preservation of antenna performances, yet antennas must be small, light weight, least affected by human body, unobtrusive to the users and ideally comfortable to the body [3]. Recently, metamaterial which is an artificially engineered material possessing negative permeability and/or negative permittivity is used to improve gain, bandwidth, directivity and efficiency of antenna [4]. While the anomalous electromagnetic features of the negative index medium were predicted by Veselago in 1968 [5], it took over thirty years to experimentally verify the feasibility of an artificial negative index medium [6].
In [7], Jaegeun et al. reported an antenna loaded with circular SRR achieving maximum frequency drift from 5 GHz to 4.5 GHz and antenna gain improvement from 2.36 dBi to 3.85 dBi. In [8], Joshi et al. presented a square slotted antenna that resonates at 8.45 GHz with gain of 4 dBi. Upon loading the antenna with square SRR, the lower resonant frequency is obtained at 4.94 GHz. To shift this resonance to 5 GHz applications, a shorting pin of 0.5 mm radius is diagonally inserted in the radiating patch and antenna gain improves to 5 dBi.
In this paper, rectangular SRR is used to load the rectangular smiley antenna as superstrate around the patch to achieve high gain and reduced size.

II. Proposed Antenna Design

The antenna design is divided into three steps—(a) design and simulations of rectangular microstrip patch antenna (b) making rectangular smiley by etching out slots in the rectangular

patch to excite the desired lower resonant frequency for size reduction (c) loading the designed metamaterial SRR to the rectangular smiley antenna.

Fig. 1(a) depicts the geometrical structure of metamaterial loaded rectangular smiley antenna. The rectangular smiley antenna is obtained by etching out slots in the form of eyes and smile. The dimensions of the antenna are; length L = 20mm and width W = 15mm. Slotting is done to achieve frequency drift towards lower resonant frequency which assists in antenna miniaturization. The optimum dimensions of eye slot length, eye slot width, smile slot length and smile slot width for maximum drift are calculated using trial and error method as 4.5 mm, 3.375 mm, 10 mm and 3.375 mm respectively. The dimensions of SRR are; length L_m = 40 mm, W_m = 30 mm, width of the ring 'w' spacing 's' between the adjacent rings and gap at the splits 'g' are; w = s = 2mm, g = 1 mm respectively. RT Duroid substrate of thickness h = 0.787 mm and dielectric constant (ε_r) = 2.2 is used to simulate the antenna. In this work the HFSS simulator is used.

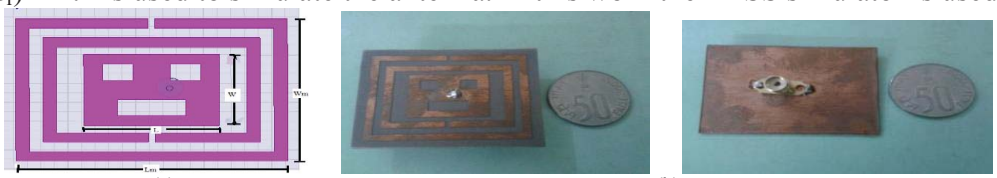

(a) (b)

Fig. 1: Metamaterial Loaded Rectangular Smiley Antenna. (a) Geometrical Structure (b) Photograph (Top View and Ground Plane view).

Fig. 1(b) depict the photographs of radiating patch and ground plane with SMA connector of the fabricated metamaterial SRR loaded wearable rectangular smiley antenna.

III. Results and Discussions

Initially, the metamaterial characteristics of the SRR are verified before analyzing its loading effect on the proposed rectangular smiley antenna. Fig. 2 (a) depicts the reflection coefficient (S_{11}) and transmission coefficient (S_{12}) of the proposed metamaterial structure. The characteristics show that the structure exhibits metamaterial behaviour and shows the phase reversal properties of +180º and -180º within the resonant frequency band of 5.0253 GHz as shown in Fig. 2(b).

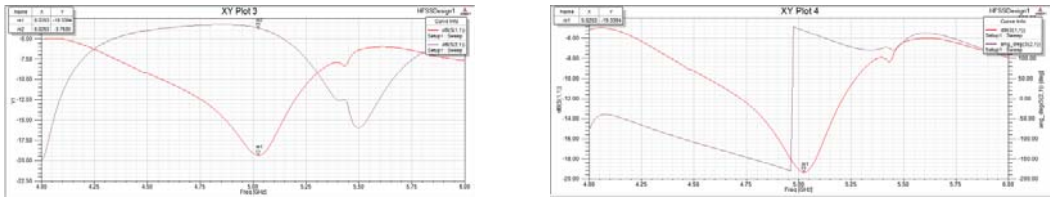

(a) (b)

Fig. 2: (a) Reflection and Transmission Characteristics of Proposed Metamaterial Structure. (b) Phase Reversal Characteristics of Proposed Metamaterial Structure.

The effective medium theory is used to extract the permeability (μ) and permittivity (ε) from the S-parameters using Nicolson-Ross- Weir (NRW) approach [9]. In this approach the metamaterial characteristics are verified using equation (1) to (3) given below:

$$V1 = S_{21} + S_{11} \quad (1)$$

$$V2 = S_{21} - S_{11} \quad (2)$$

$$\mu_r = \frac{2}{jkd}\frac{1-V2}{1+V2} \qquad (3)$$

Where k is wave number, d is the thickness of substrate, V1 and V2 are the composite terms to represent the addition and subtraction of the S-parameters. The graph shown in Fig. 3 signifies the negative permeability characteristics of the metamaterial structure. The retrieved parameters of the antenna show broadband negative permeability since the multiple slots have improved the bandwidth. As such it is not so broad as compared to S_{11} achieved for the antenna.

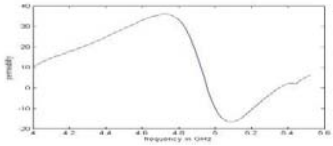

Fig. 3: Relative Permeability Characteristics of SRR Structure.

Fig. 4(a) depicts the simulated S_{11} characteristics of rectangular microstrip patch antenna and rectangular smiley antenna. The simple rectangular patch antenna resonates at 9.98 GHz with S_{11} parameters -17.89 dB having a gain and directivity of 2.79 dBi and 2.72 dBi respectively. The rectangular smiley antenna resonates at 5.24 GHz and 9.56 GHz with S_{11} parameters -21.74 dB and -17.17 dB respectively. The gain and directivity at 5.24 GHz is 1.38 dBi and 1.71 dBi respectively and the same at 9.56 GHz is 1.83 dBi and 1.91 dBi respectively. Fig. 4(b) shows the S_{11} parameter under loaded conditions which depicts that the antenna resonates at 4.46 GHz and 5.31 GHz with S_{11} parameters -20.70 dB and -20.71 dB respectively. The gain and directivity at 4.46 GHz is 4.82 dBi and 5.08 dBi respectively and the same at 5.31 GHz is 5.84 dBi and 5.96 dBi respectively. The gain plots of the antenna under loaded conditions are shown in Fig. 5. The two symmetric notches in the azimuth plane pattern are due to complementary opposite arms of SRR that cancel in x-y planes. The results are presented in Table 1.

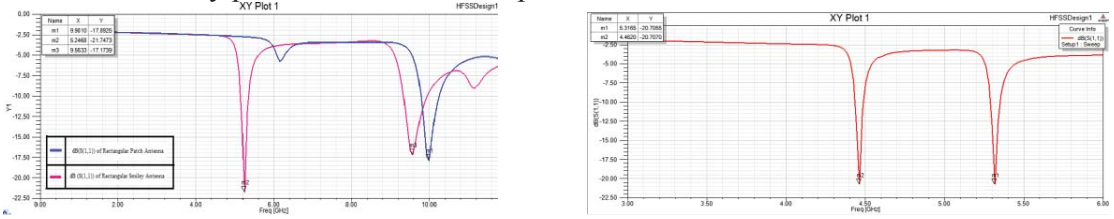

(a) (b)

Fig. 4: (a) Return Loss Obtained from Rectangular Microstrip Patch Antenna and Rectangular Smiley Antenna. (b) Return Loss Obtained from Rectangular Smiley Antenna Loaded with Metamaterial.

(a) (b)

Fig. 5: Gain Obtained from Metamaterial Loaded Rectangular Smiley Antenna (a) Azimuth (b) Elevation.

Table 1: Performance Comparison of Rectangular Smiley Antenna under unloaded and loaded conditions

Structures / Parameters ⇨ ⇩	f_{r1} (GHz)	f_{r2} (GHz)	S_{11} at f_{r1} (dB)	S_{11} at f_{r2} (dB)	Gain at f_{r1} (dBi)	Gain at f_{r2} (dBi)	Directivity at f_{r1} (dBi)	Directivity at f_{r2} (dBi)
Rectangular Smiley Antenna	5.24	9.56	-21.74	-17.17	1.38	1.82	1.71	1.91
Metamaterial Loaded Rectangular Smiley Antenna	4.46	5.31	-20.70	-20.71	4.85	5.91	5.08	5.96

In order to verify the antenna performance experimentally, the fabricated antennas are tested using Rohde & Schwarz (R & S) ZVL Network Analyzer as shown in Fig. 6. The measured resonant frequencies are 4.554 GHz and 5.28 GHz. So, the simulated and experimental results are in good agreement, which indicates that only small amount of waves are reflected back to the source and most of the power is radiated from the patch.

(a) (b)

Fig. 6: (a) Photograph of Experimental Set-up. (b) Measured Return Loss of Metamaterial Loaded Rectangular Smiley Antenna.

IV Conclusion

In this paper metamaterial loaded wearable antenna has been developed. Slotting and metamaterial loading achieves frequency drift from 10 GHz to 4.46 GHz antenna assisting in antenna miniaturization. In terms of radiation patterns, after loading the proposed antenna with metamaterial structure it is observed that the gain is enhanced from 1.38 dBi to 4.82 dBi and directivity too is improved from 1.71 dBi to 5.08 dBi at lower resonant frequency of 4.46 GHz. Comparing the theoretically calculated antenna size at 4.46 GHz with the designed antenna size, it is observed that the designed antenna size is reduced by 49.3%.

References

1. N.H.M. Rais, P.J. Soh, F. Malek, S. Ahmad, N.B.M. Hashim and P.S. Hall, "A Review of Wearable Antenna", *Proceedings of Loughborough Antennas & Propagation Conference (LAPC 2009)*, Loughborough, 2009, pp. 225-228.
2. S. Rao, N. Llombart, E. Moradi, K. Koski, T. Bjorninen, L. Sydanheimo, J. M. Rabaey, J. M. Carmena, Y. Samii and L. Ukkonen, "Miniature Implantable and Wearable On-Body Antennas: Towards the New Era of Wireless Body-Centric Systems", *IEEE Antennas and Propagation Magazine*, vol. 56, 1, pp. 271-291, 2014.
3. H. Wang, Z. Zhang, Y. Li and Z. Feng, "A Dual-Resonant Shorted Patch Antenna for Wearable Application in 430 MHz Band", *IEEE Transactions on Antennas and Propagation*, vol. 61, 12, pp. 6195-6200, 2013.
4. J.B. Pendry, A.J. Holden, D.J. Robbins and W.J. Stewart, "Magnetism from Conductor and Enhanced Non-Linear Phenomena", *IEEE Transaction on Microwave Theory & Techniques,* vol. 47, 11, pp. 2075-2084, 1999.
5. V.G. Veselango, "Electrodynamics of Substances with Simultaneously Negative Values of ε and μ", *Soviet Physics Uspekhi*, vol. 10, 4, pp. 509-514, 1968.
6. D.R. Smith, W.J. Padilla, D.C. Vier, S.C. Nasser and S. Schultz, "Composite Medium with Simultaneously Negative Permeability and Permittivity", *Physical Review Letters 1*, vol. 84, 18, pp. 4184-4187, 2000.
7. H. Jaegeun, K. Kwon, Y. Lee and J. Choi, "Hybrid Mode Wideband Patch Antenna Loaded with a Planar Metamaterial Unit Cell", *IEEE Transactions on Antennas and Propagation,* vol. 60, 2, pp. 1143-1147, 2012.
8. J.G. Joshi, S.S. Pattnaik and S. Devi, "Metamaterial Loaded Square Slotted Dual Band Microstrip Patch Antenna", *Proceedings of IEEE Applied Electromagnetic Conference (AEMC-2011),* Kolkata, 2011, pp. 1-4.
9. R.W. Ziolkowski, "Design, fabrication, and testing of double negative metamaterials", *IEEE Transactions on Antennas and Propagation,* vol.51, 7, pp. 1516-1529, 2003.

Isolation Enhancement Using Thin Wire Metamaterial for Closely Spaced Microstrip Antenna

A.Nilam.T.Kadam[1], B.Kiran.S.Janwalkar[1], C.Anuja.A.Odhekar[1]

D.J.Sanghvi College of Engineering, Mumbai. India-400056, Email-id:-anuja.odhekar@djsce.ac.in

Abstract: *Miniaturization is very important in today's modern wireless communication systems and to achieve this, physical separation between transmitting and receiving antenna has to be as low as possible for trans-receiver system. This introduces mutual coupling between the two antennas due to surface wave interference and near field radiations when both antennas shares common ground plane. This degrades antenna performance. The paper suggests a technique to improve electrical isolation between two patch antennas sharing common ground and separated by distance of λ/24. Thin wire (TW) metamaterial (MTM) which exhibits negative permittivity. Plasma frequency for TW was same as resonance frequency of patch. At this frequency direction of propagation is reversed. Thus it can be used as electrical insulator to surface waves and near field radiations. An array of TW MTM had been inserted at the center of two patches. Insertion of TW array enhances the isolation between closely spaced patches. This reduces mutual coupling due to surface waves. Thus 10 to 12 dB improvement in isolation had been observed. This had improved antenna parameters such as impedance bandwidth and antenna efficiency. There is no improvement in radiation pattern. One more TW array of the same dimensions had been inserted at the radiating edge of the one patch. Number of unit cell of TW in both array had been kept same. Insertion of this TW array results in overall improvement of 20 dB isolation. This improves radiation pattern and antenna gain. Also simulations had been carried out for various positions for TW array. Results for all these configurations had been compared. Increase in number of TW array does not affect antenna parameters and isolation as compare to configuration in which one array is placed at the center and another array is placed at the radiating edge of single patch. Thus this configuration can be the optimized one as compared with other configurations. This configuration was fabricated and measurements were carried out. Hence close resemblance had been observed between experimental and simulated results and was within tolerable engineering limits. Simulated and experimental results show that insertion of TW array enhances isolation almost 20dBs. Enhancement in isolation improves antenna impedance bandwidth. Also this improves radiation pattern. This also results in improvement in gain. Thus placement of TW array enhances isolation due to which improvement in antenna parameters had been observed. This allows close placement of microstrip antenna elements. Limitation of suggested technique is that range of frequencies over which isolation enhancement was obtained is narrow.*

Introduction: Increase in Mutual coupling for patch antennas due to less physical distance between them affects sensitivity and selectivity of trans-receiver system. The paper suggests a technique to reduce mutual coupling between two closely spaced patch antennas. Proposed antenna structure is composed of two Microstrip antennas occupying a space with the dimensions of 85.2mm*40mm*1.568mm and was resonate at 2.1 GHz on RT-Duroid substrate having dielectric constant 2.2. An array of TW MTM had been inserted at the center of two patches and at the radiating edge of the one of the patch. Proposed structure is simulated using HFSS-11 software and was fabricated.

Proposed technique for isolation enhancement: Initially **s**imulation was carried out for two patch antennas without thin wire array physically separated by distance λ/24 (5.2mm). This very less spacing between two patches, disturbs the antenna parameters and its radiation pattern[1][4]. To avoid the mutual coupling between these two patches an array of TW were inserted at the center of the proposed structure and was shown in figure 2. Initially parameters were extracted [2] for TW Unit cell and were noted in table 1. At desired frequency, the designed unit cell

exhibits negative permittivity. As mentioned in [2], method of parameter extraction is independent of cell size. Thus designing of unit cell give negative permittivity but it does not satisfies periodicity of metamaterial structure. As mentioned in [5][3] negative group velocity signifies reversing direction of propogation. Practically it had been proved which is tabulated in table 2. When number of Unit cells for TW satisfies cell size (p) that is distance between two thin wire cells in mm, mutual coupling reduces which enhances isolation between two patches. Since at this band of frequencies, array of TW exhibits negative permittivity, they reverts direction of surface waves and reduces mutual coupling between two patch elements. Insertion of this array at the center of two patch elements enhances isolation almost by 10 to 12 dBs. This improves antenna parameters. But still mutual coupling was there due to near field radiations. Therefore one more TW array had been added at one of the radiating edge of a single patch. This helps to reduce mutual coupling due to near field radiations. The final proposed structure was shown in figure 1. Simulations were carried out for various positions for TW array which is shown in figure 2 but there is no measurable difference in isolation enhancement. The results for all these configurations are same as the proposed structure. Thus configuration 2 was finalized and prototype was fabricated accordingly. Simulation results with two TW array was shown in figure 3a. Whereas figure 3c represents the radiation pattern for the same. Tabulated simulation results were shown in Table 3, gave comparison between proposed technique and two closely spaced antennas. Placement of two array of TW MTM had enhanced isolation by 20 dBs and improved antenna parameters and its radiation pattern. Prototype for the proposed antenna structure was fabricated and was shown in figure 1. Measurements were carried on vector network analyzer and model details for the same was ZVH8 (100 KHz to 8 GHz). Experimental results for without and with TW array were compared in Table 4. This experimental results table shows that, 17 dB enhancement in isolation was obtained in the same impedance band.

The proposed technique differs from the technique of via fencing since practically it was observed that via fencing does not uses array of thin wire. Array of thin wire results in degradation in quality factor which in turn improves isolation bandwidth. Though proposed technique offers narrow band but as compared to via fencing it was broadband technique.

Conclusion: The paper suggests innovative technique to improve isolation between trans-receiver antennas separated by physical separation of $\lambda/24$. Minimum physical separation between them affects antenna performance and also its radiation pattern degrades. The proposed technique uses an array of TW MTM which exhibits negative permittivity placed at the center of trans-receiver antenna. This reduces mutual coupling between them almost by 17 dBs. It results in improvement in antenna parameters due to reduction in surface waves. Placement of one more array at the one of the radiating edge of any one patch reduces mutual coupling between them due to near field radiation. Thus overall improvement of 17-19 dB in isolation had been observed. Measurement carried out with fabricated prototype showed close resemblance between simulated and experimental results. Insertion of both TW array improves antenna parameters along with its radiation pattern over the desired impedance band which allows close placement of trans-receiver antennas. Limitation of the proposed technique was that isolation bandwidth i.e. range of frequencies over which enhancement in isolation was obtained was narrow within the same impedance band.

REFERENCES

[1]Anuja A Odhekar , G Arunkumar, D D Poddar,"Mutual coupling reduction using metamaterial structure for closely spaced microstrip antennas",ICCT-2013.

[2] D. R. Smith,D.C.Vier, ThKoschny,C.M.Soukoulis, Phys. Rev E **71**, 036617,2005.

[3] C. Caloz and T. Itoh, Electromagnetic metamaterials: Transmission line theory and microwave applications, New York: Wiley, 2004.

[4] Anuja A Odhekar , G Arunkumar, D DPoddar," Isolation Enhancement for closely coupled microstrip antenna " ICMARS ,2012.

[5] Jiangfeng Zhou, Thomas Koschny, Maria Kafesaki, Costas M. Soukoulis," Size dependence and convergence of the retrieval parameters of metamaterials", Photonics and Nanostructures – Fundamentals and Applications 6 (2008) 96–101.

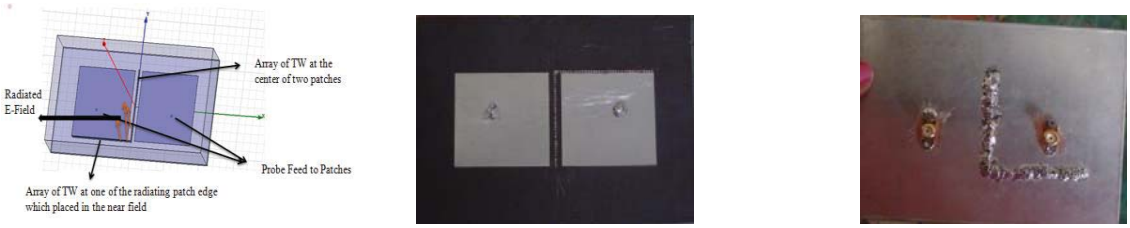

a) Top view (b) Back view

Figure 1.Proposed structure for isolation enhancement with TW array

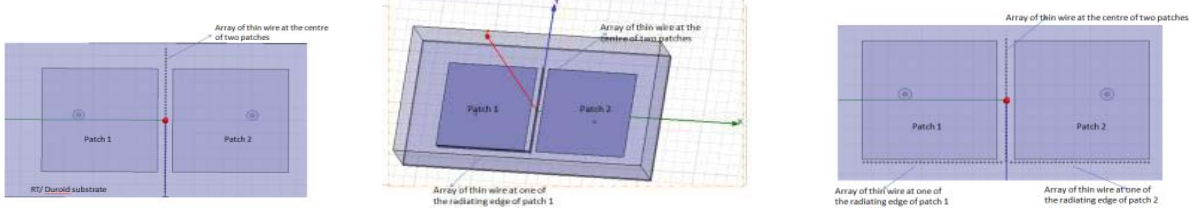

a) Configuration 1 b) Configuration 2 c) Configuration 3

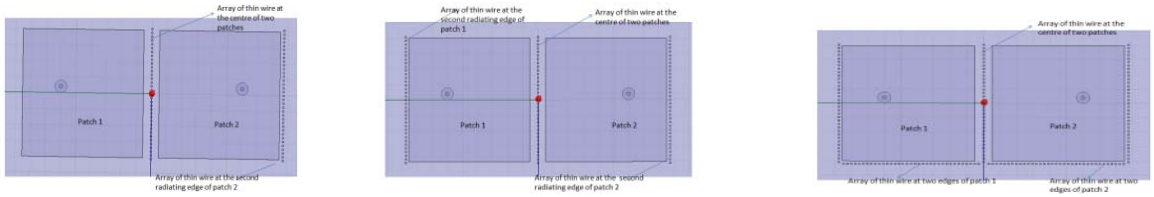

d) Configuration 4 e) Configuration 5 f) Configuration 6

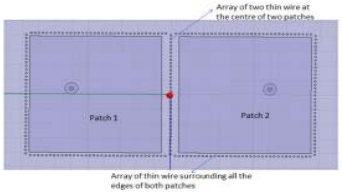

g) Configuration 7

Figure 2: Various positions for TW arrays

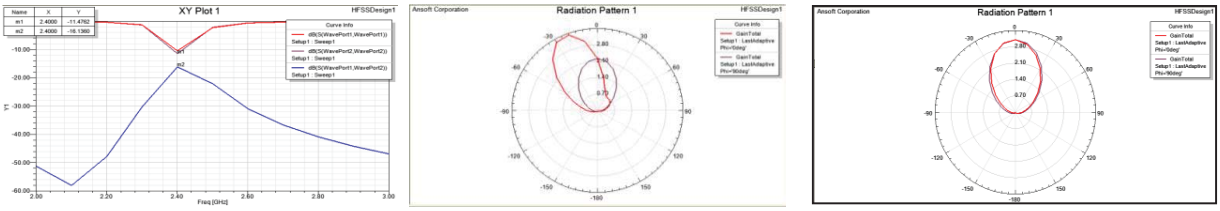

Figure 3:a)Scattering parameters of the proposed antenna without thin wires b) radiation pattern of the proposed antenna without thin wires c) improved radiation pattern of proposed antenna with thin wires

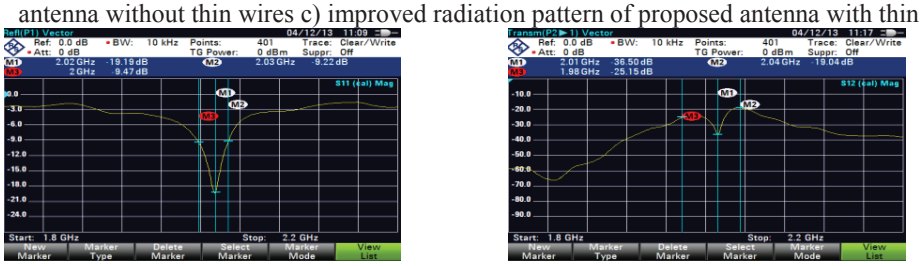

Figure 4: Experimental results of proposed antenna with thin wire array taken on VNA

Table-1: Extracted permittivity for TW Unit Cell

Frequency in GHz	Permittivity
2.09	-4.010+77.2168i
2.102	-3.80+63i
2.105	-3.2+56i
2.11	-2.9+32i
2.12	-5.+45i

Table -2: Number of thin wire cells vs. isolation

Number of Unit cell of TW in an array	**P(cell size i.e. distance between two thin wire cells) in mm**	**S_{21}(Isolation between two patches) in dB**
3	20	-16.11
6	5	-16.75
12	2.5	-17.07
24	1.667	-18.2
31	1.33	-19.8
34	1.2	-22.6

Table 3. Simulated results for closely spaced microstrip patch antenna using TW metamaterial

Antenna parameters	Patch elements separated by distance of λ/24 without TW structure	Patch elements separated by distance of λ/24 with TW structure
Resonant frequency(GHz)	2.4	2.39
Return loss(S_{11} in dB)	-11.47	-16
Impedance bandwidth(MHz)	40	60
Gain(dB)	1.63	3.4
Beamwidth(degrees)	-	62
Isolation(S_{21} in dB)	-16.3	-36.76
Isolation(S_{12} in dB)	-16.3	-36.76

Table 4. Experimental results for fabricated prototype without and with TW array

Antenna parameters	Patch elements separated by distance of λ/24 without TW structure	Patch elements separated by distance of λ/24 with TW structure
Resonant frequency(GHz)	2.01	2.02
Return loss(S_{11} in dB)	-13.7	-20.43
Impedance bandwidth(MHz)	40	50
Gain(dB)	1.63	3.4
Beamwidth(degrees)	-	62
Isolation(S_{21} in dB)	-17.9	-34.54
Isolation(S_{12} in dB)	-17.9	-36.5

A Compact ACS fed Electrically Small Antenna

U. Deepak [1], Susan Thomas [1], T. K. Roshna [1] and P. Mohanan [1]
(1) CUSAT, Cochin., India, 682022, Email: deepak.palath@gmail.com, shonasusan@gmail.com, roshnatk03@gmail.com, drmohan@gmail.com

Abstract: *A novel compact asymmetric coplanar strip line fed electrically small antenna for wireless local area network is proposed in this paper. The antenna resonates at 2.4 GHz (WLAN) band. The antenna has an overall dimension of only 1cm X 1.6cm which shows a good size reduction compared to antennas operating in the WLAN band. The uniplanar design, simple feeding and compactness make it easy to be integrated in circuit boards.*

Introduction: The rapid advancement in mobile communications has increased the demand for electrically small antennas that can be easily integrated within mobile devices. Due to electronic device miniaturization, the modern antennas are required to have small size, light weight and easy fabrication.

The 2.4 GHz ISM band is a very common and widely used communication band for many devices like Bluetooth, wireless printers, WLAN etc. The devices operating in this band has to comply with the IEEE 802.11 standards. The antennas used in such devices should be compact and easy to fabricate. Typical electrically small and low profile antennas have disadvantages of narrow bandwidth, low radiation efficiency and difficulty to achieve impedance matching. Many attempts have been done for making antennas which overcomes these difficulties [1-2]. Zeroth Order Resonance (ZOR) antennas based on Composite Right Left Handed (CRLH) transmission lines are widely used to achieve compactness in the antenna design [3-6]. The impedance matching can be improved by employing capacitive feed.

A novel, compact, electrically small antenna is presented in this paper. The antenna occupies a space of 16.1 x 10.5 mm^2 on an FR4 substrate of thickness 1.6mm and relative permittivity (ε_r) 4.4. The antenna offers a good gain and efficiency compared to typical ZOR antennas. The 2:1 VSWR bandwidth of the antenna is 95 MHz, which is sufficient to cover the entire 2.4 GHz ISM band.

I. Antenna Design & Geometry

The geometry of the proposed antenna is as shown in Fig. 1. The antenna is printed on a substrate with relative permittivity 4.4, loss tangent (δ) 0.02 and a thickness 1.6 mm. The antenna consists of three parts. The first one is the meander line which is acting as the main radiating element of the antenna, the second is the signal patch and third is the metal ground. The meander line is capacitively coupled to the signal patch. The other end of the meander line is connected to the metal ground. The antenna occupies a total area of 16.1 x 10.5 mm^2.

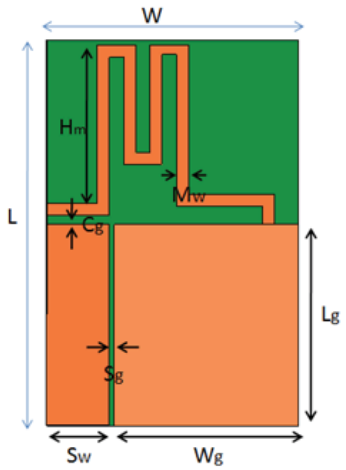

Fig. 1. Geometry of the proposed antenna.

The proposed antenna is fed by an asymmetric coplanar strip line. A traditional coplanar strip line has two conductors with same width. Since one line is substantially wider than the other line, the asymmetric coplanar strip line can be treated as a coplanar strip line with infinitely wide ground plane (CPSWG). The antenna geometry at the optimum design is as given in TABLE I

TABLE I
DIMENSIONS OF THE PROPOSED ANTENNA

Parameter	Value (mm)
L	16.1
W	10.5
Lg	8.4
Wg	7.7
Sw	2.6
Hm	6.6
Mw	0.5
Cg	0.5
Sg	0.2

II. RESULT & DISCUSSION

The simulated and measured reflection characteristics of the proposed antenna are shown in Fig. 2. The antenna is resonating at 2.48 GHz with a 2:1 VSWR bandwidth of 95 MHz, ranging from 2.429 GHz to 2.524 GHz. All the measurements of the antenna are done using PNA E8362B Network Analyzer.

The capacitance produced by the coupling gap Cg, along with the distributed inductance of the meander line, which is connected to the ground plane of the antenna, produces a series resonance at 2.48 GHz. This LC combination acts as the radiating element of the antenna.

A series of variation studies are conducted on the antenna. The variation analysis conducted on the coupling gap Cg shows that, when there is no coupling gap present, the antenna is not showing any resonance. As the coupling gap is increased, the antenna resonates around 2.4

GHz with an increase in its resonant frequency with Cg. This is because, when the coupling gap Cg is increased, this causes a decrease in the coupling capacitance, thereby increasing the resonant frequency. An optimized value of Cg is selected at 0.5mm where the impedance matching is maximum. An increase in the width of the meander line shows an increase in the resonant frequency of the antenna, because of the decrease in the inductance of the meander line with the increase in its width. Similarly an increase in the height (Hm) of the meander line makes the antenna resonate at a lower frequency because of the increase in its inductance.

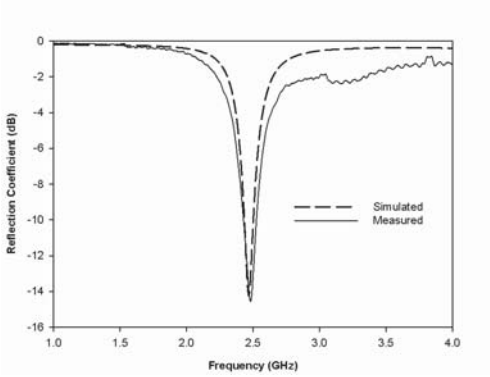

Fig. 2. Simulated and Measured reflection coefficient of the antenna

Fig. 3 shows the measured radiation pattern of the antenna at 2.48 GHz. In the E plane the antenna shows a nearly omni directional radiation pattern. Fig. 4 shows the measured gain plot of the antenna. Antenna shows a nearly uniform gain in the 2.4 GHz band with a peak gain of -0.23 dBi at 2.48 GHz. The measured efficiency of the antenna using Wheeler Cap [7] method is 96%.

According to Chu, [8] an antenna is considered as electrically small if the following two conditions are met,

$$ka < 0.5 \tag{1}$$

$$Q_{antenna} > Q_{min} \tag{2}$$

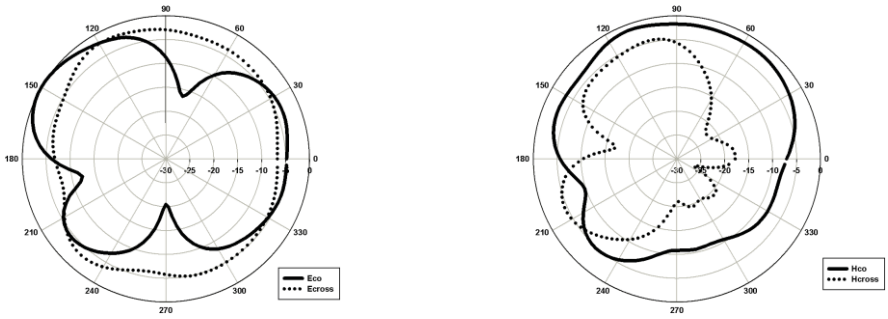

(a) (b)

Fig. 3. Measured radiation pattern of the antenna. (a) E Plane, (b) H Plane

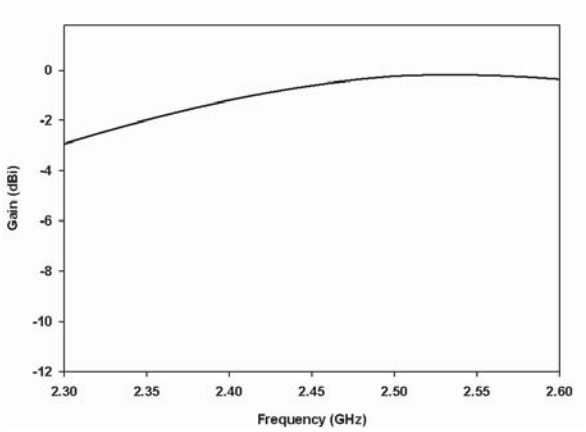

Fig. 4. Measured gain of the antenna

Where k is the free space wave number at resonant frequency and a is the radius of the sphere circumscribing the largest dimension of the antenna. Qmin is given by,

$$Q_{min} = \frac{1}{ka} + \frac{1}{(ka)^3} \tag{3}$$

For the proposed antenna, the k value is 0.519 rad/sec and a is 0.961 cm at resonant frequency. Hence ka is 0.499 < 0.5. The calculated Qmin of the antenna for this ka value is 10.052. The measured Q of the antenna is 33.513, which is greater than the Qmin of the antenna. Hence by definition, the antenna is electrically small.

III. Conclusion

A novel compact asymmetric coplanar strip line fed electrically small antenna for wireless local area network is proposed and investigated. The antenna resonates at 2.4GHz with a bandwidth of 95MHz. The measured peak gain of the antenna is -0.23 dBi in spite of its small size. The antenna has a measured radiation efficiency of 96% at 2.48 GHz

Acknowledgement

The authors acknowledge University Grant Commission and Department of Science & Technology under Government of India for the financial support.

References

[1] Steven R. Best, Senior Member, IEEE, "LowQElectrically Small Linear and Elliptical Polarized Spherical Dipole Antennas," *IEEE Trans. Antennas Propag.*, vol. 53, no. 3, March 2005.
[2] Richard W. Ziolkowski, Fellow, IEEE, and Aycan Erentok, "Metamaterial-Based Efficient Electrically Small Antennas," *IEEE Trans. Antennas Propag.*, vol. 54, no. 7, July 2006.
[3] A. Lai, T. Itoh, and C. Caloz, "Composite right/left-handed transmission line metamaterials," *IEEE Microw*. Mag., vol. 5, no. 3, pp. 34–50, Sep. 2004.
[4] T. Jang, J. Choi, and S. Lim, "Compact coplanar waveguide (CPW)-fed zeroth-order resonant antennas with extended bandwidth and high efficiency on vialess single layer," *IEEE Trans. Antennas Propag.*, vol. 59, no. 2, pp. 363–372, Feb. 2011.
[5] P. W. Chen and F. C. Chen, "Asymmetric Coplanar Waveguide (ACPW) Zeroth-Order Resonant (ZOR) Antenna with High Efficiency and Bandwidth Enhancement," *IEEE Antenna Wireless Propag. Lett.,* vol.11, pp. 527-530, 2012.
[6] S.-Y. Yang and M. N. M. Kehn, "A bisected miniaturized ZOR antenna with increased bandwidth and radiation efficiency," *IEEE Antenna Wireless Propag. Lett.*, vol. 12, pp. 159–162, 2013.
[7] Karstadt P. and Gupta A., "Radiation efficiency measurement of communication antennas with Wheeler Cap method" International Students and Young Scientist Workshop, Photonics and Microsystems,2011.
[8] Chu, L.J., "Physical limitation of omnidirectional antennas," J. Appl. Phys, 19, (64), pp. 1163–1175

BANDWIDTH ENCHACEMENT OF DUAL BAND DAVID FRACTAL MICROSTRIP ANTENNA

Jacob Abraham [(1)], and ThomaskuttyMathew[(2)]
Department of Electronics, School of Technology and Applied Science
M G University, Regional Center, Edapally, Kochi India
tjacobabra@gmail.com

Abstract: In this work David fractal concept is introduced in to the basic hexagon shaped microstrip antenna for miniaturization and multiband characteristics. It produces multiple resonances at 1.8 GHz and 3.4 GHz, which are suitable for cellular communication and Wimax applications respectively. Series of narrow slots with varying lengths are introduced in the ground plane, in order toenhance the bandwidth of the antenna. The band width of the second resonance is enhanced by 36.4% forfirst level iterated David fractal microstrip antenna with three slots in the ground plane, when compared with a reference antenna, antenna without slots.

Introduction: Microstrip antennas plays a key role in wireless communication due to many attractive features like light weight, small size, mechanically robust, easy to integrate with radio frequency devices, relatively easy to fabricate and inexpensive. Even though microstrip antennas have several advantages when compared to other standard antennas, it has few inherent limitations like narrow bandwidth, not multiband and low gain. Multiple resonances with good gain in a single patch is not directly attainable in simple microstrip antenna. One simple way to obtain multiple resonances is by introducing fractal geometry in to microstrip patch antenna. This technique offers minimizing the antenna size and simultaneously achieving multiband characteristics. Fractal composed of multiple iterations of a single elementary shape. The iterations can continue infinitely, thus forming a shape within a finite boundary but of infinite length or area. By applying fractal geometries in to ordinary microstrip antenna, size can reduce with good radiation characteristics and also multiband performance at non harmonic frequencies are produced. Fractal antennas can be of various shapes and forms [1-3]. One of the key limitations with multiband fractal antennas is the inherently narrow bandwidths. Several techniques have been reported to increase impedance bandwidth of multiband fractal antenna. A CPW fed printed double L patch antenna [4] is proposed for Wimax application with good radiation characteristics for the desired frequency band. The concept of defected ground plane for multiband antenna design is reported in [5] which is an effective method**.**

This paper investigates the possibility to use novel fractal geometry, David fractal [6] in to antenna structure. First level iterated David fractal microstrip antenna is proposed with four different ground planes. Here the reference antenna is the first level iterated David fractal microstrip patch with normal ground plane, it produces two bands.This antenna is compared with antenna having one slot, two slot and three slots in the ground plane. The slots are placed in such a way that variations are dominant in higher frequency band. As the

number of slot increases better bandwidth and better matching is achieved in higher band, band used for Wimax application, to support higher information data transmitting and receiving rate. The design and optimization of the proposed antenna was conducted using electromagnetic solver CST microwave studio.

Antenna design architecture: The basic patch is the microstrip hexagon patch antenna resonating at 1.8 GHz and is excited using proximity coupled fed method. The antenna is printed on FR4 substrate with dimension L x W x h = 72 x 84 x 1.6 mm^3. The David fractal is a class of fractal geometries. Its recursive procedure is demonstrated in figure [1]. The David fractal pattern is formed from the basic hexagon shaped patch or the initiator as in figure 1(a), by dividing it in to six smaller hexagons, six equilateral triangles and a David star at the center; the triangles and star are removed. It results in first level of iteration as shown in figure 1(b). The mentioned process is repeated in all smaller hexagons to obtain the second iteration level as shown in the figure 1(c).

1(a) (b) (c)

Figure 1:Different iteration stages of David Fractal

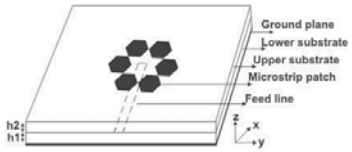

Figure 2: Configuration of the proposed dual band fractal antenna

Cross-sectional view of the proposed first level iterated David fractal hexagon patch antenna is shown in the figure 2. Here two substrates are used and the fed line is between the substrates, and the radiating patch is on the top side of the upper substrate and the ground plane is at the bottom side of the lower substrate. The figure 3(a) shows the photograph of the fabricated 1st level iterated David fractal hexagon patch antenna and 3(b) ground plane with three slots. The dimensions of slots in the ground plane is shown in the figure 4. The H P 8510 C network analayzer was used to measure the return loss

3(a) 3(b)

Figure 3: Photograph of the fabricated antenna
(a) First iteration level David fractal antenna
(b)Ground plane with three slots

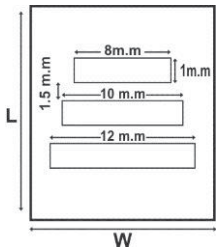

Figure 4: Dimension of the slots in the ground plane

Results and discussions: The figure 5 shows the simulated and measured return loss variation with frequency for the first level iterated David fractal microstrip antenna. The -10 dB bandwidth for the measured return loss reaches 65 MHz (1.75 – 1.815 GHz) and 45 MHz (3.37 – 3.415 GHz) respectively, and can cover GSM mobile communication system and Wimax applications in the 4G mobile phones. Since the upper band is used forWimax, studyis concentrated to increase the band width of the upper band without changing the basic configuration of the proposed antenna so that information data at higher speed can be communicated between users.

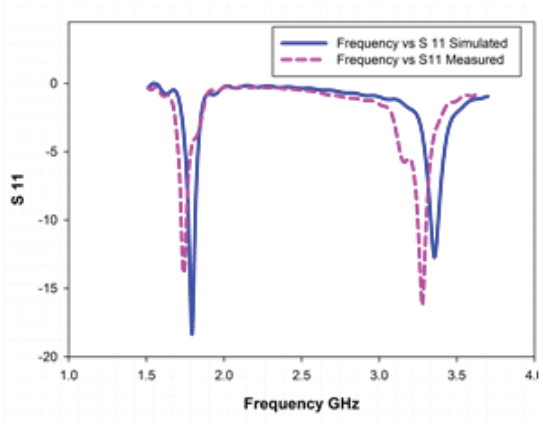

Figure 5: Measured and simulated S_{11} plot

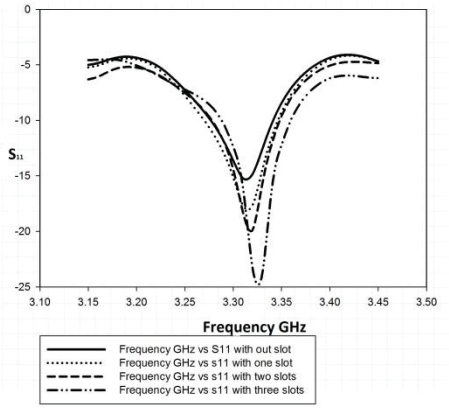

Figure 6: Measured S11 plot of upper band

Table 1 shows the measured and simulated results of antennas with varying number of slots in the ground plane. It is observed that, presence and number of slots in the ground plane has very small effect at low frequency band while it has a significant effect at higher frequency band. In this table antenna one is used to denote first level iterated David fractal hexagon antenna without slot which is the reference antenna in this study, antenna two represents antenna with a single slot on the ground plane, antenna three represents antenna with two slots in the ground plane and antenna four represents antenna with three slots in the ground plane. It can be seen from the results that as the number of slot increase from one to three, the bandwidth at the desired frequency increases from 18.2 % to 36.41 % with respect to the reference antenna. The figure 6 shows the measured return loss plot against frequency for all four antennas, of the upper band, the band used for Wimaxapplication. The antenna exhibits moderate gain at the operating frequencies.

	Resonant frequency GHz	S_{11} dB	Band	Band width MHz	% enhanced
Antenna 1 Simulated	3.4	-14.635	3.3646 – 3.428	63.4	
Antenna 1 Measured	3.31	-15.21	3.280 – 3.335	55	
Antenna 2 Simulated	3.3854	-18.07	3.3489 – 3.420	71.1	12.7
Antenna 2 Measured	3.32	-17.65	3.275 – 3.340	65	18.2
Antenna 3 Simulated	3.3851	-22.65	3.3474 – 3.427	79.6	25.9
Antenna 3 Measured	3.32	-19.88	3.275 – 3.345	70	27.3
Antenna 4 Simulated	3.39	-25.48	3.3522 – 3.434	81.8	29.6
Antenna 4 Measured	3.31	-23.86	3.280 – 3.355	75	36.41

Table 1: Comparison between antennas

The co-polar and cross polar radiation pattern in the E and H plane for the lower band of the first iterated level David fractal microstripantenna is shown in figure 7, and that of upper band with three slots is shown in figure 8 respectively.

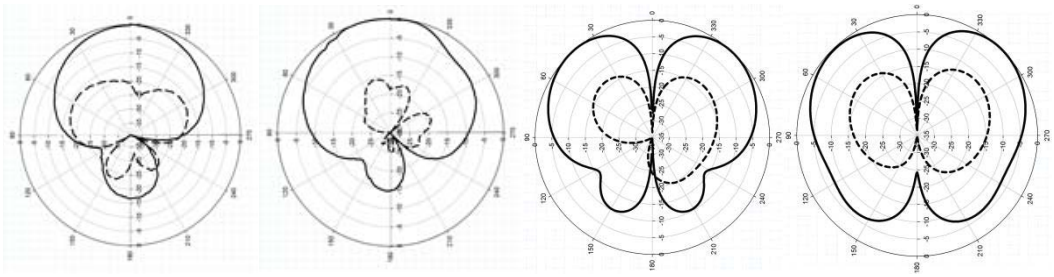

7 (a) 7 (b) 8 (a) 8 (b)

Figure7 & 8:Measured normalized radiation patterns of the antenna at resonant frequency 1.8GHz 7(a) E Plane 7(b) H Plane (co-polarized, ———solid line and cross polarized, ...dashed line) and normalized radiation pattern at 3.31 GHz with three slots 8 (a)E Plane 8(b) H Plane (co-polarized, ———solid line and cross polarized, ...dashed line)

Conclusion: The proposed hexagon shaped David fractal antenna has demonstrated its potential for multiband operation. The antenna produces two bands; the first band find application in mobile phone communication and the second band find application in Wimax. It is also observed that size reduction up to 18.3% in terms of overall size and 23.4% in terms of copper cladding remaining in comparison with a hexagon patch antenna operating in the first resonant frequency band. With the introduction of three slots in the ground plane upper band width has enhanced by 36.4% when compared with reference antenna.The proposed David fractal antenna will have significant impact on reducing the size, cost and reliability of the mobile device.

Acknowledgment: Authors would sincerely express the gratitude to Mr. Kuruvilla George, Verdant Telemetry and Antenna Systems private Limited for providing the measurement facilities.

Reference:

[1] Lin s, L Z Wang, Y Wang, X Y Zhang and H J Zhang "Design and analysis of a circular polarization microstrip antenna with Koch fractal edges" Progress in electromagnetic research letters Vol 34, 9-19, 2012.
[2] Oraizi H and Hedayati S, "Miniaturization of microstrip antenna by the novel application of the Giuseppe Peano fractal geometries", IEEE Transaction on Antenna and Propagation Vol.60, Issue 8, Pages 3559-3567, 2012.
[3] Dong Jun Kim, Jun Ho Choi and Young Sik Kim, " CPW fed ultra wide band flower shaped circular fractal antenna", Microwave and optical Technology Letters, Vol. 55, Issue 8, pages 1792-1795, August 2013
[4] A. A. Abdelaziz, "Bandwidth enhancement of microstrip antenna", Progress In Electromagnetics Research, PIER 63, 311–317, 2006
[5] Pei J,A G Wang, S Gao and W Leng, " Miniaturized triple band antenna with a defected ground plane for WLAN/ WiMAX applications", IEEE Antenna wireless propagation letter, Vol.10, 298-301. 2011.
[6] Armin Bunde and ShlomoHavlin, "Fractals in science" Published by Springer Verlag, ISBN 3-540-56220-6.

DECEMBER 18, THURSDAY
08.30AM TO 10.30AM
RESEARCH SESSION 8
UWB ANTENNAS
S N MITRA- HALL

Chair: Dr. Hema Singh NAL Bangalore, India.

No	Papers	Page
8.1	**A Triple Band-Notched UWB Antenna Design for Wi-MAX, WLAN and SATCOM Applications** Tessa Mathew [1] and Deepti Das Krishna [2] Department of Electronics and Communication, Rajagiri School of Engineering and Technology, Rajagiri Valley, Kakkanad, Cochin. 682 039 *Email: [1] tessamathew16@gmail.com, [2] deeptidk@rajagiritech.ac.in.*	223
8.2	**Compact CPW-Fed UWB Antenna with Dual Notch Bands** Saira Joseph[1], Binu Paul[1], Mridula S[1] and P Mohanan[2] [1] Division of Electronics, SOE, CUSAT. *Email:[1]saira_joseph@ymail.com, binumpaul@gmail.com, mridulahari@gmail.com.* [2]Department of Electronics, CUSAT. *Email:drmohan@cusat.ac.in*	227
8.3	**Planar UWB Antenna with Dual Band-notched Characteristics** Sarah Jacob[1], Anila P.V[1], S. Mridula[2] and P. Mohanan[1] [1]CREMA, Department of Electronics, CUSAT, Kerala, India, Pin 682 022. *Email: sarahjacob12@gmail.com.* [2]Division of Electronics, School of Engineering, CUSAT, India 682 022. *E-mail:mridula@cusat.ac.in.*	232
8.4	**Multi-Fractal Monopole Antenna for UWB Applications** Merin Mary Mathews, K Shambavi and Zachariah C Alex Vellore Institute of Technology Vellore, India. *E-mail: kshambavi@vit.ac.in.*	*236*
8.5	**Wideband Printed Monopole Antenna for Airborne Applications** Mary Rani Abraham, Sona O. Kundukulam, Abdul Wahab, and U. Ganesan Naval Physical & Oceanographic Laboratory, Kochi, India-682021. *E-mail: maryraniabraham@gmail.com.*	240
8.6	**A Spur Line Loaded Microstrip-Fed Uwb Linear Taper Slot Antenna With Frequency Notch Characteristics** C. Sarkar [1], C. Saha[2], and J.Y. Siddiqui[3] [1]Swami Vivekananda Institute of Science and Technology, Kolkata, India , Pin-700145. *E-mail: chittajit_sarkar@yahoo.co.in.* [2]Indian Institute of Space Science & Technology , Government of India. *E-mail: csaha@ieee.org.* [3]Department of Radio Physics and Electronics, University of Calcutta, India. E-mail: jysiddiqui@ieee.org.	244
8.7	**A CPW Fed Compact UWB Antenna with Modified Ground Plane and Corrugated Fractal Patch for Bandwidth Enhancement** V. Rajeshkumar [1] and S. Raghavan [2] National Institute of Technology, Tiruchirappalli, India 620015. *Email:vrajeshme@gmail.com[1], raghavan@nitt.edu[2]*	248

A Triple Band-Notched UWB Antenna Design for WiMAX, WLAN and SATCOM Applications

Tessa Mathew [(1)] *and Deepti Das Krishna* [(2)]
Department of Electronics and Communication, Rajagiri School of Engineering and Technology, Rajagiri Valley, Kakkanad, Cochin, Pin: 682039
Email: (1) tessamathew16@gmail.com, (2) deeptidk@rajagiritech.ac.in

Abstract: *A microstrip fed UWB monopole antenna design with triple band-notches is proposed in this paper. The antenna has a T-shaped stub introduced in the radiation patch, two U-shaped stubs beside the feeding line and two slits in the bevel shaped ground plane. The proposed antenna has an overall size of 32×26mm² with a VSWR<2 performance over the operating frequency range of 2.8 - 11.0GHz. The stubs and slits are so designed that three bands of frequencies, namely, 3.3 - 4.0GHz (WiMAX), 5.05 -5.90GHz (WLAN) and 8.0 - 8.4GHz (SATCOM) are the notched. The proposed antenna is simulated using a frequency domain solver and a time domain solver with comparable results, indicating that it is a good candidate for various UWB applications.*

Introduction: In recent years, ultra wide band (UWB) technology has undergone significant developments. The frequency band allotted for UWB by the Federal Communication Commission (FCC) is 3.1–10.6 GHz [1]. UWB communication systems attracted attention in the wireless world because of their advantages, including high speed data rate, low cost, resistance to severe multipath and jamming, low cost, and low complexity [2]. However, there still remain certain challenges for the UWB antenna technology such as the interference of UWB signals with the already existing wireless networking technologies namely WiMAX, WLAN and SATCOM which operate in bands 3.3 - 4.0GHz, 5.15 - 5.825GHz and 8.0 - 8.4GHz, respectively. Therefore there is a need for filtering out these interfering frequencies and introducing stop bands which will help to reduce the interference.

Till recently, various dual notched antennas have been reported. The band notched UWB antennas have been achieved by using techniques like etching slots in the patch and/or ground plane or by introducing parasitic strips near the feeding line [3 - 5]. By proper design of the radiation patch and ground plane, this idea can be extended to triple band-notched antenna designs as in [6] - [8].

In this paper, a UWB planar antenna design with triple band notches is proposed with an overall size of 32×26mm². To realize three notched frequency bands, a T-shaped stub in the radiation patch, a pair of U-shaped stubs near the feeding line and two slits in the ground plane are incorporated. A detailed parametric study of the effect proposed filtering geometry on the antenna performance is carried out. It is observed that the proposed antenna design operates over 2.8 to 11.0GHz band with triple bands rejected at 3.7 GHz (3.3 - 4.0 GHz), 5.7 GHz (5.05 - 5.90 GHz) and 8.2 GHz (8.0 - 8.4 GHz), with excellent notched band characteristics.

Antenna Design: The proposed design is given Fig. 1. The radiating monopole and feeding mechanism is printed on top of the substrate, and a modified defected ground plane is printed on the bottom. The antenna is designed on Rogers4003 substrate with a thickness of 0.8 mm, and dielectric constant 3.8. The width of the microstrip feed line is fixed at 2mm to achieve 50Ω characteristic impedance.

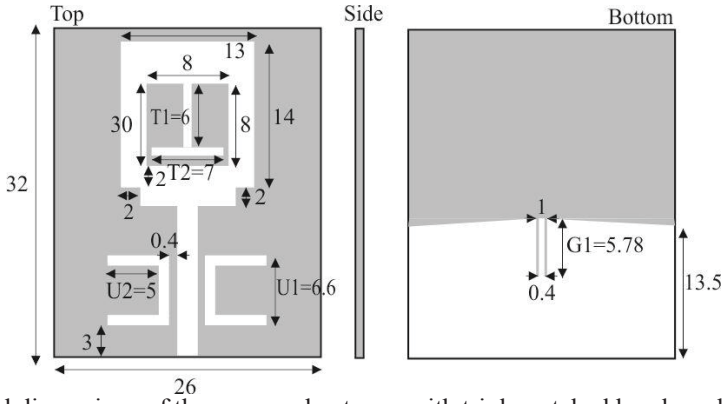

Fig. 1. Geometry and dimensions of the proposed antenna with triple notched bands and dimensions in mms.

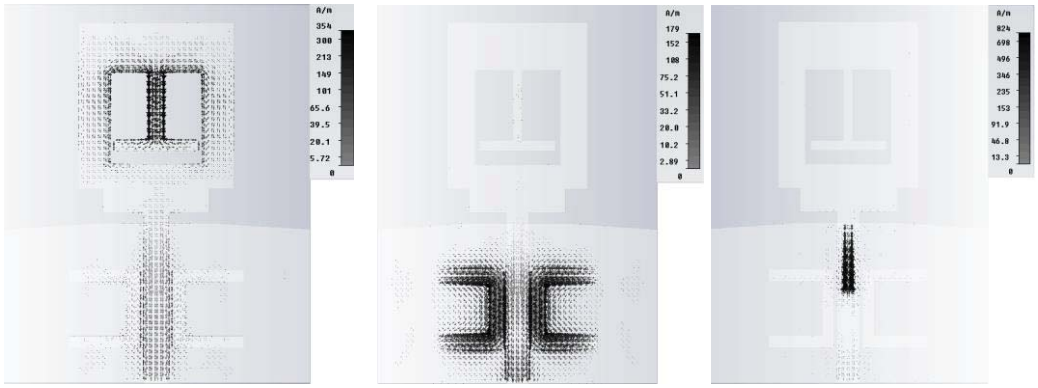

(a) (b) (c)

Fig. 2. Simulated current distributions at the different notch frequencies (a) 3.7 GHz (b) 5.7 GHz (c) 8.2 GHz.

The wideband operation of the antenna is obtained by optimizing the patch and ground plane edges in the vicinity of the gap between them and the gap itself. A beveled defected ground structure is used to ensure good impedance match and stable gain over a broad frequency range and to obtain a smooth transition from one resonant mode to another. An equivalent dipole antenna is formed by the monopole antenna and the ground plane.

The impedance characteristics of the antennas are affected by distribution of current on the patch. By etching a T-shaped stub in the radiating patch, by inserting two U-shaped stubs on either side of feed line and by etching two slits in the beveled ground plane, the current distribution on the antenna is disturbed in such a way that stop bands with center frequencies at 3.7, 5.7 and 8.2GHz is generated. It is around these structures that the current flows at the notch frequencies in such a way that their flow along the interior and exterior edges is oppositely directed. The current distribution on the proposed antenna design is simulated at the notched frequencies and is shown in Fig.2. A high attenuation near the notched frequencies is observed as a result of the radiated fields being cancelling out each other. Hence, the antenna filters out the notched frequencies.

A detailed parametric analysis is carried out by varying the dimensions T1 and T2 of the T shaped stub in the patch; U1 and U2 of the U shaped stub; and the length G1 of the slit in the ground plane. The VSWR plots, shown in Fig 3, clearly indicates that the T shaped stub in the patch, the U shaped stub and the slits independently controls the notched band center frequencies at 3.7, 5.7 and 8.2GHz respectively.

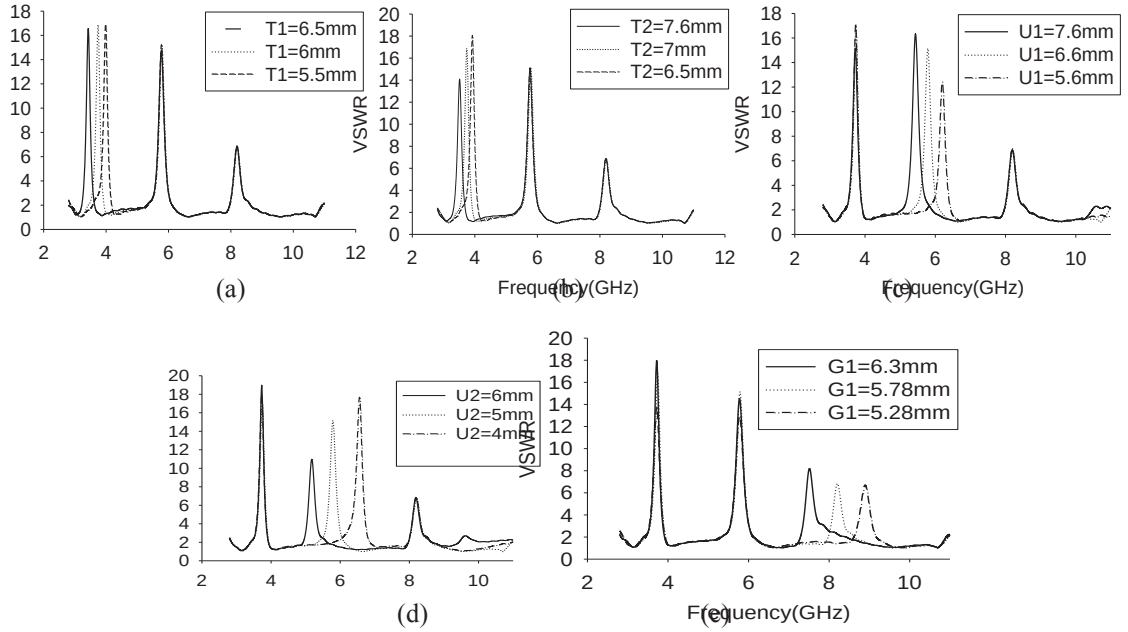

Fig. 3. Band-rejection characteristics (VSWR Vs Frequency in GHz) of the proposed antenna for different values of (a) T1, (b) T2, (c) U1, (d) U2 and (e) G1

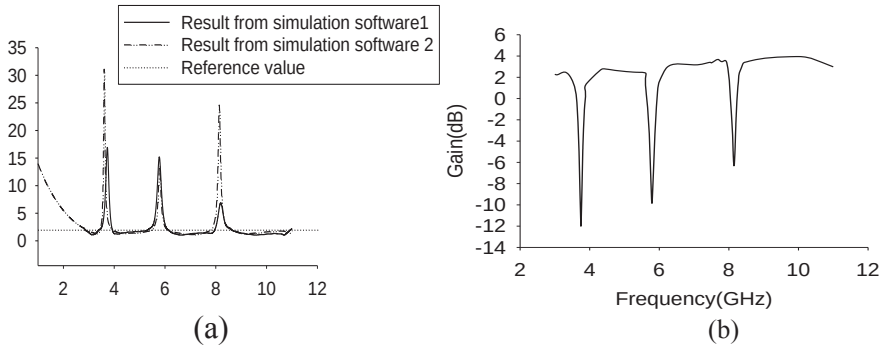

Fig. 4. (a) Band-rejection characteristics (VSWR Vs Frequency in GHz) of the proposed antenna design simulated using two different simulation softwares; and (b) Antenna gain over the entire UWB frequency band

Fig. 4(a) plots the simulated VSWR of the proposed antenna design using two different classes of commercial 3D full wave EM simulation softwares where one is time domain based (ANSYS HFSS) and another based on frequency domain (CST). The plots are observed to be comparable and thus confirm the results. The antenna gain is plotted in Fig.4 (b), which further vindicates the triple band notched performance of the antenna. The gain is observed to be decreasing in the vicinity of stop bands (3.7, 5.7 and 8.2GHz) by an order of 10dB, with a stable gain with a variation of less than 3 dB achieved outside the notched bands.

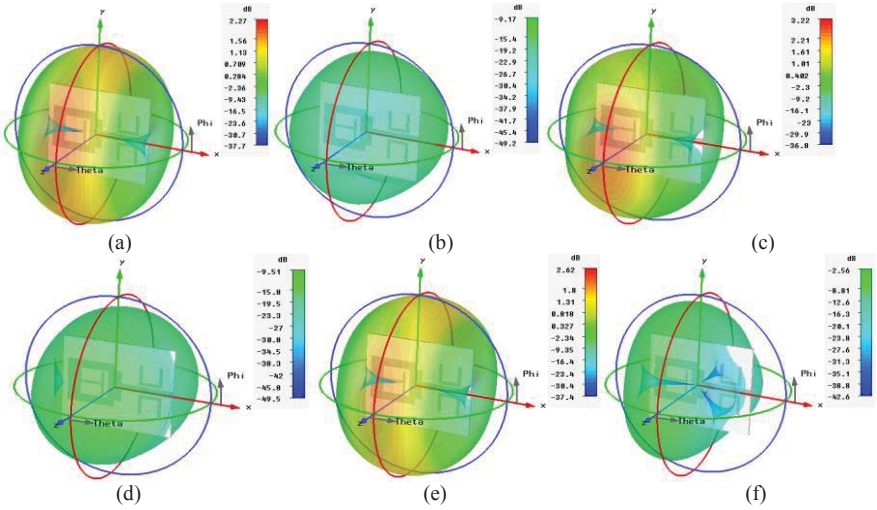

Fig. 5. 3D patterns of the antenna at frequencies (a) 3.1GHz, (b) 3.7GHz, (c) 4.17GHz, (d) 5.7GHz, (e) 6.64GHz and (f) 8.2GHz

The 3D radiation pattern of the antenna is plotted in Fig. 5 at 3.1GHz, 3.7GHz, 4.17GHz, 5.7GHz, 6.64, and 8.2GHz which clearly shows a near omni directional radiation patterns in the pass band and an almost no radiation at the notched frequencies.

Conclusion: To avoid interference of existing narrow band wireless networking technologies namely WiMAX, WLAN and SATCOM with the UWB's operating frequencies, a microstrip fed planar UWB antenna with multiple notched bands is proposed in this paper. A T-shaped stub in the radiation patch, a pair of U-shaped parasitic elements near the feed line and a slit in the beveled ground plane are used to introduce triple notched bands at 3.7GHz, 5.7GHz, and 8.2GHz. The radiation pattern of the proposed antenna shows a near omni-directional pattern throughout the UWB operating range with the antenna gain being almost flat in the operation frequency band with sharp dips in notched bands.

References:

[1] FCC 1st report and order on UWB technology, Feb 2002.
[2] I. Oppermann, M. Hamalainen, and J. Iinatti, *UWB Theory and Applications*. New York: Wiley, 2004, Ch. 1, pp. 3–4.
[3] Wen Jiang and Wenquan Che, "A Novel UWB Antenna with Dual Notched Bands for WiMAX and WLAN", IEEE antennas and wireless propagation letters, Vol. 11, 2012 293.
[4] Qing-Xin Chu, Member, IEEE and Ying-Ying Yang, "A Compact Ultrawideband Antenna with 3.4/5.5 GHz Dual Band Notched Characteristics" IEEE Transactions on Antennas and Propagation, Vol. 56, No. 12.
[5] M. Abdollahvand, G. Dadashzadeh, and D. Mostafa, "Compact Dual Band-Notched printed Monopole Antenna for UWB Application", IEEE Antennas and Wireless Propagation Letters, Vol. 9, 2010.
[6] Pu Zhuo, Hongyan Tang, Xiulei Gao, Feifei Zhao and Fuyun Zhang, "Investigation on Planar UWB Antenna with Triple Band-Notched Characteristics", iWEM 2012 Proceedings
[7] Jia-cheng Tang, Min Chen, Yu-jiao Li," A Novel Planar UWB Antenna With Triple Band-Notched Characteristics" , IEEE APS, 2012
[8] Y. F. Weng, S. W. Cheung and T. I. Yuk , "Triple Band-Notched UWB Antenna using Meandered Ground Stubs", 2010 Loughborough Antennas & Propagation Conference, 8-9 November 2010, Loughborough, UK.

Compact CPW-Fed UWB Antenna with Dual Notch Bands

Saira Joseph[*], *Binu Paul*[#], *Mridula S*[#] *and P Mohanan*[**]
*Division of Electronics, SOE, CUSAT, Email: saira_joseph@ymail.com
#Division of Electronics, SOE, CUSAT, Email:binumpaul@gmail.com, mridulahari@gmail.com
**Department of Electronics, CUSAT, Email:drmohan@cusat.ac.in

Abstract: *The paper presents a CPW-fed printed semicircular monopole UWB antenna with slots etched in the ground plane and feed line for band notching. L-shaped slots are inserted in the ground plane to notch out the frequency band for world inter operability for microwave access (WiMax 3.3-3.7 GHz) and a U-shaped slot is inserted in the CPW feed line to notch out the frequency band for wireless local area network (WLAN 5.15-5.825 GHz). The design is simulated using Ansys HFSS and radiation characteristics of the antenna show high rejection in the notch bands, omnidirectional radiation patterns and low group delay.*

1. Introduction: The Federal Communications Commission released the frequency band 3.1-10.6 GHz for the UWB system in 2002. However, in some European and Asian countries, there exist narrowband wireless services such as WiMax operating from 3.3 to 3.7 GHz and WLAN operating from 5.15-5.825 GHz within the UWB spectrum. UWB systems can pose interference to these bands if the UWB devices are within close proximity. To address this problem, additional filters may be used to notch out the interfering bands. But this will increase the complexity of the UWB system. A simpler band notching technique is to insert a thin slot in the patch antenna with a length that is an integral multiple of $\lambda_g/4$ where λ_g is the wavelength of the notched frequency [1]. Other reported techniques include using a parasitic strip or stub and using a transmission line with band stop characteristic to feed the antenna [2-4]. Recently, hybrid techniques have been adopted to attain two notched bands [5-7]. In this article, by incorporating a slot in the ground plane, the first notched band from 3.25-4.04 GHz is achieved. A second notched band from 5-6.25 GHz is realized by embedding a U-shaped slot in the coplanar waveguide (CPW) feed line. Both notching techniques leave the patch undisturbed and so this approach can be used for any CPW-fed monopole antenna. The antenna is compact, simple in design and because of the CPW-feed it is easy to integrate with MMICs.

2. Antenna Design: The geometry of the proposed antenna is shown in Fig. 1. The substrate used is of thickness h=1.6 mm, relative dielectric constant ε_r=4.4 and loss tangent tan δ=0.02. A semicircular disc monopole of diameter D is used as the radiating patch. The antenna of size WxL is fed using a 50-Ω CPW feed of width W_f. The feed line is spaced by a gap g from the ground plane of width W_g and length L_g [8].The monopole is fed with a spacing s from the ground plane. The L-shaped slot is inserted in the ground plane and has two arms of length LS_1 and LS_2 and the width of the slot is LS_t. Both L-shaped slots have the same dimensions and are positioned at a distance Lp from the outer edge of the ground plane. The overall length of each slot is approximately a quarter wavelength of the notched frequency.

$$LS_1 + LS_2 \approx \lambda_g/4 \quad (1)$$

where λ_g is $\frac{\lambda}{\sqrt{\varepsilon_{eff}}}$ and ε_{eff} is the effective dielectric constant.

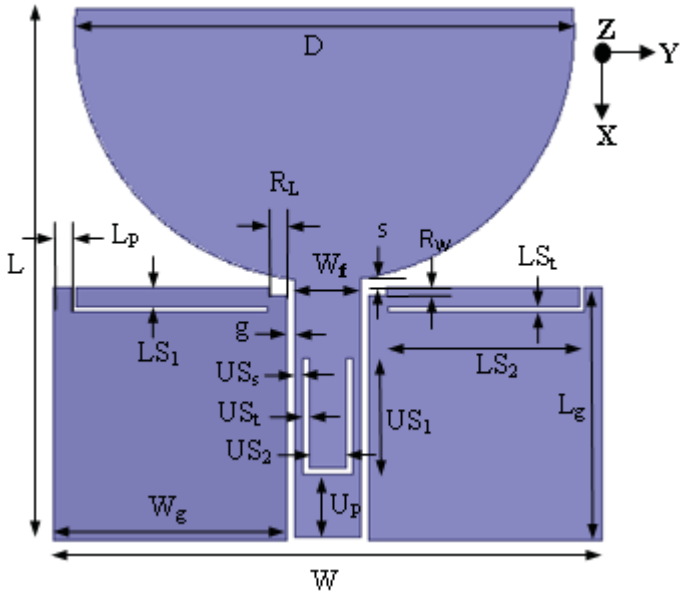

Figure 1. Geometry of the proposed antenna

Parameter	Dimension
L	32
W	31.6
D	30
L_g	15
W_g	14
R_L	1
R_W	0.5
W_f	3
g	0.3
s	0.5
LS_1	1.5
LS_2	11.5
LS_t	0.3
Lp	1.5
US_1	7
US_2	2.4
US_t	0.3
US_s	0.5
Up	4

Table1. Antenna dimensions (mm)

The U-shaped slot inserted in the CPW feed line has two vertical arms each of length US_1, one horizontal arm of length US_2 and the slot width is US_t. The slot is spaced at a distance US_s from the edge of the feed line and U_p from the end of the feed line. The overall length of this slot is approximately a half wavelength of the notched frequency.

$$US_1 + US_2 + US_1 \approx \lambda_g/2 \quad (2)$$

Optimized parameters for band notch performance in the WiMax and WLAN range are listed in Table 1.

3. Simulation Results: The simulated VSWR plot for the antenna with optimized dimensions is shown in Fig. 2. The plots show that VSWR<2 for the entire UWB range except in the notch bands.

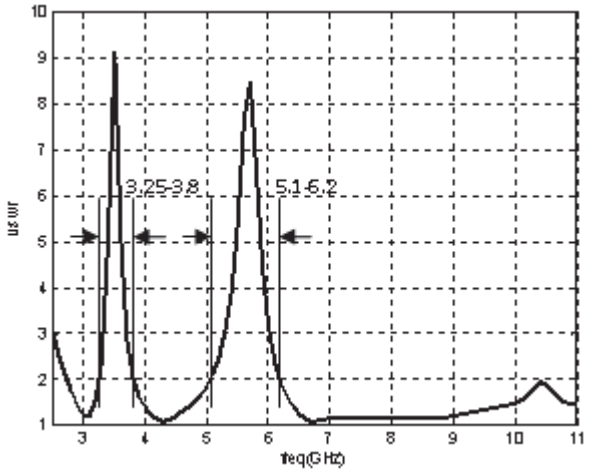

Figure 2. Simulated VSWR vs frequency for proposed antenna

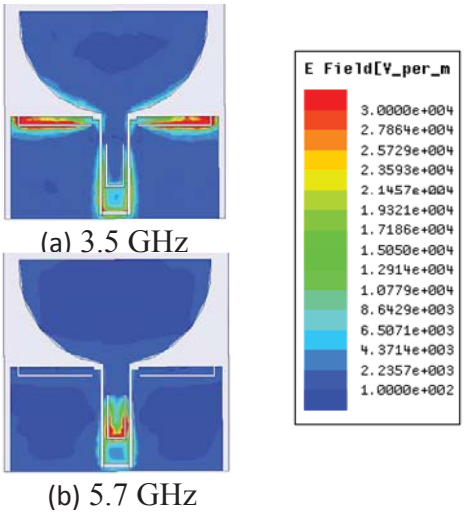

(a) 3.5 GHz

(b) 5.7 GHz

Figure 3. Electric field distribution at notch frequencies

The electric field distribution on the surface of the antenna at the notched frequencies is shown in Fig. 3. The figures clearly show that the L-shaped slots are responsible for the first notched band while the U-shaped slot controls the second notched band.

4. Radiation Characteristics: The simulated and measured reflection characteristics of the proposed antenna are shown in Fig. 4. The peak rejected level is -1.69 dB at 3.55 GHz in the first notch band and -2.37 dB at 5.75 GHz in the second notched band. Measured results are found to be in good agreement with simulated results in the second notch band. The bandwidth of the first notch band is however slightly higher than simulated results. Also there is a mismatch in readings at higher frequencies but this can be attributed to soldering effects that have not been accounted for in simulation studies.

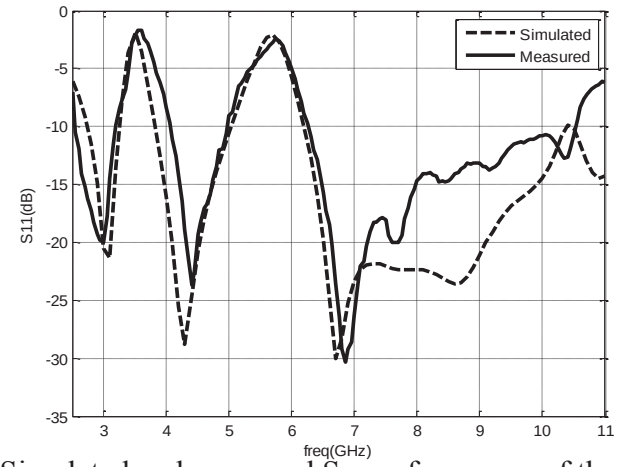

Figure 4. Simulated and measured S_{11} vs frequency of the proposed antenna

The normalized radiation pattern measured at three radiated frequencies is plotted in Fig. 5.

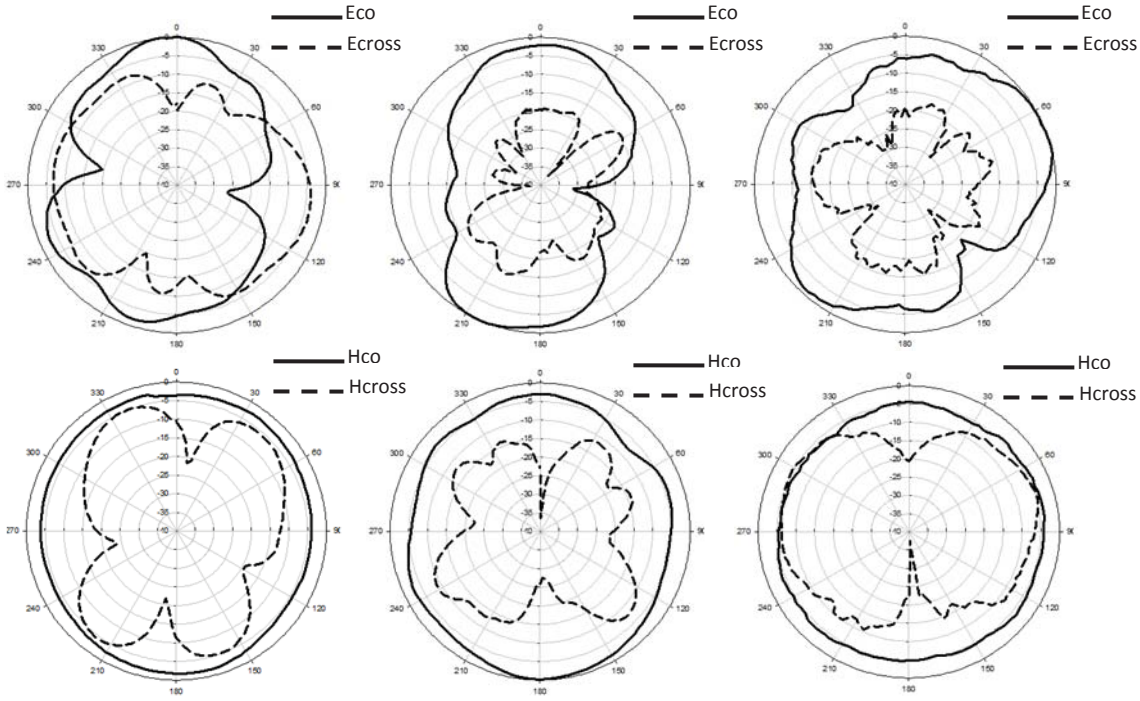

Figure 5. Normalized radiation patterns measured at (a) 3.1 GHz (b) 6.8 GHz (c) 10 GHz

The group delay for the antenna measured for two antennas placed in face to face configuration 15 cm apart is shown in Fig. 6. It is less than 1 ns throughout the UWB range except in the notched bands.

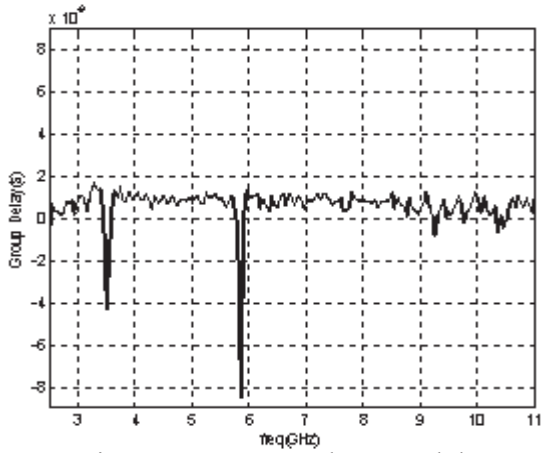

Figure 6. Measured group delay

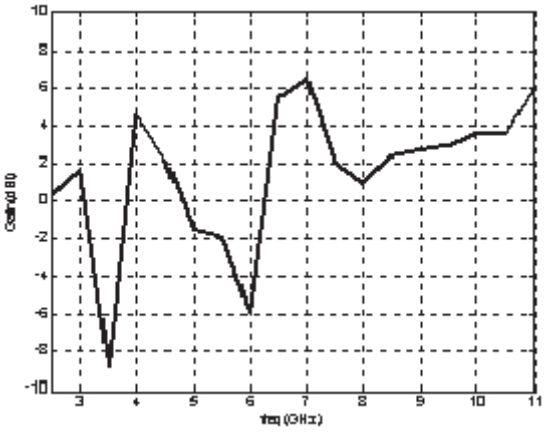

Figure 7. Measured gain

The measured gain of the antenna is shown in Fig. 7. The gain is low in the notch bands and decreases sharply at 3.5 GHz and 6 GHz. In the rest of the UWB range gain is positive with a peak gain of 6.44 dBi at 7 GHz. Table 2 shows the comparison with a few recently proposed CPW-fed antennas. The proposed antenna has high notch bandwidths in both bands but lowest gain at the notch frequencies.

Antenna	[5]		[6]		[7]		Proposed antenna	
Antenna size (mm^2)	30x30		32x32		Not specified		32x31.6	
Notch bandwidth (GHz)	3.3-4.2	5.0 - 6.0	3.3 - 3.75	5.07-5.83	3.2-3.8	5.0-6.0	3.25-4.04	5.0-6.25
Minimum Gain in notch band (dBi)	-4	-4.8	-1.5	1	-6	-5	-8.8	-5.86

Table 2. Comparison with recently proposed antennas

5. Conclusion: A compact CPW-fed UWB antenna with dual notched characteristic is presented. Slots are inserted in the ground plane and feed line to notch out the frequency bands corresponding to WiMax and WLAN applications which can cause possible interference to UWB applications. The design allows independent control of the two notch bands with strong rejection and since the radiating patch is left undisturbed, omni-directional radiation pattern is obtained throughout the UWB range.

References:

[1] Fei Yu, Chunhua Wang, "A CPW-Fed Novel Planar Ultra-Wideband Antenna with a Band Notch Characteristic" Radioengineering, Vol. 18, No. 4, December, 2009.

[2] James R. Kelly, Peter S. Hall, and Peter Gardner, "Band-Notched UWB Antenna Incorporating a Microstrip Open-Loop Resonator", IEEE Transactions on Antennas and Propagation, Vol. 59, No. 8, August 2011.

[3] Xiaoyin Li, Lianshan Yan, Wei Pan, and Bin Luo, "A Compact Printed Quadruple Band-Notched UWB Antenna", International Journal of Antennas and Propagation, Article ID 956898, 6 pages, 2013.

[4] Khalil H. Sayidmarie, Tariq A. Najm, "Performance Evaluation of Band-Notch Techniques for Printed Dual Band Monopole Antennas", International Journal of Electromagnetics and Applications, 3(4): 70-80, 2013.

[5] K Vyas, A K Sharma and P K Singhal, "Design and analysis of two novel CPW-fed dual band-notched UWB antennas with modified ground structures", Progress in Electromagnetics Research, Vol. 49, 159-170, 2014.

[6] A Wu, B Guan, "A compact CPW-fed UWB antenna with dual band notched characteristics", International Journal of Antennas and Propagation, Vol. 2013, Article ID 594378, 7 pages, 2013.
[7] C M Li, L H Ye, "Improved dual band-notched UWB slot antenna with controllable notched bandwidths", Progress in Electromagnetics Research, Vol. 115, 477-493, 2011.
[8] J Liang, L Guo, C C Chiau, X Chen, "CPW-fed circular disc monopole for UWB applications", Antenna Technology: Small Antennas and Novel Metamaterials, IWAT 2005, 505-508, 2005.

Planar UWB Antenna with Dual Band-notched Characteristics

Sarah Jacob[(1)], Anila P.V.[(1)], S. Mridula [(2)] and P. Mohanan[(1)]
(1) CREMA, Department of Electronics, CUSAT,
Kerala, India, Pin 682 022, Email: sarahjacob12@gmail.com
(2) Division of Electronics, School of Engineering, CUSAT
Kerala, India, Pin 682 022, mridula@cusat.ac.in

Abstract: *A compact coplanar waveguide (CPW) fed ultra wide band (UWB) monopole antenna with dual band-notched characteristics is presented. The antenna consists of a truncated circular disc and a semi-elliptical ground plane with an overall size of 25 mm x 20 mm x 1.6 mm. The band-notched performance is achieved by etching two simple resonant structures, a folded U-slot and a U-slot, on the radiating patch. The measured 10 dB return loss bandwidth covers 3.1 GHz to more than 12 GHz, with one notch frequency band at WiMAX (3.35– 3.8 GHz) and the other at WLAN (5.5–5.9 GHz).The antenna has promising features, including good impedance match, moderate gain and small group delay variations (<1 ns) over the entire UWB band.*

Introduction: Since the Federal Communications Commission (FCC) approved the frequency band from 3.1 to 10.6 GHz for commercial UWB applications in 2002 [1], the demands on the UWB systems and subsequently the research activities in various UWB antenna designs have been increased tremendously. Challenges of the feasible UWB antenna design include omni-directional and stable radiation patterns, flat gain response, low group delay and compact size. However, over the designated bandwidth of UWB system, there exist narrow band services that occupy frequencies within the UWB band, such as WiMAX system operating at 3.3–3.7 GHz and WLAN system operating at 5.15–5.825 GHz. To improve the co-existence of UWB systems with other wireless standards, antennas with band-notched characteristics have been proposed [2-4] to avoid the potential interferences.

In this paper, a simple UWB monopole antenna with dual band-notched characteristics is proposed. The UWB antenna consists of CPW-fed truncated circular disc and modified rectangular ground plane covers 10 dB return loss bandwidth extending from 3.4 GHz to more than 12 GHz. To realise the dual band-notched characteristics, a folded U-slot is etched near the truncated edge of the disc which produces a notch band (3.35–3.8 GHz) for WiMAX and also decreases the lower edge frequency from 3.4 to 3.1 GHz. Further, by etching a U-slot on the disc near the feed point, the second rejection band (5.5–5.9 GHz) for WLAN is obtained. It is observed that the antenna exhibits fairly good performance over the entire operating bandwidth as expected.

Antenna geometry and design: Fig.1a shows the geometry of the proposed dual band-notched UWB antenna having a size of 25 mm x 20 mm, fabricated on a substrate of relative permittivity $\varepsilon_r = 4.4$, $\tan\delta = 0.02$ and thickness h = 1.6mm. The proposed antenna consists of a truncated circular disc and a rectangular ground plane with semi-elliptically shaped upper edge. This structure is actually derived from a conventional circular disc monopole antenna

where the current is mainly concentrated over the lower edge of the disc [5] for the fundamental mode. So the antenna can be made more compact by removing the upper portion of the disc without disturbing the radiation characteristics severely. A 50 Ω CPW feed line, which has a signal strip of width W_s and a gap G between the strip and the coplanar ground plane, is used to excite the antenna. R is the radius of the circular disc which is truncated at a point L_t below the topmost point on its circumference. On the ground plane, since the current is mainly distributed along its upper edge, the impedance characteristics can be tuned by optimizing the dimensions of the ground plane [6]. Hence, the upper edge of the rectangular ground plane of size L_g x W is made semi-elliptical in shape with R_M and R_m as the major and minor axes.

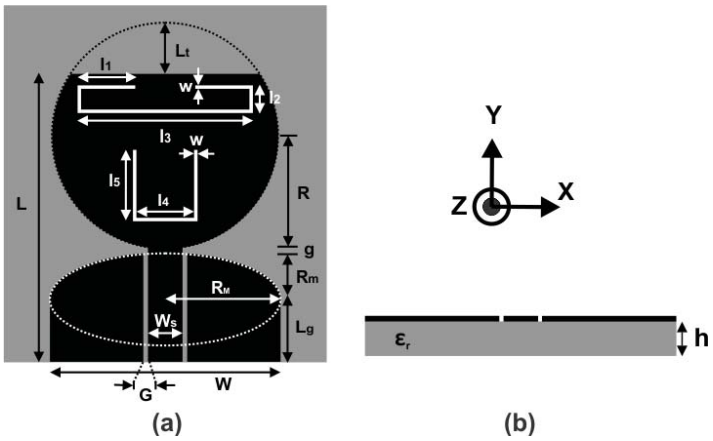

Fig.1 Geometry of the proposed dual band-notched antenna a) top view b) side view

By etching two resonant slots on the radiating patch of the UWB antenna, a dual band-notched characteristic is realized. The design concept of the notch function is to adjust the total length of the slot to be approximately half the guide wavelength at the desired frequency, which makes the input impedance resistive. The simulations are performed using CST Microwave Studio. The optimised design parameters are L = 25 mm, W = 20 mm, R = 9.8 mm, L_t = 4.4 mm, W_s = 3 mm, G = 0.4 mm, L_g = 5.5 mm, R_M = 10 mm, R_m = 4 mm, g = 0.3 mm, w = 0.4 mm, $l_1 = 0.08\lambda g_1$, $l_2 = 0.04\lambda g_1$, $l_3 = 0.29\lambda g_1$, $l_4+2w = 0.17\lambda g_2$, $l_5 = 0.18\lambda g_2$ where λg_1 and λg_2 are the guide wavelength corresponding to the notch frequencies at WiMAX and WLAN respectively.

Results and discussions: The measurements are carried out using Rhode & Schwarz ZVB 20 vector network analyser. Fig.2 shows simulated and measured return loss of the proposed antenna. It can be seen that the proposed antenna exhibits two steep rejection bands of 3.35-3.8 GHz and 5.5-5.9 GHz, while maintaining 10 dB return loss performance from 3.1 GHz to more than 12 GHz. The measured return loss agrees very well with the simulated results.

The measured normalised radiation patterns of the antenna in the H-plane (x-z plane) and E-plane (y-z plane) inside an anechoic chamber for four different frequencies 3.2, 6, 8 and 10 GHz are shown in Fig.3(a)-(b).The antenna exhibits nearly omni-directional radiation patterns in the H-plane (x-z plane). The measured E-plane (y-z plane) patterns are similar to 'figure of eight', like in printed monopole antennas.

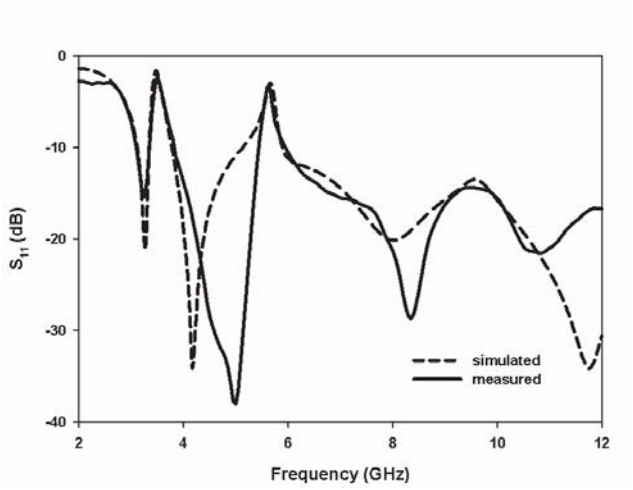

Fig. 2 Measured and simulated return loss of the proposed dual band- notched UWB antenna

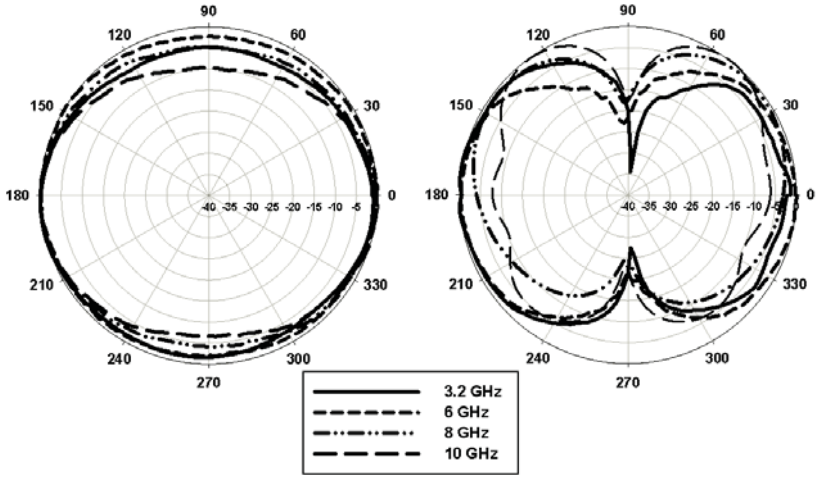

(a) (b)

Fig.3 Measured radiation patterns of the proposed antenna
a) H-plane (x-z plane) b) E-plane (y-z plane)

The simulated and measured peak gain (gain comparison method) of the antenna are shown in Fig.4 exhibits significant gain suppression at 3.5 GHz and 5.65 GHz. For frequencies outside the rejected bands, the gain remains stable with variations less than 2.5 dB, i.e. the proposed antenna has a moderate gain response and at the same time effectively minimizes the potential interferences between UWB system and co-existing narrow band wireless systems.

The antenna transfer function (S_{21}) and group delay measurements are carried out outside anechoic chamber considering the real-world situation with multiple reflecting objects. The antenna system involves two identical band-notched UWB antennas, transmitting and receiving are separated by a distance of 15 cm. Fig.5 describes the measured S_{21} and group delay for two different orientations of the proposed antenna, face to face and face to side. It is observed that the S_{21} is almost similar for both the orientations with sharp dip at notched frequencies. The variation of the group delay over the UWB band is much less than 1ns except in the vicinity of notched bands, which demonstrates that the proposed antenna exhibits excellent phase linearity at desired UWB frequencies.

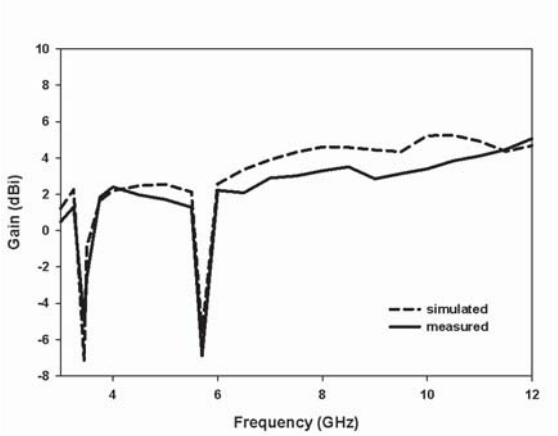

Fig.4 Measured and simulated peak gain of the proposed antenna

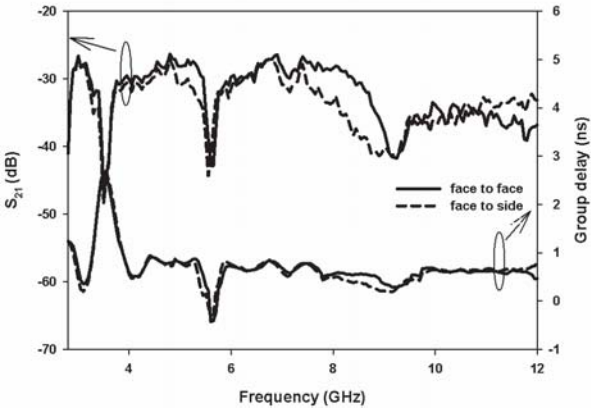

Fig.5 Measured S_{21} and group delay for two different orientations of the proposed antenna

Conclusion: A truncated circular disc UWB monopole antenna etched with two slots for achieving dual band-notch characteristics is discussed. The proposed antenna exhibits two steep rejection bands at 3.35-3.8 GHz and 5.5-5.9 GHz, while maintaining 10 dB return loss performance from 3.1GHz to more than 12 GHz. This antenna exhibits nearly omni-directional radiation patterns in H-plane throughout the UWB frequency range with a moderate gain response. The measured results indicate that the proposed UWB antenna can not only prevent the interference produced by the co-existing narrow band services but also has an excellent transient response within the UWB operating bandwidth. Therefore, the proposed antenna is a good candidate in various UWB systems.

Reference:

[1] First report in the matter of revision of part 15 of the Commission's rules regarding ultra-wideband transmission systems, Federal Communications Commissions, 2002.

[2] X. Wang, L. Wang, H. Zhou and W. Lu, " A compact CPW-fed antenna with dual band-notched characteristics for UWB applications', Microwave and Optical Technology Letters, Vol. 56, No. 5, pp.1047-1050, 2014.Authors Name,

[3] X. Liu, Y. Yin, P. Liu, J. Wang and B. Xu, "A CPW-fed dual band-notched UWB antenna with a pair of bended dual-L-shape parasitic branches", Progress In Electromagnetics Research, Vol. 136, pp. 623-634, 2013.

[4] P. Gao, L. Xiong, J. Dai, S. He and Y. Zheng, "Compact printed wide-slot UWB antenna with 3.5/5.5-GHz dual band-notched characteristics", IEEE Antennas and Wireless Propagation Letters, Vol. 12, pp. 983-987, 2013.

[5] J. Liang, L. Guo, C.C. Chiau, X. Chen and C.G. Parini, "Study of CPW-fed circular disk monopole antenna for ultra-wideband applications", IEE Proc. Microwaves Antennas & Propagation, Vol. 152, No. 6, pp.520-526, 2005.

[6] P. Li, J. Liang, and X. Chen, "Study of printed elliptical/circular slot antennas for Ultra wideband applications", IEEE Transactions on Antennas and Propagation, Vol. 54, pp. 1670–1675, 2006.

Multi-Fractal Monopole Antenna for UWB Applications

Merin Mary Mathews, K Shambavi, Zachariah C Alex
Vellore Institute of Technology
Vellore, India
kshambavi@vit.ac.in

***Abstract*- A multi-fractal monopole antenna for Ultra wide band applications is presented in this paper. The proposed antenna consists of a combination of Koch and Sierpinski fractals within a ring. Use of multi-fractal technique leads to improved bandwidth, radiation efficiency and reduced size. The proposed antenna size is 19.5*19.5*1 mm^3 which operates over a frequency range of 4.2 to 10.3 GHz. Radiation pattern of the proposed antenna is stable over the operating range.**

***Keywords*- Multi-Fractal antenna, Ultra wide band, Bandwidth, Sierpinski fractal, Koch fractal**

I. INTRODUCTION

Recently the Ultra Wide Band has experienced a rapid growth in wireless communication applications, since federal communication commission (FCC) declared the frequency band (3.1-10.6 GHz) as unlicensed band. The UWB technology is very attractive because of its high data rate transmission and low power consumption, simple hardware configuration and excellent immunity to multipath interference when compared with existing wireless communication systems [1].

FCC and the International Telecommunication Union Radio Communication Sector (ITU-R) now define UWB as transmission from an antenna, for which the emitted signal bandwidth is more than 20% of the center frequency or it exceeds 500 MHz [2]. There are so many UWB planar antennas existing so far, but these antennas are having large size [3]-[6]. By incorporating fractal structures compact size UWB antennas can be realized.

Fractals are complex geometric designs that repeat themselves and the fractal antenna concept was first introduced by Nathan Cohen in 1955. Fractals have self-similarity and space filling properties which leads to wideband operation, and therefore are suitable for UWB applications. Fractal structures introduce discontinuities in patch which results in better current distribution and hence radiation efficiency increases. Several fractal techniques have been proposed for UWB antennas so far, such as Pythagorean Tree [7], Minkowski [8], Giusepe peano [9] etc.

In this paper we make use of Sierpinski and Koch fractal inside a ring for obtaining the UWB band. Combining two or more fractal structures into a single structure leads to the multi-fractal concept. Introduction of multi-fractal concept results in more discontinuities in the form of cuts and bends, which leads to improved radiation characteristics. Here the multi-fractals are incorporated within the ring, which further improves the radiation characteristics.

II. ANTENNA DESIGN

The proposed UWB antenna is realized on FR4 Substrate with dielectric constant =4.4, loss tangent of 0.019 and thickness "h" of 1 mm. The designed UWB antenna is validated by simulation using High Frequency Structure Simulator (HFSS) v13.0.

Initially a circular patch monopole antenna of radius 7 mm is designed using equation (1) where f_r is the resonant frequency (GHz), C is speed of light (m/s), and r is radius of the circular patch [10]. To improve the radiation efficiency, fractals are added in the circular patch. As the current distribution is mainly along the circumference of the circular patch, etching its centre portion can have less effect on the radiation characteristics. Therefore a ring structure can be formed where fractal structures can be easily incorporated.

$$f_r = \frac{1.841c}{2\pi r_{eff}\sqrt{\varepsilon_{eff}}} \quad (1)$$

Where

$$r_{eff} = r\left[1+\frac{2h}{\pi r_0 \varepsilon_{eff}\left\{\ln\left(\frac{r}{2h}\right)+\left(1.41\varepsilon_r+1.77\right)+\frac{h}{r}\left(0.268\varepsilon_{eff}+1.65\right)\right\}}\right]^{\frac{1}{2}}$$

The Sierpinski and Koch fractal curves are added to the triangular patch which is placed inside the circular ring. The side length of triangular patch (W_t) can be determined using equation (2) .

$$W_t = \frac{2c}{3f_r\sqrt{\varepsilon_{eff}}} \quad (2)$$

III. RESULTS AND DISCUSSION

A. Ring with triangular patch structure

In this section a ring with and without triangular patch is designed and implemented as shown in Fig. 1. A ring of width 0.7 mm and equilateral triangular patch of sides 10.8 mm are taken into consideration. It can be inferred from Fig.2 that using only ring structure results in narrow band operation. The bandwidth of ring structure is increased by introducing triangular patch as shown in Fig. 2.

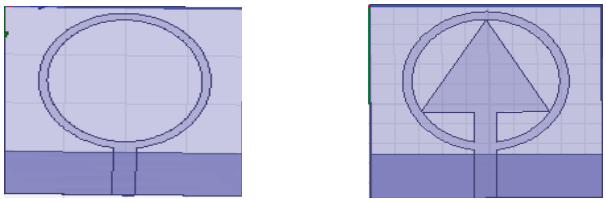

(a) (b)

Fig. 1. Structure of (a) initial ring (b) Triangular patch with ring

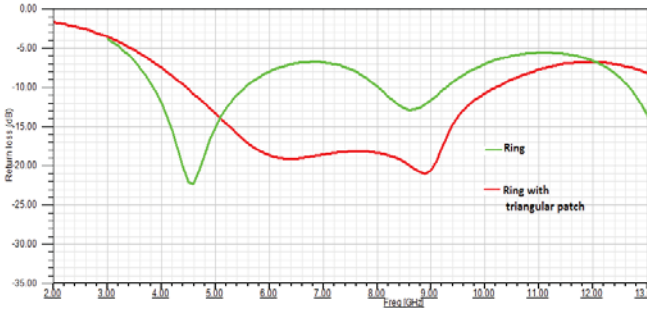

Fig. 2. Return loss characteristics of ring and triangular patch with ring.

B. Stages of development of proposed Antenna

In order to achieve the required bandwidth, different types of fractals are introduced in triangular patch structure. Assume "C" represents the iterations of Koch, "S" represents iterations of Sierpinski and m, n represents number of iteration. Hence, C[m]S[n] represents the m^{th} iteration of Koch and n^{th} iteration of Sierpinski fractal. Fig.3 (a) represents the 0^{th} iteration of Koch and Sierpinski fractal, Fig. 3 (b) represents 0^{th} iteration of Koch and 1^{st} iteration of Sierpinski, Fig. 3 (c) represents 1^{st} iteration of Koch and Sierpinski fractal. From Fig. 4 it can be observed that as the number of iterations of fractals increase, the return loss performance is improved. Here single iteration of Koch fractal and Sierpinski fractal can be used to obtain the desired multi-fractal monopole UWB antenna.

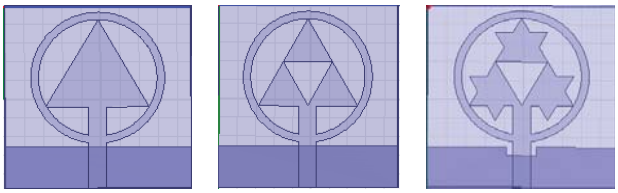

(a) (b) (c)

Fig. 3. Stages of development (a) C[0]S[0] (b) C[0]S[1] (c) C[1]S[1]

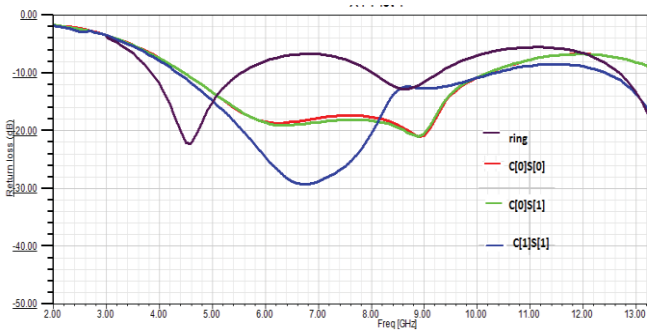

Fig.4. Return Loss characteristics of different iterations

Return loss characteristics for each iteration are shown in Fig. 4 . It can be observed that resonant frequency decreases with each iteration, which results in large operating band. The proposed UWB antenna is found to cover a frequency range of 4.34 to 10.35 GHz with return loss of -29.29 dB at resonant frequency of 6.7 GHz. The proposed antenna (C [1]S[1]) is exhibiting a 10 dB bandwidth of 89.7%.

C. Proposed multi-fractal UWB antenna

As discussed above the proposed UWB antenna is formed using single iteration of Koch and Sierpinski fractal (C[1]S[1]). The Sierpinski triangle which is cut off from the equilateral triangular patch having side length of 5.4 mm is taken for first iteration. The Koch curve added to the Sierpinski triangle is having dimension Lk = W_t / 6 = 1.8 mm. Two Koch curves are introduced to each sides of the Sierpinski triangle.

Proposed antenna is designed on FR4 substrate with dielectric constant =4.4, and loss tangent of 0.019. Dimension of the substrate is optimized to be (W_{sub} x L_{sub} x h_{sub}) 19.5 x 19.5 x 1 mm^3. The width and length of the feed

line is calculated using transmission line model equation [11] and obtained as (W_f x Lf) 1.9 x 8.6 mm^2. The partial ground plane beneath the substrate is having a dimension of (L_g x W_g) 4.4 x 19.5 mm^2.

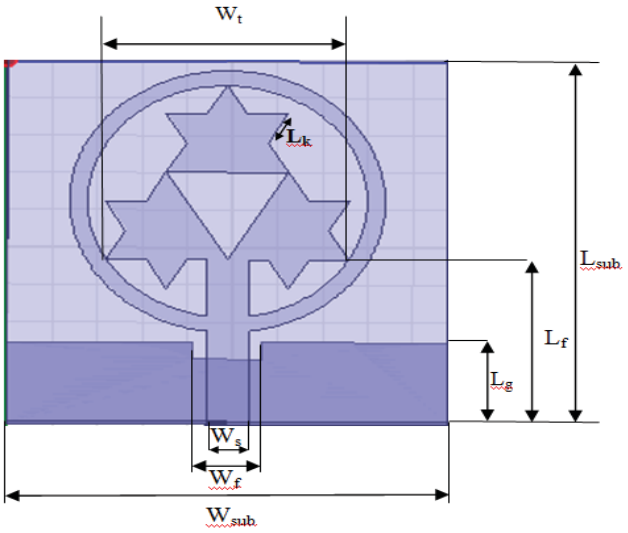

Fig. 5. Configuration of proposed multi-fractal UWB antenna (C[1]S[1])

1. Return loss

To obtain wide bandwidth and improved return loss characteristics, a rectangular slot is introduced at the feed position in the partial ground. Length of slot (Ls) is fixed as 0.9 mm and width is varied to get better return loss characteristics. The optimized dimension of the slot (L_s x W_s) is 0.9 x 3 mm^2. Effect of introducing slot in ground plane is shown in Fig.6.

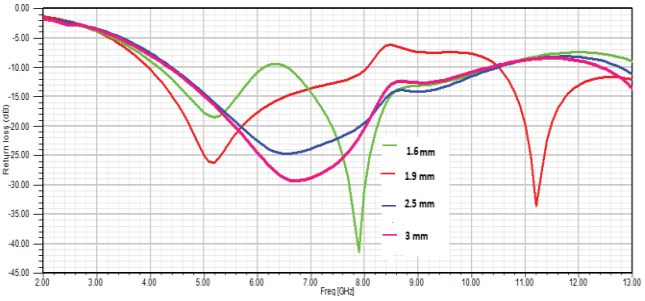

Fig. 6. Return Loss characteristics for different width of slots in ground

2. Surface current distribution

The surface current distribution of the proposed antenna was studied at different frequencies in the operating range as shown in Fig. 7. It is observed that at high frequencies, current distribution is mainly along the angular regions of the multi-fractal structure and hence enhancing the radiation efficiency of the antenna.

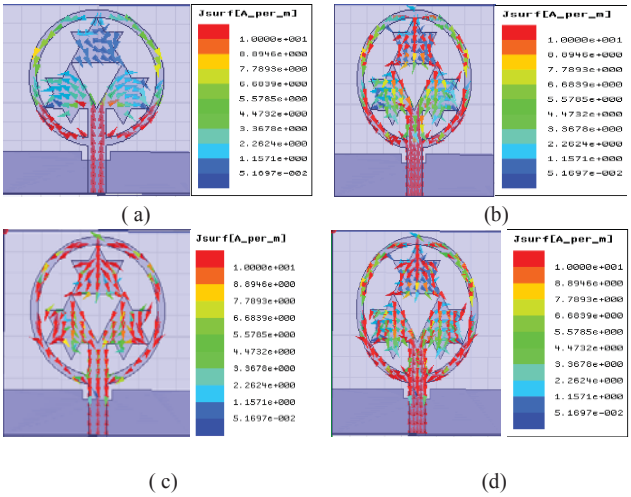

Fig . 7. Surface current distribution (A/m) at (a) 5 GHz (b) 7 GHz (c) 8 GHz (d) 9 GHz.

3. Radiation pattern

The radiation pattern of the proposed antenna in both elevation and azimuthal planes is shown in Fig.8. It is found to be symmetric and stable patterns in the form of figure eight in E plane. In H plane it provides Omni directional radiation pattern. The proposed antenna (C[1]S[1]) is exhibiting a radiation efficiency of 89.5% which is better when compared to the other iterations (C[0]S[0] and C[0]S[1]).

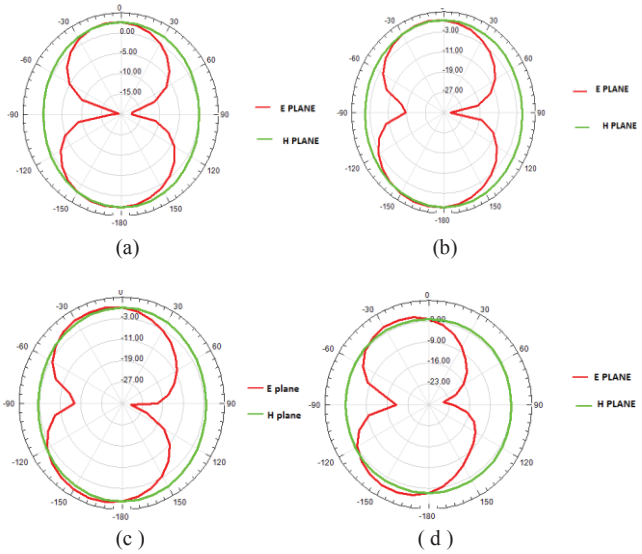

Fig . 8. Radiation pattern of proposed antenna at (a) 5 GHz (b) 7 GHz (c) 8 GHz (d) 9 GHz

4. Group delay

In order to verify the capability of the proposed antenna to operate in the UWB range, it is necessary to study its group delay characteristics. Analysis of group delay is performed by exciting two identical prototypes of the multi fractal UWB antenna kept in the far field for side by side orientation and face to face orientations. The distance of separation between them is 60 cm. Fig. 9 shows the group delay characteristics. It can be inferred that the group delay is consistent over entire UWB range.

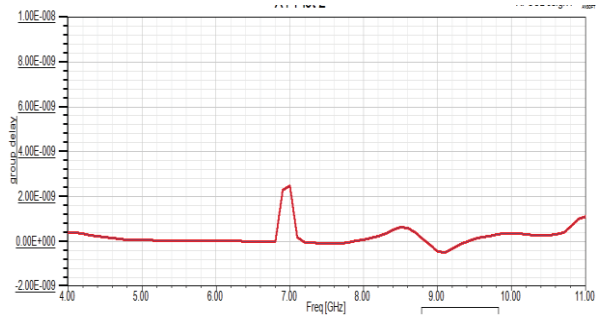

Fig . 9a. Group delay characteristics of (side be side) proposed antenna

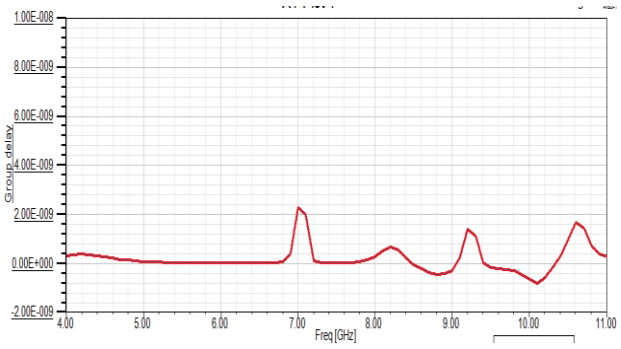

Fig . 8. Group delay characteristics (face to face) of proposed antenna

IV. CONCLUSION

The proposed multi-fractal antenna is exhibiting a bandwidth of 89.7 % ranging from 4.34 to 10.35 GHz, with a radiation efficiency of 89.5%. Comparing to other existing fractal antennas it is having a compact size of 19.5x19.5x1 mm^3. The multi-fractal techniques help to improve the bandwidth and return loss characteristics with stable radiation pattern. The bandwidth can be further enhanced by the addition of more fractals.

REFERENCES

[1] Waladi, Nooshin Mohammadi, Yashar Habashi, and Javad Nourinia, " A novel modified star-triangular fractal (MSTF) monopole antenna for super wideband applications", IEEE Antennas and Wireless Propagation Letters, VOL.12, 2013

[2] Basil K Jeemon , K Shambavi, Zachariah C Alex, "A Multi-fractal Planar Antenna for Wireless Applications", International conference on Communication and Signal Processing, April 3-5, 2013,

[3] K. Shambavi and Zachariah C Alex, " Printed Dipole Antenna with Band Rejection Characteristics for UWB Applications", *IEEE* Antennas and Wireless Propagation Letters, Vol. 9, pp.1029-1032,Nov. 2010

[4] K. Shambavi and Zachariah C Alex, " Design of Printed Multistrip Monopole Antenna for UWB Appliction", Microwave and Optical Technology Letters, Vol. 53,No.8,pp 1570-1572,Aug 2011

[5] C.Y Huang and W.C Hsia, "Planar Elliptical antenna for Ultra-wideband Communications", Electronic letters March 2005, Vol. 41 No. 6

[6] J. Jung, K. Seol, W. Choi and J. Choi, "Wideband Monopole Antenna for Various Mobile Communication applications", Electronic letters November 2005, Vol. 41

[7] Javad Pourahmadazar,Changiz Ghobadi, and Javad Nourinia, "Novel Modified Pythagorean Tree Fractal Monopole Antennas for UWB Applications" ,IEEE Antennas and Wireless Propagation Letters, Vol. 10, 2011

[8] Sayantan Dhar, Rowdra Ghatak, Bhaskar Gupta,"A Wideband Minkowski Fractal Dielectric Resonator Antenn", IEEE Transactions on Antennas and Propagation, Vol. 61, NO. 6, June 2013

[9] Homayoon Oraizi and Shahram Hedayati, "Miniaturized UWB Monopole Microstrip Antenna Design by the Combination of Giusepe Peano and Sierpinski Carpet Fractals", IEEE Antennas and Wireless Propagation Letters, Vol. 10, 2011

[10] A. K. Verma and Nasimuddin, "Analysis of circular microstrip antenna on thick substrate", Journal of Microwaves and Optoelectronics, Vol. 2, No. 5, July 2002.

[11] Constantine A. Balanis, Antenna Theory Analysis and Design, 2nd Edition, Wiley India(P.) Ltd., 2007

WIDEBAND PRINTED MONOPOLE ANTENNA FOR AIRBORNE APPLICATIONS

Mary Rani Abraham, Sona O. Kundukulam, Abdul Wahab and U.Ganesan

Naval Physical & Oceanographic Laboratory, Kochi, India-682021

Email: maryraniabraham@gmail.com

***Abstract**: A printed monopole antenna for airborne applications is presented. Blade antennas are preferred antenna structure in airborne applications due to their light weight and aerodynamic shape. Airborne platforms may fail to provide sufficient ground plane for blade antennas due to space constraints. As a solution for this, various configurations of printed monopole antenna have been studied and arrived at an optimum design. The proposed ground plane independent antenna provides a 2:1 VSWR bandwidth of 25% using resistive loading.*

Introduction: The rapid advancements in communication technologies are the driving force in design and development of broadband antennas with desirable mechanical features like compact size and light weight. Airborne antennas must not only meet the strict electrical requirements, but also be mechanically strong, compact, light in weight, and have a low profile [1].

Monopole antenna owing to their simple structure, small size and feasibility of implementation in planar configuration, is preferred for airborne applications. Airborne monopole antennas utilize the skin of the airborne platform as its ground plane. The wideband monopole antennas presented in [2-4] require very large ground plane. But in some cases due to space constraints, there may not be sufficient ground plane. As a solution for insufficient ground plane printed monopole antennas are introduced in this paper.

Microstrip antenna is a narrowband device having bandwidth of operation of the order of 1% to 5% [5]. However, present day applications demand broadband antennas. The narrow band microstrip antennas can be transformed into broadband radiating structure by using various techniques. Resistive loading of a quarter-wave patch antenna has already been proposed as an effective method of increasing the bandwidth of microstrip antennas by five to six times [5-6]. By lowering the antenna quality factor, an improved bandwidth can be achieved. The design and development of a broadband printed folded monopole antenna with resistive loading, which meet the requirements of airborne platforms, is presented here.

Antenna Design: A monopole antenna should have $\lambda_0/4$ height at lowest frequency of operation, where λ_0 is free space wavelength. In this proposed design, the printed folded monopole antenna has a height of 27% of that of standard monopole antenna. The glass epoxy substrate (relative dielectric constant = 4.4) of size 145mm X 270mm is used for the fabrication of the antenna. The antenna has two layers, the top layer contains the radiating

element and bottom layer contain the ground patch, placed back to back. An aluminium base plate in rectangular shape was used to hold the connector and provide interface to platform. A 50Ω SMA connector is used to excite the antenna. The centre conductor is connected to the printed radiating element of the antenna and outer to the bottom portion of the patch and to the aluminium base plate. The antenna schematic is shown in Fig.1 which shows the dimensional details of the antenna.

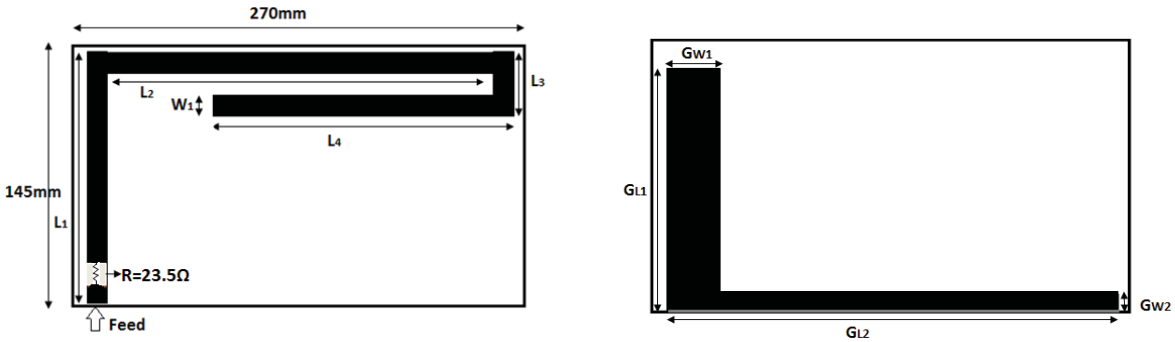

Top Layer Bottom Layer

Fig 1 Geometry of printed folded monopole antenna

Thickness of the substrate is 2mm. Dimensions of radiating patch: L_1=140mm; L_2= 255mm; L_3=36mm; L_4=180mm; W_1=12mm and dimensions of bottom patch: G_{L1}=130mm; G_{L2}=255mm; G_{W1}=30mm; G_{W2}=10mm.

The wideband performance is achieved by resistive loading. Since the resistor absorbs a part of energy, the radiation efficiency of the antenna will decrease. Therefore, by considering the trade off between impedance matching of antenna and the radiation efficiency, the resistance value is chosen as 23.5Ω. This value is sufficient to accomplish the required bandwidth while maintaining the required radiation efficiency. The antenna is then mounted on an aluminium sheet of size 50mm X 290mm. The photograph of the antenna is shown in Fig 2. The whole antenna assembly is a single integral structure encompassing the printed monopole antenna and the aluminium base plate.

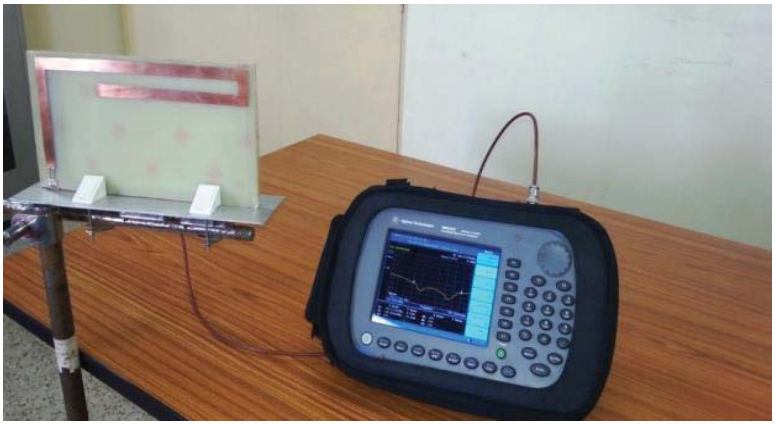

Fig 2 Measurement of fabricated antenna using N9342C Agilent Handheld spectrum analyser

Results and Discussion: The printed monopole antenna was evaluated for its performance using N9342C Agilent Handheld Spectrum Analyser. The measured VSWR of the antenna has been found to be less than 2 over the entire frequency band of interest. The simulated and measured return loss plots of the antenna are shown in Fig 3. The simulated radiation characteristics of the antenna at centre frequency f_0 MHz is shown in Fig 4. The gain of the antenna is comparatively low. This is expected as the loaded resistance absorbs part of the energy. The gain can be improved by using various techniques like using dielectric substrate of less loss tangent, using radome etc.

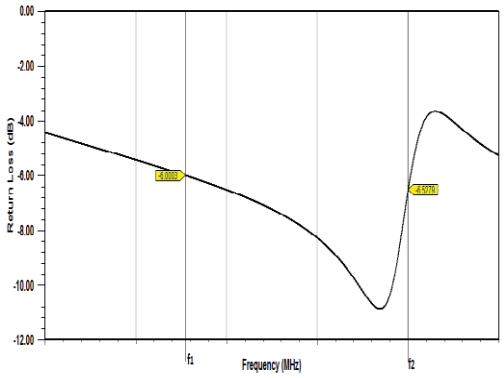

Fig 3a Simulated Return loss

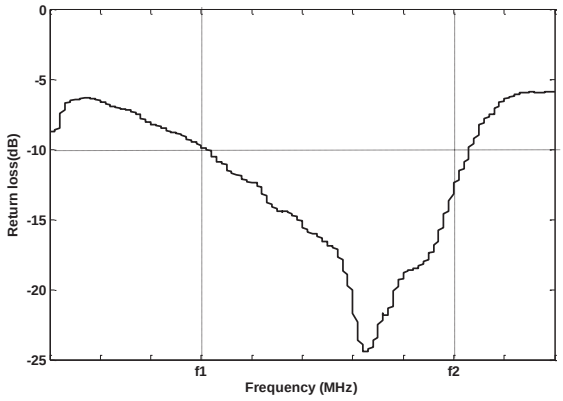

Fig 3b Measured Return loss

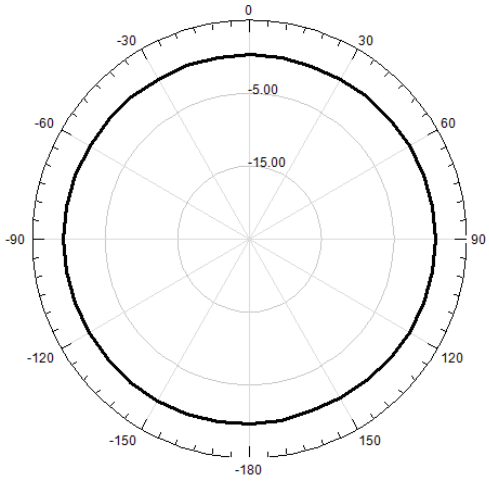

Fig 4a Simulated Azimuthal pattern at f_0 MHz

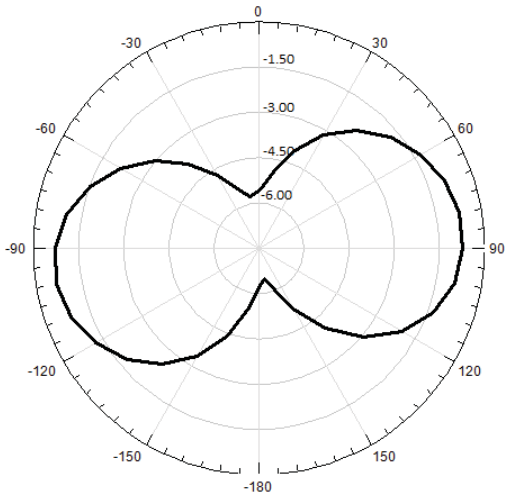

Fig 4b Simulated Elevation pattern at f_0 MHz

Conclusions: A broadband printed folded monopole antenna for airborne platforms has been developed. The antenna shows a VSWR less than 2 in the entire band of interest. The bandwidth and VSWR criteria have been achieved without ground plane. It finds applications on airborne platforms for antisubmarine warfare operations and direction finding Systems.

Acknowledgement: Authors would like to thank Shri. S Anantha Narayanan, Director, NPOL, Shri. Suresh M, Sc G, NPOL and Smt. Jayamma T.M, Sc F, NPOL for their encouragement and motivation towards achieving our goal.

References

[1] Thereza M. Macnamara, "Introduction to Antenna Placement and Installation", United Kingdom: Wiley, 2010

[2] Jiahui Chu, Chengli Ruan, Xingliang Liao, Yaoyao Cui, "A Small Size Broadband Antenna Used in VHF/UHF Band", Proceedings of International Symposium on Antenna Propagation and EM Theory, Kunming, pp 254-256, Nov 2008.

[3] Wenxuan Wei, Aixin Chen, Tiehua Jiang, Donglin Su "Design of a Novel UHF Shorted Planar Monopole Antenna", Proceedings of International Symposium on Antennas, Propagation and EM Theory, Kunming, pp 364-367, Nov 2008.

[4] S.D.Ahirwar, C.Sairam, Ashwani Kumar "Broadband Blade Monopole Antenna Covering 100-2000 MHz Frequency band", Proceedings of Applied Electromagnetic Conference, Kolkata, pp 1-4, Dec 2009.

[5] Ramesh Garg, Prakash Bhartia, Inder Bahl, Apisak Ittipiboon "Microstrip Antenna Design Handbook" Artech House, 2001.

[6] K. Wong, "Compact and Broadband Microstrip Antennas" New York: Wiley, 2002

A Spur Line Loaded Microstrip-Fed UWB Linear Taper Slot Antenna with Frequency Notch Characteristics

C. Sarkar, [(1)], C. Saha [(2)], and J.Y. Siddiqui [(3)]

(1) Swami Vivekananda Institute of Science and Technology, Kolkata, India , Pin-700145,
Email:chittajit_sarkar@yahoo.co.in
(2) Indian Institute of Space Science &Technology , Department of Space, Government of India,
Email: csaha@ieee.org
(3) Department of Radio Physics and Electronics, University of Calcutta, India,
Email: jysiddiqui@ieee.org

Abstract: *A compact micro strip-fed linearly tapered slot antenna (LTSA) is proposed for frequency notched Ultra-Wide Band (UWB) applications. The notch frequency is achieved by introducing a quarter wavelength spur-line in the feeding microstrip line of the antenna. The designed antenna is highly compact with an over-all size of 38mmX36mm exhibiting a -10 dB impedance bandwidth ranging from 1 GHz to 18GHz. The antenna provides consistent gain and stable radiation pattern. The L-shaped spur line contributes to the notch frequency aimed to avoid interference from 5-6GHz WLAN band.*

Introduction:

UWB technology has achieved an unprecedented growth and popularity amongst academic researchers and wireless industries over last ten years after the FCC permitted [1] its civil application within the frequency band from 3.1 GHz to 10.6 GHz. This ever-increasing demand and use of UWB technology has raised new challenges for antenna engineers to design highly compact, cost effective, low profile antennas with UWB bandwidth, high radiation efficiency and low group delay for minimal dispersion effect. Coexistence of few narrow band services such as fixed broad wideband access (FBWA) mainly around 3.15 GHz, WiMAX ranging from 3.3-3.7 GHz, IEEE 802.11 - wireless local area network (WLAN) in the frequency band of 5.15-5.85 GHz, and 7.25-7.75 GHz downlink of the X-band satellite communications systems with the FCC licensed UWB band requires the efficient design of frequency notched UWB antenna to reject signals from these interfering band/bands depending on user's requirement. Various techniques have been proposed to design such UWB antennas with single or multiple frequency notch characteristics. Most of the designs are based on defecting the radiators and / or the ground planes with single or multiple etched slots [2]-[4]. Complementary split ring resonator (CSRR) has also been used to achieve such frequency notches in the UWB antennas [5]. Very recently a new design concept of such frequency notched UWB antennas have been reported in [6] and [7] by loading single/multiple split ring resonator (SRR) pair along the CPW feed line of a quarter wave circular monopole antenna.

This paper describes a new and simple technique of designing frequency notched UWB antennas by embedding a quarter wavelength spur line on the feeding microstrip line of the radiator. A linearly tapered slot antenna (LTSA) has been chosen as the radiator covering a wide frequency spectrum as discussed in next section. Launched electromagnetic power is coupled from microstrip to the slot line which is gradually tapered giving rise to the radiation power along the length of slot and the antenna behave as an end fire radiator. Figure 1 shows the schematic of the proposed antenna. The linearly tapered slot antenna having starting and terminating slot-widths S_1 and W_s and tapered slot-length L_{ST} is excited by a microstrip line

of width t_1 and length x_1 having impedance of 50 Ω. The antenna is printed on a substrate having thickness h and dielectric constant ε_r. Proper impedance matching is ensured by properly terminating the microstrip and slot with a circular stub of diameter D_2 and D_1 respectively. A quarter wavelength spur line corresponding to a resonance frequency of 5 GHz and width S_2, is embedded in the transition region of the feed microstrip line.

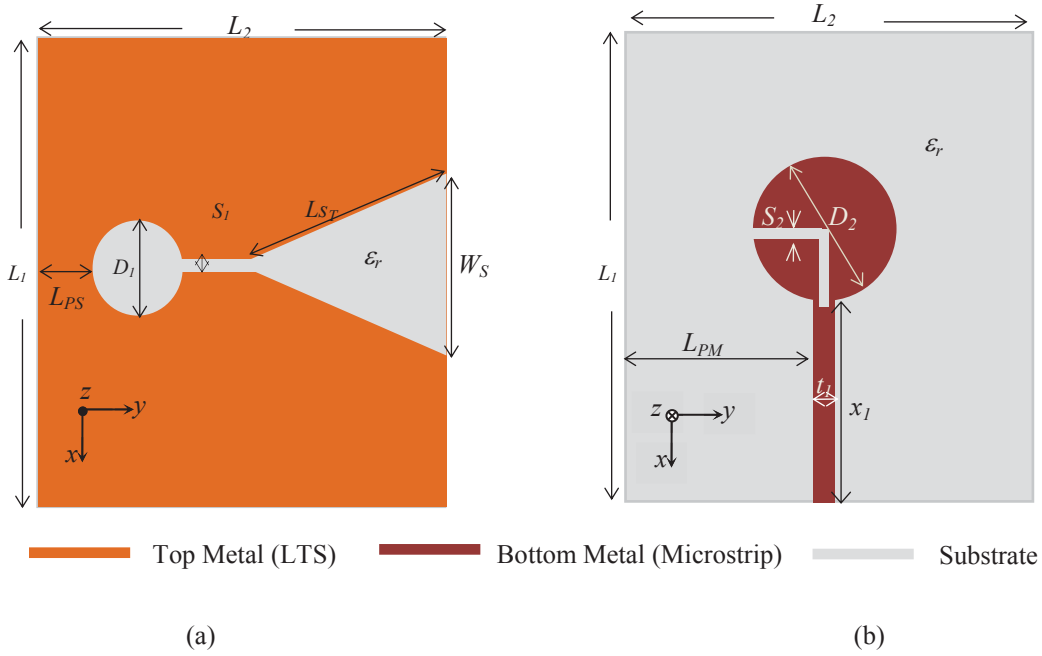

Fig. 1. Schematic of the spur-line coupled microstrip fed linearly tapered UWB slot antenna (a) Top view of the antenna showing the linearly tapered slot with circular stub matching at the transition region (b) Bottom view of the antenna showing the feed microstrip line embedded with quarter wavelength spur line

Antenna Design:

Figure 1 shows the schematic of the proposed microstrip line fed linearly tapered slot antenna. The antenna is etched on a substrate of thickness h = 0.813mm and dielectric constant ε_r = 3.55 with an over-all dimension of 38mm×36mm. The antenna is designed in a full wave commercial electromagnetic simulator [8]. Details of all the design parameters of the antenna is shown in TABLE-I.

Table I

DESIGN PARAMETERS OF THE PROPOSED SPUR LINE BASED FREQUENCY NOTCHED UWB ANTENNA PRINTED ON A DIELECTRIC SUBSTRATE WITH THICKNESS, h = 0.813 mm AND DIELECTRIC CONSTANT ε_r =2.33

Parameters	L_1	L_2	L_{ST}	W_S	t_1	L_{ps}	L_{PM}	S_1	S_2	D_1	D_2	x_1
Value (mm)	38	36	16	09	1.7	8	17.25	0.32	0.32	11	10	24

The length and the width of the tapered slot line (L_{ST}, W_S) are optimized to achieve the desired traveling wave mode of radiation as these parameters greatly impact the radiation characteristics of the antennas. The desired frequency notch is achieved by accommodating a quarter wavelength spur line along the length of the feed microstrip which is highly non dispersive band-gap structure [9].

Results and Discussion:

The proposed antenna, with and without the spur-line in feeding microstrip line, is designed and simulated using a commercial EM simulator [8]. Figure 2 shows the simulated S_{11} magnitude of the proposed LTSA antenna with and without the spur-line loaded in the feed of the radiator. As can be seen from the figure, the conventional LTSA without any spur line coupled to the feed line operates from 2 GHz to 18 GHz. The same antenna when loaded with a quarter wavelength spur line in the feeding microstrip line, a distinct frequency notch is observed at 5.1 GHz corresponding to the resonance frequency of the spur line.

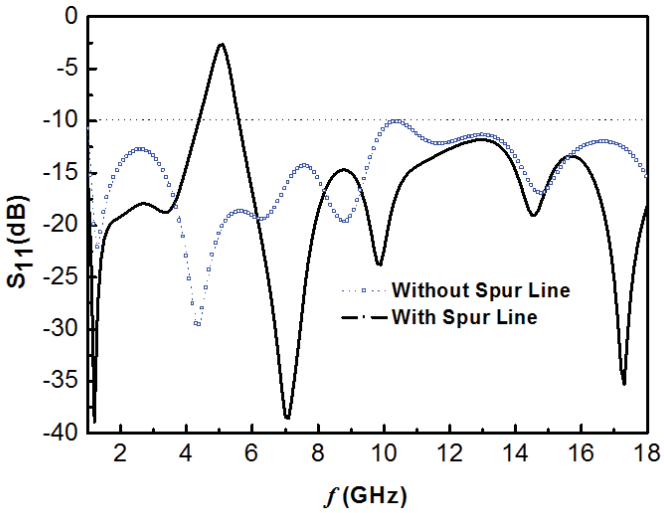

Fig. 2. Simulated S_{11} characteristics of the proposed spur line loaded microstrip fed linearly tapered slot antenna (LTSA) compared with a conventional LTSA without spur line. Design parameters as in TABLE-I.

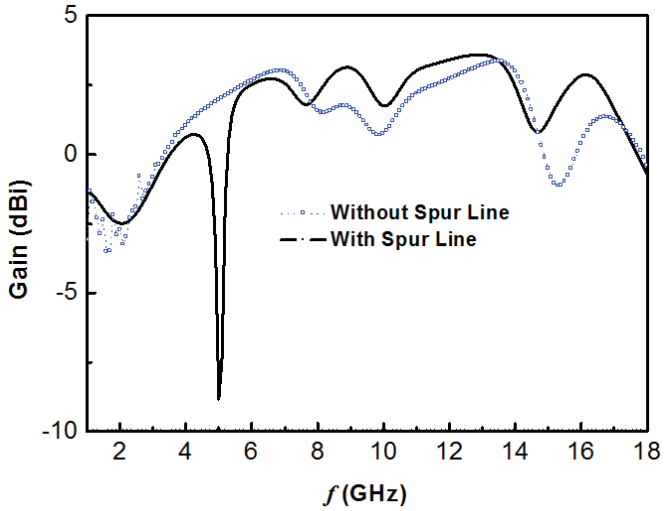

Fig. 3. Simulated Gain characteristics of the proposed spur line loaded microstrip fed linearly tapered slot antenna (LTSA) compared with a conventional LTSA without spur line.

The simulated peak gain as a function of frequency of the proposed antenna with and without the spur line is shown in Fig. 3. The plot shows a sharp reduction in gain of -9 dBi at the notch frequency contributed by spur line resonance. The overall gain of the antenna at other frequencies (3.5-14 GHz) is well above 1 dBi with a peak gain of 3.6 dBi at around 13 GHZ for both the configurations.

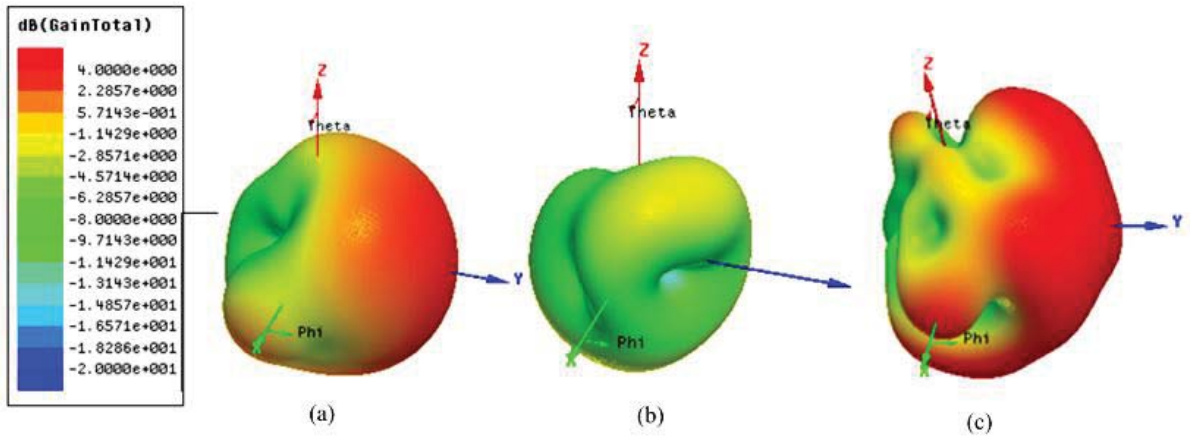

Fig. 4. Simulated 3D polar plot of the proposed spur line loaded microstrip fed linearly tapered slot antenna at (a) 4 GHz (b) 5.1 GHz (notch frequency) and (c) 13 GHz. All the plots are in same scale.

Figure 4 shows the simulated three dimensional radiation pattern of the proposed antenna at 4 GHz, 5.1 GHz and 13 GHz all plotted in same scale. The peak gain of the antenna at 5.1 GHz, corresponding to the notch frequency is very less as the antenna is effectively in non-radiating mode due to the spur-line resonance, whereas at rest of the frequencies it offers acceptable gain and pattern.

Conclusion:

A new concept of designing frequency notched UWB antenna is proposed by loading a spur line along the feeding microstrip line of a linearly tapered slot antenna. The concept can be extended to design multiple notched antennas by accommodating more number of spur lines on the microstrip. It can also be customized for wideband rejection purpose.

Reference:

[1] Federal Communications Commission (FCC) , Washington,DC, “First report and order in the matter of revision of Part 15 of the commission's rules regarding ultra-wideband transmission systems,” ET-Docket 98-153, 2002 .

[2] Nguyen, Dang Trang, Dong Hyun Lee, and Hyun Chang Park. "Very compact printed triple band-notched UWB antenna with quarter-wavelength slots." *IEEE Antennas and Wireless Propag. Let.,* Vol. 11, pp. 411-414, 2012.

[3] Y. Zhang, W. Hong, C. Yu, Z.Q. Kuai, Y.D. Don and J.Y. Zhou, “Planar Ultrawideband antennas with multiple notched bands based on etched slots on the patch and/or split ring resonators on the feed line,” *IEEE Trans. Antennas Propag.*, vol. 56, pp. 3063–3068, 2008.

[4] X.J Liao., H.C Yang, N. Han, and Y. Li, Y.H. Sun, “UWB antenna with dual narrow band notches for lower and upper WLAN bands,” *Electron. Lett.*, vol. 46, pp. 1593–1594, 2010.

[5] D. Jiang, Y. Xu, R. Xu and W. Lin, “Compact dual-band-notched UWB planar monopole antenna with modified CSRR,” *Electron. Lett.*, vol. 48, No.20, Sep. 2012.

[6] J.Y.Sidiqui, C.Saha, and Yahia M.M. Antar , “Compact SRR loaded UWB Circular Monopole Antenna with Frequency Notch Characteristics”, *IEEE Trans. Antennas Propag.*, vol 62, no.8, pp 4015-4020, 2014.

[7] J.Y.Sidiqui, C.Saha, and Yahia M.M. Antar , “Compact Dual SRR Loaded UWB Monopole Antenna with Dual Frequency and Wideband Notch Characteristics”, *IEEE Antennas and Wireless Propag. Lett* (Accepted for Publication).

[8] High Frequency Simulation Software, Ansoft corp. v.14.

[9] Sánchez-Hernández, David, and I. Robertson. "Triple band microstrip patch antenna using a spur-line filter and a perturbation segment technique." *Electronics Letters* 29.17 (1993): 1565-1566.

A CPW Fed Compact UWB Antenna with Modified Ground Plane and Corrugated Fractal Patch for Bandwidth Enhancement

V. Rajeshkumar [(1)] *and S. Raghavan* [(2)]
National Institute of Technology, Tiruchirappalli, India 620015,
Email: [(1)]vrajeshme@gmail.com, [(2)]raghavan@nitt.edu

Abstract: *A compact coplanar waveguide (CPW) fed corrugated fractal monopole antenna with a modified ground plane is presented. The main objective is to obtain ultra wideband (UWB) characteristics from a simple microstrip monopole antenna while maintaining their features. A wideband behavior and good impedance matching are obtained by modifying the ground plane to semi-trapezoidal shape. Further, the self-similar fractal property is utilized in the radiating element to enhance the bandwidth. The proposed antenna exhibits a wider impedance bandwidth from 3 GHz to 11.2 GHz for S11 ≤ –10 dB. By increasing the number of fractal iterations to three, a fractional bandwidth of about 125.3% (impedance bandwidth ratio 3.73:1) is achieved. The total volume of the presented antenna is 18×12×1.6 mm^3. The simulated antenna characteristics are presented and discussed.*

Introduction: The official release of 7.5 GHz spectrum to the ultra wideband technology has increased the use of unlicensed UWB wireless communication systems drastically. High data transmission rate, immunity to multipath interference, low power consumption, omnidirectional radiation characteristics and larger bandwidth are the main features of UWB systems [1, 2]. However, one of the major issues in the design of UWB system is to obtain larger fractional bandwidth and desired radiation characteristics over the entire band. Hence the design of such compact antenna with simple geometry has received significant interest among antenna designers. In recent times, different types of UWB monopole antennas with modified radiating patch and ground planes are reported [1]. Particularly in [2-5], for enhancing the impedance bandwidth and better impedance matching; the techniques like adding slots, strips, shorting pins, and asymmetrical patch are reported. In addition, by modifying the feed line, employing defected and electronic band gap structures in the ground plane [6,7], bandwidth enhancement are demonstrated which in turn affect the radiation characteristics as well as increases the difficulty. The self-similarity and space filling fractal properties are successfully utilized in the radiating patch for designing compact wideband [8, 9] and UWB antennas [10]. Particularly in self-similar fractal concept, the similar structure repeats several times with different scale sizes, leading to multiple resonant modes. Since each resonant part of the antenna is similar to each other, makes it promising one to design ultra wideband antennas.

In the proposed monopole antenna, the modification to both the ground plane as well as the radiating element is employed. The modification to the ground plane is used to obtain good impedance matching over a wider bandwidth. Then the self-similar fractal concept is utilized in the conventional monopole patch antenna to enhance the bandwidth without increasing the antenna size. By increasing the number of iterations the number of smaller edges and effective current paths are increased which in turn enhances the bandwidth.

Proposed antenna design: Figure 1 shows the design procedure of the proposed CPW-fed self-similar corrugated fractal antenna configuration. It is designed on a FR4-Epoxy substrate with compact size of 18×12 mm^2, thickness 1.6 mm, relative permittivity ε_r = 4.4 and loss tangent 0.02. The initial patch has dimension of $L_P \times W_P$ (11×10 mm^2) as shown in Figure 1(a). As reported in the literature, the modification to the ground plane has a significant effect on antenna's performance. Hence it is modified into a semi trapezoidal shape as shown in Figure 1(b). Further, the self-similarity fractal property is utilized to increase the number of edges as well as to increase the effective electrical length, as depicted in Figure 1(c)-1(e). Initially, the patch monopole antenna is designed which has a length (L_p) 11 mm. For the third iteration the current path is increased which has a length of 13.25 mm (L_1+W_1+L_2+W_2+L_3+W_3+L_4) as shown in Figure 2. Hence the proposed antenna has several edges which are used to obtain multiple resonant modes. A parametric study is carried out to optimize the crucial antenna parameters. The final dimensions are as follows: W = 12 mm, L = 18 mm, L_p = 11 mm, W_p = 10 mm, g_w = 4.6 mm, g_1 = 1.5 mm, g_2 = 4.6 mm, f_w = 1.6 mm, f_L = 8 mm, f_g = 0.6 mm, L_1 = 3.5 mm, L_2 = 3.0 mm, L_3 = 2.5 mm, L_4 = 2.0 mm, W_1 = 1 mm, W_2 = 0.75 mm, W_3 = 0.5 mm. In further iterations the dimensions of L_1 & W_1 are reduced by 0.5 and 0.25 mm, respectively.

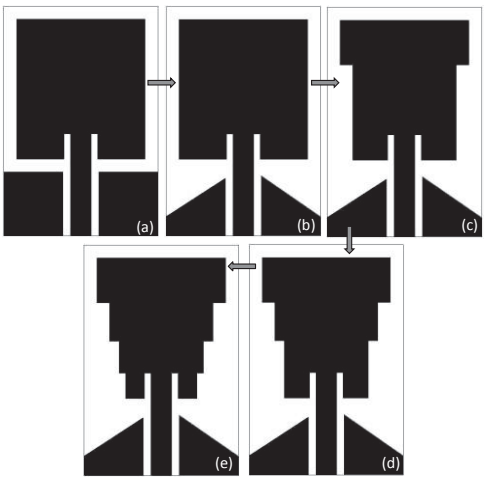

(1)

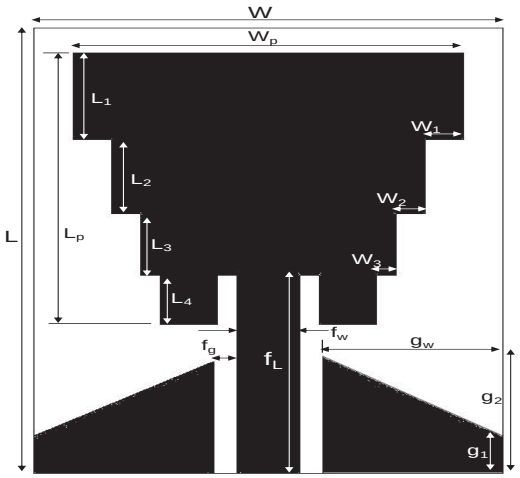

(2)

Figure 1 Evolution of proposed fractal antenna (a) Initial monopole antenna (b) With modified ground plane (c) First iteration (d) Second iteration (e) Third iteration

Figure 2 Geometry of the proposed fractal antenna

Results and discussion: The proposed antenna is first simulated and optimized using Ansoft's High Frequency Structure Simulator (HFSS) V.15. The initial patch antenna is designed for the resonant frequency of 4 GHz. Figure 3 shows the reflection coefficient less than -10 dB in the frequency range of 3.4 – 4.3 GHz, for the initial patch antenna. Then the ground plane is modified to obtain a good impedance matching over the wider bandwidth. Figure 3 shows a good impedance match over 2.9 – 8.0 GHz with the impedance bandwidth of 93.5 %. Thereby, it covers the frequency bands of major wireless applications such as 3.5 GHz WiMAX, 5 GHz WLAN and 7 GHz satellite ITU bands. Performance of the proposed corrugated fractal antenna for various iterations is compared in Table 1. The first iteration covers the frequency range 2.9 - 8.5 GHz. A bandwidth ratio of 2.93:1 and fractional bandwidth of 98.2% is obtained for the first iteration. The upper band edge extends towards from 8.0 - 11.2 GHz. Thus, for the third iteration the simulated bandwidth ratio of 3.73:1 and fractional bandwidth of 125.3% is obtained, an improvement of about 31.8% is achieved

compared to the initial CPW-fed monopole patch antenna. Such an antenna effectively meets the requirements of UWB applications.

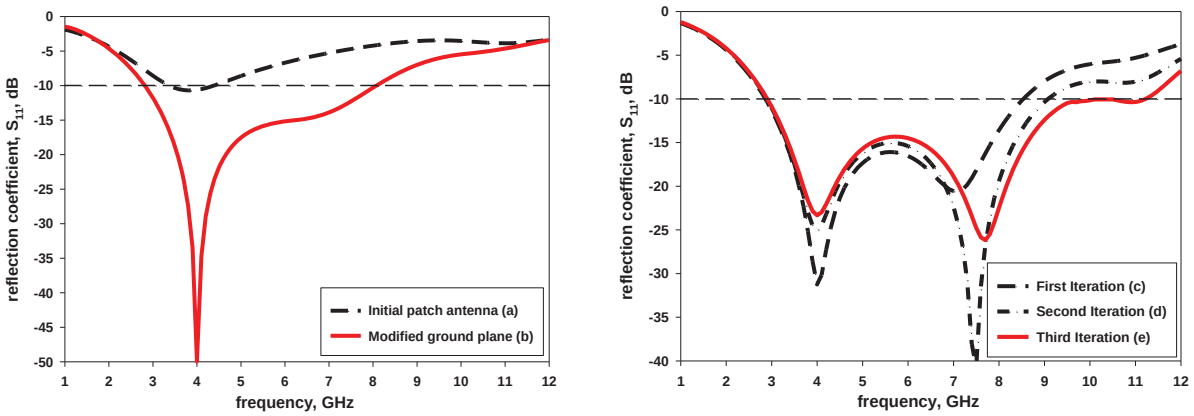

Figure 3 Simulated return loss characteristics of the antenna configurations a, b, c, d & e.

Table 1 Performance of Proposed Fractal Antenna

Iteration	Frequency band (GHz)	Band -width ratio	Fractional Bandwidth (%)
Modified ground plane	2.9 – 8.0	2.75:1	93.5
First iteration (n=1)	2.9 – 8.5	2.93:1	98.2
Second iteration (n=2)	2.9 – 9.0	3.10:1	102.5
Third iteration (n=3)	3.0 – 11.2	3.73:1	125.3

Radiation characteristics: Figure 4(a) & 4(b) depicts the simulated surface current distributions at 4 GHz and 7.7 GHz, respectively. For the 4 GHz frequency band, a strong current distribution is observed around the feed line and long edges of the fractal patch antenna. At 7.7 GHz, a strong current distribution is located at the multiple small edges of the antenna. It confirms that, the number of iterations increases the upper resonant frequency range; whereas the third iteration effectively meets the demands of UWB requirements. Figures 5(a) & 5(b) represents the radiation patterns of the proposed antenna in both H and E planes at different resonating frequencies 4 GHz and 7.7 GHz, respectively. The antenna exhibits monopole-like radiation patterns in the E-plane for all the resonant frequencies. In the H-plane, the antenna shows omnidirectional radiation patterns as desired in the UWB applications; which indicates that the antenna can receive the signals from all the directions.

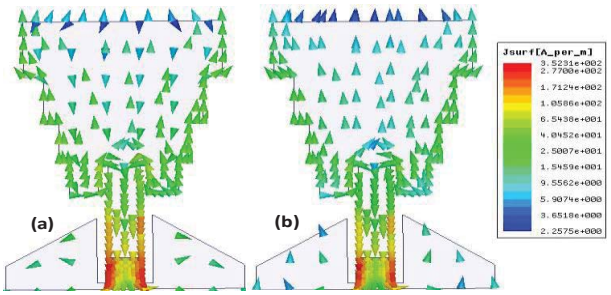

Figure 4 The simulated surface current distributions at (a) 4 GHz (b) 7.7 GHz

Conclusion: A very compact, ultra wideband fractal antenna with enhanced bandwidth by using self-similarity concept and modified ground plane is presented. The impedance

bandwidth of about 125.3% is achieved under the matching criterion of reflection coefficient less than – 10dB. It meets the demands of major wireless and UWB applications which occupy the frequency band in between 3 to 11.2 GHz. The applied fractal concept has increased the fractional bandwidth by 31.8%. Extensive impedance bandwidth, reasonable gain and the omnidirectional radiation characteristics are observed over the entire operating band. In addition, a very compact size compared with recently reported antennas and low profile make the antenna ideally suitable for modern UWB as well as wireless applications.

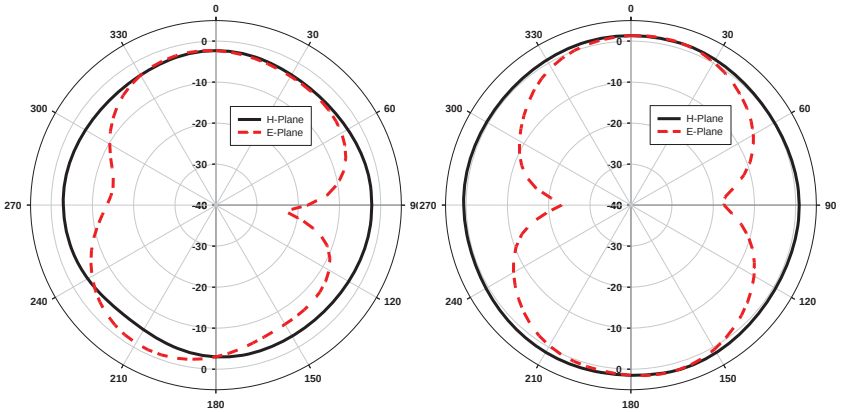

Figure 5 Simulated radiation patterns at (a) 4 GHz (b) 7.7 GHz

Reference:

[1] X. L. Liang, "Ultra-wideband antenna and design, Ultra wideband - Current status and future trends, Dr. Mohammad Matin (Ed.), ISBN: 978-953-51-0781-1, InTech, DOI: 10.5772/47805, 2012.

[2] A. Subbarao, S. Raghavan, "Compact coplanar waveguide-fed planar Antenna for ultra-wideband and WLAN Applications", Wireless Pers Commun Vol.71, No.4, 2849–2862, 2013.

[3] N. Ojaroudi, M. Ojaroudi, "Novel design of dual band-notched monopole antenna with bandwidth enhancement for UWB applications", IEEE Antennas Wireless Propag Lett, Vol. 12, 698–701, 2013.

[4] W. Liu, Y. Yin, W. Xu, S. Zuo, "Compact open-slot antenna with bandwidth enhancement", IEEE Antennas Wireless Propag Lett, Vol.10, 850–853, 2011.

[5] D.C. Chang, J.C. Liu, M.Y. Liu, "Improved U-shaped stub rectangular slot antenna with tuning pad for UWB applications", Electron Lett, Vol.41, 1095–1096, 2005.

[6] Z. Guo, H. Tian, X. Wang, Q. Luo, Y. Ji, "Bandwidth enhancement of monopole UWB antenna with new slots and EBG structures", IEEE Antennas Wireless Propag Lett, Vol. 12, 1550–1553, 2013.

[7] S. R. Emadian, C. Ghobadi, J. Nourinia, M. Mirmozafari, J. Pourahmadazar, "Bandwidth enhancement of CPW-Fed circle-like slot antenna with dual band-notched characteristic", IEEE Antennas Wireless Propag Lett, Vol.11, No.7, 543–546, 2012.

[8] S. Dhar, R. Ghatak, B. Gupta, D. R. Poddar, "A Wideband Minkowski fractal dielectric resonator antenna", IEEE Trans Antennas Propag, Vol.61, 2895–2903, 2013

[9] D. D. Krishna, M. Gopikrishna, C. K. Aanandan, P. Mohanan, K. Vasudevan, "Compact wideband Koch fractal printed slot antenna, IET Microw Antenna Propag, Vol.3, No.5, 782–789, 2009.

[10] H. Fallahi, Z. Atlasbaf, "Study of a class of UWB CPW-Fed monopole antenna with fractal elements", IEEE Antennas Wireless Propag Lett, Vol. 12, 1484–1487, 2013.

DECEMBER 18, THURSDAY
03.30PM TO 06.00PM
RESEARCH SESSION 9
ANTENNAS
J C BOSE- HALL

Chair: Prof. C S Sreedhar, BIT, Bangalore

No	Papers	Page
9.1	**C-Band Omni-Directional Antenna for Stealth Application** Pramendra Kumar Verma, Raj Kumar, and Mahakar Singh. Defence Electronics Application Laboratory, Dehradun, India, 248001. *Email: pramendra@deal.drdo.in*	255
9.2	**New Superstrate for Resonance Gain Antenna with Reduced Side Lobe Level** Koushik Dutta[1], Debatosh Guha[1], and Chandrakanta Kumar[2]. [1]Institute of Radio Physics and Electronics, University of Calcutta, Kolkata-700009, India. *Email: koushikdutt@ieee.org, dguha@ieee.org* [2]Communication Systems Group, ISRO Satellite Centre, Department of Space, Government of India, Bangalore 560017, India. *Email: kumarchk@ieee.org*	259
9.3	**Controlling of Higher Harmonics and Modes in Dielectric Resonator Antennas** S. Biswas [1], D. Guha [2], and C. Kumar[3] [1]NITMAS, WB 743 368, India. *Email: sbiswas@ieee.org.*[2]Institute of Radio Physics and Electronics, Calcutta University, Kolkata, India, 700009. *Email: dguha@ieee.org* [3]Comm. Systems Group, ISRO Satellite Centre, Bangalore 560017, India,. *Email: kumarchk@ieee.org*	263
9.4	**A High Gain & Low Side Lobe Level Pillbox based Fan Beam Antenna at Ka Band** Raj kumadhavar, Pramendra Kumar Verma, and Mahakar Singh Defence Electronics Application Laboratory, Dehradun, India, 248001. *Email: raj.kumar@deal.drdo.in*	267
9.5	**FDTD Analysis of Conformal Strip Excited Rectangular Dielectric Resonator Antenna Array** Anshul Gupta[1], Ravi Kumar Gangwar[2] [1]National Institute of Technology Raipur, Raipur, India, 492010. *Email:* agupta.etc@nitrr.ac.in. [2]I.S.M. Dhanbad, Jharkhand, India, 826004. *Email: ravi8331@gmail.com*	270
9.6	**A Novel ANFIS based CAD Model to Predict the Return Loss Performance of a Hexa-band PIFA** Aarti Gehani and Dhaval Pujara Department of Electronics and Communications Engineering, Institute of Technology, Nirma University, Ahmedabad 382481. *Email: aarti.gehani@nirmauni.ac.in, dhaval.pujara@nirmauni.ac.in*	274

9.7 **Dual Circularly Polarized and High Power Capable Medium Gain Antenna for Mars Orbiter Mission** 278
B Pavan Kumar[1], Chandrakanta Kumar, V Senthil Kumar, K M Subrahmanyam and V V Srinivasan[2]
Communication Systems Group, ISRO Satellite Centre, Bangalore, India.
E-mail: [1]pavanb@isac.gov.in, [2]vvs@isac.gov.in

9.8 **Design and Simulation of W Band Cassegrain Antenna System** 283
Eaineesh Pundir, Raj Kumar, and Pramendra Kumar Verma.
College of Engineering Roorkee, Roorkee, India-247667.
Email:eaineesh@gmail.com

9.9 **Theoretical Analysis of Double Step Junction Coupled Waveguide fed DRA** 287
P. M. Jasmine[1], P. Abdulla[2], and P. M. Raphika[3]
School of Engineering, Cochin University of Science & Technology, Kochi - 22, India.
Email:[1]jasmine.maiyn@gmail.com,[2]abdulla@cusat.ac.in, [3]pmraphika@yahoo.co.in

9.10 **Design and development of a Wideband Radiator for EMI Testing** 291
Ajal.A.J, Chikku Jose.
ECE Department Govt. Engineering College, Idukki. ECE Department Govt. Engineering College, Kozhikode.
Email: ec2reach@gmail.com.

9.11 **A Novel Coplanar antenna design for wearable gadgets with high speed and low power.** 295
Peter Cyriac, Stephen Rodrigues
Department of Instrumentation, Cochin University of Science and Technology, Cochin-682022, India.
Email: mybibin123@gmail.com, dr3stephen@yahoo.co.in

C-Band Omni-Directional Antenna for Stealth Application

Pramendra Kumar Verma, Raj Kumar and Mahakar Singh
Defence Electronics Application Laboratory, Dehradun, India, 248001,
Email: pramendra@deal.drdo.in

Abstract: *The paper describes the realization of C-band omni-directional antenna for stealth application. RCS is an important parameter for stealth applications. RCS analysis of designed antenna has been carried out using Integral Equation solver of ANSYS's HFSS full wave EM Software. Designed antenna has been simulated for monostatic RCS in both Azimuth as well as elevation plane at C-band. Measured RCS of antenna is less than 20 dBsm in both planes. Measured results closely resemble to simulated one.*

Introduction: Low Radar Cross Section (RCS) is one of the major requirements for the stealth application. RCS of antenna is important parameter for this application because it decides the resultant RCS of low observable platforms. RCS of antenna can be due to either structural mode scattering or antenna mode scattering. These two scattering phenomena take place due to short circuit, open circuit and matched load termination. When an electromagnetic signal falls on an antenna surface, some part of the electromagnetic energy is scattered back to the space. This is called structural mode scattering. The remaining part of the energy is absorbed due to the antenna effect. Some part of this absorbed energy is again scattered back into the space due to the impedance mismatches, called antenna mode scattering. Antenna for stealth applications should be designed very carefully as sometimes it enhances the overall RCS of host platform [1-3].

RCS is the measure of an object's ability to reflect radar signal in the direction of the radar receiver i.e. it is the measure of the ratio of backscatter per steradian (unit solid angle) in the direction of the radar (from the target) to the power density that is intercepted by the target. The RCS of a target can be visualized as a comparison of the power of the reflected signal from a target to the reflected signal from a perfectly conducting smooth sphere of RCS area of 1 m^2.

Omni-directional radiation patterns are generally used where the direction of incoming signal in azimuth plane is not known. Generally, omni-directional radiation pattern is obtained by a quarter wave monopole antenna, biconical antenna, discone antenna etc.. In these, quarter wave monopole antenna is generally used for narrow band and cone shaped antenna is used for wideband application[4-6]. A low RCS omni directional antenna is required for line of sight communication for stealth aircraft.

Present paper describes the design, simulation and realization of low RCS modified monocone antenna at C-Band.

Design & Simulation: It is well known fact that increasing the diameter of a monopole increases its bandwidth. Bandwidth of monopole antenna is function of length to diameter ratio. As the thickness increases the bandwidth also increases. From this technique, we can increase the bandwidth of antenna only up to 10%. An antenna that further increases the

bandwidth of a monopole is a conical or monocone antenna. A common method for enhancing the bandwidth of a conical monopole is to make the antenna having a bulbous or spherical shape. For further enhancement of bandwidth we modify the monocone antenna[7]. This modification can be done by merging a cone with circular cylindrical at the junction location.

Designed modified monocone antenna consists of a conical structure integrated with a cylindrical structure on a circular ground plane. The ratio of cone size to cylinder size decides the azimuth and elevation coverage of antenna over the desired frequency band. In present case , height of cone, height of cylinder and radius of ground plane are 12.6mm , 10.5mm and 30mm respectively.

The designed antenna has been modeled on ANSYS's HFSS software (finite element method based) using HFSS modeler. 3 -D CAD model of antenna with hemispherical Teflon radome is shown in fig.1. After applying proper boundary conditions, the antenna has been solved for desired frequency of operation. After initial simulation, the antenna was optimized for desired VSWR and radiation pattern.

HFSS-IE (integral equation) full wave EM solver has been used for RCS analysis of antenna. It creates a triangular surface mesh on all objects for calculation of currents on the surface of objects due to incident field. Designed antenna has been simulated for monostatic RCS in both azimuth as well as elevation plane over the desired frequency band (4-8 GHz). Simulated RCS of the antenna in Az plane is less than -30 dBsm and in El plane, it is less than -20 dBsm over the desired elevation angle i.e. 0 to +60 degree. The simulated results of the optimized antenna are shown in figure 2 to figure 6.

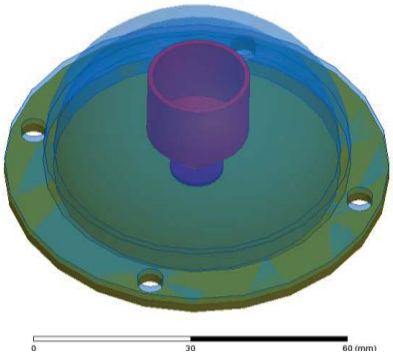

Fig1. CAD model of antenna with radome

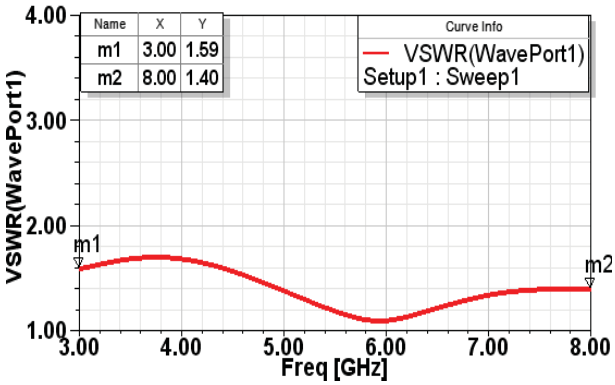

Fig2. Simulated VSWR plot

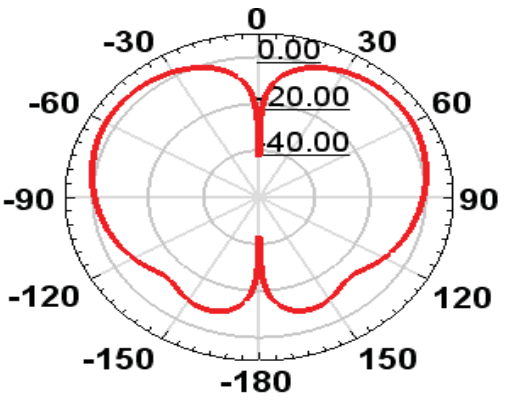

Fig3. El pattern of antenna at 6 GHz

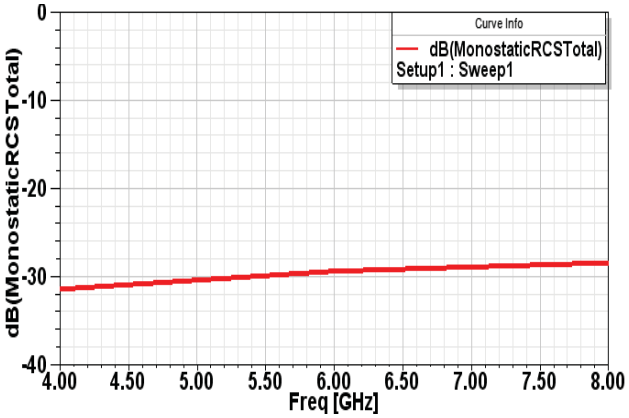

Fig4. Simulated Normalized RCS over C-Band

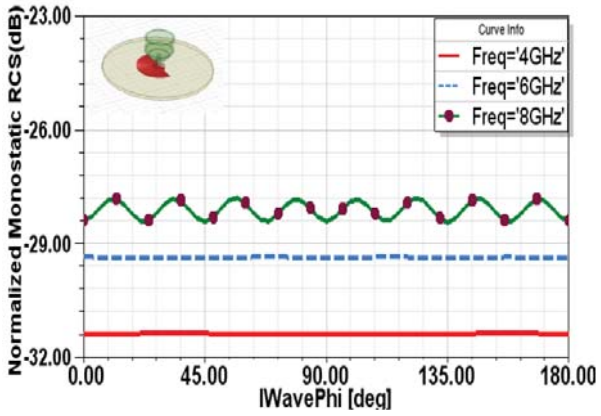

Fig5. Simulated RCS over Azimuth plane

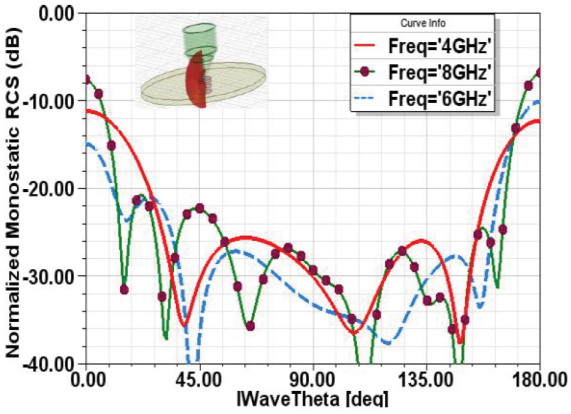

Fig6. Simulated RCS over Elevation plane

Results & Discussion: Developed antenna and its radome is shown in figure 7. Measured VSWR is less than 1.7 over the desired frequency band which is shown in figure 8. Measured elevation pattern of antenna at 5 GHz is shown in figure 9, it shows that elevation coverage of antenna is from -10 to 45 degree. RCS measurement of antenna with and without radome has been carried out over the frequency band with different load condition. Measurement of RCS depicts that its values changes with and without radome but in both cases the values remain better than -20 dBsm over the frequency band.

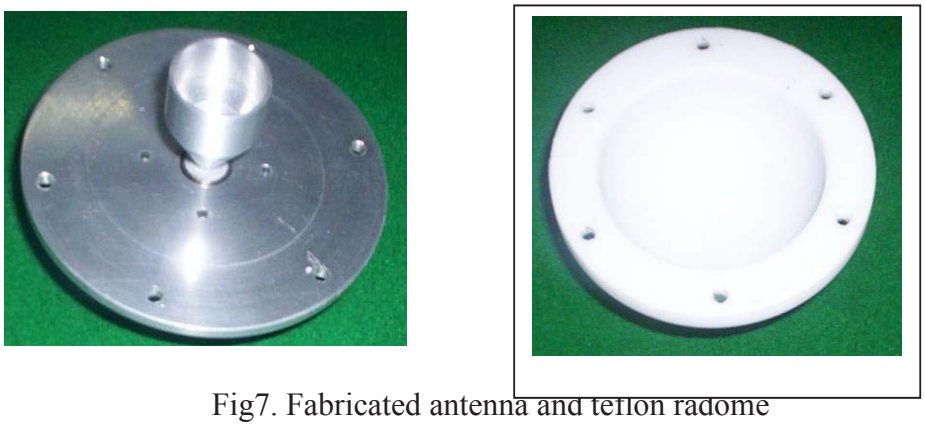

Fig7. Fabricated antenna and teflon radome

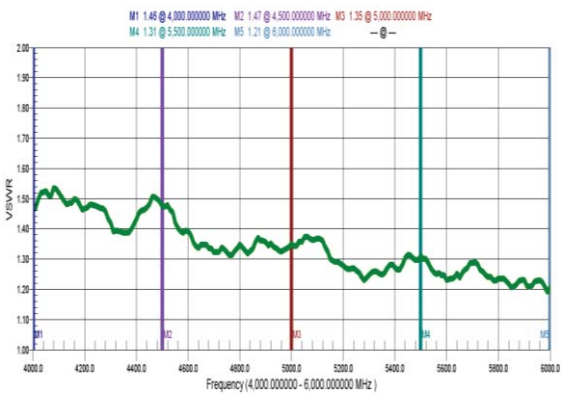

Fig8. Measured VSWR of antenna

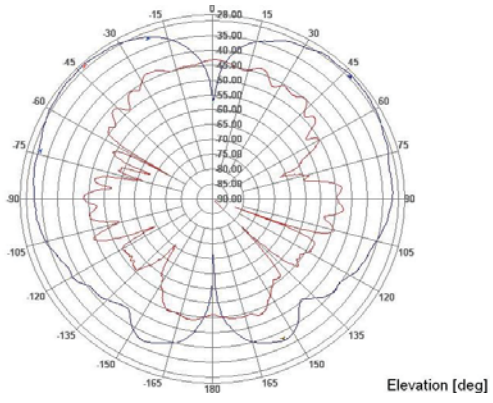

Fig9. Measured elevation pattern @5GHz

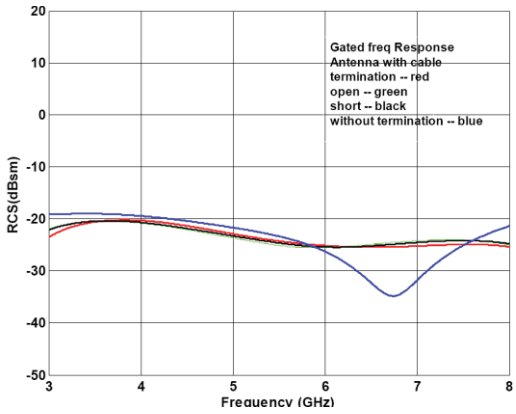

Fig10. Measured RCS without radome

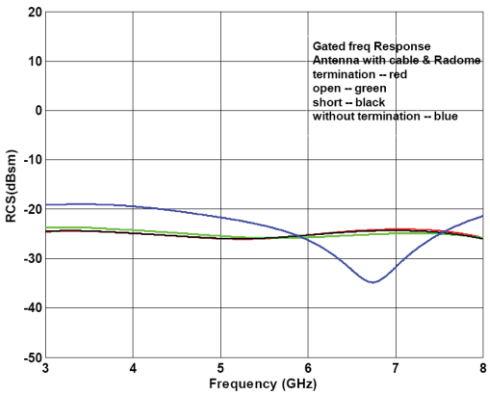

Fig11. Measured RCS of antenna with radome

Conclusion: A very compact, lightweight, low volume and low RCS omni antenna has been designed and developed. The measured parameters of the antenna are very close to the simulated results. Antenna shows omni coverage in azimuth plane and 55 degree coverage in elevation plane. The other outstanding features of the antenna are elegant configuration, light weight, robust design and most suitable for fast moving airborne as well as ground platforms. This antenna is highly suitable for stealth platform. It can also be used for tracking , telemetry & command and electronic support measures as well.

Acknowledgment: The authors are thankful to Director, Defence Electronics Applications Laboratory for granting permission to publish this paper.

Reference:

[1] Collin, R.E., "The Receiving Antenna", Antenna Theory, Part l, McGraw-Hill, New York, 123-133, 1969.
[2] Hansen, R.C., "Relationships Between Antennas as Scatters and as Radiators", Pro. IEEE, Vo1.77 (5), 659-662, 1989.
[3] L. Ying, Gong Shu-xi, and Fu De-min, "Theoretic Study of Antenna Scattering," ACTA ELECTRONICA SINICA, Vol. 33, No. 9, Sep. 2005.
[4] J. D. Kraus, Antennas, Mc Graw- Hill Book Company, New York, pp.217-229
[5] H. Jasik, Antenna Engg. Handbook, 1st ed., Mc GrawHill Book Company, NewYork, 1961,pp3-10, 3-13
[6] Richard C. Jonson and Henry Jasik, Antenna Applications Reference guide, Mc.Graw-Hill Book Company, NewYork, 1984, pp.l7.2-17.3.
[7] M.Singh, P.K.Verma. R. Kumar, V.K. Singh, "Design and Simulation of a Modified Monocone Antenna for Ultra wide Bandwidth" Int. Conf. on Microwave,2008, Jaipur, India.

New Superstrate for Resonance Gain Antenna with Reduced Side Lobe Level

Koushik Dutta[(1)], Debatosh Guha[(1)], and Chandrakanta Kumar[(2)]*
(1) Institute of Radio Physics and Electronics, University of Calcutta, Kolkata-700009, India, Email: koushikdutt@ieee.org, dguha@ieee.org*
(2) Communication Systems Group, ISRO Satellite Centre, Department of Space, Government of India, Bangalore 560017, India, Email: kumarchk@ieee.org

Abstract: *The A resonance gain antenna (RGA) has been designed using a compact nontransparent elliptical superstrate. A probe-fed cylindrical dielectric resonator antenna (CDRA) has been used as a primary radiator of the proposed RGA to achieve impedance bandwidth above 18%. Such compact elliptical superstrate geometry of size $\lambda \times \lambda/2$ assures to give about 13.3 dBi of gain with significant side lobe level (SLL) below -11 dB.*

Introduction: Resonance gain antenna (RGA) is a class of high gain antenna, which follows the principle of Fabry-Perot resonance. In an RGA, a primary radiator sits on a ground plane. A superstrate layer is employed to satisfy the condition of Fabry-Perot resonance, which in turn enhances gain of broadside radiation of the antenna. Microstrip patch [1] or dielectric resonator [2] is normally used as a primary radiator. A variety of partially reflecting surfaces (PRSs) were investigated earlier and they include electromagnetic bandgap material [3], metamaterial [4], frequency selective surface [5], and metal grid [6]. Usually, PRSs bear complex geometries and larger size.

A fully reflecting surface (FRS) has been demonstrated as superstrate for the first time in [7]. This design employs a square metal sheet with $\lambda \times \lambda$ size, λ being the resonant wavelength. Side lobe level (SLL) is a major concern of such FRS [8].

In this paper, we have explored an improvised shape or geometry of the superstrate, which can take care of the SLL issue. Its design approach along with the basic concept of using the shape has been discussed. Like [7], a probe-fed cylindrical dielectric resonator antenna (CDRA) has been used as a primary radiator to operate in S-band. Possibility of reduction of SLL by 7-16 dB has been demonstrated based on simulated data using [8]. Fabrication of the prototype is under process for experimental investigations.

Proposed Configuration of Superstrate: Fig. 1 shows a schematic diagram of the proposed RGA. A probe-fed CDRA with radius r = 10 mm, height h = 10 mm, and relative permittivity ε_r = 10 has been used. The superstrate is conceived as an elliptical metal sheet (size $a \times b$; thickness t). It is symmetrically placed and the mode of alignment is clearly shown in Fig. 1. To meet the Fabry-Perot resonance condition, the height of the cavity has been optimized to $h_r \approx \lambda_{mb}/2$ = 36 mm, where λ_{mb} is the mid-band wavelength. Fig. 2 describes the modification of superstrate geometry from a square FRS [7] to an Ellipse (Fig. 2(b)).

Results: S_{11} as a function two types of superstrate geometry (Fig. 2) has been depicted in Fig. 3(a). Their corresponding peak-gain variations are shown in Fig. 3(b). Compared to [7], marginal decrement in matching bandwidth (from 20% to 18%) is observed. Elliptical superstrate (S#2) is able to enhance the peak-gain by 1 dB.

The principal plane radiation patterns are compared in Fig. 4 and are summarized in Fig. 5. Superstrate #2 shows remarkably low SLL (improved by 7-16 dB) compared to square superstrate #1.

The effect of superstrate size has been studied in Fig. 7 keeping the dimension b (~ λ) unchanged. In terms of matching bandwidth, gain, and SLL, $a = 0.5\lambda$ appears to be the optimum choice.

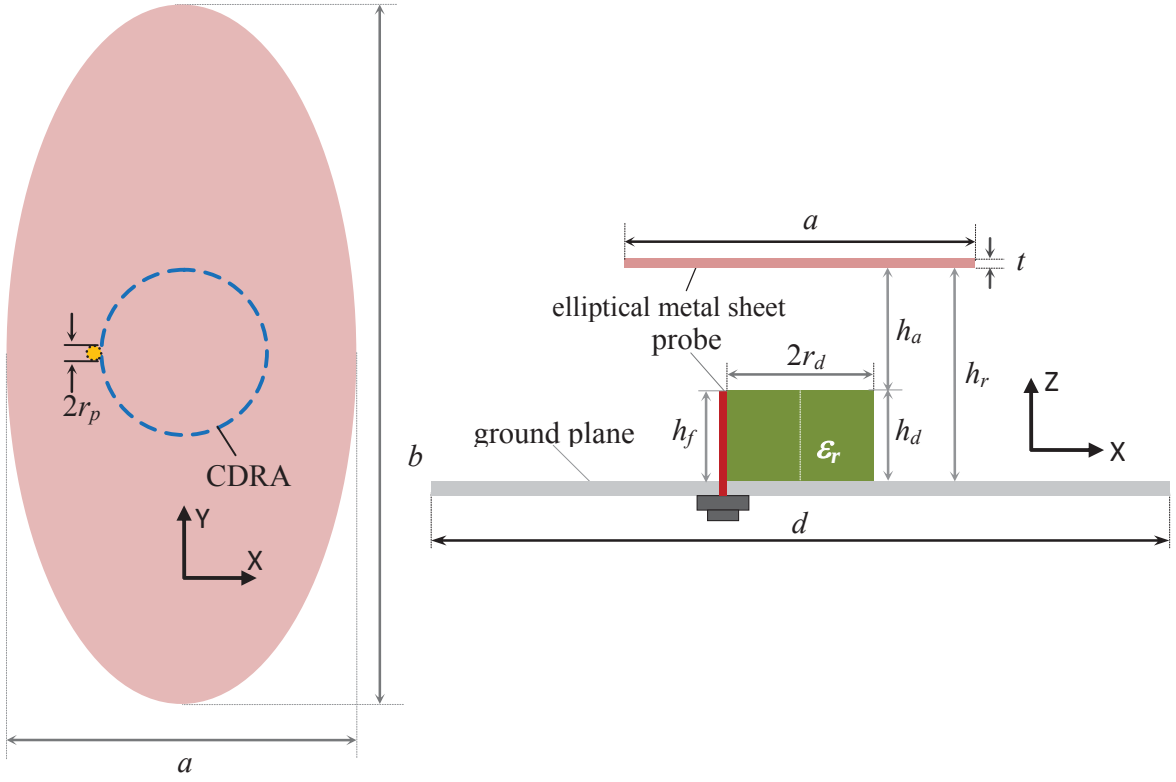

(a) (b)

Fig. 1. Schematic diagram of the proposed resonance gain antenna using elliptical solid metal sheet as superstrate: (a) Top view, (b) Side view.

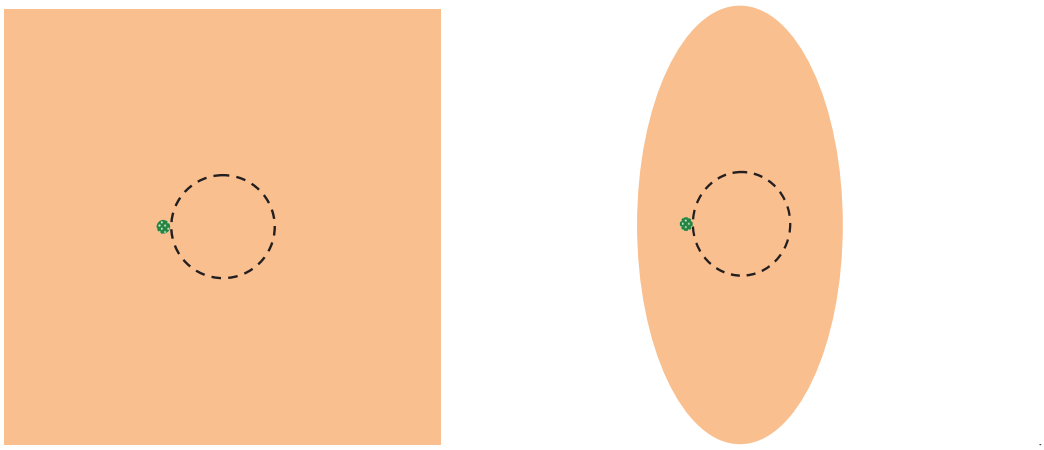

(a) (b)

Fig. 2. Schematic diagram of the superstrate geometries: (a) S#1: square metal sheet [8] (size: 96 mm × 96 mm), (b) S#2: elliptical metal sheet (size: 48 mm × 96 mm).

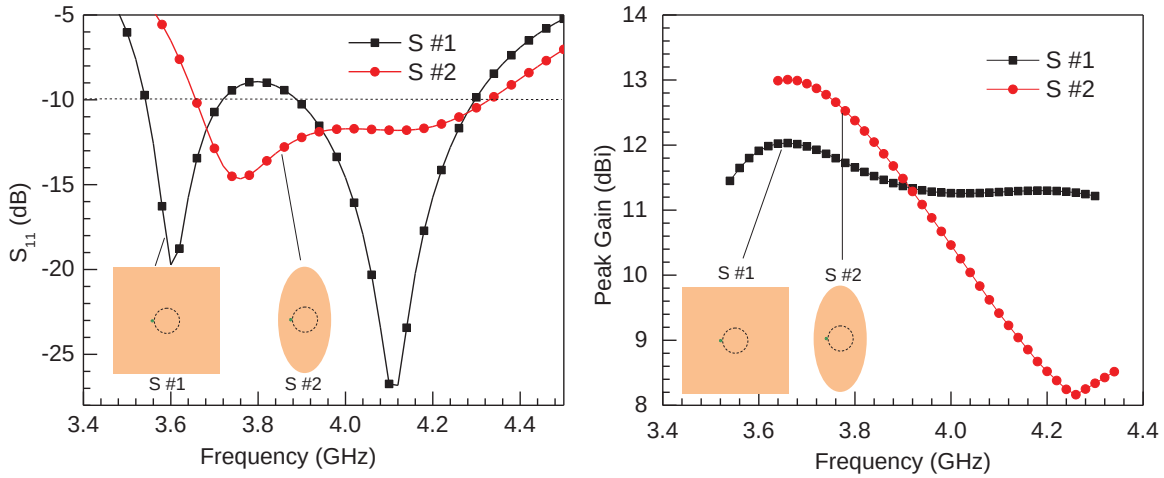

Fig. 3. (a) S_{11} and (b) Peak-gain variations of the RGA as a function of frequency using two superstrate geometries (S#1, and S#2). CDRA: ε_r = 10, r_d = 10 mm, h_d = 10 mm; Ground plane: d = 200 mm; Probe: diameter = 1.3 mm, h_f = 10 mm; Superstrates → S#1: a = 96 mm, b = 96 mm; Superstrates → S#2: a = 48 mm, b = 96 mm; t = 0.3 mm. Other antenna parameters are as in Fig. 2.

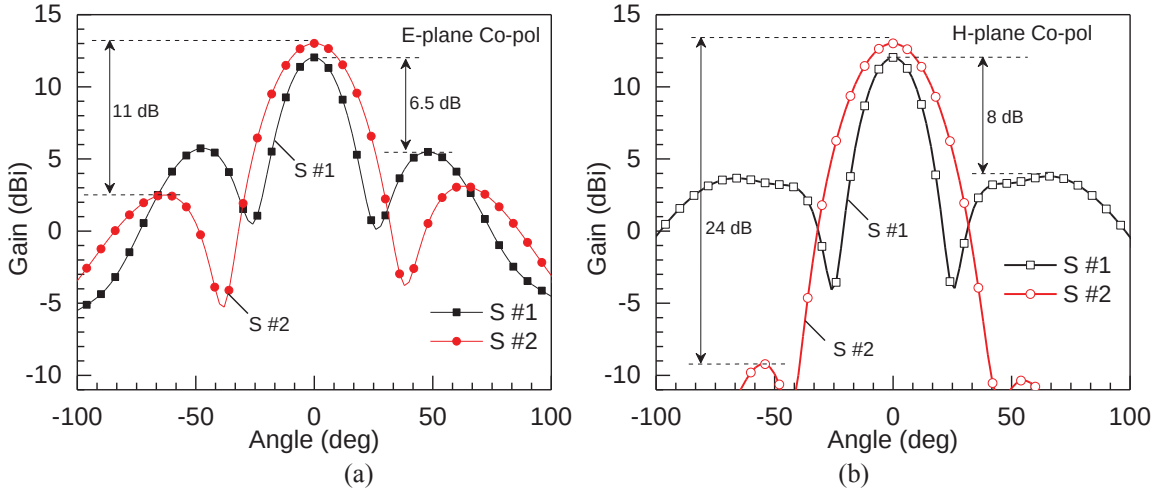

Fig. 4. (a) E-plane and (b) H-plane radiation patterns of the antenna at 3.7 GHz using superstrate geometries S#1 and S#2. All other antenna parameters are as in Fig. 2 and Fig. 3.

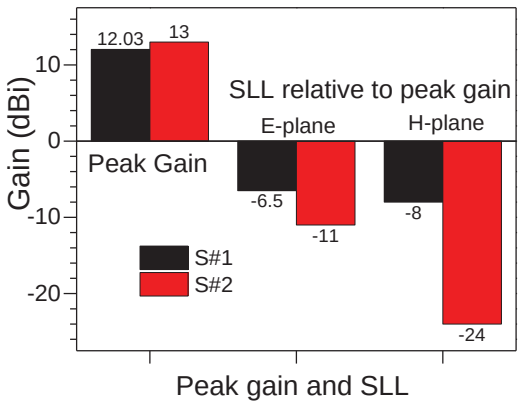

Fig. 5. Comparison of peak-gain, E-plane and H-plane SLL of the antennas using square and elliptical superstrates.

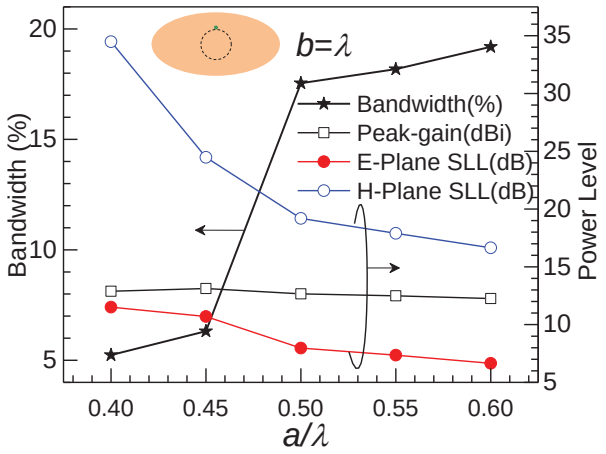

Fig. 6. Variation of bandwidth, peak-gain, and E-plane/H-plane SLL of the proposed RGA with normalized X-dimension (a/λ) of the elliptical superstrate keeping its Y-dimension fixed ($b \approx \lambda$ = 96 mm).

To understand the radiation characteristics, its surface current over each superstrate has been portrayed in Fig. 7. Uniform current distribution across H-plane of S#2 (Fig. 7(b)) indeed causes considerable improvement in H-plane SLL.

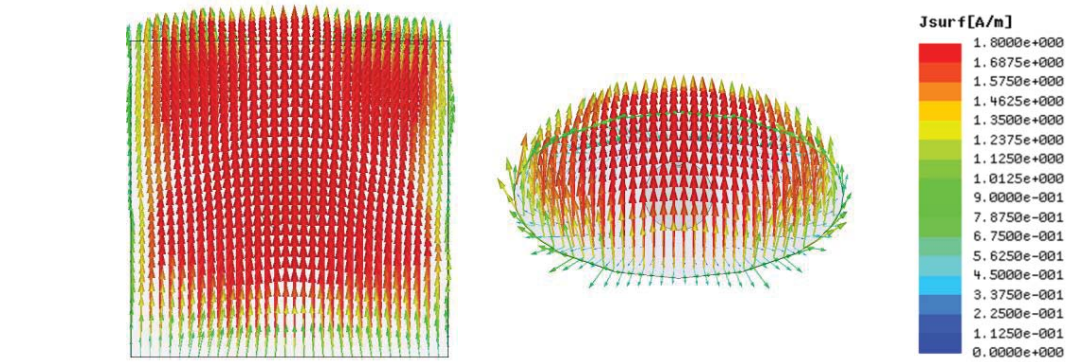

(a) (b)

Fig. 7. Surface current distributions at 3.7 GHz over the superstrate (a) S#1 and (b) S#2.

Conclusions: Elliptical shape of solid metallic superstrate is found to be much improved, especially from SLL aspect, compared to its earlier version. This improvement in radiation property may establish it as a practically viable design. Also, this may encourage the researchers in exploring newer shape of RGA superstrate to modify the aperture field and hence to improve the radiation characteristics.

Reference:

[1] F. Kaymaram and L. Shafai, "Enhancement of microstrip antenna directivity using double-superstrate configurations," Can. J. Elect. Comput. Eng., vol. 32, no. 2, pp. 77–82, June 2007.

[2] Y. Coulibaly, M. Nedil, Larbi Talbi, and T. A. Denidni, "High gain cylindrical dielectric resonator with superstrate for broadband millimeter-wave underground mining communications," 14th Int. Symp. on Antenna Technology and Applied Electromagnetics the American Electromagnetics conf. (ANTEM-AMEREM), pp. 1–4, July. 2010.

[3] Y. J. Lee, J. Yeo, R. Mittra, and W. S. Park, "Application of electromagnetic bandgap (EBG) superstrates with controllable defects for a class of patch antennas as spatial angular filters," IEEE Trans. Antennas Propag., vol. 53, no. 1, pp. 224–235, Jan. 2005.

[4] H. Attia, L. Yousefi, and O. M. Ramahi, "Analytical model for calculating the radiation field of microstrip antennas with artificial magnetic superstrates: theory and experiment," IEEE Trans. Antennas Propag., vol. 59, no. 5, pp. 1438–1445, May 2011.

[5] D. H. Lee, Y. J. Lee, J. Yeo, R. Mittra, and W. S. Park, "Design of novel thin frequency selective surface superstrates for dual-band directivity enhancement," IET Microw. Antennas Propag., vol. 1, no. 1, pp. 248–254, Feb. 2007.

[6] A. Foroozesh and L. Shafai, "On the characteristics of the highly directive resonant cavity antenna having metal strip grating superstrate," IEEE Trans. Antennas Propag., vol. 60, no. 1, pp. 78–91, Jan. 2012.

[7] K. Dutta, D. Guha, C. Kumar, and Y. M. M. Antar, "Resonance Gain Antenna Using Fully Reflecting Surface (FRS): New Boundary Condition to Realize Wideband High Gain Operation", in IEEE conference APS-URSI 2014, pp. 1978–1979, July 2014.

[8] High Frequency Structure Simulator (HFSS) v12.1, Ansoft.

Controlling of Higher Harmonics and Modes in Dielectric Resonator Antennas

S. Biswas (1), D. Guha (2), and C. Kumar(3)*
(1) NITMAS, West Bengal, India, WB 743 368, Email: sbiswas@ieee.org
(2) Institute of Radio Physics and Electronics, Calcutta University, Kolkata, India, 700009, Email: dguha@ieee.org
(3) Communication Systems Group, ISRO Satellite Centre, Bangalore, India, 560017, Email: kumarchk@ieee.org

Abstract: *Controlling of higher order modes and harmonics in an aperture coupled Dielectric Resonator Antenna (DRA) has been explored. A compact design employing Defected Ground Structure (DGS) has been used at antenna input to suppress the unwanted frequencies appearing up to 4 times the fundamental one. Application of DGS has been discussed and the suppression characteristics have been experimentally demonstrated. No detrimental effect caused by the DGS on the radiations of the fundamental mode has been ensured experimentally.*

Introduction: Radiation at harmonics of fundamental mode from an integrated antenna is a serious issue. At the same time, pickup of signals at higher order resonant modes is equally alarming. In Dielectric Resonator Antenna (DRA), harmonics of the fundamental mode may not exactly match with the higher order resonances, but appear close to those frequencies. The issue remains serious if not addressed carefully.

For practical design of DRA, microstrip-fed aperture coupled structure appears more convenient to be integrated with source and active devices on a single circuit board. One earlier work explored harmonic tuning in such a Ku band rectangular DRA employing additional slots in the feed [1]. But to the best of our knowledge, control of harmonics along with higher modes of DRA over a wide frequency range has not yet been reported in open literature.

In this paper, we have tried to alleviate these lacunae and have experimentally demonstrated the possibility of suppression of higher frequencies up to four times the fundamental resonance. We have extended the concept of using defected ground structure (DGS) beneath the microstrip feed-line, first explored by Horri [2] in printed antenna application. The technique was improvised later on for printed circuit antennas [2]-[6]. They exploited the band-stop characteristics of DGS beneath a microstrip feed to isolate the antenna from the oscillator/amplifier units.

In present investigation, a cylindrical DRA operating in S-band has been experimented. Higher order modes, occurring in its aperture-fed configuration, and their proximity to harmonic frequencies of fundamental resonance have been studied. A simple design using DGS-integrated feed line has been examined and experimentally demonstrated indicating promising feature of suppressing higher harmonics over a range covering more than 80% of impedance bandwidth.

DGS-integrated Feed: Unlike a microstrip patch, a DRA is preferred to be placed directly on a metallic ground plane. Hence aperture coupled microstrip-fed design is ideal to realize DRA with integrated feed and associate circuitry. Thus the DRA is deployed on the copper-clad face of the grounded substrate (upper side) and the microstrip feed line is etched on the other side of the substrate (bottom side) as shown in Fig. 1. The DGS which needs to be coupled to the feed-line, therefore, appears on the same side of the radiating DRA. Any leakage through the DGS thus may affect the radiation characteristics. We, therefore, have taken care of this aspect in our design and have used a pair of compact DGS which occupies minimal space in terms of the operating wavelength λ_0. A schematic diagram is shown in Fig. 2. Each partial ring DGS is obtained by truncating a full ring at a distance t_r

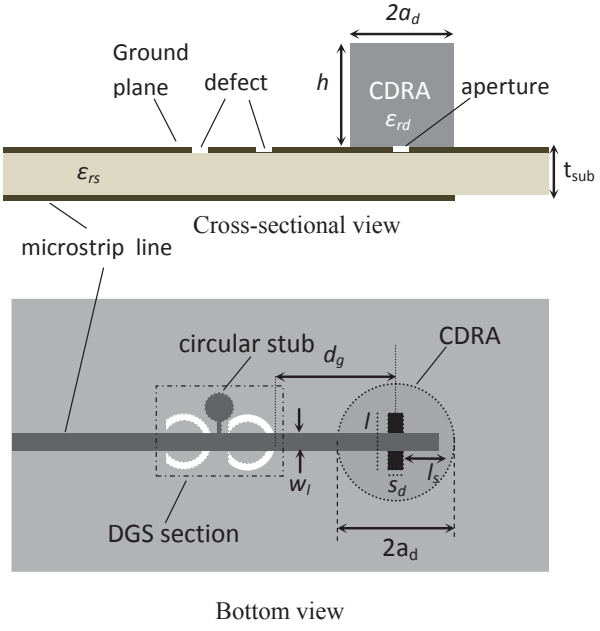

Fig. 1. Schematic of an aperture coupled cylindrical DRA (CDRA) integrated with DGS feed-filter. Parameters: d_g = 19.3 mm, w_l = 1.6 mm, l = 10 mm, s_d = 2 mm, l_s = 14 mm, a_d = 10.8 mm, h = 10.9 mm, ε_{rd} = 14.2; Substrate thickness t_{sub} = 0.508mm, relative permittivity ε_{rs} = 2.2. DGS filter parameters as in Fig. 2.

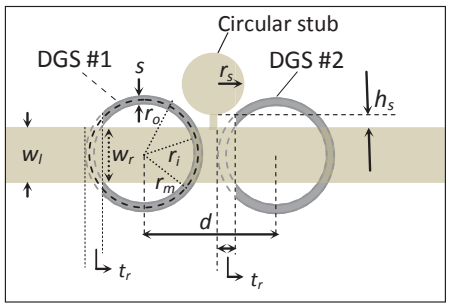

Fig. 2. DGS feed-filter with two cascaded units and open ended circular stub integrated with 50Ω microstrip line. Stub parameters: r_s = 1.9 mm, h_s = 1.2 mm. DGS Parameters: r_0 = 2.75 mm, r_i = 2.25 mm, $s = r_0 - r_i$ = 0.5 mm, t_r = 0.647 mm, w_l = w_r = 1.6 mm, and d = 6.25 mm, t_{sub} = 0.508 mm and ε_{rs} = 2.2.

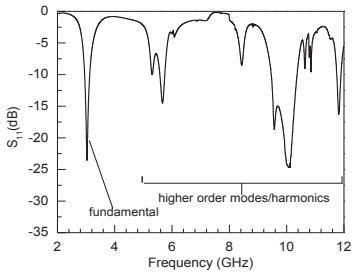

Fig. 3. Simulated S_{11} versus frequency of a microstrip line fed aperture coupled CDRA with normal ground plane. CDRA and substrate parameters as in Fig. 1.

from its outer edge. The resulting DGS looks like a partial-ring with parameters: outer radius r_0, inner radius r_i, ring width s and mean ring radius r_m (=r_i+0.5s). Parameter t_r is determined to achieve ring opening $w_r \approx$ microstrip width w_l, which results in strong coupling between the microstrip line and the DGS. The feed-filter uses two cascaded DGS units along with an open ended stub. The design procedure is described below.

Figure 3 shows simulated S_{11} of a simple aperture-fed CDRA. The fundamental resonance occurs at 3.03 GHz and subsequent higher order resonances occur over 5.3–12 GHz. Calculated resonant frequency and first three harmonics are provided in Table I. The higher order modes are close to the 1st and 2nd harmonics. But 3rd harmonic at 11.92 GHz exactly matches with a higher order mode near 11.8 GHz. Controlling of these higher frequencies is discussed in following section.

The aim of the design is, therefore, to realize a DGS-integrated feed to suppress these higher frequencies. The DGS dimensions are primarily estimated using fundamental

TABLE I
DOMINANT MODE, HARMONICS, AND FIRST FEW HIGHER ORDER MODES IN APERTURE FED CYLINDRICAL DR. PARAMETERS AS IN FIG. 1.

Calculated dominant mode and harmonics (GHz)	First few resonant frequencies (GHz)	
	Simulated (S_{11} < -10 dB)	Measured
2.98 (fundamental)	3.0	2.95
5.96 (1st harm.)	5.7	5.55
8.94 (2nd harm.)	9.5	9.4
-	10.1	10.15
11.92 (3rd harm.)	11.8	11.85

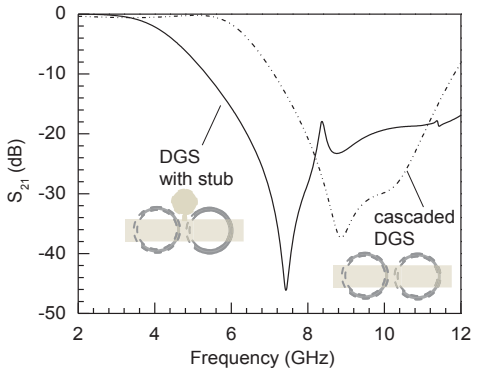

Fig. 4. Simulated S_{21} versus frequency of the cascaded DGS and DGS integrated feed with stub shown in Fig. 2.

resonance condition $2\pi r_m - w_l \approx \lambda_m/2$, where λ_m corresponds to the mid stop-band wavelength. For present study, w_l = 1.6 mm (50Ω transmission line using t_{sub} = 0.508 mm, ε_{rs} = 2.2), $\lambda_m \approx$ 33 mm, and r_m = 2.9 mm. The width of the defect s is 0.5 mm (≈ 0.015 λ_m). The value of r_m is finally tuned using simulated results [7]. Cascading of two identical DGS units helps in extending the stop-band, especially towards the higher side of spectrum, as shown in Fig. 4. Following the approach of [6], a stub is introduced to achieve stop-band towards the lower frequencies. This is clearly shown in Fig. 4. Proximity of the DGS with reference to DRA is determined by d_g (Fig. 1) and $d_g \geq 0.12\ \lambda_0$ is found to be ideal showing no effect on the matching of input impedance.

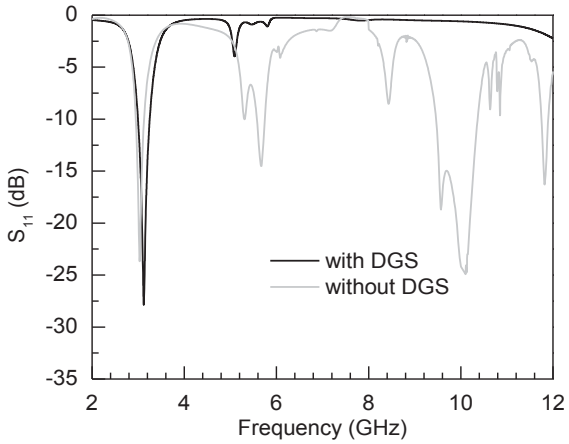

Fig. 5. Simulated S_{11} versus frequency of the CDRA shown in Fig 1 with and without DGS-integrated feed. Parameters as shown in Fig. 1.

Results: Some representative results for DRA with DGS integrated are furnished below. Fig. 5 shows simulated S_{11} of aperture coupled DRA with conventional and DGS integrated feed. The dominant mode appears exactly at the theoretically predicted value of 2.98 GHz. Higher order resonances listed in Table I is not revealed in case of DRA with DGS integrated feed. However the dominant mode remains unaffected.

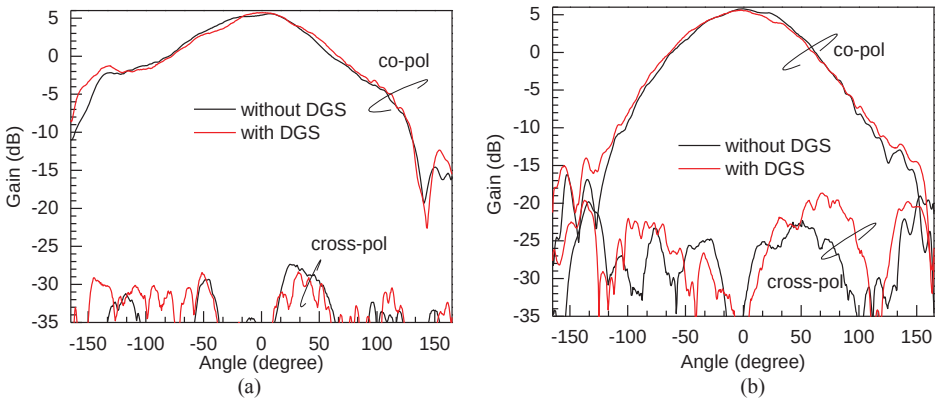

Fig. 6. Measured radiation patterns due to the fundamental resonant frequency of the CDRA shown in Fig. 5 with and without DGS integrated feed (a) E-plane, (b) H-plane. Parameters as in Fig. 1.

Measured radiation patterns due to the primary resonance obtained with and without DGS are compared in Fig. 6. No considerable change in patterns or in peak gain is revealed. This ensures the fact that the DGS causes no considerable leakage through it affecting the primary radiation of the antenna.

Conclusion: This work demonstrates a new harmonic control technique for DRA with a promise for very wide band operation. The design is compact in nature, and practically viable in integrated circuit design. The feed is fully planar and involves no additional component or circuitry and as such cost effective for mass production.

Reference:

[1] A. Guraliuc, G. Manara, P. Nepa, G. Pelosi, and S. Selleri, "Harmonic tuning for Ku-band dielectric resonator antennas," *IEEE Antennas and Wireless Propag. Lett*., vol. 6, pp. 568–571, Jan. 2007.

[2] Y. Horri and M. Tsutsumi, "Harmonic control by photonic bandgap on microstrip patch antenna," *IEEE Microwave Guided Lett*., vol. 9, pp. 13–15, Jan. 1999.

[3] I. Chang and B. Lee, "Design of defected ground structures for harmonic control of active microstrip antenna," *IEEE Antennas and Propagation Society International Symposium*., vol. 2, pp. 852–855, 2002.

[4] H. Liu, Z. Li, X. Sun, and J. Mao, "Harmonic suppression with photonic bandgap and defected ground structure for a microstrip patch antenna," *IEEE Microw. Compon. Lett.*, vol. 15, no. 2, pp. 55–56, Feb. 2005.

[5] Y. J. Sung and Y.-S. Kim, "An improved design of microstrip patch antennas using photonic bandgap structure" *IEEE Trans. Antennas Propagat*., vol. 53, no. 5, pp. 1799-1803, May, 2005.

[6] M. K. Mandal, P. Mondal, S. Sanyal, and A. Chakrabarty, "An improved design of harmonic suppression for microstrip patch antennas," *Microwave and Opt. Technol. Lett*. Vol. 49, no. 1, pp. 103-105, Jan. 2007.

[7] High frequency structure simulator (HFSS), *Ansoft*, v 11.1.

A High Gain & Low Side Lobe Level Pillbox based Fan Beam Antenna at Ka Band

Raj Kumar, Pramendra Kumar Verma and Mahakar Singh
Defence Electronics Application Laboratory, Dehradun, India, 248001,
Email: raj.kumar@deal.drdo.in

Abstract: *The paper discuses realization of high gain pillbox based fan beam antenna at 38 GHz with low side lobe level. The antenna consists of a pillbox structure fed by a sectoral horn antenna. The feed horn has been simulated and optimized on ANSYS HFSS software. This antenna is vertically polarized and is fed by dominant mode of WR-28 waveguide. Realized gain of the antenna is 36 dBi and side lobe level lower than -17 dB.*

Introduction: A pillbox antenna consists of a cylindrical reflector embedded between two parallel plates. It is generally fed by either waveguide or horn antenna [1-3]. The pillbox is member of a family of antennas called fan beam antennas which produce a wide beam in one plane and a narrow beam in the orthogonal plane [4]. Compared to other configurations, Pillbox is preferred as easy to design, low cost, high power handling and wide band of operations. The side plates of a pillbox antenna act as a parallel plate waveguide. Their main purpose in the antenna is to guide the radiated EM energy from the primary feed to the secondary antenna. The separation of the plates determines the beam-width of the antenna in the plane of separation. Parallel-plate systems may be classed into two groups, firstly If $h < \lambda/2$, propagation between the plates is limited to the principal or TEM mode and secondly Parallel-plate systems with spacing $h > \lambda$ which support additional modes. These are called cheese antennas. 'h' is the separation of the plates[4-5].

The paper describes design, simulation and realization of a high gain and low side lobe level pillbox antenna at 38 GHz.

Description of Geometry: Pillbox antenna system consists of a pillbox fed by a horn antenna. A pillbox is a reflector sandwiched between two parallel plates. Pillbox being a secondary antenna requires a waveguide feed horn to excite it which acts as primary antenna. The parameters such as polarization, side lobe level are decided by radiation pattern of primary feed antenna and focal point of pillbox. The equation of parabolic curve of pillbox antenna is given as

$$x^2 + y^2 = 4 * f * z \qquad (1)$$

A parabolic structure with F/D of 0.2 has been used to develop pillbox antenna. The aperture of the antenna is taken to obtain a gain of 33 dBi. Azimuth size of the antenna is 300 mm while in elevation its height is 90 mm. The feed is placed at the focus of reflector antenna which is 60 mm away from the vertex of parabola. The edges of pillbox make an angle of 36.8 degree in elevation plane and 118 degree in azimuth plane at its focus.

An E-plane sectoral horn has been used as feed for designed pillbox antenna. Dimensions of the feed horn have been designed in such a manner that it provides required tapering in both azimuth and elevation plane to get the side lobe level lower than -17 dB. The sectoral horn is fed by WR-28 waveguide having dimensions of the order of 7.11 mm x 3.56 mm. The 3D model of pill box antenna, sectoral feed horn along with their dimensions is shown in figure 1.

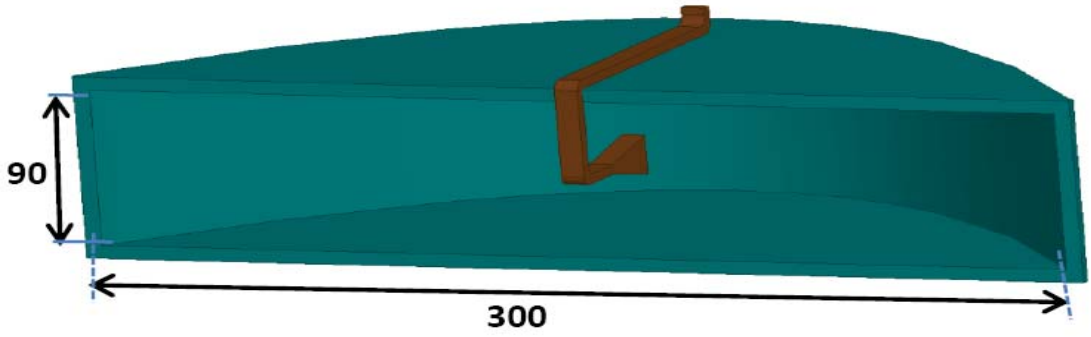

Fig1. 3D CAD model of fan beam antenna

Simulation and Optimizations: The feed horn which is a sectoral horn antenna has been simulated on ANSYS HFSS software using proper boundary conditions. The simulation of the antenna has been carried out over a frequency band of 37-39 GHz. The simulated results of feed horn are shown in figure 2. TE_{10} mode has been selected to propagate in feed horn which is also the dominant mode of waveguide. The feed horn has been designed in such a manner that it provides a tapering of 5 dB in azimuth plane and 7.5 dB in elevation plane.

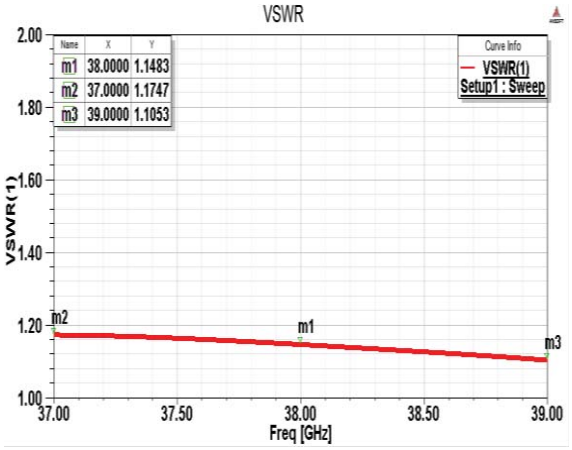

Fig 2a. Simulated VSWR of feed

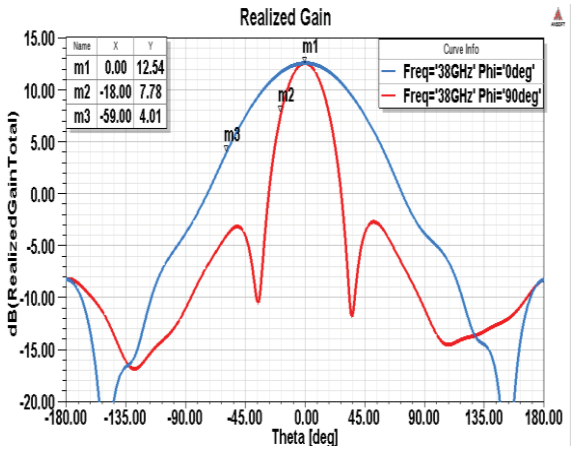

Fig2b. Simulated radiation pattern of feed

Results: The photograph of the developed antenna is shown in figure 3. Integration of pillbox and feed horn has been done so that phase centre of feed horn remains at the focus of pillbox antenna. After integrating the pillbox antenna it has been evaluated for its VSWR, radiation pattern and gain on Antenna Test range. Measured VSWR of the developed antenna is below 1.4 over 37 - 39 GHz. Measured radiation pattern of pillbox antenna at 38 GHz is shown in figure 4. From the figure it is observed that beam-width of the developed antenna is 7.1 degree in elevation plane and 2.1 degree in azimuth plane. Measured side bole level is lower than -17 dB and its gain at 38 GHz is 33 dBi.

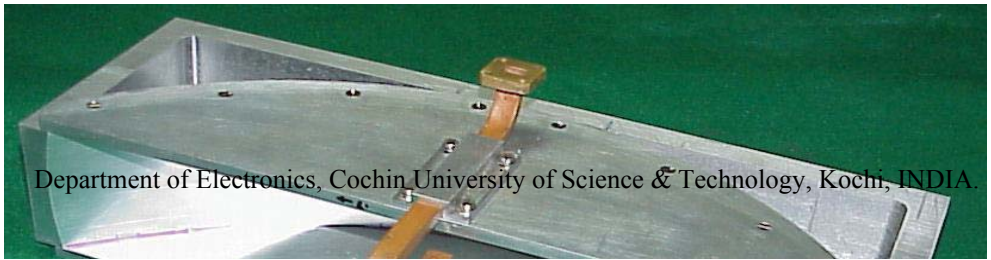

Figure 3 Photograph of developed pillbox antenna

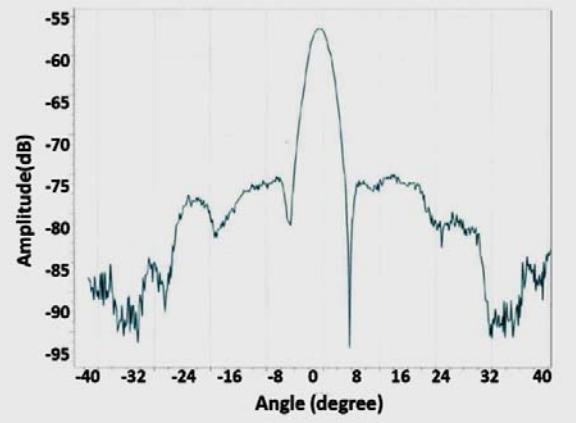

Fig 4 a. Measured Az radiation pattern

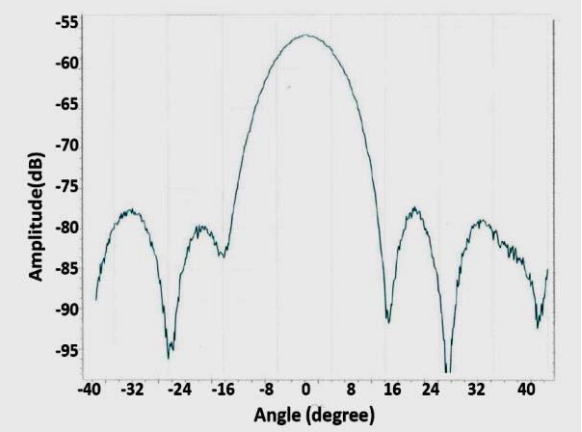

Fig 4b. Measured El radiation pattern

Conclusion: A high gain and low side lobe level pillbox antenna has been designed, simulated and developed. Measured gain of the antenna is 33 dBi & measured side lobe level of the antenna is lower than -17 dB. The antenna provides fan beam radiation pattern having small azimuth beam-width and large elevation beam-width. The antenna has several advantages like simple & rugged design, high power handing capability & wide band of operation. The developed antenna can be used in long distance communication system where coverage is wide in one plane and narrow in orthogonal plane.

Acknowledgment: The authors thank Director, Defence Electronics Applications Laboratory, for permission to publish this paper.

References:

[1] Holzman L., "Pillbox Antenna Design for Millimeter Wave Base-station applications" IEEE Antennas and Propagation Magazine, Vol.45(1): 30–37, Feb 2003.
[2] Silver S., "Microwave Antenna Theory and Design", McGraw-Hill Book Company, 1949.
[3] IEEE Standards Online Antennas and Propagation Standards.
[4] Balanis C A., "Antenna Theory: Analysis and Design.", John Wiley and Sons, 1997.
[5] Elliott R S., "Antenna Theory and Design" Prentice Hall, Jan 1981.

FDTD Analysis of Conformal Strip Excited Rectangular Dielectric Resonator Antenna Array

Anshul Gupta [1, 2], *Ravi Kumar Gangwar* [2]
[1]National Institute of Technology Raipur, Raipur, India, 492010, Email: agupta.etc@nitrr.ac.in
[2]I.S.M. Dhanbad, Jharkhand, India, 826004, Email: ravi8331@gmail.com

Abstract:*In this paper, the theoretical and simulation study of two-element linear broadside rectangular dielectric resonator antenna array has been carried out. Conducting conformal strip excitation is proposed to excite the DRA array. The Return loss and input impedance characteristics of the proposed array have been investigated in S-band of microwave frequencies using the finite-difference time-domain (FDTD) method. Numerical results have been compared with Simulation results using Ansoft HFSS 2014 simulation software. Good agreement between the calculated and simulated results is obtained.*

Introduction: The dielectric resonator antenna (DRA) is an open resonating structure, fabricated from a low loss dielectric material and offers several advantages such as small size, high radiation efficiency, flexible feed arrangement, and wide range of material dielectric constant. The rectangular shaped DRAs offer practical advantages over cylindrical and hemispherical ones in that they are easier to fabricate and provides more design flexibility.

DRAs are commonly low gain antennas with a broad radiation pattern. As with other conventional low gain antennas, DRAs can be arrayed to acquire higher gain. There are various methods for gain enhancement of dielectric resonator antennas have been reported in the literature, like by using several DRA configurations in an array can increase the gain in the boresight direction [1-3], the use of electromagnetic band gap (EBG) [4, 5] and stacking two dielectric resonators with an air gap in between [6,7].

Direct microstrip coupling is one of the most suitable feeding methods due to its simplicity especially for array applications. This coupling has been employed in the design of linear and planar DRA arrays [8, 9]. However, one shortcoming observed with this type of coupling is that obtaining critical coupling for DRAs having dielectric constants lower than 20 [10].To remove this restriction we have connected the conducting conformal strip to microstrip feed line and achieved the critical coupling for lower dielectric constant of less than 10.This excitation scheme shares the same advantage over a coaxial probe, but the effort in drilling a hole for the probe penetration and the errors that an oversized hole introduces will be avoided. On the other hand, it allows the whole electric current to flow on the DRA surface and thus, is more efficient in energy coupling than the probe-feed counterpart. This method also provides the less cross-polarization compare to probe feed method and can easily be implemented by just cutting a strip from adhesive conducting tape [11, 12].

This paper presents the theoretical and simulation studies of two element linear broadside rectangular DRA (RDRA) Array, which is fed by a conformal strip connected to 50 Ω microstripline. The numerical study of the proposed antenna array is carried out using FDTD and compared with simulation results of Ansoft HFSS. Proposed antenna provides a good bandwidth of 20% with appreciable gain of 7 dBi at $\emptyset = 90^0$.

Antenna Geometry: Each element of proposed antenna array consists of lower segment made from Teflon and an upper segment of alumina as shown in Fig. 1. The proposed structure is placed on a substrate of Roger RT/Duroid 5880 having dielectric constant 2.2, and copper thickness 35µm. The rear side of the substrate has a finite ground plane. The lower and upper segmentsof each DRA have dimensions of $l \times w \times h_1$ and $l \times w \times h_2$ respectively. In an antenna array, the mutual coupling effect will deteriorate the radiation properties of the array. To avoid mutual coupling and at the same time grating lobes, the separation between the elements must be in the range between ($\lambda_0/2$) and λ_0 depending on the angular scan range. The spacing (d) between each element is 37.5 mm ($\lambda_0/2$). The DRAs are fed by conducting conformal strip connected to microstrip line. The width (w_c) and height (h_c) of conformal strip are found to be 4.91 mm and 11.8 mm through extensive simulation using HFSS software to provide minimum return loss. The microstrip line was 4.91 mm wide (W_1) to give a characteristic impedance of 50Ω. A metallic plate of 13.4 mm height and negligible thickness covers the one side of each DRA just opposite the side where conformal strip is located.

The two RDRAs were fed in phase by implementing simple one-to-two (1:2) power dividers made of one $\lambda/4$ transformer (width W_2 = 7.97 mm, length L = 13.52 mm, and Z_0=35.35 Ω) connecting the microstrip lines of width (W_1) 4.91 mm (Z_0= 50Ω) as shown in Fig 1. Each microstrip line has at its centre a resulting input impedance of 25 Ω, and $\lambda/4$ transformer (Z_0= 35.35 Ω) changes it to 50 Ω. Table I shows the value of parameters used in our proposed structure.

The proposed antenna has been analysed with numerical technique FDTD with uniform Cartesian grid [13]. The space steps used in the FDTD method are Δx = 0.715mm, Δy = 0.615mm, Δz = 0.513mm. All of them are smaller than ($\lambda_{min}/20$), where λ_{min} is the minimum operating dielectric wavelength. The time step satisfies the Courant stability condition [14, 15]. A simple voltage gap approximation is used to model the feed of the strip. Voltage and current are sampled across and around the voltage source and they are tied together to form a port. A baseband Gaussian pulse is applied, with parameters T = 0.083ns and t_0 = 3T. To terminate the boundary, an 8-cell-thick convolutional perfectly matched layer (CPML) [15] absorber with polynomial spacing scaling (cpml-order = 3 and cpml-kappa-max = 7) is used for all sides. In each direction, the distance form rectangular DRA array to the inner CPML interface is 10 space steps. 10,000 time steps are needed to allow the input response to vanish.

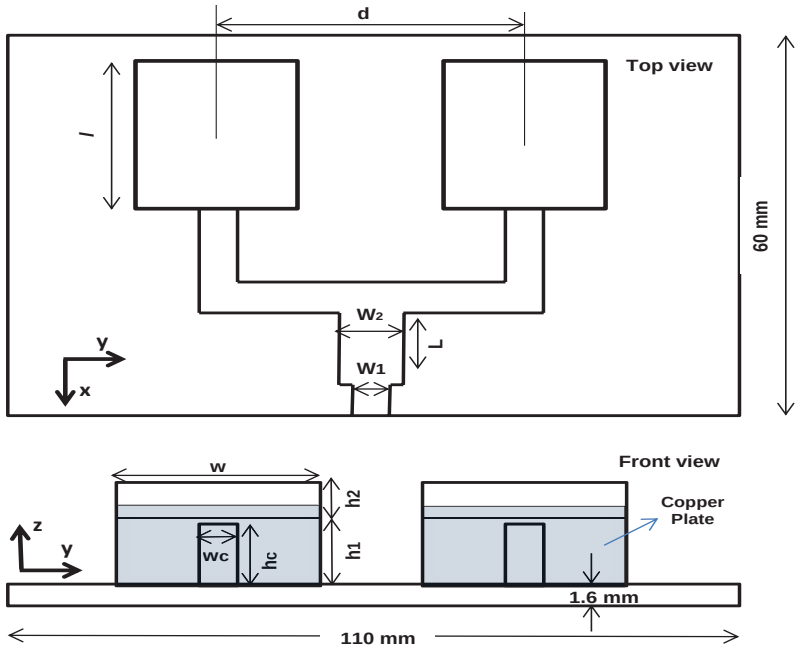

Fig.1. Proposed two element RDRA array with conducting conformal strip excitation

Table I
Antenna Design Parameters

Antenna Parameter	Value
Length of DRA; (*l*)	20 mm
Width of DRA; (*w)*	12 mm
Height of upper segment; (h_2)	5 mm
Height of lower segment; (h_1)	12 mm
Dielectric constant of upper segment DRA; (ε_r)	9.8
Dielectric constant of lower segment DRA; (ε_r)	2.1
Thickness of Substrate	1.6 mm
Substrate dimensions	$60\ mm \times 110\ mm$
Ground plane dimensions	$60\ mm \times 110\ mm$
Spacing between element (d)	37.5 mm
Height of metallic plate	13.4 mm

Results and Discussion: The simulated and calculated return loss comparison is shown in Fig. 2, where a good agreement between theory and simulation is found which validate our FDTD method for conformal strip excited DRA array. It is found that simulated and calculated resonant frequencies and impedancebandwidths are 3.44 GHz, 20.43%, 3.46 GHz & 19% respectively. Again a good agreement can be observed between calculated and simulated input impedance in Fig. 3.

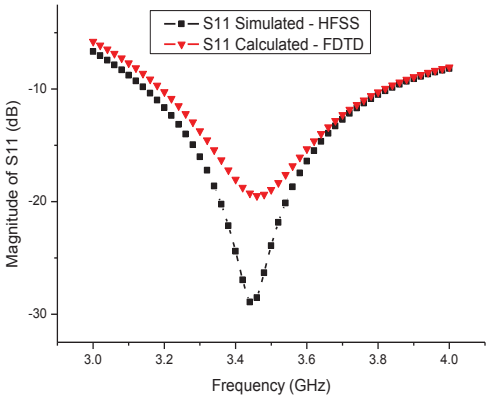

Fig.2. Comparison between simulated & calculated S11 versus frequency characteristics for proposed array

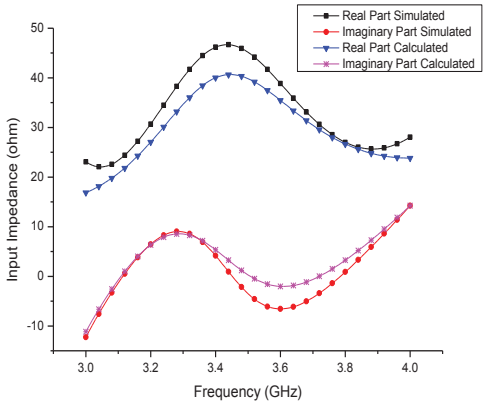

Fig.3.Simulated and calculated input impedances for proposed array

Conclusion: In this paper, two element conformal strip coupled RDRA array excited in the $TE^{y}_{1\delta1}$ mode has been studied. The resonant frequency, return loss and impedance bandwidth of the proposed array has been discussed. Calculated results of the uniform grid FDTD method have been compared with simulated results ofAnsoft HFSS software. This can be a particularly useful feature manifesting that conformal strip coupling is an efficient, simple, and easy to implement feeding system for RDRAs and arrays, enabling their integration in MMIC applications. The proposed antenna array offerswide bandwidth, appreciable Gain,

and good impedance matching, making them a good alternative to patch antennas in array applications. Finally, although the strips would add conduction losses to the antenna, the antenna efficiency should be significantly higher than that of the microstrip antenna, especially at millimetre-wavefrequencies where the skin effect is strong. The results obtained may be useful for designing and developing antennas for Radar application in S-band.

References:

[1] G. Drossos, Z. Wu, and L. E. Davis, „„Aperture-coupled cylindrical dielectric resonator antennas forming four-element linear arrays,"" *Electronics Letters*, Vol. 20, 1999, pp. 151-153.

[2] Wee, F. H., F. Malek, S. Sreekantan, A. U. Al-Amani, F. Ghani, and K. Y. You, "Investigation of the characteristics of barium strontium titanate (BST) dielectric resonator ceramic loaded on array antennas," *Progress In Electromagnetics Research*, Vol. 121, 181-213, 2011.

[3] G. Drossos, Z. Wu, and L. E. Davis, „„Two-Element Broadside Arrays Using Cylindrical Dielectric Resonator Antennas,"" *Microwave Opt. Technol. Lett*., Vol. 11, No. 6, 1996, pp. 342-345.

[4] Denidni, T. A., Y. Coulibaly, and H. Boutayeb, "Hybrid dielectric resonator with circular mushroom-like structure for gain improvement,"*IEEE Transactions on Antennas and Propagation*, Vol. 57, No. 4, 1043-1049, 2009.

[5] Biancotto, C. and P. Record, "Dielectric EBG corner reflector antenna," *Journal of Electromagnetic Waves and Applications*," Vol. 24, Nos. 14-15, 2107-2118, 2010.

[6] Leung, K. W., K. Y. Chow, K. M. Luk, and E. K. N. Yung, "Offset dual-disk dielectric resonator of very high permittivity," *Electronics Letters*, Vo1. 32, No. 22, 2038-2039, 1996.

[7] A. Gupta, R. K. Gangwar, and S. P. Singh, "Three element dual segment triangular dielectric resonator antenna for x-band applications," *Progress In Electromagnetics Research C*, Vol. 34, 139-150, 2013.

[8] A. Petosa, R. K. Mongia, A. Ittipiboon, and J. S. Wight, "Design of microstrip-fed series array of dielectric resonator antennas," *IEE Electronics Letters*, Vol. 31, pp. 1306-1307, 1995.

[9] A. Petosa, R. Larose, A. Ittipiboon, and M. Cuhaci, "Low profile phased array of dielectric resonator antennas," *IEEE International Symposium on Phased Array Systems and Technology*, pp. 182-185, 1996.

[10] R.K. Mongia, and A. Ittipiboon, "Theoretical and experimental investigations on rectangular dielectric resonator antennas," *IEEE Transactions on Antennas and Propagation*, Vol. 45, pp. 1348-1356, 1997.

[11] K. W. Leung "Conformal strip excitation of dielectric resonator antenna", *IEEE Transactions on Antennas and Propagation*, Vol. 48, No. 6, pp.961 -967 2000.

[12] B. Li and K. W. Leung "Strip-fed rectangular dielectric resonator antennas with/without a parasitic patch",*IEEE Transactions on Antennas and Propagation*, Vol. 53, No. 7, pp.2200 -2206, 2005.

[13] Y. S. Yee, "Numerical solution of initial boundary value problems involvingMaxwell""sequationsinisotropicmedia,"*IEEE Transactions on Antennas and Propagation*, Vol. 14, No. 3, pp. 302–307, May 1966.

[14] A. Taflove, Computational Electrodynamics: The Finite Difference TimeDomain Method. Norwood, MA: *Artech House*, 2000.

[15] A. Elsherbeni and V. Demir, "The FiniteDifference Time Domain Method for Electromagnetics: With MATLABSimulations," *SciTech Publishing,* 2009.

A NOVEL ANFIS BASED CAD MODEL TO PREDICT THE RETURN LOSS PERFORMANCE OF A HEXA-BAND PIFA

Aarti Gehani and Dhaval Pujara
Department of Electronics and Communications Engineering, Institute of Technology, Nirma University, Ahmedabad 382481,
Email: aarti.gehani@nirmauni.ac.in, dhaval.pujara@nirmauni.ac.in

Abstract: *In the present work, the Artificial Neuro-Fuzzy Inference System (ANFIS) based CAD model is proposed to predict the return loss performance of a hexa-band Planar Inverted-F Antenna (PIFA). The PIFA physical parameters are given as inputs to the proposed CAD model, while the antenna return loss characteristics over a desired frequency band is obtained as the output. The CAD model output is compared with that of the commercially available full wave solver and it is found in close agreement. Moreover, for the given model, various ANFIS parameters are changed and their effects on the results are studied and thoroughly summarized.*

Introduction: Antenna design for mobile handsets has become a subject of interest amongst the researchers since its inception. Prior to 1990s, external antennas like helix, monopole or a combination of helix and monopole antenna were used in mobile handsets [1]. The technological advancements, increasing demands for flexibility in industrial design and reduction in SAR has led to the development of planar antennas. One of the most employed planar antennas in mobile handsets is PIFA [1]. Structurally, PIFA consists of a ground plane, substrate, a metallic patch, a shorting pin/plate and a feed line. It operates at λ/4 length and is very suitable for a small and light weight application such as, an internal antenna of a mobile handset [2].

Till recent years, conventional electromagnetic modelling techniques were being used to design and analyze the performance of PIFA. However, it is known that, the conventional techniques involve complex analytical models and extensive computations which make them complicated and time consuming. In the recent years, researchers have explored many soft computing techniques, such as artificial neural networks, genetic algorithm, fuzzy logic, etc. to predict the performance of various complicated antennas including PIFA. The present paper proposes an ANFIS based CAD model to predict the return loss characteristics of a compact hexa-band PIFA over a broad frequency spectrum. The results obtained through ANFIS model are validated with that of the commercially available full wave solver. Also, various ANFIS parameters, such as, types of membership functions, number of membership functions, the size of training data set, etc. are varied and their effects on the overall performance of the CAD model are studied and discussed at a length.

Planar Inverted-F Antenna: In the present work, the PIFA geometry suggested in [3] is referred for developing the ANFIS based CAD model. The PIFA geometry under consideration consists of a long radiator, a short radiator and is designed to have triple-resonance characteristics. The first resonance frequency operates at GSM (880–960 MHz) band while the second and third resonance frequencies operate at DCS (1710–1880 MHz), PCS (1880–1990

MHz), UMTS (1920–2170 MHz), WiBro(2300–2390 MHz) and Bluetooth (2400–2480 MHz). Thus, in true sense the geometry offers hexa-band performance. The said antenna geometry is shown in Fig. 1.

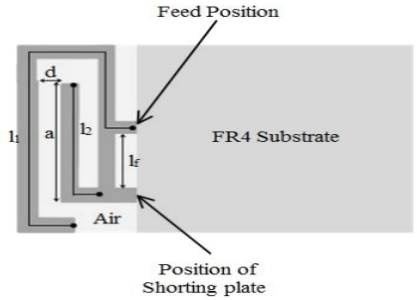

Fig. 1. Schematic of PIFA under consideration

l_1 = total length of the long radiator
l_2 = total length of the short radiator
a = length of the horizontal portion of the short radiator
d = distance separating long and short radiator
l_f = distance between the feed point and the shoring pin

Artificial Neuro-Fuzzy Inference System: Artificial Neuro-Fuzzy Inference System (ANFIS) is a combination of fuzzy system and artificial neural networks [4]. It combines the explicit knowledge representation of a fuzzy inference system with the learning capability of artificial neural networks. The advantages of ANFIS include: fast convergence due to hybrid learning, ability to construct good input membership functions and automatic search of non-linear connection between inputs and outputs. A simple ANFIS structure is shown in Fig. 2.

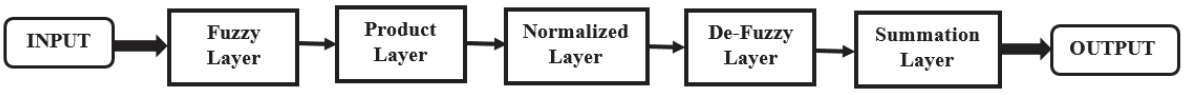

Fig. 2. Simplified ANFIS architecture

Development of ANFIS based Model: In this section, development of ANFIS based CAD model is discussed. For the present PIFA problem, antenna physical parameters a, d and l_f are taken as input to the model, while antenna return loss is expected as the model output. The proposed ANFIS model is suitable for obtaining return-loss over a frequency band of 0.5 to 3 GHz. As it may be difficult to cover entire band using a single ANFIS model, it is decided to develop 51 such models as shown in Fig. 3. Each of the models provides the value of return loss at single frequency starting from 0.5 to 3 GHz with a step size of 0.05 GHz. The necessary data for training and testing the ANFIS model are generated using full wave solver (FWS). The complete description of the proposed ANFIS model including the size of training and testing data set is given in Table I. The next step in the sequence is to train each model such that it results into minimum error (below 5 %). Once, all the models are trained properly, they are tested for their effectiveness. Generally, the testing data set is different from the training data set. The effectiveness of the proposed model is assessed based on the two statistical parameters, namely the Coefficient of Determination (R^2) [5] and the Root Mean Square Error (*RMSE*).

Results and Analysis: This section presents: (i) the results obtained from the proposed ANFIS model, (ii) their comparison with the results obtained through full wave solver and (iii) effects on results due to change in different model parameters. The effect of change in the number of training data sets is summarized in Table II. Later on, for a given set of input data, the outputs are obtained by changing the type of membership functions. The outcomes of this study are summarized in Table III. From the table, it can be observed that the *trapezoidal* type of membership function can produce the best results as compared to the other types for the present problem.

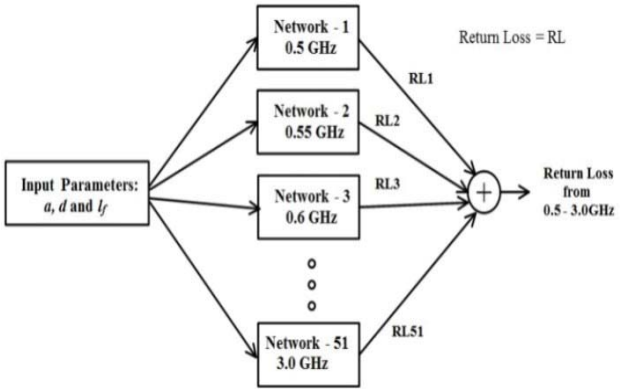

Fig. 3. Proposed ANFIS based CAD model

TABLE I
DESCRIPTION OF THE ANFIS BASED CAD MODEL

Parameters	Value
Number of training datasets	1300
Number of testing datasets	288
Number of membership function	5
Number of epochs	20
Type of membership function	*Trapmf*
Number of nodes	286
Number of fuzzy rules	125
Total number of parameters	560

TABLE II
EFFECT OF CHANGE IN NUMBER OF TRAINING DATASETS ON MODEL STATISTICAL PARAMETERS

Size of Training Dataset	R^2	RMSE
700	0.958	1.74
1040	0.973	1.38
1300	0.979	1.23

TABLE III
EFFECT OF CHANGE IN TYPE OF MEMBERSHIP FUNCTIONS ON MODEL STATISTICAL PARAMETERS

Type of MF	R^2	RMSE
Gaussian	0.956	1.79
Generalized bell	0.974	1.38
Pi-shaped	0.978	1.24
Sigmoidal	0.978	1.24
Two Gaussian	0.978	1.23
Trapezoidal	**0.979**	**1.23**

The number of membership functions for trapezoidal type of membership function are changed and the results for all the cases are obtained for a = 33mm, d = 4mm and l_f =15mm case. All such results are plotted in Fig. 4. From the careful observation of the results, it can be concluded that the accuracy of results increases as the number of membership function increase. However, it is also noticed that the increase in number of membership functions also increases the computation time.

The proposed ANFIS model is also checked for different sets of testing data sets. Based on the exhaustive study and analysis of all 288 combinations of testing data sets, it is found that the *trapezoidal* membership function gives very accurate results for all the combinations. Considering the space constraints, the results for only two testing datasets are presented in Fig. 5. For all these cases, it can be easily seen that the results from the proposed ANFIS model are in close agreement to FWS.

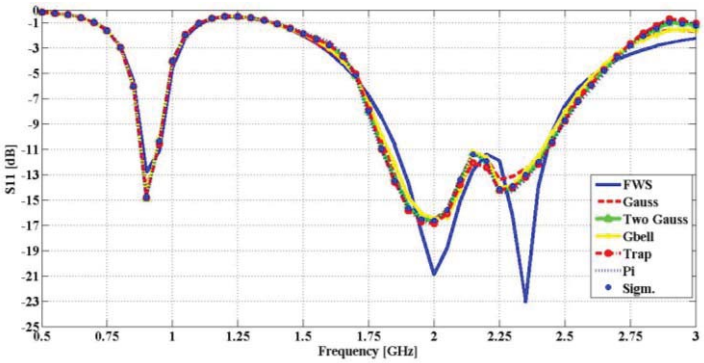

Fig. 4. Return loss characteristics for different number of MFs for Trapezoidal MF

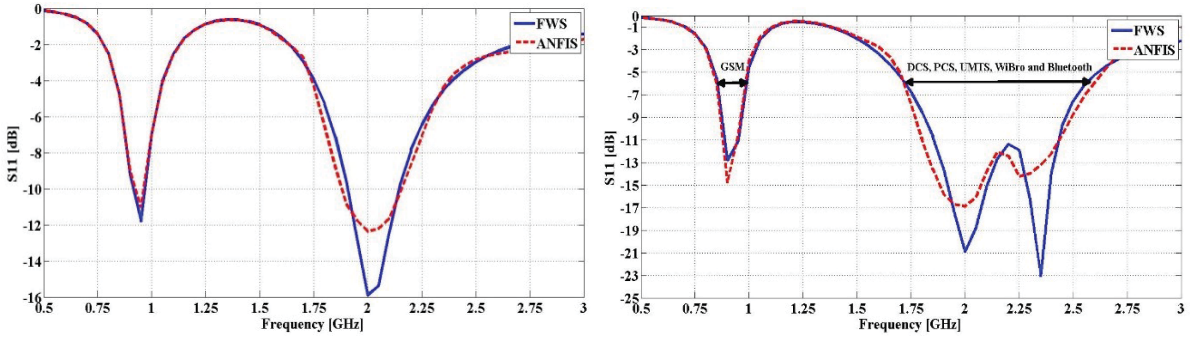

(a) (b)

Fig. 5. (a) Comparison of return loss characteristics for a = 16.5mm, d = 4.5mm and l_f = 11.5mm
(b) Comparison of return loss characteristics for a = 33mm, d = 4mm and l_f = 15mm

Conclusion: In the present work, a novel ANFIS based CAD model is proposed to analyze the return-loss characteristics of a PIFA. It is observed that the return-loss obtained from the ANFIS based model resembles closely to that obtained through the full wave solver. For the antenna geometry under consideration, the *trapezoidal* membership function gives accurate results as compared to other membership functions. However, there is no thumb-rule for selection of the type and number of membership functions. Increase in the number of training datasets will increase the accuracy of the results but at the cost of computation time. Also, increase in the number of membership functions will increase the accuracy of the results but with a rise in the computation time. As compared to the FWS which takes hours to solve the problem, the proposed model takes very less computation time, in terms of few minutes, and gives accurate return-loss characteristics of the antenna. Computer RAM of the order of GB is required to design the hexaband PIFA using a FWS, while only a few KBs file is required by the proposed model. Utmost care should be taken in generation of training datasets, selecting the type and the number of membership functions and validation of the models.

References:

1. C. Rowell and E. Y. Lam, "Mobile-Phone Antenna Design," IEEE Antennas Propag. Mag., Vol. 54, No. 4, pp.14-34, 2012.
2. Y. X. Guo, M. Y. W. Chia, and Z. N. Chen, "Miniature built-in multiband antennas for mobile handsets," IEEE Trans. Antennas Propag., Vol. 52, No. 8, pp. 1936–1944, 2004.
3. D. G. Kang and Y. Sung, "Compact Hexaband PIFA Antenna for Mobile Handset Applications," IEEE Antennas and Wireless Propagation Letters, Vol. 9, No. 3, pp. 1127-1130, 2010.
4. J.-S. R. Jang, "ANFIS: Adaptive-Network-Based Fuzzy Inference System," IEEE Trans. Syst., Man and Cybern., Vol. 23, pp. 665-685, 1993.
5. O. Kisi, J. Shiri and B. Nikoofar, "Forecasting Daily Lake Levels using Artificial Intelligence Approaches," Computers & Geosciences, Vol. 41, pp. 169-180, 2011.

Dual Circularly Polarized and High Power Capable Medium Gain Antenna for Mars Orbiter Mission

B Pavan Kumar[(1)], Chandrakanta Kumar, V Senthil Kumar, K M Subrahmanyam, V V Srinivasan[(2)]
Communication Systems Group, ISRO Satellite Centre, Bangalore, India, PIN-560017
[(1)]pavanb@isac.gov.in, [(2)]vvs@isac.gov.in

Abstract— *This paper gives design and optimization of a medium gain antenna operating in dual circular polarization and can handle high power onboard a satellite. The antenna has to provide coverage in some specific directions off the satellite's principal axes to have RF link during critical mission operations. A novel way of adjusting the boresight and at the same time minimizing the antenna weight is discussed. This antenna is proposed to be used for satellite telemetry, tracking and command operations along with transmitting payload data in S-band for India's Mars Orbiter Mission.*

Introduction: ISRO's Mars Orbiter Mission is equipped with three antenna systems for TT&C (Telemetry, Tracking and Command) and payload communications in S-band during different phases of the mission. They are Low Gain Antenna (LGA) system for communication during the near Earth phase, Medium Gain Antenna (MGA) that can support during the initial part of cruise phase (Helio-centric phase) and also during some critical mission operations and the High Gain Antenna (HGA) which will be helpful during lateral part of cruise phase and also for communication from Martian orbit.

The LGA is an omni-antenna system which consists of a set of four Quadrifilar Helix Antennas (QFAs) for both uplink and downlink on two opposite sides of the spacecraft similar to the one mentioned in [1]. The HGA, which is an offset fed parabolic reflector antenna with its boresight along the +Roll axis of the spacecraft is designed [2]. By continuously pointing the spacecraft's +Roll axis towards Earth, continuous communication will be ensured. But there are two problems associated with this arrangement. The spacecraft has two large appendages – the 2.2m reflector (for HGA) and the solar panels. During the long cruise phase (almost 300 days), there are many external forces acting on the satellite and the most important one is the solar radiation pressure (SRP). Due to this SRP acting on the appendages, there will be a marginal but continuous change in the velocity of the satellite. For a deep space mission, if there is any such unpredicted change in the velocity of the satellite, the chances of reaching the target decreases. Another problem is communication during Mars orbit insertion (MOI) which is the most important event for this satellite. The satellite's engine is also aligned along the Roll axis. During MOI, the satellite has to be aligned such that Roll axis should be along the velocity vector. Hence communication through HGA is not possible and LGA also cannot support during MOI.

To overcome these problems, a new antenna called MGA is introduced. The boresight is chosen such that both the above mentioned problems can be solved. During

MOI, +Roll axis will be away from Earth by 35° and increase as the engine burn progress till the communication is blocked by Mars planet itself. Hence a wide beam antenna with its boresight 35° away from +Roll axis and that can handle an RF power of 200-250 W will serve the purpose. As there is a stringent constraint in the spacecraft mass, necessary novelty and engineering is implemented to minimize the MGA weight.

Design considerations for MGA: During the cruise phase and till MOI, maximum range from Earth to satellite is 220 million kilometers. To support TT&C from different ground station antennas and with onboard power of about 230W, an antenna with moderate gain of about 8-9 dBi is required. This can be achieved by a simple open ended circular waveguide. An antenna with waveguide interface is selected so as to withstand high power downlink. For TT&C application, circularly polarized antenna is usually preferred. Hence dual circularly polarized antenna is chosen so that any ground station antenna can communicate with the satellite. The allotted TT&C frequencies in S-band for deep space communication are 2.11 – 2.12 GHz for uplink and 2.29 – 2.3 GHz for downlink. Since both uplink and downlink are in same frequency band, same antenna can be used.

Thus, ideally, to meet all the above requirements, MGA should have an open ended circular waveguide connected to a septum polarizer by a circular to rectangular waveguide transition, a septum polarizer to generate dual circular polarization, a 90˚ bend after septum polarizer for any one port to physically separate the two ports, a 35˚ bend to meet the mission requirement. Even though both ports (RHCP and LHCP) can be used, we are considering using only RHCP port. Hence a matched waveguide termination to terminate the LHCP port is also required. But, having all these components, and at S-band, would result in an antenna with large weight and volume. This large volume and with the antenna inclined by 35˚ with one of the principle axes will call for a stronger supporting structure to withstand severe launch vibrations. Such a luxury is not affordable in a satellite especially in this mission where large volume of fuel needs to be carried. Hence MGA configuration is optimized in several ways as explained below to reduce the overall weight without compromising on RF performance.

(i) Firstly, WR-340 waveguide is selected instead of WR-430 which is the recommended standard waveguide for operating in S-band. WR-340 waveguide is having a cut-off frequency of 1.73 GHz. Thus the starting frequency of operation (2.11 GHz) is 20% more than the cut-off frequency of WR340. Hence WR-340 is sufficient to be used for the required frequency of operation.

(ii) The circular waveguide is totally removed and the circular end of the rectangular to circular waveguide transition itself is used as radiating open ended waveguide.

(iii) A 35˚ bend is introduced between septum polarizer and the rectangular to circular waveguide transition. Thus by using one end of the bend for mounting the antenna, only this bend and the rectangular to circular waveguide transition are projected outside the satellite panel. This reduces the need for complex supporting structure and thus reducing the overall weight considerably.

(iv) The unused port of the polarizer which has to be terminated is shorted with a simple metal plate and thus saving the weight of the waveguide termination.

(v) Ideally, the taper length of the rectangular to circular waveguide transition should be larger than the operating wavelength for proper impedance matching over the complete frequency band [3]. This will be more than 140 mm at 2.11 GHz. But here the transition is optimized to a length of 120 mm (< 1λ) such that impedance matching is ensured within the required frequency of operation (2.1 to 2.3 GHz).

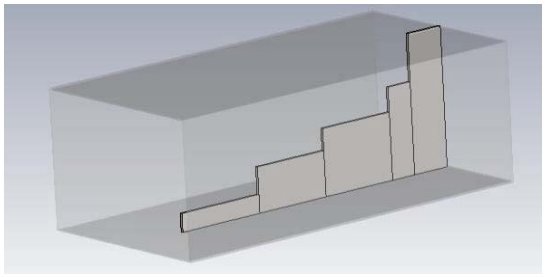

Fig.1. Schematic of the Septum Polarizer with 4 steps

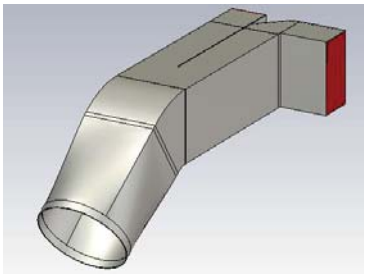

Fig.2. Schematic of MGA with all the components

(vi) The diameter of the circular waveguide is chosen such that its cut-off frequency is at least 20% less than the minimum frequency of operation and also small enough to minimize the weight. The chosen diameter is 108mm. The cutoff frequency of the dominant mode is TE_{11}-1.628 GHz. It can be noted that the minimum frequency of operation is higher by more than 20% of the cut-off frequency of the dominant mode. By lowering the waveguide diameter further, it is noted that there is a beam squint. Thus the chosen diameter of the waveguide is optimum for the application.

Simulated Results: Since the required bandwidth is <10%, a septum polarizer with four steps is sufficient. A schematic of septum polarizer with four steps is shown in Fig.1. The working principle and design guidelines of a septum polarizer are available in articles like [4]-[5]. Septum polarizer is chosen because it provides a simple, compact and easy to realize structure for generating dual circular polarization with very good polarization purity within the required frequency band [6]. Initially, only the septum polarizer is optimized over several iterations using the software CST Microwave Studio to keep the return loss of the ports and the isolation between the ports better than 20 dB and Axial ratio less than 0.5 dB over complete bandwidth. Since a standard WR-340 waveguide is followed after the polarizer, the rectangular waveguide containing the polarizer is having the dimensions of 86.36 mm x (86.36+1) mm, where 1 mm is the septum thickness.

Once the dimensions of the septum polarizer are optimized, the complete structure - 90° bend, septum polarizer, 35° bend and rectangular to circular waveguide transition are integrated and simulated. The schematic of the MGA with all the components is shown in Fig.2. Introduction of the 35° bend after the septum polarizer and shorting plate for the unused port will degrade the cross-polar isolation of the antenna. Hence several parameters are optimized over iterations to meet the required performance. Simulation results shows that the cross polar isolation in integrated MGA is degraded. The on-axis cross-polar isolation details are tabulated in Table.1. Since the cross-polar isolation is better than 20 dB, this is acceptable.

Table.1. Cross-polar isolation for septum polarizer alone and integrated MGA

Frequency	Septum Polarizer	Integrated MGA
2.1 GHz	41 dB	24 dB
2.3 GHz	37 dB	23 dB

Measured Results: The fabricated antenna is shown in Fig.3. This antenna is tested for its performance. The first parameter to be tested is the reflection coefficient (S_{11}) of the antenna which is done using a Vector Network Ananlyzer. The measured S_{11} plot of the antenna is shown in Fig. 4. At the frequency of interest, S_{11} is about -22 dB and is less than -20 dB over the complete bandwidth. The co and cross-polarized radiation patterns of the antenna are measured in an automated RF shielded anechoic chamber. Pattern for co-polarized (RHCP) radiation of the antenna are measured in 4 planes at an interval of 45° at

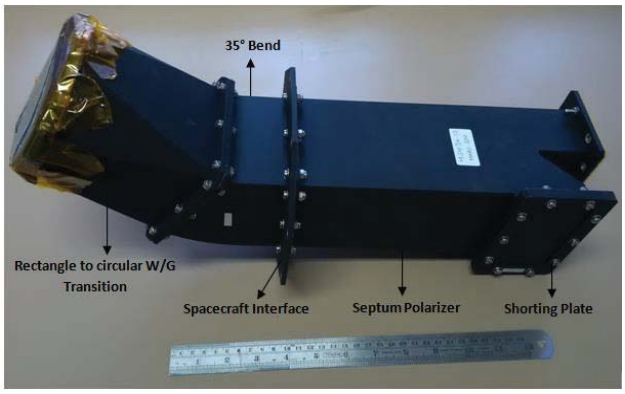

Fig. 3. Photograph of the fabricated MGA indicating different components

2.1 GHz and 2.3 GHz. In each plane the pattern is measured over ±90˚ about the antenna axis. The radiation patterns at 2.1 GHz and 2.3 GHz in all the measured planes are shown in Fig. 5 (a) and Fig. 5 (b) respectively. These pattern over four planes help understand the typical 3D behavior of the radiation characteristics of the antenna. It is seen from this plot that antenna is radiating symmetrically about antenna axis with pattern dispersion less than 1 dB over ±45˚. Measured peak gain is around 8.2 dBi at 2.1 GHz and 8.7 dBi at 2.3 GHz.

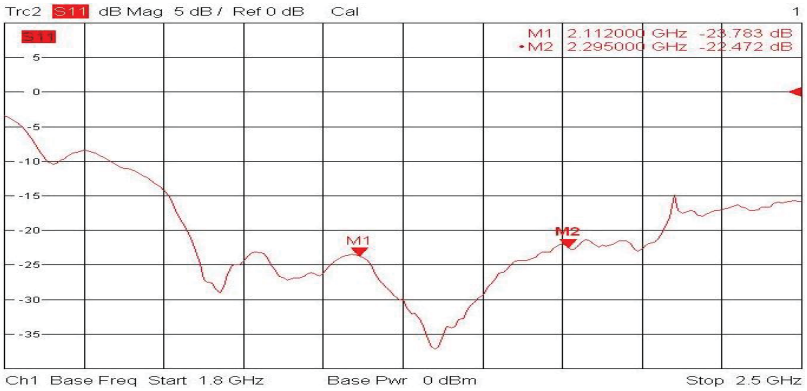

Fig. 4. Measured retun loss of RHCP port with LHCP port shorted

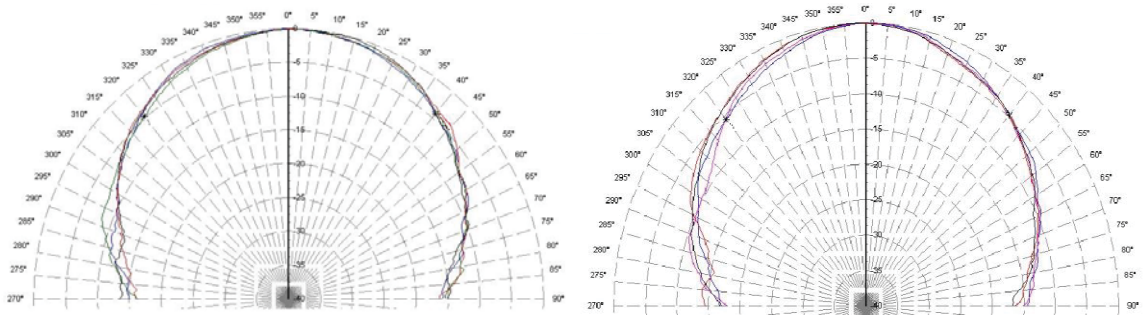

(a) (b)

Fig. 5. Measured co-polar radiation pattern in four planes at (a) 2.1 GHz and (b) 2.3 GHz

The polarization purity of the antenna can be analyzed by measuring the co to cross-polar isolation or by measuring axial ratio (AR) pattern. Here co and cross-polarized patterns are measured at 2.1 GHz and 2.3 GHz and are compared as shown in Fig. 6 (a) and Fig. 6 (b). It can be seen that the cross-polarized radiation is less than 22 dB compared to the co-polarized pattern along antenna axis and this corresponds to an AR less than 1.4 dB. This is sufficient for the present application under consideration. Thus the measured results have a very close match with the simulated values.

(a) (b)

Fig. 6. Measured cross polar isolation at (a) 2.1 GHz and (b) 2.3 GHz

Conclusion: A waveguide antenna providing a good circularly polarized radiation and with moderate gain is designed. The need for MGA in Mars Orbiter Mission is explained. The constraints and objectives for designing MGA are also listed. A novel way of providing the boresight at the intended direction is implemented in a compact manner. The weight of the realized antenna is about 1.6 Kg. Simulation results and measurement results of MGA are also presented The measured results are in good agreement with the simulated results and meet all the requirements. Since the antenna is intended for space application and has to handle high power, all the necessary precautions and care are taken during the design and handling the antenna. An analysis is also done to verify the power handling capability of the antenna. The in-orbit performance of the antenna is also satisfactory.

Acknowledgements: The authors are exremely thankful to our Group Director, Sri. Yateendra Mehta, for his timely suggestions and guidence in designing the antenna.

References:

[1] B .P. Kumar, M. Kumar, C. Kumar, V. S. Kumar, V. V. Srinivasan, "Integrated Quadrifilar Helix at C-band for spacecraft omni antenna system," Applied Electromagnetics Conference, Kolkata, Dec. 2011.

[2] C Sriharsha, B. P. Kumar, K. M. Subrahmanyam, V. S. Kumar, V. V. Srinivasan, Y. Mehta, "Design and development of High Gain Antenna for Mars Orbiter Mission," Journal of Spacecraft Technology, vol. 25, No.2, pp.21-28, June 2014.

[3] P. A. Rizzi, "Microwave Engineering –Passive Circuits", Prentice Hall of India, New Delhi, 2001.

[4] M.H.Chen, G. N.Tsandoulas, "A wide-band square waveguide array polarizer," IEEE Trans. AP., vol.21, pp.389-391, May 1973.

[5] J. Bornemann, V. A. Labay," Ridge waveguide polarizer with finite and stepped-thickness septum," IEEE Transactions on Microwave Theory and Techniques, vol. 43, no. 8, pp. 1782-1787, Aug. 1995

[6] J. Uher, J. Bornemann, U. Rosenberg, "Waveguide components for antenna feed systems: Theory and CAD", Artech House, London, 1993.

DESIGN & SIMULATION OF W BAND CASSEGRAIN ANTENNA SYSTEM

Eaineesh Pundir, Raj Kumar, PK Verma
College of Engineering Roorkee, Roorkee, India.247667
Email:eaineesh@gmail.com

Abstract: *Present paper describes design, simulation & optimization of 300 mm narrow beam cassegrain antenna at 94 GHz for long distance communication system. The feed for the antenna has been simulated on ANSYS HFSS software while reflector and sub reflector have been simulated on TICRA's GRASP9 software. Simulated gain of antenna is 48 dBi and its side lobe level is better than 25 dB at 94 GHz. The simulated results of the antenna closely resemble with the designed values.*

Introduction: Antenna is one of the important sub systems of any system. The performance of system depends on the performance of antenna as it is the sub system that faces the signal first. High gain antennas are the prime requirement of long distance communication system. Besides gain, other parameters of antenna which affect the performance of system are side lobe level, VSWR and polarization. Side lobe level dictates the signal received from direction other than the required direction. VSWR of the antenna determines the mismatch of the input power to the antenna. For better communication system the side lobe of the antenna should be as low as possible at the same time the VSWR should not exceed 2.

Reflector antennas are generally used for high gain applications in microwave frequencies. Out of several configurations of reflector configurations (prime focus, offset, Cassegrain etc.) Cassegrain antenna are compact as compared to other configurations and it also offers ease of integration of RF to antenna as it's input lies at the back of antenna. Other advantages of Cassegrain over other configurations includes ability to place the feed in a convenient location resulting in reduction of spillover and minor lobe radiation, ability to obtain an equivalent focal length much greater than the physical length and reduction of noise temperature [1].

This paper describes the design, simulation and optimization of 94 GHz Cassegrain antenna system.

DESIGN CONSIDERATIONS

The Cassegrain antenna mainly consists of two reflecting structure from which the wave gets reflected before being radiated in a definite direction. Out of these two reflectors the primary or usually the larger reflector is a paraboloid structure and the secondary one is a hyperboloid / ellipsoid structure resulting in Cassegrain or Gregorian antenna. In a Cassegrain arrangement the beam of radio waves from the feed illuminates the secondary reflector which reflects it to the main reflector and main reflector reflects the rays again in the forward direction. The geometrical condition for radiating a collimated, plane wave is that the feed antenna must be placed at the far focus of the hyperboloid, while the focus of the primary reflector coincide with the near focus of the hyperboloid [4-5].

Design of casegrain antenna depends on the design of primary antenna i.e. feed horn and design of secondary antenna (reflector and sub reflector). To get gain of the order of 48 dBi, the aperture of antenna has been chosen as 300 mm taking aperture efficiency of the order of 70 %. f/D of the antenna (which defines the volumes of antenna) has been taken as 0.35. Side lobe level of the antenna is decided by the edge tapering to the antenna. To get side lobe level of less than 25 dB the total edge tapering (beam edge tapering and tapering due to reflector surface) should be around -11 dB[6]. This edge tapering reduces the power level at the edge to -11 dB down compared to centre and hence making spill over negligible (<3%). Based on above parameters all other dimensions of the paraboloid reflector and hyperboloid sub reflector are calculated and are listed below.

Focal length of the parabolic reflector (f) = 105 mm
Focal length of the hyperbola = (30+25) = 55 mm

Effective f/D = $\frac{1}{4\tan\left(\frac{\Psi}{2}\right)}$ = 0.902 Magnification M = $\frac{\text{Effective}\frac{f}{D}}{\frac{f}{D}}$ = 2.57

Eccentricity e = $\frac{M+1}{M-1}$ = 2.27

c = f of hyperbola/2 = 27.5 mm a = c/e = 12.11 mm

b=$\sqrt{c^2 - a^2}$ = 24.69 mm

Feed blockage

$\Phi_b = \sin^{-1}(\frac{d}{2F})$ = =9.87

Using equations given in [2-3] all the dimensions of Cassegrain antenna has been calculated and are shown in figure 1.

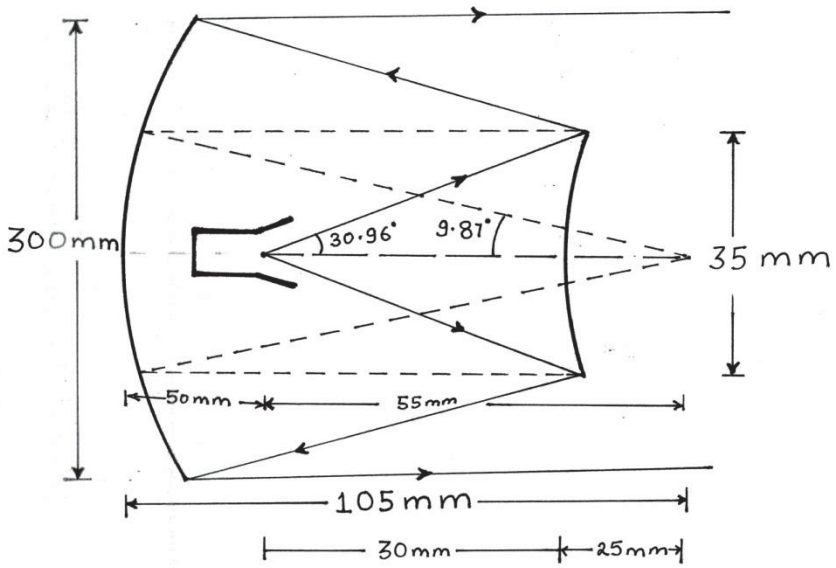

Figure 1. Calculated dimensions of Cassegrain antenna

The design of feed horn antenna is made based on the edge tapering requirement at the edges of reflector by placing the feed horn at the focus of the sub reflector. To feed the above design antenna a conical feed horn has been selected. Aperture of feeding waveguide has been selected as 3 mm for dominant mode (TE_{11}) propagation. The aperture of conical horn has been selected as 8 mm so that required tapering may be obtained at the edge of the sub reflector. The phase centre of the designed conical horn is located at the focus of the sub reflector antenna. Other calculated dimensions of the primary antenna are shown in figure 2.

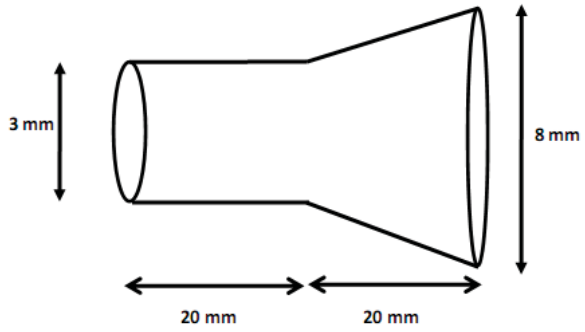

Figure 2. Calculated dimensions of feed horn antenna

Simulation and optimization: Designed feed horn was simulated on ANSYS HFSS software using proper boundary conditions. Optimized simulated radiation pattern of horn antenna is given in figure 3.

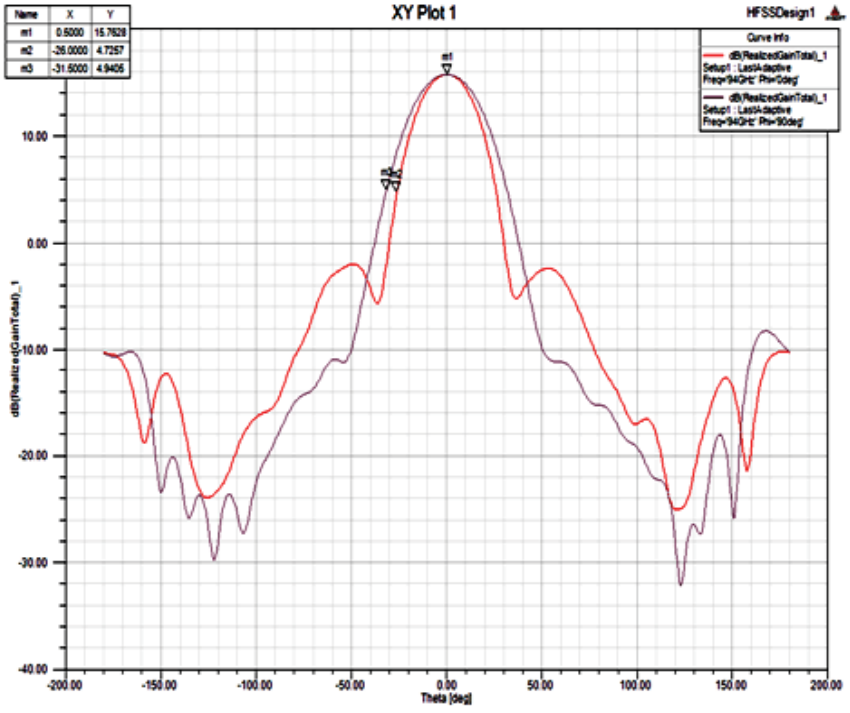

Figure 3. 3D model and simulated radiation pattern of horn antenna

Simulated parameters of feed horn have been used in TICRA's GRASP9 software for simulation of dual reflector Cassegrain antenna. 3D model of reflector antenna and its simulated radiation patterns are shown in figure 4.

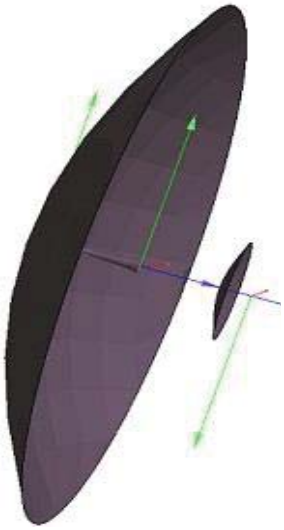

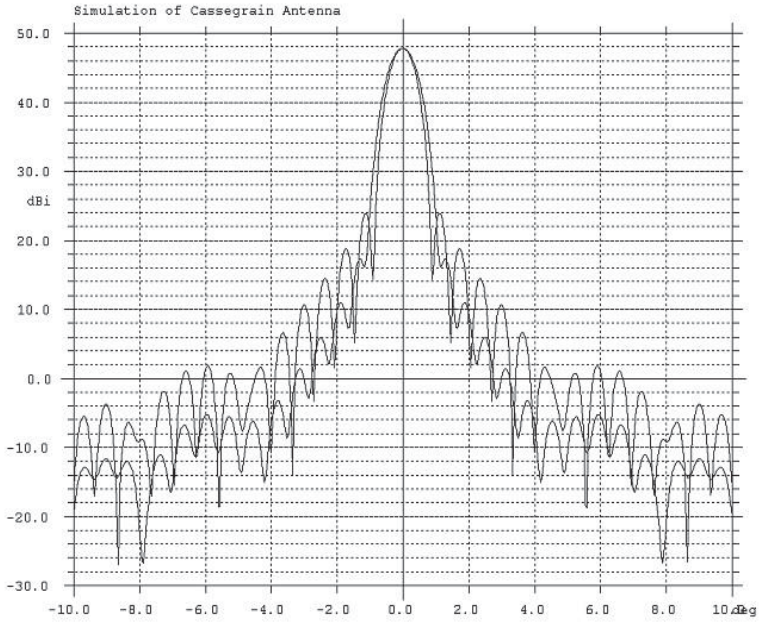

Figure 4. 3D model a

Results & discussion: The simulated radiation pattern of feed horn and reflector antenna are shown in figure 3 and 4 respectively. The 11 dB beamwidth of the feed horn antenna has been taken equal to angle subtended by reflector edges at its focus. The simulated gain of antenna is 48 dBi and side lobe level of better than 25 dB.

Conclusion: A 300 mm cassegrain antenna has been modeled, simulated and optimized at 94 GHZ on TICRA's GRASP9 software and ANSYS HFSS software. Designed antenna has very high gain of 48 dBi (narrow beamwidth) and side lobe level lower than -25 dB. This antenna posses aperture efficiency of 70 % and spill over less than 3 %. Side lobe level of -25 dB has been obtained by taking edge tapering of -11 dB at the sub reflector. This high pencil beam antenna may be used in long distance line of sight communication system

Acknowledgement: Author is thankful to Director, DEAL for allowing for training in antenna division of DEAL. Thanks are also due to Mr. Mahakar Singh, Head, Antenna system group for his guidance during my training period at DEAL. We are also thankful to Mr. B.D.Patel (HOD-Electronics and Telecommunication department, COER).

References

1. Constantine A. Balanis, "Antenna Theory Analysis and Design", Second edition,
2. Paul Wade, "Multiple Reflector Dish Antennas", www.w1ghz.org
3. Christophe Granet, "Designing Axially Symmetric Cassegrain or Gregorian Dual-Reflector Antennas from Combinations of Prescribed Geometric Parameters," IEEE Antennas and Propagation Magazine, June 1998, pp. 82-85.
4. J.S. Cook, E.M. Elam and H. Zucker "The open Cassegrain Antenna: Part I. Electromagnetic Design and Analysis", The Bell system technical journal, September 1965.
5. Divya Gupta, R.A. Deshpande "A review on designing of the dual reflector axially symmetric Cassegrain Antenna" IOSR Journal of Electronics and Communication Engineering (IOSR-JECE) ISSN: 2278-2834, ISBN: 2278-8735. Volume 4, Issue 1 (Nov. - Dec. 2012), PP 48-51.
6. L. V. Blake, "Antennas", Artech House Inc. 1984.

Theoretical Analysis of Double Step Junction Coupled Waveguide fed DRA

P. M. Jasmine[(1)], P. Abdulla[(2)], and P. M. Raphika[(3)]
(1), (2), (3) School of Engineering, Cochin University of Science & Technology, Kochi - 22, India.
Email: (1) jasmine.maiyn@gmail.com (2) abdulla@cusat.ac.in (3) pmraphika@yahoo.co.in

Abstract: *A hemispherical dielectric resonator antenna (DRA) excited by a double step junction coupled waveguide is studied theoretically. The double step junction is used to increase the coupling from waveguide to DRA. The problem has been analyzed by solving coupled integral equations obtained by imposing magnetic field boundary conditions at various apertures using method of moments. The DRA, slot and the steps are analyzed using Green's function and modal analysis is performed for waveguide. The proposed structure guarantees more than 98% coupling.*

Introduction: During the last three decades, microstrip antennas were used extensively because of their low profile and conformability with curved surfaces. As the operating frequency is increased to millimetre wave region, conductor loss of metallic patch becomes too high for efficient operation. Using dielectric resonators, small size and low cost antennas can be fabricated with very good radiation capabilities. Without any metallic portion, the loss of dielectric resonator antenna is mainly due to dielectric, which is very small compared to conductor loss. For this reason, DRA has been studied extensively over the years since first reported in [1]. Different shapes of DRAs like cylindrical, rectangular, hemispherical, triangular, and conical can be designed to radiate efficiently. Hemispherical DRA is used in this paper due to its simple interface with free space. Also closed form solution exists for hemispheres, which makes analytical solution possible.

Different types of feeding mechanisms can be used with DRA, such as coaxial probe, direct microstrip line, aperture coupled by microstrip or coplanar waveguide, and conformal strip. The main drawback of all these feeding mechanisms is that the feed line losses are considerable at millimetre wave frequencies. Instead, if waveguide is used for feeding the DRA, feed line losses can be avoided. Since waveguide has metallic walls, it has excellent shielding between the interior and exterior regions, avoiding radiation loss even in the millimetre wave band. Since waveguide and DRA are of very low loss, they form excellent combination for low loss millimetre wave communication systems.

In the literature, very little studies have been reported on waveguide fed DRAs either at the waveguide shorted end or at broad wall. Although a high permittivity DRA can be efficiently excited by an empty waveguide [2], which is not the case with DRAs of low dielectric constants. This is due to the fact that the inductive susceptance offered by the DRA loaded slot gives poor coupling from waveguide. K. W. Leung and K. K. So have reported an experimental study of waveguide fed cylindrical DRA with a cylindrical DR inside the waveguide to increase coupling [3]. Keeping the cylindrical dielectric inside the waveguide is extremely difficult and not very robust mechanically. Moreover using two DRAs will increase the cost. To improve the coupling of waveguide shorted end slot excited rectangular DRA, P. Abdulla *et al.* [4] proposed a technique using capacitive waveguide junction.

However, the very small narrow wall dimension of the capacitive junction makes the fabrication difficult at millimeter wave frequencies. Improvement in coupling can also be obtained by using multilayer hemispherical DRA [5]. But fabrication of multilayer DRA is very difficult.

The analysis of a novel coupling enhancement technique of waveguide fed hemispherical DRA is presented in this paper. Improvement in coupling is achieved by incorporating two steps with respect to the centre of the waveguide at the end, and is terminated by a thick ground plane. A slot is cut at the ground plane on which the DRA is placed. The steps act as a capacitive junction, cancelling the inductive susceptance present in the direct fed case. More than 98% coupling is possible through this technique. Theoretical study of the double step junction coupled waveguide fed DRA has been carried out using method of moments (MoM).

Theoretical Formulation: The three dimensional view of the proposed structure is shown in Fig. 1(a). A hemispherical DRA of radius, a_{dr} and dielectric constant, ε_r excited by a narrow slot of length, 2L and width, 2W is located at the centre of the ground plane. The ground plane with thickness, 2t is assumed to extend to infinity in both x and y directions. The slot can be given offset along the x and y directions as shown in Fig. 1(b) to obtain wide and dual band operations. The height of the first step is 2h1 and second step is 2h2, as shown in Fig. 1(c), while the width of the steps is same as the broad wall dimension of the waveguide. The length of the first and second step is 2L1, 2L2 respectively. In the following formulations, the fields are assumed to have a time dependence of $e^{j\omega t}$ which is suppressed throughout.

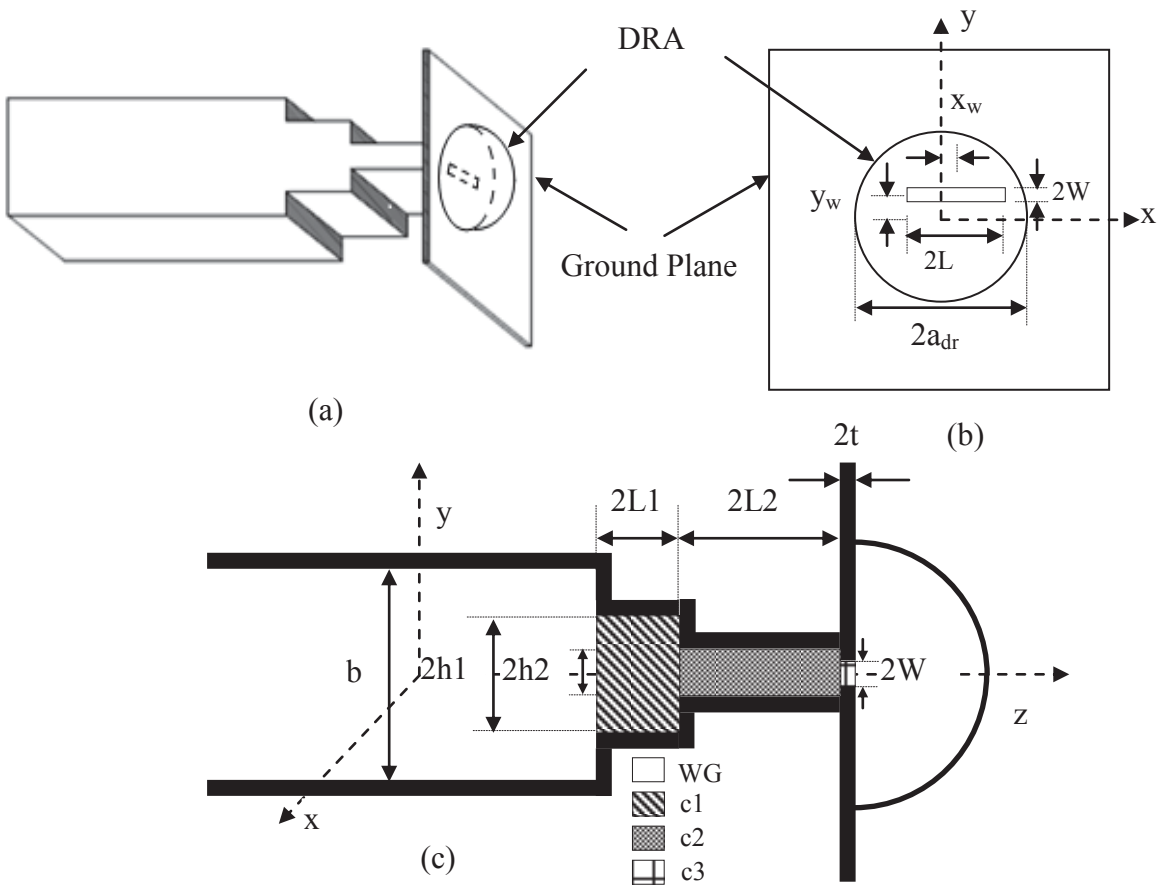

Fig. 1. Double step junction coupled waveguide fed DRA (a) 3D view (b) top view (c) longitudinal cross section

Invoking surface equivalence principle, the slot can be closed by a perfect electric conductor which divides the problem into two: the slotted waveguide part and the DRA placed above the ground plane. Applying magnetic boundary conditions at various apertures, the magnetic field, H(M) can be expressed as:

At aperture 1(between waveguide and first step)

$$-H_x^{WG}(\vec{M}_x^1)-H_x^{c1}(\vec{M}_x^1)+H_x^{WG}(\vec{M}_y^1)+H_x^{c1}(\vec{M}_y^1)+H_x^{c1}(\vec{M}_x^2)-H_x^{c1}(\vec{M}_y^2)=-2H_x^{inc} \quad (1)$$

$$-H_y^{WG}(\vec{M}_x^1)-H_y^{c1}(\vec{M}_x^1)+H_y^{WG}(\vec{M}_y^1)+H_y^{c1}(\vec{M}_y^1)+H_y^{c1}(\vec{M}_x^2)-H_y^{c1}(\vec{M}_y^2)=0 \quad (2)$$

At aperture 2 (between first step and second step)

$$H_x^{c1}(\vec{M}_x^1)-H_x^{c1}(\vec{M}_y^1)-H_x^{c1}(\vec{M}_x^2)-H_x^{c2}(\vec{M}_x^2)+H_x^{c1}(\vec{M}_y^2)+H_x^{c2}(\vec{M}_y^2)+H_x^{c2}(\vec{M}_x^3)=0 \quad (3)$$

$$H_y^{c1}(\vec{M}_x^1)-H_y^{c1}(\vec{M}_y^1)-H_y^{c1}(\vec{M}_x^2)-H_y^{c2}(\vec{M}_x^2)+H_y^{c1}(\vec{M}_y^2)+H_y^{c2}(\vec{M}_y^2)+H_y^{c2}(\vec{M}_x^3)=0 \quad (4)$$

At aperture 3 (between second step and ground plane)

$$H_x^{c2}(\vec{M}_x^2)-H_x^{c2}(\vec{M}_y^2)-H_x^{c2}(\vec{M}_x^3)-H_x^{c3}(\vec{M}_x^3)+H_x^{c3}(\vec{M}_x^4)=0 \quad (5)$$

At aperture 4 (between ground plane and DRA)

$$H_x^{c3}(\vec{M}_x^3)-H_x^{c3}(\vec{M}_x^4)-H_x^{DRA}(\vec{M}_x^4)=0 \quad (6)$$

Where $H_{x,y}^{\alpha}(\vec{M}_{x,y}^{i})$ (i = 1, 2, 3, 4 and α = WG, c1, c2, c3, DRA) is the magnetic field due to magnetic current at aperture *i*. H_x^{inc} is the incident magnetic field in the waveguide. If E_p^i is the unknown coefficient for the electric field at aperture *i*, then the magnetic currents are assumed to be of the form

$$\vec{M}_{x,y}^{\,i}(x,y)=\sum_{p=1}^{M}E_{yp,xp}^{i}e_p^i(y/x) \quad (7)$$

Where $e_p^i(x)$ (p = 1, 2, 3 ... M) is defined by

$$e_p^i(x)=\begin{cases}\sin\left[\dfrac{p\pi}{2L_i}\left(x-x_{wi}+L_i\right)\right], & \begin{matrix}x_{wi}-L_i\le x\le x_{wi}+L_i\\ y_{wi}-W_i\le y\le y_{wi}+W_i\end{matrix}\\ 0, & \text{elsewhere}\end{cases} \quad (8)$$

Since each component of the field is described by M basis functions, 6M unknowns are to be determined from the boundary conditions. Galerkin's specialization of MoM [6] is used to obtain 6M equations from the boundary conditions. Once the magnetic current and fields are determined, reflection coefficient can be computed using:

$$\Gamma=\frac{E_y^1+E_y^2}{E_y^{inc}}=-1+\frac{WL}{ab}\sum_{p=1}^{M}E_{yp}^1\left[\cos\left\{\frac{\pi}{2}\left(-\frac{x_w}{a_i}+p-1\right)\right\}\sin c\left\{\frac{\pi L_i}{2}\left(\frac{p}{L_i}-\frac{1}{a_i}\right)\right\}\right.$$
$$\left.-\cos\left\{\frac{\pi}{2}\left(\frac{x_w}{a_i}+p+1\right)\right\}\sin c\left\{\frac{\pi L_i}{2}\left(\frac{p}{L_i}+\frac{1}{a_i}\right)\right\}\right] \quad (9)$$

Where E_y^{inc} is the incident electric field due to the TE_{10} excitation and E_y^1 is the reflected electric field when the aperture is shorted. When the generator in the feed waveguide is removed and replaced by a perfect match, the electric field is represented by E_y^2.

Result and Discussion: A general MATLAB code is developed to analyse the theory for the proposed work. DRA of radius, a_{dr} = 7.5 mm, ε_r = 10, WR90 waveguide and ground plane of dimension 100 mm x 100 mm x 1.27 mm is used in the analysis. Convergence checks for the moment method solution has been performed, and it is found that the result using the number of basis function, M = 1 is very close to those using M = 5. The simulation has been carried out using the electromagnetic simulation software Ansoft HFSS. The theoretical result is in good agreement with simulation result as shown in Fig. 2. The resonant frequency obtained by performing theoretical study is 8.65 GHz, which is very close to the DRA resonant frequency 8.63 GHz. The 10 dB bandwidth obtained by theoretical study is 3.6% at resonant frequency.

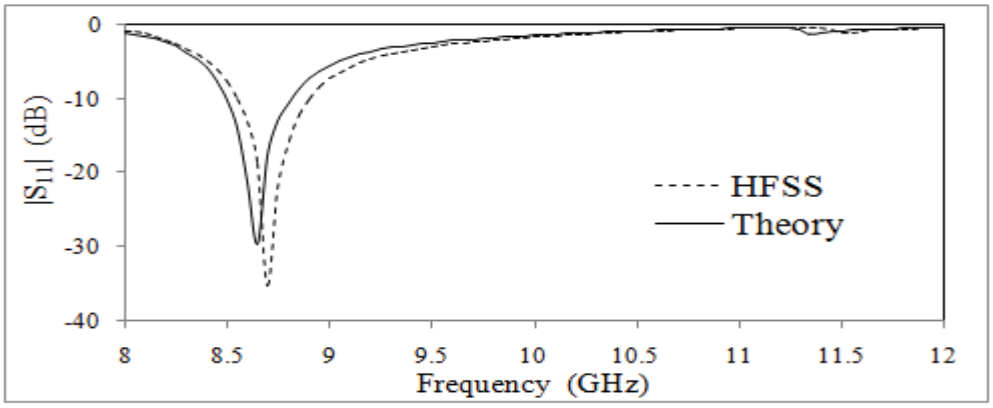

Fig. 2. Computed and simulated return loss characteristics of the double step junction coupled waveguide fed DRA with 2h1 = 6.5 mm, 2h2 = 3.4 mm, 2L = 9.5 mm, 2W = 1.0 mm, 2t = 1.27 mm, 2L1 = 4.0 mm, 2L2 = 8.0 mm.

Conclusion: The MoM analysis of double step junction coupled waveguide fed hemispherical DRA has been presented. The step junction placed between the waveguide and the ground plane acts as an impedance transformer which provides more than 98% coupling. The coupling enhancement technique proposed in this paper can be extended for DRAs of other shapes like cylindrical, rectangular etc.

Reference:

[1] Long S. A., M. W. McAllister, and L. C. Shen, "The resonant cylindrical dielectric cavity antenna", IEEE Trans. Antennas Propagat. vol.31, pp.406-412, May 1983.
[2] K. W. Leung, H. Y. Lo., K. K. So, and K. M. Luk, "High-permittivity dielectric resonator antenna excited by a rectangular waveguide", Microwave. Opt. Tech. Lett., vol.34, no. 12, pp. 157-158, August 2002.
[3] K. W. Leung and K. K. So, "Rectangular waveguide excitation of dielectric resonator antenna", IEEE Trans. Antennas Propagat., vol. 51,no. 9, pp. 2477- 2481, Sept. 2003.
[4] P.Abdulla, Yatendra K. Singh, and A. Chakrabarthy, "Coupling enhancement of waveguide fed dielectric resonator antenna", Microwave and Optical Technology Letters, vol.53, No.4, pp.769-770, April 2011.
[5] A. B. Kakade, B. Ghosh, "Analysis of the rectangular waveguide slot coupled multilayer hemispherical dielectric resonator antenna", IET Microwaves, Antennas & Propagation, vol.6, pp. 338-347, Feb. 2012.
[6] Harrington R. F., "Field Computation by Moment Methods", Roger E. Krieger Publishing Company, USA.

Design and development of a Wideband Radiator for EMI Testing

[1] AJAL.A.J , [2] CHIKKU JOSE
ECE Department GEC IDUKKI
ECE Department GEC kozhikode
ec2reach@gmail.com , Mobile: 8907305642

Abstract- Wideband radiator has been designed and constructed for operating in the frequency range from tens of kilohertz to few MHz. Our radiator is exited by a pulse source, which generates a rectangular waveform of small ON time and large OFF time. The pulse waveform is amplified in a current amplifier in order to provide the required amplitude to the radiating loop. The radiation is realized using a radiating loop printed on a glass epoxy PC board. The Pulse Source circuit hardware as well as the radiating loop is realized on a single PC board for miniaturization and simplicity.

In order to avoid radiated emission directly from the pulse source circuit components a metal enclosure is used to shield the pulse source. To avoid conducted emission pulse source is covered by a metal enclosure. Wideband radiator is self contained, housing the pulse generator PC board, chargeable battery as well as the radiating loop all with in a plastic cabinet.

Key words – Hot spot , Gaussian monocycle , degradation , scaling factor , activity factor

INTRODUCTION

The wide band radiator can be used for measuring shielding effectiveness of enclosures which are generally used for housing Electronic / IT / communication systems hardware.

1.Pulse generator – Circuit operations:

When supply voltage, V_{CC}, is applied, one transistor conducts more than the other due to imbalance in resistance and capacitance values. Suppose that Q1 is on and Q2 is off. The voltage at the output of Q1 is approximately V_{cesat}, which is zero. Immediately after Q1 turns on, C1 charges with the time constant R2C1 toward the supply voltage through R2. That is, V_{be} of Q2 increases asymptotically towards V_{CC}.When V_{be} of Q2 crosses the turn-on voltage, Q2 turns on and voltage at the output of Q2 drops to approximately zero. Immediately after Q2 turns on, V_{be} of Q1 falls due to capacitive coupling between the collector of Q2 and the base of Q1. As a result, Q1 turns off. Immediately after Q2 turns on, C2 charges with the time constant R3C2 toward the supply voltage through R3. That is, V_{be} of Q1 increases asymptotically towards V_{CC}.When V_{be} of Q1 crosses the turn-on voltage, Q1 turns on again and the process repeats. The diodes D1, D2 prevent breakdown of base-emitter junctions of the transistors are turned off, and D3

isolates the collector of Q2 from C2 when Q2 switched off. In this way, a fast-rising waveform can be obtained.

Derivation of time period:

$$V_C = V_{INIT} + (V_{FIN} - V_{INIT})(1 - e^{-t/RC}) - (1)$$

$$V_C = V_{FIN} + (V_{INIT} - V_{FIN})e^{-t/RC} - (2)$$

V_C - the capacitor voltage,

V_{INIT} – the initial capacitor voltage, V_{FIN} – the final capacitor voltage

t – the time period of charging.

R and C – the resistor and capacitor through which charging occurs.

The capacitor discharges from $-V_{CC}$ to V_{CC}.

Therefore $V_{IN}=(-V_{CC})$, $V_{FIN}=V_{CC}$, V_C 0V.

Substituting this in equation (2)

$$0 = V_{cc} + (-V_{cc} - V_{cc})e^{\frac{-t}{RC}}$$

$$-V_{cc} = -2V_{cc} \times e^{\frac{-t}{RC}}$$

$$0.5 = e^{\frac{-t}{RC}} - (3)$$

$$\ln 0.5 = \frac{-t}{RC}$$

$$t = 0.693RC - (4)$$

2.DESIGN OF CURRENT AMPLIFIER

We need to amplify the output pulse of a pulse generator. Since we want high magnetic field radiation from the radiating element we have to amplify the current of the pulse. The current amplifier output must be in the range about 10 mA.

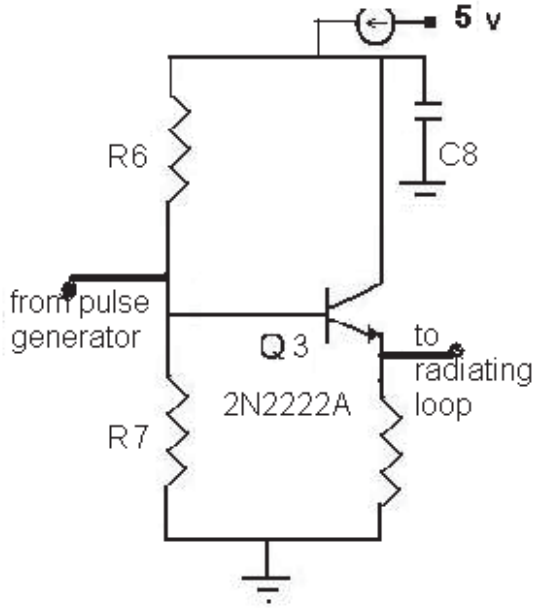

Figure.4.Current amplifier circuit

The component list for this circuit is given in the table 2. We are using BJT 2N2222A for this current amplifier. Here the bandwidth should be of few 100 MHz. To have wideband in cascade connection all (pulse generator, amplifier) must have wide bandwidth. Even a single circuit in the cascade is narrowband the overall bandwidth will also be limited.

3. FABRICATION AND TESTING

A CAD of the PCB layout was made considering high frequency (fast switching) Performance of the multivibrator and the pulse current amplifier. Short length of tracks was used by appropriately placing the components to reduce track inductance undesired track radiation. Ground plane was incorporated on the PCB in order to realize the high-speed performance. Printed track of 44.9 mm length was used as a radiating loop. PCB dimension is 120 * 120 mm fabricated a glass epoxy substrate. The single PCB includes the pulse generator and the radiating loop.

In order to avoid radiated emissions from the pulse generator circuit a shield metallic shield is used to enclose the pulse generator circuit hardware. This enclosure is on the component side whereas the radiating loop is on the other side of the PCB to reduce the effect of the enclosure on the performance of the radiator. The component placement detail of the PCBoard

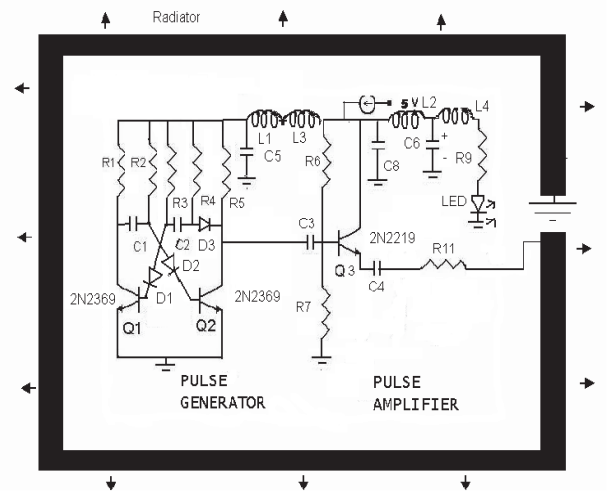

Figure . The circuit schematic of the pulse generator

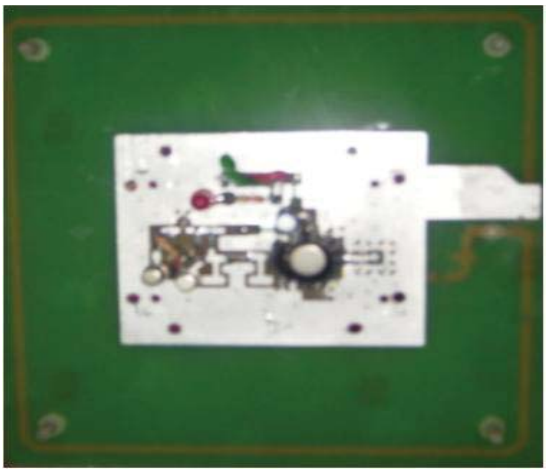

Figure .Pictorial view of the PCB components side.

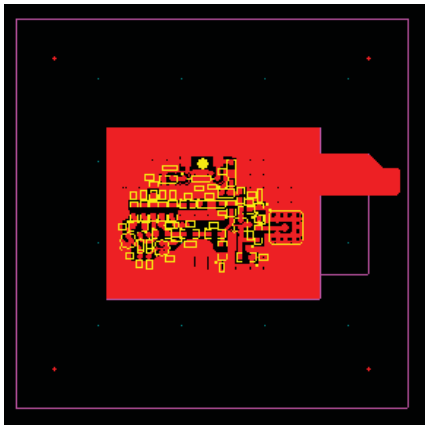

Figure The component placement detail of the PCB component side

Figure.Test setup for time domain analysis photograph.

Figure :Test setup using biconical antenna in an anachoeric chamber

References

1.Vaughan-Nichols, S.J.: 'Achieving wireless broadband with Wi-Max',IEEE Comput., 2004, 37, (6), pp. 10–13

2.Ghosh, A., et al.: 'Broadband wireless access with WiMax=8O2.16:Current performance benchmarks and future potential', IEEE Commun.Mag., 2005, 43, (2), p. 129136

3. Revision of part 15 of the Commission's rules regarding ultra-wideband transmission systems, First Report and Order, Federal Communications Commission (FCC), Washington, DC, ET Docket 98-153, FCC 02-48,2002

4.Hamalainen,M.,etal.:'OntheUWBsystemcoexistencewithGSM900,UMTS=WCDMA,andGPS',IEEEJ.Sel.AreasCommun.,2002,20,(9),pp. 1712–1721

5. Giuliano,R., and Mazzenga, F.: 'On the coexistence of power-controlledUltrawide-bandsystemswithUMTS, GPS, DCS1800, and fixed wirelesssystems', IEEE Trans. Veh. Technol., 2005, 54, (1), pp. 62–81

6.802.16-2004 IEEE Standard for Local and Metropolitan Area Networks,Part 16: Air interface for fixed broadband wireless access systems

7.Ghavami,M.,Michael,L.B.,andKohno,R.:'Ultra widebandsignalsandsystems in communications systems in communications engineering' (John Wiley & Sons Ltd)

A Novel Coplanar antenna design for wearable gadgets with high speed and low power

Peter Cyriac [(1)], Stephen Rodrigues [*]

Department of Instrumentation, Cochin University of science and technology, Cochin-682022, India.
[1]Email: mybibin123@gmail.com
[*] Email: dr3stephen@yahoo.co.in

Abstract: *Antenna plays a vital role in communication. Now days, several factors are considered in the design of an antenna. In many electronic gadgets, microwave antennas, especially micro strip type finds many fold applications. The improper design of the antenna may lead to several biological problems, like tissue heating, cancer and other behavioral symptoms, if these electronic gadgets come so close to our body. In the present work, we proposed a novel coplanar strip line fed compact antenna design with high speed data rate, low near field power and compact structure, suitable for next generation wearable gadgets. Reduced Specific Absorption Rate (SAR) can be achieved with proper reflective masking. The proposed antenna works in the 5GHz frequency band and satisfies the most advanced wireless standards of IEEE 802.11/ac. The antenna is fabricated on low cost and light weight single sided FR4 (εr=4.4, Loss Tangent = 0.02, Thickness = 0.8mm) epoxy based material. It can be equipped with any wearable gadgets having minimum size of 10x10mm that needs data connectivity.*

Index Terms: *Wearable gadgets antenna, coplanar printed antenna, Low power radiation, near field communication, 5GHz.*

1. Introduction

Short range or near field communication will be most advancing in the future. The wearable gadgets which are primarily used for short range communication should have optimum size, shape, weight and battery backup [6]. The battery size cannot be increased much; the only solution is to reduce the radiation power loss. The newly developed antenna design is suitable for some special, dedicated and noise free closed environment networks such as a network in an operation theatre where all the body sensors and monitoring devices are connected wirelessly, which make room more wire free.

2. Antenna Design Highlights

The present antenna is designed to be as a front end antenna for wearable RF devices. Here we have to look at the baud rate and structure of data which can be supported by the back end communication. Most of our copper cables will be replaced with optical fiber in near future[10]. This will reduce electromagnetic interference and lightning damage problems.

The modern Wi-Fi gadgets are switched to the most advanced near field wireless architecture of 5GHz band - IEEE 802.11/ac - which has the following special features of wider channel bandwidth, higher modulation and coding scheme, CSI Feedback for multi-user beam forming, IEEE 802.11ac PHY frame format and Spatial multiplexing [2]. A multiband antenna with frequencies of 2.45GHz and 5GHz for wearable gadgets makes the system more

complex with higher processing overhead, duel microwave sources for transmission, more energy profile, heavy and bulky antenna size. The present antenna is designed for a single band frequency of 5 GHz. The main advantages of this frequency design are high baud rate and several times larger number of user support than the previous band. IEEE 802.11ac has spatial multiplexing allows the quality of operation even during noise conditions.

3. Antenna Fabrication

Figure 1 shows the design details of the present antenna. Light green shaded portion is the copper or metallic coved radiating region. The given coplanar antenna design structure have a space difference of 0.5mm in between the two poles. The yellow shaded portion is the dielectric material, FR4 epoxy. Figure 2 shows the physical appearance of the fabricated antenna. Coplanar feed of the antenna helps to resolve the antenna connector complexity and improve system compatibility. If we place a reflective metallic strip on the other side, the antenna can be made directive. This helps to maintain Specific Absorption Rate (SAR) value within the limit.

The present work is initially simulated in the ANSOFT High Frequency Structure Simulation software (HFSS). Designed parameters are obtained by the continuous evaluation of HFSS by considering the parameters like omnidirectional radiation pattern, better value of return loss S11 and resonance frequency with 0.5GHz of bandwidth. Then, the antenna fabricated on a single sided, low cost FR4 epoxy based material of thickness 0.8mm. The obtained optimum dimensions are L=10mm, L1=7.5mm, L2=2.5mm, L3=2mm, H=10mm, H1=4mm, H2=3mm, H3=2mm, H4=1.5mm Thickness (T) = 0.8mm, Total Dimension=10x10mm, εr = 4.4, Loss Tangent = 0.02. And Weight = 0.1307gm (without connector).

Even though the present antenna is not flexible, because of its smaller size of 10X10 mm, it can also be used in flexible devices. The device can bend over this dimension without affecting antenna parameters like radiation pattern, resonance frequency and efficiency[5]. Connector de-soldering and metal crack are other problems encountered. Usually all flexible antennas are facing such above mentioned problems in their continuous use. So it is better to design an antenna as small as possible without sacrificing its primary parameters and fold over that, if there is an application of folding in wearable gadgets. So we took much concern about that. The prototype dimension satisfies the far field condition for proper electromagnetic coupling.

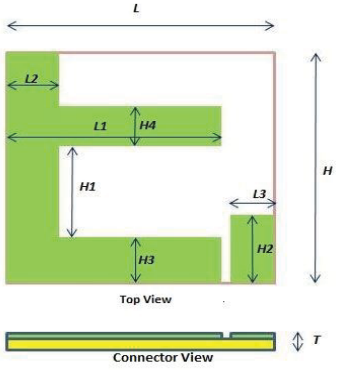

Figure1. Antenna geometry

Figure2. Photograph of fabricated 5GHz antenna

The proposed antenna is an omnidirectional antenna. The antenna can be tuned directive in desired direction, with the help of a reflective type mask. Practically it's a metallic strip. Wearable gadgets are designed to be located in different parts of the body. *Like google glass,*

smart watches etc[9]. All the gadgets are made as compact as possible, so the position antenna may not be predictable. So we cannot make an antenna in a particular direction, but it can be made directive according to the gadgets. Thus with the help of proper masking in proper position, we can achieve the Specific Absorption Rate (SAR) value in desired limit.

4. Results and discussions

All the radiation parameter measurements are carried out in an anechoic chamber using Agilent PNA E8362B Microwave Network Analyzer. Figure 3 shows the variation practically measured return loss S11 chart. The minimum return loss is -35dB at the frequency 5GHz. This value is significantly sufficient for the desired bandwidth. The band width of the present antenna is from 4 GHz to 5.8GHz, with the center frequency at 5GHz. From 4GHz to 5.8GHz the minimum value of S11 is better than -10dB.

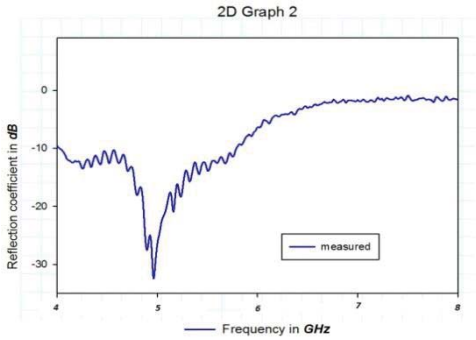

Figure3. Measured Return loss (S11)

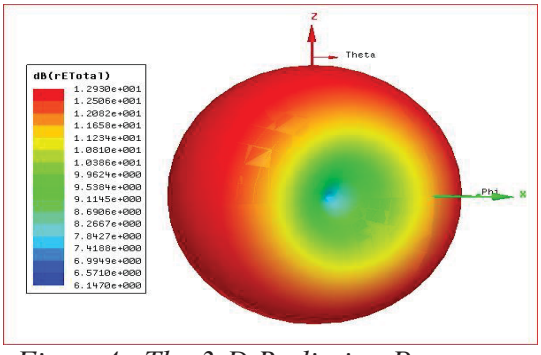

Figure4. The 3-D Radiation Pattern

This is perfectly suitable for the most advanced with the center frequency of IEEE 802.11/ac. IEEE 802.11/ac-defined for near field high speed data transfer; huge number of device connectivity, which ensures the low power radiation[3] [4]. It's suitable for low power wearable smart mobile gadgets.

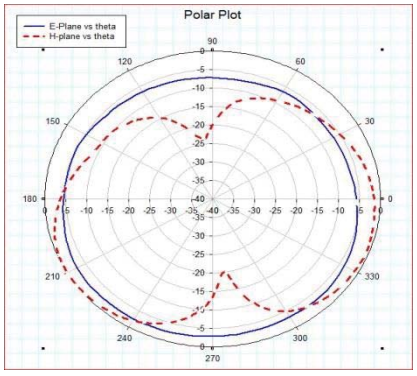

Figure5. The 2-D Measured Radiation pattern

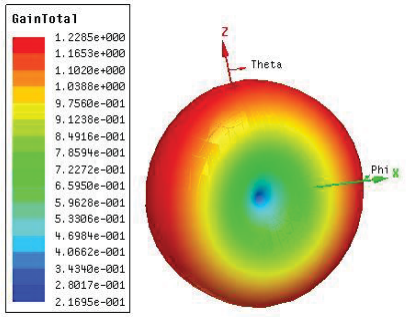

Figure6. The 3-D Gain chart

Figure 4 and figure 5 show the radiation pattern. Figure 4 is the 3Dimension radiation pattern obtained from the simulating software and the figure5 is the measured 2Dimension graph. From both figure it's clear that the present antenna exhibits omnidirectional radiation pattern. Figure 6 shows the simulated 3-Dimensional gain chart of the present antenna. The antenna uniformly distributes its energy in all directions. Peak gain obtained is 1.18469dB. For an omnidirectional micro strip patch antenna this is sufficient to transmit efficiently. As we discussed earlier, we can make the antenna more directive according to our antenna

placement location in the gadgets and operating environments. This is the best way to improve the gain more effectively.

Radiation parameter shows that, the peak gain is 1.18dB. Radiation efficiency between accepted power and radiated power is 88%. Front to back ratio is 1.02 which means it's an omnidirectional antenna. Thus we could design and develop low cost, light weight, FR4 epoxy based, low profile antenna for wearable gadgets. It can support the latest wireless standard of IEEE[3].

5. Conclusion

From the experimental analysis, it's clear that, this is a well-designed, low cost, lightweight, low profile coplanar strip line antenna for "mobile devices" which come very close to our body. It is also suitable for some "closed environment" applications which have high noise profile and needs more user support[2]. It satisfies the most advanced near field, high speed wireless architecture with 5GHz band -IEEE 802.11/ac**.** We chose locally available materials to fabricate this prototype. Further improvements can be obtained in the antenna performance, with high quality dedicated low loss epoxy material of the same dimension.

6. Acknowledgement

I express my immense gratitude to the *Kerala state council for science, technology and environment (KSCSTE)* for their financial support for the work.

7. References

[1] Constantine A. Balanis, "Antenna Theory" Second Edition. John wiley& sons (asia) Pte Ltd. ISBN 9971-51-233-5

[2] Ruizhi Liao**,** Boris Bellalta**,** Jaume Barcelo**,** Victor Valls and Miquel Oliver**,** "Performance analysis of IEEE 802.11ac wireless backhaul networks in saturated conditions". EURASIP Journal on wireless communications and networking 2013. Springer Open Journal ID:2013:226

[3] IEEE 802.11- 2012, "Wireless LAN Medium Access Control and physical Layer Specifications". IEEE standards.

[4] IEEE 802.11ac™-2013 "Wireless LAN Medium Access Control and physical Layer Specifications, Enhancement for very high throughput for operation in bands below 6 GHz", IEEE standards.

[5] M.E de Cos and F. Las-Heras, "Polypropylene-Based Duel-Band CPW-Fed monopole Antenna". IEEE Antennas and propagation Magazine Vol.55 No. 3, June 2013.

[6]B.Gupta, S. Sankaralingam and S. Dhar, "Development of wearable and implantable antennas in the last decade: A Review" Proceedings of 10th Mediterranean microwave symposium, August 2010, pp.251-267.

[7] Q.B ai, R. L angley, "Crumpled textile antennas". Electronic letters Vol. 45, Issue: 9, pp.436-438, 2009.

[8] B. Sanz-Izquierdo and J.C. Batchelor, "A duel band Belt antenna".Proceedings of IWAT-2008, Chiba, Japan, pp.374-377, 2008.

[9] Stephen Kirk, "The Wearable Revolution: Is Standardization a Help or a Hindrance?" IEEE Consumer Electronics Magazine, pp. 45-50, 2 October 2014.

[10] Sudhir K. Routray "The changing trends of optical communication" IEEE POTENTIALS. Date of publication: 7 January 2014. Page 28-33.

DECEMBER 18, THURSDAY
03.30PM TO 06.00PM
RESEARCH SESSION 10
RFID & FSS
S N MITRA- HALL

Chair: Mr. Adnan Bohori, GE, Bangalore

No	Papers	Page
10.1	**Electromagnetic Frozen modes in cascaded frequency selective surfaces** Sarin V. Pushpakaran, Anju Pradeep, Anila P.V, Jayakrishnan M.P, Mridula Haridas, C.K Aanandan, P. Mohanan, and Vasudevan K [1]Govt. College Chittur, Palakkad 678104, Kerala, *Email: sarincrema@gmail.com* [2] School of Engineering, CUSAT, Cochin -22, *Email:mridula@cusat.ac.in.*[3]CREMA, CUSAT, Cochin-22. *Email: vasudevankdr@gmail.com*	301
10.2	**Absorption Behaviour of a Four-layered Plasma-RAM Structure** Simy Antony, and Hema Singh Centre for Electromagnetics (CEM), CSIR – National Aerospace Laboratories, Bangalore 560017, India. *Email: hemasingh@nal.res.in, jha@nal.res.in*	305
10.3	**Chipless RFID Tag Based on Stepped Impedance Resonators** V.R. Sajitha, C.M. Nijas, T. K. Roshna and P. Mohanan. Department of Electronics, Cochin University of Science and Technology, Kochi-22, India. *Email: svrk1989@gmail.com, nijasmhmmd@gmail.com, roshnatk03@gmail.com.*	309
10.4	**Compact Polarization Independent Chipless RFID Tag** Laila .D[1], Riny Thomas[1], Nijas C M [2] and P. Mohanan [1]Model Engg. College, Thrikkakara, India, 682021, *Email: lailacusat@gmail.com,* [2]Department of Electronics, Cochin University of Science and Technology, Cochin-22, Kerala, India. *Email:nijasmhmmd@gmail.com ,drmohan@gmail.com*	315
10.5	**Bistatic RCS measurement of Electromagnetic Absorbers Using Stacked Ring-Patch Arrays** M. N. Sujatha[1], K. J. Vinoy[2] [1]Siddaganga Institute of Technology, Tumkur 572103, India. *Email: mnsujathaguddu@rediffmail.com* [2]Indian Institute of Science, Bangalore 560012, India. *Email: kjvinoy@ece.iisc.ernet.in*	318
10.6	**A Frequency Selective Surface for GSM 900 MHz Band Shielding** Ayan Chatterjee[1], Susanta Kumar Parui[2] Indian Institute of Engineering Science & Technology, Shibpur-711103, WB, India. *Email:[1]ayanmrinal26@gmail.com, [2]arkapv@yahoo.com*	322
10.7	**A UHF RFID Tag Based on modified Folded Dipole Antenna** K.K. Aju John, Manju Abraham and Thomaskutty Mathew Department of Electronics, School of Technology and Applied Sciences, Mahatma Gandhi University Regional Center, Edappally, India, 682024. *Email: mwrfgroupstas@gmail.com*	326

10.8 **A Novel UHF RFIDTag Based On Multi-Fractal Cantor Structure for Enhanced Read Range** 330

Manju Abraham, Fijo Jose K and Thomaskutty Mathew
Department of Electronics, School of Technology & Applied Science, M.G. University, Regional center, Edappally, Kochi 682024, Kerala, India.
Email: mwrfgroupstas@gmail.com

Electromagnetic Frozen modes in cascaded frequency selective surfaces

Sarin V. Pushpakaran[(1)], Anju Pradeep [(2)], Anila P.V[(3)], Jayakrishnan M.P[(3)], Mridula Haridas [(2),] C.K Aanandan [(3)], P. Mohanan [(3)]and K. Vasudevan[(3)]

(1) Govt. College Chittur, Palakkad, Kerala, Pin-678104, Email: sarincrema@gmail.com

(2) School of Engineering, CUSAT, Email:mridula@cusat.ac.in

(3) CREMA Lab, CUSAT, Email: vasudevankdr@gmail.com

Abstract: *Electromagnetic wave slow down using cascaded FSS layers is presented in this paper. The slow wave propagation scenario is attained by introducing the tunnel band corresponding to the magnetic resonance of the stacked plates. The dispersion analysis of the structure is done using the simulation and is verified in the experiment by conducting the transmission and reflection measurements*.

Introduction:

The invention of metamaterials is a paradigm shift in the field of electromagnetic research. Artificial dispersive materials are showing some unusual phenomenon like negative refraction, subwavelength focusing etc. [1-2]. The slow light or the electromagnetic wave slow down is a byproduct of the metamaterial research [3]. The stacked hole arrays and stacked metal slab pairs can be used as an alternative for getting left handed behavior [4-5]. The slow wave frozen modes are also observed in this particular propagation scenario. When the perforated metal plates are very much close to each other, the propagation mode is identified as the left handed mode. When the arrays are distant apart, propagation will be right handed. In between these extremes, the transmission will be enabled by the slow wave frozen modes. The dispersion curve of the frozen modes will be almost flat with a slight positive slope. Sorolla has given an important observation that the interaction between the left handed mode and the Fabry-Perot modes gives the essential flat pass band for the frozen mode propagation [6]. This peculiar dispersion properties of the stacked subwavelength hole arrays makes it useful for the implementation of electromagnetic absorbers in the millimeter wave ranges [7].

Here we are addressing the same issue. We have achieved the frozen mode in a cascaded homogeneous FSS layers. The geometry of the proposed FSS structure constitutes a simple meander line inductor loaded cut wire element. This Unit cell is arranged in two dimensional manner and two such arrays are cascaded to get the required electromagnetic tunneling mechanism. Experiments were conducted using the HP 8510C network analyser and simulation studies were done using FEM based Ansoft HFSS.

Geometry and Results:

The geometry of the proposed FSS structure is shown in fig.1. The unit cell of the FSS constitutes a simple meander line inductor loaded cut wire. The geometrical parameters of the unit cell are L_s=2mm, W_s=2mm, g=0.2mm, d=2.5mm and h=5mm. The unit cell is repeated to form and 20X20 element array and two such layers are cascaded to obtain the final structure. The inter array period is represented by d_z.

We have calculated the dispersion of the cascaded structure using simulation using the Eigen mode solver method for d_z=3mm. The resultant dispersion diagram is shown in fig.2. It is observed that the structure shows a slow wave frozen mode in between two right handed modes. The slow wave frozen mode extends from 4.15 GHz to 4.24 GHz. Inorder to validate

the dispersion diagram we have taken the reflection and transmission measurements and the results are summarized in fig. 2(b). The transmission slow wave band can be easily detected from the dip at 4.2 GHz in

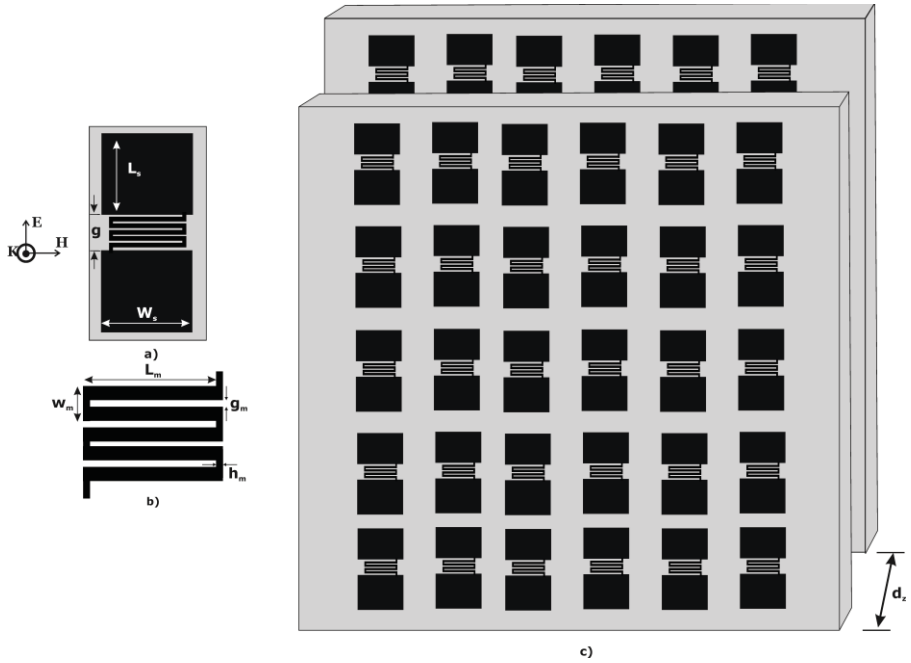

Fig.1. Geometry of the FSS structure a) unit cell b) meanderline inductor and c) final cascaded cell

the reflection measurement. The magnitude of transmission can be increased by increasing the number of layers or by increasing the inter array distance.

The single array of meander loaded inductor can be represented as a series LC shunt circuit. The single layer structure shows the band reject property at the series resonant frequency. At the series resonant frequency, the impedance offered by the structure will be zero and the wave will be completely reflected back. Below the resonant frequency, the structure will be capacitive and above the resonant frequency, the structure will be inductive. Cascaded array of the FSS layers excites the parallel resonance between the layers and this parallel resonance can be identified as the magnetic resonance of the stacked FSS layers. The magnetic resonance shows anti symmetric current distribution between the plates and it shows a magnetic field maximum at the exact centre of the plate.

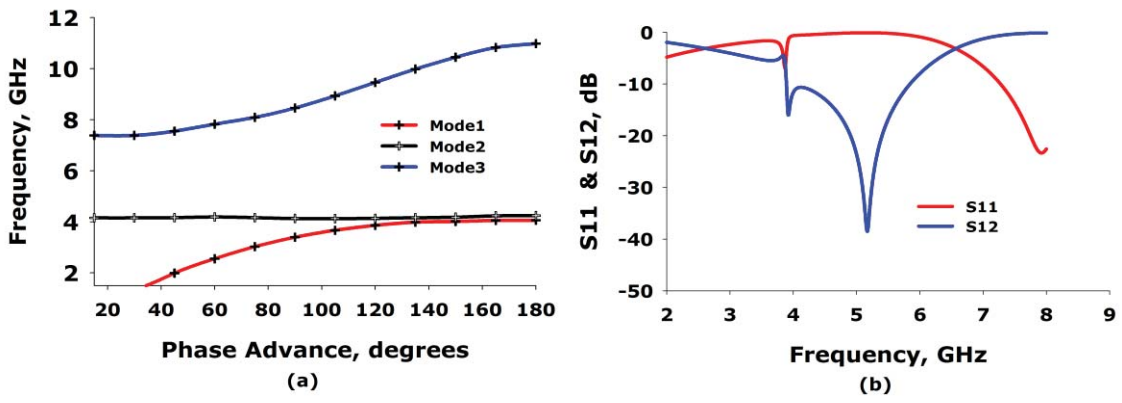

Fig. 2 a) Dispersion diagram of the structure and b) reflection and

transmission measurements

The variation in dispersion characteristics against the inter array distance d_z is studied next. The corresponding variation is included in fig.3. It is observed that for very small value of the inter array spacing ($d=7d_z$), the transmission mode excited will be right handed indicated by the black lines in the diagram. As d_z increases, the dispersion curve will be almost flat corresponding to the frozen mode slow wave regime. For larger spacing, it shows left handed property, giving negative slope. Here the magnetic resonance will be merged with the lower TE mode.

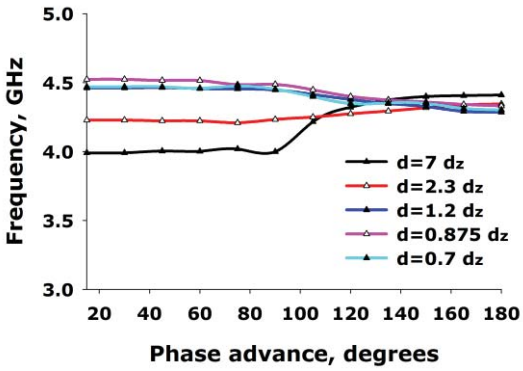

Fig. 3 Variation in dispersion with varying d_z for the second mode

Conclusions:

We have achieved electromagnetic wave slow down in cascaded homogeneous frequency selective surfaces. Wave slow down is accomplished by creating a magnetic resonant tunnel band within the band gap of single layer FSS structure. The unit cell of the FSS constitutes a simple meander line inductor loaded rectangular metal strip and the design is devoid of the conventional conjugate metamaterial bilayer and conjugate FSS layers. We are sure that the proposed technique will surely paves ways for obtaining light slow down in THz regime The high group refractive index profile makes the structure suitable for antenna size reduction and increasing the gain of antennas.

Reference:

[1] D.R Smith, W.J Padilla, D.C Vier, S.C Nemat, S. Schultz, "Composite medium with simultaneously negative permeability and permittivity", Physical Review Letters, Vol. 84, No. 18, pp. 4184-4187, 2000.

[2] J.B Pendry, "Negative refraction makes a perfect lens", Physical Review Letters, Vol. 85, No. 18, pp. 3966-3969, 2000.

[3] E. Shamonina, "Slow waves in magnetic metamaterials: history, fundamentals, and applications", Physics stat. sol. (b), vol.245, no.8, 2008.

[4] Jiangfeng Zhou, Lei Zhang, Gary Tuttle, Thomas Koschny, Costas M. Soukoulis," Negative Index Materials using simple short wire pairs", Physical Review B., Vol. 73, 2006.

[5] Miguel Beruete, Mario Sorolla, Igor Campillo, "Left handed extraordinary optical transmission through a photonic crystal of subwavelength hole arrays", Optics Express, vol.14, no.12,5445, 2006.

[6] M. Beruete, P. Rodriguez-Ulibarri, V. Pacheco-Pena, M. Navarro Cia, A.E Serebryannikov, "Frozen mode from hybridized extraordinary transmission and Fabry-Perot resonances", Physical Review B, 87, 205128, 2013.
[7] M. Navarro-Cia, V. Tores, M. Beruete, M. Sorollo, "A slow wave fishnet like absorber in the millimeter wave range", Progress in Electromagnetics research, vol.118, pp.no.287-301, 2011.

Absorption Behavior of a Four-layered Plasma-RAM Structure

Simy Antony, and Hema Singh
Centre for Electromagnetics (CEM),
CSIR – National Aerospace Laboratories, Bangalore, India 560017
Email: hemasingh@nal.res.in, jha@nal.res.in

Abstract: *The radar cross section reduction can be achieved by controlling the reflections from the surface of the structure. Plasma envelope is one of the ways to control the reflections and scattering from the surface. The overall reflection characteristics of homogeneous plasma over a RAM covered conducting surface are discussed in this paper. The reflection coefficient of the plasma covered RAM structure is derived using impedance transformation in multiple dielectrics method. The effect of plasma parameters, such as electron density, collision frequency, plasma thickness on absorption behavior of plasma-RAM-conductor structure.*

Introduction: In a low-observable design, reflections and scattering can be reduced significantly by using plasma. The absorbing property of plasma depends on its configuration. In order to avoid the problems associated with an open plasma cloud such as plasma trail, visible glow etc. a plastic envelope is used to cover the plasma. The problem of EM propagation within the bounded plasma can be approximated as multi-layered dielectric problem [1]. In this paper, the reflection coefficient of the plasma covered RAM structure is derived using impedance transformation in multiple dielectrics method [2]. The total reflection from the plasma covered conducting structure includes reflection at the plasma-air interface, partial reflection within the plasma layer and the reflections from the conductor. The reflections from the conducting surface can be reduced by covering it with radar absorbing material (RAM) [3].

Model of the plasma-RAM structure: An EM wave propagating in -z direction is assumed to be normally incident on a four-layered structure consisting of plastic envelope, plasma layer, RAM, and perfectly electric conductor (PEC), as shown in Figure 1. The incident wave will be reflected at each interface. The parameters that controls the overall reflection from the structure are the impedances (Z_o, Z_1, Z_2, Z_3) , the wave numbers (k_o, k_1, k_2, k_3), permeability (μ_o, μ_1, μ_2, μ_3), and permittivity (ε_o, ε_1, ε_2, ε_3) in air (0^{th}), 1^{st}, 2^{nd} and 3^{rd} layer respectively. d_1, d_2 and d_3 are the thicknesses of 1^{st}, 2^{nd} and 3^{rd} layer respectively. Z_{in1} is the impedance at the first interface. The dielectric constant of plasma depends upon the plasma frequency (ω_p), the plasma collision frequency (V_{en}), and is expressed as [4]

$$\varepsilon_2 = \left(1 - \frac{\omega_p^2}{\omega^2 + V_{en}^2}\right) - j \times \frac{V_{en}}{\omega} \frac{\omega_p^2}{\omega^2 + V_{en}^2} \tag{1}$$

$$\omega_p = \sqrt{\frac{N_e e^2}{m_e \varepsilon_o}} \tag{2}$$

where ω is the incident wave frequency, N_e is the plasma electron density, e is the electron volt, m_e is the mass of electron and ε_o is the free space permittivity.

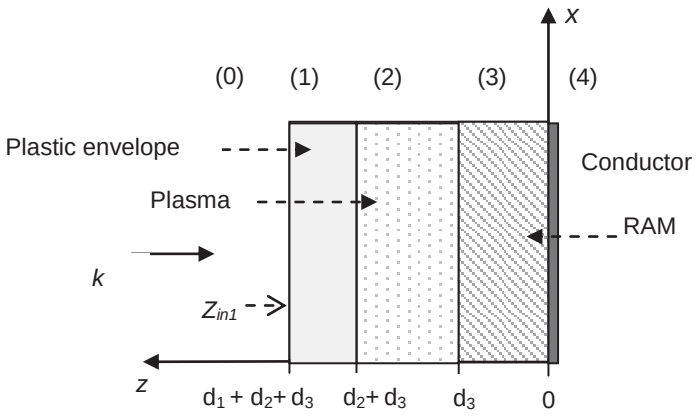

Figure 1 Four layered structure: Plasma with RAM covered PEC

Impedance transformation method in four layered structure: By transforming impedance from right side of the structure to left side, reflection from the structure can be determined. The overall reflection coefficient from the structure is expressed as

$$\Gamma = \frac{Z_{in1} - Z_o}{Z_{in1} + Z_o} \tag{3}$$

where Z_o is the free space impedance. The total reflected power, is given by

$$R = |\Gamma|^2 \tag{4}$$

In order to find Z_{in1} , the impedance at each interface is required. It is expressed as

$$Z_{in1} = \frac{Z_2 Z_3 \delta_3 + Z_2^2 \delta_2 + Z_1 Z_3 \delta_1 \delta_2 \delta_3 + Z_1 Z_2 \delta_1}{Z_2 Z_3 \delta_1 \delta_3 + Z_2^2 \delta_1 \delta_2 + Z_1 Z_3 \delta_2 \delta_3 + Z_1 Z_2} \times Z_1 \tag{5}$$

where, $\delta_i = \tanh jk_i d_i$

Results and Discussion: Figure 2 shows the reflected power for four-layered structure (plastic-plasma-RAM-PEC), and three layered structures (plastic-plasma-PEC), (plastic-RAM-PEC). It may be observed that the reflected powers of the bounded plasma, with and without RAM layer, are different. This is mainly due to the significant absorption of propagating EM wave within the RAM layer.

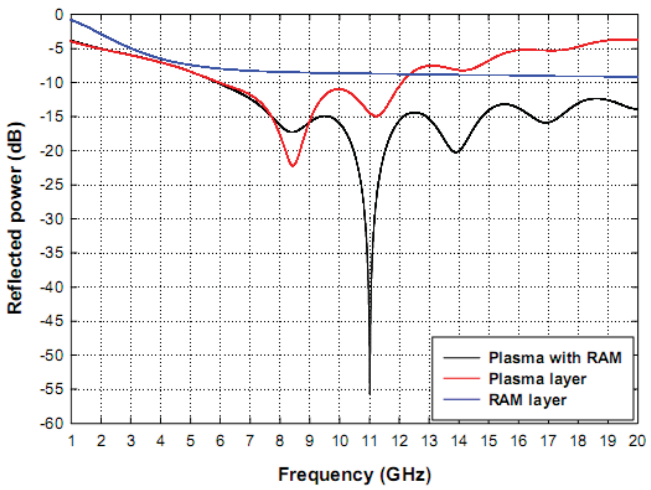

Figure 2 Comparison of the reflection behavior of four-layered and three-layered structures $N_e = 5\times10^{17}m^{-3}$, $V_{en} = 28$ GHz,$d_2 = 4.5$ cm

At low incident frequencies, the plasma with RAM follows the same trend as the plasma without RAM case and it becomes different when the incident wave frequency is increased beyond the plasma frequency. This is because that the incident frequencies greater than the plasma frequency can enter the plasma and get absorbed both in plasma and RAM layers. At high frequencies plasma with RAM shows reduced reflected power, where the main absorption is due to the RAM layer. In order to achieve more absorption in plasma at high frequencies ($\omega >> \omega_p$), thicker plasma layer is required. Further, choosing optimum plasma and RAM parameters, a broad absorption band can be achieved.

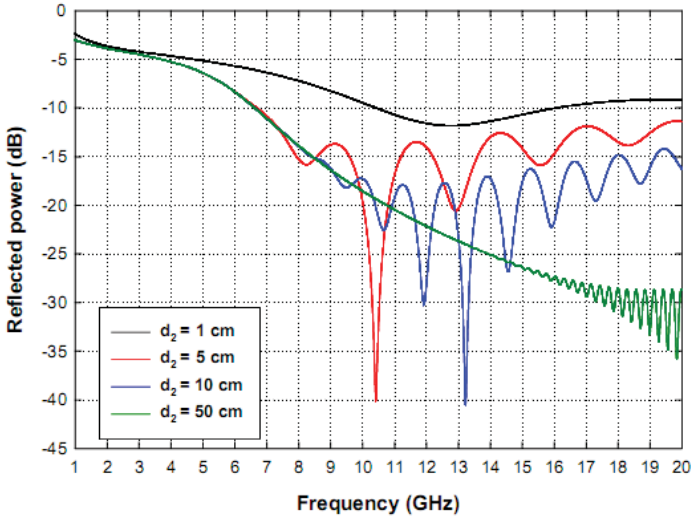

Figure 3 Effect of plasma thickness on four-layered plasma-RAM

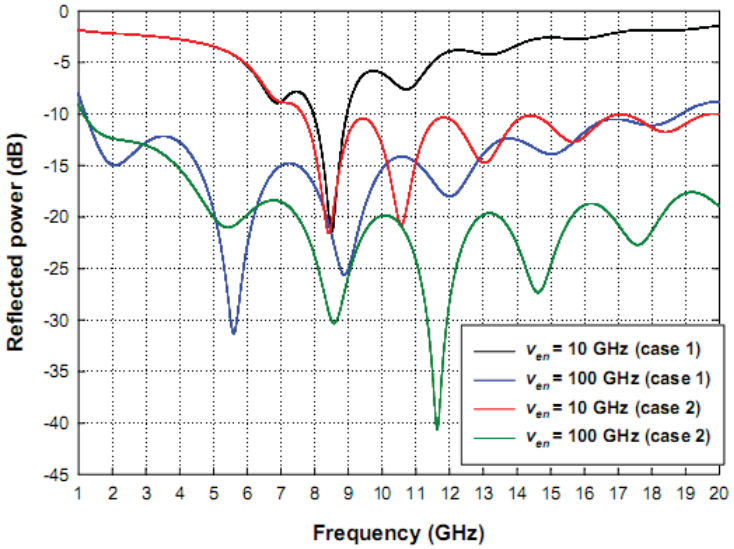

Figure 4 Effect of collision frequency on reflected power
Case1: Plasma without RAM, Case 2: Plasma with RAM

Figure 3 shows the effect of plasma thickness on the reflection behavior of four-layered plasma-RAM structure (N_e=5×10^{17}m^{-3}, ω_p=6.35 GHz, V_{en} = 20 GHz). For thin plasma (5cm and 10cm) maximum EM wave absorption occurs for an incident frequency greater and close

to plasma frequency ($\omega > \omega_p$). For thick plasma (50 cm) maximum EM wave absorption occurs for an incident frequency much greater than the plasma frequency ($\omega >> \omega_p$).

Next, Figure 4 shows the effect of collision frequency on the reflection characteristics of three-layered conductor-backed plasma and four layered plasma-RAM structure (N_e=5×10^{17}m^{-3}, d_2=5cm). It may be seen that both the structures follow the same trend. Higher collision frequency shows better absorption. For high collision frequency, the effect of RAM layer parameters is visible in the reflection characteristics and for low collision frequencies it is visible only at high incident wave frequencies ($\omega > \omega_p$).

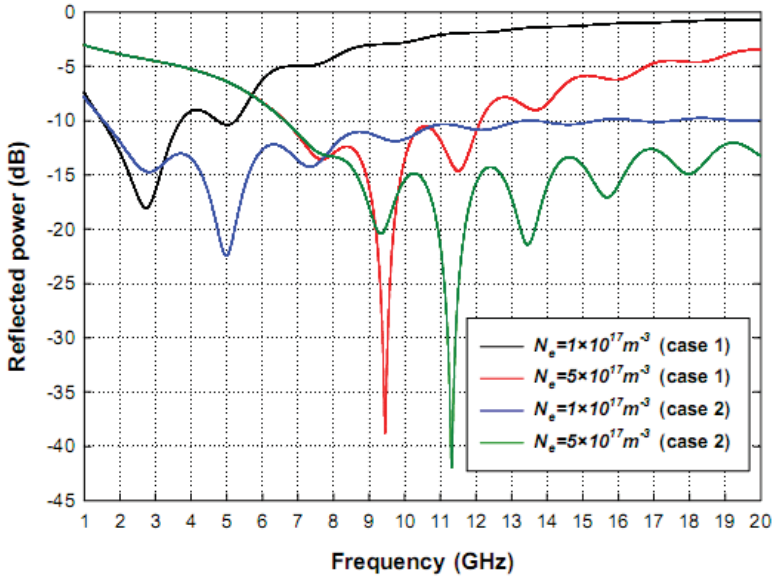

Figure 5 Effect of electron density on the reflected power
Case1:Plasma without RAM, Case 2:Plasma with RAM

Figure 5 shows the effect of electron density with V_{en} = 20 GHz, d_2 = 6 cm, on the performance of two structures. The plasma electron density plays the same role in both the four-layered and three-layered plasma structures. The plasma frequency, obtained from the plasma electron density, determines the resonant absorption band. The RAM layer slightly shifts the resonant absorption band, depending on the RAM parameters.

Conclusion: The reflected power from a plasma covered RAM structure is analyzed using impedance transformation method. It is shown that the overall performance of the structure can be improved by including RAM layer over the conductor. The matching between plasma and RAM parameters is required to achieve maximum EM wave absorption. However other plasma parameters are also required to be chosen appropriately.

References:

[1] C.X. Yuan, Z.X. Zhou, and H.G. Sun, "Reflection properties of electromagnetic wave in a bounded plasma slab," *IEEE Transactions on Plasma Science* , vol. 38, no. 12, pp. 3348-3355, December 2010

[2] W.H. Hayt, and J.A. Buck, *Engineering Electromagnetics.* McGraw-Hill Publishing, New York, ISBN: 0073380660, 608 p., 2011.

[3] C.X. Yuan, Z.X. Zhou, J.W. Zhang, X.L. Xiang, Y. Feng, and H.G. Sun, "Properties of propagation of electromagnetic wave in a multilayer radar absorbing structure with plasma and radar absorbing material," *IEEE Transactions on Plasma Science,* vol. 39, no. 9, pp. 1768-1775, September 2011.

[4] D.C. Jenn, *Radar and Laser Cross Section Engineering*. 2nd ed., AIAA Education Series, Washington DC, ISBN-13: 9781563477027, 505 p., 2005.

CHIPLESS RFID TAG BASED ON STEPPED IMPEDANCE RESONATORS

V.R. Sajitha, , C.M. Nijas, T. K. Roshna and P. Mohanan
Dept. of Electronics, Cochin University of Science and Technology, Kochi-22, India
, Email: svrk1989@gmail.com, nijasmhmmd@gmail.com, roshnatk03@gmail.com.

Abstract: *A fully passive printable chipless RFID tag based on Stepped Impedance Resonator (SIR)is proposed. By suitably selecting impedance ratio(K) and length ratio (α) of the SIR structure first order harmonic frequencies are shifted away from the desired band. The tag is fabricated on RT Duriod ($\varepsilon_r = 2.2$ and tanδ=0.0009) substrate. . Data is encoded in frequency domain and Frequency Shift Coding is used to enhance data encoding capacity of the tag. The proposed RFID tags have an operating range of 40cm in the outdoor environment. Theoretical and numerical methods are used to verify the measured resonant frequencies of the tag.*

Keywords: *Chipless RFID, Stepped Impedance Resonator, Backscattering, Frequency Shift Coding*

Introduction: Radio Frequency identification is one among worldwide top 10 technologies which is used mainly for automated identification purposes. Chipless RFID tag is an emerging field in this context and is an attempt to reduce the cost of RFID transponders by eliminating Integrated Circuits [1]. A lot of chipless RFID tag designs are available in literature. Data is encoded either in time domain [2] or in phase domain [3] or in frequency domain or in multiple domains [4]. Among these frequency domain tags are seemed to be more compact and have higher data encoding capacity.

Within frequency domain tags itself there are reception/retransmission based [5] and backscattering based tags. Back scattering based tags are compact due to the absence of reception/retransmission antennas. In these tags multiple resonators or scatterers perform all the three functions of reception, filtering and retransmission. The first RFID tag using multiple scatterers was reported by Jalaly et. al. [**6**] based on RF barcodes which are constructed with arrays of opaque metallic microstrip dipoles on an opaque dielectric substrate with metallic back plane. Design rules for chipless RFID tags based on multiple scatteres and a comparison of performance of different scatteres is discussed in [7]. A compact printable dual polarized chipless RFID system is presented in [8]. Here two sets of slot resonators are placed in horizontal and vertical polarizations to double the number of bits within the same frequency bandwidth. An SIR based tag for low cost application is proposed in [9] where both fundamental and first harmonic frequencies are used for coding.

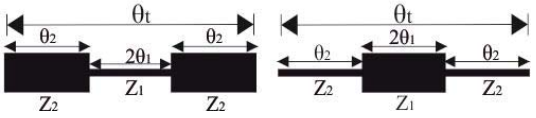

Figure 1: structure of λ/2 SIR K < 1 (left) and K > 1 (right)

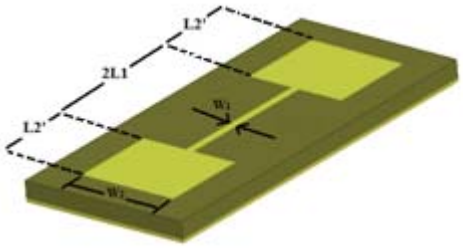

Figure 2: Microstrip version of SIR for K < 1

Most of the reported tags based on backscattering did not provide any means to avoid higher order harmonic frequencies from the desired band except symmetric excitation[8]. In this paper an SIR based chipless RFID tag is proposed. The first order harmonic frequencies are effectively shifted away from the used band by appropriately choosing the impedance ratio (K) and length ratio (α) of the SIR structure. Also high Q nature of SIR structure provides best bandwidth utilization. Structural information in the tag can be decoded using magnitude or group delay of the backscattered signal. Theoretical and numerical results are used to verify the measured data. The tag has a surface coding density of 1.35bits/cm^2 and a faithful reading range of 40 cm from the reader.

Stepped Impedance Resonators: Main attraction of stepped impedance resonators as scatterers in chipless RFID tags are their flexibility in design and their independent control over fundamental and higher harmonic frequencies. Two important parameters of SIR are impedance ratio and length ratio and are defined as follows.

$$K = Z_2/Z_1 \quad (1)$$
$$\alpha = \theta_2/(\theta_1+\theta_1) \quad (2)$$

Where Z and θ represent the impedance and electrical length of respective sections. Mathematical method for finding the fundamental and first harmonic frequency is reported in [10]. Basic λ/2 SIR structures for K<1 and K>1 is shown in Figure 1. Microstrip version of typical half wavelength SIR is shown in Figure 2 for K<1. Physical dimensions are obtained from this Z and θ. The effect of fringing should include in the Length calculations ie., $L_2' = L_2 - \Delta L$, where L_2 is the length corresponding to the electrical length θ_2 and ΔL is the fringing field end correction.

Equation (3) and (4) represent the even and odd resonant conditions of an SIR, respectively.

$$K.\cot\theta_2 = \tan\theta_1 \quad (3)$$
$$K.\cot\theta_2 = -\cot\theta_1 \quad (4)$$

Expressing Equations (3) and (4) in terms of α,

$$K.\cot(\alpha.\theta_t/2) = \tan[(1-\alpha).\theta_t/2] \quad (5)$$
$$K.\cot(\alpha.\theta_t/2) = -\cot[(1-\alpha).\theta_t/2] \quad (6)$$

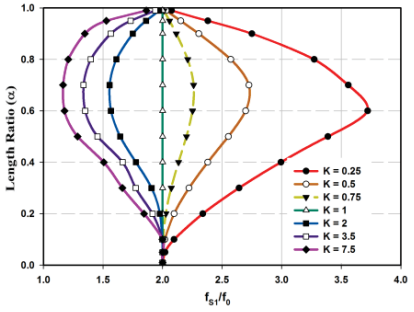

Figure 3: Dependence of fundamental and first harmonic separation on K and α

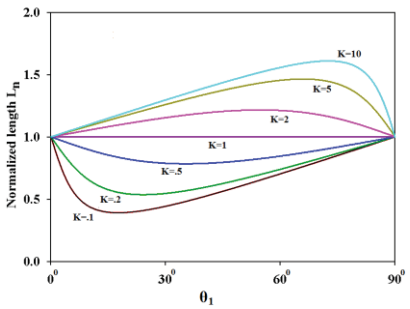

Figure 4: Physical length variation with K

By solving transcendal equations (5) and (6) separately, value of θ_t for both modes can be obtained. Plot between α, K and the ratio f_{s1}/f_0 is depicted in Figure 3 where f_{s1} is the first harmonic frequency and f_0 is fundamental frequency. It is noted from the figure that larger the impedance ratio, the closer will be the separation between f_{s1} and f_0 and vice versa.

For α=0.6 there will be maximum and minimum separation for K<1 and K>1 SIR, respectively. Figure 4 shows the relationship between physical length, electrical length and impedance ratio. K<1 SIR is used in this paper for the purpose of miniaturization. An orthogonally polarised wave incident on SIR will not induce any surface current on it. This polarization property of SIR is utilized here to increase the encoding capacity by employing orthogonal SIRs .Current distributions on SIR for parallel and orthogonal excitation are shown in Figure 5. In the present analysis, effect of step junction at the high impedance to low impedance transition is neglected.

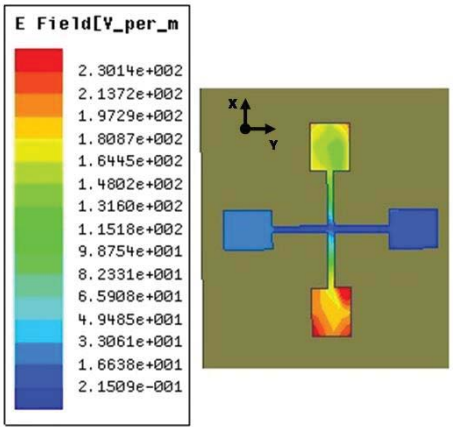

Figure 5: Electric Field distribution for excitation in Y direction

TAG DESIGN

A single scatterer in the tag is a combination of two SIRs placed orthogonal to each other. So the scatterer encodes different data for orthogonal polarizations. As shown in figure 12, eight independent resonators are designed at 3.6 GHz, 3.9 GHz, 4.2 GHz, 4.9 GHz, 5.6 GHz, 6 GHz, 6.4 GHz, 7 GHz. They are grouped into four scatterers. Careful selection of impedance ratio and length ratio ensures that no harmonics of any SIR will interfere in the desired band. Positioning of orthogonal SIRs is done to minimise mutual coupling effects between them. A separation not less than 3mm between adjacent scatterers is required to minimize mutual coupling. The tag has an overall dimension of 4.35x4.52cm^2. Dimensions of each resonator are given in table1 and these are calculated using MATLAB and AppCad.

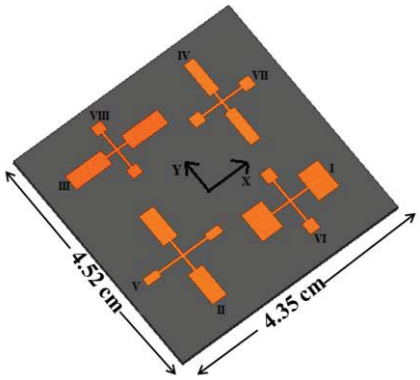

Figure 6: Chipless RFID Tag with 8 SIRs

TABLE **1**

SIR	K	α	W_1	L_1	W_2	L_2	ΔL
I	.25	.6	0.5	3.79	5.9	4.38	0.95
II	.4	.7	0.5	3.29	3.05	6.74	0.61
III	.4	.8	0.5	2.17	3.06	7.67	0.61
IV	.5	.8	0.5	1.98	2.155	7.14	0.52
V	.6	.4	0.5	5.16	1.57	2.89	0.46
VI	.5	.4	0.5	4.50	2.16	2.38	0.52
VII	.5	.4	0.5	4.22	2.16	2.20	0.52
VIII	.5	.4	0.5	3.86	2.16	1.97	0.52

Total bit combination expression with frequency shift coding given in [11] is modified for calculation of total bit encoding capacity of the tag with N resonators and can be rewritten as

$$Tb = \log_2 \left[\prod_{i=1}^{N} \left(\frac{\Delta f}{df}\right)\right] \qquad (7)$$

where frequency span (Δf) for fundamental mode is 500MHz and bandwidth resolution (df) for detecting the resonance in the fundamental mode is 50MHz. Here N=8 and as a whole the tag is designed to operate in a band from3.2 GHz to 7.2 GHz

Simulation and Measurement: The designed tag is fabricated on RTDuroid substrate with relative permittivity 2.2, loss tangent 0.0009 and height 1mm. Finite Element Method (FEM)based Ansys HFSS with plane wave excitation is used for simulation in which, source is placed at a distance of 18cm from the tag. Agilent PNA E8362B Network analyser with 1 mW input power is used as reader. Two orthogonally polarized medium gain (10dB) horn antennas are used as the reader antennas. In this measurement two degrees of freedom are given in the tag positioning, vertical and horizontal. The measurement setup is shown in figure 7.

A simple but effective calibration is performed by subtracting S_{11} without tag from S_{11} with tag [9]. Measurements are carried out inside and outside the anechoic chamber with sufficient averaging to minimize the white noise level. In the present work, the measurements are carried out with an averaging of 16.

Results: Reflection coefficient and backscattered group delay are measured to decode data. The measured results are shown in Figure 7 and it can be seen from the figure that the measured values are in good agreement with designed ones except for slight variation due to the neglected step junction effect and coupling effect between orthogonal SIRs in the design. In figure 7, each resonance can have one of the 10 digits in the assigned span of 500 MHz with a resolution of 50 MHz according to the design. In the figure the represented digits are highlighted with dashed lines and are written down.

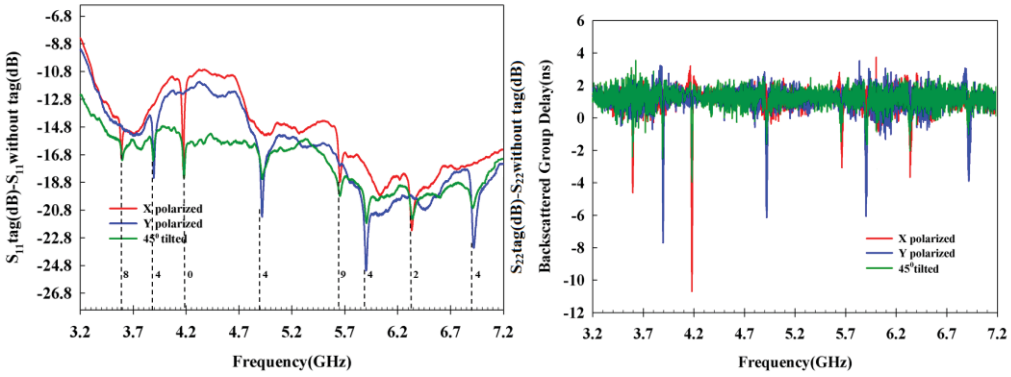

(a) (b)

Figure 7: Measured (a) S_{11} (b) Group delay

Figure 8 shows rotation of the x polarized tag for four different angles along x-y plane. The tag maintains its performance for rotation up to 30^0 in x-y plane. Beyond 30^0 the resonances of orthogonal SIRs appear in the desired band. For 45^0 tilted tag in x-y plane excited with a single linearly polarized antenna(X or Y polarized for this case), all the eight resonances are obtained. Measurements for four different distances are shown in figure 9. Up to 40 cm from the reader the tag is readable.

The tag has an overall dimension of 4.35x4.52cm^2.The total bit capacity of the tag for N = 8 is found as 26.58 and surface coding density is 1.35 bits /cm^2.

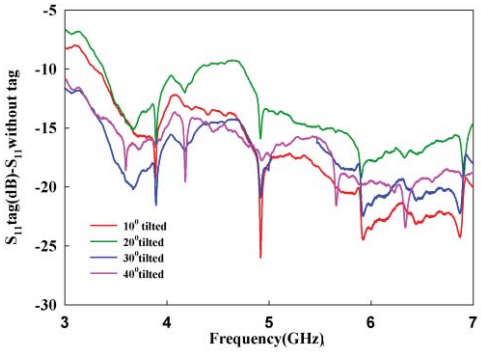

Figure 8: tag tilted for different polarizations

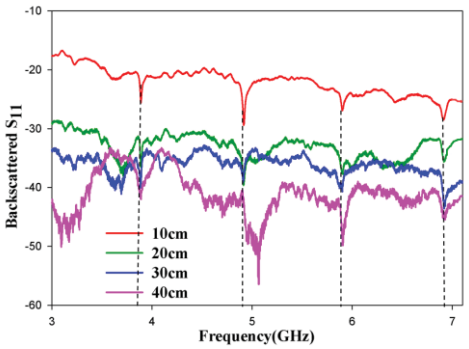

Figure 9: tag performance at different distances

Conclusion: An SIR based chipless RFID tag having eight is designed and fabricated. Complete harmonic suppression in the desired band is obtained. Frequency shift coding is employed to enhance data density. The tag can be read up to 40 cm. Surface coding density for the presented tag is calculated as 1.35 bits/cm^2.

Acknowledgement: The Authors acknowledge Kerala State Council for Science Technology and environment, University Grants Commission Government of India and Department of Science and Technology for financial support.

Reference:

[1] S. Preradovic, N. Karmakar "Chipless RFID: bar code of the future", Microwave Magazine, IEEE,vol.11, No.7, pp.87–97 December 2010.

[2] A. Chamarti and K. Varahramayan, "Transmission delay linebased ID generation circuit for RFID applications", IEEE Microwave Wireless Compon. Lett., vol. 16, no. 11, pp. 588–590, Nov. 2006.

[3] I. Balbin, , N. Karmakar, "Phase-Encoded Chipless RFID Transponder for large-scale low-cost applications", Microwave and wireless Components Letters, IEEE,vol.19,No.8, pp.509–511, 2009.

[4] A. Vena, E. Perret, S. Tedjini, " Chipless RFID Tag Using Hybrid Coding Technique", Microwave thory and techniqies,IEEE, vol.59, No.12, pp. 3356–3364,2009.

[5] S. Preradovic, I.Balbin, , N. Karmakar, , & Swiegers, G. F., "Multiresonator-based chipless RFID system for low-cost item tracking", IEEE Transactions on Microwave Theory and Techniques, vol.57,No.5, pp.1411–1419, 2009.

[6] I. Jalaly and D. Robertson, "RF barcodes using multiple frequency bands," in IEEE MTT-S Microwave Symp. Dig., Long Beach, CA, pp. 139–141, Jun. 2005,.

[7] A. Vena, E. Perret, S. Tedjini., "Design rules for chipless RFID tags based on multiple scatteres" Antenna telecommunication, vol.68, pp.361-374, 2013

[8] A. Islam and N. Karmakar, "A novel compact printable dual polarized chipless rfid system", IEEE transactions on microwave theory and techniques, vol.60, No.7,pp.2142-2151, july2012.

[9] C M Nijas, U Deepak, R Sujith, S Mridula, K Vasudevan , P mohanan, "Low cost multiple bit encoded chipless RFID tag using stepped impedance resonator." IEEE transactions on Antennas and propogation, vol.62,No.9, pp.4762-4770, sep2014

[10] M Makimoto and S Yamashita "Microwave resonators and filters for wireless communication theory design and application",advanced Microelectronics, springer.

[11] A.Vena, Perret, E., Tedjini, S., "A Depolarizing chipless RFID tag for Robust Detection and Its FCC Compliant UWB Reading system" IEEE Transactions on microwave theory and techniques, vol.61,no.8,aug 2014.

Compact Polarization Independent Chipless RFID Tag

Laila .D [(1]Member IEEE, Riny Thomas[(1)], Nijas C M[(2)], Mohanan P[(2)],Senior Member IEEE
(1) Model Engg College, Thrikkakara,India, 682021, lailacusat@gmail.com
(2) Department of Electronics, Cochin University of Science and Technology,Cochin-22, Kerala, India.nijasmhmmd@gmail.com ,drmohan@gmail.com

Abstract:*A compact polarization independent RFID tag employing multiple resonators is proposed. The prototype of the tag is fabricated on a low loss FR4 substrate of dielectric constant 4.4with height 1,6mm. Designing a reader for chipless RFID is a hard task since both the polarization and operating frequency agility have to be implemented. The tag design proposed in this paper is polarization independent, making the design of the reader easier. A prototype of 3bit data encoded tag is demonstrated. This new design is experimentally validated in the frequency domain.*

Introduction: Chipless RFID has the potential in the field of automated identification, tracking, and safety management. Chipless technology does not require any IC or communication protocol. Commercially available chipless RFID tags developed by the Surface Acoustic Waves(SAWs) [1] are not fully printable. The tags can be coded in the time domain [2-3], or in the frequency domain [4-6]. To detect the tag regardless of its orientation, the reader needs to have polarization agility. Also the detection reliability in harsh environment having multiple paths can be improved by polarization diversity.The best performance in terms of coding capacity and miniaturization is achieved by frequency encoded chipless tags.

A fully printable chipless RFID system on a 1.6-mm thin FR4 laminate is presented. The tag is encoded in frequency and can be easily decoded corresponding to the presence and absence of a bit.

TAG DESIGN:

The symmetric and polarization independent tag is composed of multiresonators. The basic structure of the tag is shown in Fig.1. To encode data within a frequency band, the classical way is to create some notches or peaks in the backscattering signal at specific frequencies, which can be controlled by changing the physical dimensions of the resonators. The proposed three bit microstrip based structure consists of microstrip resonators operate in Ultra Wide Band(UWB) frequency range, i.e. 3.1GHz to 10.6 GHz. To make tag independent of incident polarisation four microstrip resonators working in the same frequency arranged in all direction in a symmetric pattern as shown in Fig. 1. Increasing the number of unit cell will also enhance the level of backscattered signal; hence more readable range is also possible up to a distance of 30cm with a lossy substrate.

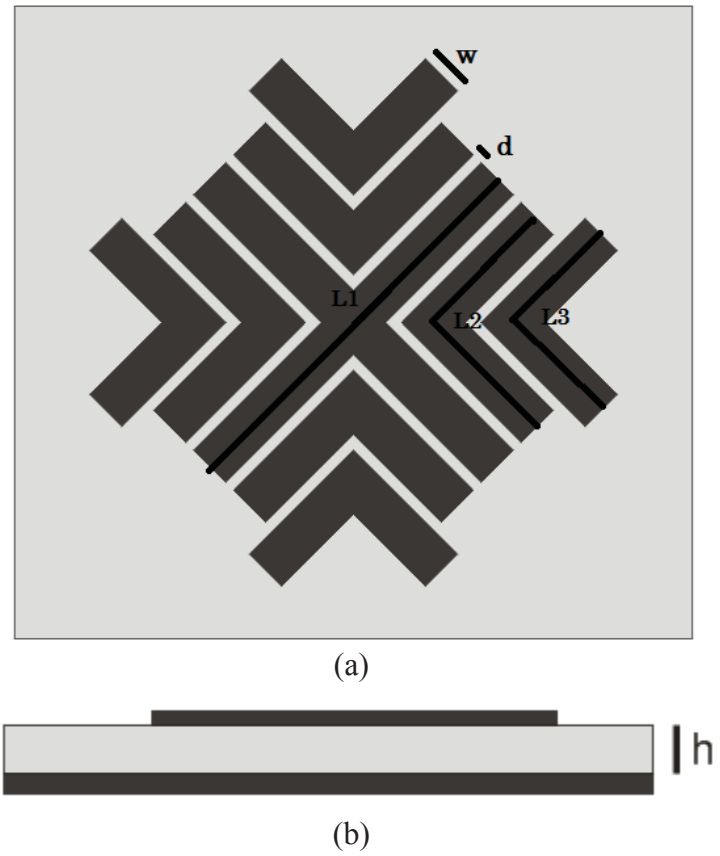

Fig 1.Structure of multiple resonators(a) top view(b)side view

TABLE 1.DIMENSION OF COMPACT MULTIPLE STRIP RESONATOR

Dimension	L1	L2	L3	w	d
Value (mm)	18	12	8	2	0.5

The width of resonator (w) is fixed at 2 mm and interelement gap (d) is 0.5 mm. The inter element gap is optimized to 0.5 mm. Due to the symmetry of the structure, any of the resonator in the basic model will resonate for random incident wave polarization. The tag is fabricated on FR4substrate of thickness 1.6mm with relative permittivity 4.4 and loss tangent 0.02.The structure is simulated using Ansoft HFSS.

MEASUREMENT AND RESULTS

The measurement was carried out using Agilent PNAE8362B with 1mW output power. A linearly polarised horn antenna is used at the reader end, which will work as both transmitter and a receiver.The structure resonates at 4.54 GHz,6.72GHz and 10.34GHz.Each resonator independently resonates at its half wavelength frequency. The backscattered measured field response of the tag for different angles $\pm 0^0$,$\pm 45^0$ and $\pm 90^0$ are shown in Fig.2. Tag is measured at a distance of 20 cm away from the antenna.

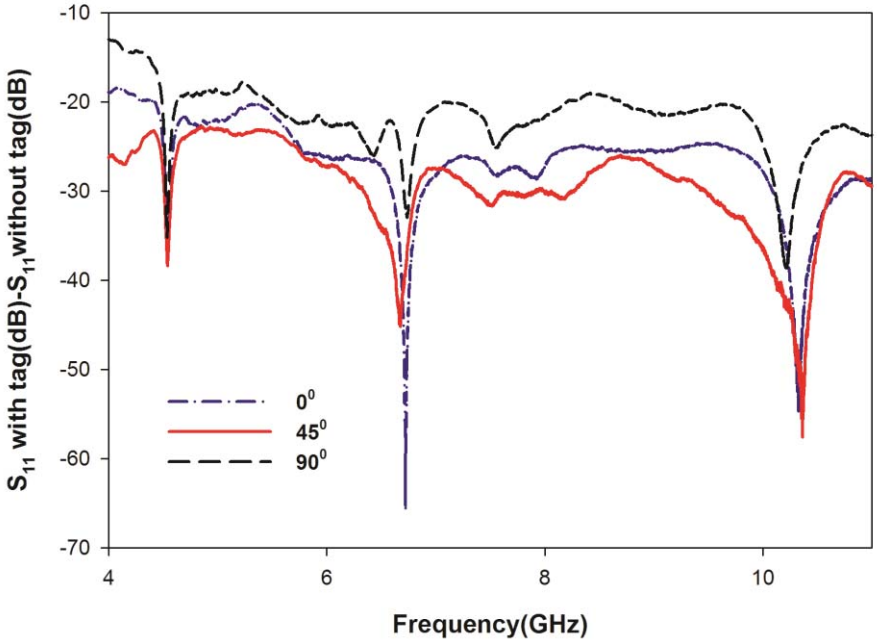

Fig 2.Measured field response of the tag for different angles

CONCLUSION

A polarization independent RFID tag with muliresonator is proposed. The structure is symmetric and 3 bits encoding can be done. The structure is implemented on a FR4substrate. The polarization independent property reduces the cost of the design of the reader.

Reference:

[1] C. S. Hartmann, "A global SAW ID tag with large data capacity," in Proc.IEEEUltrason. Symp., Munich, Germany, Oct. vol. 1, pp.65-69, 2002

[2] R. Nair, E. Perret, and S. Tedjini, "Temporal multi-frequency encoding technique for chipless RFID applications," in IEEE MTT-S Int.Microw.Symp. Dig., pp. 1-32012.

[3] . A. Ramos, D.Girbau,A. Lazaro, and S. Rima, "IR-UWB radar system and tag design for time-coded chipless RFID," in EUCAP, pp.2491- 2494, 2012

[4] A. Vena, E. Perret, and S. Tedjini, "High capacity chipless RFID tag insensitive to the polarization," IEEE Trans. Antennas Propag., vol.60, no. 10, pp. 4509-4515, Oct. 2012.

[5] S. Preradovic and N. Karmakar, "Design of fully printable planar chipless RFID transponder with 35-bit data capacity," in Eur. Microw.Conf., pp. 13-16, 2009.

[6] I. Jalaly and I. Robertson, "RF barcodes using multiple frequency bands," in IEEE MTT-S Int. Microw. Symp. Dig., pp. 1-4, 2005.

BISTATIC RCS MEASUREMENT OF ELECTROMAGNETIC ABSORBERS USING STACKED RING-PATCH ARRAYS

M. N. Sujatha[(1)], *K. J. Vinoy* [(2)]
(1) Siddaganga Institute of Technology, Tumkur, India, Pin: 572103 Email: mnsujathaguddu@rediffmail.com
(2) Indian Institute of Science, Bangalore, India, Pin: 560012, Email: kjvinoy@ece.iisc.ernet.in

Abstract: *A near Perfect electromagnetic absorber is designed by the addition of a ring layer below the square patch AMC structure. This is characterized by bistatic radar cross section measurements to ensure that there are no scattered fields in other directions. The resulting absorber structure is thin, polarization independent and consists of a low cost commercial substrate (FR4).*

1. INTRODUCTION

Radar Absorbing materials (RAM) are used in military and civil applications to reduce the electromagnetic interference among microwave components or electronic circuits mounted on the same platform. Conventional microwave absorbers proposed in [1]-[4] is good in terms of reflectivity and bandwidth their thickness is not less than λ/4 (λ is operating wavelength). Recently thin absorbers based on resistive frequency selective surfaces (FSS) have been proposed in [5]-[7]. Perfect metamaterial absorber based on magnetic and electric resonance have been proposed in [8]-[10] and operation is explained using complex effective medium parameters ε and μ [11], usually consists of two resonators one for electric resonance and other for magnetic resonance. The direction of incident wave must couple to both the structures, due to this, reflection properties of the structures proposed in [8]-[10] depend highly on the polarization state of incident wave. Also thickness of these materials in the direction of wave propagation affects the material properties.

This paper demonstrate that the high surface impedance of a square patch AMC structure can be matched to free space impedance by the addition of an array of metal rings below these patches. Impedance matching results in near perfect absorption of the incident electromagnetic waves. The structure is designed to operate at a certain frequency using formulas given in [12]. The structure makes use of commercially available metal laminated FR4 material with loss tangent $tan\delta$= 0.025. Bistatic RCS measurement reported here proves that there are no scattering of waves in other directions.

II. GEOMETRY OF THE STACKED RING-PATCH ABSORBER

Metal square patches are printed on the top substrate and metal square rings are printed on the metal backed bottom substrate. Metal rings and patches in the array have the same lattice constant 'a'. Geometrical parameters, 2D and side views of the structure are shown in Figure 1. FR-4 material with loss tangent $tan\delta$= 0.025 and thickness h=0.8mm is used as the substrate.

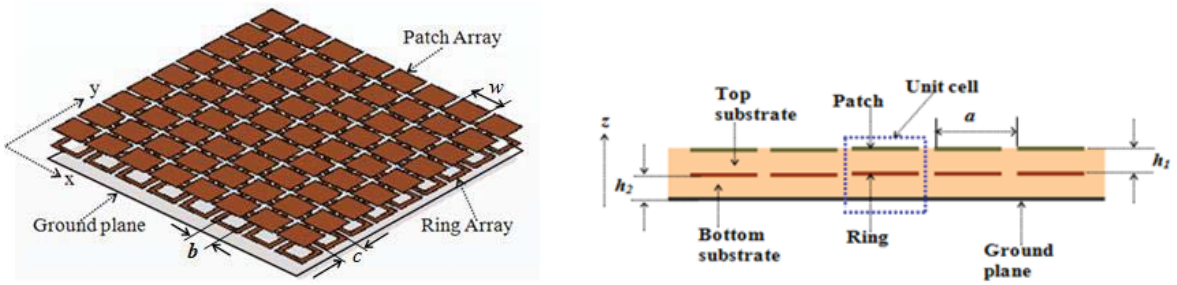

(a) (b)

Figure 1: Stacked Ring-Patch structure (a) 2D view of the structure (b) Side view of the structure

III. SIMULATION STUDIES

Numerical simulations have been performed using CST Microwave Studio software. Simulation setup is formed by a unit cell, the side walls are set with unit cell boundary conditions, so the simulated structure could be regarded as infinite in the x- y plane. Top wall is assigned with open boundary and bottom is with electric boundary. Floquet port is used to incident plane wave normally on the unit cell.

Initially array of patches is designed to operate at the given frequency. Using transmission line theory, patch AMC can be modeled as a parallel combination of L and C components. *L* is the input impedance of the metal backed dielectric slab of thickness '*h*'.

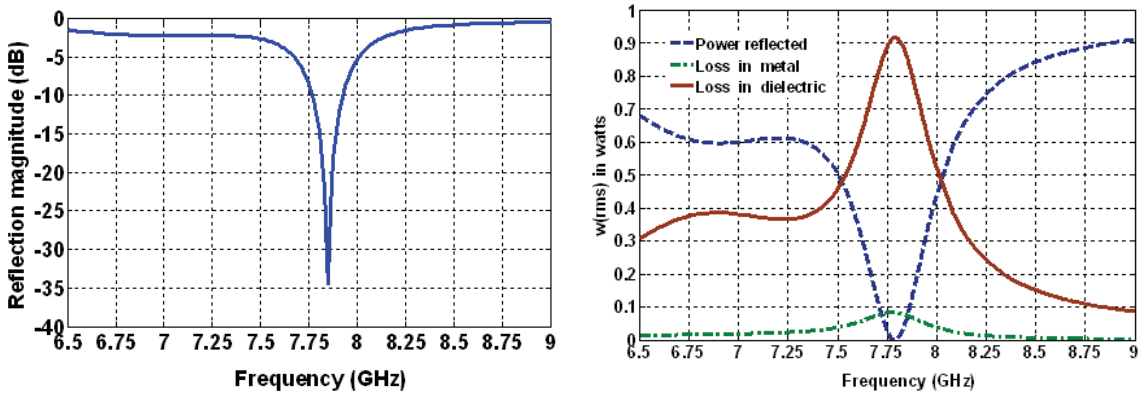

(a) (b)

Figure 2: Simulation results (a) Reflection magnitude plot (b) Losses in different materials of the structure

Top layer patch dimensions are calculated using equations given in [12]. For the given substrate parameters ε_r and thickness '*h*', value of inductor is given by $L=\mu_o h$, where $\mu_o=4\pi x10^{-10}$ H/mm and $h= h_1+ h_2$. *C* is the capacitance of the patch array, with expected resonant frequency f_r , the value of *C* is calculated. In the present study Width of the gap '*g*' between the patches is taken equal to $g= 0.1w$, width of the patch ($w=a-g$) is found using Equation (1) [12]

$$C = \frac{a\varepsilon_0 (1+\varepsilon_r)}{\pi} log\left(\frac{8a}{g}\right) \quad (1)$$

To get the dimensions of the rings in bottom layer, outer width of the ring is taken as c=0.85w and inner width b=0.65w. Finally outer and inner width of the rings is varied to get the maximum absorption through impedance matching. Geometrical parameters of the structure to operate at 7.86GHz using FR4 substrate with dielectric constant ε_r=4.3 and $h_1= h_2$ =0.8mm are *a*=7mm, *w*=6.4mm, outer width of the ring *c*=5.4mm, inner width of the ring

b=4.3mm, *g*=0.6mm. Reflection coefficient plot extracted through this model with above structural dimensions is shown in Figure 2(a). It can be seen from the Figure 2(a) that there is a good absorption at 7.86GHz, with 2% bandwidth at 10dB. Figure 2(b) shows the comparison of contribution of losses in different materials of the structure. Out of total incident power, 90% appears as loss in dielectric material and remaining 10% appears as loss in metal.

IV. EXPERIMENTAL RESULTS

The proposed structure is fabricated with an array of 57x57 unit cells with overall size (40cmx40cm). Array of patches printed on FR-4 material with backside metallization removed and thickness h1=0.8mm, dielectric constant ε_r=4.3 and loss tangent tanδ= 0.025. Metal square rings are also printed on FR4 substrate backed by a metal ground plane with thickness h2=0.8mm. Two layers are properly aligned together using alignment marks and tightly bonded together to form the final structure, fabricated structure is shown in Figure 3(a).The Arch method is used to study the bistatic RCS of the structure.

(a) (b)

Figure 3: Fabricated structure and measurement setup (a) Fabricated structure (b) Bistaic RCS measurement setup

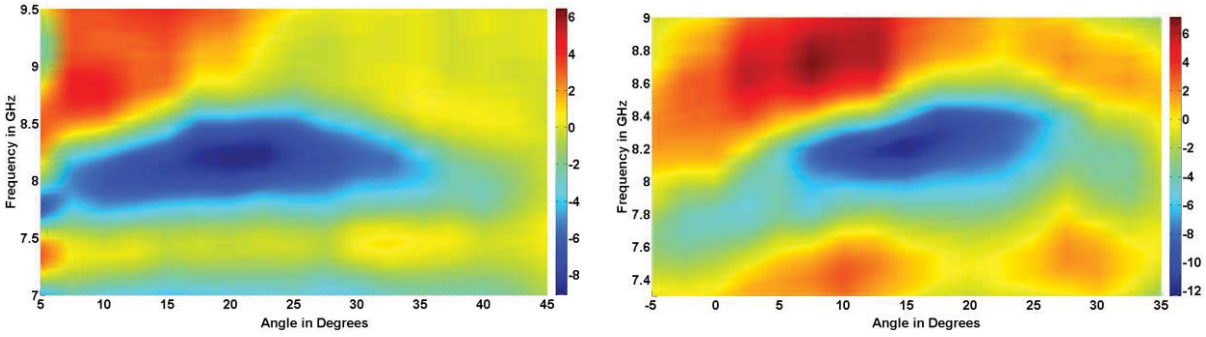

(a) (b)

Figure 4: Bistastic RCS measurement result with TE polarized incident wave (a) Transmitting antenna at 10° (b) Transmitting antenna at 20°

Two wideband horn antennas are used as transmitting and receiving antennas. The transmitting antenna mounted on a wooden carriage is placed closed to the arch. The proposed structure is fixed on a turntable at the centre of the Arch. The receiving antenna is moved on the Arch for measuring the reflected power from the structure of interest, measurement setup is shown in Figure 3(b). Transmitting antenna fixed at 10^o (and 20^o) from

the bisector of the Arch, receiving antenna is moved on either side of bisector of Arch, angle is negative to the left of Arch bisector and positive to right of bisector, while receiving antenna is moved over an arch in steps of 2.5^o and at each position S_{21} is measured as a function of frequency. Measured Bistatic RCS shown in Figure 4 proves that there is no scattering in other directions. Further, only small changes are observed as the angle of incidence is increased.

V. CONCLUSIONS

Bistatic RCS measurement of square loop and patch array structure are studied in this work. It has been demonstrated through simulation and experiment that the addition of square loop layer below the patch layer is a simple method to get perfect EM wave absorption. Proposed structure is thin, simple for design, polarization independent and makes use of commercially available FR4 material. From experimental results it is observed that, the structure exhibits 7% bandwidth at 10dB. The performance of the structure does not degrade for low angles on incidence, as reported here.

ACKNOWLEDGMENTS

Author would like to thank Prof C.K. Anandan of Cochin Universityof Science and Technology (CUSAT) Kochi, for allowing us to use his Lab facilities for NRL arch bistatic RCS measurements.

REFERENCES

[1] L. Dallenbach, W. Kleinsteuber , " Reflection and Absorption of Decimeter-Waves by Plane DielectricLayers," *Hochfreq. u Elektroak*, Vol.51, pp. 152-156, 1938

[2] W. W. Salisbury, Absorbent Body of Electromagnetic Waves," U. S. Patent 2,599,944, Jun 10, 1952.

[3] R. L. Fante, and M. T. McCormack, "Reflection Properties of the Salisbury Screen," *IEEE Trans. on Antennas and Propagatio*n, Vol. 36, No. 10, pp. 1443-1454, 1988.

[4] B. A. Munk, P. Munk, J. Pryor, "On designing Jaumann and Circuit Analog absorber (CA absorber) for oblique angel of incidence," *IEEE Trans. Antennas Propag*.55, pp. 186–193, 2007.

[5] N. Engheta, "Thin Absorbing Screen Using Metamaterial Surfaces," *Proc. IEEE International Symposium on Antennas and Propagation,* Vol. 2, pp. 392-395, 2002.

[6] D. J. Kern and D. H. Werner, "A genetic algorithm approach to the design of ultra-thin electromagnetic bandgap absorbers," *Microwave Optical Technology Letters*, Vol. 38, pp. 61–64, 2003.

[7] H. Mosallaei and K. Sarabandi, "A one-layer ultra-thin meta-surface absorber," *Proc. IEEE International Symposium on Antennas and Propagation*, Washington DC, USA, July 2005.

[8] N. I. Landy, S. Sajuyigbe, J. J. Mock, D. R. Smith, and W. J. Padilla, "Perfect metamaterial absorber," *Phys. Rew. Lett.*, Vol. 100, May 2008.

[9] Y Cheng and H Yang , "Design, simulation, and measurement of metamaterial absorber," *Journal of Applied Physics*, Vol. 108, Issue: 3, Aug 2010.

[10] Y. Cheng, H. Yang, Z. Cheng, N. Wu, "Perfect Metamaterial Absorber Based on a Split-Ring-Cross Resonator", *Appl Phys A*, Vol. 102, Issue: 1, pp 99-103, Jan 2011.

[11] F. Costa, S. Genovesi, A. Monorchio, "A Circuit-Based model for the Interpretation of Perfect Metamaterial Absorber," *IEEE Antennas and Wireless Propagation Letters*, Vol. 61, No.3, pp. 1201-1209, March 2013.

[12] S. Tretyakov, *Analytical modeling in applied electromagnetics*, Artech House Publishers, 2003.

A Frequency Selective Surface for GSM 900 MHz Band Shielding

Ayan Chatterjee[(1)], *Susanta Kumar Parui*[(2)]
Indian Institute of Engineering Science & Technology, Shibpur-711103, West Bengal, India
[(1)]ayanmrinal26@gmail.com, [(2)]arkapv@yahoo.com

Abstract: *This paper presents a Frequency Selective Surface (FSS) that functions as a band stop filter to shield the GSM 900 MHz downlink band, allowing the uplink frequency signals to pass through it without significant attenuation. The FSS is designed to exhibit a stopband in the 935-960 MHz band with a transmission below -15 dB and a passband in the 890-915 MHz band. The structure based on a transparent acrylic substrate can be used in the wall, window or balcony of the top floors of high rise buildings near the mobile phone towers to reduce the radiation hazards along with successful communication.*

Introduction: With the enormous use of wireless communication, electromagnetic interference due to undesired radiation from different sources has become a serious problem in this field. To overcome this problem, shielding has become an important technology [1] that generally uses frequency selective surfaces (FSS) of both patch and aperture types for the protection against undesired radiation from external sources. Frequency Selective Surface, the counterpart of the filters of traditional radio frequency (RF) circuit in wireless communication, is a periodic array consisting of conducting patch or aperture elements having band-stop or band-pass spectral behavior [2]. In order to protect a flat array antenna system operating in the Ku-band from damage caused by the external environment such as rain, moisture, aerodynamic effects, etc., FSS coated on the glass [3-4] has been used to effectively pass the Ku-band signals and stop interference of external noises. A band-pass shielding enclosure of dimensions 16x10x2.1 cm for the portable digital wireless device was designed [5] using single layer of multi-pole slot array FSS, with high transmittance in the specified wireless-signal band and high shielding effectiveness outside this band. This FSS wall is made by printing metal aperture array on the FR4substrate.

Now-a-days with the increasing number of mobile phone users, density of cell phone towers has been increased very much especially in the urban areas with huge population. As a result, radiation from base station antennas are affecting people more who live in the high rise buildings near to these towers at a line of sight. In this paper, a FSS design has been proposed in the GSM 900 frequency band that can be used in such building walls, curtains, window glass, and balcony to reduce the radiation hazards at the same time allowing successful communication.

Description of the FSS Structure:

The FSS has been designed to reduce the power level of the signal radiated from the mobile phone tower in the GSM 900 frequency band. The proposed design is shown in the Fig. 1 and the detail dimensions (in mm) are given the figure. A dual layer FSS has been chosen for the purpose. The upper layer is of patch type and is a convoluted dipole here whereas the lower layer contains inductive wire grid elements that are basically aperture type FSS. Transparent

acrylic sheets have been used as the dielectric material between the two layers of FSS, with a dielectric constant (ε_r) of 2.8 above 1 MHz frequency and a dielectric loss tangent (tanδ) of 0.02. Apart from being transparent as shown in the Fig. 1 acrylic substrates are inexpensive and easily available. In the proposed design thickness of the substrate is chosen h = 2mm.

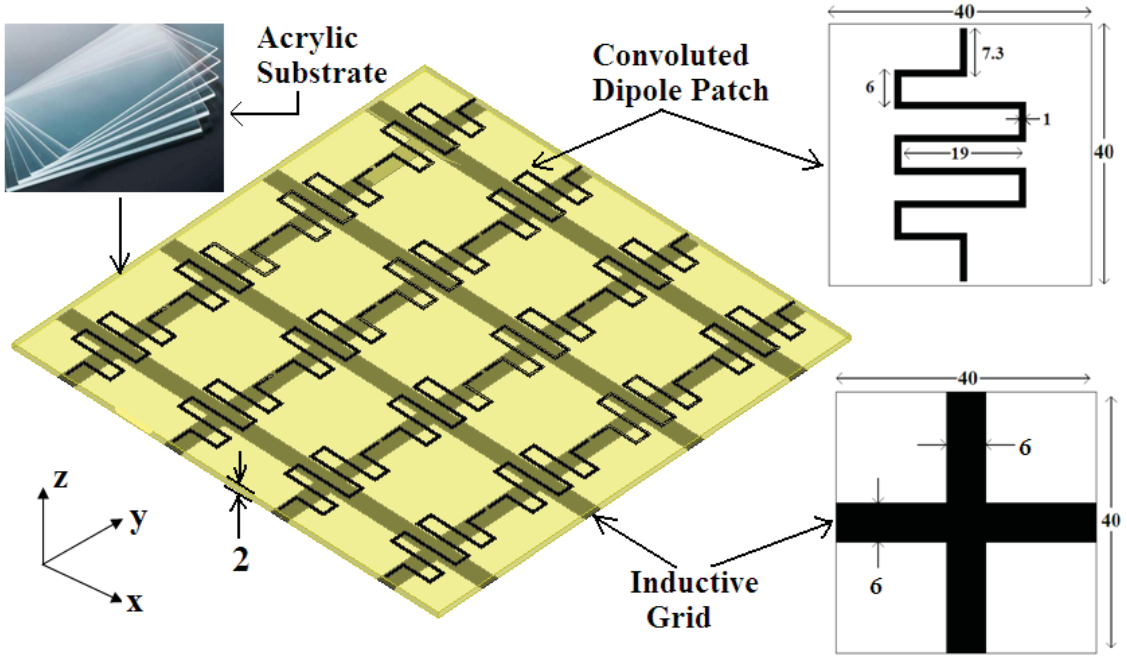

Fig. 1 Three dimensional view of the FSS and the unit cells (all dimensions are in mm)

Principle of Operation:

The proposed design contains two layers of FSS. The purpose of upper patch type layer of convoluted dipole is to offer a stop band at the downlink frequency of 935-960 MHz in the GSM 900 band where a huge amount of power is radiated from the base station antenna at the tower for reducing the power level by a certain amount. Whereas the aperture type grid layer acts as a high pass filter but when coupled with the other layer via dielectric, leads to a passband for the uplink frequency of 890-915 MHz used by the mobile phones to send signals at a very low power towards the base station antenna so that the power level does not fall by a significant amount.

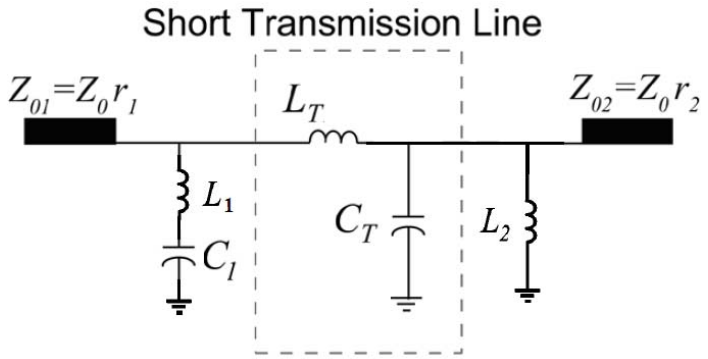

Fig. 2 An equivalent circuit model for the proposed design of Fig. 1

An equivalent circuit model for the proposed design has been given [2] for analysis in the Fig. 2. The convoluted dipole shaped patches are modeled as inductor L_1 and the capacitance between two such elements in the presence of E field is modeled as C_1. The series combination of L_1 and C_1 acts as band stop filter at 935-960 MHz. The cross shaped grids can be modeled as inductor L_2 offered by the grids mainly parallel to the incident E field and a acts as a high pass filter. The dielectric substrate is represented by a short piece of transmission line section and is replaced with its equivalent circuit model [6] composed of a series inductor and shunt capacitor namely L_T, C_T given by the following equations.

$$L_T = \mu_0\mu_r h \qquad C_T = (\varepsilon_0\varepsilon_r h)/2$$

The parallel combination of L_2 and C_T gives the response of a bandpass filter and when coupled to the Bandstop filter through the inductor L_T, it leads to a passband near 890-915 MHz. The half-spaces on the two sides of the FSS are modeled with semi-infinite transmission lines with characteristic impedances of $Z_{01}=Z_0r_1$ and $Z_{02}=Z_0r_2$, where r_1 and r_2 are normalized source and load impedances and $r_1= r_2=1$ for free space as considered in this case and $Z_0=377\Omega$ is the free space impedance.

Results and Discussion:

Full wave EM simulations have been performed for the proposed structure using Ansoft HFSS that uses Finite Element Method (FEM) for analysis. Analysis has been done for the composite structure and the simulation result for normalized transmission coefficient (dB) along with the transmission phase is given below in the Fig. 3 (a) and (b).

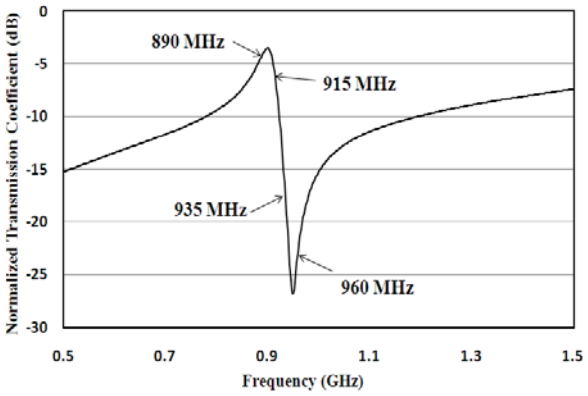

Fig. 3(a) Transmission response for the FSS

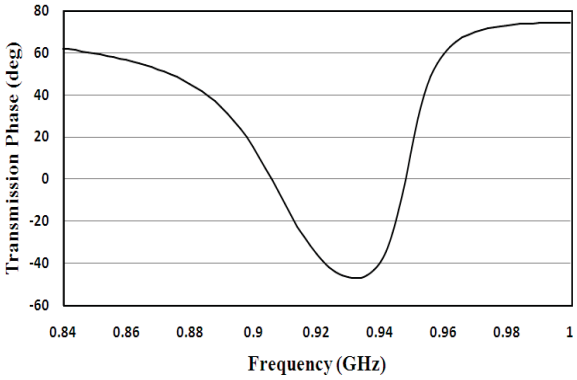

Fig. 3(b) Transmission phase of the FSS

As can be seen from the transmission response of the FSS, it passes the uplink frequency (890-915 MHz) signals from the mobile handset well and the signal power is reduced by around 20 to 25 dB in the downlink frequency (935-960 MHz) coming from the base station tower having a strong radiation for the nearby buildings and top floors.

It can be observed from the transmission phase response of Fig. 3 (b) that in both the uplink as well as downlink frequencies, the FSS layer does not lead to a significant change in phase for the signals passed through it. The proposed design provides a -15 dB bandwidth of 74 MHz covering the downlink band of GSM 900.

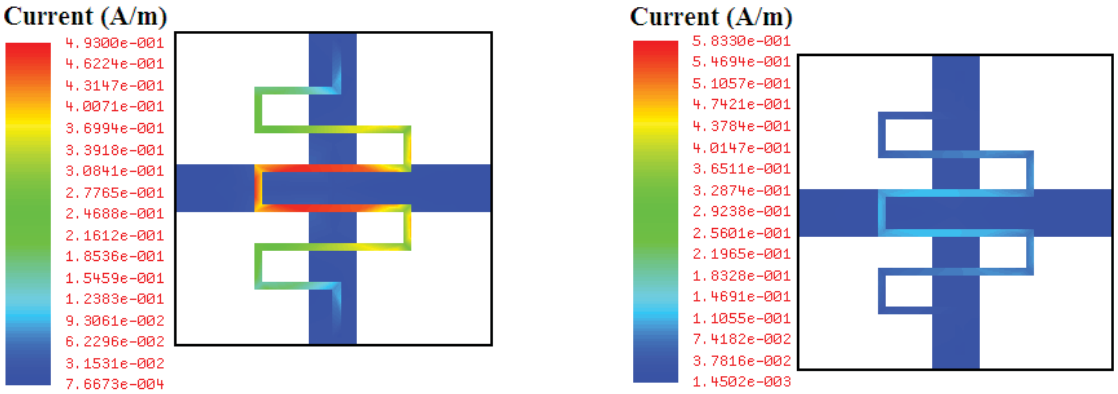

(a) (b)

Fig. 4 Surface current distribution on the unit cells of the FSSat (a) 950 MHz (b) 902 MHz

Surface current distribution for the individual FSS layers at two different frequencies of 902 MHz with maximum transmission and 950 MHz with minimum transmission is shown in the Fig. 4. It can be seen that surface current flows mainly on the convoluted dipole shaped patch allowing transmitted power to be reduced at downlink frequency of 950 MHz whereas at uplink frequency of 902MHz, inductive grid layer allows maximum transmission of power.

Conclusions:

A frequency selective surface for shielding the GSM 900 MHz downlink band is proposed with theoretical analysis. The design provides a reduction in power level by about 20 dB for the downlink frequency band only, allowing the uplink frequency signals to pass through it without much attenuation. The proposed structure uses a transparent material as substrate for visibility. The future scope of this work will be implementing the design into fabrics for curtain as well as air as the substrate for the structure.

Reference:

[1] Salvatore Celozzi, "Electromagnetic Shielding", 2nd Edition, Wiley Interscience Publication, 2008, pp.164.
[2] Farhad Bayatpur, "Metamaterial-Inspired Frequency-Selective Surfaces", Dissertation submitted for Doctor of Philosophy (Electrical Engineering), in The University of Michigan, 2009.
[3] R. Vincenti Gatti, L. Marcaccioli, E. Sbarra, and R. Sorrentino, "Flat array antennas for Ku-band mobile satellite terminals," Proc. of the 30th ESA Antenna Workshop on Antennas for Earth Observation, Science, Telecommunications and Navigation Space Missions, Noordwijk, The Netherlands, pp. 534-537, 2008.
[4] Hsing-Yi Chen and Yang-Kai Chou, "An EMI Shielding FSS for Ku-Band Applications", IEEE Antennas and Propagation Society International Symposium (APSURSI), 2012.
[5] Cheng-Nan Chiu, "Bandpass Shielding Enclosure Design Using Multipole-Slot Arrays for Modern Portable Digital Device", IEEE Transactions on Electromagnetic Compatibility, Vol. 50, No. 4, November 2008.
[6] Mudar Al-Joumayl and Nader Behdad, "A New Technique for Design of Low-Profile, Second-Order, Bandpass Frequency Selective Surfaces", IEEE Transactions on Antennas and Propagation, Vol. 57, No. 2, February 2009.

A UHF RFID TAG BASED ON MODIFIED FOLDED DIPOLE ANTENNA

K.K. Aju John [(1)], Manju Abraham [(2)], and Thomaskutty Mathew [(3)]
Department of Electronics, School of Technology and Applied Sciences,
Mahatma Gandhi University Regional Center, Edappally, India, 682024,
Email: mwrfgroupstas@gmail.com

Abstract: *The Design and development of a UHF RFID tag which exhibits good read range over the entire azimuth and elevation angular ranges is reported in this paper. The proposed RFID tag is designed to operate in the UHF RFID frequency bands in India, which is 865-867 MHz's. A T-matching is employed to achieve good impedance matching between the RFID chip and the tag antenna.*

Introduction: Radio frequency identification (RFID) is a rapidly developing wireless technology which utilizes radio waves for identifying objects. It is widely being used in automatic identification, asset tracking and security surveillance [1].RFID system is composed of a tag, reader and middleware. In a passive RFID system, the reader transmits a modulated RF signal to the tag consisting of an antenna and an IC. The chip receives power from the antenna and responds by varying its input impedance and thus modulating the backscattered signal. Recently there has been intense research on RFID technology in the UHF band (860-960) MHz and a large number of papers were published on the various design aspects of tag antennas [2-3].

Dipole structures and its many variations were reported for the design of RFID tag antennas. Folded dipole antennas are attractive structures for RFID tag and are investigated by many researchers for RFID tag design. Meandered structures are dipoles where the arms are folded, producing a distributed capacitive and inductive reactance [4-6].Designing an RFID tag with good read range is the major challenge that exist in today's RFID research, which needs better impedance matching between the chip and the tag antenna [7-8].

In this paper we present an RFID tag, based on modified folded dipole that operates in the UHF RFID bands (865-867 MHz), which is the UHF RFID band used in India. The main consideration of this work is to improve the read range of the RFID tag as well as the impedance matching for maximum power coupling to the chip, employing a T-matching technique and modified folded dipole structure [9]. Most of the tags reported are found to give good read range only over limited angular range in azimuthal and elevation. This novel tag exhibits good read range over the entire azimuth and elevation angular ranges.

TAG DESIGN AND FABRICATION

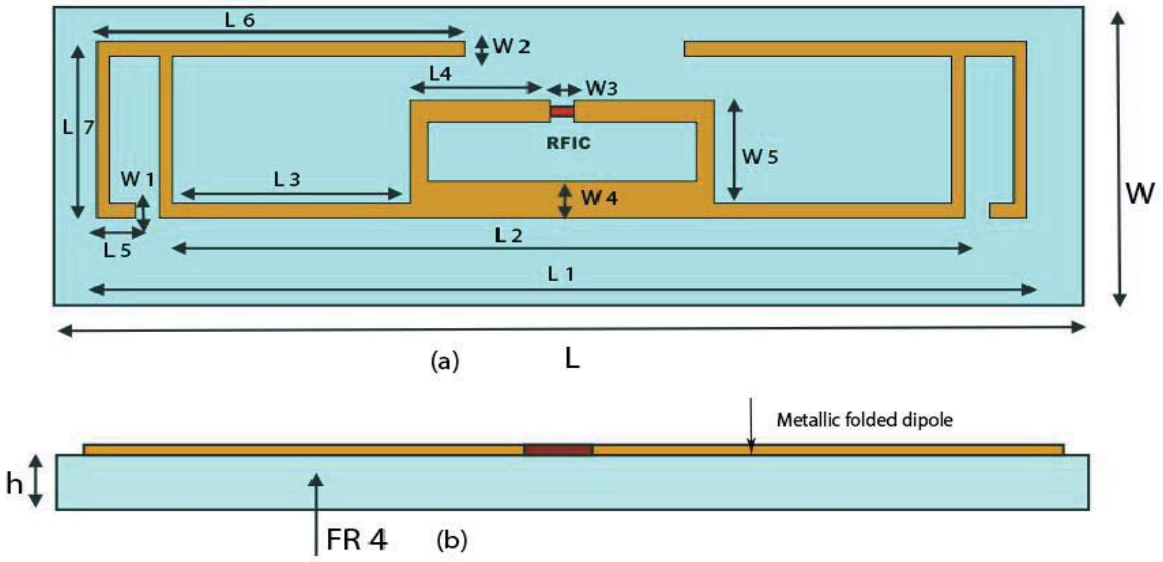

Fig 1.Geometry and structure of the UHF RFID tag (a) Top View (b) Side view

Geometry and structure of the proposed UHF RFID tag is shown in Fig 1, in which a folded dipole structure with additional arms on each side is employed. RFID chip is connected between the arms of the folded dipole. The impedance of the IC is matched to the impedance of the tag antenna to obtain a maximal power transfer from tag antenna to IC which results in maximal read range. A T-match network is implemented in the antenna design using CST Microwave studio for the optimization of the parameters of the RFID tag [10-11].The parameters W_3, L_4, W_4 and W_5 in the geometry are the T match parameters, which are properly tuned using simulations to get a conjugate impedance match with the chip at resonant frequency 866 MHz . The RFID tag is printed on the top side of a 1.6 mm thick FR-4 substrate with a loss tangent of 0.02 and relative permittivity $\varepsilon_r = 4.4$.

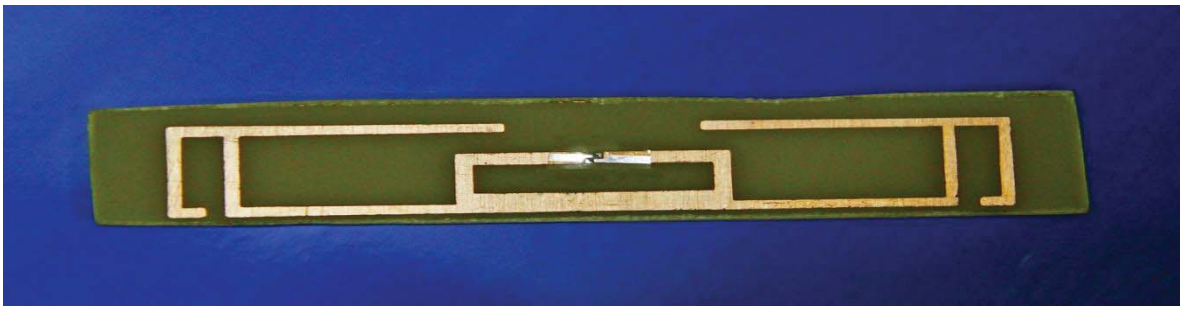

Fig 2. Fabricated UHF RFID tag.

Fig 2. shows the fabricated UHF RFID tag based on a modified folded dipole structure. The RFID chip with an impedance of 27-j211 at 866 MHz is used. The tag is a combination of the folded dipole and the T-matching network, consists of length L=80mm and width W=16mm. Table (1) shows the design parameters of the optimized antenna.

Parameter	Dimension [mm]	Parameter	Dimension [mm]
L	80	L6	30.1
W	16	L7	12
L1	76.2	W1	1
L2	66	W2	1
L3	19.5	W3	2
L4	11.5	W4	2.5
L5	3.1	W5	7

Table (1) Parameters of the proposed Tag

The read range measurement carried out with an STA IR0507E reader with a receiver sensitivity of -80 dBm and RF power of 28 dBm with circularly polarized waves. The tag is mounted on a movable platform with an arrangement for placing the tag for different azimuth and elevation angles. Placing the tag at a particular orientation, the read range is measured by moving the turn table with the tag to the maximum distance to which the tag is read for that orientation. This distance is taken as the read range for that particular orientation.

RESULTS AND DISCUSSION

Fig 3 (a) and (b) shows the simulated results of the variation of real and imaginary input impedance of the modified folded dipole Tag antenna with frequency. It can be seen from the graph that the real and imaginary part of the antenna impedance at 866 MHz are 24 ohms and 211 ohms respectively, which are very close to the corresponding values of the RFID chip.

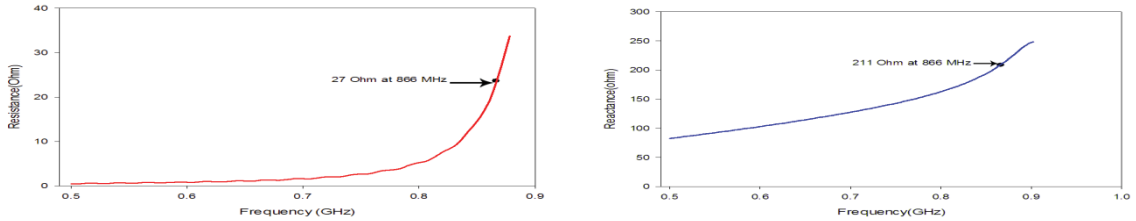

Simulated input impedance variation with frequency for the proposed UHF RFID tag antenna

Fig.3 (a) (Resistance Vs Frequency) Fig.3 (b) (Reactance Vs Frequency)

Figure 4 shows the simulated results of the variation of return loss with frequency of the RFID tag antenna. It can be seen that the antenna structure resonates in the desired frequency of 866MHz.

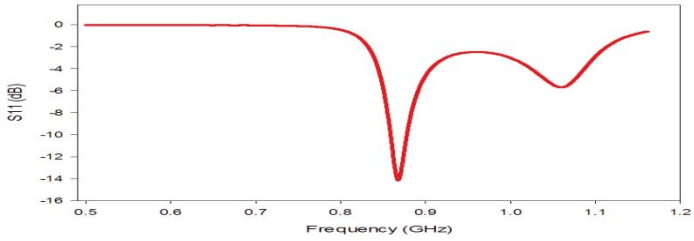

Fig 4.Simulated return loss of the proposed RFID tag antenna.

Figure 5 (a) and (b) show the measured variation of read range with the azimuth and elevation angles of the RFID tag. The measured read range versus elevation value shows a constant read range throughout the elevation angle. The azimuth angle value shows a constant read range in the -50 degree to +50 degree and slight variation in other angles. The read range at higher values of the azimuthal angle is appreciably better than conventional RFID tag.

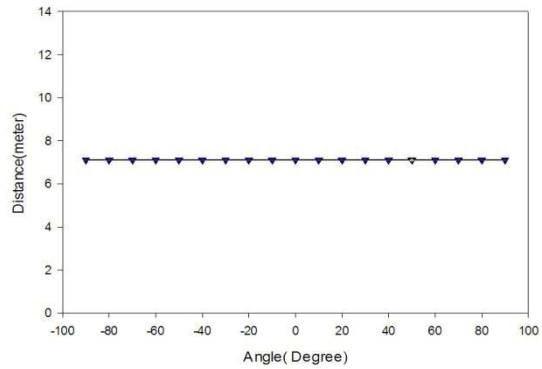

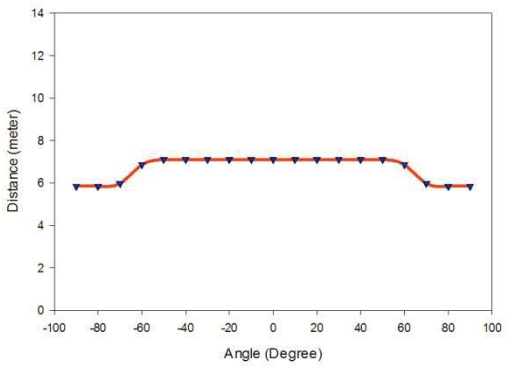

Measured read range versus Elevation and azimuth angle of the UHF RFID Tag.

Fig.5 (a) (Read range Vs. Elevation angle) Fig.5 (b) (Read range Vs. Azimuth angle)

CONCLUSION

A UHF RFID tag based on modified folded dipole with enhanced performance over the azimuthal and elevation angular ranges is presented. An effective T-matching technique is employed to obtain good impedance match between the antenna and RFID chip. Read range measurements shows that this UHF tag exhibits almost constant read range in the entire azimuth and elevation angle.

Acknowledgment

Authors wish to acknowledge the encouragement and support received from Dr. C. K Aanandan, Professor, Department of Electronics, Cochin University of Science & Technology, Kochi, India.

Reference:

[1] K. Finkenzeller, "RFID Handbook: Radio-frequency Identification Fundamentals and Applications", Second edition, 2004.

[2] K.V.S. Rao, P.V.Nikitin, and S.F.Lam, "Antenna design for UHF RFID tags: a review and a practical application", IEEE Transactions on Antennas and Propagation, vol.53, No.12, pp.3870-3876, 2005.

[3] Thomaskutty Mathew and John Batchlor, "RCS and Read Range of UHF RFID tag", Asia Pacific International Symposium on Electromagnetic Compatibility, 978-1-4244-56239/10, 2010.

[4] Chi di Diugwu, J Bachelor and T Mathew "Complementarity in the optimization of RFID dipole tag antennas", Antennas and Propagation Society International Symposium, 978-1-4244-20, 2008.

[5] Hubregt.J.V, "Printed Folded Dipole Antenna Design for Rectena and RFID Applications", 7th European conference on Antennas and propagation, 978-88-907018-3-2/13 IEEE. 2013.

[6] Ferran paredes,Gerad Zamora, "Dual Band UHF-RFID tags based on Meander line Antennas Loaded with Spiral Resonators", IEEE Antennas and Wireless Propagation letters, vol.10.1109/ LAWP.2162716/11 IEEE.2011.

[7] Jinlan.Gao, Johan Siden and Hans-E.N, "An Analytical Model for Electromagnetically Coupled UHF RFID Sensor Tags", IEEE International conference on RFID, 978-1-4673-5750-0/13, 2013.

[8] Alimenti.F, M.Viril li and L. Roselli, "Design of Paper Substrate Dipole Antennas Magnetically Coupled to UHF RFID Silicon Chips", International Conference on RFID Technologies and Applications, 978-1-4577-0027-9/IEEE, 2011.

[9] Micheal T.Reich and Cherish Baur-R, "UHF RFID Impedance Matching: When is a T-Match not A T-Match", International Conference on RFID (IEEE RFID),978-1-4799-3587-1/14/IEEE.2014.

[10] Tae-Wan.K, Dongsu Kim, "Design of a Label Typed UHF RFID Tag Antenna for metallic objects", IEEE Antennas and Wireless Propagation letters, vol.10.1109/ LAWP. 2166370, 2011.

[11] Karoliina Koski, Eveliina K, Leena U,"Effects of Laboratory Scale IC attachment methods on Passive UHF RFID tag performance", IEEE International Symposium on Antennas and Propagation(APSURSI), 978-1-4244-9561-0-/11,2011.

A NOVEL UHF RFID TAG BASED ON MULTI-FRACTAL CANTOR STRUCTURE FOR ENHANCED READ RANGE

Manju Abraham [(1)], Fijo Jose K [(2)] and Thomaskutty Mathew[(3)]
Department of Electronics, School of Technology & Applied Science, M.G. University, Regional center, Edappally, Kochi, Kerala, India 682024.
Email: mwrfgroupstas@gmail.com

Abstract: *The design and development of a novel RFID tag based on multi-fractal cantor structure for operation at UHF band (865-867 MHz) are presented. The performance of the tag is evaluated by measuring the read range using STA IRO507E RFID reader and a read range of 8.1m at boresight direction is obtained. The read range measurements of the tag for different azimuth and elevation angular ranges of the tag orientation are presented. The tag exhibits good read range over wide azimuth angular range and over the entire elevation angular range.*

Introduction: Radio Frequency Identification is an automated wireless data collection technology which is widely used as a substitute for barcodes[1]. Identification of objects using RFID has become very popular in areas such as electronic toll collection, logistics, inventory management, animal tracking etc. A passive backscattering RFID system generally consists of two basic components, the reader and the tag, which communicate with each other by electromagnetic waves. The reader uses an antenna to transmit an electromagnetic wave to wake up the passive tag, which is mounted on the object being identified. The tag consists of an antenna and a chip. The chip is usually placed right at the terminals of the antenna, and both the chip and the antenna have complex input impedance. RFID tag antenna must be directly matched to the complex impedance of the chip to maximize the tag performance.

Several papers have been published on various design aspects of RFID antennas and their performance evaluation [2-4]. In the design of an antenna the size of the geometry is treated equally important as the impedance matching, since they tend to look for light, low profile, and portable RFID equipment [5]. The space filling property of fractals offers size reduction to the tag antenna and also provides necessary inductance that is required for impedance matching with the chip impedance.[6]. The use of multi-fractal structures in antenna design has been reported recently [7].But the use of multi-fractal structure for RFID tag antenna design is not seen in literature. In this paper we present a novel passive multi-fractal cantor printed dipole tag antenna operating in the UHF RFID band. Each arm of the antenna is designed and developed using multi-fractal cantor technique because this geometry will itself provide some sort of size reduction and impedance matching by tuning the fingers of the multi-fractal cantor geometry. Additional inductance is provided by the closed loop.

Multifractal Cantor Structure: Fractal structures are characterized by using a single fractal dimension. But multi-fractals are characterized by not the unique fractal dimension but by a set of dimensions. Thus multi-fractals are objects, which tentatively can be considered as any synthesis of fractal structures with various dimensions [8]. Since the cantor geometry is the simplest one dimensional fractal possessing all the main fractal properties, multi-fractal geometry based on cantor geometry is used for making each arm of the proposed printed dipole. In the multi-fractal cantor geometry the initiator (Ko) of length 'L' and width 'w' is divided into three non overlapping segments with the middle segment removed as shown in figure1(a).

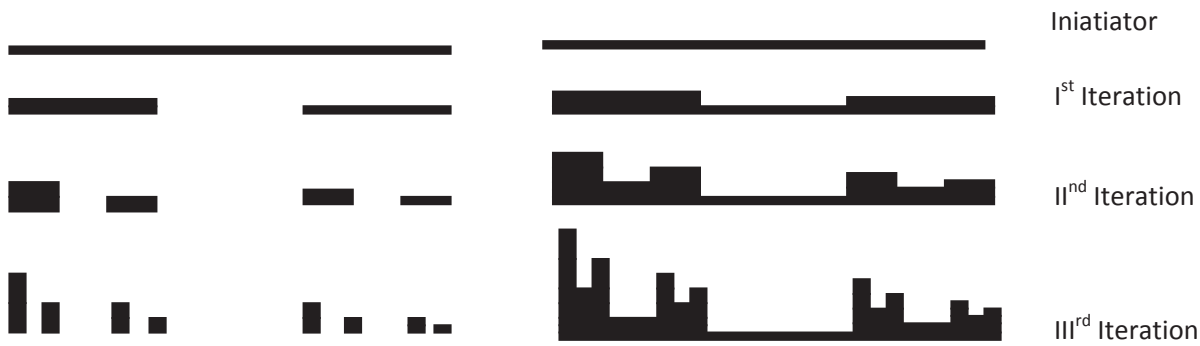

Figure1a. Different levels of iteration of multi-fractal cantor geometry

Figure1b. Different levels of iteration of the revised multi-fractal cantor geometry

The three overlapping segments are generated by applying the IFS(Iterated Function System) transformation coefficients of Table 1 into the transformation matrix shown below.

$$w_i \begin{bmatrix} x_1 \\ y_1 \end{bmatrix} = \begin{bmatrix} a_i & b_i \\ c_i & m_i * d_i \end{bmatrix} \begin{bmatrix} x \\ y \end{bmatrix} + \begin{bmatrix} e_i \\ f_i \end{bmatrix}$$

w_i	a_i	b_i	c_i	d_i	e_i	f_i	m_i
Left segment	1/3	0	0	1	0	0	2
Right segment	1/3	0	0	1	2/3	0	1

Table1. IFS Transformation Coefficient for multi-fractal cantor set

Here (x_1,y_1) represents the coordinates of the transformed layer, (x,y) represents the co-ordinates of the initiator, a_i, b_i, c_i, d_i, and m_i are the scaling coefficients and e_i and f_i are the translation coefficients. In the multi-fractal cantor geometry, instead of removing the middle segment a Revised Multi-fractal Cantor Geometry is developed by retaining the middle segment and concatenating each layer of iteration with the previous layers of iteration starting with the initiator as shown in figure 1(b).

RFID Tag Design and Testing: The Configuration of the proposed UHF RFID tag based on multi-fractal cantor printed dipole antenna is shown in figure 3. Each arm of the dipole is

developed using the revised multi-fractal cantor geometry which is shown in Figure 1b, with an initiator of length 49mm ,width 2mm and IFS Transformation Coefficients of Table 1. The separation between two arms is 2mm. The dipole is fabricated on an FR4 substrate of thickness 1.6mm and dielectric constant ϵ_r =4.9. The cantor geometry will itself provide some inductance. Additional inductance is provided by the closed loop. The tag consist of an antenna and a chip which has an impedance of 27-j211 at 866 MHz.

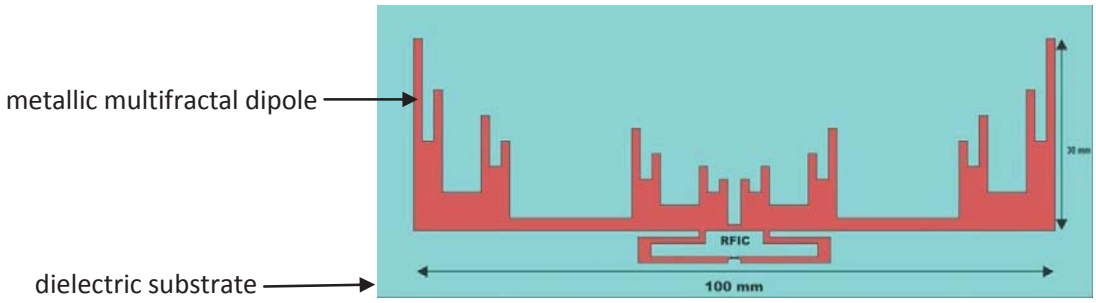

Figure 3. Structure of the RFID tag based on multi-fractal structures

The read range measurement is carried out with STA IR0507E reader with a receiver sensitivity of -80 dBm and RF power of 28 dBm with circularly polarized waves. The tag is mounted on a movable platform with an arrangement for placing the tag for different azimuth and elevation angles. Placing the tag at a particular orientation, the read range is measured by moving the turn table with the tag to the maximum distance to which the tag is read for that orientation.

Results And Discussions: The design and simulation of the antenna is performed in the CST environment to get optimum performance. The plot of the real and imaginary part of the impedance of the antenna is shown in Figure4(a) and Figure4(b). It can be seen that the tag antenna has an impedance of 31+j151 at 866 MHz which is close to the chip impedance.

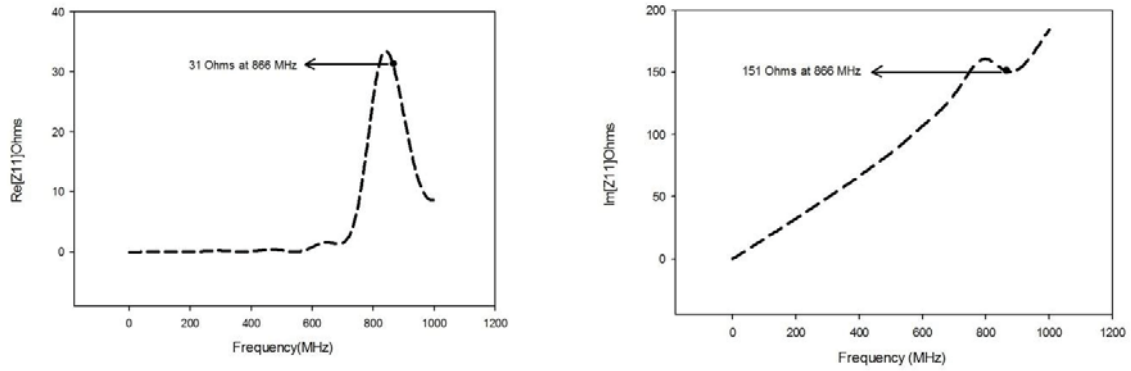

Figure 4. Variation of Antenna impedance with frequency for the tag antenna with …..

(a). Real Part of Antenna Impedance (b). Imaginary part of antenna impedance

The measured read range of the tag antenna in the UHF RFID band for elevation and azimuth angular angle is illustrated in Figure 5(a) and 5(b) respectively.

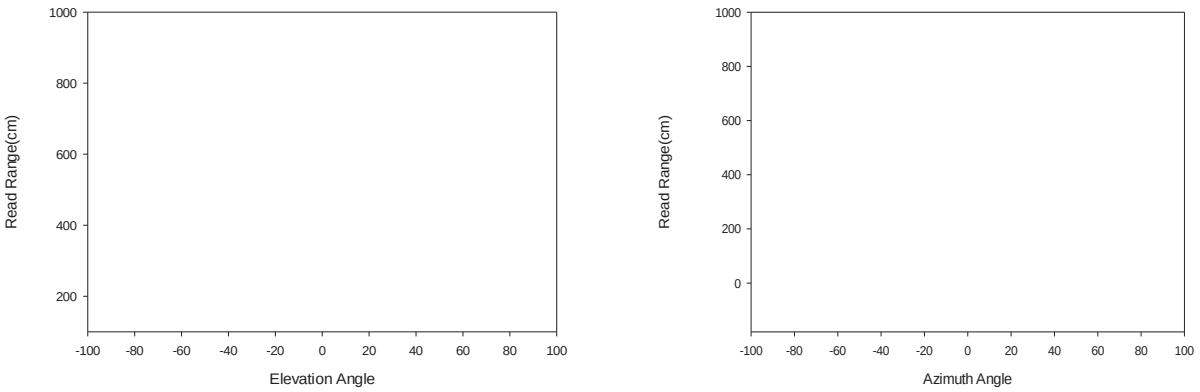

Figure 5. Measured variation of read range for (a) elevation angle. (b) azimuth angle.

Figure 5(a) shows that the read range is almost constant over the entire elevation angular range with a maximum value of 8.1 m . From figure 5(b) it is clear that read range is maximum at Θ=0, and decrease with azimuth angles on either side.

Conclusion: A novel design of a UHF RFID tag whose dipole arms are developed using multi-fractal cantor geometry is reported. The antenna has an impedance of 31+j151. The impedance of the antenna can be adjusted by tuning the fingers of the cantor structure and also by varying the parameters of the closed loop. The tag exhibits a read range of 8.1m over the entire elevation range and over wide angular range in the azimuth angular range.

Acknowledgement: One of the authors Mrs. Manju Abraham acknowledges the University Grants Commission (UGC) Govt. of India for providing a research fellowship under the Faculty Development Programme for Ph.D degree.

References:

1. K. Finkenzeller, RFID Handbook, 2nd edition. John Wiley &son, England 2003.
2. K. V. S. Rao, P. V. Nikitin, and S. F. Lam, "Antenna design for UHF RFID tags: a review and a practical application," IEEE Transactions on Antennas and Propagation, vol. 53,No. 12, pp. 3870–3876, 2005.
3. Yang P.H., Yan Li, Lijun Jiang" Compact Metallic RFID Tag Antennas With a Loop-Fed Method "IEEE Transactions on Antennas and Propagation",Vol.59,pp 4454-4462,Dec 2011
4. Juno Ahn, Hyungmin Jang, Hyosang Moon, Jong Wook Lee," Inductively Coupled Compact RFID Tag Antenna at 910 MHz With Near-Isotropic Radar Cross-Section Patterns", IEEE Antennas and Wireless Propagation Letters , vol 6, pp 518-520,2007
5. Design Fundamentals and Advanced Techniques of RFID Antennas, Open Access Database, www.intech.web.org.RFID Applications",
6. Yalin Guan, Zhuming Zhou, Huaibao Xiao and Yanfei Li," A Novel Design of Compact Dipole Antenna for 900 MHz and 2.4 GHz", Progress in Electromagnetic Letters, Vol. 45. pp 99-104, 2014.
7. B. Manimegalai, S. Raju,"A MultiFractal Cantor Antenna For Mutiband Wireless Applications", Antenna and Wireless Propagation Letters, vol 8, pp 359- 362,2009
8. O.Angelsky, A.Kovalchuk, P.Maksimyak," Diffraction of Optical Fields on Multifractals", http://optics.sgu.ru/SFM99/Angelsky

DECEMBER 19, FRIDAY
08.30AM TO 10.30AM
RESEARCH SESSION 11
MICROWAVE DEVICES 3
J C BOSE- HALL

Chair: Prof. K T Mathew, Viswajyothi College of Engineering and Technology, Vazhakulam.

No	Papers	Page
11.1	**Application of Resonance Microwave Probes as Electron Density Sensor** S. K. Karkari[1], M. P. Jayakrishnan[2] and P. Mohanan[2] [1]Institute for Plasma Research, Bhat Gandhinagar, Gujarat, 382428, India. [2]Center for Research in Electromagnetics and Antennas, Cochin University of Science and Technology, Cochin, Kerala. *E-mail: skarkari@ipr.res.in*	337
11.2	**EM Performance Predictions of a Hypersonic Radome** Raveendranath U. Nair, Sandhya S, and R. M. Jha Centre for Electromagnetics, CSIR-National Aerospace Laboratories (CSIR-NAL) Bangalore-560017, India. *Email: raviunair@nal.res.in*	343
11.3	**Compact Planar Lowpass Filter with sharp roll-off and wide stopband using Multiple Patch Resonators** Raphika P.M.[1], Abdulla P.[2], and Jasmine P.M.[3] Division of Electronics, School of Engineering, CUSAT, Kochi, Kerala, India, Pin-682022, *Email:[1]pmraphika@yahoo.co.in,[2]abdullaece@gmail.com* *[3]jasmine.maiyn@gmail.com*	347
11.4	**RF MEMS Based Switchable Tri/Dual/Single-Band Bandstop Filter using Stub Loaded Open Loop Resonator** Nagendra Kumar and Yatendra Kumar Singh Indian Institute of Technology, Patna 800013, India. *Email: nagendra@iitp.ac.in*	351
11.5	**Compact MEMS DMTL Phase Shifter** B. Anudeep[1] , and Usha Kiran .K [2] *VIT University Chennai Campus, Chennai 600127, India.* *Email: [1]anudeep.b2013@vit.ac.in, [2]usha.kiran@vit.ac.in*	355
11.6	**Low Voltage RF Mems Capacitive Shunt Switches** B.K.Arun Chowdhary [1] , Usha Kiran K. [2] VIT university, Chennai, Tamilnadu 6000127. *Email: bkarun.chowdhary2013@vit.ac.in , usha.kiran@vit.ac.in,*	359

11.7 **Compact Dual-Band Band Pass Filter Using λ/2 ACS-SIR** 363
A.Kamalaveni [1] and M.Ganesh Madhan [2]
MIT Campus, Anna University, Chennai, India 600044.
Email: [1] kamalaveniganesh@gmail.com, [2]mganesh@annauniv.edu

11.8 **Microwave dielectric properties of $Ca_3V_4O_{13}$ ceramics for ULTCC applications** 367
Suersh E.K., Arun.N.S. , Naveen Raj. R, and Ratheesh.R
Microwave Materials Group, Centre for Materials for Electronics Technology (C-MET), Department of Information Technology, Government of India, Thrissur, Kerala 680771, India.
E-mail ratheeshr@yahoo.com

11.9 **Compact Hexagonal Split Ring Resonator Dual Band Bandstop Filter** 371
Jasmi .J[1], Manju Bhaskar[1], and Thomaskutty Mathew[2]
[1]KMEA Engineering College, Ernakulam 683561, India.
Email: jasmijalal@yahoo.co.in[1], mbr.ec@kmeacollege.ac.in[1]
[2]School of Technology and Applied Sciences , Ernakulam 682024, India.
Email: drtkmathew@yahoo.co.in

11.10 **Dual Band Circular Polarizer using Superstrate with Split Ring Structure** 375
Anindya Ghosh, Binay Kumar Sarkar
Indian Institute of Technology, Kharagpur 721302. India.
Email: anindyaghosh.ghosh4@gmail.com, bks@ece.iitkgp.ernet.in

11.11 **Biphasic Calcium Phosphate-Arrowroot film for microwave phantom applications** 379
Ullas G Kalappura[1] and K. T. Mathew[2]
[1]Microwave Materials Research Laboratory,Department of Electronics, Cochin University of Science and Technology, Cochin- 682022, India.
E-mail: ullasgk@gmail.com.
[2]Viswajyothi College of Engineering and Technology,Vazhakulam, 686670, India. *E-mail: kattackalmathew@gmail.com*

Application of Resonance Microwave Probes as Electron Density Sensor

S. K. Karkari [1], M. P. Jayakrishnan [2] and P. Mohanan [2]
[1] Institute for Plasma Research, Bhat Gandhinagar, Gujarat, India, 382428
[2]Center for Research in Electromagnetics and Antennas, Cochin University of Science and Technology, Cochin, Kerala
E-mail:skarkari@ipr.res.in

Abstract: A concept of measuring local electron density in weakly magnetized plasma based on quarter wave resonator was introduced by Stenzel in 1976. In the recent years, the technique has attracted noticeable interest for diagnosing industrial plasmas. The resonance probes, also popularly known as hairpin probe (HP) because of its characteristic shape, have been successfully applied in many industrial plasma systems including deposition plasmas and dual radio-frequency operated confined CCP discharge.The principle is based on supporting a standing wave that corresponds to the plasma permittivity in the near field region around the resonator. The above probing technique has the advantage over microwave interferometer because they are capable of providing local measurement of electron density.

One important application of resonance microwave probe is its capability of providing spontaneous response to the change in dielectric medium around the probe head. This unique property can therefore be employed as a sensor for monitoring the plasma during long-pulse operation in industrial plasma tools. In this paper we describe the underlying principle behind the resonance hairpin probe and finally introduce the concept of split-ring-resonator as a possible substitute for plasma surface diagnostics. The split-ring-resonator (SRR) is unique in the sense that it can be mounted on the wall of the plasma chamber therefore it is less perturbing to the plasma. Additionally the diagnostics can provide useful information about the state of plasma adjacent to the substrate during dielectric etching and plasma deposition treatments. A comparative study of SRR with the conventional hairpin probe applied in a magnetized linear plasma device is presented and its prospective role as a diagnostic sensor is discussed.

Introduction: Microwave based diagnostics are the heart of many professional hi-tech systems across the world as they are extensively used in wide range of research applications including radio-communication, medical diagnostic, surface engineering and for evaluating material properties. In plasma physics, applications of microwave diagnostic is well known from the study of ionosphere plasma. The plasma behaves as a dielectric medium since it has a natural tendency to react as an absorber, or reflector of electromagnetic waves. The dielectric property of plasma is a function of electron density. Therefore when electromagnetic wave traverses through the plasma, it can get reflected or absorbed after encountering different layers with variable electron density inside the plasma. This is the underlying principle behind the microwave interferometry technique which provides the precise measurement of electron density. However, the technique is by far limited to measurement of averaged density of the plasma and it is complex to interpret the state of bulk plasma having steep density gradients.

In 1976 Stenzel introduced the concept of quarter wave resonator for diagnosing local electron density in weakly magnetized plasmas. Unlike the microwave interferometry technique, which relies on the propagation of electromagnetic waves through the medium of plasma, the quarter wave resonator on the other hand is based on change in the resonance frequency due to the variation of plasma permittivity in the vicinity. Therefore in the recent years, this technique has attracted noticeable interest for diagnosing industrial plasmas. The resonance probes, are also

popularly known as hairpin probe due to its characteristic shape, have been successfully applied in many industrial plasma systems including deposition plasmas and dual radio-frequency operated confined CCP discharge. Beside hairpin probe, several variations of microwave resonator probes have been developed. The commonly employed probes are the plasma oscillation, plasma absorption, plasma transmission, plasma cut-off, multi-pole resonance, LC resonance, and the curling probes. The above names mainly differ in terms of the measurement technique applied but their principle is originally based on dielectric response of the plasma towards the incident EM wave. The above probing techniques have the advantage over the microwave interferometer because of their capability to provide local measurement of electron density.

Although having the unique property to detect the changes in adjunct plasma dielectric, its usefulness remained largely underexplored, primarily because of its physical dimension. A promising application is to develop a diagnostic tool that can monitor the plasma density adjacent to the physical substrates introduced inside the plasma. In this regard a compact probe head that can be adapted to the chamber wall as well at the substrate can be highly beneficial as a tool for diagnosing plasma characteristics at the plasma-sheath interface.

The resonance hairpin probe: The hairpin probe is represented as two-wire parallel transmission line whose one end is short-circuited while the other end is kept open. The length of each arm is equivalent to a quarter wavelength while the effective path-length is λ/2 from tip to tip. A given dielectric medium will support a quarter-wave that will correspond to a unique frequency. The formula for the probe's resonance is given by,

$$f_r = \frac{c}{4L\sqrt{\kappa_p}} \tag{1}$$

Where κ_p is the Plasma permittivity and c is is the speed of EM waves in vacuum.

When the resonance condition is achieved, an intense time varying electric field is sustained in the region around the open ends of the hairpin. With the introduction of plasma dielectric, the resonance frequency shifts towards the higher frequency. Naturally $\kappa_p < 1$ and is expressed as.

$$\kappa_p = 1 - \frac{f_{pe}^2}{f_r^2} \tag{2}$$

Where f_{pe} is the Electron Plasma Frequency.

In (2) $f_{pe} = 9000\sqrt{n_e}$ is the plasma frequency with n_e per cm^3, while f_r is the frequency of the resonator. Combining equations (1) and (2), the electron density is,

$$n_e[10^{10} cm^{-3}] = 1.23\ (f_r^2 - f_{vac}^2) \tag{3}$$

where f_r and f_{vac} are the resonant frequencies in plasma and vacuum respectively.

Measurement Methodology: A $\frac{\lambda}{4}$ hairpin excited with a small loop antenna is used for the study gives rise to a lumped inductance and distributed capacitance along the length of the hairpin. A small loop antenna is situated at the short-circuited end to inductively drive the hairpin from a voltage controlled variable microwave source typically in the range of 2.0 – 18.0 GHz. When the drive frequency corresponds to the quarter-wavelength of the hairpin, intense electric field is developed around the open ends. A directional coupler and schottkey diode is placed in the path of the microwave source and the 50 Ω coax to the loop-antenna to measure the reflected power. When the applied frequency is tuned to resonance, a significant power is dissipated in the hairpin causing reduction in the reflected power. This enables detecting the resonance frequency by

monitoring the r.m.s. value of the reflected signal verses the voltage controlled signal to the microwave source on the oscilloscope. This is shown in figure-2.

Instead of applying variable frequency scan, one can apply a fixed frequency to the hairpin and detect the dynamic value of resonance frequency in the case of pulse-plasmas in which the electron density is periodically varying due to modulation of discharge power. The technique can be automated and the synchronous value of resonance frequency corresponding with the pulse discharge waveform is obtained to find the time-modulated electron density.

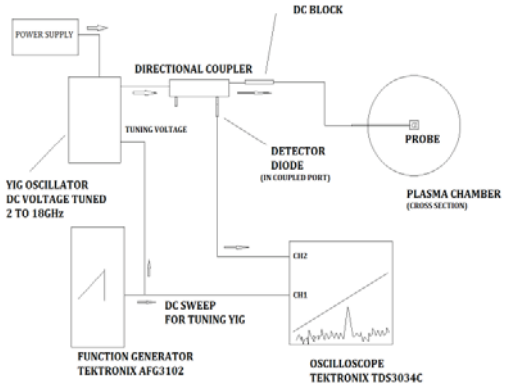

Figure-1 *The Experimental Setup.*

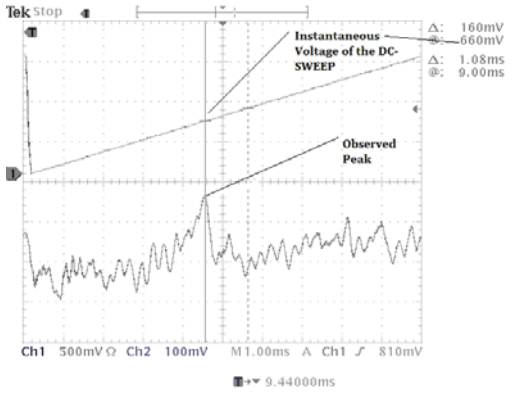

Figure - 2 *The Data extraction technique.*

Split ring resonator: The split-ring-resonator (SRR) comprise of two concentric circular rings having splits at diametrically opposing ends. The structure is constructed on a dielectric substrate. A loop antenna situated at the back of the dielectric couples the microwave signal to the resonator. A resonance condition is achieved when maximum transfer of energy takes place from the coupling loop to the SRR. A Matlab based GUI calculator [2] is used in this study to calculate the dimensions of the SRR. The parameters of the Split Ring Resonator are detailed below.

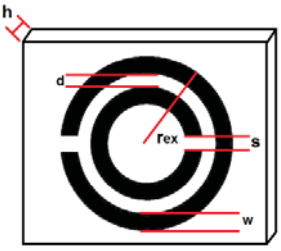

Figure-3 *The Proposed SRR geometry.*

Desired frequency = 3GHz.
Substrate used = FR4 (Relative permittivity 4.4).
External radius (rex) = 4.2mm.
Width of rings (w) = 0.6mm.
Gap between the rings (d) = 0.6mm.
Slot width(s) = 0.3mm
Predicted frequency = 2.9697GHz (Calculator).

The resonance characteristic of an SRR depends on the substrate as well as the dielectric properties of the material adjacent to the splits. In order to investigate the spatial resolution of the sensitive region, a dielectric slab (Teflon) is systematically displaced from infinity to the surface of the SRR. Figure 4 plots the resonance frequency as a function of axial distance z of the dielectric block. The sensitive region above the SRR is found to be of the order of 0.4 – 0.5 mm.

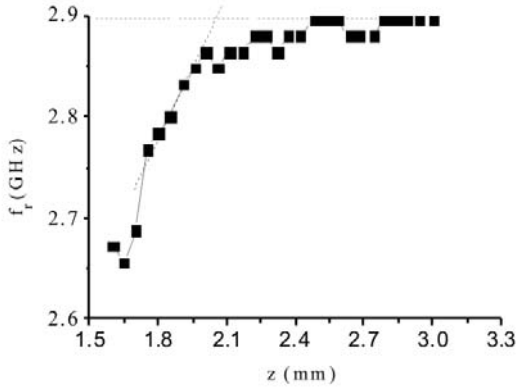

Figure-4 The Spatial Resolution analysis result.

Experimental set-up and results: The experiments are carried in the linear plasma device which comprises of a cylindrical vacuum chamber equipped with 5 sets of external electromagnet coils to produce an axial magnetic field up to 50 mT. This system is named APPEL-Device (Applied Plasma Physics Experiment on Linear Device) figure 5. Note that the Vacuum seals, cooling jacket, power supply unit and supporting structures are not shown, in order to simplify the diagram. The plasma source based on dc magnetron discharge is situated at one end of the chamber while the plasma column emanated from the source is suspended along the magnetic field. The experimental result showing the variation of resonant frequency with the electron Plasma frequency is depicted in figure 6.

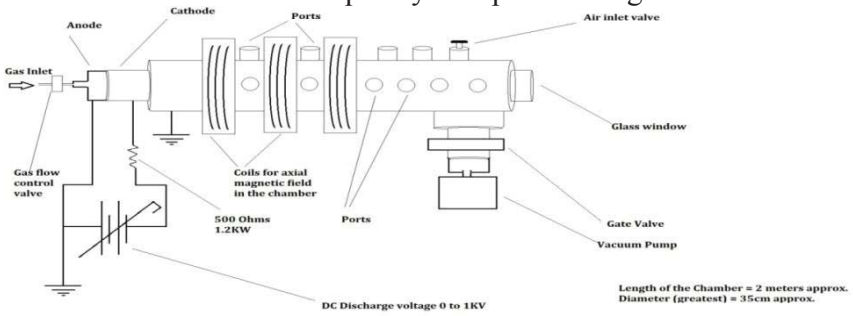

Figure-5 *the Plasma column(APPEL Device)*

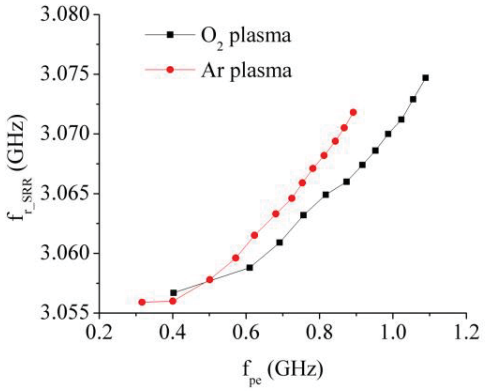

Figure-6 *The SRR resonance Frequency against the Electron Plasma Frequency.(* Pressure = 1.2 Pa, No magnetic field central**)**

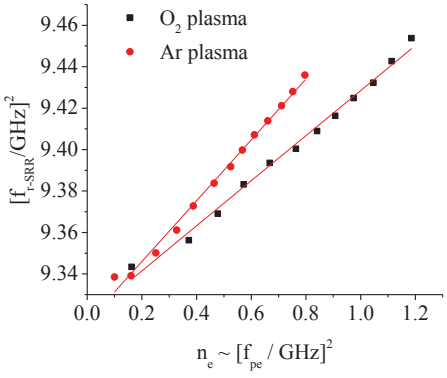

Figure-7 *The SRR resonance Frequency(Square) against the Electron Plasma Frequency (Square).(*Pressure = 1.2Pa,No magnetic field central)

The figure 7 shows the variation of the square of the resonance frequency of the SRR against the square of electron plasma frequency. This confirms that the square of the SRR resonance frequency is linearly proportional to the square of the electron plasma frequency. This behavior is similar to [1] as found in the case for the hairpin probe. Therefore it is possible to interpret the electron density by means of SRR probe provided a suitable scaling factor is found.

As expected the plot of the resonance frequency v/s the discharge power (figure 8) show a linear variation. This is consistent with the view that the electron density is linearly related with the power. In figure 9, the electron density which is proportional to the square of $f_{r\text{-}SRR}$ increases with the magnetic field to reach a peak value. Higher the discharge power higher is the plasma density. However the electron density tends to fall as the magnetic field is increased above 10 mT. This observation is consistent with the fact that the secondary electrons which are the primary source of ionization in dc operated magnetron source are reabsorbed at the cathode surface owing to strong magnetic field transverse to the cathode. The initial rise in the density with modest magnetic field B < 10 mT is because of efficient trapping of the secondary electrons within the cylindrical volume of the hollow cathode. Therefore the SRR technique is useful for determining the variation in electron density parameters in a discharge.

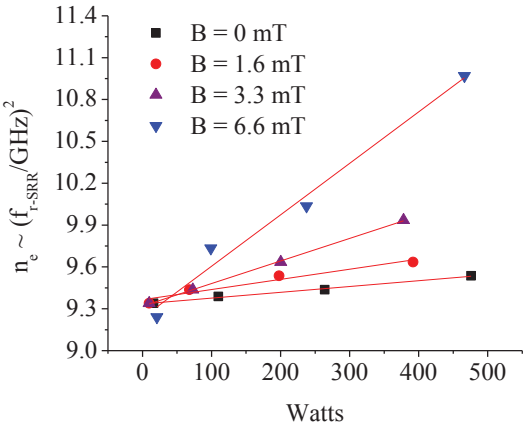

Figure-8 *The behavior of SRR to varying DC discharge-power.(* Oxygen, Pressure = 1.2 Pa, center of the plasma column)

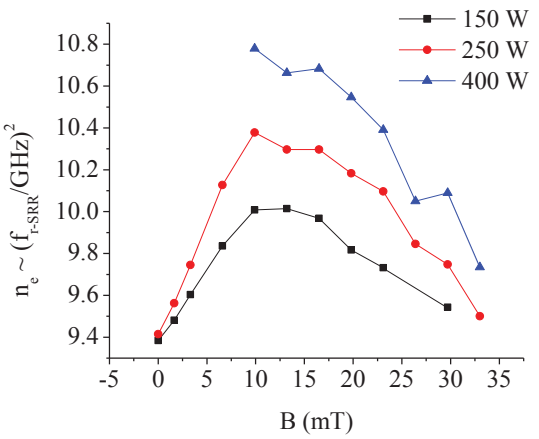

Figure-9 *The behavior of SRR to varying Magnetic field.(* Oxygen, Pressure = 1.2 Pa, center of the plasma column)

Discussion: The resonance microwave probe is a simple yet a powerful diagnostic tool for the measurement of electron density in the discharge plasma. The underlying principle is based on the resonance of the probe entity which is determined by the lumped inductance and distributed capacitance of the resonator. Indirectly this is related to the effective dielectric constant of the medium surrounding the probe.

The response of the SRR towards the presence of adjunct dielectric is systematically carried with the CST microwave studio. The study finds that the sensitive region around the SRR is confined within 1 mm. Therefore the probe can be ideally suited for observing the effects near the plasma surface. Due to its flat compact profile, the SRR can be embedded on the walls of the vacuum chamber. The benchmarking of the SRR technique against the standard hairpin probe displays linear variation with the plasma density. Hence the technique can be suitable as a method for determining relative variation in the plasma parameter adjacent to the probe surface.

Conclusion: In this paper we demonstrate an alternative design based on SRR. The performance of this technique is demonstrated against the conventional microwave resonance probe in magnetized linear plasma device. The variation in electron density with the external discharge parameters such as operating discharge power and the external magnetic field are found to be in reasonable agreement with the expected parameters of the discharge. Due to the compact design of the SRR, it is considered as one of the potential technique which can give valuable information in the vicinity of the target surface exposed to the plasma. A detail investigation is currently under progress to benchmark this technique against standard diagnostic technique. This will be helpful in finding the absolute formula for interpreting the electron density directly using this device.

References

[1] R. B. Piejak, V. A. Godyak, R. Garner, and B. M. Alexandrovich, "The hairpin resonator: A plasma density measuring technique revisited". Applied Physics Letters, 2004.
[2] Anju Pradeep, S. Mridula and P.Mohanan, "Design of an Edge-Coupled Dual- Ring Split-Ring Resonator", Antennas and Propagation Magazine, IEEE Volume: 53, Page(s): 45 – 54, 2011.
[3] G. S. Gogna, C. Gaman, S. K. Karkari, and M. M. Turner, "Dielectric covered hairpin probe for its application in reactive plasmas", Applied Physics Letters, 2012.
[4] G. S. Gogna, S.K. Karkari, D. Boilson, M.M. Turner, "Theory and application of hairpin probe in strongly magnetized plasma", 37thEPS Conference on Plasma Physics.
[5] Frank Hesmer, et al. "Coupling mechanisms for split ring resonators: Theory and experiment" phys. stat. sol. (b) 244, No. 4, 1170 – 1175 (2007) / DOI10.1002/pssb.200674501, © 2007 WILEY-VCH Weinheim
[6] Alfred Grill, "Cold Plasma Materials Fabrication: From Fundamentals to Applications", ISBN: 978-0-7803-4714-4, March 1994, Wiley-IEEE Press
[7] Robert J Goldston and Paul H Rutherford, "Introduction to Plasma Physics", 1995 IOP Publishing Ltd.
[8] Christophe Caloz and Tatsuo Itoh, "Electromagnetic Metamaterials: Transmission Line Theory and Microwave Applications", 2006 John Wiley & Sons, INC., Hoboken, New Jersey.
[9] Filippo Capolino, "Metamaterials Handbook: Theory and Phenomena of Metamaterials", 2009, CRC Press - Taylor & Francis Group.
[10] Edward C. Jordan and Keith G. Balmain, "Electromagnetic Waves and Radiating Systems", 1994, Prentice Hall, New-Delhi.

EM Performance Predictions of a Hypersonic Radome

Raveendranath U. Nair, Sandhya S., and R. M. Jha
Centre for Electromagnetics
CSIR-National Aerospace Laboratories (CSIR-NAL)
Bangalore-560017, India
Email: raviunair@nal.res.in

Abstract: *The electromagnetic (EM) performance of nosecone radomes of hypersonic flight vehicles degrade due to variation of dielectric properties resulting from large temperature gradient existing across the radome wall. Such radome walls can be modeled as inhomogeneous planar layer (IPL) structures consisting of stacked layers of dielectric materials with varying dielectric parameters. In the present work, the EM modeling of radome wall of a tangent ogive nosecone radome made of RBSN Ceralloy 147-010F in a hypersonic environment has been carried out based on IPL model. 3-D Raytracing in conjunction with Aperture Integration Method has been used for the computation of EM performance parameters of antenna-radome system. The present study establishes the potential application of IPL based radome wall model for better EM performance predictions of streamlined airborne radomes in hypersonic environments.*

Introduction: Streamlined nosecone radomes are used to protect the radar seeker antenna systems of hypersonic aerospace vehicles [1]. During such high mach flight operations, the temperature of the outer surface of the radome wall is much higher than that of inner surface due to high aerodynamic drag. The large temperature gradient existing across the radome wall results in drastic variations in the dielectric properties of the radome wall and hence radome EM performance parameters [2]. So the radome EM performance predictions during hypersonic flight operations based on conventional design of radome wall configurations (using average dielectric constant and electric loss tangent of radome material) may not be accurate. As the dielectric properties have significant effect on the EM wave propagation through the radome wall, the temperature-dependent EM performance predictions of streamlined nosecone radomes are in great demand for hypersonic airborne applications. For this purpose, temperature dependent EM performance predictions of a streamlined nosecone radome in a hypersonic environment based on *Inhomogeneous Planar Layer (IPL)* model are presented in this work.

IPL modeling of the radome wall: RBSN Ceralloy 147-010F is a promising radome material due to high-temperature resistance, excellent dielectric and mechanical properties [3]. The temperature dependant dielectric properties of this material are shown in Figure 1. The tangent ogive nosecone radome considered in this work is made of RBSN Ceralloy 147-010F (height = 400 mm; and base diameter = 200 mm). It encloses a monopulse slotted waveguide planar array antenna (diameter = 120 mm) operating at 10 GHz with cosine aperture distribution and TE polarization. The antenna is located at a distance of 80 mm from the radome base. The azimuth and elevation antenna scan ranges are ±60° respectively. The optimized half-wave wall thickness is 7.13 mm, which corresponds to maximum power transmission for TE polarization at high incidence angle 62° (applicable for the streamlined

radome considered here). For the estimation of the optimized wall thickness mentioned above, the average dielectric parameters (ε_r = 5.21; tanδ_e = 0.0033) of the material over 25°C - 1400°C are considered. In hypersonic applications (Figure 2), the large temperature gradient existing across the RBSN Ceralloy 147-010F radome wall makes it an *inhomogeneous planar layer* (IPL). This IPL radome wall configuration is assumed to be made up of stacked dielectric layers with varying temperature-dependent dielectric parameters. Polynomial curve fitting is used for identifying the boundaries of dielectric layers of the IPL model of radome wall based on the temperature-dependent dielectric data of the material. Further the dielectric parameters corresponding to the average bulk temperature of each layer are estimated. Then the IPL radome wall is considered as a transmission line with different sections corresponding to different dielectric layers (Figure 3).

EM performance predictions of antenna-radome system: The interaction of the slotted waveguide planar array antenna with the radome is carried out by a 3-*D Raytracing* procedure in conjunction with *Aperture Integration Method* [4]. The EM performance parameters of the radome are computed by considering the antenna-radome system w.r.t. the antenna alone reference. Here '*Monolithic Model*' refers to the conventional monolithic half-wave radome wall design based on average dielectric parameters, whereas '*IPL Model'* refers to the radome wall of same material and thickness in actual operating conditions (*i.e.* in hypersonic environment) at the high mach speeds. In the present work, three EM window regions (R1, R2, and R3) are considered for the EM performance predictions based on the temperature profile available for a radome in a hypersonic environment [5]. Table 1 shows the approximate temperature ranges existing across the radome wall in the hypersonic environment corresponding to different window regions. As discussed above, the radome wall in each window region is considered as an IPL structure due to large temperature gradient existing across it. Polynomial curve fitting is used for identifying the boundaries of dielectric layers of the IPL model of the radome wall for each window region based on the measured dielectric data of the material over the corresponding temperature range.

Table 1. Approximate temperature ranges across the radome wall in EM window regions

EM window region	Antenna scan range	Approximate temperature range across the radome wall
R1	0°-15°	860°C - 1400°C
R2	15°- 45°	775°C - 1300°C
R3	45°- 60°	240°C - 775°C

It is noted that the angle of incidence is maximum at the radome nose-tip as the antenna beam is pointing along the radome-axis and it decreases with the increase in antenna scan angle. For the antenna-radome system considered in the present work, the angle of incidence is varying from 56°-62° in window region R1. Figures 4a and 4b show the co-pol power transmission and boresight error (BSE) characteristics of the radome in the window region R1, respectively. It is observed that the co-pol power transmission is low for *IPL Model* as compared to that of *Monolithic Model*. Further the boreseight error of *IPL Model* is higher than that of *Monolithic Model* in this window region. In window region R2, the angle of incidence is varying from 34°-56°, corresponding to the antenna scan range. The EM performance characteristics of the radome in the window region R2 are shown in Figures 5a and 5b. Here the co-pol power transmission of *IPL Model* shows drastic degradation as compared to *Monolithic Model*. Further BSE characteristics of *IPL model* also show

degradations as compared to monolithic case. It is observed that the EM performance characteristics of *IPL Model* do not vary considerably from that of *Monolithic Model* in window region R3 and hence those results are not included.

Conclusion: The EM performance analysis of a tangent ogive radome (made of RBSN Ceralloy 147-010F) has been carried out for conventional *Monolithic Model* and *IPL Model* of radome wall for given EM window regions corresponding to the angular sectors of antenna scan range. The study establishes the efficacy of the *IPL Model* over the conventional *Monolithic Model* for the EM performance predictions of radome in a hypersonic environment. Further, the present work indicates that the radome wall thickness has to be selectively chosen for given window regions of the radome to obtain better impedance matching required for superior EM performance in a hypersonic environment.

Reference:

[1] D. J. Kozakoff, *Analysis of Radome enclosed Antennas*, Artech House, Norwood, USA, ISBN 13: 978-1-59693-441-2, p. 265, 2010.

[2] W. H. Poisl, C. Solecki, and J. M. Wahl, "Mission challenges spur next generation missile radome materials innovations," *Raytheon Technology Today*, No. 2, pp. 64-65, 2012.

[3] J. Mangles, B. Mikijelji, and B. Lockhart, "Ceramic radomes for tactical missile systems," www.ceradyne-thermo.com.

[4] R. U. Nair and R. M. Jha, "Electromagnetic performance analysis of a novel monolithic radome for airborne applications," *IEEE Transactions on Antennas and Propagation*, Vol. 57, No. 11, pp. 3664-3668, 2009.

[5] N. R. Kilcoyne, "A two-dimensional ray-tracing method for the calculation of radome boresight error and antenna pattern distortion," ElectroScience Laboratory, Dept. of Electrical Engineering, The Ohio State University, Columbus, Ohio, USA, Tech. Rep. 2767-2, p. 114, 1969.

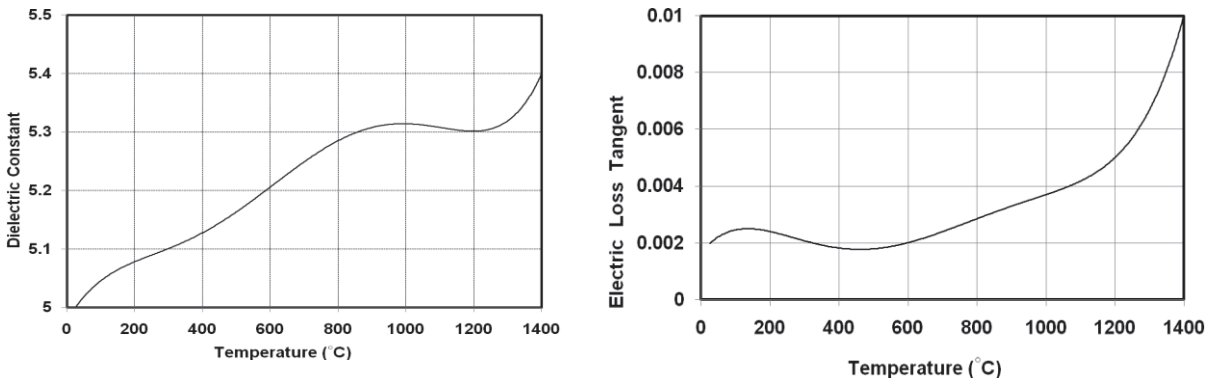

(a) (b)

Figure 1. Variation of dielectric parameters of RBSN Ceralloy 147-010F with temperature (based on [3]). (a) Dielectric constant, (b) Electric loss tangent.

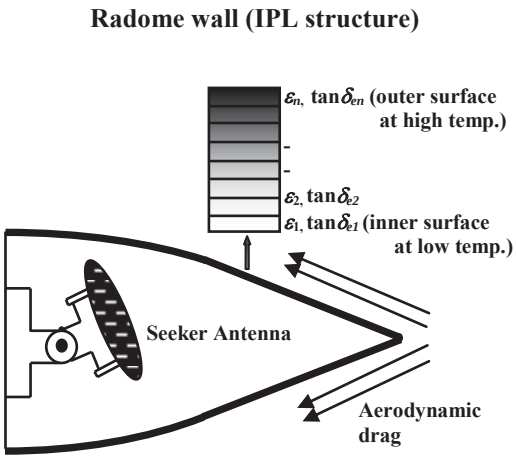

Figure 2. Schematic of hypersonic radome under actual operating conditions.

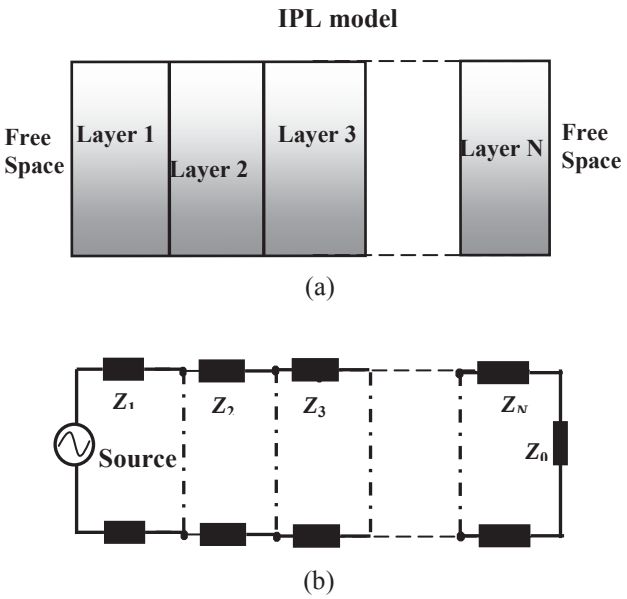

Figure 3. (a) IPL model of radome wall. (b) Equivalent circuit model of IPL structure.

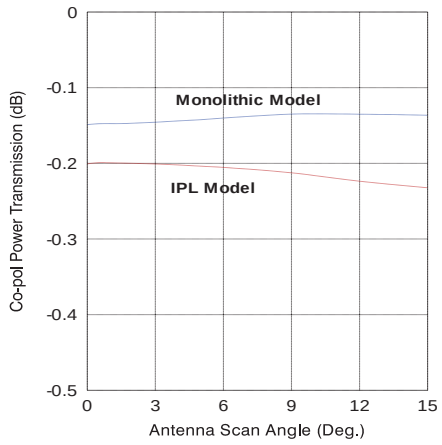

Figure 4a. Co-pol power transmission characteristics in Window Region R1.

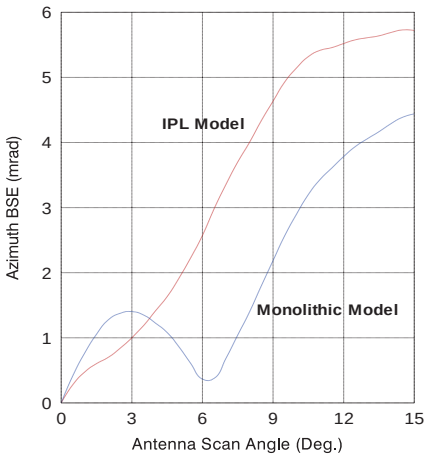

Figure 4b. BSE characteristics in Window Region R1.

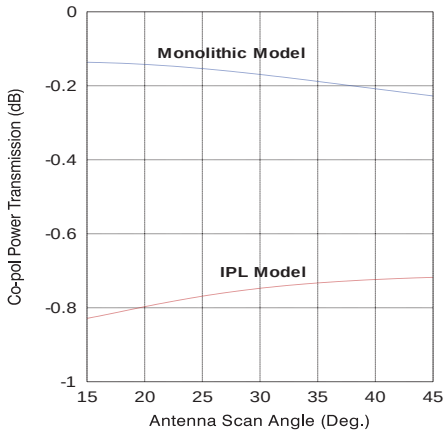

Figure 5a. Co-pol power transmission characteristics in Window Region R2.

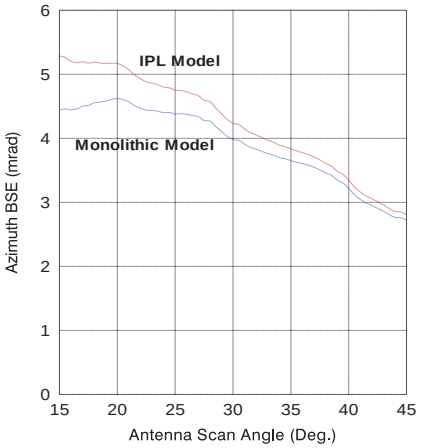

Figure 5b. BSE characteristics in Window Region R2.

Compact Planar Lowpass Filter with sharp roll-off and wide stopband using Multiple Patch Resonators

Raphika P.M.[(1)], *Abdulla P*[(2)], *and Jasmine P.M.*[(3)]
(1, 2, 3) Division of Electronics, School of Engineering, CUSAT, Kochi, Kerala, India, Pin-682022,
Email: (1) pmraphika@yahoo.co.in, (2) abdullaece@gmail.com, (3) jasmine.maiyn@gmail.com.

Abstract: *This article presents a new compact microstrip lowpass filter with sharp roll-off and ultra wide stopband using corner cut triangular patch and modified funnel patch resonators. The patch resonators are placed symmetrically about a high impedance central microstrip line. The filter has been designed and fabricated using low cost FR4 material. The experimental results show very good agreement with the simulated results and demonstrate that, the sharp roll-off and good stopband performance is obtained by the proposed filter. The 3 dB cutoff frequency of the proposed filter is at 2.5 GHz with a roll-off of 85 dB/GHz and its stopband extends up to 9.95 GHz.*

Introduction: High performance and compact lowpass filters are in great demand for present communication systems to suppress harmonics and spurious signals. Microstrip filters offer low insertion loss in the passband and infinite attenuation in the stopband together with compact size, low cost and ease of fabrication. Filtering of undesired frequencies using microstrip can be accomplished with conventional design techniques such as stepped impedance lines or tuned stubs. However, these filter structures require large layout area in order to obtain sharp frequency characteristics [1]. Compactness and sharp roll-off will be obtained by introducing defective ground structure, which also exhibits wide harmonic suppression and slow wave characteristics [2]–[3]. But these filters have additional radiation due to partially opened ground plane and cannot be fixed on a metal base due to the inherent defects in the ground plane. Various methods have been proposed to develop a high performance, compact microstrip lowpass filters by cascading multiple resonators [4]–[8]. A microstrip lowpass filter using the stepped impedance hairpin resonator was reported in [4]. Even though the size reduction was achieved in this configuration, the response is not very sharp. Good stopband performance was achieved by multiple resonators and meander transmission line [5]–[6], the filter passband was too narrow and its transition characteristics were very poor. Moreover the above mentioned filters are designed using high cost substrate. Sharp roll-off lowpass filter with wide stopband using stub loaded coupled line hairpin unit fabricated on FR4 was reported in [7], but its passband is too narrow and there exist periodic fluctuation of more than 15 dB of return loss in the stopband. A compact microstrip lowpass filter with sharp roll-off and ultra wide stopband using low cost substrate have been reported by the authors [8], in which, cutoff frequency was 5.55 GHz and the fractional stopband bandwidth achieved was only 66.96 %.

In this paper, a compact and low cost lowpass filter with very sharp roll-off and wide stopband is presented. The cutoff frequency of the proposed filter is 2.5 GHz. The filter achieves a roll-off of 85 dB/GHz and an ultra wide stopband better than 23 dB from 2.73 GHz to 9.95 GHz. The size of the filter is very compact and has a physical dimension of about 15.4 mm x 12.6 mm.

Filter Design and Simulation: We can enhance the fractional stopband bandwidth as well as the compactness of the filter already reported [8] by scaling the geometry of the filter. As physical size increases, the effective inductance and capacitance of the filter will increase, that leads to the decrease in the cutoff frequency. But mere scaling up will introduce transverse resonance due to the decrease in the capacitance of the resonant patch [1]. The structure of the proposed filter is derived from TPRs and FPR by cutting the base corner of TPRs symmetrically, one corner is attached to FPR on both sides, as shown in Fig. 1. and the other corner is eliminated.

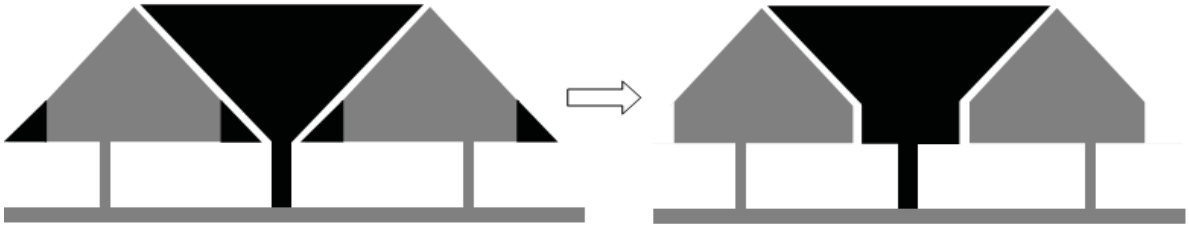

Fig. 1. Equivalent relation between TPRs and FPR & corner cutting TPRs and modified FPR.

Fig. 2. shows the layout of the proposed filter with corner cutting TPRs and modified FPR, are placed symmetrically about the high impedance central microstrip line. Since lower impedance patch results in a better approximation of a lumped-element capacitor and higher impedance leads to better approximation of a lumped-element inductor, the resonator parameters are selected accordingly to get a complete elliptic function response lowpass filter with sharp attenuation near the cutoff frequency. The impedance of the connecting stub of the centre resonators is 118 Ω and that of corner cutting TPRs is 146 Ω.

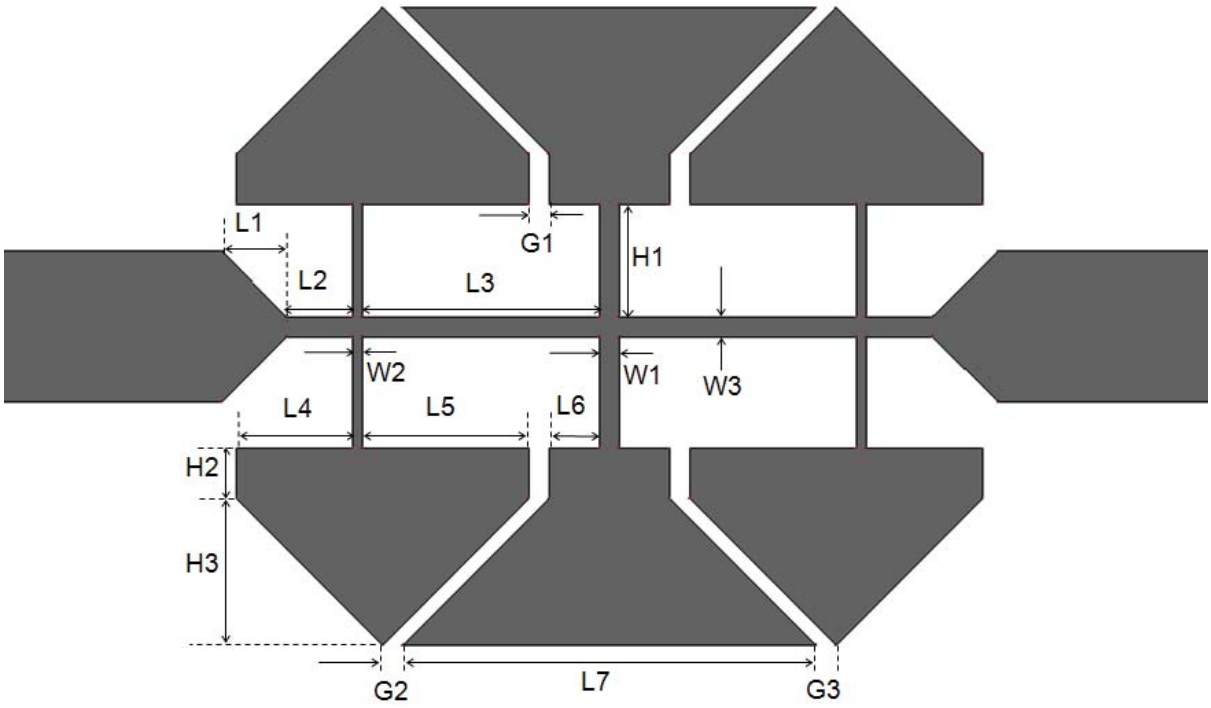

Fig. 2 Layout of proposed low pass filter

By suitably combining both resonators we can enhance the roll-off rate as well as the stopband performance. The sharp transmission zero near the cutoff frequency is due to the presence of patch resonators and the tight coupling between them, which enhances the shunt capacitance of the main transmission line. The wide stopband performance is achieved under

the combined effect of the three resonators. Cascading the separate resonators also increases the effective inductance and capacitance, which makes the structure a slow-wave transmission line. The cutoff frequency of the proposed lowpass filter is 2.5 GHz. The tapered microstrip line at the input and output feed line reduces the discontinuity effect associated with the step junction, which provides impedance matching with 50 Ω feed line and 118 Ω central microstrip line.

Fabrication and Measurement: The proposed filter has been designed and fabricated on a low cost FR4 substrate with relative permittivity 4.4 and thickness of 1.6 mm. The dimensions are L1 = 1.3 mm, L2 = 1.3 mm, L3 = 4.7 mm, L4 = 2.3 mm, L5 = 3.3 mm, L6 = 1 mm, L7 = 8.2 mm, W1 = 0.4 mm, W2 = 0.2 mm, W3 = 0.4 mm, H1 = 2.2 mm, H2 = 1 mm, H3 = 2.9 mm, and G1 = G2 = G3 = 0.4 mm. Excluding the microstrip feed line, the filter has a size of about 15.4 mm x 12.6 mm, which corresponds to the normalized circuit size of $0.23395\ \lambda_g$ x $0.191415\ \lambda_g$, where λ_g is the guided wavelength at 2.5 GHz. The simulation has been accomplished using electromagnetic simulation software Ansoft HFSS and fabricated using photolithographic process. The measurement was carried out using R&S ZVL 13 Vector Network Analyzer and 1.6 mm SMA connector.

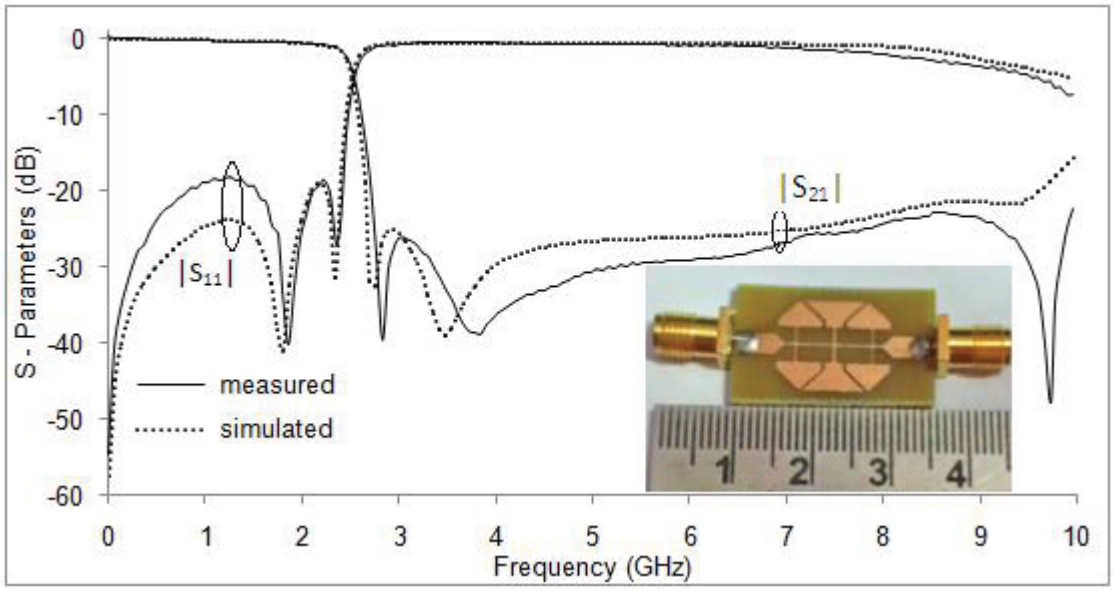

Fig. 3. Simulated and measured results of the proposed filter along with the photograph of fabricated structure

As shown in Fig. 5, the measured results are in good agreement with the simulated results. The measured result shows that the proposed filter has an insertion loss less than 0.6 dB in the passband up to 2 GHz, with a cutoff frequency of 2.5 GHz and stopband attenuation better than 23 dB from 2.73 GHz to 9.95 GHz and the return loss is less than 18 dB in the passband and close to 5 dB at 9.5 GHz. The high value of insertion loss in the passband and return loss in the stopband of the measured filter is due to the inherent dielectric losses associated with FR4 material (loss tangent 0.02). The measured roll-off rate of the proposed filter is 85 dB/GHz (20 dB attenuation frequency is 2.7 GHz). The roll-off rate, ξ is defined as:

$$\xi = \frac{\alpha_{max} - \alpha_{min}}{f_s - f_c} \text{ dB/GHz} \qquad (1)$$

where α_{max} is the 20 dB attenuation point and α_{min} is the 3 dB attenuation point; f_s is the 20 dB stopband frequency and f_c is the 3 dB cutoff frequency. A comparison of designed filter with the previous works is shown in Table I. From the table it is clear that the proposed filter, which is made of low cost FR4 substrate, gives high roll-off rate and suppression level among the quoted filters.

Table I: Comparison between proposed filter and previous work

Ref.	ξ	Stopband (GHz)	SL (dB)	Dielectric material	3 dB cutoff frequency (GHz)
[4]	18	2.0 - 15.0	10	RT/duroid 5880	1.5
[5]	18	1.57 - 12.64	15	Rogers RO4003	0.85
[6]	20	2.0 – 14.60	17	RT/duroid 5870	1.3
[7]	63	0.8 – 4.6	20	FR4	0.53
[8]	42	5.88 – 11.8	15	FR4	5.55
This Work	85	2.73 – 9.95	23	FR4	2.5

ξ – roll-off rate, SL – Suppression Level

Conclusion: A novel compact microstrip lowpass filter using patch resonators with tapered microstrip transmission line is presented. The filter has a cut-off frequency of 2.5 GHz with a sharp roll-off of 85 dB /GHz and an ultra wide stopband from 2.73 GHz to 9.95 GHz with fractional stopband bandwidth of 113.8 %. Its low insertion loss, wide stopband, sharp roll-off, low cost and compact size with simple topology make the filter suitable for various practical applications.

Reference:

[1] J. S. Hong and M. J. Lancaster, "Microstrip Filters for RF/ Microwave Applications," John Wiley, New York, 2001.
[2] C. J. Wang and C. H. Lin, "Compact lowpass filter with sharp transition knee by utilizing a quasi-π-slot resonator and open stubs," IET Microwaves Antennas & Propagation, vol. 4, no. 4, pp. 512 – 517, April 2010.
[3] A. S. Mohra, "Microstrip lowpass filter with wide rejection using open circuit stubs and z-slots defective ground structure," Microwave Opt. Technol. Lett., vol. 53, no. 4, pp. 811-815, February 2011.
[4] M. H. Yang and J. Xu, "Design of compact broad-stopband lowpass filters using modified stepped impedance hairpin resonators," Electronics Lett., vol. 44, no. 20, pp. 1198–1200, September 2008.
[5] H. Cui, J. Wang and G. Zhang, "Design of microstrip low pass filter with compact size and ultra-wide stopband," Electronics Lett., vol. 48, no. 14, pp. 856 – 857, July 2012.
[6] L. Ge, J. P. Wang and Y-X Guo, "Compact microstrip lowpass filter with ultra-wide stopband," Electronics Lett., vol. 46, no. 10, pp. 689 – 691, May 2010.
[7] V. K. Velidi and S. Sanyal, "Sharp roll-off lowpass filter with wide stopband using stub-loaded coupled-line hairpin unit," IEEE Microw. and wireless Compon. Lett., vol. 21, no. 6, pp. 301 – 303, June 2011.
[8] Raphika P.M., Abdulla P., Jasmine P.M., " Compact lowpass filter with a sharp roll-off using patch resonators," Microwave and Opt. Technol. Lett., Vol. 56, Issue 11, pp. 2534-2536, Nov. 2014.

RF MEMS Based Switchable Tri/Dual/Single-Band Bandstop Filter using Stub Loaded Open Loop Resonator

Nagendra Kumar[(1)] *and Yatendra Kumar Singh*[(1)]
(1) Indian Institute of Technology, Patna, India, 800013, Email: nagendra@iitp.ac.in

Abstract: *The paper presents a radio frequency micro-electro mechanical system (RF MEMS) based switchable tri/dual/single band bandstop filter (BSF). Tri-band BSF is designed using stubs loaded open-loop resonators. It is shown that three stopband of bandstop filter is fully and separately controllable using the length of stubs and the length of open loop resonators. This property of controlling stopbands using stubs are used to design switchable tri/dual/single band bandstop filter using RF MEMS switches. Based on the selection of RF MEMS switches four different kind of responses are achieved.*

Introduction: Multiband bandstop filters are one of the essential components in the wireless communication due to its property to reject spurious or unwanted signal at more than one frequency band without increasing the size of the filter. With the design of multiband filters, control and switching over those stopbands are highly desirable. Switchable stopband filters allow users to choose the stopband frequency according to the requirement. In recent radio frequency micro-electro mechanical system **(**RF MEMS) switches are one of the best devices to achieve switchable stopband filter due to their linear behavior and low insertion loss[**1**].

Recently RF MEMS switches are proposed to design a switchable filter with different functionality. In [**2**], bandpass to banstop switchable filter is designed using RF MEMS switch. RF MEMS switches are also used to design a filter having second, third and fourth order responses depending upon the condition of various switches [**3**].

In this paper a novel idea to design a tri-band bandstop filter is proposed. The proposed structure consists of open-loop resonators loaded with open and shorted stubs. The three stopbands are separately controllable using the length of open-loop resonators and the length of open and shorted stubs. RF MEMS switches are used to switch between these two stubs to achieve tri/dual/single stopband responses in a single structure without changing the dimensions.

Proposed Filter: Fig.1(a) shows the layout of the proposed second-order tri-band BSF. The open loop resonators are loaded with open stubs of length, l_2 with admittance, Y_2 and shorted stubs of length, l_3 with admittance, Y_3 as shown in Fig.1(b). The total length of the open loop is l_1 having admittance of Y_1. The feed lines and resonators are separated by a gap, s. As the circuit is symmetric, so even and odd mode analyses are performed to analyze the circuit. For odd mode excitation there is a voltage zero at the center of the loop. This simplifies the circuit to Fig. 1(c). So the odd mode resonant frequencies can be deduced as:

$$f_{odd} = \frac{c}{2l_1\sqrt{\varepsilon_{eff}}} \quad , \tag{1}$$

where c is the speed of the light in free space and ε_{eff} represents the effective dielectric constant of the substrate. It is clear that odd mode resonance is unaffected by the length of open and short stubs.

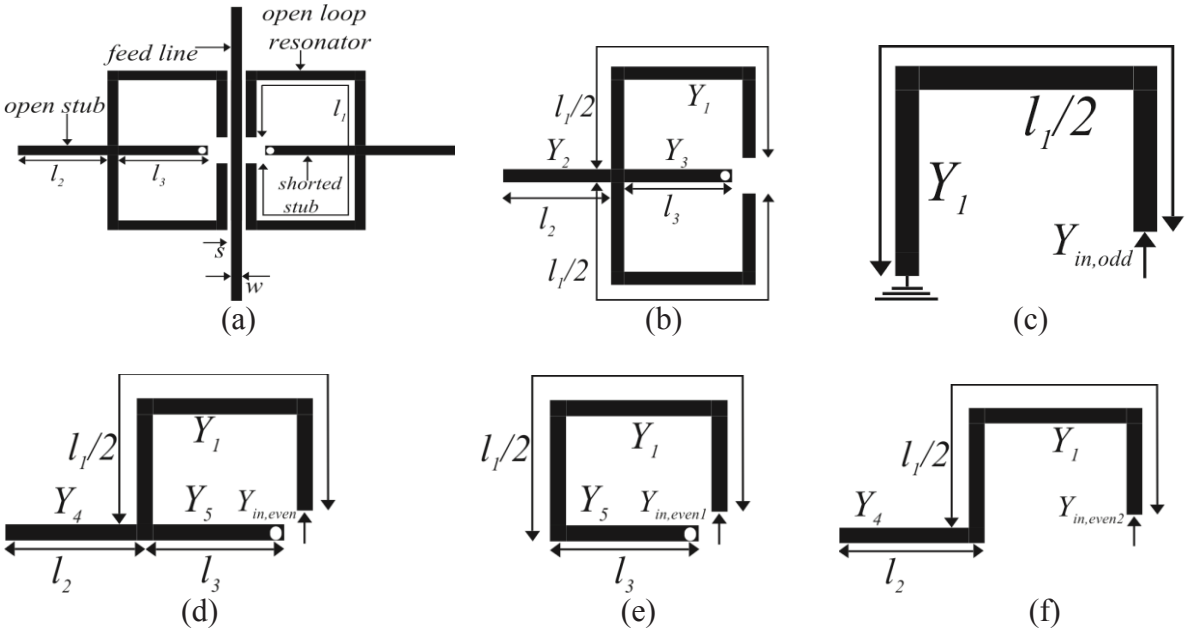

Fig.1(a) The proposed bandstop filter **(b)** resonator loaded with open/short stubs **(c)** odd mode **(d)** even mode **(e)** even 1 mode **(f)** even 2 mode.

For even mode excitation the circuit is bisected at symmetrical plane with open stubs and shorted stubs are at the middle to achieve the equivalent circuit shown in Fig.1(d). As shown in Fig.1(d) the new admittance of open stub and shorted stub (having half width of the original) are Y_4 and Y_5 respectively. Now two even mode frequencies are obtained. The frequency, f_{even1} is due to the shorted stub and half of the open-loop resonator and the frequency, f_{even2} is due to the open stub and half of the open-loop resonator as shown in Fig.1(e) and Fig.1(f) respectively. So the two even mode frequencies f_{even1} and f_{even2} for the case of $Y_4=Y_1$ and $Y_5=Y_1$ are achieved as:

$$f_{even1} = \frac{c}{(2l_1 + 4l_3)\sqrt{\varepsilon_{eff}}} \quad , \tag{2}$$

$$f_{even2} = \frac{c}{(l_1 + 2l_2)\sqrt{\varepsilon_{eff}}} \quad . \tag{3}$$

Now for the similar lengths of l_2 and l_3 frequency f_{even1} is smaller than f_{even2}. So these three frequencies $f_{even1} < f_{odd} < f_{even2}$ represents three stopband. The lengths l_1 and l_3 control the frequency, f_{even1} and the lengths l_2 and l_1 control the frequency, f_{even2}. To show the validity of the above concept a filter is designed and simulated using ADS on the substrate RT/duroid 6010.2 with dielectric constant of 10.2 and thickness of 0.635 mm.

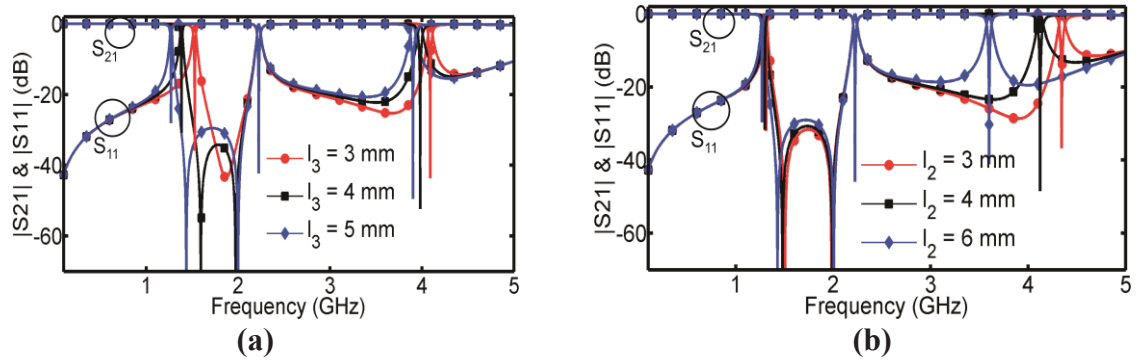

Fig.2(a) Response of the filter with respect to l_3 **(b)** Response of the filter with respect to l_2.

The layout of the filter is depicted in Fig.1(a). Fig. 2(a) and 2(b) plot the response of the tri stopband bandstop filter with changing shorted stub length, l_3 and changing open stub length, l_2 respectively. The dimensions used in the simulation are l_1 = 25.6 mm, w = 0.59 mm, s = 0.2 mm. As shown in Fig.2(a), while changing l_3 (for l_2 = 4.8 mm), to higher value, first stopband is shifting to lower frequency, second stopband is unaffected and there is a slight change in third stopband. Similarly on changing l_2 (for l_3= 4.8 mm) as depicted in Fig.2(b) there is no change in the position of first and second stopband of bandstop filter.

RF MEMS switch: Metal-contact SPST RF MEMS switches from Radant MEMS [**4**] is used for the switching operation. Fig. 3(a) shows the side view of the RF MEMS switch. The gold cantilever beam is used to design the switch. Normally without actuation voltage switch is in the up-state position. A dc voltage of 90 V is used to pull the gold beam to make a direct contact with the transmission line [4]. The lumped circuit representation of the RF MEMS switch for the two conditions - down state and up state- are shown in Fig.3(b) and 3(c) respectively. In up-state condition this RF MEMS switch show a good isolation of 80 fF and in downstate the switch shows a resistance of 0.7 Ohm. Due to low resistance at down-state Radant MEMS switch is better than Omron RF MEMS switch.

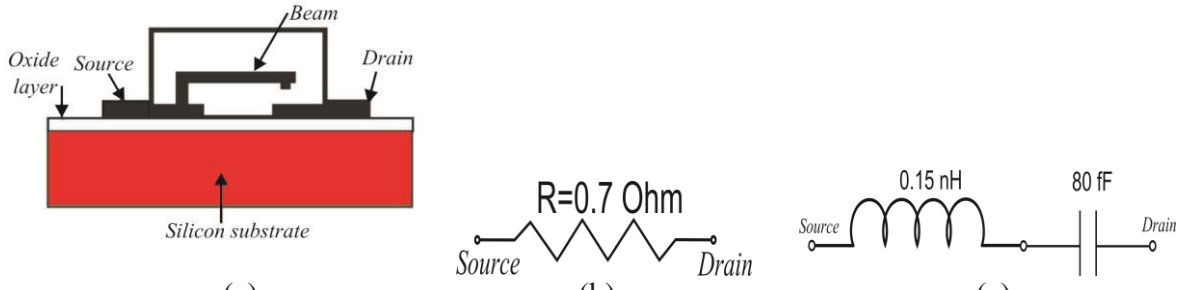

Fig.3 (a) RF MEMS switch **(b)** Downstate equivalent circuit **(c)** Upstate equivalent circuit

Proposed Filter with RF MEMS switch: Fig. 4 shows the layout of the proposed second-order switchable BSF with RF MEMS switches. Two switches are used to connect short stub and open stub. Switch, sw1 is connected to shorted stub and switch, sw2 is connected to open stub.

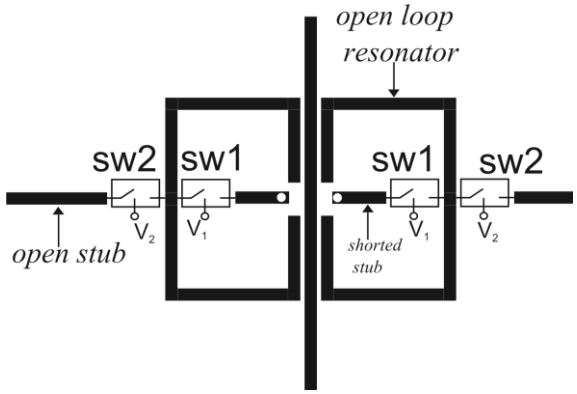

Fig.4 Topology of the switchable stopband bandstop filter using RF MEMS switches.

Case 1:-When both switches sw1 and sw2 are given a voltages $V_1 = V_2 = 0$ V, then both open and shorted stubs are unconnected to open-loop resonators. Only the open-loop resonators decide the position of the stopband. So this results a single stopband at the response. Fig. 5(a) shows the simulated response of the filter when both switches sw1 and sw2 are OFF.
Case 2:-When switches sw1 are given a actuation voltage of V_1 = 90 V and sw2 are given a voltage of V_2 = 0 V, then sw1 close to give a direct connection of open-loop filter to shorted

stubs but open stubs are remain unconnected. As discussed earlier shorted stub creates a stopband before the centre frequency of open-loop filter. Fig. 5(b) shows the simulated response of the filter when sw1 is ON and sw2 is OFF. Two stopband at 1.3 GHz and 2.2 GHz are achieved .

Case 3:-When 0 V is given to sw1 and 90 V is given to sw2 then open stub get connected to open-loop resonators but shorted stubs are remain unconnected. In that case dual stopband is achieved with stopband at 2.2 GHz and 3.7 GHz due to open-loop and open stub respectively as shown in Fig 5(c).

Case 4:-When both switches sw1 and sw2 are given $V_1 = V_2 = 90$ V then both the stubs get connected to open loop resonators. The connection of both stubs provide a tri-stopband at 1.3 GHz, 2.2 GHz and 3.7 GHz as depicted in Fig. 5(d). For all cases the dimensions of the filter are $l_1 = 25.6$ mm, $l_2 = 6$ mm, $l_3 = 4.5$ mm, $s = 0.2$ mm, $w = 0.59$ mm.

So when both switches are OFF single stopband is achieved. If any one of the switches are ON, then filter response results a dual stopband. Condition of switches decide the position of second stopband. Finally when both switches are ON, the tri-stopband can be achieved.

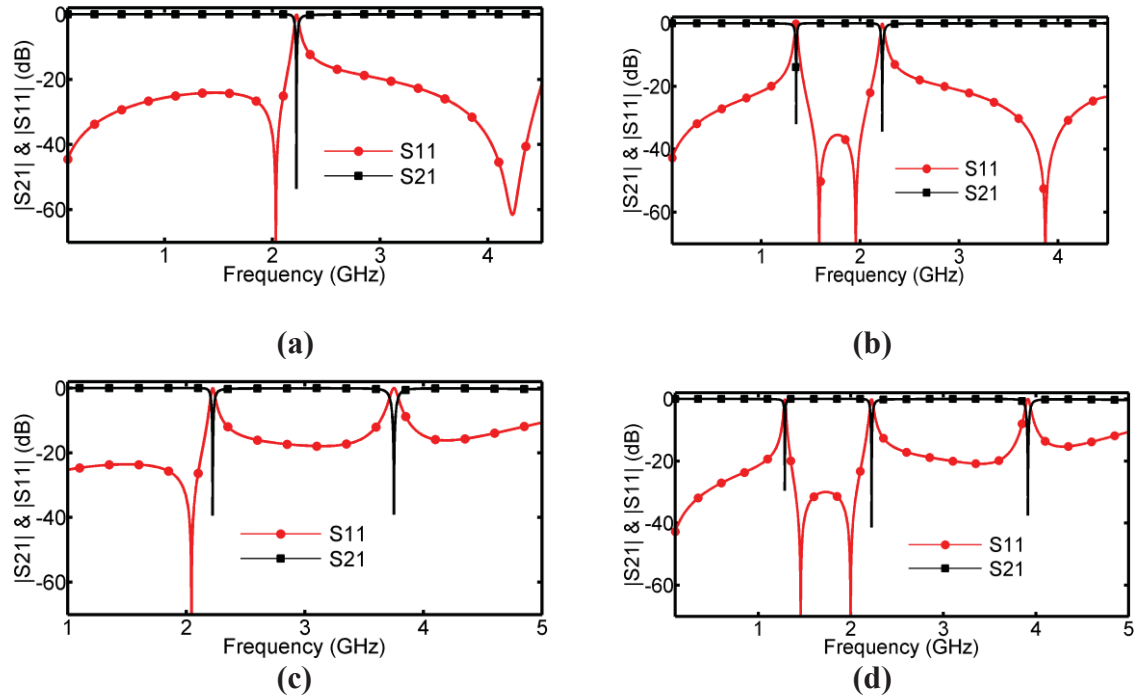

Fig 5. (a) When sw1 and sw2 both are OFF **(b)** when sw1 is ON and sw2 is OFF **(c)** when sw1 is OFF and sw2 is ON **(d)** when sw1 and sw2 both are ON.

Conclusion: In this paper, open and shorted stubs loaded open loop resonators are presented to exhibit bandstop characteristic. The Radant RF MEMS switches are used to design tri/dual/single stopband bandstop filter.

Reference:

[1] G. M.Rebiz, RF MEMS Theory, Design, and Technology. John Wiley and Sons, 2003.

[2] N. Kumar and Y.K.Singh, "Bandpass to Bandstop Switchable and Tunable Filter," International Conference on MEMS and Sensors (ICMEMSS) 2014.

[3] Y.-H. Cho and G. M. Rebeiz, "0.73–1.03-GHz tunable bandpass filter with a reconfigurable 2/3/4-pole response," IEEE Trans. Microw. Theory Tech., vol. 62, pp. 290–296, Feb. 2014.

[4] S. Majumder et al., "A packaged, high-lifetime ohmic MEMS RF switch," in IEEE MTT-S Int. Microw. Symp. Dig., Jun. 2003, pp. 1935–1938.

Compact MEMS DMTL Phase Shifters

B. Anudeep [(1)], and Usha Kiran .K [(2)]
VIT University Chennai Campus, Chennai., India, Pin: 600127,
Email: (1) anudeep.b2013@vit.ac.in
(2) usha.kiran@vit.ac.in

Abstract: *MEMS Phase shifters have received a lot of attention as an enabling technology for low cost, high performance passive phased arrays. Compact structure is important to increase process consistency and reliability of the device. In this paper, we present compact MEMS DMTL phase shifter using RF MEMS switch. The miniaturization is obtained by incorporating DGS structure in the ground. These DGS structure increase the current path hence enabling more phase shift. This helps in reducing the number of MEMS switches. So, the DGS structure is implemented and phase shifts of 11.25, 22.5, 45 and 90 degree are obtained.*

Introduction:

Microelectromechanical Systems (MEMS) have been developed since 1970s for various types of sensors, switches; accelerometers etc. MEMS are essentially miniature devices that use a mechanical movement to achieve a short circuit or an open circuit in a transmission line. RF MEMS results in -0.3db/bit and -0.6 dB/ bit phase shifters at X-band (10 GHz) and Ka – band (35 GHz) respectively. This is much better than GaAs FET phase shifters which result in -1 dB/bit and -2 dB/ bit at the same frequency. [1] MEMS include low insertion loss, high isolation, great linearity, low power consumption, and very low fabrication cost. It is for these reasons as well as for the simplicity of their biasing networks that most of the developed switches are electrostatic in nature.

The distributed phase shifters are attractive for its simple fabrication and wide bandwidth. So, distributed MEMS transmission line (DMTL) phase shifters are essential components in phased array antennas for telecommunications or radar applications [3]. The distributed MEMS transmission line (DMTL) consists of a high impedance line that is capacitively loaded by the periodic placement of MEMS bridges [1]. There is often understated drawback of the distributed phase shifter is its long length. If the number of sections can be decreased or if the individual sections are shortened while maintaining the desired phase shift, the overall phase shifter length can be reduced.

In this paper, a design of H shaped low actuation voltage RF MEMS shunt switch is developed as MEMS bridge on the CPW line. The unit cell is considered and the spacing between the bridges is optimized to obtain the desired phase shift. The MEMS switch is designed on CPW (Coplanar Waveguide) line because it is easy to implement and compared to other designs it offers a wide performance and works well at high frequencies.

Design Descriptions:

The compact MEMS DMTL phase shifter is obtained by the different methods and designs which are discussed below.

A. RF MEMS Switch:

The design is H shaped membrane suspended above a coplanar waveguide (CPW) line with G/S/G of 60/100/60 µm and 50 Ω characteristic impedance. It has been built on a GaAs substrate with 12.9 dielectric constant and 270µm thickness. It is covered by a 0.5µm silicon dioxide buffer layer. Figure 2 shows the schematic representation of the H shaped bridge with fixed – fixed flexure suspensions, which are connected to each other by the contact area.

The H shaped bridge with fixed – fixed flexures is made of Gold with 80GPa Young's modulus, 0.44 Poisson's ratio, and thickness of 0.8µm. It is suspended above lower electrode with 3µm with initial gap height. A silicon nitride layer of 0.1µm thickness and a relative permittivity of 7.6 cover the lower end of the bridge to avoid the direct electrical contact. The specifications of the design are given in the Table 1.

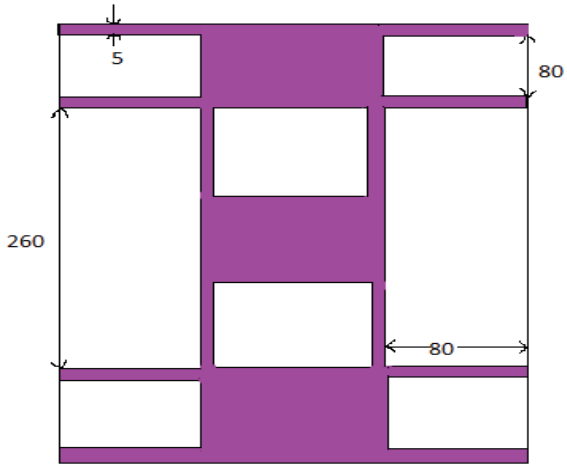

Fig. 1: Schematic representation of the H shaped bridge with fixed – fixed flexure suspensions.

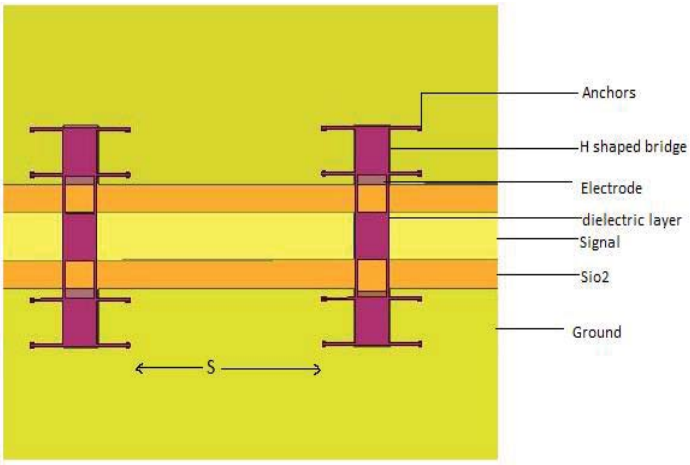

Fig. 2: Unit Cell with two H shaped bridges on CPW line

Description	Specifications (in µm)			
	Material	***Length***	***Width***	***Thickness***
Substrate	Galium Arsenide	1220	1000	270
Substrate Dielctric	Silicon dioxide	1220	1000	0.5
CPW(G/S/G)	Gold	60	100	60
Signal line Dielectric	Silicon Nitride	100	80	0.1
Anchors	Gold	20	10	2
CPW Ground	Gold	500	1000	3
Signal line	Gold	100	1000	3
Bridges	Gold	100	80	0.8
Flexures	Gold	80	5	0.8

TABLE 1: SPECIFICATIONS OF THE DESIGN

The main advantage of these switches is that the bias voltage has not to be applied between the center-conductor (RF line) and the ground planes; hence no interference occurs with other semiconductor devices in a practical circuit. This separation between the RF and DC signals allows modeling practical circuits more flexible.

B. Defected Ground Structure:

DGS is an etched periodic or non-periodic cascaded configuration defect in ground of a planar transmission line (e.g., microstrip, coplanar and conductor backed coplanar wave guide) which disturbs the shield current distribution in the ground plane cause of the defect in the ground. This disturbance will change characteristics of a transmission line such as line capacitance and inductance. In a word, any defect etched in the ground plane of the device can give rise to increasing effective capacitance and inductance. [2]

Fig.3: Circular Headed Dumbbell Shaped DGS Structure.

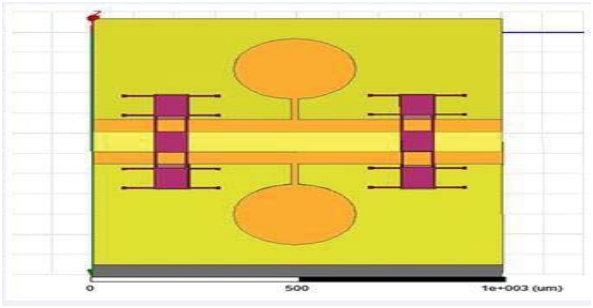

Fig. 4: DGS for 11.25 phase shifter in HFSS

C. Mechanical Parameters of the Switch:

The parameters of the switch can be calculated by using the formulas as listed below:

The pull in voltage is given by

$$Vp = \sqrt{\frac{8\,K\,g^3}{27 \epsilon o A}} \quad (1)$$

$$K = 4\,Ew\left(\frac{t}{l}\right)^3 \quad (2)$$

The switching time is given by

$$ts = 3.67\,\frac{Vp}{Vs\;\omega o},\; fo = \sqrt{\frac{K}{m}} \quad (3)$$

$$m = 0.35(lwt)\rho \quad (4)$$

where (ωo, fo) is resonant frequency,

fo is the natural frequency of vibration (in Hz), k= spring constant of the beam

m= mass of the beam, l= length of the beam, w= width of the beam

t= thickness of the beam, ρ = density of gold 19,320 Kg/m^3

Design Developments for Compact Phase Shifter:

Initially the unit cell with two bridges of same H shaped fixed – fixed flexure is implemented and observed the phase. Later the numbers of bridges are increased to three to obtain the 11.25 degree phase shift.

As the number of bridges increases the design becomes complex so the concept of DGS in introduced in the ground plane due to which the electrical path length increases and contributes more amount of phase shift by which the desired phase of 11.25 degree is obtained with less number of bridges as shown in figure 2.

Similarly 22.5, 45 and 90 degree phase shifters are obtained by periodically increasing the radii of the dumbbell shaped DGS.

S.no	Design	S Parameters (in dB)	Phase shift in degrees
1.	Dumbbell shaped DGS with two bridges	-42.1888	11.252
2.	Dumbbell shaped DGS with three bridges	-52.7202	22.58
3.	Dumbbell shaped DGS with four bridges	-75.4783	44.93
4.	Dumbbell shaped DGS with six bridges	-120.3839	89.8

Table 2: Results regarding different phase shifts in degrees

Description	Value Obtained
Pull in voltage	7.842 V
Return loss	-31.21 dB
Insertion loss	0.1 dB
Switching time	9.10 µ sec

Table 3: Results for the Single Bridge

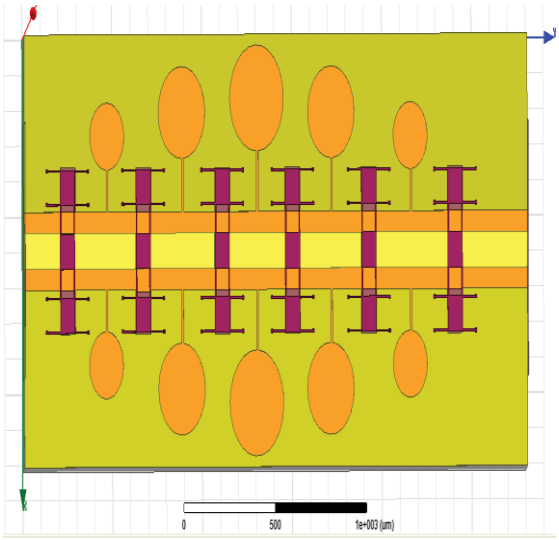

Fig. 5: Dumbbell Shaped DGS model for 90^0phase shift

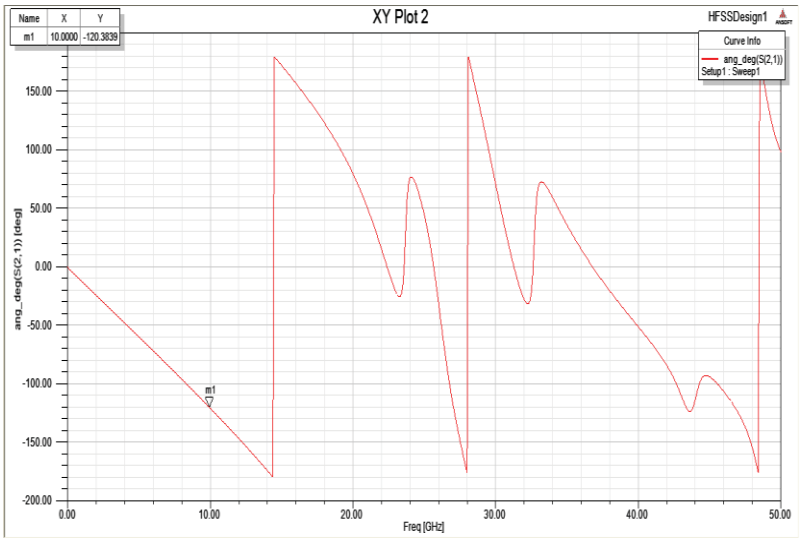

Fig. 6: Phase shift observed for 90^0 phase shift in HFSS

Conclusion:

In this paper we have seen the effect of DGS structure in obtaining the phase shifters with less number of MEMS bridges. In the designed phase shifters the return loss and insertion loss are maintained at -20 to -26 dB and -0.09 to -0.2 dB respectively operating for 10 GHz. The further work can be carried on optimizing the design by choosing meander coplanar waveguide (CPW) line. .

Reference:

[1] Gabriel M. Rebeiz, "RF MEMS Theory Design and Technology", John Wiley and Sons 2003.

[2] L.H.Weng, Y.C. Gyo, X.W.Shi and X.Q.Chen, "An Overview on Defected Ground Structure (DGS)", Progress in Electromagnetics Research, Vol 7, pp 173-189, 2008.

[3] Y. Du, J. Bao and X. Zhao, "5-bit MEMS distributed phase shifter", Electronics Letters, Vol. 46 No. 21, pp 1452 -1453, 14th October 2010.

[4] Sharma. T, Tyagi. A, "Review of mechanical modelling of fixed- fixed beams in RF MEMS switches", Advanced Computing and Communication Technology (ACCT), Third International Conference, pp 211 – 214, 6-7th April 2013.

Low Voltage RF Mems Capacitive Shunt Switches

Bk.Arun Chowdhary[(1)], *Usha Kiran K.*[(2)]
(1) VIT university, Chennai, tamilnadu,6000127, email: bkarun.chowdhary2013@vit.ac.in
(2) VIT university,Chennai,tamilnadu,6000127, email: usha.kiran@vit.ac.in

Abstract—*This paper presents a low voltage RF MEMS capacitive switch based on fixed-fixed beam structure using meanders designed on silicon substrate having stiff anchors around the membrane. The performance of the switch for four different shapes of the membrane is been proposed in this paper. The buckling effect in the switch and stiction problem has been the primary concern and can be reduced with this proposed design approach due to stiffness of the anchors around the membrane. Lower mass of the beam and lower spring constant is achieved as the meanders are included on the sides of the membrane. The proposed switches are optimized to operate in k-band that results in low insertion loss of -0.034 dB, -0.21 dB, -0.28 dB and 0.47 dB, high isolation of 36 dB, 43.5 dB and 48.1 dB and 38 dB, and pull-in voltage of 8.1V, 10.2V and 9.6V and 3.5V respectively are achieved.*

Keywords—RF MEMS; low-actuation voltage; silicon substrate; capacitive switch; high isolation; spring constant; meanders; anchors

I. INTRODUCTION

Radio frequency Micro-Electro-Mechanical-Systems (RF MEMS) based switches play a key role in the field of microwave switching. The radio-frequency MEMS switch is defined as a contact switch fabricated using micro-machining technology. RF MEMS switches are known to have the excellent features like low insertion loss and high isolation. Additionally these provide benefits such as reduced power consumption, weight, size and cost etc.

Typically MEMS switches are fabricated using surface micro-machining processes and have a suspended thin membrane which allow or block the electronic transmission through the mechanical moment of the membrane above the electrode. MEMS switches are actuated by various methods, such as electromagnetic, electrostatic, piezoelectric and thermal actuation. Due to low power consumption and linearity, electrostatic actuation is widely used, in which electrostatic force is generated between fixed electrode and movable membrane for switching operation. Several disadvantages include slow switching speed, high actuation voltage in high power RF applications. This paper presents a design of RF MEMS capacitive switch on silicon substrate with silicon nitrate(Si3N4) as dielectric material, which results in excellent RF performance with high isolation and low insertion loss. With the inclusion of anchors around the membrane, the bucking effect and stiction problem can be reduced. Two actuation electrodes, thin membrane and meanders further helps to lower the actuation voltage of switch.

II. STRUCTURE AND OPERATION OF SWITCH

The proposed model of RF MEMS switch has a coplanar waveguide(CPW) line for RF transmission on a 200 µm thick silicon substrate and dielectric layer of Silicon dioxide (Si02). The coplanar waveguide of 50Ω impedence with ground/signal/ground (G/S/G) configuration is used for design. The CPW consists of a 100µm wide signal line with gap of 60µm i.e the G/S/G dimensions for CPW configurations are 60/100/60. A dielectric material (Si3N4) is used above the signal line.

In this paper, we focus on designing of a low actuation voltage of MEMS switch by reducing the spring constant and by increasing the actuation area. An serpentine and meander type membrane is designed to achieve the lower spring constant. By adding more meanders the spring constant can be further reduced without increasing the required space as miniaturization is necessary for a device to be embedded in RF applications. The transmission characteristics of a RF switch are determined by the up-state capacitance of the switch.
The proposed switch is actuated using electrostatic force. When the voltage is applied to pull-down electrodes, the membrane connected to grounds of the CPW line snaps down on signal line and dielectric surface forming a low impedence RF path to ground, and hence down-state capacitance value is increased. When the membrane is in up-state, the capacitance value gets low thus, allows the excellent transmission of signal.

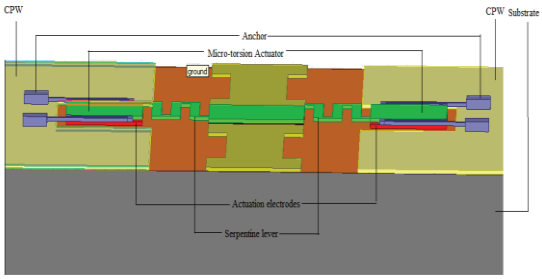

Fig. 1 Side view of the designed switch

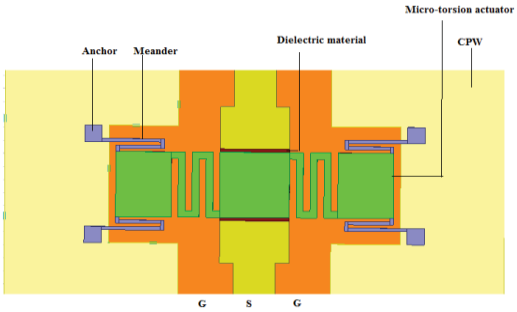

Fig. 2 Top view of switch(a)

III. SELECTION OF MATERIALS

RF/microwave devices and circuits are mechanically supported by a substrate. The nature of the substrate (i.e whether it is conductive, semi-insulative or insulating) plays a major role in the ultimate performance of the devices and circuits disposed on it. It should have uniform electrical properties and chemical resistance. These requirements make silicon a good candidate, as it fulfils all these requirements. It can withstand high temperatures.

Silicon nitrite (Si3n4) of 0.5 thickness is used over substrate beneath CPW line made of Gold (Au). Si3n4 has dielectric constant of 7.9. It is always preferable to use materials with high dielectric constant.

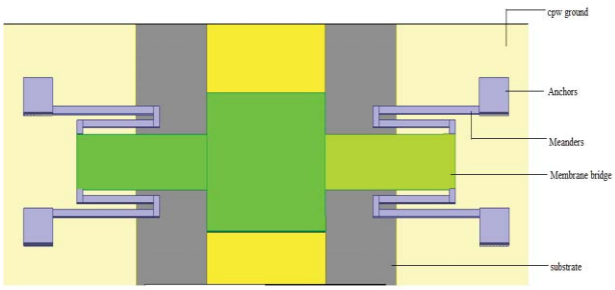

Fig. 4 top view switch (b) of fractal switch switch

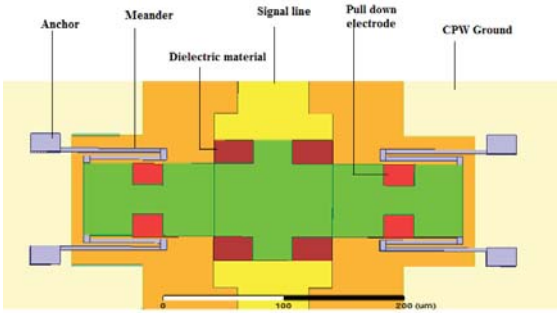

Fig. 5 Top view of switch(c) second order fractal

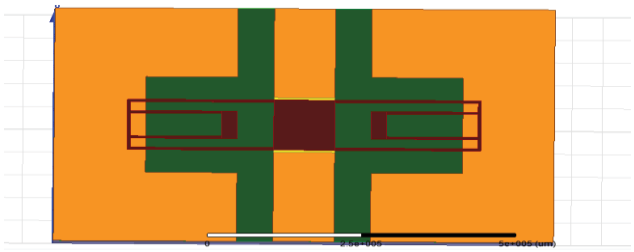

Fig. 6 Top view of switch(d) folded flexure switch

IV. SWITCH CHARACTERISTICS

Due to approach used to design the membrane the load on membrane is shifted towards the ends, it has meanders to lower the overall spring constant k. The load is distributed because of the anchors fixed around the edges of the membrane.

The actuation voltage V_P , of the MEMS switch with spring constant, k is given by

$$V_P = \sqrt{\frac{8kg^3}{27\varepsilon_0 A}}$$

Where ε_0 is the permittivity of free space, g_0 is the gap between membrane and electrode, A is the area of the electrodes which actually used for actuation operation. The pull-in voltage depends on the spring constant, k, air-gap between the electrode and membrane and the area of the electrode.

Up-State Capacitance:

The up-state capacitance of the switch can be calculated by using

$$C_{up} = \left(\frac{\varepsilon_0 A}{g_0 + t_d}\right)$$

Down-state capacitance:

The down-state capacitance of the switch is calculated when the switch is in down state. In this case, the thickness of the dielectric is so small that the fringing capacitance can be neglected. The switch capacitance in down-state can be calculated using

$$C_{down} = \frac{\varepsilon_0 \varepsilon_r A}{t_d}$$

Switching time:

The switching time of the switch can be calculated by using

$$t_s = \frac{3.67 V_p}{V_s\, \omega}$$

where k is the spring constant , V_p is the pull-in voltage and V_S is the source voltage.

V. PERFORMANCE ANALYSIS

The isolation loss, return loss and insertion loss of the proposed switches are measured using Ansoft HFSS software. The performance of the switch after the calculations of various components of design for three different switches shown in the fig.1 ,fig.4 and fig.5 is shown in the table II.

components	Switch performance			
	Switch(a)	Switch(b)	Switch(c)	Switch(d)
Dielectric layer	0.5µm (Si_3N_4) ε_r 7.9	0.5µm (Si_3N_4) ε_r =7.9	0.5µm (Si_3N_4) ε_r =7.9	0.5µm (Si_3N_4) ε_r =7.9
Air gap	2.5µm	2.5µm	2.5µm	2µm
Spring constant, k	2.07 N/m	1.08 N/m	6.7 N/m	0.076 N/m
Up-state capacitance	17.7 fF	14.1 fF	19.1 fF	39.5 fF
Down-state capacitance	3.3 pF	2.65 pF	2.67 pF	3.7 pF
Insertion loss	<0.034 dB	<0.28 dB	<0.21 dB	<0.47 dB
Isolation	36 dB	43.5 dB	48.1 dB	38 dB
Actuation voltage	8.1 V	10.2V	9.6V	3.5V
Switching time	18.2µs	7.2 µs	19.3 µs	18.6 µs

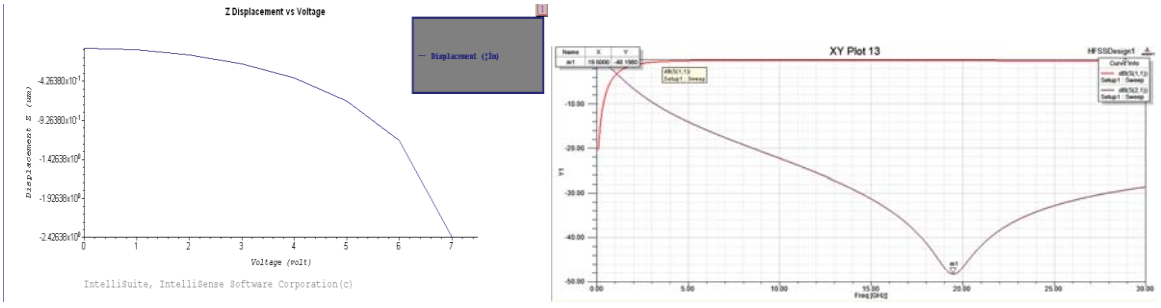

Fig.6 Displacement vs voltage graph

Fig.7 isolation performance of switch(a) in down state at 19 GHz

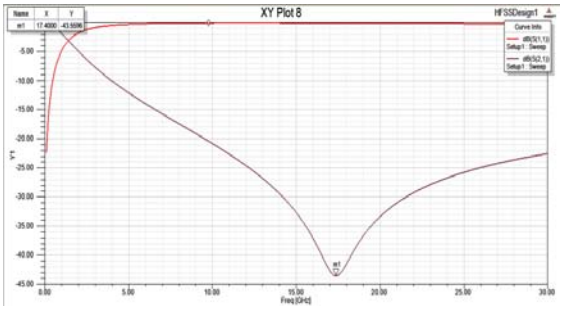

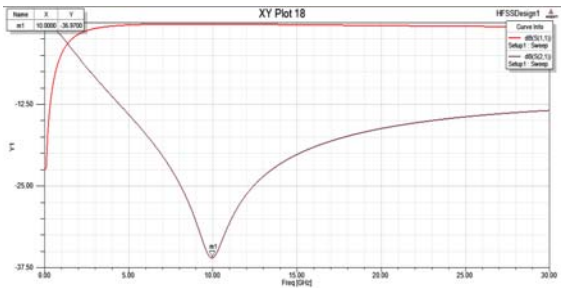

Fig.8 Isolation performance of switch(b) at 17GHz

Fig.9 Isolation performance of switch(c) at 10 GHz

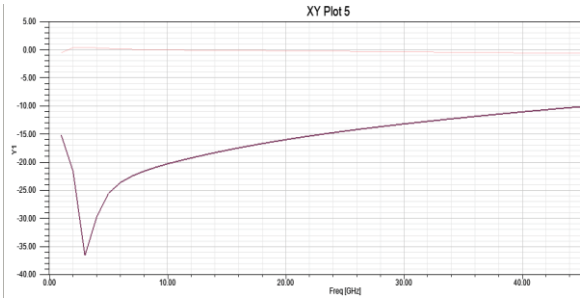

Fig.10 isolation performance of switch(d) at 3 GHz

VI. CONCLUSION:

A low voltage RF-MEMS capacitive shunt switch is designed and simulated. These switches have actuation voltages of 11.2V, 10.2V, 9.6V and 3.5 respectively depending on the membrane design. The RF characteristics shows that these switches provides high isolation and have low insertion loss. The low actuation voltage is achieved which results in an excellent RF response and can be used in the applications where the low power is the primary concern such as in communication and space systems.

REFERENCES

[1] ll-Joo Cho,taeksang song, Sang-Hyun Baek, and Euisik Yoon, "A Low-Voltage and Low-Power RF MEMS Series and Shunt Switches Actuated by Combination of Electromagnetic and Electrostatic Forces" *IEEE TRANSACTIONS ON MICROWAVE THEORY AND TECHNIQUES*, VOL. 53, NO. 7, JULY 2005.

[2] Jeremy B. Muldavin and Gabriel M. Rebeiz, "Inline Capacitive and DC-Contact MEMS Shunt Switches" *IEEE MICROWAVE AND WIRELESS COMPONENTS LETTERS,* VOL.11, NO.8, AUGUST 2011.

[3]Poonam Verma and Surjeet Singh, "Design and simulation of RF MEMS Capacitive type Shunt Switch & its Major Applications" *IOSR Journal of Electronics and Communication Engineering*. Volume 4, Issue 5, pp.60-68, (Jan-Feb. 2013).

[4]Divya Varma and Ajay Kaushik, "Analysis of RF MEMS Capacitive Switch based on Fixed-Fixed beam structure" *International journal of Engineering Reasearch and Applications (IJERA)* Vol.2, Issue 5, pp.391-394, September-october 2012.

[5]Montserrat Fernandez-Bolanos Badia, Elizabeth Buitrago, and Adrian Mihai Ionescu "RF MEMS Shunt Capacitive Switchs Using AIN compared to Si3n4 Dilectric" *Journal of microelectromechanical systems*, vol. 21, no.5, October 2012.

[6] Richard Chan, Robert Lesnick, David Becher. "Low Actuation Voltage RF MEMS Shunt Switch with Switching Lifetime of Seven Billion Cycles", *Microwave Theory Tech- S Int. Microwave Symp*., vol.1, pp.165-168,2001.

[7] Yasser Mafinejad, Abbas Kouzani and Khalil Mafinezhad "Review of low actuation voltage RF MEMS electrostatic switches based on metallic and carbon alloys" *Journal of microelectronics, Electronic Components and Materials* Vol.43, No. 2, pp. 85-96, 2013,

COMPACT DUAL-BAND BAND PASS FILTER USING $\lambda/2$ ACS-SIR

A.Kamalaveni [(1)] *and M.Ganesh Madhan* [(2)]
(1), (2) MIT Campus, Anna University, Chennai, India 600044.
Email: (1) kamalaveniganesh@gmail.com, (2) mganesh@annauniv.edu

Abstract: *A microstrip bandpass filter (BPF) using asymmetric coupled short-circuit terminated stepped impedance resonator (ACS-SIR) is designed. In this approach, asymmetric coupled lines are used to replace the normal SIR structure. The structural parameters of the ACS-SIR are calculated analytically according to the center frequencies of the filter. To validate the design, a fourth order chebyshev ACS-SIR dual band bandpass filter for dual-band mobile applications (UMTS and WIFI bands: 1920-2170MHz and 5.6-5.875GHz) was fabricated and measured. The filter provided an insertion loss of 1.05 dB and 1.38 dB, return loss of -19 dB and -15 dB, and bandwidth of 32.30% and 10.3% at 1.95 GHz and 5.8 GHz, respectively. The proposed method is compact and provides high roll off between the two pass bands compared to the existing schemes.*

Introduction: For wireless communication applications, RF passive filter components are required to separate multiple frequency bands in order to access different services. For such applications, asymmetric coupled line helps to obtain high rejection compared to the conventional methods discussed in the literature. Traditionally dual-band filters are designed as a cascade connection of a bandstop filter (BSF) and a bandpass filter (BPF), and the filter response is expressed using transfer function of the filter combination. The bandwidth of each pass band is controlled by adjusting the characteristics of both filters [1]. This is not efficient for practical applications due to its characteristics and loss performance. On the other hand, resonators with open or short stubs connected in parallel or series can be used to create dual-band filters [2] [3]. These circuits have complicated configurations and occupy larger area. Introduction of coupling resonators may provide high performance dual-band response [4], but the fixed position of standing waves, may lead to insufficient rejection between two pass bands. Stepped impedance resonators (SIR) based design overcomes many of the limitations imposed by conventional filter designs. The conventional method of designing SIR dual-band filter is to draw a design graph of coupling coefficient for each pair of SIRs. Moreover for filter of larger order, more than one design graph is needed. Hence this method is also not effective for the design of higher order dual-band filters. However, short stub loaded SIR [5] improves the selectivity of the dual-band filter with reduced losses. Recently, asymmetric coupled-line [6] has been attempted in bandpass filter design to suppress the spurious pass band at the second harmonic. The effect of asymmetric coupled line in filter design is explained in [7]. The different width of asymmetric coupled line decreases the stop band slope. It is envisaged that introduction of Asymmetric Coupled Short-stubs in both ends of the high impedance section of the SIR may improve the controllability of the two pass bands and out-of-band rejection performance. The proposed method involves asymmetric coupling only in the low impedance section with short stubs, along with regular design procedure of the dual-band SIR. Hence the electrical lengths and characteristics impedance can be easily derived as per the steps provided in [8]. As a test case, a fourth order dual-band filter is designed, simulated and fabricated. Performance comparison is carried out by fabricating and

testing two filters for the same frequency bands, one without coupling section and another with ACS.

Dual Band Filter Design: The basic structure of a Stepped Impedance Resonators (SIR) consists of three stepped impedance segments, and two of them have the same impedance and electrical length. The short-circuited stub is connected in series with the λ/2 SIR by using K-inverters and the values are obtained as per the procedure reported in [8]. Introducing the asymmetric coupled line with short stub leads to the implementation of transmission zero that will eliminate filter harmonics. Choosing the correct width and length dimensions, the transmission zero can be placed in the proximity of those harmonics allowing wider stop bands and it contributes to the modulation of characteristic impedance of the coupled line, thus reallocating the 2nd harmonics and transmission zero.

A dual-band filter was initially designed by serially connecting the SIR using K-inverters. Here the short-circuited stub is grounded via hole. A fourth order dual-band filter with the center frequencies f_0 =1.95 GHz and f_{s1}=5.8 GHz ($f_0/f_{s1}>2$) having fractional bandwidths of Δ_1=0.2 and Δ_2=0.082, is considered for the study. The element values of the fourth order chebyshev frequency response with 0.1 dB ripple level are consider for this design. The design approach exactly follows the procedure of [8]. A numerical technique is used to determine the value of θ_1 (0.4560 rad) and θ_2 (0.5674 rad) respectively. The characteristics impedances are chosen as $z_2=z_d$=102Ω and by using R_z, the value of the z_1 is calculated as 31.875Ω. Then the impedance value of the K-inverter is chosen as $z_k^{12}=z_k^{23}$= 86Ω. The superscripts denote the number of SIRs which is connected by the inverter. Due to the symmetry, z_k^{12} equals z_k^{34}. In the proposed dual band filter design; SIR is short circuit terminated at both the ends and also in the low impedance section by using asymmetric coupled line. Here asymmetric coupled line is added without affecting the electrical characteristics of the SIR. It has the same impedance characteristics and has more or less same electrical length, but the width of the asymmetric line is adjusted to get better rejection characteristics, when compared with the conventional SIR scheme. Based on this approach, a fourth order filter with similar specification used in SIR section is designed. Fig.3 shows the layout of the SIR designed as per ref [8] and proposed ACS-SIR dual-band band pass filter.

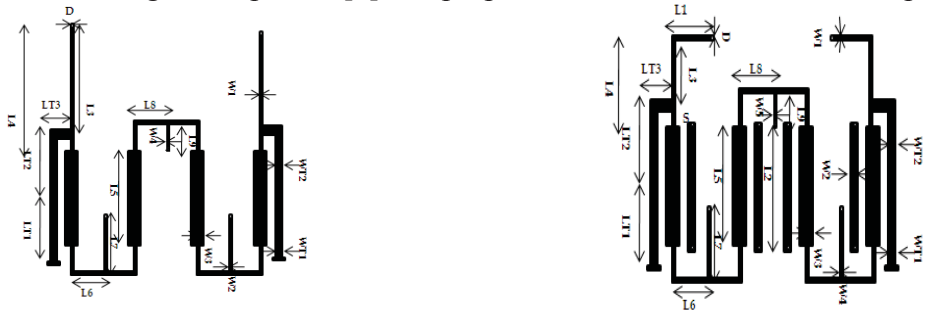

(a) (b)

Fig.3. Design of the fourth order dual-band (a) SIR filter W_1=0.5962, W_{T2}=1.4328, W_{T1}=1.36159, W_2=1.2097, W_3=2.864, W_4=0.5426, L_A=18.6438, L_3=18.195, L_{T3}=2.6173, L_{T2}=6.4376, L_{T1}=10.7011, L_5=13.1848, L_6=4.3415, L_7=4.4415, L_8=4.4419, L_9=1.6266 (b) ACS-SIR filter W_{T2}=1.4328, W_5=0.2713, S=0.1524, L_1=7.664, L_3=7.664, L_{T3}=2.6173, L_A=16.6438, L_2=13.7697.

Results and Discussion: This proposed design is initially simulated in ADS simulator using ideal transmission line, later converted in to EM simulation by ADS momentum. Here we added the transmission loss parameter to match the practical result. After simulation and optimization by ADS, the dual band ACS-SIR BPF was fabricated on the substrate with

relative dielectric constant of 2.55 and thickness of 0.762 mm, and its photograph is shown in Fig.4. Comparison of the dual band filters performances are shown in Fig.5. Both of them are found to be in good agreement with each other. The S parameter values are compared and listed in Table I. The pass band group delay variations in both the bands and the simulated results of filter performances for various spacing between the coupling sections of ACS-SIR are illustrated in Fig.6 (a) and (b) respectively.

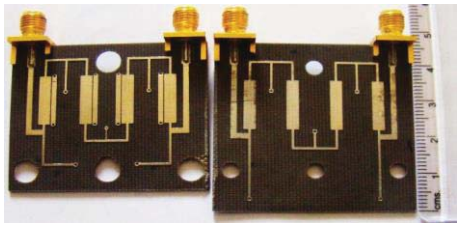

(a) (b)

Fig.4. Photograph of the fabricated dual-band bandpass filters. (a). ACS-SIR dual band Filter and (b) SIR dual band Filter.

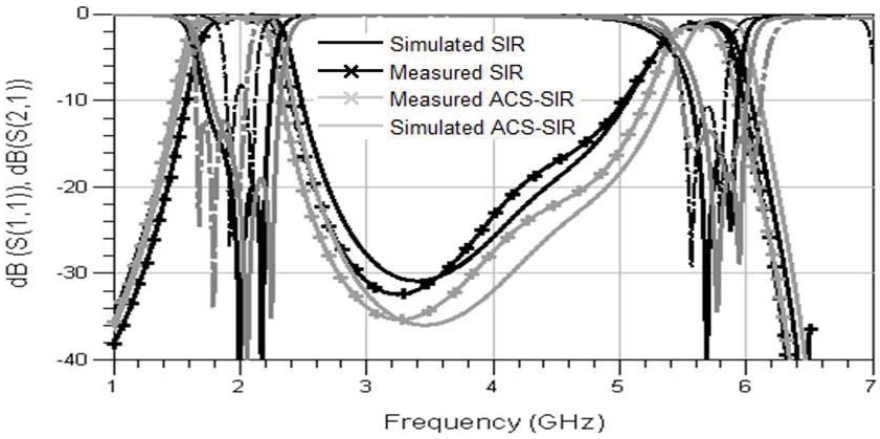

Fig.5. Comparison of the dual band filters performances

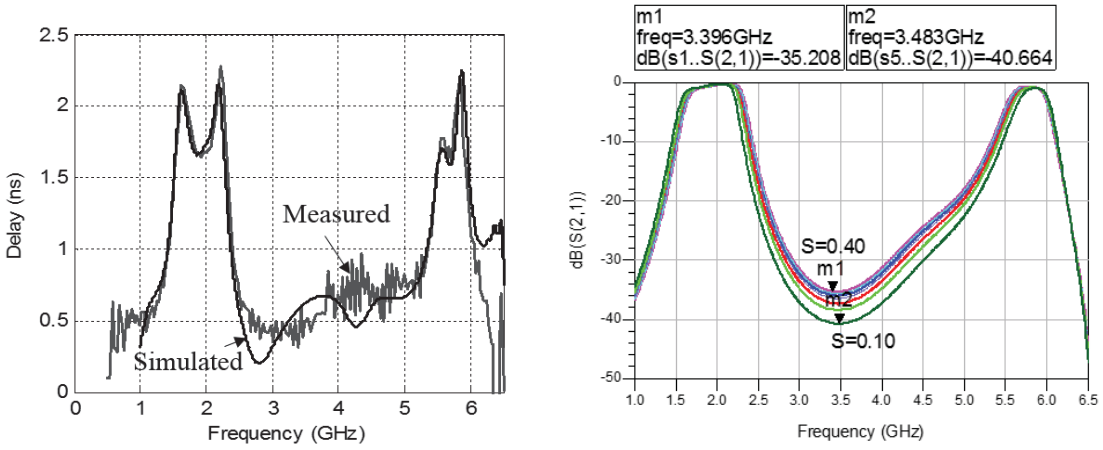

(a) (b)

Fig.6. (a) Pass band group delay variations of both the bands (b) Simulated results of filter performances with various spacing between the coupling sections of ACS-SIR

Detailed analysis on the impact of ACS-SIR line has been investigated in terms of out of band rejection. A very narrow spacing between the coupled line (s) results in high coupling of signal between ground and filter line. Hence a compromise has been made by choosing the space which is practically feasible without affecting the characteristics of the filter. The

rejection of stop band was improved by the proper selection of width and length of ACS SIR line. Table I compares the band pass filter design. It clearly shows that the proposed design in this study is better than the reported references.

Table: Performance Comparision of Dual-band Filters

BPF	Simulated / Measured (GHz)				Roll off @20dB (GHz)	FBW I / II Band (%)	Volume (mm^3)
	S11 (dB)		S21(dB)				
	1.9	5.8	1.9	5.8			
Ref.[7]	20/19.7	15/14.2	0.5/0.6	1.2/1.5	4.8/4.9	16.2/9.5	79x22.5x1.27
SIR [8]	17/16	20/16	1.1/1.2	0.8/2.4	4.5 / 4.3	33.5 / 11.4	45x39.5x0.762
ACS-SIR	20/19	20/15	0.3/1.0	0.6/1.3	5.0/4.8	35.8/10.6	39.5x35x0.762

Conclusion: A new filter design based on ACS-SIR and the combination of series λ/2 SIR connected by K-inverters was designed and fabricated for operating at 1.9/5.8 GHz. The simulation and measurement results are in good agreement. The roll off is improved by 6 dB compared to the existing SIR Filter design. The proposed dual-band filter has a good performance with very compact size.

Reference:

[1] Tsai, L.C., and Huse, C.-W.:"Dual-bandbandpass filters using equal-length coupled-serial-shunted lines and Z-transform techniques', *IEEE Trans. Microw. Theory Tech.,* Vol.52, No.4, pp.1111-1117, 2004.

[2] M. Sagawa, M. Makimoto, and S. Yamashita, "Geometrical structures and fundamental characteristics of microwave stepped-impedance resonators," IEEE Trans. Microwave Theory Tech., vol. 45, pp. 1078–1085, Jul. 1997

[3] Miyake,H.S.Kitazawa, T.Ishizaki, T.Yamada, and Y.Nagatom, " A miniaturized monolithic dual band filter using ceramic lamination technique for dual mode portable telephones," *IEEE MTT-S Int.Dig.,*Vol.2, 789-792, Jun.1997.

[4] H.M.Lee and C.M.Tsai, "dual-band filter design with flexible passband frequency and bandwidth selections," *IEEE Trans. Microw.Theory Tech.,* Vol. 55, No.5, pp.1002-1009, May2007.

[5] Y.H. Cho, H.I. Beak, H.S. Lee, and S.W. Yun, "A dual-band comblinebandpass filter loaded by lumped series resonators," *IEEE Trans. Microw. Theory Tech.,* Vol. 19, No.10, pp.626-628, Oct, 2009.

[6] X.Y.Zang, Y.X.Chen, Q.Xue, and J.Shi, "dual-band band pass filter design using a novel feed scheme", *IEEEMicrow. Wireless Compon. Lett.*, vol. 19, no. 6, pp. 350–352, Jun. 2009.

[7] Songbai Zhang, Lei zhu, "Synthesis Design of Dual-Band Bandpass filter with λ/4 Stepped Impedance Resonators," ", *IEEE Trans. Microw. Theory Tech.,* Vol.61, No.5, May2013.

[8] Wei-Shin Chang and Chi-Yang Chang, " Analytical design of microstrip short circuit terminated stepped –impedance resonator Dual-band Filters", *IEEE Trans. Microw. Theory Tech.,* Vol.59, No.7, July2011.

Microwave dielectric properties of $Ca_3V_4O_{13}$ ceramics for ULTCC applications

Suersh E.K., Arun.N.S. , Naveen Raj. R, and Ratheesh.R

Microwave Materials Group, Centre for Materials for Electronics Technology (C-MET), Department of Information Technology, Government of India, Thrissur, Kerala 680771, India *E-mail address:*ratheeshr@yahoo.com (R. Ratheesh)

Abstract

Ultra low temperature sintarable $Ca_3V_4O_{13}$ ceramics have been prepared through solid state ceramic route. Phase purity and structural properties of the ceramics are studied using X-ray diffraction and Laser Raman spectroscopy. SEM studies reveal a dense microstructure for the well sintered ceramics. The sample sintered at 650°C for 4h shows maximum density of 2.62 g/cc together with ε_r=9.4, Q×f=28000GHz and τ_f= -51ppm/°C.

Introduction

The rapidly growing modern microwave circuit fabrication industry demands high density circuit packaging in order to attain circuit miniaturization for portable electronic devices. Low temperature co-fired ceramic (LTCC) technology is well known for high integration of passive components through 3-D conductor network, which will lead to better performance, reliability, miniaturization, cost reduction etc. Hence, this technology represents adequate packaging technique to meet the demands for circuit miniaturization. In LTCC technology high conductive Ag, Al, Cu etc. are used as the conducting layers. Therefore chemical compatibility between ceramics and metal electrodes is of prime importance in addition to its low sintering temperature. Many material systems such as $MgO\text{-}Al_2O_3\text{-}TiO_2$, $BaO\text{-}Nb_2O_5$ (1-2) etc. possess good microwave dielectric properties however the higher sintering temperatures (>1000°C) limits their wider usage in LTCC applications. Liquid phase sintering by the addition of low melting oxides such as Bi_2O_3, B_2O_3, CuO etc., are used to lower the sintering temperature of the ceramics (3-4). But most of the ceramics reported so far in this class are having inferior microwave dielectric properties especially the quality factor (5-6). Now the trend is to develop single phase material systems having chemical compatibility with metal electrodes. Current development in LTCC ceramics shows that molybdates (7-9) and vanadates (10) based ceramics will have more potential use in circuit design. Recently material researchers are focused on the development of new material system having ultra low sintering temperature (≤ 650°C). In the present work, the structural and microwave dielectric properties of new $Ca_3V_4O_{13}$ ceramics sintered at ultra low temperature are studied and results are presented.

Experimental procedure

The $Ca_3V_4O_{13}$ ceramics were prepared through solid state ceramic route. High purity $CaCO_3$ (99%, Sigma Aldrich) and V_2O_5(99%, Loba Chemie) were used as the starting materials. The stochiometric amounts of oxides and carbonates were weighed and wet mixed in distilled

water for about an hour and then dried. The $Ca_3V_4O_{13}$ ceramic was calcined at 550°C for 2hrs in a programmable SiC furnace. The calcined powders were ground in to fine powders and 5wt% polyvinyl alcohol (PVA) solution was added to the powders and then dried. The powder was again ground well and pressed uniaxially in tungsten carbide die of 11mm diameter by applying a pressure of 250 Mpa. The cylindrical compacts of $Ca_3V_4O_{13}$ samples were sintered at 650°C for different soaking hours. The density of the sintered pellets was determined using dimensional method. The phase purity of the specimens was analyzed using X-ray diffraction technique (M/S Brucker AXS, Germany). Raman spectrum of $Ca_3V_4O_{13}$ ceramic was recorded using a Bruker RFS 1001 s spectrophotometer with a Nd:YAG laser of wavelength 1064 nm using Ge target. The microstructures of the samples were studied using scanning electron microscope (JEOL model JSM-6390 LV, Tokyo, Japan).The dielectric constant and the unloaded quality factor of the sintered samples were studied using Hakki and Coleman (11) post resonator technique and resonant cavity method (12) respectively, using a Vector Network Analyzer (Agilent, E8362b, USA). The temperature coefficient of resonant frequency (τ_f) was measured in the temperature range 30-100°C.

Result and Discussion

Fig.1 shows the powder X-ray diffraction pattern of $Ca_3V_4O_{13}$ ceramic sintered at 650°C for 4h. The large number of diffraction peaks observed in the XRD pattern reveals a lower symmetry for $Ca_3V_4O_{13}$ ceramic. A close examination of the powder X-ray diffraction pattern confirms the co-existence of both CaV_2O_6 and $Ca_2V_2O_7$ phases.

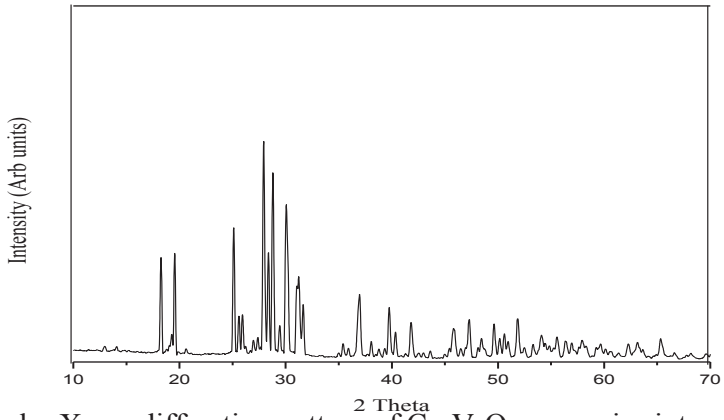

Fig.1. Powder X-ray diffraction pattern of $Ca_3V_4O_{13}$ ceramic sintered at 650°C for 4h.

The Raman spectrum of the sintered $Ca_3V_4O_{13}$ ceramic is studied and results are presented in Fig. 2. It is reported that the structure of $Ca_2V_2O_7$ contains pyrovanadate $(V_2O_7)^{4-}$ anions whereas vertex sharing $(VO_4)^{3-}$ groups are present in the structure of CaV_2O_6. The appearance of internal vibrations of VO_3 groups and bridging V-O-V bonds of the poyvanadate anions in the 900 to 1000 cm^{-1} region confirms the existence of $Ca_2V_2O_7$ groups in the Raman spectrum. In addition to $Ca_2V_2O_7$, the presence of CaV_2O_6 is also evident from the symmetric stretching vibration of the $(VO_4)^{3-}$ molecular groups observed in the 800 to 870 cm^{-1} region. Hence, Raman results also confirm the co-existence of both $Ca_2V_2O_7$ and CaV_2O_6 groups in $Ca_3V_4O_{13}$ ceramic.

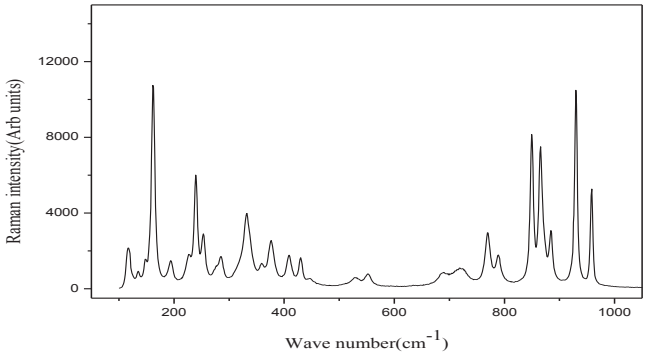

Fig.2. Raman spectrum of $Ca_3V_4O_{13}$ ceramic sintered at 650°C for 4h.

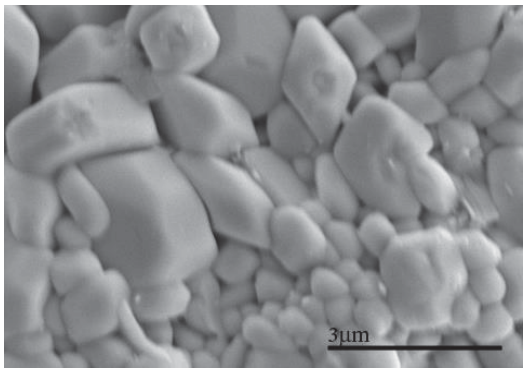

Fig.3. SEM picture of $Ca_3V_4O_{13}$ ceramics sintered at 650°C for 4h.

Fig.3 shows the SEM image of $Ca_3V_4O_{13}$ ceramic sintered at 650°C for 4h. The ceramic shows well sintered grains with small amount of porosity. The microstructure of $Ca_3V_4O_{13}$ ceramic possesses uniformly distributed polygonal grains having an average size of 2μm.

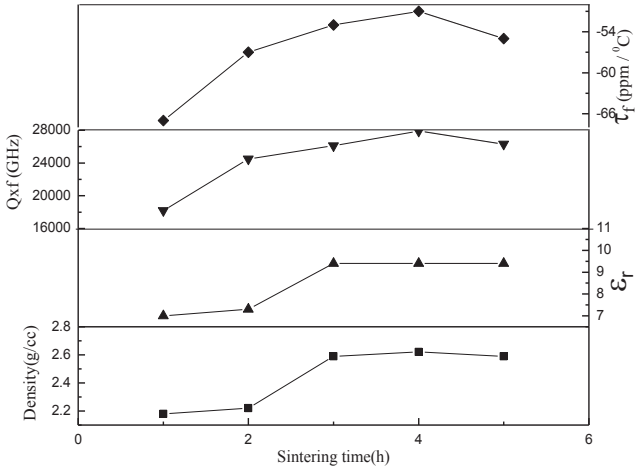

Fig.4. Variation of density and dielectric properties $Ca_3V_4O_{13}$ ceramics sintered at 650°C with different sintering time.

The variation of density and microwave dielectric properties of $Ca_3V_4O_{13}$ ceramics sintered at 650°C for different sintering time is shown in Fig.4. For $Ca_3V_4O_{13}$ ceramics, density and dielectric properties show an increasing trend with respect to sintering time. The sample sintered at 650°C for 4h possesses an optimum density of 2.62 g/cc together with ε_r=9.4, Q×f=28000 GHz and τ_f= -51ppm/°C. Further increase in sintering time slightly decreases the density.

Conclusion

$Ca_3V_4O_{13}$ ceramic has been prepared through solid state ceramic route. X-ray diffraction and Raman spectroscopic studies show that both $Ca_2V_2O_7$ and CaV_2O_6 groups co-exist in $Ca_3V_4O_{13}$ ceramics. SEM analysis shows dense microstructure with well sintered polygonal grains. The sample exhibits excellent microwave dielectric properties at optimum sintering temperature of 650°C for 4h and hence can be used as an ideal candidate material for ULTCC applications.

References

1. S.Jayanthi, T.R.N,Kutty "Microwave dielectric properties of $Mg_4Al_2Ti_9O_{25}$ ceramics", J.Mater.Lett.62,556-560,2008.
2. H.Zhou, X.Chen, L.Fang, C.Hu, H.Wang "Microwave dielectric properties of $Ba_5Nb_4O_{15}$ ceramic by molten salt method",J.MaterSci: Mater Electronics. 21,939-942,2010.
3. P.Liu, H.Ogawa, E.S.Kim, A.Kan, 'Microwave dielectric properties of low temperature sinterdCa[$(Li_{1/3}Nb_{2/3})$,Ti]$O_{3-\delta}$ceramics', J.Eur.Ceram.Soc., 24,1761-1764,2004.
4. H.Zhou, X.Liu, H.Wang, X.Chen, 'Low temperature co-firing and compatibility with silver electrode of ZnO-SnO_2-TiO_2-Nb_2O_5 ceramics with $BaCu(B_2O_5)$ addition' J.Ceram.Inter., 38,367-372,2012.
5. N.Santha, M.T.Sebastian, 'Low temperature sintering and microwave dielectric properties of $Ba_4Sm_{9.33}Ti_{18}O_{54}$ ceramics',J.Mater.Res.Bull., 43,2278-2284,2008.
6. C. L. Huang, M. H. Weng, H. L. Chen,Effects of additives on Microstructures and microwave dielectric properties of (Zr, Sn)TiO4 Ceramics,J. of Mater. Chem. and Phy.71,17-22,2001.
7. N.K.James, R.Ratheesh, 'Microwave dielectric properties of low-temperature sintarable$BaCe_2(MoO_4)_4$ Ceramics', J.Am.Ceram.Soc.,93,4,931-933,2010.
8. D.Zhou, C.A. Randall, H.Wang, L.X. Pang, X.Yao, 'Microwave dielectric ceramics in Li_2O-Bi_2O_3-MoO_3 system with ultra-low sintering temperature', J.Am.Ceram., 93,4, 1096-1100,2010.
9. A.Surjith, R.Ratheesh, 'High Q ceramics in the $ACe_2(MoO_4)_4$ (A=Ba,Sr and Ca) system for LTCC applications', J.Alloy. and Comp., 550,169-172,2013.
10. E.K.Suresh, A.N.Unnimaya, A.Surjith, R.Ratheesh. 'New vanadium based $Ba_3MV_4O_{15}$(M=Ti and Zr) high Q ceramics for LTCC applications', J.Ceram.Inter.,39, 3635-3639,2013.
11. B.W.Hakki and P.D.Coleman, 'A dielectric resonator method of inductive capacities in the millimeter range,'IRE Trans. Microwave Theory Techn., 8,402-410,1960.
12. J.Mazierska, M.V.Jacob, A.Harring, J.Krupka, P.Barnwell, T.Sims, 'Measurments of loss tangent and relative permittivity of LTCC ceramics at varying temperatures and frequencies', J.Eur.Ceram.Soc.,23,2611-2615,2003.

COMPACT HEXAGONAL SPLIT RING RESONATOR DUAL BAND BANDSTOP FILTER

Jasmi .J[*(1)], *Manju Bhaskar*[(1)], *and Thomaskutty Mathew*[(2)]
(1) KMEA Engineering College, Ernakulam, India, Pin: 683561
Email: jasmijalal@yahoo.co.in[*(1)], mbr.ec@kmeacollege.ac.in[(1)]
(2) School of Technology and Applied Sciences , Ernakulam, India, Pin: 682024
Email: drtkmathew@yahoo.co.in.

Abstract: *Dual band bandstop filters are realized by etching periodic patterns of split ring resonators(SRR) on either sides, in close proximity to a transmission line. This article presents a modified hexagonal SRR in the design of dual band bandstop filter with narrow stopbands at 2.07GHz and 2.55GHz. The new structure shows size miniaturization and increased stopband rejection level than the conventional hexagon shaped SRR filter. Simulation results of the structures are validated through measurements.*

INTRODUCTION: Filters have got a vital role in communication devices and systems, and metamaterial structures are a solution to reduce the size of the circuits [1]. There have been many different types of ring resonator structures in research studies, because these structures can be applied to planar technologies and they are found to have applications in compact microwave filters [2]. As the manufacturing processes and materials are very economical, microstrip technology has found its place in the design and implementation of communication system devices which have reduced area than the lumped element devices.

THEORY OF SRR: The planar structures which consist of two concentric conducting rings made of nonmagnetic metal like copper with slits etched on opposite sides is a split ring resonator. They can be considered as an LC circuit which is externally driven, and its dimensions determine the resonant frequency. The small electrical size of SRR makes it useful in the design of compact filters.

Fig.1 shows a schematic diagram of hexagonal SRR having strip width 'c' and spacing 'd' between the rings. The split gaps in the inner and outer rings are of equal width and denoted as 'g'. The inner and outer rings have dimensions a_{avg} and a_{ext}. The resonant frequency of the split ring resonators is given by [3],

$$f = \frac{1}{2\pi\sqrt{L_T C_{eq}}} \tag{1}$$

$$= \frac{1}{2\pi\sqrt{L_T[\left(\left(3a_{avg}-\frac{g}{2}\right)C_{pul}\right)+\left(\frac{\varepsilon_0 ch}{2g}\right)]}} \tag{2}$$

The effective inductance 'L_T' [4] is determined by the metal rings and effective capacitance 'C_{eq}' is determined by the gaps and splits in the rings. Here, a_{avg} is the distance of the two

constituent rings from the centre, ε_0 is the absolute permittivity, h is the height of the substrate and C_{pul} is the per unit length capacitance [5].

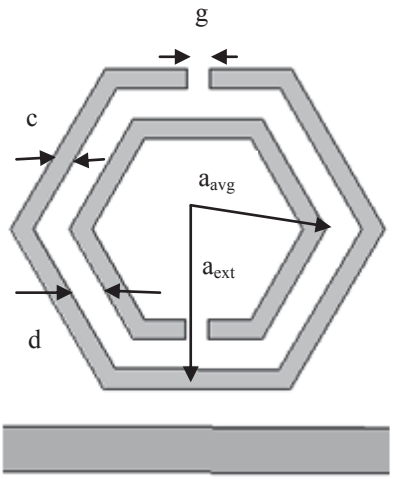

Fig.1 Hexagonal SRR Fig.2 Regular hexagon Fig.3 Modified hexagon

A regular hexagon is shown in Fig.2 which has all the six sides of equal width. This hexagon can be modified to another shape in such a way that it has the same perimeter but occupying smaller area than a regular hexagon which is shown in Fig.3. The modified hexagonal shaped split ring resonator has been used to implement dual band bandstop filter in this paper.

TOPOLOGY OF THE FILTER: A dual band bandstop filer is designed with resonant frequency at 2.07 GHz and 2.6 GHz in regular hexagonal shaped split ring resonator and modified hexagonal shaped split ring resonator. The filters are fabricated on Arlon substrate having a relative dielectric constant of 2.2, thickness of 0.787mm and loss tangent 0.0009. The hexagonal shaped split ring resonator bandstop filter has lengths 48mm and 36mm.The width of the rings, r is 0.5mm and the split width, g is 1mm. The top SRR has inter-ring spacing, c_1, as 1mm and bottom resonator has inter-ring spacing, c_2, as 0.5mm. The resonators are placed very close to the central transmission line to ensure maximum coupling. The gap between the resonators and microstrip transmission line, w, is 0.4mm.The second structure consists of modified hexagonal shaped SRRs which also has same resonator lengths, split width, ring width and inter-ring distance as the first structure. The length of the transmission line in regular hexagonal shaped SRR is 60mm and modified hexagon is 48mm.The layout of the filters is shown in Fig.4 and Fig.5.

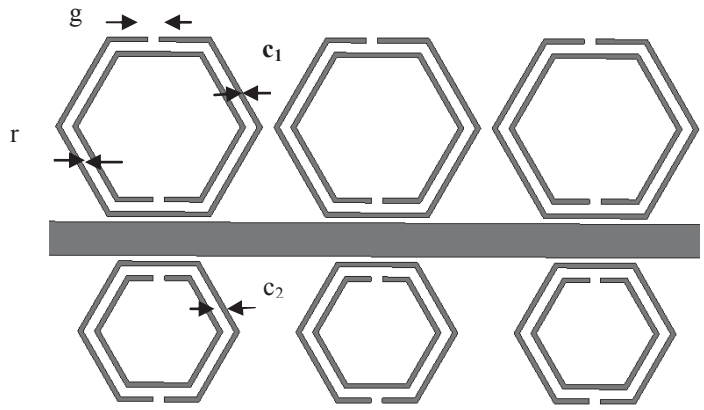

Fig.4 Layout of regular hexagonal dual band BSF

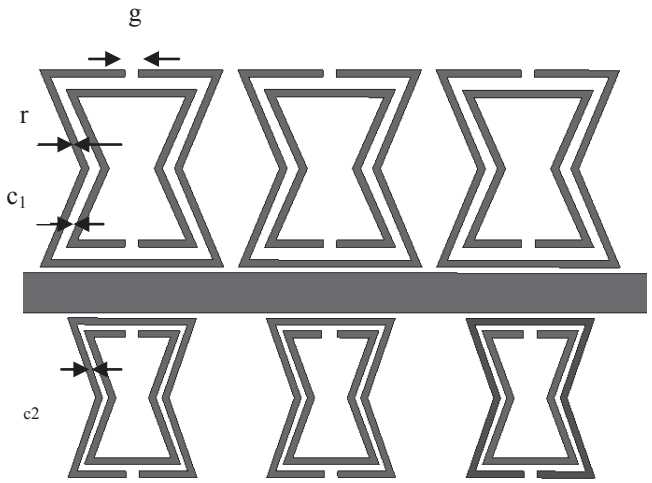

Fig.5 Layout of modified hexagonal dual band BSF

RESULTS: The measurements S_{11} and S_{12} are taken using a PNA network analyzer. The simulated and measured frequency response of S_{12} is compared and shown in Fig.6 and Fig.7. For modified hexagon, the measured results show centre frequencies at 2.07 GHz and 2.58 GHz, with rejection levels of -26dB and -23dB respectively, while the simulated results show centre frequencies at 2.07 GHz and 2.55 GHz, with rejection levels of -28dB and -27dB respectively. The results show a sharp cut-off and low return loss.

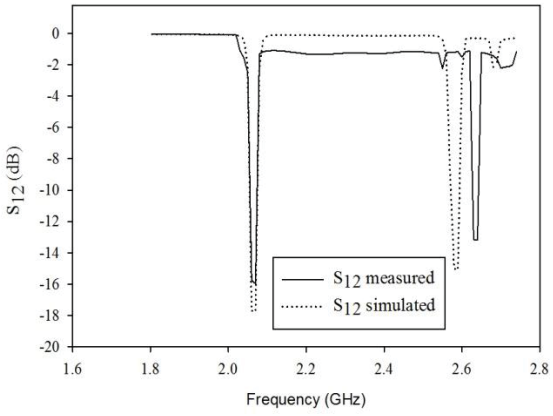

Fig.6 Comparison of S_{12} of regular hexagonal SRR BSF

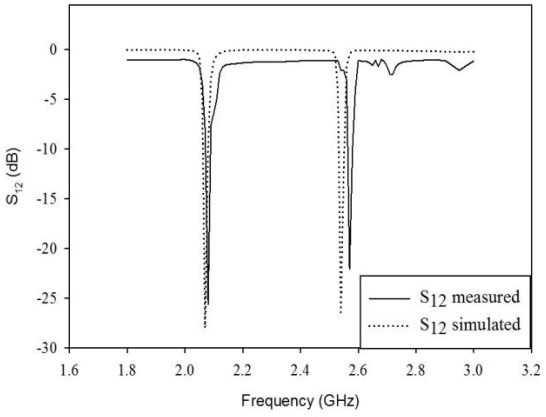

Fig.7 Comparison of S_{12} of modified hexagonal SRR BSF

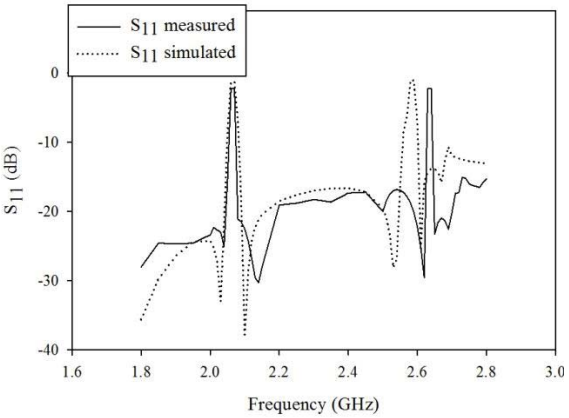

. Fig.8 Comparison of S_{11} of regular hexagonal SRR BSF

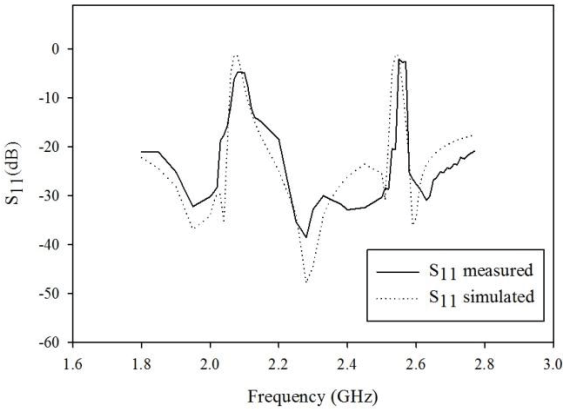

Fig.9 Comparison of S_{11} of modified hexagonal SRR BSF

A higher stop band attenuation is observed in the modified hexagonal than the regular hexagonal BSF, which can be related to the magnetic coupling of the rings which are much closer in modified hexagon than the regular hexagon. The simulated and measured frequency response of S_{11} is compared and shown in Fig.8 and Fig.9. The measured and simulated results show comparable values. The difference between the simulated and measured values can be due to the substrate material and the fabrication intolerances. The photograph of the fabricated filters is shown in Fig.10 and Fig.11. The modified hexagonal shaped split ring resonator dual band bandstop filter is found to have a size reduction of 25.15% than the regular hexagonal shaped bandstop filter.

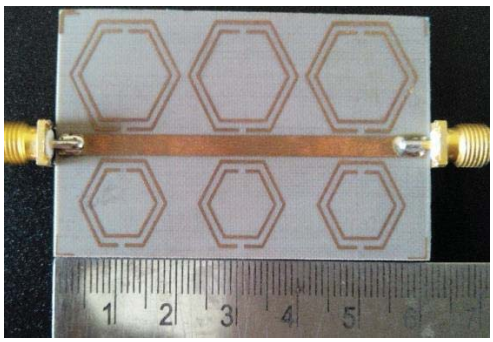

Fig.10. Photograph of fabricated regular hexagonal SRR BSF

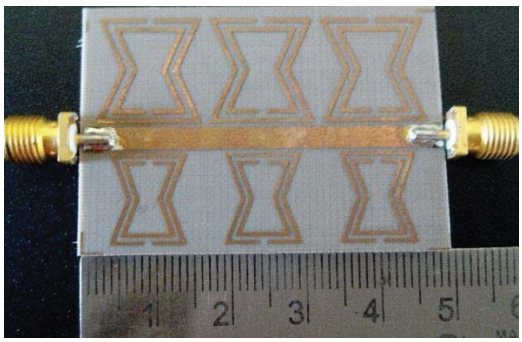

Fig.11. Photograph of fabricated modifed hexagonal SRR BSF

CONCLUSION: A dual band bandstop filter has been developed using split ring resonators in modified hexagonal shape. The new structure shows enhanced performance and a miniaturization of 25.15% than the conventional hexagonal split ring resonator. The filters being easy to design and fabricate, can find applications in multi-band wireless communication systems.

ACKNOWLEDGEMENT: The authors are grateful to Prof. (Dr.) P. Mohanan and Dr. S. Mridula, Cochin University of Science and Technology for their help and support in completion of this work.

REFERENCES

[1] J.de Dios Ruiz and J.Hinojosa, “Microstrip bandstop filter design from a modified version of split ring resonator”, The fifth International Congress on Advanced Electromagnetic Materials in Microwave and Optics, 2011.
[2] J.B.Pendry, A.J.Holden, D.J.Ribbins and W.Stewart, “Magnetism from conductors and enhanced nonlinear phenomenon”, IEEE Trans. Microwave Theory Tech,vol.47,pp2075-2084
[3] Chinmoy Saha and Jawad Y.Siddiqui, “A Comparative Analysis for Split Ring Resonators of Different Geometrical Shapes”, IEEE 2011.
[4] F.E.Terman, Radio Engineers’ Handbook, Mcgraw-Hill,Nw York,1943I.Bahl and P. Bhartia,Microwave Solid State Circuit Design, Ch.2, John Wiley & Sons, New York,1998.
[5] I.Bahl and P. Bhartia,Microwave Solid State Circuit Design, Ch.2, John Wiley & Sons, New York.

Dual Band Circular Polarizer using Superstrate with Split Ring Structure

Anindya Ghosh[(1)], *Binay Kumar Sarkar* [(1)]
(1) Indian Institute of Technology, Kharagpur.,India, 721302,
Email: anindyaghosh.ghosh4@gmail.com, bks@ece.iitkgp.ernet.in.

Abstract: *A dual band polarizer is proposed in this work which is capable to convert dual frequency, dual linear polarized wave into dual frequency circular polarized wave. The polarizer is designed and measurement results are presented.. Achieved Axial ratio from experimental results is 0.801dB and 1.8dB at 1.486 GHz and 2.592GHz respectively.*

Introduction: Circular polarized wave is widely used in GPS, Radar, Satellite Communication systems to avoid environmental interferences. Unwanted multipath reflection can also be mitigated with circular polarized wave. Polarization properties of propagating wave can be changed from linear to circular by using Superstrate. A multilayer split ring frequency selective surface reported in [1] to change wave polarization over wide frequency range. Single layer split ring FSS is implemented as circular polarizer in [2]. A Single layer Superstrate which convert the polarization and also improve antenna directivity, is proposed in [3].Mender line FSS can also convert the linear polarized wave to circularly polarized wave [4]. Most of the cases the polarizer layer is multi layered or it operate with a frequency ranges. Linear polarized wave within the frequency range of operation is either Vertical or Horizontal polarized.

A dual band polarizer for dual polarized wave is proposed in this work which gives circularly polarized wave for both frequencies. A dual polarized dual band antenna is used as linear polarized wave and polarizer FSS is placed H=48mm above the radiating source as shown in Fig.1. Unit cell of proposed polarizer FSS is designed in such a way so that parallel and perpendicular component of electric field amplitude and phase satisfy the condition of circular polarization at both frequencies.

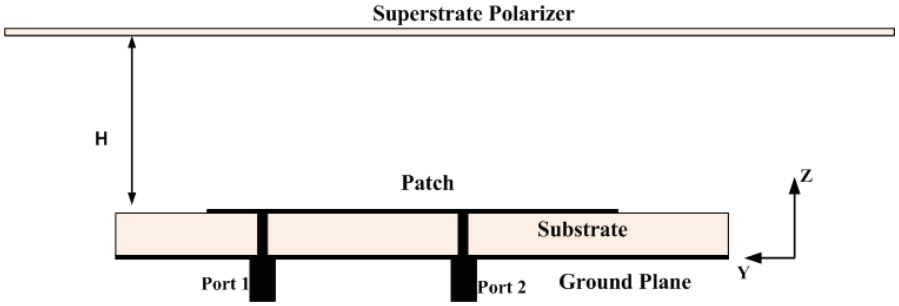

Fig.1. Polarizer with dual band antenna.

Working Principle: Linear polarized incident electric field propagating through the polarizer FSS which placed 48mm above the radiating source. If incident electric field is Y polarized, transmitted electric field can be stated as [5]

$$\vec{E} = (T_{XY}\vec{x} \pm T_{YY}\vec{y})E_0 \quad (1)$$

Where,
E_0= Incident Electric Field.
$\vec{E}$ = Transmitted electric field after passing through Polarizer.

T_{XY} = Transmission of Y polarized incident wave along X direction after passing through polarizer.

T_{YY}= Transmission of Y polarized incident wave along Y direction after passing through polarizer.

To get circularly polarized wave the amplitude and phase difference of T_{XY} and T_{YY} should be equal and 90 degree respectively.

At 1.48 GHz X polarized wave incident on the FSS and its orthogonal components are maintaining the required condition for polarization conversion as stated in equation.1. In other hand for Y polarized wave which radiated at 2.592 GHz, FSS maintaining the same condition of equation1.

Dual periodicity is maintain in polarizer FSS to operate it dual frequency of operation. Unit cell of the FSS is both cases are circular ring with a split cut. Position of splits are adjusted for polarization conversion. The proposed FSS polarizer structure is given in Fig.2. Dimension of proposed FSS is 228mm X 228mm X 1.57mm (A X B X h) where 'h' is the thickness of polarizer. FSS is fabricated on a substrate which is having dielectric constant 2.2. Unit cell dimension for 1.486GHz is 32.57mm X 32.57mm and for 2.58 GHz is 28.5mm X 28.5mm.

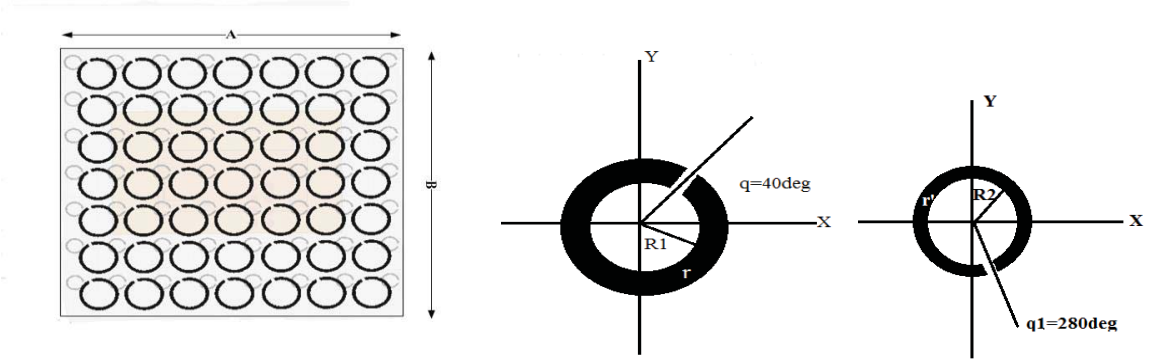

Fig.2. Dual band Polarizer and split rings.

Unit cell of polarizer FSS is simulated in CST microwave studio [6]. The unit cell structure is given in Fig.2. and dimensions are presented in Table-I. Periodic boundary conditions are applied along X and Y direction. Magnitude and phase difference of two orthogonal component of transmission coefficient are presented in Fig.3-4 which shows that the magnitude of two components are nearly equal. Phase difference between two components is also close to 90 deg.

Table I
Unit cell dimensions

Split Ring at	Ring width	Split gap	Inner radius	Split angle
Top layer	2mm	1.4mm	11mm	40deg
Bottom layer	1mm	1mm	5mm	280deg

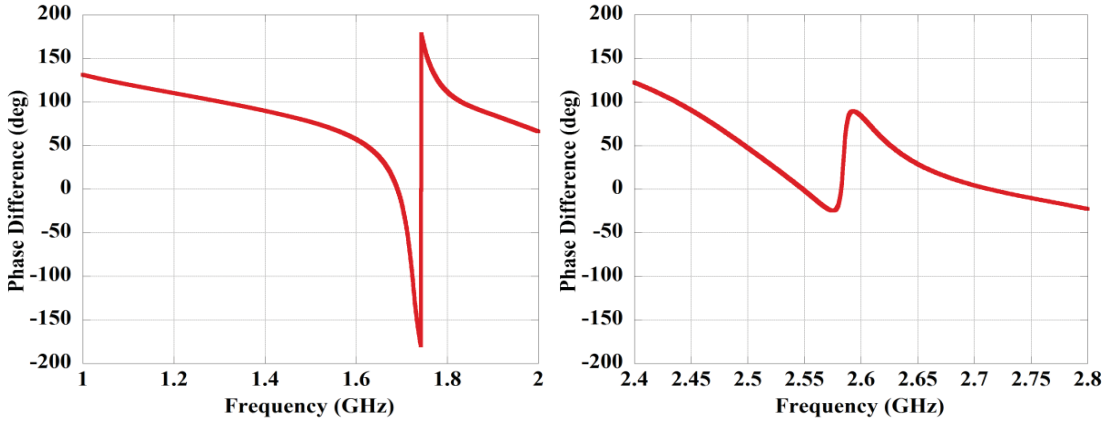

Fig.3. Phase difference of two orthogonal transmission components.

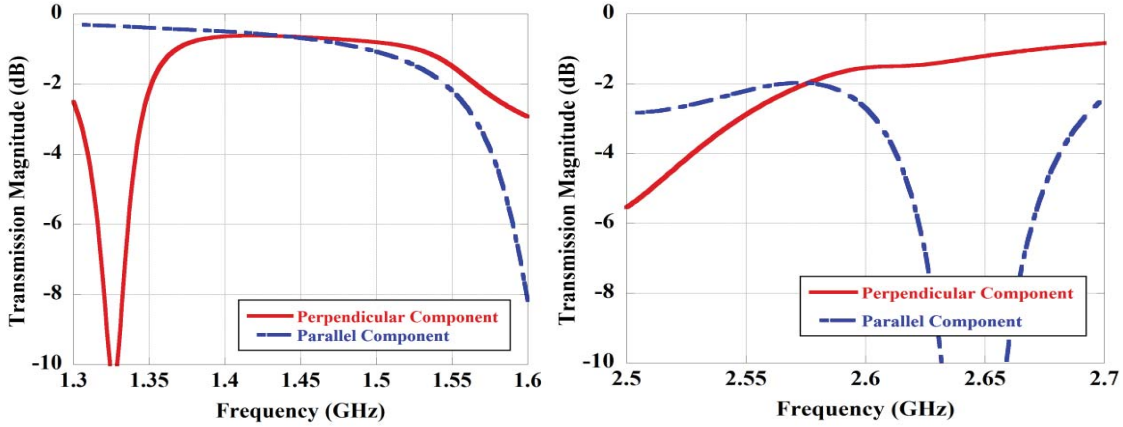

Fig.4. Transmission Magnitude of two orthogonal components.

Measurement Result: The polarizer is fabricated on Roger-rt-duroid 5880 substrate. Measurement has done in laboratory environments. The measured axial ratio at 1.468 GHz and 2.592 GHz is 0.66 and 0.801respectively. Experimental data is given in Table-II, which are slightly varying due to the finite structure of polarizer.

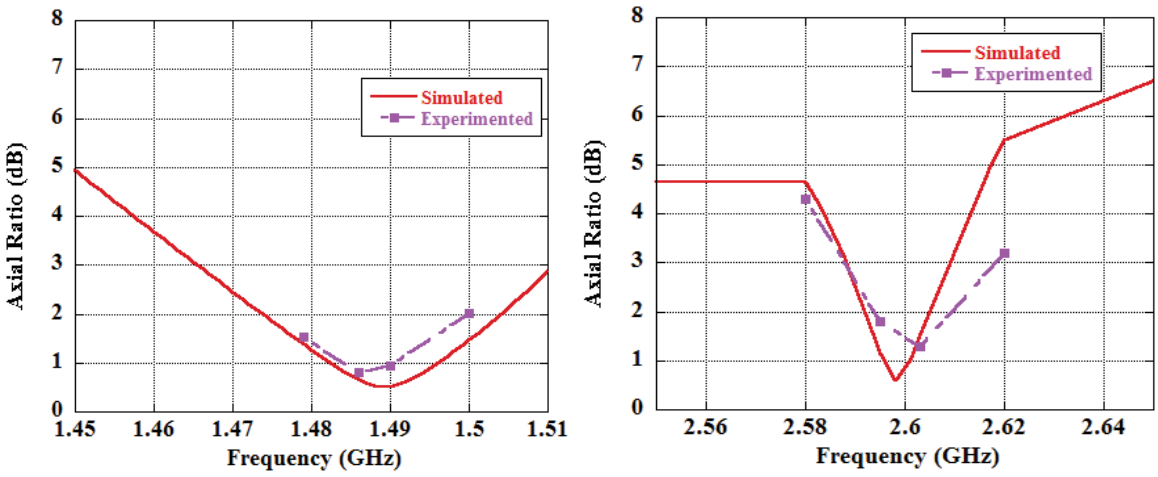

Fig.5. Simulated and Measured Axial ratio of transmitted wave after passing through the polarizer.

Table II
Comparison between simulation and experimental results

Frequency	Simulated Axial ratio (dB)	Measured Axial ratio(dB)
1.486GHz	0.66	0.801
2.592 GHz	1.1	1.8

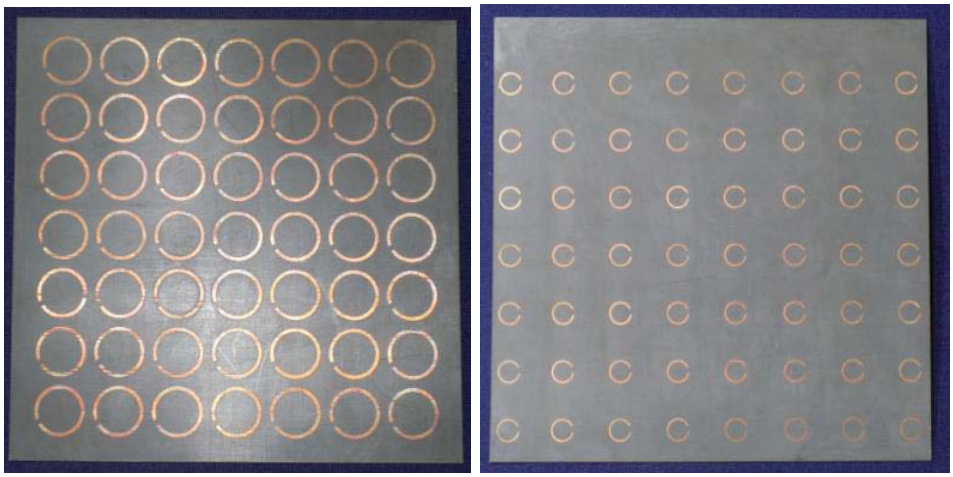

(a) (b)

Fig.6. (a)Top and (b) bottom view of polarizer.

Conclusion: A dual band circular polarizer is designed and fabricated. In this work a dual band dual linear polarize wave is converted to a dual band circularly polarized wave by using a suitable Superstrate having circular split rings. The height of the Superstrate from patch is same for both frequencies. Experimental results show a good agreement with the simulation results.

Acknowledgement: We are obelized to ISRO Bangalore for their financial support to carry out this work.

Reference:

[1] Martinez-Lopez, L., Rodriguez-Cuevas, J., Martinez-Lopez, J.I., and Martynyuk, A.E.:'A multilayer circular polarizer based on bisected split-ring frequency selective surfaces',IEEE Antennas Wirel. Propag.Lett., 2014,13, pp. 153–156

[2] M. Euler, V. Fusco, R. Cahill, and R. Dickie, "325 GHz single layer sub-millimeter wave FSS based split ring linear to circular polarization convertor,"IEEE Trans. Antennas Propag., vol. 58, no. 7, pp.2457–2459, Jul. 2010.

[3] X.L.Ma,C.Huang,M.B.Pu,C.G.Hu,Q.Feng,andX.G.Luo,"Single-layer circular polarizer using metamaterial and its applicationin antennas,"Microw.Opt.Tech.Lett., vol. 54, no. 7, pp. 1770–1774,Jul. 2012.

[4] M. Joyal and J. Laurin, "Analysis and design of thin circular polarizers based on meander lines,"IEEE Trans. AntennasPropag., vol. 60, no.6, pp. 3007–3011, Jun. 2012.

[5] X. Ma, C. Huang, M. Pu, C. Hu, Q. Feng and X. Luo, "Multi-band circular polarizer using planar spiral metamaterial structure", Opt. Express., vol. 14, no. 20, pp. 16050-16058, July 2012.

[6] CST Studio Suite 2006 Advanced Topics CST-Comp. Simulation Technology, 2014.

Biphasic Calcium Phosphate-Arrowroot film for microwave phantom applications

Ullas G Kalappura[(1)] *and K. T. Mathew*[(2)]
(1) Microwave Materials Research Laboratory,Department of Electronics,
Cochin University of Science and Technology, India-682022, E-mail: ullasgk@gmail.com
(2) Viswajyothi College of Engineering and Technology, Vazhakulam, India-686670,
E-mail: kattackalmathew@gmail.com

Abstract: *Bioceramics are widely used for medical implantation applications. Biphasic Calcium Phosphate is popular for its bioresorbability and balanced mechanical properties. A biofilm based on biomaterial Arrowroot and Biphasic Calcium Phosphate is prepared, and tested for its suitability as microwave phantom material. Cavity perturbation method was used for dielectric characterization of the film.*

Introduction: In 1970-80s, bioglass (CaP containing glass) and hydroxyapatite ceramic (HAp) were found to be osteoconductive. Since then Calcium phosphate biomaterials became the most interesting artificial bone grafts. HAp has good mechanical properties, but is less bioresorptive as compared to β-Tricalcium Phosphate (β-TCP) ceramics. The Biphasic Calcium Phosphate (BCP) is formed by the mixture of HAp and β-TCP in different ratios [1,2]. Hence the dissolution of BCP highly depends on the β-TCP/HAp ratio. Synthetic films that possess either or any of the characteristic features such as biodegradability, biocompatibility, bioresorption etc. can be termed as biomaterial films. Biomaterial films found significant applications in complex surgeries involving skin transplantation, plastic surgery and they even found use as a medium for drug delivery as some of these films were edible and non-toxic. Arrowroot is from the family Marantaceae. It has tuberous roots which stores starch. Because of its medicinal properties [3,4], it is considered to be an effective antidote to vegetable poisons.

Microwave phantoms are usually used to evaluate quantitative performance of imaging systems [5]. The purpose and use of a phantom is to explore the interaction between body tissues and electromagnetic fields. A phantom used to evaluate an imaging device should respond in a similar manner to how human tissues and organs would act in that specific imaging modality. Munro *et al* [6] performed measurements to determine dielectric properties of liquids and gels for use in as microwave phantoms. In this work, we have prepared Arrowroot-BCP films for different ratios of Arrowroot and BCP. The prepared films were characterized using cavity perturbation technique. The developed films were found to be compatible for use as microwave phantoms.

Preparation:

For preparing Biphasic Calcium Phosphate, HAp and β-TCP are mixed in the ratio 1:4 and ground well. The resultant mixture is calcinated at 700^{o}C for 3 hours. The mixture is allowed to cool, ground again and then kept in air tight container. The BCP powder is not as flimsy as β-TCP powder, but is grainier in appearance.

Arrowroot (Maranta Arundinacea) has therapeutic use as it is mainly used as a traditional wound healing medicine. Arrowroot powder (10g) is dissolved in water (100ml) and is heated to obtain Arrowroot gel. To this gel, the BCP is added in different ratios (1:4,

2:3, 1:1, 3:2 and 4:1) and are casted to obtain films. The films are dried in room temperature and are cut into long strips for dielectric characterization studies. The films were of uniform thickness and are devoid of air gaps.

Experimental setup and Theory:

Microwave characterization of Arrow and Arrow-Ch films were performed using Agilent 8714 ET vector network analyzer. Cavity perturbation technique [7] was used for the purpose. The properties such as Complex permittivity, Microwave heating coefficient and Absorption coefficient were calculated.

The complex permittivity can be obtained from the measured data as below

$$\varepsilon_r' - 1 = \frac{f_c - f_s}{2f_s}\left(\frac{V_c}{V_s}\right) \quad (1)$$

$$\varepsilon_r'' = \frac{V_c}{4V_s}\left(\frac{Q_c - Q_s}{Q_c Q_s}\right) \quad (2)$$

Where V_c,V_s are the volumes of the cavity and sample respectively.

For absorption coefficient measurements, the samples were placed in a perspex sample holder of 2.5mm thickness and hold in between two S-band waveguide adapters.

Absorption coefficient, A=1- (R + T)

Where $R=|S_{11}|^2$, the reflection coefficient and $T=|S_{21}|^2$, the transmission coefficient.

Characterization: The dielectric properties of Biphasic Calcium Phosphate: Arrowroot (BCP: Arrow) film were studied with the aid of HP 8714ET Network Analyzer. The measurements were taken at 2.685GHz which is one of the resonant frequencies of the cavity. Films with varying BCP/Arrow ratio were used for dielectric characterization measurements. The thickness of the film is immaterial as the films are homogeneous. However, uniform thickness was maintained for individual samples.

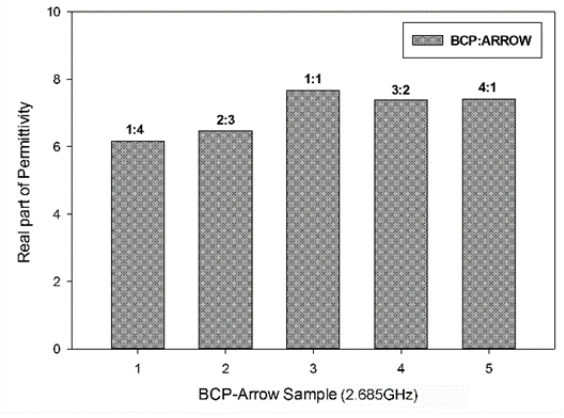

Figure1. Variation of real part of Permittivity with frequency

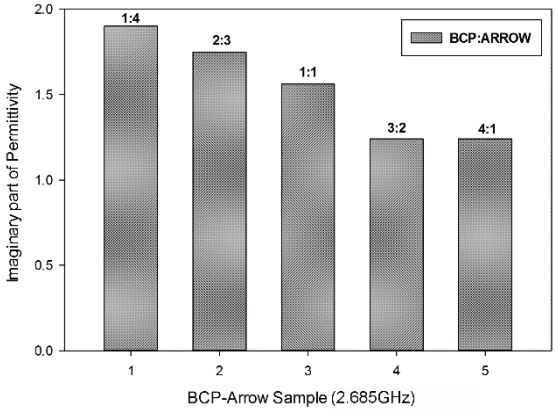

Figure2. Variation of imaginary part of Permittivity with frequency

Figure 1 shows the variation of real part of complex permittivity at 2.685 GHz for BCP: Arrow films with ratios 1:4, 2:3, 1:1, 3:2 and 4:1. It can be observed that the ratio 1:4

shows minimum permittivity which is around 6. The body tissue collagen exhibits permittivity value in between 5.5 and 6.5. Hence the BCP:Arrow film can be used as a phantom material representing collagen. As the amount of BCP is increased in film, an increase in permittivity value is observed. And when the amount of BCP exceeds that of Arrowroot, the permittivity doesn't show further variation. It might be due to the saturation of BCP particles in vacant spaces of the film. Further increase of the BCP amount in the film significantly affects its mechanical properties and structural stability of the film. It will make the film brittle and useless.

The imaginary part of permittivity or the Loss factor (figure 2) depends on the dielectric relaxation property of the film. The film is assumed to be non-polar due to the absence of water in it. Hence it gets only weakly polarized in an applied field owing to a faster relaxation time. And it accounts for the nominal value of Loss factor. The Arrowroot gel is highly polar in nature when compared to BCP powder. As the amount of BCP is increased in the film, the Loss factor also shows a corresponding variation by lowering its value.

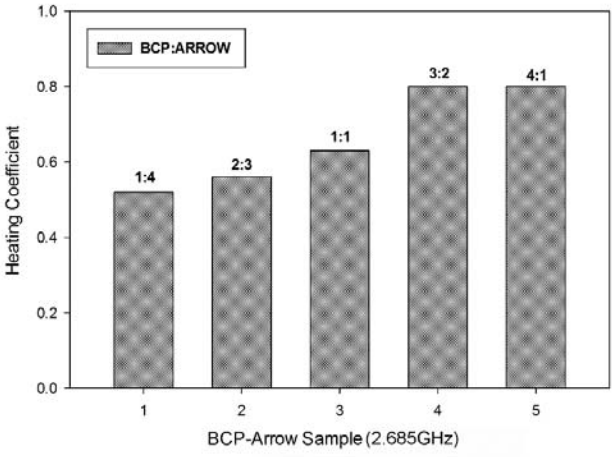

Figure3. Variation of heating coefficient with frequency

The heating coefficient defines how microwave interacts with a material. Dielectric relaxation phenomenon is responsible for dielectric heating. Heating coefficient is the efficiency of heating of a dielectric material. A low value of heating coefficient indicates that

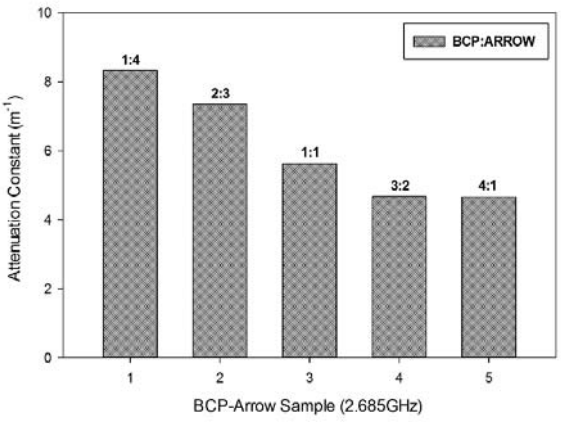

Figure4. Variation of attenuation constant with frequency

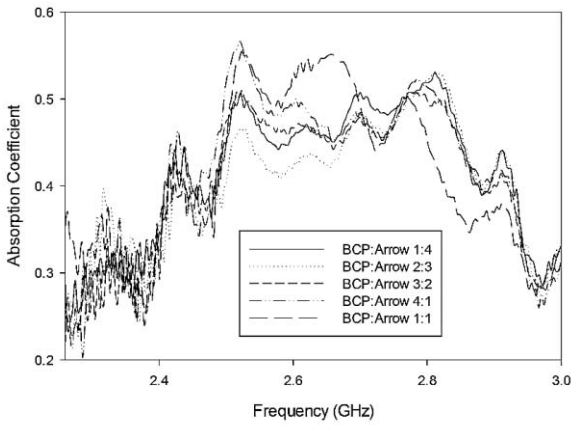

Figure5. Variation of absorption coefficient with frequency

the material is good for dielectric heating purposes [8]. As evident from Figure 3, the BCP: Arrow samples in ratios 3:2 and 4:1 have the highest Heating coefficients. Thus they undergo less dielectric heating. Hence they are better than the other BCP: Arrow combinations for implantation/phantom applications.

The attenuation constant (Figure 4) shed light on the material's transparency to microwaves. It is directly related to the Loss factor of the material. Hence it shows the same variation as that of the loss factor. It is observed that BCP: Arrow with the ratio 1:4 has the highest attenuation constant which means it can attenuate much of the microwave power within the material. This is also evident from the variation of heating coefficient (figure 3). The ratios 3:2 and 4:1 are more transparent to microwaves and are better dielectrics. Figure 5 shows the Absorption coefficient variation with frequency for different ratios of BCP: Arrow powder samples. It can be seen that there is not much variation between the curves. The minor variations can be attributed to the slight variations in packing density of the samples within the sample holder. The absorption is nominal at the start of the band then increases to reach a maximum and again shows a declination at the upper end.

Conclusions: The dielectric characterization of Biphasic calcium phosphate-Arrowroot film was done. The amount of BCP is the key factor which determines the mechanical stability of the film. The films obtained have low dielectric constant and loss factor. They could be used as phantom materials representing collagen.

References:

[1] S. Lin, R. Z. Legeros, R. Rohanizadeh, D. Mijares, and J. P. Legeros, "Biphasic Calcium Phosphate (BCP) Bioceramics: Preparation and Properties," *Key Engineering Materials*, vol. 242, pp.473-476, 2003.

[2] E. C. Victoria and F. D. Gnanam, "Synthesis and characterisation of Biphasic Calcium Phosphate", *Trends Biomater. Atrif. Organs*, vol. 16, no. 1, pp. 12-14, 2002.

[3] C. Cooke, I. Carr, K. Abrams and J. Mayberry," Arrowroot as a treatment for diarrhoea in Irritable bowel syndrome patients: a pilot study", *Arq Gastroenterol,* 37**,** 20-24.

[4] Lajvardi, A., Mazarin, G.I., Gillespie, M.B., Satchithanandam, S. & Calvert, R.J., " Starches of varied digestibilities differentially modify intestinal function in rats", *Journal of Nutrition*, 123, pp. 2059-2066, 1993.

[5] M.A. Miller and G. D. Hutchins, "Development of Anatomically Realistic PET and PET/CT Phantoms with Rapid Prototyping Technology", *IEEE Nuclear Science Symposium Conference Record*, pp.4252-4257, 2007.

[6] K. M. Munro, J. W. Reeves, M. J. Birch and R. Collier, "Standing wave measurements to determine the dielectric properties of liquids and gels for use in microwave phantoms", 11th International Conference on Antennas and Propagation, Conference Publication No. 480, pp.111-114, 17-20 April 2001

[7] K.T. Mathew,Perturbation theory, Encyclopaedia of RF and Microwave Engineering, Kai Chang (Ed.), Vol 4, Wiley Interscience, 3725-35, 2005.

[8] K. Lakshmi, H. John, R. Joseph, K. E. George, and K. T. Mathew, "Comparison of Microwave and Electrical properties of selected Conducting polymers," *Microwave and Optical Technology Letters*, vol. 50, no. 2, pp. 504-508, 2008.

DECEMBER 19, FRIDAY
08.30AM TO 10.30AM
RESEARCH SESSION 12
MICROSTRIP ANTENNAS 3
S N MITHRA- HALL

Chair: Prof. Girish Kumar,IIT Mumbai, Mumbai.

No	Papers	Page
12.1	**Design of a Compact Antenna for the Wireless Networking of Energy Meters** Sandeep Kumar, Srinaga Nikhil and KJ Vinoy ECE Department, IISc, Banglore, India *Email:skiisc14@gmail.com, naganikhil@gmail.com, kjvinoy@iisc.ernet.in*	385
12.2	**Design and Development of Dual-Band CPW- Fed Antenna for Wireless Application** Sreelekshmi P Communication Engineering, KMEA Engg College, Kerala, India. *Email: sreelekshmis040@mail.com*	389
12.3	**A Novel Broad Band Parasitic Microstrip Ring Antenna for 5.8 GHz ISM Band Applications** A.Kamalaveni[1]and M.Ganesh Madhan[2] MIT Campus, Anna University, Chennai, India 600044. *Email: [1] kamalaveniganesh@gmail.com, [2] mganesh@annauniv.edu*	395
12.4	**Multiband Antenna Using Slotted Techniques for Wireless Applications** Rebecca Abraham[1], Usha Kiran K.[2] VIT University, Chennai , Tamil Nadu, 600127, *Email: rebecca.abraham2013@vit.ac.in[1], usha.kiran@vit.ac.in[1]*	399
12.5	**Development of a Novel Microstrip Patch Antenna For TCAS Application** Debajit De[1] , Prasanna Kumar Sahu[2] National Institute of Technology, Rourkela 769008, India. *Email: 514ee1016@nitrkl.ac.in[1], pksahu@nitrkl.ac.in[2].*	403
12.6	**Gain enhancement of antenna using proposed Hexagonal EBG with cylindrical structures for Wi-Max Applications** Naveen Kumar P [1] and Shambhulingappa K V[2] [1]SDM College of Engg. & Tech., Dharwad, India. *Email: itznavkumar@gmail.com* [2]Jain College of Engg. & Tech., Bengaluru, India. *Email: shambu91@gmail.com*	412
12.7	**A Reflector Based Compact UWB MIMO Antenna** T. K. Roshna, U. Deepak, V. R. Sajitha, Sumitha Mathew, and P. Mohanan CREMA, Department of Electronics, Cochin University of Science and Technology, Cochin -22, Kerala, India. *Email: roshnatk03@gmail.com*	418
12.8	**Null placement and Side Lobe Level Reduction in Beam Steered Linear Antenna Array using Restricted Search Particle Swarm Optimization** Soumyo Chatterjee[1] and Sayan Chatterjee [2]	422

[1] Heritage Institute of Technology, Kolkata700107, India. *Email: soumyo.chatterjee@heritageit.edu*
[2] Jadavpur University , Kolkata700075, India.
Email: sayan1234@gmail.com

12.9 **WIDEBAND DIPOLE ANTENNA OVER HIGH IMPEDANCE SURFACE** 426

V.A. Libi Mol, B. Rahul, C.K. Aanandan
Cochin University of Science and Technology, Kerala, India.
Email: libi.riyaz@gmail.com

Design of a Compact Antenna for the Wireless Networking of Energy Meters

Sandeep Kumar, Srinaga Nikhil and KJ Vinoy
ECE Department, IISc, Banglore, India
skiisc14@gmail.com, naganikhil@gmail.com, kjvinoy@iisc.ernet.in

Abstract: *This paper proposes the design of a folded uniplanar inverted F antenna for use in the wireless networking module for energy meters. Due to space constraints within existing energy meters, the size of the wireless module is limited to 60mm x 40mm and the footprint of the antenna must be smaller than this. The wireless band dedicated for this application in India is at 865-867 MHz. In order to maximize the communication range, the antenna efficiency must be kept high. The design approach and experimental results for a prototype antenna are presented here.*

Keywords: *Printed inverted F antenna; Energy meter networking; Antenna efficiency*

Introduction: Wireless technologies have touched all aspects of human life and are enabling greater levels of convenience. Wireless energy meter networking is one of the major steps in this direction. This uses a secure wireless networking technology for providing two way communication between energy meter and the distributor system [1]. Hi-tech smart energy meters have extraordinary features such as real time or near real time energy monitoring, automatic meter reading, levying bill charges according the demand profile and online bill tracing by the hour, by the day or by the month [2, 3]. In India, SRD860 band has been proposed for this application. Designing boards with size constraint, especially with an integrated antenna is a major challenge as it is the heart of wireless communication .

Due to various technological advancements, the size of the modern wireless system reduces by the year, and hence the design of various types of miniaturized antennas has been a hot topic among antenna researchers [4]. The size of most conventional antennas depends on the wavelength of operation. Thus for a low frequency antenna, the size will be larger as the wavelength is inversely proportional to the frequency. To reduce the size of the antenna, several approaches are available in the literature. Planar antennas such as microstrip antennas and printed dipole and monopole antennas are compact in size and are often preferred for most applications in modern wireless systems [5]. Planar Inverted-F Antenna (PIFA) is one such configuration widely used in modern wireless communication systems [4, 5]. By this approach we can reduce the size of the antenna up to $\lambda/8$ without seriously compromising other parameters such as the efficiency, gain, directivity and bandwidth. Therefore PIFA is highly suited for the wireless board of energy meters. The antenna proposed here is a modification of the PIFA that can be printed directly on the PCB of the wireless module [4]. Radiation efficiency of the antenna is measured using Wheeler Cap Method.

This paper is organized as mentioned with an overview of design considerations, then discusses the antenna design with certain parameter sweeps followed by discussion on the results of antenna and ends with conclusions of this work.

Design Considerations: Some approximate formulae based on the experimental results are used to determine the dimensions of the IFA. PIFA configuration can be analyzed using the transmission line model and Cavity model [4, 6, 7]. Based on a the current path, the total length of radiator required can be calculated from

$$L_1 + L_2 \approx \frac{\lambda}{4}$$

where L_1, and L_2 are the length of the shorting strip and patch of the antenna; The minimum width x of ground plane should be greater than L_2 and the length of ground plane should be greater than λ/4 for good efficiency and bandwidth.

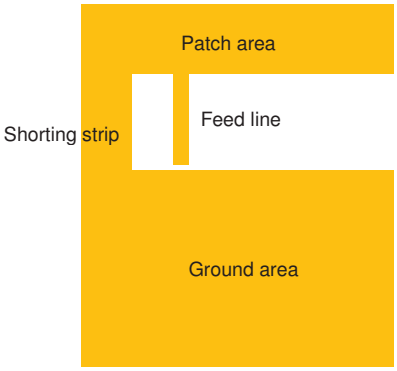

Fig 1: Geometry of the printed inverted F antenna

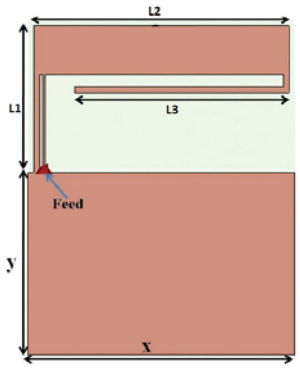

Fig. 2: Antenna design

With the operational frequency chosen as 865MHz, λ/4 is 86.7 mm. Due to limitations in space availability, the antenna designed is smaller than the above guidelines, with dimension of ground plane limited to 45×30 mm^2 and the rest of the antenna limited to an area of size 24×44 mm^2 as shown in Fig. 2. The substrate used is FR-4 with 1.6 mm thickness. The antenna length is maintained by using a folded radiator, by decreasing the antenna size and to meet the frequency specification.

Antenna Design Simulations: The performance of the antenna is analysed using CST Microwave Studio. The performance of the antenna is affected by the distance between the feeding line and the short strip [4] and the strip width. The parametric simulations of the same are shown in Fig. 3 & 4. The designed antenna has good bandwidth, efficiency and gain at the resonant frequency of 865MHz and a Omni-directional radiation pattern.

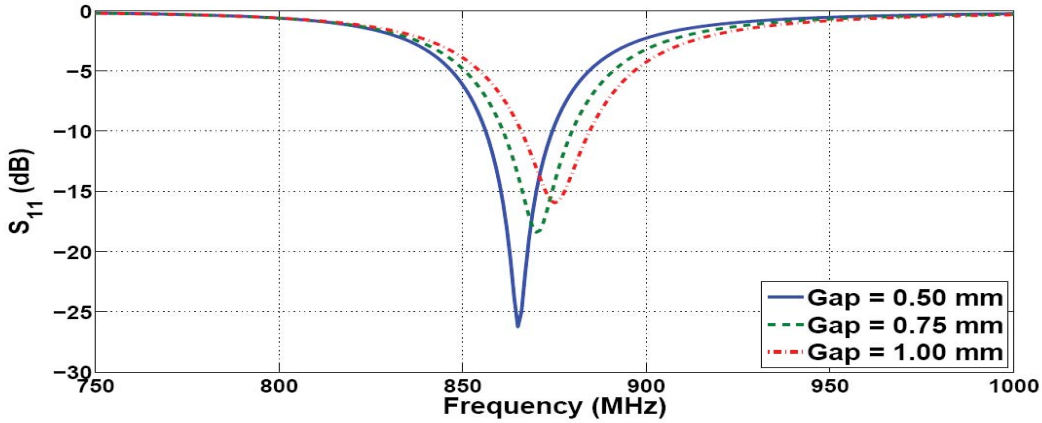

Fig. 3. S11 plot for varying gap between feed and short

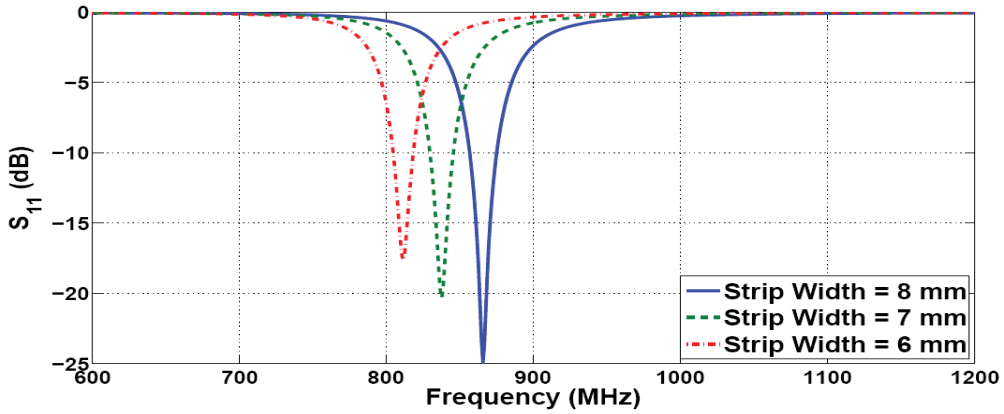

Fig. 4. S11 plot for varying the strip width.

Experimental Validation: The antenna is fabricated by standard photolithography and PCB etching process. A small coaxial cable with a connector is soldered on to the antenna to measure its performance. A photograph of the fabricated antenna is shown in Figure 5.

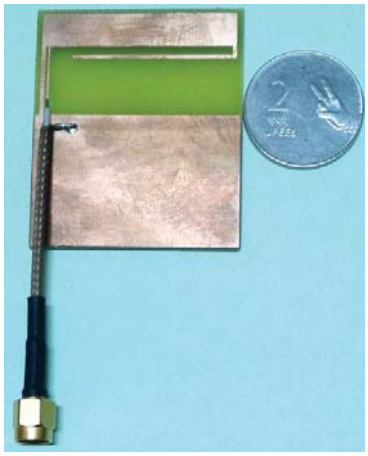

Fig. 5. Antenna Configuration

A. Return Loss Measurement

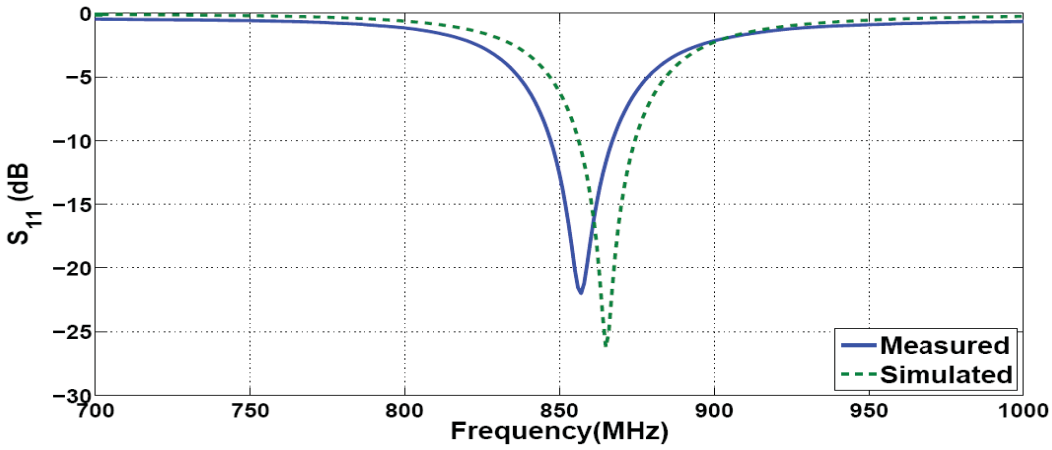

Fig. 6. S11 comparison of simulated and measured results

The antenna performance is evaluated using a vector network analyzer. The measured and simulated results are closely agreeing as shown in Fig. 6, except a slight shift due to tolerances such as loss in cable, soldering effects and fabrication errors. The resonant frequency is around 870MHz with a bandwidth (-10dB) of 19MHz. Therefore the fabricated antenna work in the wireless band of interest.

B. Radiation Efficiency measurement

Wheeler cap method is used to measure the radiation efficiency of the antenna [8]. The radiation efficiency of this antenna is experimentally evaluated using a metal (copper) box size 100×100×75 mm^3, where the real part of input impedance of the antenna changes from 57.5 Ω in free space to 1.7 Ω in the closed metal box. The radiation efficiency of this antenna calculated is

$$\frac{57.5 - 1.7}{57.5} = 0.9705$$

This implies that the radiation efficiency of the antenna is 97.05%.

Conclusion: A folded uniplanar inverted F antenna is proposed in this paper for a compact antenna with excellent performance at 865MHz. The antenna is fabricated on the commonly used FR-4 substrate and has a high value for the measured radiation efficiency. The fabricated antenna exceeds the bandwidth requirement. The large bandwidth can help in retaining the operation of the antenna by preventing any de-tuning due to other components within the energy meter.

Reference:

[1] Smart energy meter for monitoring of electricity: URL http://www.smart-energy-meters.com/

[2] Smart energy meter automatic bill charging: URL https://www.gov.uk/government/policies/helping-households-to-cut-their-energy-bills/supporting-pages/smart-meters

[3] Smart Energy freescale smart grid and metering solutions: URL www.freescale.com/files/industrial/doc/brochure/BRSMRTENERGY.pdf.

[4] Z. Zhang, Antenna design for mobile devices. Wiley-IEEE Press, Singapore , 2011.

[5] K.L. Wong. Planar antenna for wireless communication. Wiley Inerscience, Hoboken: New Jersey, 2013.

[6] Antenna theory, Planara inverted-F antenna (PIFA) : URL http://www.antenna-theory.com/antennas/patches/pifa.php

[7] Z. Qi; K. Fu; T.-Z. Liang, "Analysis of planar inverted-F antenna using equivalent models," *Antennas and Propagation Society International Symposium, 2005 IEEE* , vol.3A, pp.142,145, 3-8 July 2005

[8] W.E. McKinzie III, A modified Wheeler cap method for measuring antenna efficiency. IEEE Antennas and Propagation Society International Symposium, 1997 Digest, 1(1):542-545, July 1997.

Design and Development of Dual-Band CPW-Fed Antenna For Wireless Applications with Defected Ground Structure

Sreelekshmi.P
Communication Engineering, KMEA Engg. College, Kerala, India
Email: sreelekshmis040@mail.com

Abstract—This paper presents a small and compact dual-band microstrip antenna for wireless applications like 4G LTE and Wi-Fi. Nowadays wireless communication systems require antennas with simple structure, wide bandwidth and low cost. The microstrip monopole antennas have a lot of merits such as low-cost, low-profile, conformability, and ease of manufacture, which make them very attractive. In the proposed antenna, a Co-Planar Waveguide-fed monopole antenna with defected ground structure for dual-band Wi-Fi and 4G LTE applications is proposed. The substrate used is FR-4 substrate with dielectric constant ϵ_r=4.4 with substrate thickness 3.2mm and the size of the proposed antenna is 34×17×3.2 mm.The obtained bandwidth and radiation characteristics make the antenna proper to be used for Wi-Fi and 4G LTE applications and it covers 2.29GHz to 2.5GHz band at the center frequency 2.42GHz and 3.9GHz to 6.2GHz band at the center frequency 5.45GHz. The simulation revealed that the peak gain values of proposed antenna is 1.9dB for the lower frequency range whereas it is 3.78 dB for the upper frequency range.

Index Terms - ***Microstrip antennas; Co-planar waveguide Feed(CPW); Defected Ground Structure(DGS); Wi-Fi; 4G-LTE; Dual-band Operation .***

Introduction: As the advancement of technology, wireless communication is one of the active area in the day-to-day life. So,the use of wireless devices and many commercial applications have arisen in order to cover the demand of services such as data/video transfer with high speed. In many applications of wireless communications such as Bluetooth, IEEE 802.11 Wireless Local Area Networks (WLAN, e.g.Wi-Fi i.e. IEEE 802.11a, 802.11b, 802.11g, 802.11j etc.), it is desirable to use multi-band antennas[2] .The latest advancement in this era of wireless communication is the 4G LTE (Long Term Evolution) technology, which is the fourth generation of mobile communication standards. A 4G system provides ultra broadband internet access for wireless communication of high speed data for mobile phones and data terminals [1]. In this paper, the proposed antenna is to be used for Wi-Fi and 4G LTE applications and it covers 2.29GHz to 2.5GHz band at the center frequency 2.42GHz and 3.9GHz to 6.2GHz band at the center frequency 5.45GHz. The simulation revealed the peak gain of microstrip antenna is 1.9dB for the lower frequency range whereas it is 3.78 dB for the upper frequency range.

Antenna Design: Fig.1 shows the geometrical configuration of the proposed CPW-fed monopole antenna. The antenna is printed on only one side of an FR4 microwave substrate with the substrate thickness of 3.2 mm and the dielectric constant of 4.4. The main structure of the proposed antenna contains two folded strips, and a CPW feeding line with Defected

Ground Structure. For feeding the antenna a CPW transmission line of width Wt and gap of W_b=0.2mm is used. The strips c, g, h and f are used to provide the dual-band characteristics.

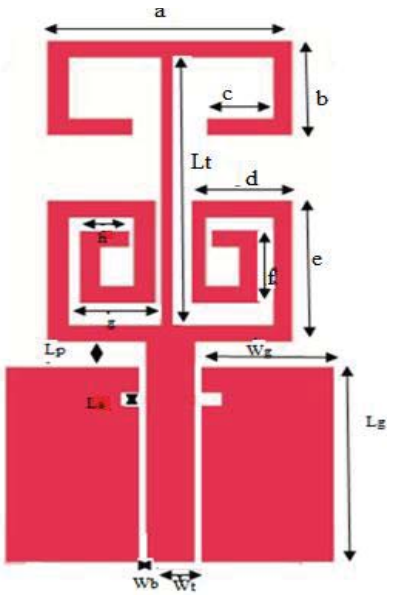

Figure 1.Geometry of Proposed Antenna

The strips Wg, Ls, Lp and a makes the antenna to resonate at the operating frequency range. The parameter a' and the DGS in the ground plane provides the upper frequency band to resonate at 5.45GHz with good return loss. The length of the ground plane and the variation in the Ls improves the return loss of both the bands. The major function of the two folded strips of equal lengths is to produce two different current paths and thus expected to effectively excite dual resonant modes.DGS in the geometry improves the resonant bandwidth. It may have various shapes like U shaped slot, E shaped slot etc.
The table shows the optimized parameter values:

Parameter	Size (mm)	Parameter	Size (mm)
a	12.7	g	1.5
b	5	h	2.8
c	3.35	Lp	1.5
Lt	17.3	Wg	2.74
d	4.5	Lg	12.5
e	8	Wt	1.59
f	3.6	Ls	0.2

Results and Discussions: The proposed antenna with various parameters has been designed and fabricated. The radiation pattern, return loss and gain were analysed. The proposed antenna is designed and optimized with CST Microwave Studio.
Return Loss: The below graph shows the simulated return loss graph which covers the frequency range from 2.29 GHz to 2.5GHz band at the center frequency 2.42 GHz and 3.95 GHz to 6.2 GHz band at the center frequency 5.45GHz . The bandwidths are of 200MHz and 3GHz.

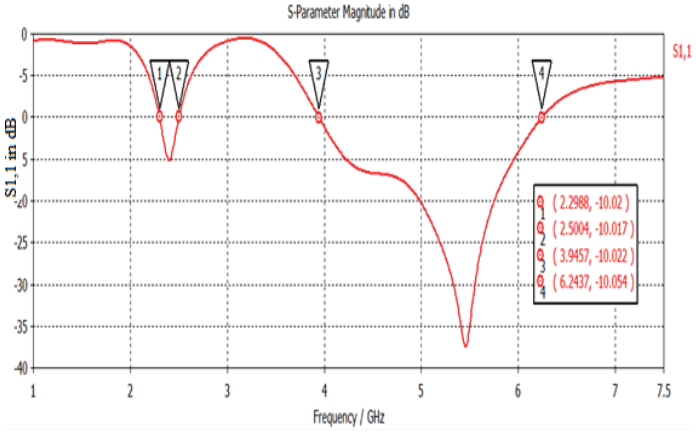

Figure 2. Simulated Return Loss Graph

Fig. 3 shows the comparison with measured and simulated return loss graph, the frequency range and return loss obtained for the lower frequency band are almost same. The return loss is less for the measured as compared to the simulated.

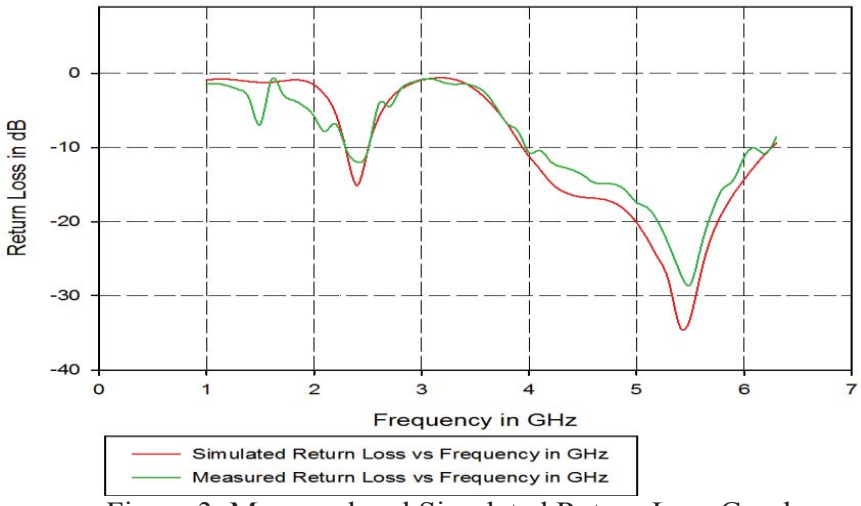

Figure 3. Measured and Simulated Return Loss Graph

Voltage Standing Wave Ratio(VSWR): VSWR is a measure of how much the antenna is matched to the impedance. The VSWR ≤ 2 for a perfectly matched antenna. At the resonating frequencies of 2.42 GHz and 5.45 GHz the VSWR is 1.4 and 1.02.

Radiation Pattern: Radiation pattern is the graphical representation of radiation properties of an antenna as a function of space co-ordinates. The proposed antenna has two resonant frequencies of which 1.9dB at the resonating frequency of 2.42GHz and 3.78 dB at the resonating frequency of 5.4GHz. Figure shows the 3D and polar radiation pattern at 2.42 GHz and 5.45GHz.

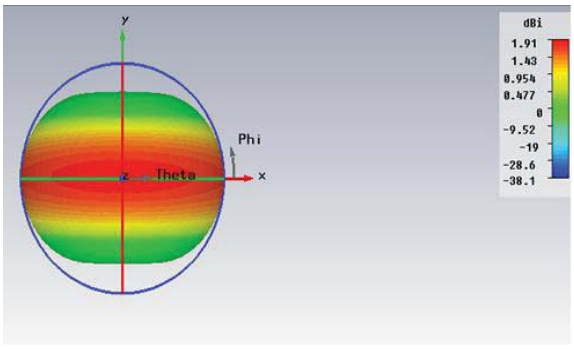

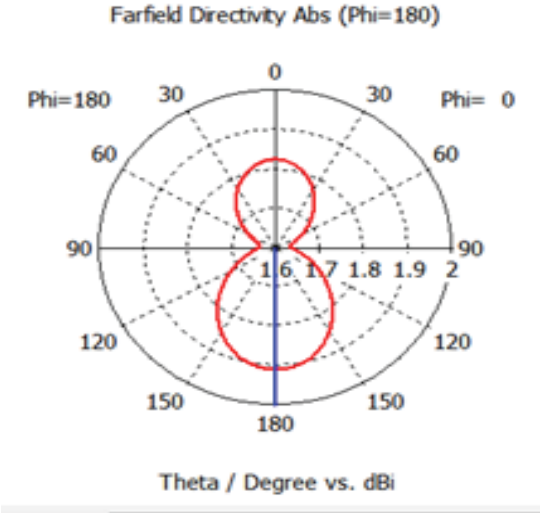

Figure 4. (a) 3D Radiation Pattern at 2.42 GHz (b) Polar Radiation Pattern at 2.42GHz

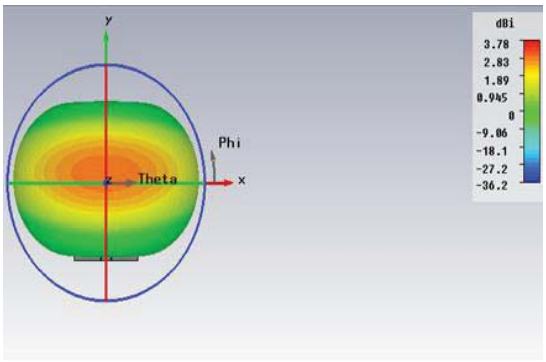

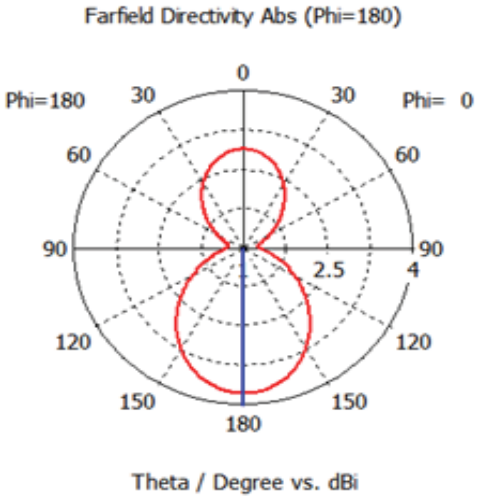

Figure 5. (a) 3D Radiation Pattern at 5.45 GHz (b) Polar Radiation Pattern at 5.45GHz

Current Distribution: The current distributions at different frequencies are illustrated in fig.6. Fig.6(a) shows that the current distributes mainly along the edges of the ground plane as well as at the strips at 2.42 GHz.

In fig.6(b) the current flowing along the two edges in the ground plane at 5.45 GHz. By optimising the parameters of the proposed antenna the operating bands for the 4G LTE, WLAN applications can be achieved.

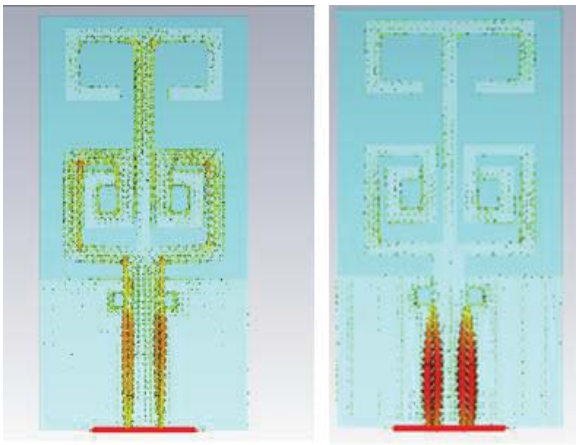

(a)2.42 GHz (b) 5.45 GHz

Figure 6. Current Distributions at 2.42 and 5.45 GHz

Structure of Proposed Antenna: Fig.7 shows the photograph of proposed antenna which is fabricated on FR-4 substrate with dielectric constant of 4.4 and screen printing technique is used for fabrication. The size of the proposed antenna is 34× 17×3.2mm.

Figure 7. Fabricated Structure of Proposed Antenna

Conclusion: A CPW-fed dual band antenna for wireless applications has been presented. The proposed antenna which supports both Wi-Fi as well as 4G LTE applications is designed, simulated and fabricated. The size of the antenna is of 34×17×3.2 mm. The simulated and measured result shows that it covers 2.29GHz to 2.5GHz band at the center frequency 2.42GHz and 3.95GHz to 6.2 GHz band at the center frequency 5.45GHz. The various antenna parameters like S11, VSWR and radiation pattern are studied. It can be concluded that the proposed antenna can be used for wireless applications. It can be concluded that the proposed antenna can be used for wireless application.

REFERENCES

[1] M.Mantash, S. Collardey, A-C. Tarot and A. Presse IETR. Institute of Electronic and Telecommunications of Rennes, France" Dual-band Wi-Fi and 4G LE Textile Antenna,"Proceedings of the 7th European Conference on Antennas and Propagation (EuCAP),2013.

[2] Supriya Arora, Davinder Parkash, Arun Kumar "Design of CPW-Fed Strips Patch Antenna for Wireless Communication Applications", International Journal of Computer Applications (0975 – 8887) Volume 83 , Dec. 2013.

[3] D. Mitra, D. Das, and S. R. Bhadra Chaudhuri,"Bandwidth Enhancement Of Microstrip Line And Cpw-Fed Asymmetrical Slot Antennas", Progress In Electromagnetics Research Lett., Vol. 32, 69-79, 2012

[4] Jyoti Ranjan Panda, Aditya Sri Ram Saladi, Rakhesh Singh Kshetrimayum,Dept. Of Electronics And Electrical Engineering, Iit Guwahati, Assam, India,"A Compact Printed Monopole Antenna For Dual-Band Rfid And Wlan Applications", Radioengg., VOL. 20, NO. 2, JUNE 2011.

[5] Jawad K. Ali, Department of Electrical and Electronic Engineering, University of Technology, Baghdad, Iraq,"A New Dual Band E-Shaped Slot Antenna Design For Wireless Applications" PIERS Proceedings, Suzhou, China, September 12-16, 201

[6] O. Tze-Meng And T. K. Geok,"A Dual-Band Omni-Directional Microstrip Antenna", Progress In Electromag. Research, Vol. 106, 363–376, 2010

A NOVEL BROAD BAND PARASITIC MICROSTRIP RING ANTENNA FOR 5.8 GHz ISM BAND APPLICATIONS

A.Kamalaveni [(1)] *and M.Ganesh Madhan* [(2)]
(1), (2) MIT Campus, Anna University, Chennai, India 600044.
Email: (1) kamalaveniganesh@gmail.com, (2) mganesh@annauniv.edu

Abstract: *This paper describes the design and analysis of a microstrip ring antenna for 5.8 GHz ISM band applications, incorporating parasitic patches. The antenna is developed from the square loop and parasitic patches are added on the rear side of the substrate. An air gap is provided between its substrate and the ground plane. A gap-coupled capacitive feeding technique is used to cancel the probe impedance and for achieving higher bandwidth. Full wave 3D simulation is carried out based on FDTD modelling technique. The proposed antenna is found to provide an impedance bandwidth of 600 MHz with the return loss of -30dB. A good agreement is found between the simulation and measured results.*

Introduction: Printed microstrip antennas are versatile for wireless applications due to its simple profile and low weight. Different antenna designs are reported for ISM band for body area networks and RFID readers [1]-[4]. The feeding mechanism for such devices depends on the applications [5]-[8]. Generally microstrip antennas are designed in shapes such as rectangular, circular, or elliptical patch. Many techniques have been reported in recent days [9], for the design of antennas for 5.8 GHz applications. However, the design of antennas operating at higher frequencies, is often challenging for the conformability with the integrated circuitry. In this paper, we propose a rectangular ring antenna with parasitic patches, designed in a FR4 substrate on a finite ground plane with air dielectric. This design provides wide bandwidth and compact size. The proposed antenna is found to efficiently radiate at 5.8GHz. The capacitive feed used in this design reduces spurious radiations, and implemented by a very small strip placed close to the radiator.

Design and Analysis of Ring Antenna: The geometry of proposed antenna consists of a rectangular ring derived from the conventional microstrip patch radiator. A rectangular ring (W=12 mm, L=20 mm) has been formed when a rectangular slot is cut in the centre of the rectangular microstrip patch. The dimension of the slot is optimized to obtain the desired resonant frequency. Hence the size of the antenna is reduced correspondingly compared to the conventional microstrip patch antenna. The loop has a larger electrical length which helps to achieve the same resonant frequency. Instead of direct feed, a capacitive coupled feed has been chosen for the further improvement in bandwidth and radiation performance. A finite ground (65 mm^2) is used in this analysis. To realize the wide band in practice the distance (air gap) between the finite ground and the radiating loop is chosen as 4.25 mm as in Fig.1. (a). To obtain a better bandwidth, the air gap should be such that $g \cong 0.16\,\lambda - h\sqrt{\varepsilon_r}$ [8]. The design of rectangular ring is improved in such a way that the radiating ring is overlapped with the parasitic patches as shown in Fig.1. (a) and (b) respectively. The bandwidth of the antenna is enhanced by introducing parasitic patches. The dimensions of the parasitic patches are chosen based upon the parametric study.

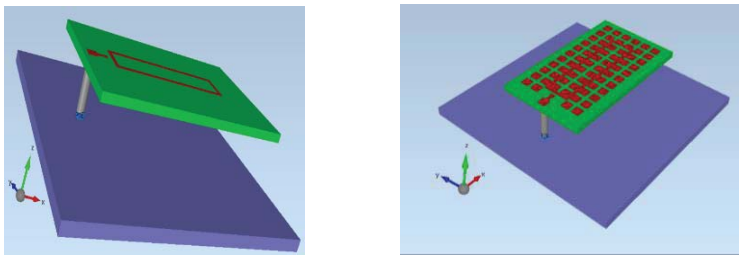

(a) (b)

Fig.1 Isometric view of the proposed antenna (a) loop alone (b) loop along with parasitic patches

Parametric Study: The dimension of the patch is directly related to the ground capacitance. As the size of the patch increases, the load capacitance of individual patch also increases resulting in reduced frequency. Eventually, the size of the square patch directly relates to the coupling capacitance between the adjacent patches. Fig.2. (a) shows the result of variation with respect to the dimension (a) of the patch. This optimization (a = 1mm) helps to determine the dimension of the patch, which leads to better transparency for the required band. The resonant frequency of the proposed antenna also depends on the inter element spacing (d_x) and (d_y) in x and y directions respectively. If either d_x or d_y is increased by a relatively small amount, the frequency is reduced and vice versa. The effect of varying the inter element spacing is shown in Fig.2.(b). This variation is directly related to the capacitance between the neighboring elements. Based on the results, the appropriate spacing is found as 0.25 mm. The antenna impedance matching is achieved by adjusting the gap between the feed patch and the radiator. Fig.2.(c) shows the effect of variation of distance between the patch and the feed strip. The optimum value of the distance between the radiator patch and the feed strip is found to be 0.4 mm, which provides the desired resonant frequency and better impedance matching. By adding air substrate between the ground and the radiating patch the effective dielectric constant reduces towards that of air. It is widely accepted that lower dielectric constant increases the bandwidth and the efficiency of the antenna. To obtain the optimum air gap without affecting the frequency of operation, optimization carried out with respect to height, provides an air gap height of 4.25 mm. An analysis on the effect of air gap in the antenna performance is carried out in full wave 3D simulation and the S_{11} characteristics are provided in Fig.2.(d).

Results and Discussion: All the simulations are carried out based on FDTD modelling technique. Fig. 3 shows the result obtained at various stages of the antenna development, which explains the bandwidth and matching improvement in subsequent stages. Finally, the complete antenna provides the maximum bandwidth with compact size. The surface current distributions on the radiating patch of the complete antenna at 5.8 GHz are shown in Fig.4. It shows that the antenna has stronger current distributions concentrated at the guiding edge of the antenna. The antenna was fabricated on the FR4 substrate with a dielectric constant of 4.4, a loss tangent of 0.02, and a thickness of 0.762 mm. The antenna is characterized for its radiation properties and gain in an anechoic chamber (SATIMO SG64 near field probing chamber) and S parameter measurements in cable and antenna analyzer (R&S ZHV8). The experimental arrangements and a comparison of simulated and measured results of the proposed antenna are reported in Fig5. It is seen that the bandwidth of the antenna is about 500 MHz and 600 MHz in simulation and experiment respectively. This may be due to the manufacturing tolerance of the PCB and the manual assembly error which is difficult to incorporate in simulation.

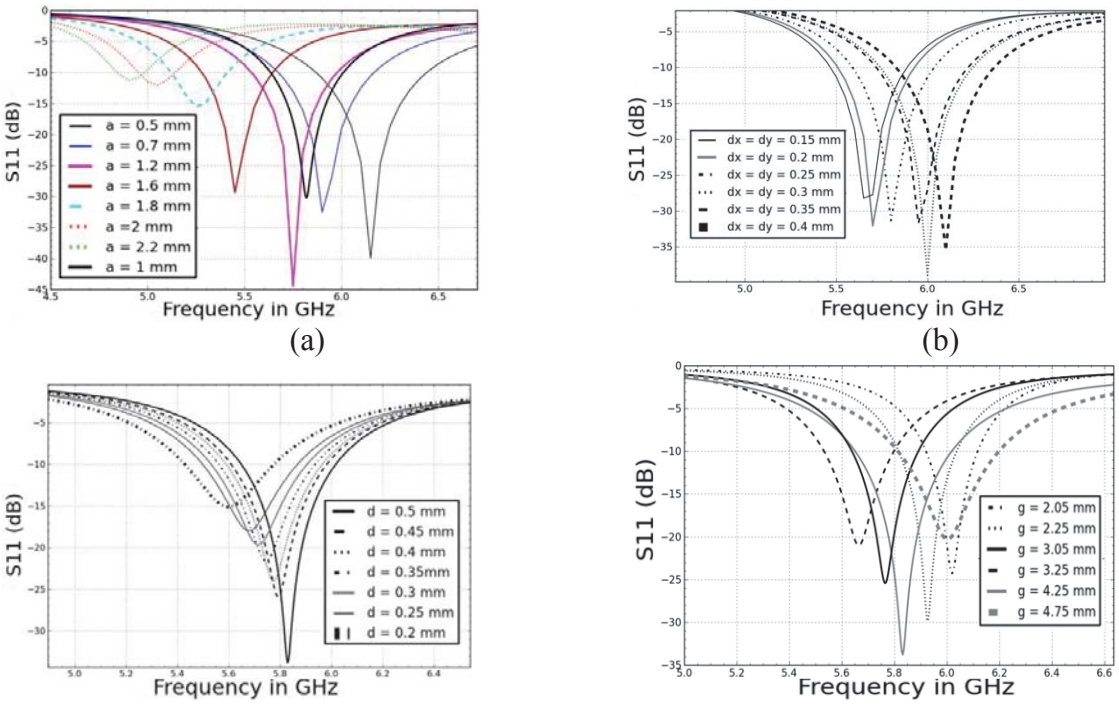

Fig.2 Parametric study for return loss characteristics of the proposed antenna (a) dimension of each patch (b) inter element spacing (c) distance between radiating element and feed strip (d) air gap

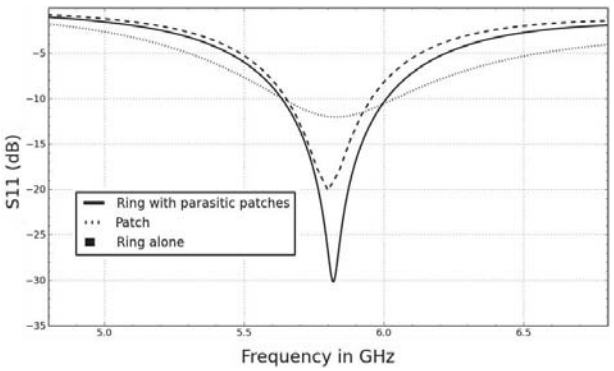

Fig.3 Simulated S11 of the design

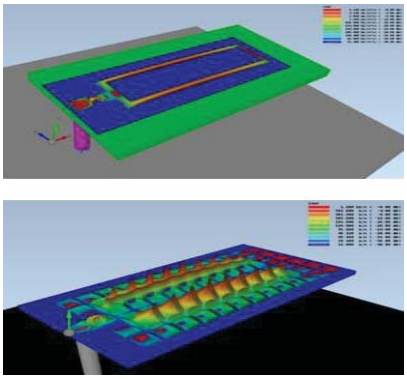

Fig.4 Surface current distribution (5.8 GHz)

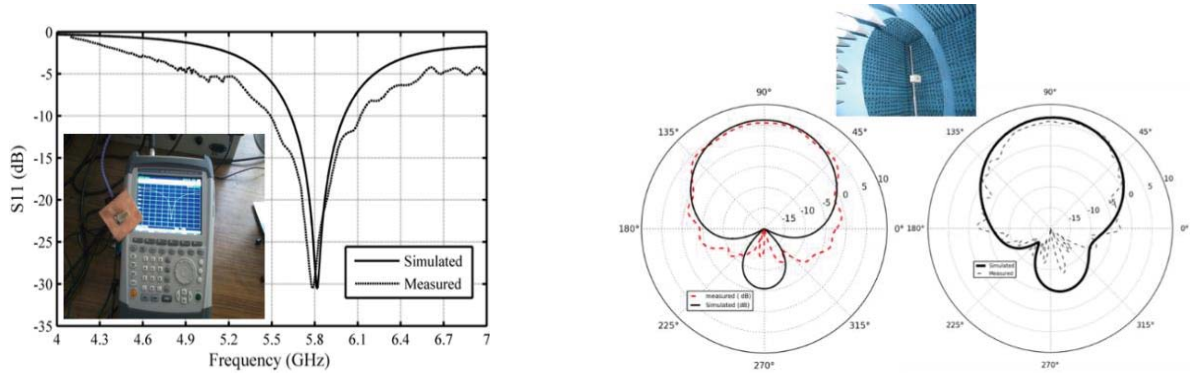

Fig.5 Measured results (a) S11 (b) simulated (solid) and measured (dotted) results of E-plane and H-plane patterns at 5.8 GHz.

The H- plane is well symmetric and yields a beamwidth of 90 deg. Compared to conventional patch this approach provides higher beamwidth. Similarly E- plane also provides an improved beamwidth. It is found that both E- plane and H-plane give a broader coverage, which is favorable for indoor environment applications. The simulated and measured antenna gains are shown in Fig. 6. The plot shows a gain of 6.5 dB at 5.8 GHz.

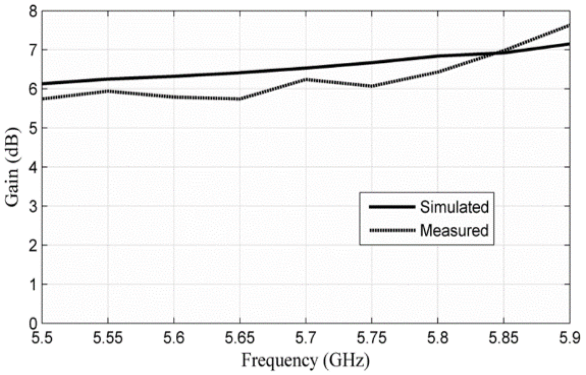

Fig.6 Antenna gain variation with frequency

Conclusion: A planar rectangular ring antenna with parasitic patches and finite ground plane is designed, analyzed and fabricated for 5.8 GHz applications. The proposed antenna provides a wide beamwidth and a bandwidth of 600 MHz with -30 dB return loss at 5.8 GHz. The bandwidth is twice compared with ring antenna without parasitic patch. However, antennas without and with parasitic patches are found to provide a similar radiation pattern.

Reference:

[1] Jayesh V. Gohil and Deepak Bhatia, "Design of 2x1Circularly Polarized Microstrip patch Antenna Array for 5.8 GHz ISM Band Applications", *Nirma University International Conference On Engineering, Dec,2012.*

[2] Zang W.S., "A dual-band dual-polarized antenna for body area network", Antennas and propagation EuCAP, April 2010.

[3]Mobashsher, AT.; Aldhaheri, R.W., "An Improved Uniplanar Front-Directional Antenna for Dual-Band RFID Readers," *Antennas and Wireless Propagation Letters, IEEE*, vol.11, no., pp.1438, 1441, 2012.

[4] S.Ononchimeg, J.H.Bang, and B.C.Ahn, "A new dual- polarized gap-fed patch antenna", PIER, vol.14, pp.79-87, 2010.

[5] Huihui Li; Yongjin Zhou; Pan Han; Lei Wang; Shuang Zhang; Xiaqing Wen, "A CPW-fed 5.8 GHz Wideband Antenna Applied on the Human Body," *Intelligent Systems Modelling & Simulation (ISMS), 2013 4th International Conference on* , vol., no., pp.157,159, 29-31 Jan. 2013.

[6] Reddy, M.A; Raghavan, S., "A novel CPW-Fed antenna for RFID tag at 5.8 GHz," *Applied Electromagnetics Conference (AEMC), 2009*, vol., no., pp.1, 3, 14-16 Dec. 2009.

[7] V.G.Kasabegoudar,"Dual frequency ring antennas with coplanar capacitive feed", PIER, vol., 23, 2011.

[8] V.G.Kasabegouder, "Low profile suspended microstrip antennas for wideband applications", Journal of Electromagnetic waves and applications vol.25, 2011.

[9] K.P. Ray, Amit A.Deshmukh and Ameya A.kadam, "Linearly Polarized Microstrip Reflectarry with microstrip Antenna Feed", IETE Journal of Research, vol.59, Issue 4, pp.294-301, Jul-Aug 2013.

Multiband Antenna Using Slotted Techniques for Wireless Applications

Rebecca Abraham[(1)], *Usha Kiran K.*[(2)]
(1) VIT University, Chennai , Tamil Nadu, 600127, Email: rebecca.abraham2013@vit.ac.in
(2) VIT University, Chennai, Tamil Nadu, 600127, Email: usha.kiran@vit.ac.in

Abstract: *A CPW(coplanar waveguide)-fed slotted microstrip patch antenna for multiband operation is proposed. Two folded C-shaped slot and a U-shaped slot are incorporated in a microstrip patch antenna. It also includes dual inverted L-shaped slots on either side of the feed to provide impedance matching. The antenna resonates at five frequencies – 2.02 GHz, 2.53 GHz, 3.13 GHz, 4.93 GHz and 6.97 GHz.*

Introduction: An increasing demand for present-day wireless communication device is the capability to integrate multiple communication standards into a single system. But it is difficult to place multiple antennas into a device. Due to the space constrain in a device, there is a huge demand for an antenna that provides various applications. Hence, the necessity to develop a multiband antenna to operate for different applications arises.

Microstrip patch antenna is widely used because of its various advantages such as low profile, light weight, low cost and simplicity of manufacture. A conventional microstrip patch antenna provides a single frequency. For providing multiband operation, techniques have to be used. Some of these techniques are planar inverted-F antennas with direct feed [1] having the advantage of small size and easy multiband operations, microstripline-fed antennas [2], probe-fed antennas [3],[4] and CPW(coplanar waveguide)-fed antennas [5]. Slot loading technique [6],[7] has received attention for obtaining multiband operation. There are a number of advantages of using CPW-fed antennas such as simple, lower radiation leakage, less dispersion than microstrip lines, easier integration with system circuits and compact structure. CPW-feed with slot loading technique provides multiband operation [8].

In this paper, a CPW-fed slotted patch antenna consisting of two folded C-shaped slot along the non-radiating edge and a symmetrical U-shaped slot for providing multiband operation. The proposed antenna also has a dual inverted L-shaped slot which are shorted provides impedance matching.

Antenna Design: The proposed antenna consists of a substrate and a patch on the top. The substrate used is FR4 glass epoxy which has a dielectric constant of 4.4 and thickness 0.072 mm. The dimension of the substrate and the patch is 30×25 mm^2 for 2.4 GHz. The dimensions are so selected that the patch behaves as a quarter wavelength antenna. The thickness of the patch is selected as 0.1 mm. The output impedance is 50Ω. Two folded C-shaped slot along the non-radiating edge and a symmetrical U-shaped slot are etched on the patch. Two inverted L-shaped slots are also included which together with the two folded C-shaped slots and U-shaped slot forms the rectangular antenna. Feeding technique used is CPW-feed. Here, the two inverted L-shaped antennas are shorted to the ground which is different from the conventional CPW-fed antenna. This slot provides the required impedance matching. The width of all the slots is 0.5mm.

The configuration of the proposed antenna and the fabricated prototype is shown in Fig. 1. The dimensions of the proposed antenna are tabulated in Table I. The simulation is done using Ansoft's High Frequency Structural Simulator (HFSS) software which employs Finite Element Method (FEM).

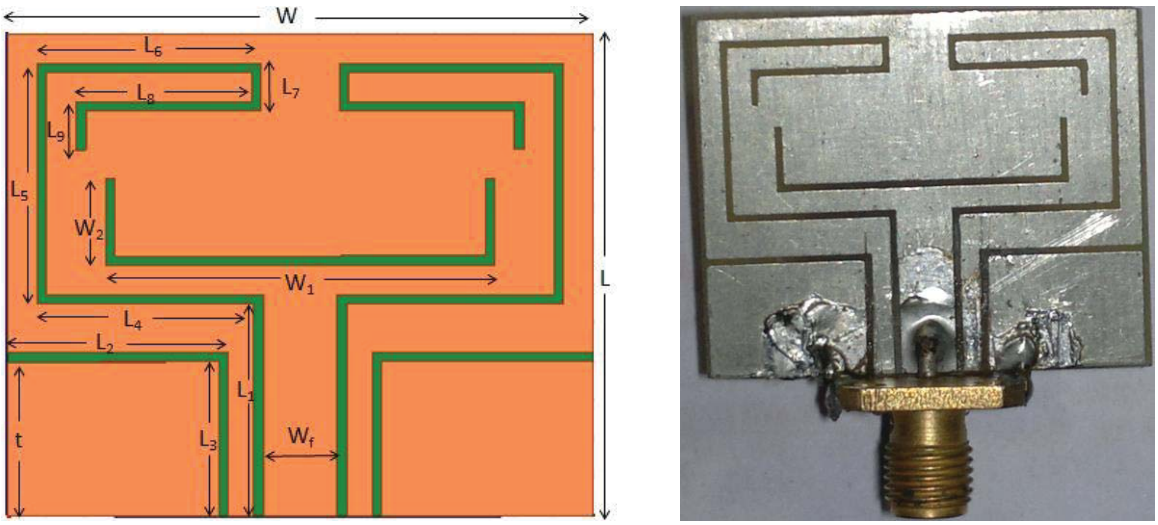

Fig. 1. Configuration of the Proposed Antenna and the fabricated prototype

TABLE 1. Dimensions of the Proposed Antenna

Parameter	*L*	*W*	L_1	L_2	L_3	L_4	L_5	L_6	L_7	L_8	L_9	W_f	W_1	W_2	*t*
Value(mm)	25	30	11	11.3	8	11.1	12.5	11.5	2.5	9	2.5	3.8	20	4.5	8

Simulation Result: The proposed multiband antenna includes two folded C-shaped slot along the radiating edge,a symmetrical U-shaped slot and two inverted L-shaped slots. The two inverted L-shaped slots which are shorted provides the required impedance matching. This multiband antenna resonates at frequencies 2.02 GHz, 2.53 GHz, 3.13 GHz, 4.93 GHz and 6.97 GHz. The absolute gains at these frequencies are 0.5905, 0.5437, 1.056, 1.5736 and 1.4633 respectively. The simulated return loss for the proposed multiband antenna is shown in Fig. 2. The measured return loss is shown in Fig. 3. The fabricated antenna resonates at four frequencies 3.34 GHz, 4.915 GHz, 5.878 GHz and 7.596 GHz with a wide band of 2.094 GHz from 7.267 GHz to 9.361 GHz.

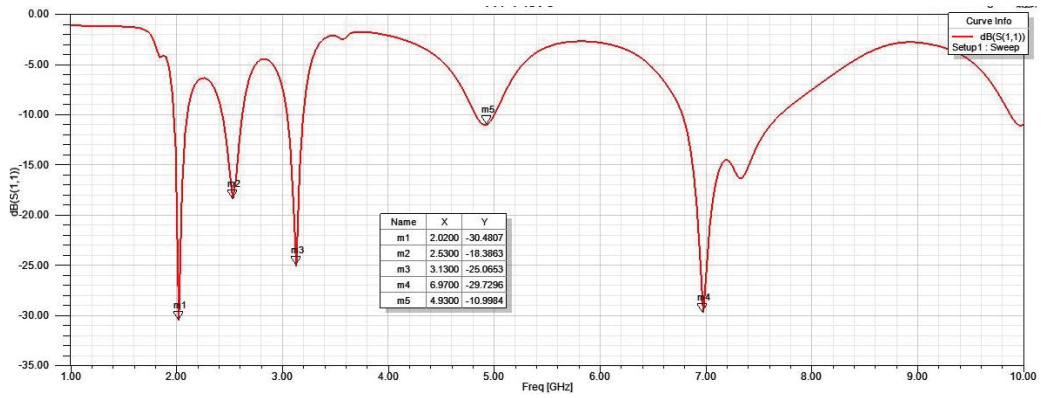

Fig. 2. Simulated return loss for proposed antenna

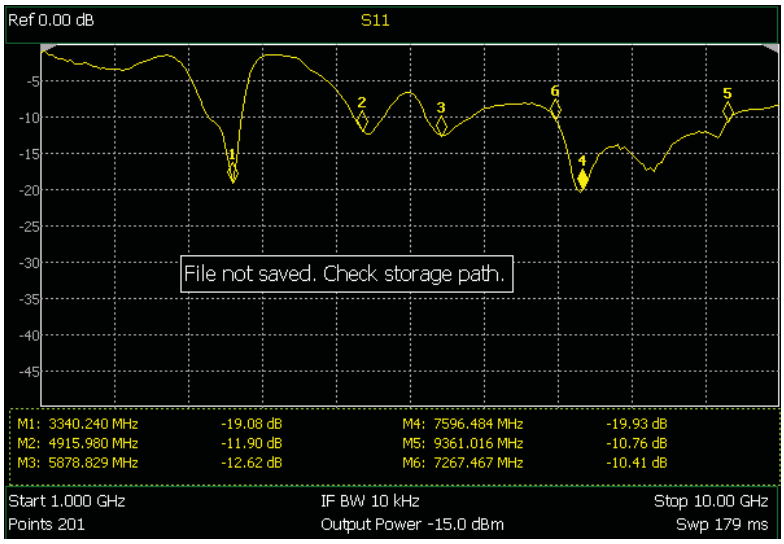

Fig. 3 Measured return loss of fabricated antenna

Radiation Patterns: The radiation patterns of the proposed antenna simulated using Ansoft's HFSS for the proposed multiband antenna is shown in Fig. 4. The antenna operates at frequencies 2.02 GHz, 2.53 GHz, 3.13 GHz, 4.93 GHz and 6.97 GHz.

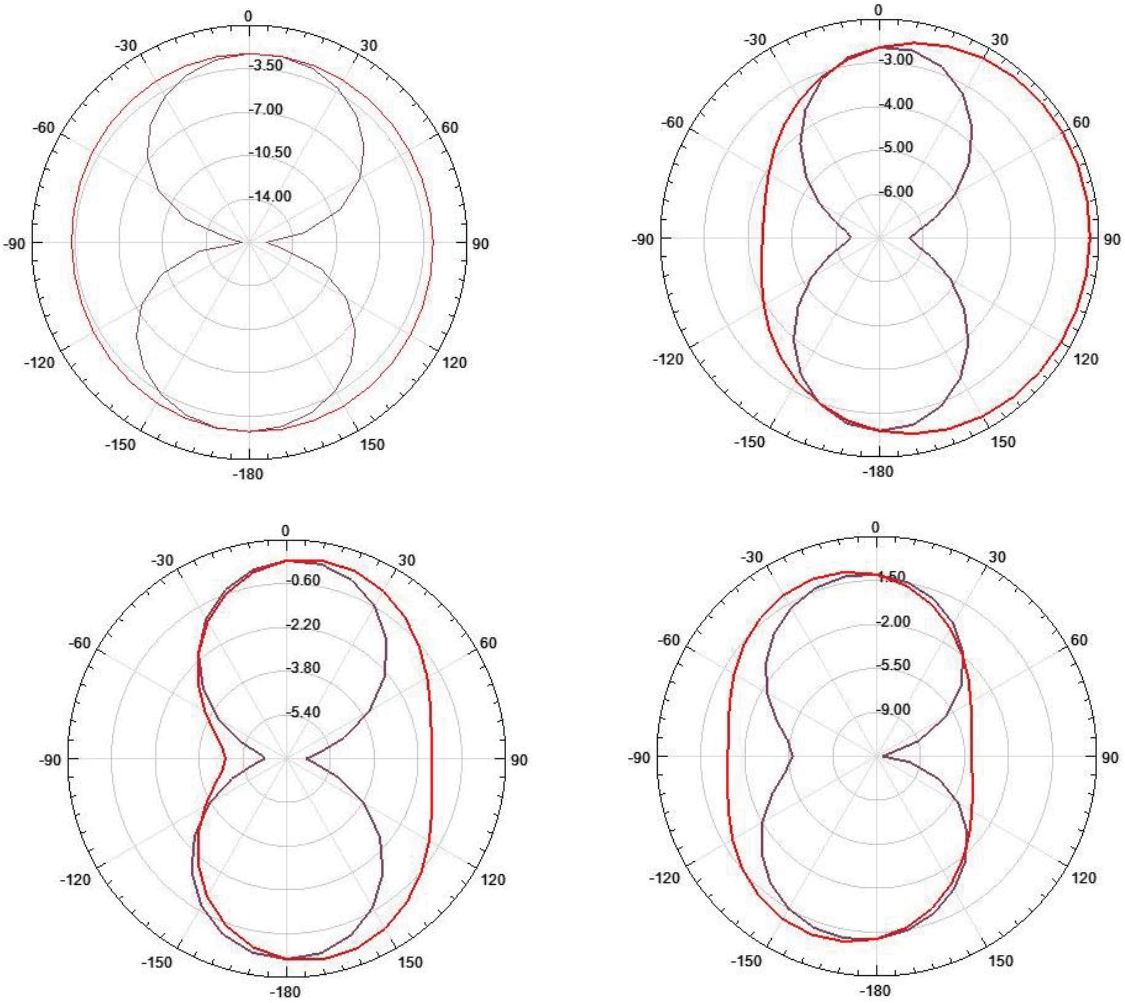

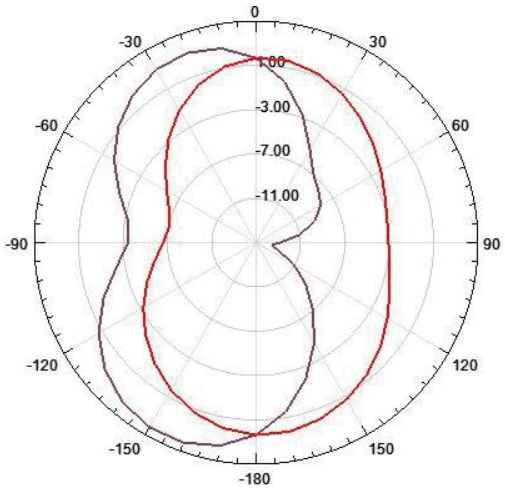

Fig. 4 Radiation patterns- E plane(red) and H plane(grey) for the frequencies 2.02 GHz, 2.53 GHz, 3.13 GHz, 4.93 GHz and 6.97 GHz.

Conclusion: A CPW-fed slotted microstrip patch multiband antenna that comprises of two folded C-shaped slot along the non-radiating edge, a symmetrical U-shaped slot and a dual inverted L-shaped slot has been implemented using HFSS. The antenna size is 30 x 25 x 0.072 mm^3. Since CPW-feed is used, the antenna can be easily integrated with CPW-based microwave circuits. The proposed CPW-fed slotted multiband antenna resonates at frequencies - 2.02 GHz, 2.53 GHz, 3.13 GHz, 4.93 GHz and 6.97 GHz. The fabricated antenna resonates at frequencies 3.34 GHz, 4.915 GHz, 5.878 GHz and 7.596 GHz with a wide band of 2.094 GHz from 7.267 GHz to 9.361 GHz.

References:

[1] P. W. Chan, H. Wong and E. K. N. Yung ,"Wideband planar inverted-F antenna with meandering shorting strip", *Electron. Lett.,*vol. 44, no. 6, pp. 395-396, 2008.

[2] W. C. Liu, M. Ghavami, and W. C. Chung, "Triple-frequency meandered monopole antenna with shorted parasitic strips for wireless application," *IET Microw., Antennas, Propag.*, vol. 3, pp. 1110–1117, 2009.

[3] R. K. Raj, M. Joseph, B. Paul, and P. Mohanan, "Compact planar multiband antenna for GPS, DCS, 2.4/5.8 GHz WLAN applications," *Electron. Lett.*, vol. 41, pp. 290–291, 2005.

[4] Z. Wang, S. Fang, S. Fu, and S. Lu, "Dual-band probe-fed stacked patch antenna for GNSS applications," *IEEE Antennas Wireless Propag. Lett.*, vol. 8, pp. 100–103, 2009.

[5] G. Augustin, P. C. Bybi, V. P. Sarin, P. Mohanan, C. K. Aanandan, and K. Vasudevan, "A Compact dual-band planar antenna for DCS-1900/PCS/PHS, WCDMA/IMT-2000, and WLAN applications," *IEEE Antennas Wireless Propag. Lett.*, vol. 7, pp. 108–111, 2008.

[6] K. F. Lee, S. L. S. Yang, and A. A. Kishk, "Dual- and multiband U-slot patch antennas," *IEEE Antennas Wireless Propag. Lett.*, vol. 7, pp. 645–647, 2008.

[7] C. Hsieh, T. Chiu, and C. Lai, "Compact dual-band slot antenna at the corner of the ground plane," *IEEE Trans. Antennas Propag.*, vol. 57, no. 10, pt. 2, pp. 3423–3426, Oct. 2009.

[8] Xin Sun, Gang Zeng, Hong-Chun Yang,and Yang Li, "A Compact Quadband CPW-Fed Slot Antenna for WiMAX/WLAN Applications," *IEEE Antennas Wireless Propag. Lett.*, vol. 11, 2012.

Development of a Novel Microstrip Patch Antenna For TCAS Application

*Debajit De * (1), Prasanna Kumar Sahu (2), Neela Chattoraj (3)*
(1) National Institute of Technology, Rourkela, Pin - 769008, India. Email: de.debajit118@gmail.com
(2) National Institute of Technology, Rourkela, Pin - 769008, India. Email: pksahu@nitrkl.ac.in
(3) Birla Institute of Technology, Mesra, Pin: 835215, India. Email: nchattoraj@bitmesra.ac.in

Abstract: *In this paper, a new model of TCAS (Traffic Collision Avoidance System) Antenna, installed in an Aircraft has been proposed. This proposed model is a Dual Patch Slotted Microstrip Antenna designed with HFSS to meet the current needs of traffic collision avoidance system and to overcome the possible limitations associated with the existing techniques. All simulated parameters of the proposed antenna have been verified with the fabricated one. A good Reflection Coefficient and VSWR with good 50 Ohm Impedance matching, high Gain and perfect directional Radiation Pattern at the operating frequencies make this proposed antenna a good candidate as a TCAS Antenna.*

I. Introduction: After many years of extensive analysis, development, and flight evaluation by the Federal Aviation Administration (FAA), other countries‟ Civil Aviation Authorities (CAAs), and the aviation industries, Traffic Collision Avoidance System (TCAS) was developed to reduce the risk of mid-air collisions between aircraft [1]. This airborne system senses the presence of nearby aircraft by interrogating the transponders carried by these aircraft. When TCAS senses that a nearby aircraft is a possible collision threat, TCAS issues a traffic advisory to the pilot, indicating the presence and location of the other aircraft. If the encounter becomes hazardous, TCAS issues a maneuver advisory [2]. The main feature of TCAS, which was first proposed by Dr. John S. Morell in 1955, is that it functions according to time criteria and not distance. From several successive replies, TCAS calculates a time to reach the CPA (Closest Point of Approach) with the intruder, by dividing the range by the closure rate [3]. If the aircraft transmit their altitude, TCAS also computes the time to reach co-altitude.

II. Existing TCAS Antenna: The antennas used by TCAS include a directional antenna (ANT-81A) that is mounted on the top of the aircraft and either an Omni-directional or a directional antenna mounted on the bottom of the aircraft. Most installations use the directional antenna on the bottom of the aircraft. So, for intruder bearing to be determined on the bottom antenna, an ANT-81A directional antenna must be mounted on the underside of the aircraft.

Fig. 1 Directional Antenna

Fig. 2 Omni-Directional Antenna

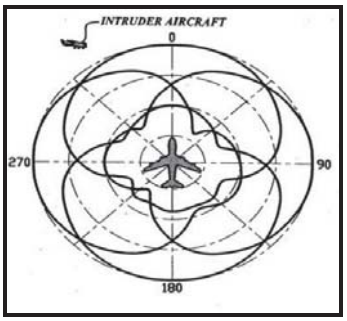

Fig. 3 Radiation Pattern

The ANT-81A Directional Antenna shown in Fig. 1 contains an array of four passive, steerable, radiating monopole elements mounted at 00, 900, 1800 and 2700 in relationship with the vertical axis of the antenna. This whole assembly is mounted directly to the fuselage of the aircraft. During Mode S and C interrogation message transmission, the directional antenna transmits 1.03 GHz pulses on the four radiating elements [3]. During TCAS receptions, each of the four directional antenna elements detects 1.09 GHz RF signals which are present.

The phasing of these received signals is determined by the direction from which the RF energy is received. These signals are directed onto the four cables those connect transmit signals between the TCAS Processor and the directional antenna. The Omni-Directional Antenna shown in Fig. 2 is mounted directly to the underside of the aircraft [4]. It consists of L-band blade type, dipole antenna. It connects the TCAS Processor via single coaxial cable. The other three bottom antenna connectors are left open (to the processor). Fig. 3 shows the radiation pattern of 4 monopole stubs used as the TCAS directional Antenna [5]. The monopoles are oriented in such a way that the overall radiation pattern can cover all the surveillance area of the aircraft.

III. Design of Proposed Microstrip Patch Antenna:

A dual Patch Slotted Microstrip Antenna having one Shorting Pin and Co-Axial Feed has been proposed as a TCAS Directional Antenna. Fig. 4 shows the proposed antenna which is designed in HFSS Software and Fig.5 shows the fabricated one.

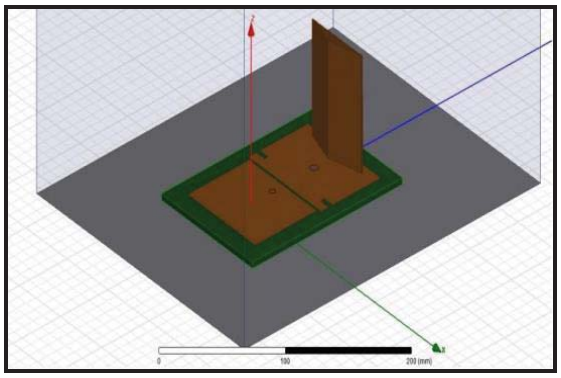

Fig. 4 Designed Dual Patch Antenna In HFSS

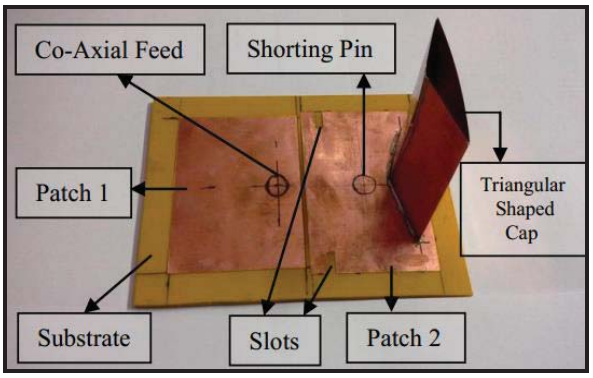

Fig. 5 Fabricated Dual Patch Antenna

In this design, the designed frequency, f_r = 1.06 GHz (Since 1.06 GHz is the center frequency of T_X f_r = 1.03 GHz and R_X f_r = 1.09 GHz). FR4 Epoxy of height 4 mm. has been taken as the substrate material whose dielectric constant (ε_r) is 4.4. After calculation, it is obtained that Width and Length of the patch 1 is given by 8.21 cm and 6.45 cm respectively; Width and Length of the patch 2 is given by 8.81 cm and 6.25 cm respectively.

The Co-axial feed will be given in the patch 1. So patch 1 is treated as primary radiator and patch 2 will be treated as secondary radiator. A triangular shaped cap made of thin copper foil has been placed upon the patch 2. This triangular cap will help that antenna to radiate in a particular upward diagonal direction which is very much important for the TCAS application.

One shorting pin/post made of copper has been put into the substrate through patch 2 and two small slots have been cut in the patch 2. Actually, this shorting pin and slots have been used for tuning purpose of that antenna. Shorting pin provides inductance and slot having

length less than λ0/4 (Length of Quarter Wave Transformer) provides capacitance to the overall patch antenna. So, varying the dimensions of shorting pin and two slots, almost exact two resonating frequencies (1.03 GHz and 1.09 GHz) have been obtained.

IV. Results and Discussions:

The designed Dual Patch Slotted Microstrip Patch TCAS Antenna has been simulated in HFSS software. After the fabrication of that antenna, it has been tested in the laboratory with the help of V.N.A (Vector Network Analyzer).

Fig. 6 Antenna Measurement Using V.N.A

Different parameters like S_{11}, VSWR and Input Impedance have been measured. Fig. 6 shows the laboratory setup for measurement of the fabricated antenna in V.N.A.

(A) Measurement of S_{11} -

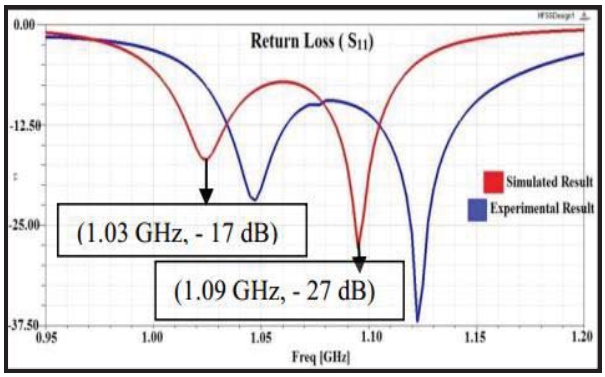

Fig. 7 S_{11} of the Patch Antenna

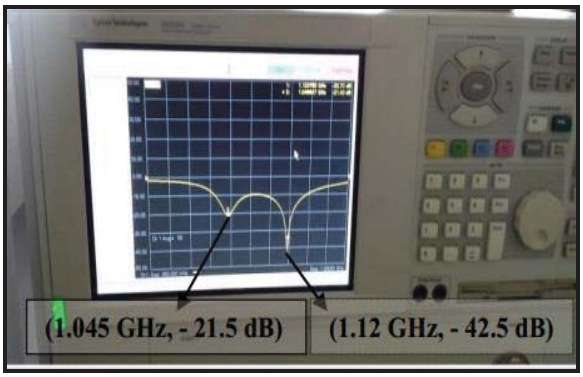

Fig. 8 Measurement of S_{11} in V.N.A

Fig. 7 shows both the simulated and experimental result of the S_{11}. Fig. 8 shows the S_{11} plot in V.N.A. The dual resonating frequency nature has been seen from this graph. In the simulation result, the antenna is resonating around at 1.03 GHz and at 1.09 GHz. In the experimental result, the resonating frequencies are slightly deviated from the simulation result. The error percentage of deviation is around 2.1%. In V.N.A, it is showing that, at 1.045 GHz, S_{11} is -21.5 dB and at 1.12 GHz, S_{11} is -42.5 dB.

(B) Measurement of V.S.W.R -

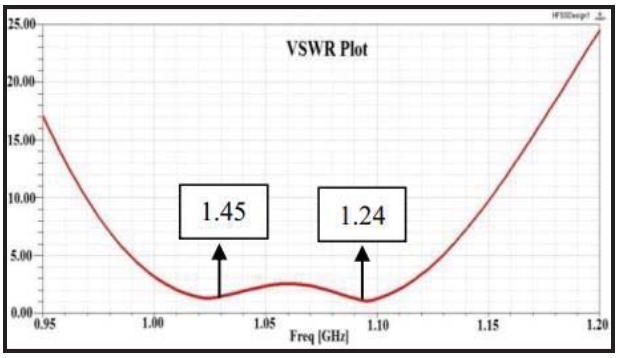

Fig. 9 VSWR Plot in HFSS

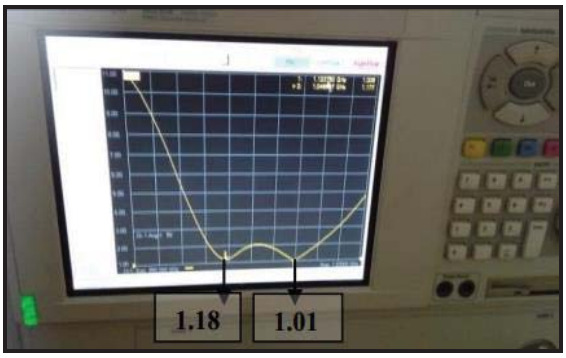

Fig. 10 Measurement of VSWR in V.N.A

Fig. 9 shows the simulation result of VSWR and Fig. 10 shows the experimental result of VSWR in V.N.A. In the simulation result, it is observed that at 1.03 GHz, VSWR is 1.45 and at 1.09 GHz, VSWR is 1.24. In V.N.A, at 1.045 GHz, VSWR is 1.18 and at 1.12 GHz, VSWR is 1.01.

(C) Measurement of Input Impedance –

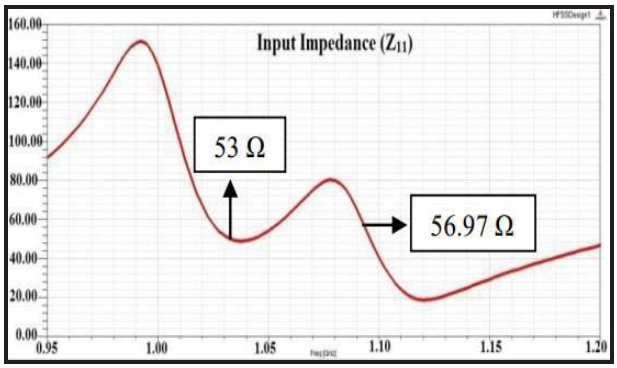

Fig. 11 Input Impedance (Z_{11}) Plot in HFSS

Fig. 12 Measurement of Input Impedance in V.N.A

Fig. 11 shows the simulation result of Input Impedance (Z_{11}) and Fig. 12 shows the experimental result of Z_{11} in V.N.A. In the simulation result, it is observed that at 1.03 GHz, Z_{11} is 53 Ohm and at 1.09 GHz, Z_{11} is 56.97 Ohm. In V.N.A, at 1.045 GHz, Z_{11} is 51.95 Ohm and at 1.12 GHz, Z_{11} is 48.02 Ohm.

(D) Simulation Result of E Field Distribution –

In Fig. 13, for 1.03 GHz, E field distribution throughout the antenna has been shown. Here, E field is very well distributed in patch 1 and a very small amount of E field distribution has been observed in patch 2 due to weak mutual induction between patch 1 and 2. In this case, the maximum E Field Distribution is 16.21 V/m.

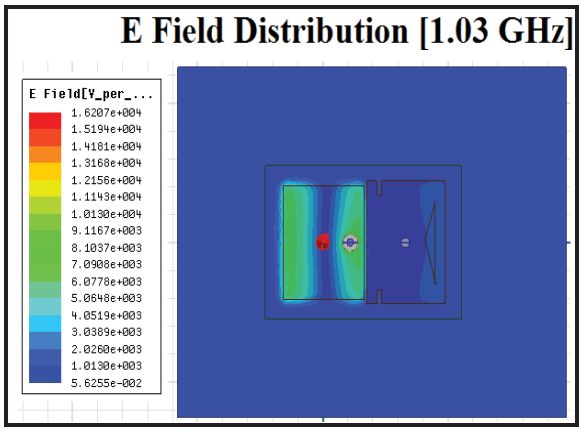

Fig. 13 E Field Distribution at 1.03 GHz

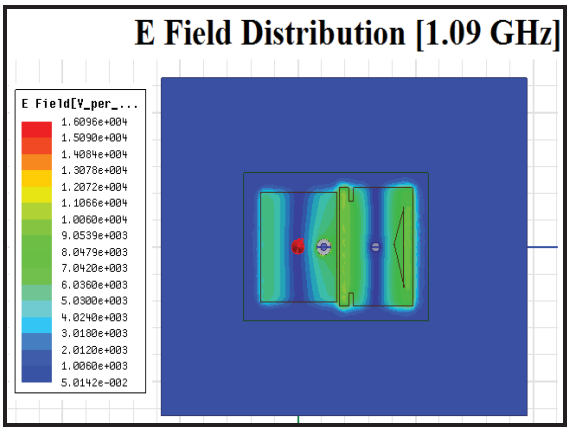

Fig. 14 E Field Distribution at 1.09 GHz

Fig. 14 shows the E field distribution in the antenna for 1.09 GHz. In this case, it is observed that, E field is very well distributed throughout the both patches due to strong mutual induction between them. In this case, the maximum E Field Distribution is 16.09 V/m.

(E) Simulation Results of Radiated Electric Field -

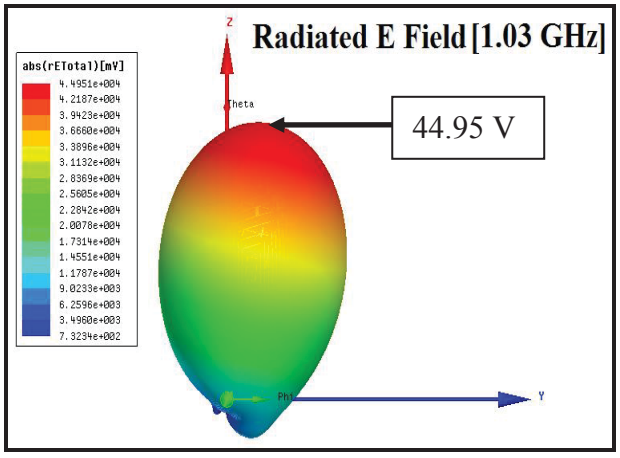

Fig. 15 Radiated Electric Field at 1.03 GHz

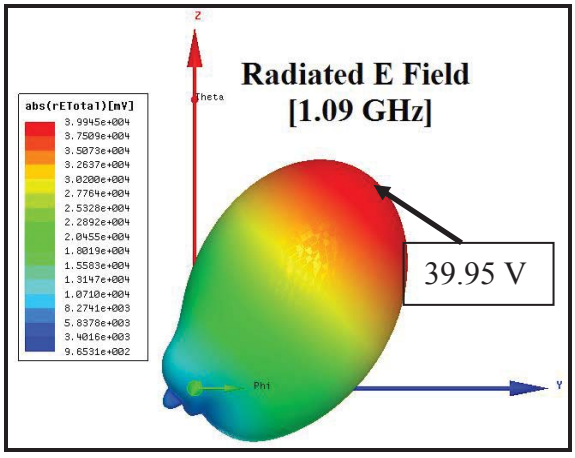

Fig. 16 Radiated Electric Field at 1.09 GHz

Fig. 15 shows the radiated electric field of the antenna for 1.03 GHz. In this case, the maximum radiated E field is 44.95 V. Here, the radiation beam is very slightly bent into the diagonal directional of the orientation of the antenna. Fig. 16 shows the radiated electric field of the antenna for 1.09 GHz. In this case, the maximum radiated E field is 39.95 V. Here, the radiation beam is very well bent into the lateral direction of the orientation of the antenna.

(F) Simulation Result of Gain Measurement –

In Fig. 17 and 18, 3D view of Gain for 1.03 GHz and 1.09 GHz has been shown respectively. At 1.03 GHz, the maximum gain is 5.39 dB and at 1.09 GHz, the maximum gain is 4.07 dB.

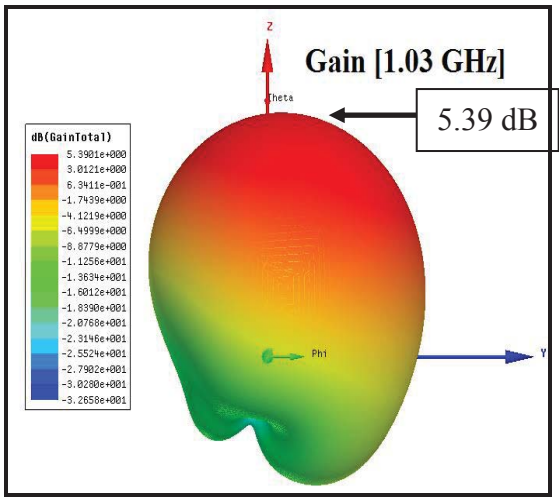

Fig. 17 3D View of Gain at 1.03 GHz

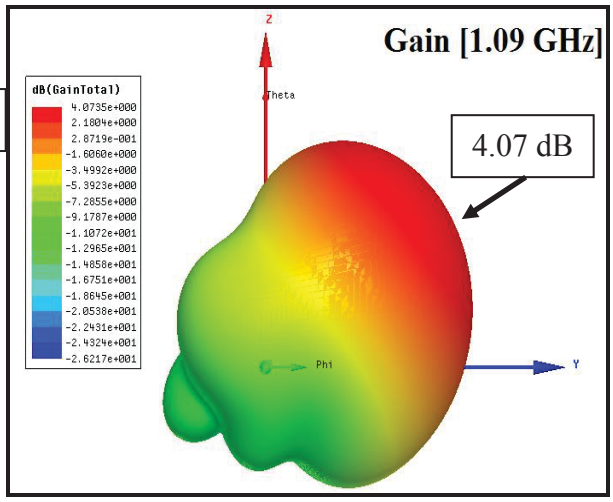

Fig 18 3D View of Gain at 1.09 GHz

(G) 2D Plot of Gain and Total Radiated Electric Field –

From the above graph shown in Fig. 19, it is obtained that, the maximum Gain of the antenna for 1.03 GHz is around 5.39 dB at $\theta = 14^0$ and for 1.09 GHz the maximum Gain is around 4.07 dB at $\theta = 44^0$. For both the cases, the gain has been obtained with respect to positive Z axis in the ZY Plane (i.e. $\phi = 90^0$).

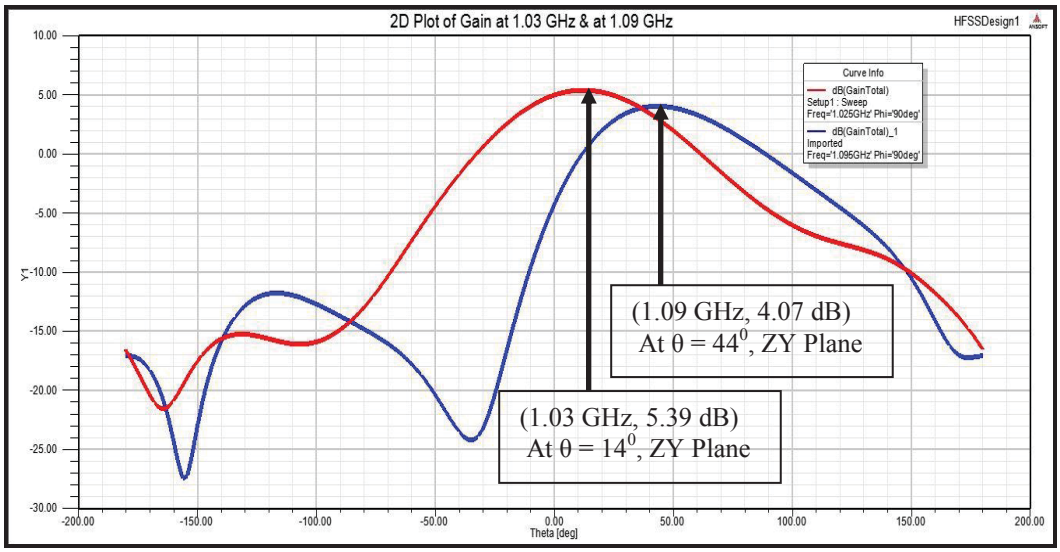

Fig. 19 2D Plot of the Antenna Gain for 1.03 GHz and for 1.09 GHz

From the graph shown in Fig. 20, it is obtained that, the maximum Total Radiated Electric Field of the antenna for 1.03 GHz is around 44.95 V at $\theta = 14^0$ and for 1.09 GHz the maximum Total Radiated Electric Field is around 33.95 V at $\theta = 44^0$. For both the cases, the gain has been obtained with respect to positive Z axis in the ZY Plane (i.e. $\phi = 90^0$).

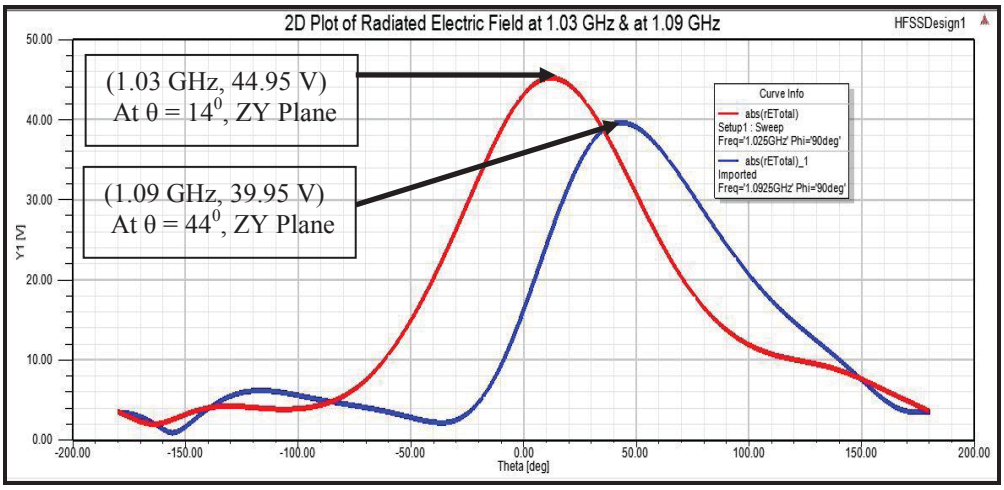

Fig. 27 2D Plot of Total Radiated Electric Field of the Antenna for 1.09 GHz

(H) Simulation Result of Radiation Pattern Measurement –

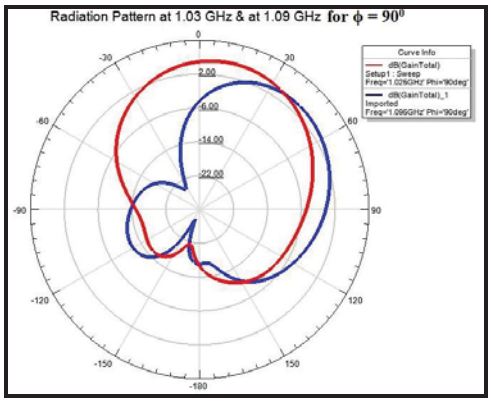

Fig. 21 Radiation Pattern in the ZY Plane

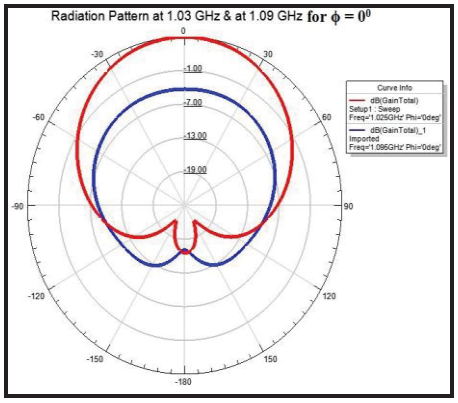

Fig. 22 Radiation Pattern in the ZX Plane

Fig. 21 and 22 represent the radiation pattern of the antenna at 1.03 GHz and at 1.09 GHz in the ZY Plane and in the ZX Plane respectively. The Radiation pattern is the nature of θ for $\phi = 90^0$ & $\phi = 0^0$ respectively.

(I) Efficiency vs. Frequency Plot -

Fig. 23 shows the graph of Antenna Efficiency. From the plot, it is obtained that, the antenna Efficiency at 1.03 GHz is around 91.2 % and at 1.09 GHz the efficiency is 88.2 %.

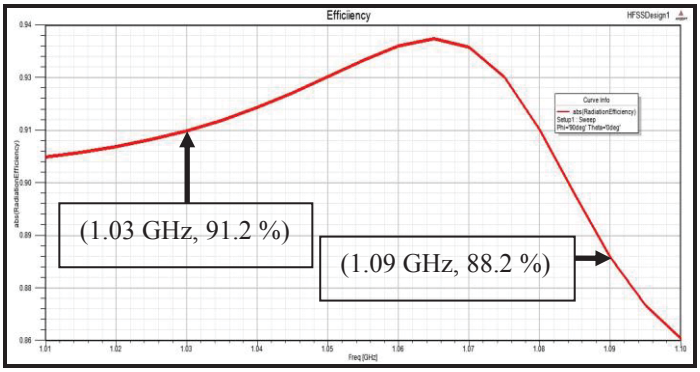

Fig. 23 Antenna Efficiency vs. Frequency Plot

(J) Parametric Studies of the Designed Antenna –

In this paper, some parametric studies of different parameters of the designed TCAS Patch Antenna have been done. These are Variation of S_{11} for different substrate heights, Variation of S_{11} for different gaps between two patches and Variation of S_{11} for different heights of triangular cap.

(i) Variation of S_{11} for Different Substrate Heights –

Fig. 24 shows the variation of S_{11} with taking different substrate heights (h). The chosen substrate thicknesses are 3 mm, 3.5 mm, 4 mm, 4.5 mm and 5 mm.

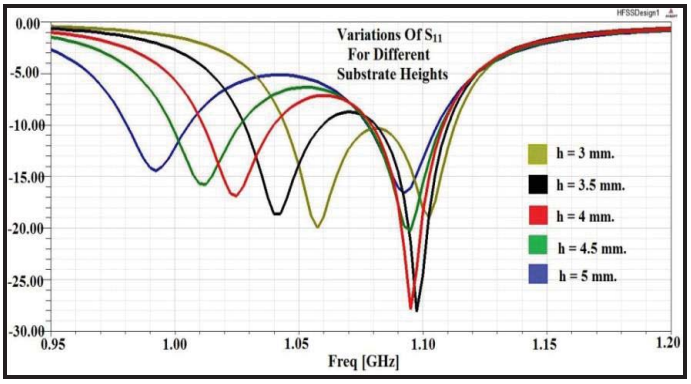

Fig. 24 Variation of S_{11} for Different h

From this plot, it is observed that, the first resonating frequency is decreasing as h is increasing. But, it is also observed that, as h is changing, a very few variations are there for the second resonating frequency. The value of S_{11} for the first resonating frequency is varied from -15 dB to -20 dB. The second resonating frequency is above -20 dB for substrate height 3 mm, 4.5 mm, 5 mm and is below -25 dB for substrate height 3.5 mm, 4 mm. Comparing all the patterns of S_{11} for different h, the best result is getting for 4 mm. substrate thickness.

(ii) Variation of S_{11} for Different Gaps between Two Patches –

Fig. 25 shows the variation of S_{11} with taking different gaps between patch 1 and patch 2.

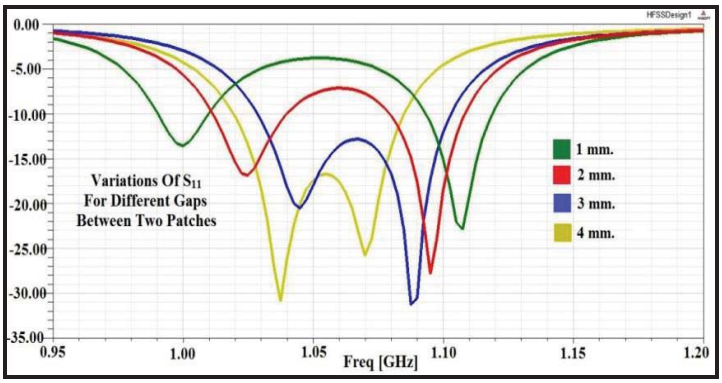

Fig. 25 Variation of S_{11} for Different Gaps between Two Patches

The chosen gaps are 1 mm, 2 mm, 3 mm and 4 mm. From this plot, it is noticed that, the gap between two resonating frequencies is decreasing as the gap between two patches is

increasing from 1 mm. to 4 mm. The gap between two resonating frequencies are almost 110 MHz, 71 MHz, 45 MHz and 33 MHz for 1 mm., 2 mm., 3 mm. and 4 mm. gaps between two patches respectively. Comparing all the patterns of S_{11}, the best result is achieved for 2 mm gap between patch 1 and patch 2.

(iii) Variation of S_{11} for Different Heights of Triangular Shaped Metal Cap –

Fig. 26 shows the variation of S_{11} with taking different heights of triangular shaped cap.

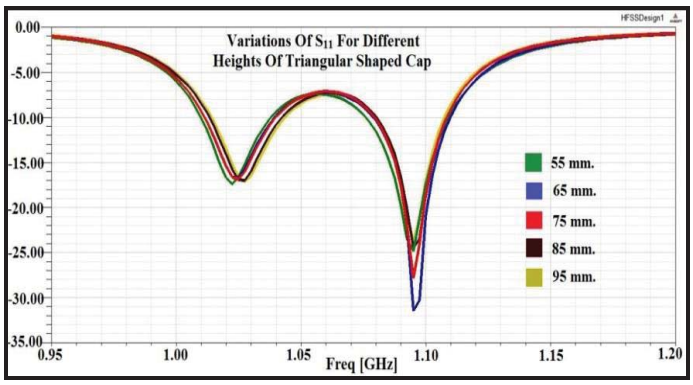

Fig. 26 Variation of S_{11} for Different Heights of Triangular Cap

The chosen heights are 55 mm, 65 mm, 75 mm, 85 mm and 95 mm. From the plot, it is observed that, the pattern of S_{11} is almost fixed for every chosen cap heights. Comparing all the patterns of S_{11} for different cap heights, the best result is obtained for triangular cap height 75 mm.

V. Conclusion:

This paper presents a designing technique to replace an existing TCAS antenna with a Dual Patch Microstrip Antenna which provides a better performance like high gain, good directivity and small beamwidth compared to that of existing monopole TCAS antenna. This new proposed antenna is also very much light in weight and cost effective. The dual patch microstrip antenna has been designed using the dielectric most suited for the intended frequency of operation. The length and width of the patch has been calculated comply with the space bracket available on the fuselage of the aircraft. The above designed antenna exhibits the parameters similar to the original antenna. This Antenna can be embedded in the body of the aircraft and hence will not offer any resistance to the airflow. Apart from the design considerations it also saves on the maintenance front as it is not directly exposed in the line of the airflow.

References:

[1] W. H. Harman, "*TCAS: A System for Preventing Midair Collisions*", in The Lincoln Laboratory Journal. Volume 2, November 3, 1989.
[2] Kim Wiolland, "*Traffic Alert Collision Avoidance System, UNCOVERED*"
[3] U.S. Department of Transportation (Federal Aviation Administration), "*Introduction to TCAS II*", Version 7.1, February 28, 2011.
[4] Amy Laboda, "*Sensor Systems Unveils Three New Antennas*", in AINonline, October 30, 2012.
[5] Ruy C P Brandao, Ruy L Brandao and Daryal Kuntman, "*Transponder having directional antennas*", in Honeywell Int Inc, WO2001011389 A1, February 15, 2001.

Gain enhancement of antenna using proposed Hexagonal EBG with cylindrical structures for WiMax Applications

Naveen Kumar P [(1)] *Shambhulingappa K V*[(2)]
(1)SDM College of engineering and technology, Dharwad, India
Email: itznavkumar@gmail.com

(2)Jain College of engineering and technology, Bengaluru, India,
Email: shambu91@gmail.com

Abstract: *This work focusses on the gain enhancement by introducing 2-D multiperiodic EBG structures in micro strip antenna for WiMax application. It is seen that the EBG structure with dielectric material FR4 (Loss tangent 0.02) in proximity can be optimally placed along with the patch antenna to increase the gain almost as double as compared the patch antenna without EBG structure. The objective of this work is to design and study the effect of gap between the patch and the Electromagnetic band gap (EBG) structure on the bandwidth and gain of the antenna by placing multi period EBG structure on the same plane of patch antenna having bandwidth of 300 MHz with VSWR 2:1 and Gain of 8.35 is observed which is almost twice when compared to Gain of patch antenna without EBG structures. The Gain found is stable over the entire frequency band. The results are obtained through simulation by using Ansoft HFSS, a commercially available simulation based on finite element method. The size of a typical near optimum antenna is 66.65mm x 70.49mm x 1.57mm with the EBG structure of periodic hexagonal patch of 5x3 can be considered suitable for WiMax application.*

Introduction: Electromagnetic band gap (EBG) structures are formed by periodical geometric arrangement of dielectric materials and conductors that may hinder, allow or confine electromagnetic waves propagating within a specified span of frequencies. The property of periodic variation in dielectric permittivity or magnetic permeability can used to overcome disadvantages such as a narrow bandwidth (Less than 5%), low gain (Less than 6dBi) and excitation of surface waves which limits their applications in many fields. EBG structure are conventionally used as focusing devices to enhance the characteristics of simple micro strip patch antennas making it a suitable candidate for applications that require low profile and inexpensive antennas. When we consider WiMax applications the antennas play a very crucial part as the WiMax was devised to deliver high speed wireless internet access, the micro strip antennas designed for WiMax applications ranges from complex base station antennas the compact antennas fabricated on printed circuit boards of portable devices. The EBG prototype proposed is intended for medium sized devices which may be used to generate local hot spots for high speed internet access. Typically these antennas consist of an EBG structure, such as a frequency selective surface (FSS) or partially reflective surface (PRS) placed approximately half a wavelength above a ground plane containing a source antenna. The exact distance between the EBG structure and the ground plane is determined by the reflection phase of both materials at the operating frequency. In this article, a 2-D multi periodic EBG with 5 X 3 hexagonal patch antennas is designed for optimized gain and directive. This article is organized by using a simple but repetitive iteration strategy. First, the rectangular patch antenna without EBG structure is designed at operating frequency 5.60 GHz. In Section 2, EBG antenna is used along with basic patch antenna

and gain of the entire system is optimized. Then simulation results are obtained and comparisons are made in Section 3. Conclusions are drawn in Section 4. The motivation of this work is to search for an applicable antenna with high gain at microwave frequencies in WiMax application**.**

Optimized antenna design

Patch Antenna: A planar antenna operating in the frequency range 5.45 -575 GHz is designed. The prototype is shown in Figure 1. From the set of available materials FR4 with dielectric constant 4.4 and thickness (h) of 1.57 mm is chosen for use as substrate. The patch dimensions have direct influence on the operating frequency and gain. The patch length (L) and width (W) are found to be 11.6 mm and 16.44 mm respectively. The patch antenna is fed with a coaxial feeding connected to a point of the patch where the input impedance is 50 ohm

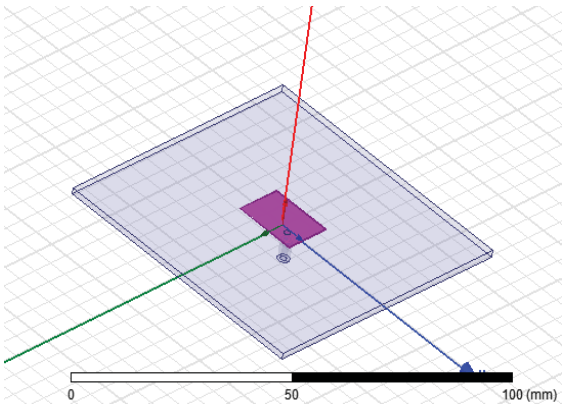

Figure 1. Patch antenna without EBG structure.

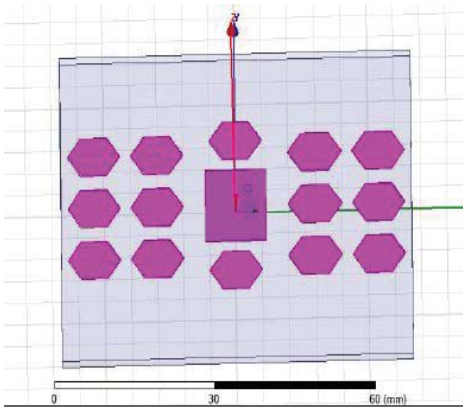

Figure 2. Patch antenna with EBG structure

EBG Antenna: The HFSS simulator tool is used to build a model for the EBG antenna. The 2-D multi periodic EBG structure antenna is designed using FR4 dielectric with 5 X 3 arrays of patches beside the rectangular patch of planar antenna on the same plane. The mushroom like EBG structure used constitutes of patches having sides of 5mm and cylindrical structures of radius 1.29mm with the height of 1.57mm placed on the plane of planar antenna with the gap of 1mm along x-coordinate and 1.15mm along y-coordinate between the patches of EBG structure as shown in Figure 2.

Optimization strategy: A simple algorithmic iterative strategy is used to optimize the physical dimensions of the antenna to maximize the gain by retaining the operating frequency and voltage standing wave ratio (VSWR) which ensures that no standing wave patterns are generated leads to reflecting a part of power that is fed to the antenna. The optimization strategy devised is based on the equations (2) and (3). Initially the roughly modeled antenna is simulated in Ansoft HFSS^{TM} for gain, return loss and VSWR. If the return loss is not at operating frequency then the width D of the conducting patches are increased or decreased to get to the correct operating frequency irrespective of the gain by retaining VSWR below the value 2.Once the operating frequency is attained then the value of D is increased very marginally and proportionately the gap δ between the patches is increased to maximize the gain of the EBG Structure. After several runs, if the gain does not improve to appreciable extent then a new geometry of placement of patches is done. The optimization curve for gain against the distance between the patches of the proposed EBG structure is given below.

$$L = h\mu o \quad (1)$$

$$C = \frac{D(\varepsilon r + 1)\varepsilon 0}{\pi} \cosh^{-1}\left(\frac{2D + \delta}{\delta}\right) \quad (2)$$

$$fo = \frac{1}{\sqrt{2\pi(LC)}} \quad (3)$$

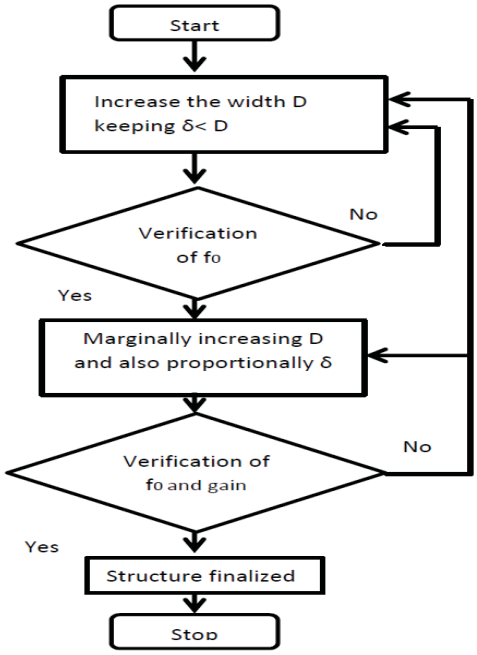

Figure 3. Optimization strategy.

X data-gap between patches
Y data-gain in dB

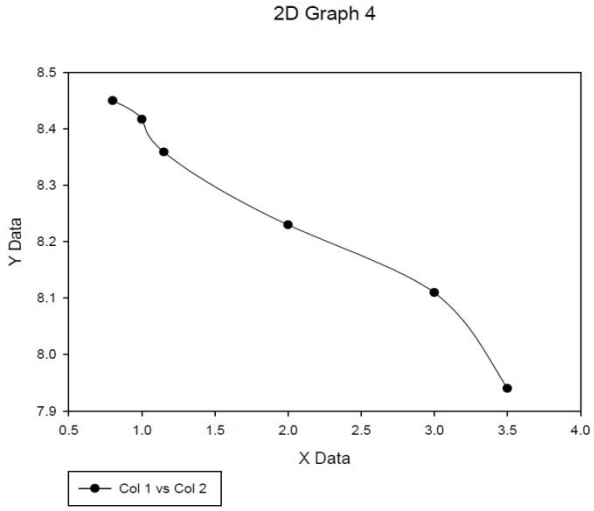

Figure 4. Optimization graph for gain enhancement in EBG structure

Optimized simulation results

Patch Antenna without EBG structure: The designed patch antenna without EBG structure has central frequency of 5.59 GHz and a –10 dB return loss bandwidth of 285 MHz as shown in Figure 3. The other parameters like gain, VSWR, Bandwidth and Bandwidth percentage are obtained as shown in TABLE I

TABLE I. DIFFERENT PARAMETERS VALUES OF PATCH ANTENNA WITHOUT EBG

Band widht(MHz)	%Band width	VSWR	Gain(dB)
285	5.13	1.94 : 1.14	4.33

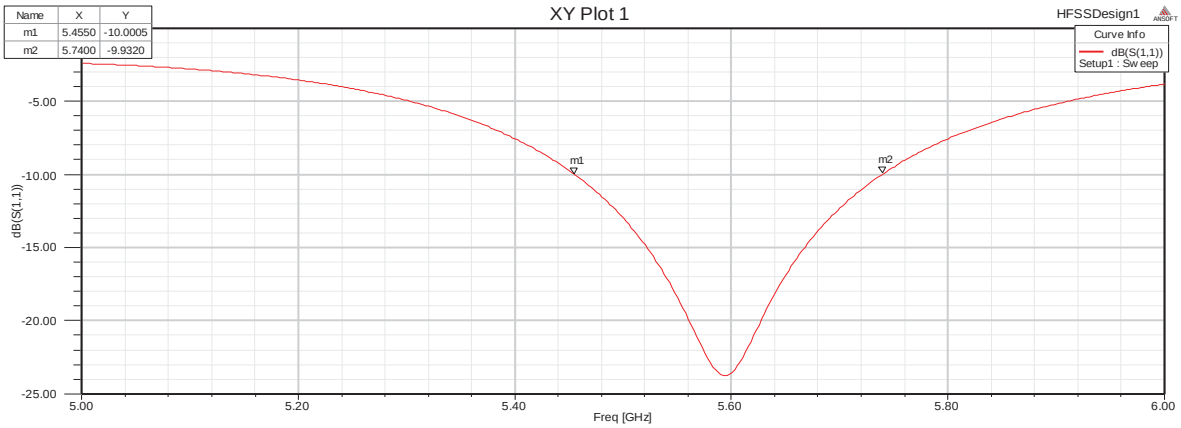

Figure 5. Return Loss of Patch antenna without EBG

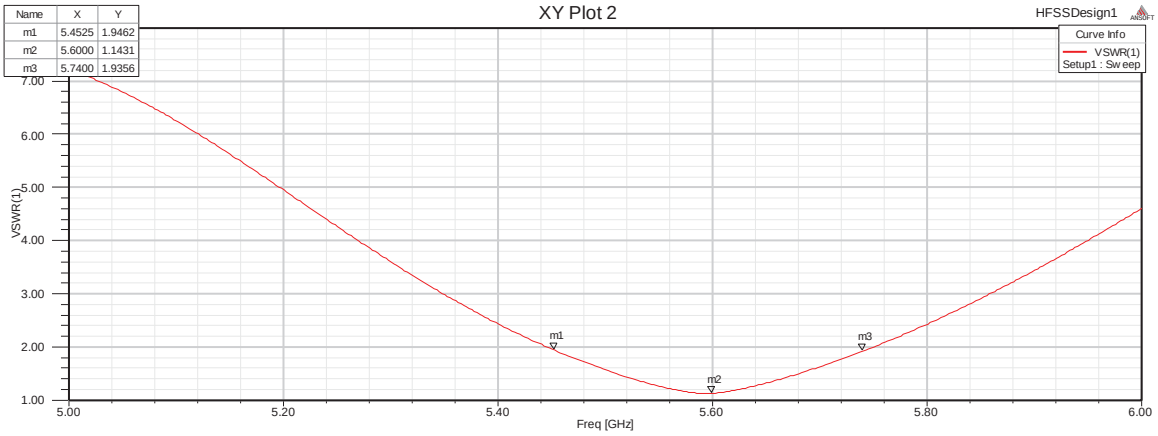

Figure 6. VSWR plot for Patch antenna without EBG

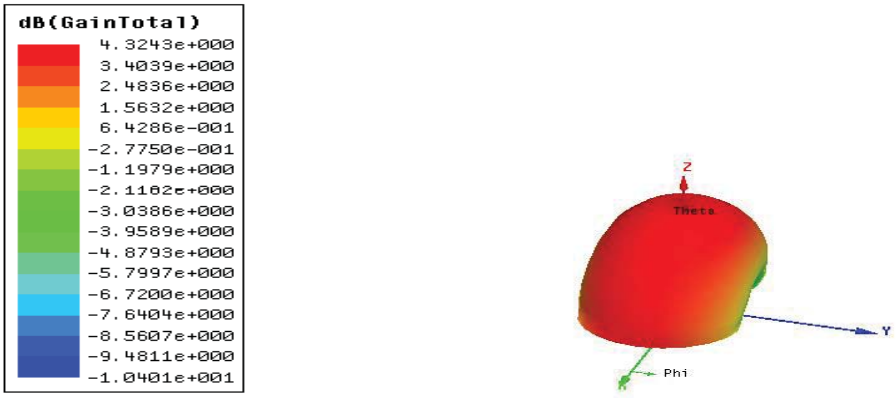

Figure 7. Polar plot for Patch antenna without EBG

Patch Antenna with EBG structure: The designed patch antenna with EBG structure has central frequency of 5.60 GHz, –10 dB return loss and bandwidth of 300 MHz as shown in Figure 6. The other parameters like gain, VSWR, Bandwidth and Bandwidth percentage are obtained as shown in TABLE II

TABLE II. DIFFERENT PARAMETERS VALUES OF PATCH ANTENNA WITH EBG

BW(MHz)	%BW	VSWR	Gain(dB)
285	5.13	1.94 : 1.14	4.33

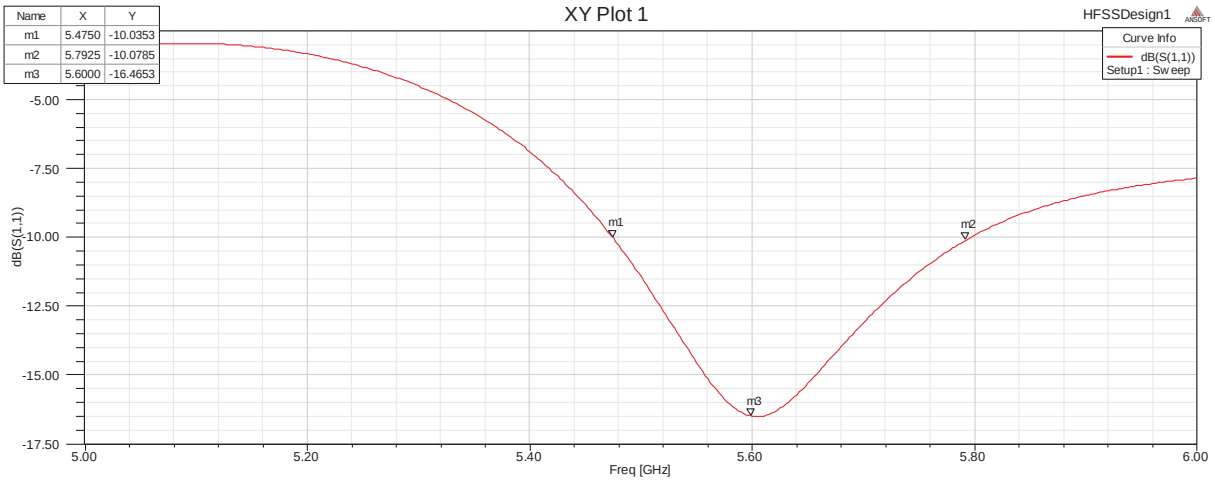

Figure 8. Return loss Patch antenna with EBG

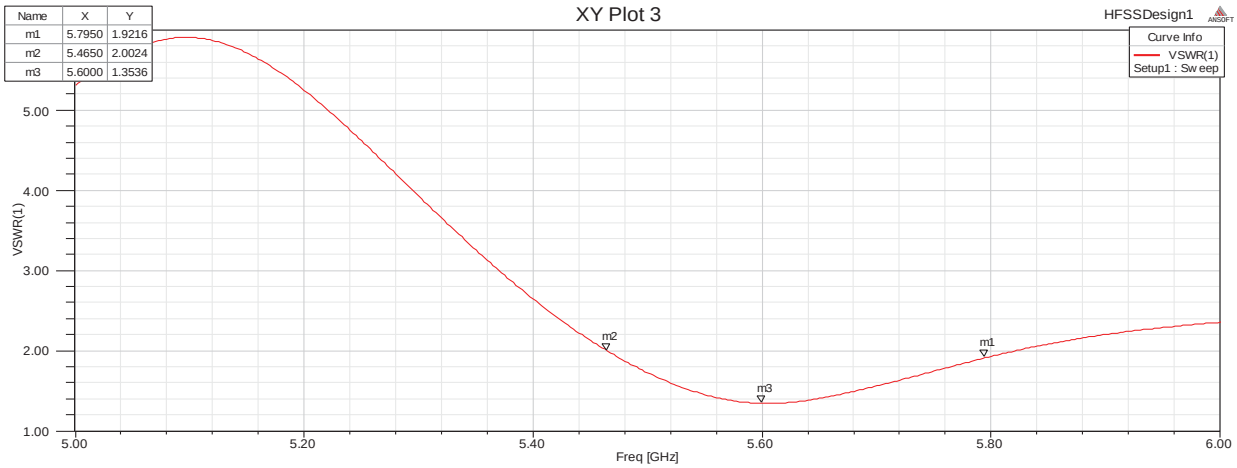

Figure 9. VS WR of Patch antenna with EBG

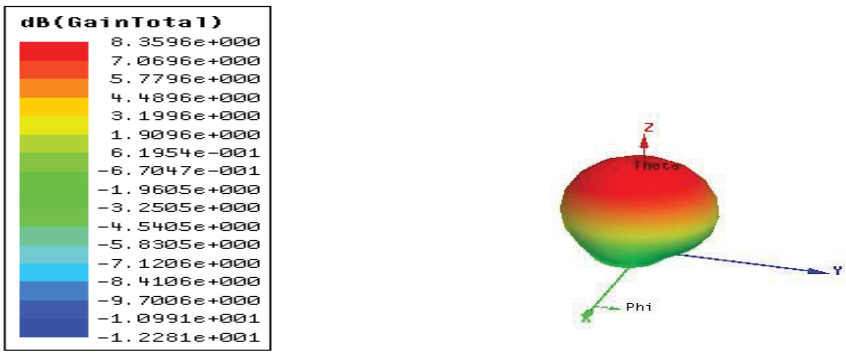

Figure 10. Polar plot of Patch antenna with EBG

Conclusion: This work demonstrates that patch antenna with FR4 substrate and 2-D multi-period EBG structure made up of FR4 with dielectric constant 4.4 on patch antenna with a distance of 1.15 mm between the patches operating at 5.45-5.75 GHz range applicable for WiMax application. The gain of patch antenna with EBG is around 8.35 dB which is almost twice as compared to patch antenna without EBG structure as shown in TABLE I.

Parameter	**Values**	
	Micro strip antenna without EBG structure	*Micro strip antenna with EBG structure*
VSWR(dB)	1.13	1.35
Gain(dB)	4.33	8.35

TABLE I. gain enhancement of Patch antenna

Reference:

[1] "Bandwidth widening techniques for directive antennas based on partially reflecting surfaces"H. Boutayeb, T. A. Denidni and M. NediL INRS-EMT, University of Quebec, 800 rue de la Gauchetiere, Montreal Quebec H5A 1K6, Canada.(2007) boutayeb@emt.inrs.ca .

[2] "Electromagnetic band gap structures in antenna engineering", Fan Yang University of Mississippi,Yahya Rahmat-Samii,University of California at Los Angeles, Cambridge University press(2009).

[3] " Microstrip Antennas:Broadband Radiation Patterns Using Photonic Crystal Substrates", Keith C. Huie ,Virginia Polytechnic Institute and State University.

[4] W. Di, Y. Yingzeng, and G. S. Minjun, "Wideband dipole antenna for 3G base stations," in Proc. IEEE Int. Symp. Microw., Antenna, Propag. and EMC Technol. for Wireless Commun., Aug. 2005, vol. 1, pp. 454–457.

[5] Y. Rahmat-Samii and H. Mosallaei, "Electromagnetic band-gap structures: Classification, characterization and applications," in Proc. 11th Interaction Conf. Antennas Propag., Manchester, U.K., Apr. 17–20, 2001, vol. 2, pp. 560–564.

[6] P. Ratajczak, P. Brachat, and J. M. Baracco, "Active reflectarray based on high impedance surface," in Proc. IEEE Antennas Propag. Symp., Honolulu, HI, Jun. 9–15, 2007, pp. 5327–5330.

[7] D. Serhal, M. Hajj, E. Rodes, and B. Jecko, "EBG antenna conformation for beamforming," in Proc. IEEE 4th Antennas Propag. Conf., Loughborough, U.K., Mar. 17–18, 2008, pp. 121–124.

[8] A.S. Pradeep, Shankar. D, Rukmini. T. S and RaviShankar. S, "A Parametric Study Of CPW Fed Slotted Antenna For Increasing Bandwidth," *Proc., ICSSC,* pp. 115-118, 2009. http://en.wikipedia.org/wiki/Microstrip_antenna.

A Reflector Based Compact UWB MIMO Antenna

T. K. Roshna [(1)], U. Deepak[(1)], V. R. Sajitha[(1)], Sumitha Mathew[(1)], and P. Mohanan[(1)]*
(1) Centre for Research in ElectroMagnetics and Antennas (CREMA),
Department of Electronics, Cochin University of Science and Technology,
Cochin -22, Kerala, India, Email: roshnatk03@gmail.com

Abstract: *A compact ultrawideband (UWB) Multiple-Input-Multiple-Output (MIMO) antenna, with high isolation is proposed for portable UWB MIMO systems. The prototype is designed on a substrate of dielectric constant 4.4 with an overall dimension of 25mm x 30mm x 1.6mm, where two coplanar stripline (CPS) fed staircase-shaped radiating elements are connected back-to-back. The proposed antenna achieved a good 2:1 VSWR impedance bandwidth covering the entire UWB band (3.1-10.6 GHz) with a high isolation of 20 dB, peak efficiency of 90% and a guaranteed value of envelope correlation coefficient ≤ 0.1641.*

Introduction: The demand for high data rate and good channel capacity is always the primary area of concern in the modern era of wireless communication systems. The race for this leads to the MIMO system [1], which utilizes the diversity technique to improve the reliability of the communication systems by mitigating the vulnerable multipath fading problem. Research field feels real scarcity while going for compact coplanar fed UWB MIMOs. Even though some CPW fed antennas are introduced for MIMO systems, they lack in compactness [2]. A 48x48 mm2, antenna with two modified CPW fed staircase-shaped radiating elements was proposed in [3]. They placed a rectangular stub at 45º between the CPW feeding points to reduce the mutual coupling.

This paper presents a novel compact coplanar stripline (CPS) fed UWB MIMO antenna with a 67% reduction in the overall area, compared to the one discussed in [3]. A metal strip reflector is placed in between them to reduce the mutual coupling between the two antenna elements for 3 – 7.5 GHz and the two antenna elements are connected back-to-back to improve the isolation for frequencies above 7.5 GHz. These decoupling methods made isolation better than 20 dB possible, throughout the UWB band, by retaining the 2:1 VSWR.

Antenna design and geometry: Fig. 1 depicts the geometry of the proposed coplanar stripline fed 2-port UWB MIMO antenna. It comprises of two symmetric antenna elements 1 and 2, arranged back-to-back, and fed through port 1 and port 2, respectively. The two antenna elements are separated by a distance of G = 16mm. In addition to that, a metal strip of length 25mm and width (W7) 0.4mm is kept at the middle of the MIMO antenna, as shown in Fig. 1. Each antenna element has staircase-shaped radiator with a shorted strip at the bottom [4]. Both the antenna elements along with the metal strip are printed on the front side of a 25mm x 30mm x 1.6mm FR4 substrate with a relative permittivity (ε_r) of 4.4 and loss tangent (tanδ) of 0.02. The 3D EM simulator software of CST Microwave Studio is used for simulating the antennas. The optimized dimensions for the antenna are L=25, L1=1, L2=1, L3=2, L4=12.3, L5=0.6, L6=10.5, L7=7.4, L8=2, W=30, W1=0.5, W2=0.5, W3=0.8, W4=1, W5=1, W6=5, W7=0.4, G=16, g=0.4, h=1.6.

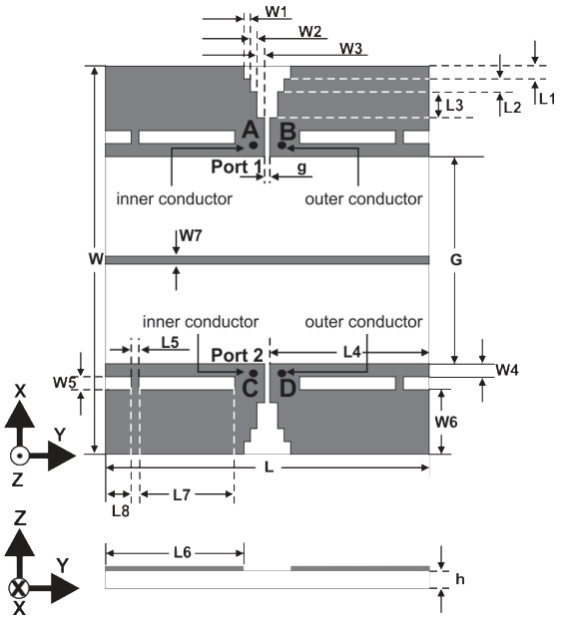

Fig. 1. Geometry of the proposed CPS fed 2-port UWB MIMO antenna.

Working Mechanism: For the proposed 2-port MIMO antenna, the two UWB antennas are configured back-to-back to attain better isolation. But the isolation is poor for 3.1-7.5 GHz, as seen in Fig. 2. It can be resolved by placing a metal strip of width 0.4mm and length 25mm between the antennas. The metal strip is kept at half the way from port 1 to port 2, as shown in Fig. 1. Here the metal strip behaves as a reflector for the frequencies between 3.1 GHz to 7.5 GHz. A comparison of the simulated reflection and transmission coefficients of the 2-port UWB MIMO antenna with and without the strip is depicted in Fig. 2. From the figure it is clear that the reflector effectively decreases the coupling between the two antenna elements and thus improves the isolation level to stand better than 20dB in the 3.1-7.5 GHz band. So, the presence of reflector together with the back-to-back configuration of the antenna elements helped the proposed MIMO antenna to get an enhanced isolation level of 20dB throughout the UWB band.

The mutual coupling between closely packed antennas is due to the large flow of surface current from the excited port to the other ports. With the help of decoupling structures, this migration of surface current can be blocked or attenuated, and hence reduce

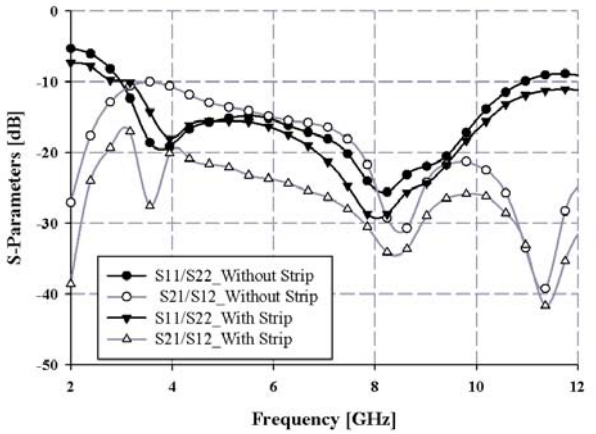

Fig. 2. Simulated S-parameters of MIMO antenna with and without strip

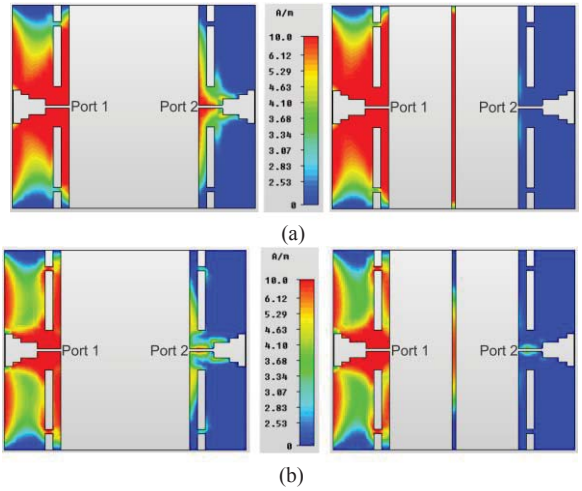

Fig. 3. Surface current distribution of antenna with and without strip at (a) 4.5 GHz and at (b) 8.5 GHz .

the mutual coupling. Here, a simple metal strip reflector is used for the decoupling purpose and its effect on surface current distribution is shown in Fig. 3, with port1 excited. For 4.5 GHz the reflector has a significant influence on the surface current distribution, which is clearly depicted in Fig. 3(a). For the frequencies greater than 7.5 GHz, the influence on the isolation of two antenna elements degrades slowly and its effect on surface current also decreases, as shown in Fig. 3(b). However, mutual coupling will not be increased for those frequencies because of the configuration of the antenna elements.

Result and Discussion: The proposed antenna in Fig. 1 is fabricated on a FR-4 substrate and tested. The measured S-parameters of the proposed antenna is depicted in Fig. 4. Fig. 2 & 4 indicates a good agreement between the simulated and measured results. The slight discrepancies in simulated and measured transmission coefficients are due to the fabrication tolerances. The measured results in Fig. 4 shows that the proposed MIMO antenna has a 2:1 VSWR bandwidth from 3.1 to 11.3 GHz for both the ports, which implies that the antenna satisfies the impedance matching requirements for UWB systems, specified by FCC. Moreover, the |S21| and |S12| are more than 20dB throughout the UWB band, which makes the proposed antenna suitable for UWB MIMO operation.

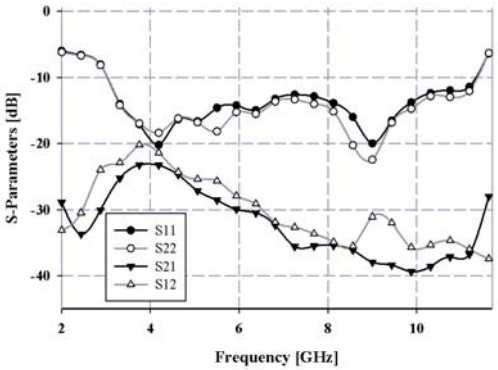

Fig. 4. Measured S-parameters of MIMO antenna with strip.

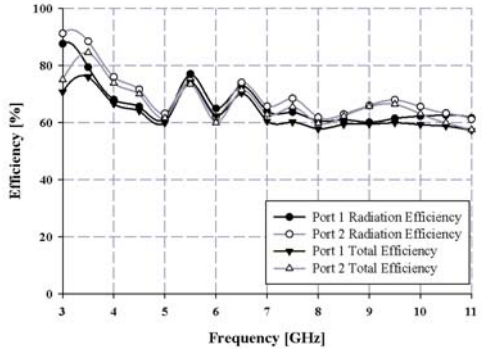

Fig. 5. Measured radiation and total efficiencies of antenna

The radiation efficiency (η_{rad}) of the 2-port UWB MIMO antenna is measured, using the Wheeler Cap method by Schantz [5], with one port excited while the other is matched with 50Ω load. From radiation efficiency, the total efficiency (η_{tot}) is calculated [6] and both

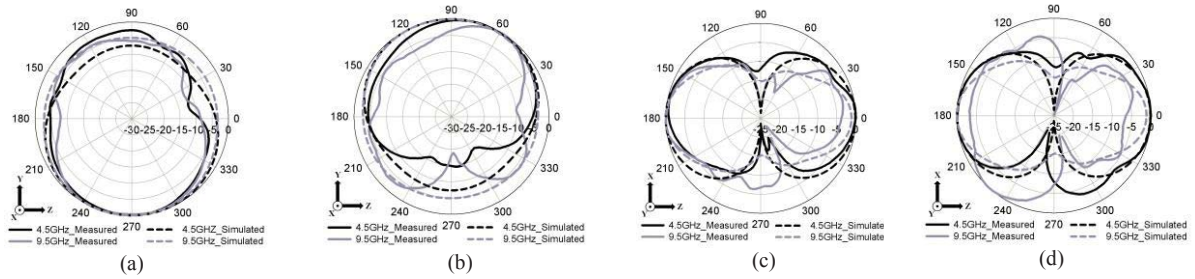

(a) (b) (c) (d)

Fig. 6. Radiation pattern at ϕ=0 plane for (a) port 1, (b) port2, ϕ= π/2 plane for (c) port 1, (d) port 2

are plotted against frequency, as seen in Fig. 5. The proposed compact MIMO antenna has an average measured radiation efficiency of about 66%, with a peak efficiency of 90% at 3.2 GHz. The radiation characteristics of the proposed antenna across the UWB band were investigated. The simulated and measured radiation patterns at 4.5 and 9.5 GHz in the ϕ=π/2 plane and ϕ=0 plane, for both port 1 and 2 are depicted in Fig. 6. For measurements, port 2 is terminated with a matched load of 50 Ω when port 1 is excited and vice versa. On comparing Fig. 6(a) & (b), it can be observed that the radiation patterns of the two antenna elements has

a complementary spatial appearance in the ϕ=0 (Y-Z) plane. Thus the polarization diversity, which contributes high isolation between the antenna elements, is achieved by this compact MIMO antenna.

The ECC measure the amount of signal fading or diversity capability of two antennas. By translating the correlation of the losses of antennas to an uncertainty in the received signal correlation, the lowest value that the correlation can be sure to lie below [7] is calculated to be ≤ 0.4051. And the guaranteed value of envelope correlation coefficient (ECC) is ≤ 0.1641 in the UWB band. Thus the proposed antenna satisfies the ECC criteria [6] for good channel characteristics in a MIMO system. MEG is used to quantify the relative mean power levels between the signal delivered from each antenna [8]. To guarantee a good diversity performance and channel characteristics, the ratio of MEG of two antenna elements should satisfy the criteria [6] of, $MEG_i / MEG_j \leq \pm$ 3dB. The ratio of MEG of the proposed MIMO antenna lies in between the above mentioned limit throughout the UWB band, with a maximum of -0.9dB at 4GHz. The calculated values of ECC and MEG_i/MEG_j show that the proposed UWB MIMO antenna is a good prospect for UWB MIMO communication systems.

Conclusion: A compact UWB MIMO antenna with enhanced isolation for portable UWB MIMO communication systems has been presented and discussed. The simulated and measured results are in good agreement. The MIMO antenna achieved a 2:1 VSWR bandwidth from 3.1 – 11.3 GHz covering the entire UWB band with high isolation of more than 20dB between the antenna elements. It has a peak radiation efficiency of 90% at 3.2 GHz. Throughout the UWB band the guaranteed value of ECC is found to be ≤ 0.1641 and ratio of MEG $< \pm$1dB, which indicates that the proposed UWB MIMO antenna is a good candidate for UWB MIMO communication systems.

Reference:

[1] M. S. Fernández, E. R. Iglesias, Ó. Q. Teruel, and M. L. Pablo-González, "Spectral efficiency in MIMO systems using space and pattern diversities under compactness constraints," IEEE Trans. Veh. Technol., vol. 57, no. 3, pp. 1637-1645, May 2008.

[2] L. Xiong and P. Gao, "Compact dual-polarized slot UWB antenna with CPW-fed structure," in Proc. IEEE Antennas Propag. Society Int. Symp. (APSURSI'2012), Chicago, IL, USA, 2012, pp. 1–2.

[3] P. Gao, S. He, X. Wei, Z. Xu, N. Wang, and Y. Zheng, "Compact printed UWB diversity slot antenna with 5.5-GHz band-notched characteristics," IEEE Antennas Wirel. Propag. Lett., vol. 13, pp. 376–379, March 2014.

[4] T. K. Roshna, U. Deepak, V. R. Sajitha, and P. Mohanan, "Coplanar stripline-fed compact UWB antenna," IEEE Electron. Lett., vol. 50, no. 17, pp. 1181–1182, Aug 2014.

[5] H. Schantz, "Radiation efficiency of UWB antennas," in Proc. IEEE Conf. Ultra-Wideband Syst. And Tech. (UWBST'2002), Baltimore, MD, USA, 2002 pp. 350–355.

[6] M. Karaboikis, V. C. Papamichael, G. F. Tsachtsiris, C. F. Soras, and V. T. Makios, "Integrating compact printed antennas onto small diversity/MIMO terminals," IEEE Trans. Antennas Propag., vol. 56, no. 7, pp. 2067–2078, July 2008.

[7] P. Hallbjorner, "The significance of radiation efficiencies when using S-parameters to calculate the received signal correlation from two antennas," IEEE Antennas Wirel. Propag. Lett., vol. 4, pp. 97–99, June 2005.

[8] T. Taga, "Analysis for mean effective gain for mobile in land mobile radio environments," IEEE Trans. Veh. Technol., vol. 39, no. 2, pp. 117–131, May 1990.

Null placement and Side Lobe Level Reduction in Beam Steered Linear Antenna Array using Restricted Search Particle Swarm Optimization

Soumyo Chatterjee[(1)] and Sayan Chatterjee [(2)]
(1) Heritage Institute of Technology, Kolkata, India, Pin-700107,
Email: soumyo.chatterjee@heritageit.edu
(2) Jadavpur University, Kolkata, India, Pin-700075,
Email: sayan1234@gmail.com

Abstract: *In this article, multiple objectives such as null placement and Side lobe Level reduction (SLL) in beam steered linear array have been addressed using Restricted Search Particle Swarm Optimization (RSPSO). In order to achieve the objectives current excitation amplitude has been perturbed in a predefined restricted search space for improvement of convergence efficiency. Some design examples have been considered and compared for multiple and broad null placement along with SLL reduction to prove the effectiveness of RSPSO algorithm*

Introduction: Efficiency of modern wireless communication system depends upon its ability to place the desired pattern in the direction of intended user, while nulls directed towards the interferers. Consequently, null placement in beam steered linear array or phased array with prescribed side lobe level (SLL) and null depth has received a considerable amount of attention in recent past [1-7,10]. In literature, problem of null placement along with SLL reduction has been addressed either by controlling amplitude excitations or by controlling positions of array elements, with main beam positioned at broadside direction [3-7]. F. Tokan et. al. has addressed the problem of SLL reduction along with null placement in beam steered linear array by controlling the positions of array elements [2]. Genetic Algorithm has been used to obtain the optimal positions satisfying the desired objective of null placement and SLL reduction in beam steered linear array. However, according to [6], practical implementation of this technique requires servomotor controllers which in turn increases system cost. Moreover, with increase in number of elements, the computational time to find the position also increases. Hence element excitation perturbation is much easier to implement in achieving beam steering along with null placement in linear array and has been adopted in the present work

In the present work, null placement with the constraint of SLL reduction in beam steered linear array has been investigated with the aim of more efficient and easier method of implementation. In order to achieve the desired objectives, excitation amplitudes has been perturbed using a novel restricted search particle swarm optimization (RSPSO), where in the search space of the optimization problem has been pre defined using Taylor one parameter distribution for linear array. The objective function has been formulated using weighted sum method which is much easy to implement compared to other methods like pareto optimal synthesis method [2]. Effectiveness of the proposed method has been shown through some design examples and comparative study for both multiple and wide null placements with the constraint of desired SLL reduction and prescribed null depth.

Problem Formulation: In the present work, a linear beam steered of even numbered (2N) isotropic elements uniformly placed along x-axis has been considered. The array geometry is shown in Fig.1.
The normalized array factor expression for 2N isotropic elements is as represented in (1) [6].

$$AF(\theta) = \sum_{n=1}^{N} a_n \cos\left[\left(\frac{2n-1}{2}\right) kd(\cos\theta - \cos\theta_s)\right] \quad (1)$$

In (1), k is the wavenumber and a_n, d and θ_s ($0° \leq \theta_s \leq 180°$) represents the excitation amplitude, position of the n^{th} element and desired main beam position, respectively. Objective of desired $(SLL\ (dB)_d)$ and null placement positions (θ_{ni}) are mathematically represented in (2) and (3) respectively as error functions.

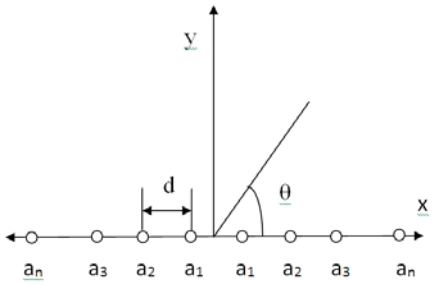

Fig. (1) Even numbered (2N) linear array uniformly placed along x- axis

$$f_1 = \left|SLL(dB)_d\right| - \left|\max\left[\max\left\{20\log\left|\frac{AF(\theta)}{AF(\theta_s)}\right|\right\}_{0^o}^{\theta_s - \theta_{nl}}, \max\left\{20\log\left|\frac{AF(\theta)}{AF(\theta_s)}\right|\right\}_{\theta_{nr} - \theta_s}^{180^o}\right]\right| \quad (2)$$

$$f_2 = \left|Null_level(dB)_d\right| - \left|\sum_{i=1}^{m} 20\log\left\{\frac{AF(\theta_n)_i}{AF(\theta_s)}\right\}\right| \quad (3)$$

In (2), θ_{nl} and θ_{nr} represents first null position on the left and right hand side of main beam position (θ_s) respectively. In (3), $Null_level\ (dB)_d$ is the desired null level, $AF(\theta_n)_i$ is the value of the array factor at the particular null position, $AF(\theta_s)$ is the value of array factor at main beam position (θ_s) and m is the maximum number of positions where the null has to be imposed.

An optimization algorithm operates on a single scalar value representing the desired objectives. Consequently, error functions of (2) and (3) are combined together to formulate a single valued scalar function called as fitness function using weighted sum method as expressed in (4).

$$\text{fitness function} = \alpha \times f_1 + \beta \times f_2 \quad (4)$$

In (4), α and β are the influence factor representing relative importance of the two objectives considered in the present work. In order to give equal importance to each objective, value of α and β has been set to 1.

Restricted Search Particle Swarm Optimization: Proposed algorithm namely restricted search particle swarm optimization (RSPSO) is basically a modified version of conventional PSO (CPSO) developed by Kennedy and Eberhart [9]. Due to limitation in space only major steps of the algorithm has been discussed in this section. Following are the steps of the algorithm:

a) Choice of optimization variables: As it is required to modify the SLL, excitation amplitudes are considered as optimization variable.

b) Search space definition: Search space comprises of set of excitation amplitudes whose initial values have to be set. For desired SLL and particular linear array configuration, Taylor one parameter method [8] facilitates the calculation of excitation amplitudes. Consequently, the range of excitation amplitude gets defined. As the search space is restricted and not defined randomly the modified algorithm is called as restricted search space PSO (RSPSO).

c) Fitness function definition: Fitness function is a single valued scalar function that represents the desired objective of desired SLL and null placement position which in turn guides the movement of each particle. The mathematical expression of cost function is as expressed in (4). Depending upon the cost function, RSPSO algorithm searches for minimum value iteratively. Each particle knows its best value of excitation amplitude at any iteration

cycle which corresponds to personal experiences of each particle and is called as personal best (p_{best}). Moreover, each particle knows the best value excitation amplitude so far in the swarm among personal bests and is called as global best (g_{best}).

d) Update of velocity and position: Velocity of each particle is updated according to the following equation:

$$v_n(t+1) = wv_n(t) + c_1 rand(\,)[p_{best} - x_n(t)] + c_2 rand(\,)[g_{best} - x_n(t)] \quad (5)$$

where $v_n(t)$ is the velocity of the particle in the n^{th} dimension and $x_n(t)$ is the particle's coordinate in the n^{th} dimension. After time step, location of each particle is updated according to the following equation:

$$x_n(t+1) = x_n(t) + v_n(t+1) \quad (6)$$

where $v_n(t+1)$ and $x_n(t+1)$ are the updated velocity and position of each particle. Details of the expressions can be seen in [10].

e) Termination criterion: In the present work termination criterion of 100 iterations has been considered.

Experimental Results: As an example, design of 12 element non uniformly excited (amplitude only) linear array with desired SLL of -20 dB, multiple null placement positions of 40° and 80° and main beam positioned at 120° has been considered. Elements of the linear array are considered to be uniformly placed with inter element spacing of 0.5λ (wavelength). The desired null level has been kept at -120 dB. Such high null depth helps in handling electromagnetic interference at the desired null positions [7]. Corresponding radiation pattern of optimized array has been shown in Fig. (1). From Fig. (1), it has been observed that optimization objective of placing multiple nulls at 40° and 80° with desired null depth of -120 dB has been achieved successfully. Moreover peak SLL value of -15.65 dB represents partial SLL reduction.

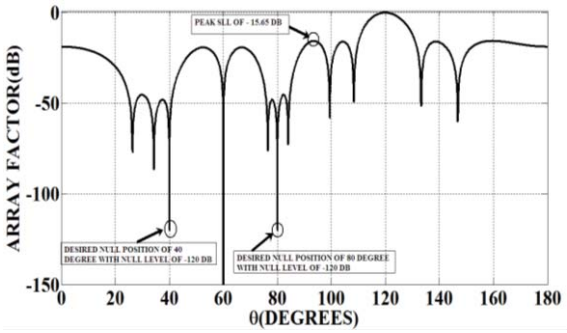

Fig. (1) Multiple nulls at 40° and 80° for 12 elements linear array with uniform spacing of 0.5λ.

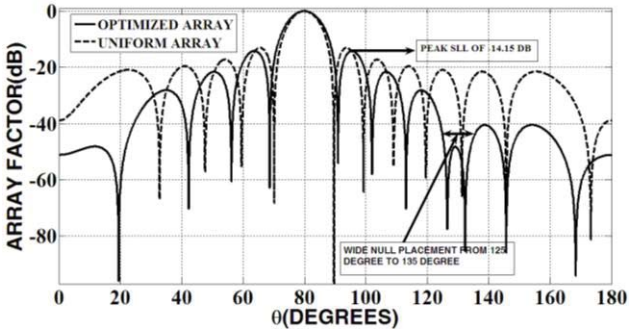

Fig. (2) Wide nulls from 125° to 135° for 12 elements linear array with uniform spacing of 0.5λ.

The same array configuration has been tested for wide null placement from 125° to 135° with desired null depth of -50 dB, desired peak SLL value of -20 dB and main beam positioned at 80°. Corresponding radiation pattern for optimized array and uniform array has been shown in Fig. (2). It must be noted that radiation pattern of uniform array has been plotted in order to compare the optimized array, on the basis of null placement and peak side lobe level. In the desired wide null placement positions from 125° to 135°, maximum SLL of -44.13 dB has been obtained which is quite acceptable with respect to peak SLL of -14.15 dB for optimized array. For optimized array peak SLL has been reduced from -13.06 dB (uniform array) to -14.15 dB. Hence, both optimization objectives of SLL reduction and wide null placement have been achieved using the proposed method. Summary of comparative study has been summarized in Table I. Table I summarizes the comparative case study of wide null

placement in 40 elements beam steered linear array. From Table I it is observed that in both cases, within prescribed null regions the maximum side lobe level (MSLL) is much less using RSPSO method compared to genetic algorithm (GA) and pareto optimal synthesis method [2]. Moreover in case-II it has been observed that using GA and pareto optimal synthesis method [2], peak side lobe level (PSLL) is -14 dB whereas using RSPSO it is -15.28 dB. Hence, it can be concluded that using RSPSO, better null placement with reduced SLL constraint can be achieved in beam steered linear array.

Table I Comparison of maximum side lobe level (MSLL) and peak side lobe level (PSLL) of 40 elements linear array in prescribed interference region.

θ_s	Interference Region	MSLL		PSLL	
		GA [2]	RSPSO	GA [2]	RSPSO
50° (Case-I)	19° - 21°	-33 dB	-51.32 dB	-13.8 dB	-13.8 dB
75° (Case-II)	15° - 25°	-33 dB	-36.58 dB	-14 dB	-15.28 dB

Conclusion: In this article, multiple and wide null placement in beam steered linear array with constraint of reduced SLL and prescribed null depth has been investigated using RSPSO. The desired objectives have been achieved by perturbation of excitation amplitude within the pre defined search space which has been defined using Taylor one parameter distribution for linear array. Experimental results show the successful implementation of multiple design objectives. For example, in case of 12 elements linear array with main beam positioned at 80° and prescribed wide null position of 125° to 135°, MSLL of -44.13 dB and PSLL of -14.15 dB has been achieved. Consequently, it can be concluded that wide null placement with SLL reduction constraint has been achieved. Moreover comparative study confirms the effectiveness of the proposed method in implementing wide null placement in beam steered linear array with constraint of SLL reduction.

Reference:

[1] M.A. Mangoud and H.M. Elragal, "Antenna Array Pattern Synthesis and Wide Null Control using Enhanced Particle Swarm Optimization" PIERS B, Authors Name, Vol. 17, pp. 1 – 14, 2009.

[2] F. Tokan and F. Gunes, "The Multi-Objective Optimization of Non-uniform Linear phased Arrays Using The Genetic Algorithm", PIERS B, Vol.17, pp. 135– 151, 2009.

[3] U. Singh, H. Kumar and T.S. Kamal, "Linear Array Synthesis Using Biogeography Based Optimization", PIERS M, Vol. 11, pp. 25-36, 2010.

[4] S. Pal, B.Y. Qu, "Optimal Synthesis of Linear Antenna Arrays with Multi-objective Differential Evolution", PIERS B, Vol. 21, pp. 87-111, 2010.

[5] X. Li and M. Yin, "Optimal Synthesis of Linear Antenna Araay with Composite Differential Evolution Algorithm", Scientia Iranica D, Vol. 19, No. 6, pp. 1780-1787, 2012.

[6] A. Recioui and H. Bentarzi, "Null Steering of Dolph Chebyshev Arrays Using Taguchi Method", WSEAS Transactions on Communications, Vol. 9, pp. 720-729, 2010.

[7] B. Goswami and D. Mandal, "A Genetic Algorithm for the Level Control of Nulls and Side Lobes in Linear Antenna Arrays", Journal of King Saud University- Computer and Information Sciences, Vol. 25, pp. 117-126, 2012.

[8] T.T. Taylor, "Design of line source antennas for narrow beamwidth and low sidelobes," IRE Transaction on Antennas Propagation, Vol. AP-7, pp. 16-28, 1955.

[9] J.Kennedy and R. Eberhart, "Particle swarm optimization", In Proceedings of IEEE International Conference on Neural Networks, Vol. 4, pp. 1942-1948, 1995.

[10] Soumyo Chatterjee, S. Chatterjee and D.R. Poddar, "Synthesis of linear array using Taylor distribution and Particle Swarm Optimisation," International Journal of Electronics, pp. 1-17, 2014.

WIDEBAND DIPOLE ANTENNA OVER HIGH IMPEDANCE SURFACE

V.A. Libi Mol, B. Rahul, C.K. Aanandan
Cochin University of Science and Technology, Kerala., India
Email: libi.riyaz@gmail.com

Abstract: *Studies on wideband folded dipole over high impedance surface is presented. The performance of different types of high impedance surfaces as ground plane for planar dipole antenna is investigated. Planar dogbone, ring and square patches printed on grounded dielectric substrate are considered. While all these structures reduced overall size of the dipole, the ring structure gives a better bandwidth compared to the other two.*

Introduction:

Since the pioneering work on high impedance surfaces (HIS) in 1999 by Daniel Sievenpiper, it found a lot of application because of its Artificial Magnetic Conductor (AMC-in phase reflection) and Electronic Band Gap (EBG-forbids surface wave propagation) properties [1]. Usually Perfect Electric Conductor plates are used as ground planes to redirect the back radiation and provide shielding to the antennas. PEC exhibit the property of phase reversal of the incident currents that result in destructive interference of the original antenna currents and the image currents. To overcome this effect, antennas are to be placed at a height of quarter wavelength above the metallic ground plane making the size of the antenna bulky at low frequencies. To reduce the size of the antenna, we need a ground plane that is dual of the conventional PECs, in other words we need a PMC. Due to its in-phase reflection property, high impedance surfaces can be used as ground plane for low profile realization [3].

Also different antenna parameters like the gain, impedance and bandwidth along with size reduction can be achieved by incorporating the HIS into the antenna structures. The PEC ground plane can provide a directive broadside pattern and narrow impedance bandwidth while PMC ground plane shows improved bandwidth with lower directivity. A properly designed HIS can achieve improved bandwidth with respect to PEC and higher forward directivity with respect to PMC case [2].

In this work, performance of wideband folded dipole antenna over different types of High impedance surface is investigated. The modelling of dipole is similar to [2] but this one shows reduced size (in terms of wavelength) and improved bandwidth performance. First, the size of planar HIS is optimized to achieve magnetic resonance at 9 GHz and then folded dipole antenna with twin line feeding is designed over these structures to achieve the wideband characteristics. Both Simulation and measurement show good agreement.

Antenna Design

HIS are planar 2-dimensional periodic array of metallic elements with specially designed sub wavelength geometry and showing in phase reflection at some particular

frequency. When we design antennas over HIS ground plane, both elements must be considered simultaneously as a single antenna structure. First of all the HIS unit cell for the desired magnetic resonant frequency is designed considering the upper dielectric layer above the unit cell to support the antenna structure. Then the balun used to feed the folded dipole antenna using coaxial cable is designed for same frequency. Finally the dipole length is varied and length is optimized using CST MW Studio.

(a)HIS Unit Cell Design-

Three different sub wavelength unit cells: square, ring and dogbone are optimized for magnetic resonance at 9 GHz on a grounded FR4 substrate (h=1.6 mm, ε_r =4.4 and tanδ=.021) as shown in figure 1(a). An upper dielectric layer of FR4 used for supporting the antenna is also considered in the design. For this application, we have considered normal plane wave incidence. By varying patch and unit cell dimensions, it is possible to obtain both EBG and AMC characteristics within same frequency band. Here optimization is done for magnetic resonance considering normal plane wave incidence in the simulation.

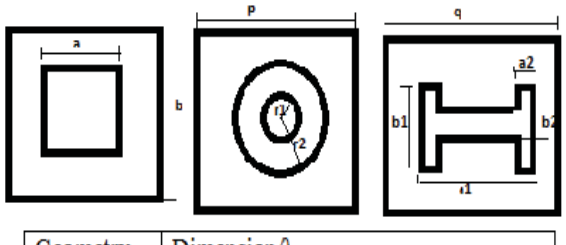

Geometry	Dimension/λ
Square	a=.12,b=.24
Ring	p=.196,r1=.03,r2=.06
Dogbone	q=.212,a1=.12,a2=.026,b1=.06,b2=.03

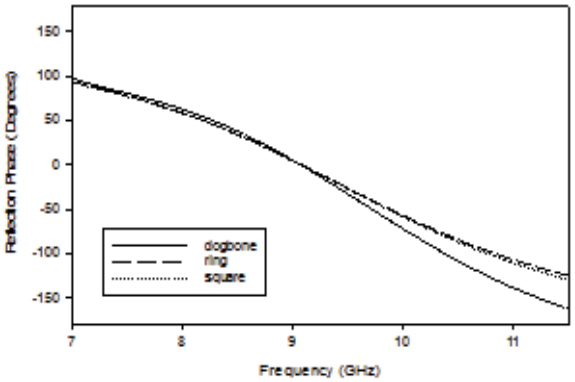

Figure1. (a) Geometry of HIS unit cell (b) Simulated reflection phase over top dielectric layer,3.2 mm from lower ground plane,

The reflection phase verses frequency is plotted in figure 1(b). All these structures show magnetic resonance at 9 GHz. Above and below the magnetic resonant frequency, these structure shows capacitive and inductive reactance. When the reflection phase become $\pm$180, these surface show the PEC characteristics.

(b)Folded Dipole over High Impedance Surface

The dipole antenna consist of two symmetrical conductors printed over High Impedance Surface. To connect this dipole antenna to the coaxial cable, a BALUN is designed. The balun geometry consist of a symmetric T junction followed by a 180^0 delay line printed on antenna plane and the ground plane printed on HIS layer as shown in figure 2(a). The length of one branch is selected as λ_g and other as $\lambda_g/2$ to provide 180^0 phase shift between two arms. To avoid the 90^0 bends standard mitering is used. The simulation result shows good reflection and transmission characteristics, phase reversal properties and broad bandwidth. The length of the antenna is optimized to .18λ to provide resonance from magnetic resonant frequency of HIS.

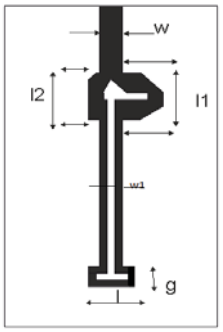

(a)

Parameters	Dimension (mm)
w	3
l	5.94
g	1
l1	19.4
l2	9.7
w1	1

(b)

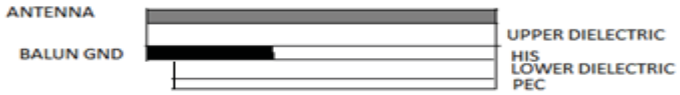

(c)

Figure 2. (a)Geometry of folded dipole (b) dimensions (c) Antenna configuration

This antenna configuration uses two layers of dielectric as shown in Fig 2(c) and the inner conductor of coaxial cable is connected to the feed line of balun and the outer conductor is connected to the balun ground. The reflection characteristics of the dipole with three types of HIS used as ground plane is shown in Fig 3(b). All these configurations show reduced antenna size and enhanced bandwidth as compared to the antenna with PEC ground plane.

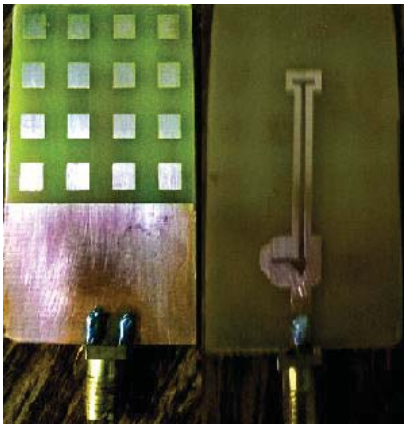

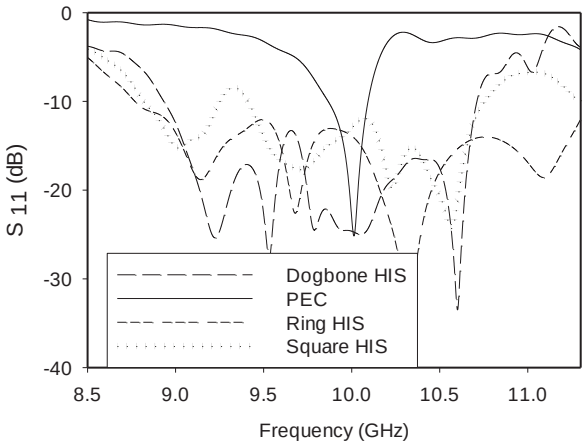

Figure 3. (a)Fabricated prototype (b) Simulation results

Ground	Square	Ring	Dogbone	PEC
Array Size	32mm (4*4)	26mm (4*4)	28mm (4*4)	
Resonant Band(GHz)	8.8-9.24 9.4-10.7	8.8-11.3	8.9-10.7	9.8-10.09
Antenna Size	.18λ	.18λ	.18λ	.25λ

Table 1.Comparison of ground planes

Results

The folded dipole over different HIS were fabricated and return loss characteristics were measured using HP 8510 network analyzer and is shown in Fig 4(a). Good agreement is shown by both measured and simulated results. The measured gain of the antenna is also shown in Fig 4 (b). Measured E and H plane radiation pattern at 8.9, 10.053 and 10.95GHz

for ring HIS are also shown in Fig 4(c) and 4(d). The cross-polar components are about 10 dB less than co- polar components.

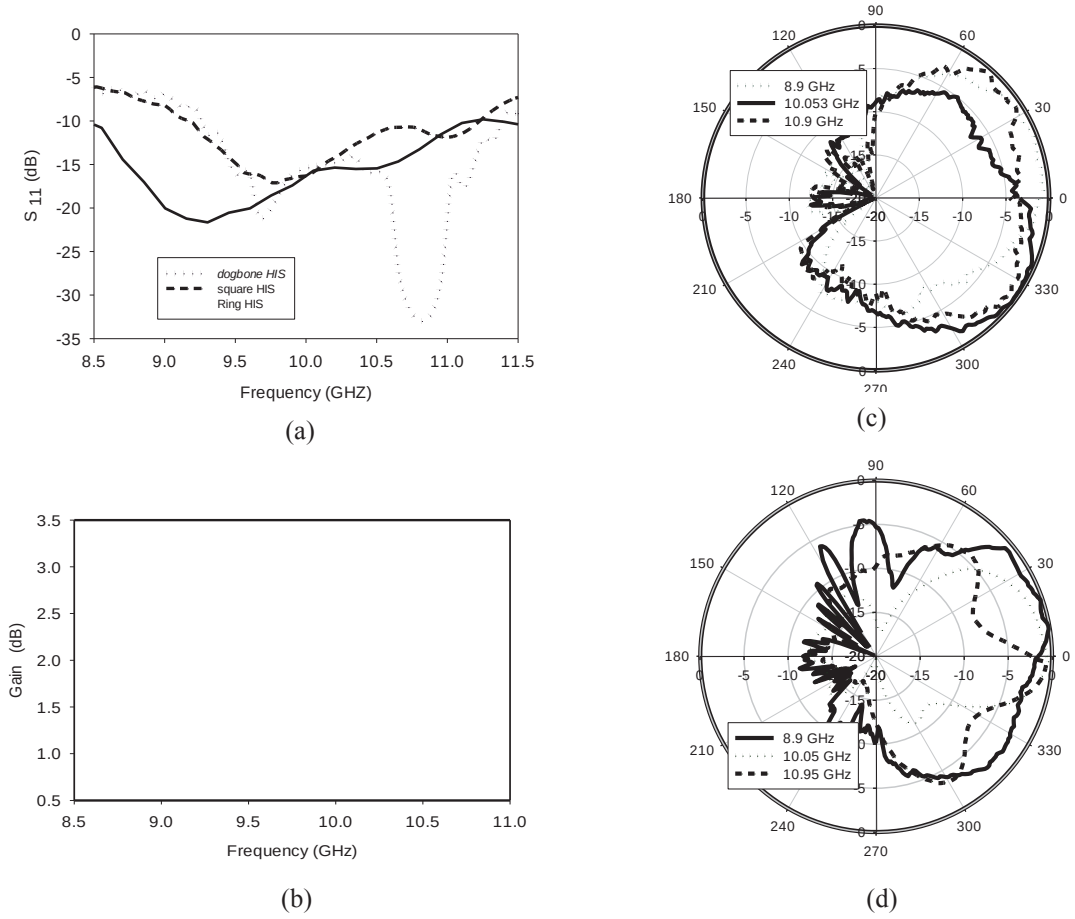

Figure 4. (a) Measured return loss (b) Gain
(c) E-plane Pattern (d) H plane Pattern

Conclusion

This paper investigates the advantages of using HIS as ground plane for low profile antenna. Different structures are used as HIS and it is found that overall antenna size is reduced with the ring structure giveing and enhanced bandwidth compared to the other two.

Acknowledgements

Authors wish to acknowledge the financial and infrastructural support from UGC and DST, Government of India.

Reference

1. D. Sievenpiper, L. Zhang, R. F. Jimenez Broas, N. G. Alexopolous,and E. Yablonovitch, "High-impedance electromagnetic surfaces with a forbidden frequency band," *IEEE Trans. Microw. Theory and Tech.*,vol. 47, no. 11, pp. 2059–2074, Nov. 1999.
2. Andrea Vallechi, Javier R De luis, Filippo Capolino and Franco De Flavis,"Low profile fully planar folded dipole antenna on a high impedance surface," IEEE Trans.on Antennas and Propn,vol.60,no.1.Jan 2012

INVITED TALKS

No	Papers	Page
1	**Terahertz Technology and its Applications** *Dr. Goutam Chattopadhyay* NASA-Jet Propulsion Laboratory, California Institute of Technology 4800 Oak Grove Drive, Pasadena, CA 91109, USA.	433
2	**Novel Multiple Radiating Modes Based Antennas and Arrays** *Prof. Satish K. Sharma* Antenna and Microwave Lab (AML), Department of Electrical and Computer Engineering, San Diego State University, 5500 Campanile Drive, San Diego, CA, 92182-1309, USA, *Email: ssharma@mail.sdsu.edu*	434
3	**Antenna Design: History and Recent Developments** *Prof. Zhongxiang Shen* Nanyang Technological University, Singapore	435
4	**3D Frequency Selective Structures: Opportunities and Challenges** *Prof. Zhongxiang Shen* Nanyang Technological University, Singapore	436
5	**R&D Opportunity in the Country – Vis-à-vis Contributions of CSIR-CEERI** *S N Joshi* CSIR-CEERI, Pilani – 333 031 (Rajasthan) *snjoshi_15@yahoo.co m, snj@ceeri.res.in*	437
6	**Story of an Unknown Radiating Mode in Dielectric Resonator Antenna** *Prof. Debatosh Guha* Institute of Radio Physics and Electronics, University of Calcutta, 92 A P C Road, Kolkata 700 009, INDIA *dguha@ieee.org*	438
7	**Research and Development Activities on Antennas in SAMEER** *K. P. Ray* SAMEER, IIT Campus, Powai, Mumbai-400 076 *E-mail: kpray@rediffmail.com, kpray@sameer.gov.in*	439
8	**Active Radar Cross Section Reduction: Theory and Applications** *Dr Hema Singh* Centre for Electromagnetics CSIR-National Aerospace Laboratories, Bangalore, India	440

Terahertz Technology and its Applications

Dr. Goutam Chattopadhyay
NASA-Jet Propulsion Laboratory, California Institute of Technology
4800 Oak Grove Drive, Pasadena, CA 91109, USA.

For more than last forty years, terahertz components and instruments have primarily been developed for space science applications in radio astronomy and planetary sciences. However, in recent years, terahertz waves are increasingly being used in commercial applications such as high speed communications, security imaging, autonomous landing and refueling of airplanes, and medicines. In spite of all these fascinating scientific and commercial potential, the terahertz frequency range (loosely defined as 300 GHz < ν < 10 THz) still remains one of the least utilized electromagnetic bands because of the unavailability of commercial source and sensor components, and sub-systems.

Recent progress in CMOS technology as well as availability of InP HEMT based amplifiers in terahertz frequency band has caught the imagination of researchers for developing terahertz instruments for commercial applications. Rapid progress in multiple fronts, such as commercial software for component and device modeling, low-loss waveguide circuits and interconnect technologies, silicon micromachining for highly integrated and compact packaging, and submicron scale lithographic techniques, is making it an exciting time for terahertz engineers and scientists.

In this presentation, an overview of the state of the terahertz technology will be presented. The talk will detail the science and other applications that specifically require technology at terahertz frequencies. The challenges of the future generation instruments and detectors at these frequencies in addressing the needs for critical scientific and commercial applications will also be discussed.

The research described herein was carried out at the Jet Propulsion Laboratory, California Institute of Technology, Pasadena, California, USA, under contract with National Aeronautics and Space Administration.

©2014 California Institute of Technology. Govt. sponsorship acknowledged.

Novel Multiple Radiating Modes Based Antennas and Arrays

Prof. Satish K. Sharma
Antenna and Microwave Lab (AML)
Department of Electrical and Computer Engineering
San Diego State University
5500 Campanile Drive, San Diego, CA, 92182-1309, USA
Email: ssharma@mail.sdsu.edu

Abstract

In this talk, novel multiple radiating modes based antennas and arrays will be discussed. By carefully choosing number of radiating modes in an antenna structure, specific radiation pattern properties such as directional and omni-directional radiation patterns, beam steering, and phase center control can be obtained. These radiation performance parameters can be realized by properly combining the radiating modes and control of the amplitude and phase of the modes. Number of radiating modes in an antenna structure determines the size of an antenna. For example, to incorporate TM_{10} and TE_{21} modes in addition to the dominant mode TE_{11} in a circular waveguide multiple mode horn antenna, radii of the waveguide sections should be according to the Bessel functions in a circular waveguide. The theory of multiple radiating modes antennas will be presented. Followed by this, novel multiple modes based microstrip patch and waveguide horn aperture antennas will be discussed, both as individual antennas and feed sources to the reflector antennas. A beam peak and null steering circularly polarized receive antenna for Global Position System (GPS) using a dual mode annular patch antenna along with its feed network will be introduced. Finally, a linear array beam steering antenna along with its beam forming network (BFN) will presented showing beam steering to $\pm 70^{o}$ with reduced gain drop. The talk will conclude with design, analysis, fabrication and experimental verification challenges and future studies.

Selected References

1. S. K. Sharma, L. Shafai and S. Rao, "*Handbook of Reflector Antennas and Feed Systems*, Volume I: Theory and Design of Reflectors", Artech House, USA, June, 2013
2. L. Shafai, S. K. Sharma and S. Rao, "*Handbook of Reflector Antennas and Feed Systems*, Volume II: Feed Systems", Artech House, USA, June, 2013
3. N. Labadie, S. K. Sharma, and G. Rebeiz, "A Circularly Polarized Multiple Radiating Modes Microstrip Antenna with Beam Peak and Null Steering Satellite Receive Applications", *IEEE Trans Antennas and Propagation*, USA, Vol. 62, No. 7, July 2014, pp. 3490 – 3500.
4. N. Labadie, S. K. Sharma and G. Rebeiz, "1D Beam Steering using Multiple Radiating Modes", *IEEE Inter. Symposium on Antennas Propagation 2014* (IEEE AP-S 2014), Memphis, USA
5. N. Labadie, S. K. Sharma and G. Rebeiz, "Investigation of Hybrid Phased Arrays Composed of Multiple Mode Subarrays", *IEEE Inter. Symposium on Antennas Propagation 2014* (IEEE AP-S 2014), Memphis, USA
6. S. K. Sharma and M. Thyagarajan, "Performance Comparison of Symmetric and Offset Reflector Antennas Adaptively Illuminated by Novel Triple Mode Feedhorn", *International Journal of Antennas and Propagation*, Volume 2012 (2012), Article ID 870318, 10 pages, doi:10.1155/2012/870318
7. T. Tran, and S. K. Sharma, "Radiation Characteristics of a Multimode Concentric Circular Microstrip Patch Antenna by Controlling Amplitude and Phase of Modes", *IEEE Transactions on Antennas & Propagation*, USA, *Vol. 60, No. 3, March, 2012, pp. 1601-1605*
8. B. Balaji, A. Damini, G. Haslam, L. Shafai, and S. Sharma, "*Multiple Phase Center Feedhorn for Reflector Antennas"* US Patent # 7,180,459 granted February 20, 2007.
9. L. Shafai, S. K. Sharma, B. Balaji, A. Damini, and G. Haslam, "Performance of Reflector Antennas with Dual Mode Feed Horn Providing Multiphase Centres", *IEEE Transactions on Antennas & Propagation*, USA, Vol. 54, No. 11, Nov 2006, pp. 3407-3417

Antenna Design: History and Recent Developments

Prof. Zhongxiang Shen
Nanyang Technological University, Singapore

Abstract: In this talk, I would like to highlight a few important contributions in antenna history and then share with the audience my personal perspective of the recent developments in antenna design. After quickly mentioning the importance of an antenna to a wireless communication, I shall introduce several antennas invented by pioneers such as Hertz and Marconi et al. After that, a few innovative antenna designs such as Yagi-Uda antenna, slot antenna, microstrip antennas, and frequency-independent antennas will be discussed. Recent developments such as design of small antennas, ultra-wideband antennas, and nano-antennas for energy harvesting will also be briefly reviewed in the end.

3D Frequency Selective Structures: Opportunities and Challenges

Prof. Zhongxiang Shen
Nanyang Technological University, Singapore

Abstract:

Conventional frequency selective surface consists of a two-dimensional (2-D) periodic array of unit-cells, which are either printed on a dielectric substrate or etched out of a conductive surface. These simple 2-D surfaces suffer from poor frequency selectivity and unstable response under different incident angles. Recently, an innovative concept of three-dimensional (3D) frequency selective structure (FSS) was proposed to alleviate the disadvantages of traditional frequency-selective surfaces. The new type of 3-D frequency selective structure is composed of a 2D periodic array of vertically placed microstrip lines, which is very promising for the realization of compact high-performance FSSs. This talk will introduce the proposed 3-D frequency selective structure. Mode-matching formulation for analyzing the structure will be briefly presented and equivalent circuit model will be employed to explain the operating principle of these three-dimensional FSSs. A number of design examples will be presented to demonstrate the high performance filtering response of 3D FSSs. Possible research topics for further investigation are suggested and existing challenges are also mentioned at the end of the talk.

R&D Opportunity in the Country – Vis-à-vis Contributions of CSIR-CEERI

Dr. S.N Joshi
CSIR-CEERI, Pilani – 333 031 (Rajasthan)
snjoshi_15@yahoo.com, snj@ceeri.res.in

ABSTRACT

Research and development has a very important role for the various advanced systems in the country. Based on the inventions made by various scientists around the globe in the past centuries, further research has been carried out based on these inventions. Today the human mankind around the globe is taking advantage of these and developing new and new technologies based on carrying out further research and development. World has really changed in last 5 – 6 decades and now the growth in technology is almost exponential particularly in Electronics and IT Sectors. Electronics R&D has paved the way for benefit of human mankind all across the globe in different sectors like communication, health medicine, education, energy and many more.

In the country, Council of Scientific and Industrial Research (CSIR) was established in 1942 with the great efforts of Pt. Jawahar Lal Nehru, the first Prime Minister of the country. CSIR was established for carrying out research and development in different areas including electronics. As on today also, CSIR has 37 laboratories in different parts of the country and one can find presence of CSIR in almost every field. Later on, as the demand grew, other agencies like DRDO, DAE, ISRO, DST, DeitY, NCSM were established with time. All these agencies have been carrying out R&D in different fields. Above organizations also provide support to other agencies including academic agencies in the country for carrying out research and development in their respective organizations. In addition to above major agencies, R&D is also being supported by IITs, NITs, IISc, TIFR, Central & State Universities and some of the private universities and reputed colleges.

CSIR-CEERI was established in 1953 and the R&D was initiated w.e.f. 1958. It has three major areas of R&D (i) Microwave Tubes, (ii) Semiconductor Devices and (iii) Electronic Systems. Over the years, all the respective areas have grown significantly with the support of CSIR, DAE, DRDO, ISRO, DST, DeitY. A strong design as well as technological base has been established with reasonably well infrastructure. This organization has met in past the requirement of various user agencies and now leaping forward to make more challenging roles. CSIR has also established an academy known as Academy of Scientific & Innovative Research (AcSIR) by an act of Parliament and under this academy CSIR-CEERI has been running Integrated M.Tech./Ph.D. Programme in three disciplines viz. (i) High Power Microwave Tubes and System Applcations, (ii) Semiconductor Electronics and (iii) Electronic Systems.

There is a great demand in the country for pursuing R&D in different areas including electronics due to the requirement of various advanced systems. I would like to thank the organizers of APYSM – 2014 for providing me an opportunity to project this work.

Story of an Unknown Radiating Mode in Dielectric Resonator Antenna

Prof. Debatosh Guha
Institute of Radio Physics and Electronics,
University of Calcutta,
92 A P C Road, Kolkata 700 009, INDIA
dguha@ieee.org

Abstract

This talk will address a story of a resonant mode newly identified and used for radiation purpose in cylindrical shaped Dielectric Resonator Antenna (DRA). The content of the talk is based on author's personal experience in dealing with the problem since 2010 and the innovations reported during 2012-2014 [1]-[4].

The boundary condition of a conventional DRA does not support the modal fields of the target mode and that has been the main constraint in realizing it in a practical antenna structure. Few novel concepts to overcome this challenging boundary condition will be discussed. They actually result in some novel feed mechanisms and provide new insight into the field coupling process in a dielectric body. This exercise ushers in several possibilities of realizing commercially viable DRAs with attractive features.

References

1. D. Guha, A. Banerjee, C. Kumar and Y. Antar, "Higher Order Mode for High Gain Broadside Radiation from Cylindrical Dielectric Resonator Antennas," ***IEEE Trans. Antennas Propagat***. Vol. 60, No. 1, pp. 71-77, Jan. 2012.
2. D. Guha, A. Banerjee, C. Kumar, and Y. Antar, "New Technique to Excite Higher Order Radiating Mode in a Cylindrical Dielectric Resonator Antenna," ***IEEE Antennas and Wireless Propagation Letters***., Vol. 13, pp. 15-18, 2014.
3. D. Guha, A. Bnaerjee, C. Kumar, Y. Antar, and M. T. Sebastian, "Design Guideline for Cylindrical Dielectric Resonator Antenna Using Recently Proposed $HEM_{12\delta}$ Mode" ***IEEE Antennas and Propagation Magazine*** , Vol. 56, No. 4, pp. 148-158, Aug. 2014.
4. D. Guha, P. Gupta, and C. Kumar, "Dualband Cylindrical Dielectric Resonator Antenna Employing $HEM_{11\delta}$ and $HEM_{12\delta}$ Modes Excited by New Composite Aperture," ***IEEE Trans. Antennas Propagat***., to appear in Vol. 63, No. 1, Jan 2015.

Research and Development Activities on Antennas in SAMEER

K. P. Ray
SAMEER, IIT Campus, Powai, Mumbai-400 076
E-mail: kpray@rediffmail.com, kpray@sameer.gov.in

Abstract

Research and development of different type of antennas is one of the main activities of SAMEER. Thus, design, development and characterization of antennas for various applications are carried out at in all the three main centers of SAMEER at Mumbai, Chenai and Kolkata. Different types of antennas for various applications under sponsored and core R&D projects have been developed for the different frequency range starting from HF to millimeter wave frequency. For various applications, all types of antennas, such as wire (element as well as array), slotted antenna array, horn antennas (both standard as well as ridge), helical antennas (normal, axial and printed), loop antennas, blade and air borne antennas, conformal (microstrip and suspended) antennas, reflector antennas, antennas with defected ground plane and meta material, etc, have been developed and are being used in different systems.. Keeping in pace with the fast changing technological scenario, most recent types of radiating systems, such as; smart antennas, shared aperture antennas, Fractal antennas, UWB antennas, space fed antennas, reflect-array antennas, active antennas, reconfigurable antennas, meta materials, frequency selective surface, etc have also been developed and tested. State of the art facilities are required to test these antennas. SAMEER has developed facilities in various centres. Some of the antennas and test facilities will be presented in the invited talk.

Active Radar Cross Section Reduction: Theory and Applications

Dr Hema Singh
Centre for Electromagnetics
CSIR-National Aerospace Laboratories,
Bangalore, India

Abstract

A low observable platform is often assumed to imply reduced radar cross section (RCS), which is primarily a function of controlled electromagnetic (EM) scattering and absorption by the structure. The RCS reduction (RCSR) involves both the passive and the active RCS reduction. While the passive RCSR has often been realized through shaping and radar absorbing materials (RAM), active RCS reduction *w.r.t.* field amplitude, phase and polarization is more difficult to achieve and is often remained an idealized goal. The active RCS may be related to the radiation pattern of the antenna mounted on the aerospace platform. This involves active cancellation of radar signals from hostile probing sources leading to eventual active RCSR and thereby invisibility of the aerospace platform in the hostile environment. When the reduced structural RCS is optimized along with the antenna RCS, the net combination of the active and passive RCSR is expected to result in an effective low observable structure. This lecture emphasizes the contemporary methods and the emerging trends in the area of active RCSR as applicable to the aerospace low observable platforms. The major aspects covered are the concept of active RCSR, adaptive algorithms for active cancellation of probing sources, RCS estimation of phased arrays with mutual coupling, multilobe beamforming, multipath mitigation, sidelobe cancellers, and emerging RCS reduction techniques.

AUTHOR INDEX

A

Aanandan C K 301 ,426
Aarti Gehani 274
Abdul Wahab 240
Abdulla P 287 , 347
Ajal.A.J, Chikku Jose 291
Aju John K K 326
Ameya A. Kadam 28, 95
Ami Desai 183 , 187
Amit A. Deshmukh 28 ,95 , 183 ,187 191
Anders Rydberg 15
Anila P.V 232, 301
Anindya Ghosh 375
Anindya Harchowdhury 136
Anitha R 195
Anju Pradeep 65, 301
Ansha K K 177
Anshul Gupta 270
Anudeep B 355
Anuja.A.Odhekar C 207
Anupam R Chandran 20
Anurag Sharma 87, 91
Arijit Majumdar 140
Arun Chowdhary B K 359
Arun.N.S 367
Ashish Meena 144
Ashish Rojatkar 61
Atrey P K 45
Ayan Chatterjee 322

B

Bala Ankaiah N 83
Balwinder S. Dhaliwal 203
Baral R N 113
Basil J. Paul 199
Beenamole K.S 144
Binay Kumar Sarkar 136, 375
Bindu.G 71
Binoy Babu B 123
Binu Paul 103, 227
Biswas S 263
Bybi P Chacko 79

C

Chandrakanta Kumar 259, 278
Chirag Arora 113

D

Darine Kaddour 131
David Koilpillai R 161
Debajit De 403
Debatosh Guha 259 , 263, 438
Deepak U 212, 418
Deepti Das Krishna 223
Devaraj V 144
Dhaval Pujara 274
Divya Sathyanath 65
Divya Unnikrishnan 131
Durga Rao M 119

F

Fijo Jose K 330

G

Galaba Sai Rajesh 148
Ganesan U 244
Ganesh Madhan M 363, 395
Gijo Augustin 79
Girish Kumar 99
Gopal Joshi 51
Goutam Chattopadhyay 438
Gurveer Kaur 203

H

Hema Singh 83, 305,440
Hemprasad Ghanta 144
Hrudya.B.Kurup 71

J

Jacob Abraham 216
Jasmine P.M 287, 347
Jayakrishnan M.P 65 , 301 ,337
Jha R.M 83 ,343
Jim Morrison 20
Joshi S.N 437

K

Kakatkar S.S 24, 169
Kamalaveni A 363 ,395
Kamaraj P 119
Karandikar R.G 24
Karkari S K 337
Karthika S. Nair 65
Kathiravan V 107
Kiran.S.Janwalkar B 207

Koushik Dutta 259
Kshitij Lele 95, 191
Kumar C 263
Kumar G 41

L

Laila .D 315
Libi Mol V A 426

M

Magdalena Salazar Palma
Mahakar Singh 87 , 255 , 267
Mahima Arrawatia 99
Manju Abraham 330 , 326
Manju Bhaskar 371
Mary Rani Abraham 177 , 240
Maryam Shojaei Baghini 99
Mathew K.T 379
Merin Mary Mathews 236
Mini P R 103
Mishra J.K 41
Mishra R K 173
Mohammad Ameen 32
Mohammed Ismail 32
Mohanan P 65 , 71 , 103 ,123, 199 , 227, 232 ,301 , 309, 315, 337 , 418
Mohankumar K 123
Mousumi Sarkar 140
Mridula S 65 , 103 , 123 , 140, 199, 227 , 232 ,301
Mugundhan 107
Mukherjee J 41
Mukherji S 45
Murali Krishna P 157 ,161

N

Nagarbowdi S 191
Nagendra Kumar 351
Nampoori V.P.N. 71
Narayanan N K 57
Naveen Kumar P 412
Naveen Raj R 367
Neelam V. Phatak 191
Nick Timmons 20
Nijas C M 309 , 315
Nilam.T.Kadam A 207

P

Pande M 41
Pavan Kumar B 278
Peter Cyriac 295
Pramendra Kumar Verma 255,267
Pramod Kumar Verma 87 ,91
Prasanna Kumar Sahu 403
Pujara D A 45
Pundir R S 47

R

Rabindra K. Mishra 165
Raghavan S 248
Rahul B 426
Raj kumadhavar 267
Raj Kumar 255
Rajalingam M 107
Rajeshkumar V 248
Rajpal Singh 87 , 91
Ramarao B.V 41
Ramesh R 107
Raphika P.M 287 ,347
Ratheesh.R 367
Raveendranath U. Nair 343
Ravi Kumar Gangwar 270
Ray K.P 24, 28 , 95 , 169, 183, 187 , 191, 439
Rebecca Abraham 399
Rejoy Rebello 123
Riny Thomas 315
Robin Augustine 15
Roshna T K 212 ,309 , 418
Ruifeng Zhang 20

S

Sachin Oberai 47
Saha V 244
Sahu P K 173
Saira Joseph 227
Sajitha V R 309 , 418
Saleha Shaikh 183 ,187
Sambhudutta Nanda 173
Sameer Babu T.P 157, 161 , 177
Sandeep Kumar 385
Sandhya S 343
Sanjib Kumar Mandal 47

Santosh K R 123
Sarah Jacob 232
Sarin V. Pushpakaran 301
Sarkar C 244
Satish K. Sharma 434
Sayan Chatterjee 422
Senan Morrison 20
Senthil Kumar V 278
Shambavi K 236
Shambhulingappa K V 412
Shyam S. Pattnaik 113 , 203
Siddiqui J Y 244
Simy Antony 305
Singh P 41
Singh V N 47
Smail Tedjini 131
Smitha C K 57
Sona O. Kundukulam 240
Sonal S 41
Soumyo Chatterjee 422
Sreelekshmi P 389
Srinaga Nikhil 385
Srinivasan V V 278
Srinivasulu P 119, 148
Sruthy Skaria 65
Stephen Rodrigues 295
Subrahmanyam K M 278
Suchitra Majumdar 24
Sudhakar Rao
Sudesh Agrawal 28
Suersh E.K 367
Sujatha M N 318
Sujith Raman 15
Sujo C.I 51
Sukhendu Bhanja 140
Sumitha Mathew 195 ,418
Susan Thomas 212
Susanta Kumar Parui 322

T

Tapen K Sarkar
Tayeb A Denidni 79
Tessa Mathew 223
Thomaskutty Mathew 216 , 326, 330 , 371
Thushara H.P 65
Titu K. Samson 123

U

Ullas G Kalappura 379
Usha Kiran .K 355 , 359 , 399

V

Vasudevan K 123 , 195 ,301
Venkata Kishore.K 148
Vibishna B 144
Vijay Kumar 148
Vijesh.K.R 71
Vikass Monebhurrun 61
Vinod Kumar Singh 87 ,91
Vinoy K J 318 , 385

Y

Yatendra Kumar Singh 351

Z

Zachariah C Alex 236
Zhongxiang Shen 435,436